

Utilizing the Trp-cage miniprotein in the design of light-responsive proteins and stable antimicrobial peptides

Dissertation

zur Erlangung des akademischen Grades Dr. rer. nat.
verliehen von der Mathematisch-Naturwissenschaftlichen Fakultät
der Christian-Albrechts-Universität zu Kiel

vorgelegt von

Nils Preußke

angefertigt am
Otto Diels-Institut für Organische Chemie

Kiel, September 2022

Die vorliegende Arbeit wurde unter Anleitung von
Prof. Dr. Frank D. Sönnichsen
in der Zeit von Oktober 2017 bis September 2022
am Otto Diels-Institut für Organische Chemie
der Christian-Albrechts-Universität zu Kiel angefertigt.

1. Gutachter: Prof. Dr. Frank D. Sönnichsen
2. Gutachter: Prof. Dr. Matthias Leippe

Tag der mündlichen Prüfung: 01.09.2022
Zum Druck genehmigt: 01.09.2022

Eigenständigkeitserklärung

Hiermit erkläre ich, Nils Preußke, die vorliegende Dissertation selbstständig und ausschließlich unter Zuhilfenahme der angegebenen Quellen und Hilfsmittel angefertigt zu haben. Abgesehen von der Beratung durch meinen Betreuer, Prof. Dr. Frank D. Sönnichsen, habe ich diese Arbeit eigenständig erarbeitet und verfasst. Teile der Arbeit gingen aus Kooperationen mit anderen Wissenschaftlern hervor – Leistungen, die nicht von mir selbst erbracht wurden sind an den entsprechenden Stellen der Arbeit immer als solche gekennzeichnet. Die folgenden wissenschaftlich begutachteten Fachpublikationen sind ein wesentlicher Bestandteil dieser Dissertation:

Nils Preußke, Widukind Moormann, Katrin Bamberg, Matthias Lipfert, Rainer Herges, Frank D. Sönnichsen, Visible-light-driven photocontrol of the Trp-cage protein fold by a diazocine cross-linker, *Organic and Biomolecular Chemistry* **2020**, 18, 2650-2660.

Nils Preußke, Matthias Lipfert, Sven Rothemund, Matthias Leippe, Frank D. Sönnichsen, Designed Trp-cage proteins with antimicrobial activity, *Biochemistry* **2021**, 60, 3187-3199.

Die Arbeit hat an keiner anderen Stelle im Rahmen eines Prüfungsverfahrens vorgelegen und mir wurde kein akademischer Grad entzogen. Diese Arbeit ist unter Einhaltung der Regeln guter wissenschaftlicher Praxis der Deutschen Forschungsgemeinschaft entstanden. Dies ist mein erster Promotionsversuch.

Kiel, den 11. September 2022

Nils Preußke

Danksagung

An erster Stelle möchte ich mich bei Prof. Frank D. Sönnichsen für die hervorragende Betreuung und die immerwährende Unterstützung meiner wissenschaftlichen Arbeit bedanken. Du hast mir stets die Freiheit gelassen eigene Entscheidungen zu treffen, doch sollten mal Probleme auftreten oder ich aus anderen Gründen Rat benötigen war Deine Tür stets offen um das weitere Vorgehen zu besprechen. Auch beim Verfassen wissenschaftlicher Texte oder dem Erstellen von Präsentationen oder Postern war Dein Rat immer unschätzbar viel wert und Deine stets konstruktiven Anmerkungen sehr willkommen. Vielen Dank, dass ich in Deinem Arbeitskreis dieses spannende Thema bearbeiten durfte – ich habe wirklich viel von Dir lernen können! Ich danke Dir weiterhin für die schöne Zeit, die wir bei der Konferenz in Israel, in Warnemünde, beim Thanks Giving Dinner, beim Grünkohlessen in der Forstbaumschule, bei unseren Gruppentreffen und bei vielen anderen Arbeits- oder Freizeitaktivitäten hatten.

Ich danke darüber hinaus auch dem AK Sönnichsen und der spektroskopischen Abteilung für die freundliche Atmosphäre. Auf Euch konnte ich immer zählen, wenn ich am NMR Gerät saß und es nicht wusste, was ich von ihm will. Besonders erwähnt sei hier natürlich die Hilfe und Unterstützung von Katrin Bamberg. Ich danke Dir, dass ich Dich immer fragen konnte, wenn ich mal schnell Rat oder eine zweite Meinung brauchte. Und wenn Du mal nicht da warst waren mir Deine perfekt geführten Anleitungen vom CD oder NMR Gerät, die ich mir abfotografieren durfte, eine große Hilfe. Außerdem danke ich Dir für die reichliche Verpflegung mit Nerven-nahrung ohne die ich sicherlich schon lange verhungert wäre.

Und natürlich bin ich dem besten Bachelor-Studenten der Welt, Widukind Moormann, zu Dank verpflichtet. Ohne Deine Bachelorarbeit hätte ich das Thema „Trp-cage Schalten“ wohl nicht weitergeführt. Die Arbeit mit Dir war – wie schon im Studium – äußerst produktiv und mir eine große Freude. Weiterhin danke ich Dir, dass ich in der Zeit als ich in Kiel an meiner Promotion und in Jena am HKI gearbeitet habe, bei Dir in Zottelstedt Unterschlupf finden konnte, wenn ich am HKI vor Ort sein musste.

Ich möchte natürlich auch Prof. Matthias Leippe danken, für die Möglichkeit die biologischen Untersuchungen durchzuführen. Ich danke Ihnen dafür, dass ich bei Ihnen im Labor in die spannende Welt der Mikrobiologie eintauchen durfte. Dies hat nicht nur meine Dissertation um viele wertvolle Ergebnisse bereichert und die AMTC-Publikation überhaupt erst in diesem Umfang ermöglicht, sondern darüber hinaus auch echt Spaß gemacht. Ich danke Ihnen weiterhin für Ihre Rückmeldungen zu verschiedenen wissenschaftlichen Texten. Durch Ihre Anmerkungen und konstruktiven Kommentare konnte ich lernen meine Formulierungen zu präzisieren und die Qualität meiner Texte erheblich steigern.

Dank gebührt auch Heidrun Ließegang. Ich danke Dir dafür, dass Du mich all die Techniken gelehrt hast, die ich für die biologischen Untersuchungen benötigt habe. Als Chemiker hatte ich zwar eine ungefähre Ahnung wie man einen Laborkittel anzieht und eine Pipette bedient, aber vieles weitere, wie das sterile Arbeiten oder das Arbeiten mit Bakterienkulturen oder Zelllinien, habe ich erst durch Deine geduldige und immer freundliche Anleitung gelernt. Dafür möchte ich Dir sehr herzlich danken.

Ich danke Dr. Reinhard Stock und Heike Knorn für die tolle Betreuung meiner Promotion seitens der Deutschen Bundesstiftung Umwelt. An Sie konnte ich mich immer wenden, wenn ich Fragen bezüglich des Stipendiums oder der DBU hatte. Darüber hinaus danke ich der gesamten DBU für die Finanzierung meiner Forschung und für die Organisation der tollen Seminare, die ich besuchen durfte. Ich habe den Austausch mit den anderen Stipendiaten und Betreuern, sei

es bei den Seminaren, Kolloquien oder der jährlichen Umweltpreisverleihung sehr genossen und empfinde es als Privileg, ein Teil der DBU sein zu dürfen.

Nicht zuletzt möchte ich meinem Chef am HKI, Dr. Florian Kloß, danken. Ohne Dein Verständnis und Deine Unterstützung hätte ich es nicht geschafft, parallel an meinem Promotionsprojekt und an dem SARS-CoV-2 Projekt zu arbeiten. Vielen Dank, dass Du dies ermöglicht hast.

Ich möchte aber auch den Menschen danken, die mein privates Leben bereichern und dadurch diese wissenschaftliche Arbeit erst ermöglicht haben. Ich danke meiner ganzen Familie, Papa, Mama, Jonas, Meike und Svenja, für den Rückhalt, den ich bei Euch immer hatte. Ihr seid mir super wichtig und ich danke Euch, für die unzählbaren glücklichen Stunden bei und mit Euch. Besonderer Dank gilt hierbei meinen Eltern. Ohne Euch gäbe es mich nicht; ohne Eure ideelle und finanzielle Unterstützung wäre ich nicht in der Lage gewesen dieses Promotionsprojekt so zu bewältigen und dafür bin ich über alles dankbar.

Die letzten Zeilen dieser Danksagung widme ich meiner Frau Chantal. Ich bin Dir für so vieles unglaublich dankbar, denn Du hast mich immer unterstützt. Du hattest Verständnis, wenn ich am Wochenende wieder im Büro war oder abends länger arbeiten musste. In Deiner Gegenwart kann ich endlich mal abschalten. Danke, dass Du ein Teil meines Lebens bist. Ich freue mich darauf, meine durch den Abschluss dieser Promotion neu gewonnene Freizeit mit Dir und unserem Kind zu verbringen.

Kurzzusammenfassung

Die Miniprotein grafting Methode (grafting = Englisch für Veredelung; im medizinischen Kontext auch im Sinne einer Transplantation verwendet) zielt darauf ab, ein Miniprotein so zu modifizieren, dass es eine bestimmte Funktion erhält. Das Miniprotein Trp-cage zeichnet sich durch eine sehr stabile Faltung aus, die eine α -Helix mit zwei Windungen und eine kurze Polyprolin-II-helix umfasst. Da es keine eigene Funktion besitzt und nur aus 20 Aminosäuren besteht, eignet sich der Trp-cage ideal für Modifikationen, die ihm bestimmte Funktionen verleihen. In dieser Arbeit werden zwei verschiedene Anwendungen des Trp-cage grafting vorgestellt.

In der ersten Anwendung soll die Trp-cage-Domäne verwendet werden, um die Sekundärstruktur von α -helikalen antimikrobiellen Peptiden (α AMPs) zu stabilisieren. Viele α AMPs besitzen eine starke antibakterielle Aktivität und sind daher potenzielle Kandidaten für neue medizinische Antibiotika. Allerdings sind sie in Lösung häufig unstrukturiert und bilden eine α -helikale Struktur nur nach Assoziation mit einer Lipidmembran aus. Daher können sie leicht von Proteasen abgebaut werden. Eine geeignete Strategie ihre Bioverfügbarkeit zu steigern, ist die Stabilisierung ihrer Sekundärstruktur, was durch die kovalente Verknüpfung zweier Seitenketten innerhalb der Helix erreicht werden kann. Miniprotein grafting wurde bisher noch nicht angewandt um die Helizität von α AMPs in Lösung zu induzieren und so ihre Resistenz gegen Peptidasen zu erhöhen. Diese Arbeit zeigt, wie die Fusion des bekannten α AMP KR-12 mit einer Trp-cage-Domäne zu einer Stabilisierung der α -helikalen Konformation im AMP-Teil des Fusionsprodukts beiträgt, das als antimikrobieller Trp-cage (AMTC) bezeichnet wird. Die Korrelation von Strukturdaten mit den Ergebnissen aus einer Analyse der enzymatischen Abbaubarkeit konnte zeigen, dass die stabilisierte Struktur des AMTC für eine höhere Resistenz gegen enzymatischen Abbau sorgt. Weitere AMTCs wurden entworfen indem das α AMP IsCT mit einer Trp-cage-Domäne fusioniert wurde und indem die α -Helix eines Trp-cage-Proteins zu einer amphipatischen Helix mit bis zu vier Windungen verändert und verlängert wurde. Die Aktivität aller entworfenen AMTCs wurde *in vitro* gegen vier verschiedene Bakterien getestet. Während die Trp-cage-Domäne allein keine Aktivität zeigte, wiesen alle entworfenen AMTCs eine antimikrobielle Aktivität auf, deren Stärke sich jedoch untereinander unterschied. Obwohl ein Liposomen-Depolarisations-Test auf einen Membran-perforierenden Wirkmechanismus der AMTCs hinwies, war die Porenbildung gegenüber menschlichen Erythrozyten nur schwach ausgeprägt. Folglich konnte das Trp-cage grafting aktive AMPs mit einer geringen hämolytischen Aktivität und erhöhter Resistenz gegen enzymatischen Abbau hervorbringen.

Der zweite Ansatz des Trp-cage grafting diente der Erlangung von Photokontrolle über die Trp-cage Faltung, also die Fähigkeit den Trp-cage durch die Bestrahlung mit Licht unterschiedlicher Wellenlängen reversibel zwischen einem gefalteten und einem ungefalteten Zustand hin- und herzuschalten. Um das switch cage genannte photoschaltbare Protein zu erhalten, wurde der Trp-cage an der α -Helix mit einem neuen Diazocinderivat intramolekular verknüpft. Das Diazocin ist in der Lage durch die Bestrahlung mit violetterem Licht von einem kompakten *cis*-Zustand zu einem längeren *trans*-Zustand zu isomerisieren. Die Rückreaktion erfolgt langsam in der Dunkelheit oder sofort bei Bestrahlung mit grünem Licht. In Konjugation mit dem Trp-cage unterstützt das *cis*-Diazocin die stabile Faltung des Miniproteins. Insbesondere konnten mittels NMR-Spektroskopie zwei Diastereomere des gefalteten *cis*-switch cage identifiziert werden, die interkonvertierbar sind und sich nur durch die Ausrichtung der Diazocin-Verknüpfungseinheit unterscheiden. Im Kontext des Proteins in wässriger Lösung

konnte das Schalten zum *trans*-switch cage mit 46% Ausbeute erreicht werden. Die Ausbeute war geringer als erwartet, da der negative Effekt des Wassers auf die Schaltbarkeit von Diazocinen zum Zeitpunkt der Konzeptionierung der Studie noch nicht bekannt war. Der *trans*-Zustand führte dennoch zu einer kompletten Entfaltung des Trp-cages, ohne eine Aggregation oder Fällung zu bewirken. Damit konnte diese Studie zeigen, dass es möglich ist die Tertiärstruktur eines Proteins mit Hilfe einer an einer α -Helix angebrachten photoschaltbaren Verknüpfungseinheit zu kontrollieren. Dank dieses Machbarkeitsnachweises kann die Strategie nun auf kleine, funktionale Proteine oder Proteindomänen übertragen werden, um Photokontrolle über ihre Funktion zu erlangen, da Funktion eines Proteins typischerweise direkt von seiner Struktur abhängt.

Abstract

The miniprotein grafting method uses a non-functional miniprotein as a scaffold that can be modified to exert a specific function. The miniprotein Trp-cage is characterized by a highly stable fold including an α -helix of two turns and a short polyproline II helix. Being non-functional and only 20 residues in length, the Trp-cage is an ideal scaffold to be modified to achieve a specific function. In this thesis, two approaches to Trp-cage grafting are presented.

The first approach aims to use the stable fold of the Trp-cage to stabilize the secondary structure of an α -helical antimicrobial peptide (α AMP). Many α AMPs possess strong antibacterial activity and are therefore considered as potential candidates for new antibiotic therapeutics. α AMPs assume an α -helical structure upon association with a lipid membrane, but are usually unstructured in solution. In consequence, they are highly susceptible to degradation by proteases. A valid strategy to increase their bioavailability is the stabilization of their secondary structure, which has been demonstrated by cross-linking two side chains of the α -helix. Miniprotein grafting has not yet been explored to induce helicity in α AMPs in solution to increase their resistance to degradation by peptidases. This thesis demonstrates how fusing the well-known α AMP KR-12 to a Trp-cage domain may stabilize the α -helical conformation in the AMP-derived section of the fusion product termed antimicrobial Trp-cage (AMTC). Correlation of structural data with results from an enzymatic degradation assay provided evidence that the stabilized structure resulted in a higher resistance to enzymatic degradation of the AMTC. Other AMTCs were designed by fusing the α AMP IsCT to the Trp-cage domain and by remodeling the Trp-cage's α -helix into an amphipathic α -helix of up to four turns. The activity of all designed AMTCs on four different bacteria was assessed *in vitro*. While the Trp-cage domain alone was completely inactive, all designed AMTCs showed antimicrobial properties – albeit with varying activities. A liposome depolarization assay indicated a pore-forming mode of action of the AMTCs, but the pore-forming activity of the AMTCs with respect to human erythrocytes was low. In conclusion, Trp-cage grafting provided active AMPs with low hemolytic activity and increased resistance against enzymatic degradation.

The second approach to Trp-cage grafting achieved photocontrol of the Trp-cage fold, i.e. the ability to reversibly switch the Trp-cage between a folded and an unfolded state by irradiation with light of different wavelengths. To obtain the photoswitchable protein termed switch cage, the Trp-cage was cross-linked at the α -helix with a new diazocine derivative. The diazocine was able to isomerize from a compact *cis*-state to a longer *trans*-state upon irradiation with violet light. The reverse reaction occurs slowly in the dark, or immediately upon irradiation with green light. When the diazocine was conjugated to the Trp-cage, its shorter *cis*-state supported a stable fold of the miniprotein. Notably, two different diastereomers of the folded *cis*-switch cage were identified by NMR spectroscopy which are interconvertible and differ only in the orientation of the diazocine cross-linker. In the context of the protein dissolved in water, switching to the *trans*-switch cage was achieved with a yield of 46%. The conversion was lower than expected because the negative effect of the aqueous environment on the switching efficiency of diazocines was not known when the study was designed. Still, the *trans*-state led to complete unfolding of the Trp-cage, but did not induce aggregation or precipitation. The study showed that it is possible to control a protein's tertiary structure by the isomerization of a photo-switchable cross-linker attached to an α -helix. With this proof of concept at hand, the strategy can be transferred to small functional proteins or protein domains to gain photocontrol over their function, because a protein's function is typically highly dependent on its structure.

A guide to this thesis

This semi-cumulative thesis is divided into eight chapters. The first chapter provides an **Introduction** to the Trp-cage miniprotein and how it has been used in a strategy termed Trp-cage grafting to stabilize α -helical peptide motifs with different functions. The second chapter briefly describes the **Objective** of this thesis, which included the planning and execution of two new Trp-cage grafting approaches.

Chapter 3 discusses the approaches to designing and characterizing different Trp-cage variants with antimicrobial activity. I would like to highlight chapter **3.2. Antimicrobial peptides** because it provides an extensive literature review on α -helical antimicrobial peptides (α AMPs). Many review papers on antimicrobial peptides (AMPs) have been published, but my review is from a chemist's point of view. The architecture of mammalian and bacterial cell envelopes are described in detail, because (1) they are not sufficiently covered by the curriculum of chemistry and (2) they are important targets of AMPs and provide the basis for their selectivity. After having established the "playground" of AMPs, the review focuses on their mode of action. Finally, it will conclude with a subchapter on α AMP design, before the thesis turns to the experimental research regarding the antimicrobial Trp-cage. Most experimental results have been published in the research article entitled "Designed Trp-cage proteins with antimicrobial activity and enhanced stability" which is also part of chapter 3.

Chapter 4 focusses on the second Trp-cage grafting approach, which is the introduction of a photoswitchable cross-linker to be able to fold and unfold the Trp-cage secondary and tertiary structure by irradiation with light. The introduction to this chapter focuses on previous approaches to gain photocontrol over functional α -helical peptides. The experimental works to achieving a switchable Trp-cage have been described in the research article entitled "Visible-light-driven photocontrol of the Trp-cage protein fold by a diazocine cross-linker" which is included in chapter 4.

Chapter 5 discusses the Trp-cage grafting approach in general and summarizes the most important findings of the experimental works. Furthermore, this chapter will answer the question whether the two grafting approaches presented in this thesis may be combined. Chapter 6 will provide experimental details one might need to reproduce the results from this thesis. It also comprises the supplementary information published with the two original articles. Chapter 7 and chapter 8 list the bibliography and the abbreviations, respectively.

Throughout the thesis, you will find references to (sub-)chapters, figures or tables in this document. Those are printed in **bold** and (if you have a digital copy of this document) contain a link to the corresponding chapter or display item. All references to the bibliography are numbered, written in super-script in square brackets (e.g. "Avian pancreatic polypeptide (aPP) is a small, globularly folded peptide.^[1]") and contain clickable links. Whenever a reference to the bibliography is given behind an expression (i.e. a word or a combination of words) the reference belongs to that expression only (and probably not to the whole sentence). However, when a reference to the bibliography is given behind a punctuation character it belongs to the whole sentence or dependent clause. Sometimes it may be hard to tell, whether a string of capitalized letters (e.g. AMTC) is an abbreviation or a peptide's sequence. Therefore, sequences of peptides or proteins will be written in the `Courier New` font (e.g. FPPPP).

Publications included in this thesis

The majority of findings discussed in this thesis is based on experimental work originally described in two publications.

- Designed Trp-cage proteins with antimicrobial activity and enhanced stability, Nils Preußke, Matthias Lipfert, Sven Rothmund, Matthias Leippe and Frank D. Sönnichsen, *Biochemistry* **2021**, *60*, 3187-3199.
- Visible-light-driven photocontrol of the Trp-cage protein fold by a diazocine cross-linker, Nils Preußke, Widukind Moormann, Katrin Bamberg, Matthias Lipfert, Reiner Herges and Frank D. Sönnichsen, *Organic and Biomolecular Chemistry* **2020**, *18*, 2650-2660.

Studies not included in this thesis

In my time as a doctoral candidate, I have contributed to collaborations resulting in several peer-reviewed publications (listed below) that are not discussed in this thesis because of their different topics. My contribution to these collaborations is briefly described in the individual publications.

- Occurrence of *fusarium* mycotoxins and their modified forms in forage maize cultivars, Tim Birr, Tolke Jensen, Nils Preußke, Frank D. Sönnichsen, Marthe De Boevre, Sarah De Saeger, Mario Hasler, Joseph-Alexander Verreet, Holger Klink, *Toxins* **2021**, *13*, 110.
- Effect of ensiling duration on the fate of deoxynivalenol, zearalenone and their derivatives in maize silage, Tolke Jensen, Marthe De Boevre, Sarah De Saeger, Nils Preußke, Frank D. Sönnichsen, Ewald Kramer, Holger Klink, Joseph-Alexander Verreet, Tim Birr, *Mycotoxin Res.* **2020**, *36*, 127-136.
- Evaluation of high-resolution mass spectrometry for the quantitative analysis of mycotoxins in complex feed matrices, Tolke Jensen, Marthe de Boevre, Nils Preußke, Sarah de Saeger, Tim Birr, Joseph-Alexander Verreet and Frank D. Sönnichsen, *Toxins* **2019**, *11*, 531.
- Different secondary metabolite profiles of phylogenetically almost identical *Streptomyces griseus* strains originating from geographically remote locations, Ignacio Sottorff, Jutta Wiese, Matthias Lipfert, Nils Preußke, Frank D. Sönnichsen and Johannes F. Imhoff, *Microorganisms* **2019**, *7*, 166.
- Antitumor anthraquinones from an Easter Island sea anemone: Animal or bacterial origin?, Ignacio Sottorff, Sven Künzel, Jutta Wiese, Matthias Lipfert, Nils Preußke, Frank D. Sönnichsen and Johannes F. Imhoff, *Mar. Drugs* **2019**, *17*, 154.

Table of content

Eigenständigkeitserklärung	I
Danksagung	II
Kurzzusammenfassung	IV
Abstract	VI

A guide to this thesis.....	VII
Publications included in this thesis.....	VIII
Studies not included in this thesis	VIII
Table of content.....	VIII
1. Introduction	1
1.1. Protein grafting of pancreatic polypeptides	1
1.2. The Trp-cage motif and exendin-4	2
1.3. Trp-cage grafting	4
1.3.1. A Trp-cage-based inhibitor of the E6 oncoprotein.....	4
1.3.2. Ice-binding Trp-cage proteins	5
1.3.3. Photocontrol of the Trp-cage fold.....	5
1.3.4. En route to photoswitchable ice-binding proteins	6
1.3.5. En route to antimicrobial Trp-cage proteins.....	7
2. Objective	8
3. Antimicrobial Trp-cage proteins	9
3.1. The antibiotic resistance crisis	9
3.2. Antimicrobial peptides	10
3.2.1. Mammalian and bacterial cell envelopes	11
3.2.1.1. Mammalian cell envelopes	11
3.2.1.2. Bacterial cell envelopes	14
3.2.1.3. Selectivity of AMPs	17
3.2.2. α -helical AMPs: Mode of action.....	18
3.2.2.1. Barrel stave mechanism.....	20
3.2.2.2. Carpet mechanism	21
3.2.2.3. Toroidal pore mechanism	21
3.2.2.4. Aggregate mechanism	22
3.2.2.5. Detergent-like mechanism.....	23
3.2.2.6. Multi-target mechanism	24
3.2.2.7. Fibrillary structures.....	26
3.2.3. α -helical AMPs: Peptide design.....	28
3.2.3.1. Rational and heuristic design of α AMPs.....	28
3.2.3.2. Computational design of α AMPs	29
3.2.3.3. α -helical AMPs: From bench to bedside?	31
3.3. Antimicrobial Trp-cage: Results	33
3.3.1. Unpublished results: AMTC33-2 and IsCT.....	34

3.3.1.1.	Antibacterial activity of AMTC33-2 and IsCT.....	34
3.3.1.2.	Pore-forming activity of AMTC33-2 and IsCT.....	35
3.3.1.3.	Hemolytic activity of AMTC33-2 and IsCT.....	35
3.3.2.	Antimicrobial Trp-cage: Publication.....	36
4.	Switch cage.....	50
4.1.	Azobenzenes.....	50
4.2.	Azobenzene-mediated photocontrol of peptides.....	52
4.2.1.	Photoswitchable α -helical peptides.....	53
4.2.1.1.	Photocontrol of peptide-protein interactions.....	54
4.2.1.2.	Photocontrol of DNA-binding peptides.....	56
4.2.1.3.	Photocontrol of peptide-RNA interactions.....	59
4.3.	Challenges of applying azobenzenes in <i>in vivo</i> applications.....	60
4.4.	Diazocines.....	61
4.5.	Switch cage: Publication.....	63
5.	Discussion and Conclusion.....	76
6.	Detailed methods and supplementary information.....	80
6.1.	Detailed description of methods regarding the AMTC.....	80
6.1.1.	Peptide synthesis.....	80
6.1.1.1.	Swelling.....	80
6.1.1.2.	Coupling.....	80
6.1.1.3.	Capping.....	81
6.1.1.4.	Deprotection of the Fmoc protecting group.....	81
6.1.1.5.	Final cleavage.....	81
6.1.2.	Peptide purification.....	85
6.1.3.	Analytical UHPLC: Settings of the mass spectrometer.....	87
6.1.4.	NMR spectroscopy: number of scans, size of FID and mixing times.....	87
6.1.5.	MIC assay: Bacterial growth and preparation of the serial dilution.....	87
6.1.6.	Hemolysis assay: preparation of the serial dilution.....	88
6.2.	Supporting information on the AMTC publication.....	89
6.3.	Supplementary information on the switch cage publication.....	89
7.	Bibliography.....	174
8.	Abbreviations.....	192

1. Introduction

1.1. Protein grafting of pancreatic polypeptides

Many peptide design approaches focus on the stabilization of the secondary and tertiary structure of peptides because their function is often dependent on a proper fold. A prominent example is the grafting of avian pancreatic polypeptide (aPP), a small and globularly folded peptide^[1]. It belongs to a family of homologous peptides that play a role in the regulatory processes of food uptake.^[2] The so-called PP family includes pancreatic polypeptides (PPs), polypeptides YY (PYYs), and neuropeptides Y (NPYs). These are each 36 residues in length and bear an amidated C-terminus, but have only limited sequence identity (**Table 1**).^[1–4] Many members of the PP family, i.e. aPP,^[1, 5] bovine PP (bPP),^[3] porcine PYY (pPYY),^[4, 6] and human PYY (hPYY),^[2] tend to fold into the same unique structure (**Figure 1**). The fold combines a polyproline type II (PPII) helix and an α -helix connected by a type II β -turn. These elements of secondary structure are in close contact through hydrophobic interactions sometimes referred to as knobs-into-holes (KIH) packing. Three proline rings within the PPII helix (Pro2, Pro5, and Pro8) are interdigitating with nonpolar residues of the α -helix forming a hydrophobic core. The crystal structure of aPP suggests stabilization of the fold through symmetrical dimerization,^[1] which was confirmed by size exclusion chromatography^[7, 8] and ultracentrifugation^[7]. The dissociation constant of the homodimer is approximately $K_d \approx 30$ nM (at 28 °C and pH = 5).^[8] Interestingly, most but not all members of the PP fold family are as susceptible to self-association in solution. The intestinal hormone PYY also folds into the unique structure of PPs,^[2, 4] but as opposed to aPP and bPP, pPYY is > 90% monomeric in solution at 1 mM concentrations.^[4, 9, 10]

Table 1: Sequences of PP family peptides. If available, their midpoint of thermal unfolding T_m is listed.

Peptide	PPII helix	β -turn	Sequence α -helix	T_m / °C	Ref. and remarks
aPP	GPSQPTYP	GDDAP	VEDLIRFYDNLQQYLNVTTRHRY-NH ₂	64 55	[1]
	GPSQPTYP	GDDAP	VEDLIRFYDDLQQYLNVTTRHRY-NH ₂		[5] a
	GPSQPTYP	GDDAP	VEDLIRFYDNLQQYLNVTTRHRY-NH ₂		[5] b
	GPSQPTYP	GDDAP	VEDLIRFYDNLQQYLNVTTRHRYC ^{AcNH₂} -NH ₂		[11] c
	GAMGPSQPTYP	GDDAP	VEDLIRFYDNLQQYLNVTTRHRY		[12] d
bPP	APLEPEYP	GDNATP	EQMAQYAAELRRYINMLTRPRY-NH ₂		[3]
pPYY	YPAKPEAP	GEDAS	PEELSRYYASLRHYLNLTQRQRY-NH ₂	43	[4, 9]
hPYY	YPIKPEAP	GEDAS	PEELNRYASLRHYLNLTQRQRY-NH ₂		[2]

a) Sequence as given in the report. b) Sequence from entry 2bf9 as deposited in the protein data bank (PDB) of the Research Collaboratory for Structural Bioinformatics (RCSB). c) The cysteine thiol group is blocked with iodoacetamide. d) The melting point was evidenced to be concentration dependent.

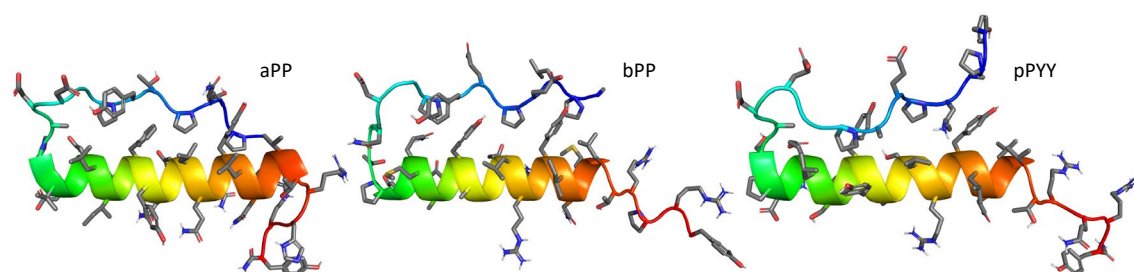


Figure 1: Structures of PP family peptides. aPP (crystal structure; PDB entry 2bf9), bPP (repaired nuclear magnetic resonance (NMR)-derived structure; 1bba) and pPYY (NMR-derived structure; 2rlk) display the typical PP fold.

The PP grafting strategy uses the stable fold of aPP and its relatives as a scaffold to stabilize a functional peptide motif. The idea is to enhance the miniprotein with new functions such as deoxyribonucleic acid (DNA) binding^[13–16], protein binding^[12, 17–28], catalytic activity^[29–31],

1. Introduction

photoswitchability^[32] or cell-penetrating properties^[11, 33, 34]. This is achieved by incorporating the functional epitope into its sequence whilst maintaining the unique fold. Mainly aPP, but also bPP or PYY were subject to PP grafting. The versatility of PP grafting was evidenced by many studies that proved successful in modifying either the α -helix or the PPII helix yielding a variety of functional PP-derived miniproteins. A highlight of the PP grafting story is the design and evolution of p007, which not only provided the proof of concept but also showed high affinity to DNA even at room temperature.^[13, 14] In addition, this study laid the grounds for using phage display in order to improve folding and binding of grafted PP family peptides.^[14, 35] Even though the majority of PP grafting approaches relied on rational design, the phage display technology was successfully applied in several studies including the development of the peptides p007 (DNA-binding)^[14, 35], PPBH3 (apoptosis-regulating)^[17, 21], PPKID4^P (regulatory domain of a transcription factor)^[18], and miniprotein 3.3 (inhibitor of an oncoprotein)^[24].

In some cases, PP grafting paved the way for new technologies or concepts. For instance, the development of KSDD, an allosteric inhibitor of an oncogenic herpesvirus protease, advanced cancer research in the field of Kaposi's sarcoma.^[20] Although its half maximal inhibitory concentration (IC₅₀) was not high enough for therapeutic applications, KSDD was the first allosteric inhibitor of an important serine protease of Kaposi's sarcoma-associated herpesvirus (KSHV). This research thus laid the grounds for a new therapeutic approach to treat KSHV infections and based on these findings, more potent small molecule allosteric inhibitors have been developed.^[36–39] Similarly, aPP-based cell-penetrating miniproteins provided the basis for developing highly potent zinc finger-derived miniproteins with the ability to deliver small molecules and even proteins into the cytosol of cells.^[11, 40]

Several properties of PPs are responsible for the versatility and hence the success of the PP grafting approach. These include synthetic and biosynthetic accessibility, many mutable surface-accessible residues that do not contribute to the fold, high stability of the fold, simple characterization by circular dichroism (CD) spectroscopy, as well as two different partly solvent-exposed secondary structures (α -helix, PPII helix) available for modification. One disadvantage of PP family peptides and their derivatives is the tendency to dimerize as this might reduce the solvent accessible surface area of the peptide and thus might influence the affinity for its target. Only a few grafted PP family peptides have been investigated with respect to homodimerization, but it seems likely that, like aPP or bPP, many of the grafted PP family peptides have a tendency to dimerize. A strictly monomeric miniprotein might avoid this drawback when being used as a scaffold for protein grafting. Many different miniproteins are available for protein grafting with potential for therapeutic applications.^[41] One of them is the Trp-cage, a monomeric and particularly small and stable protein that is the center of this dissertation.

1.2. The Trp-cage motif and exendin-4

The Trp-cage motif comprises an α -helix, one turn of a 3_{10} -helix, and a short polyproline II helix arranged in a defined tertiary structure. Its cooperative folding process is driven by the eponymous encapsulation of a tryptophan side chain. The motif was discovered when examining the 39-residue peptide exendin-4 by nuclear magnetic resonance (NMR) spectroscopy.^[42] At NMR concentrations, exendin-4 is prone to aggregation, so the structure determination required the presence of 30% 2,2,2-trifluoroethanol (TFE).^[42] In exendin-4, the Trp-cage domain is located at the C-terminus stabilizing an α -helix (**Figure 2**, bottom left). The helix succumbs to fraying at its N-terminus gradually unfolding to a flexible N-terminal strand. Exendin-4 was originally

isolated from the oral secretions of the lizard Gila monster (*Heloderma suspectum*) and was analyzed because of its sequential similarity to the human hormone glucagon-like peptide 1 (GLP-1).^[42] Exenatide, the synthetic equivalent of exendin-4, is approved as an active agent for the treatment of diabetes mellitus type 2^[43, 44] by the U.S. Food and Drug Administration (FDA) as well as by the European Medicines Agency (EMA). Exendin-4 shows several antidiabetic effects of GLP-1,^[42] but has a significantly higher bioavailability^[43] and a 30-fold longer half-life in human blood plasma.^[45] These effects are the results of a higher resistance against enzymatic proteolysis^[45] which partly results from exendin-4's tertiary structure.

Exendin-4:	HGEGTFTSDL	SKQMEEEAVR	LFIEWLKNNG	PSSGAPPPS-NH ₂
TC5b:			N LYIQWLKDGG	PSSGRPPPS
TC10b:			D AYAQWLKDGG	PSSGRPPPS
E19:	HGEGTFTSDL	SKQMEEEAVR	LYIQWLKEGG	PSSGRPPPS

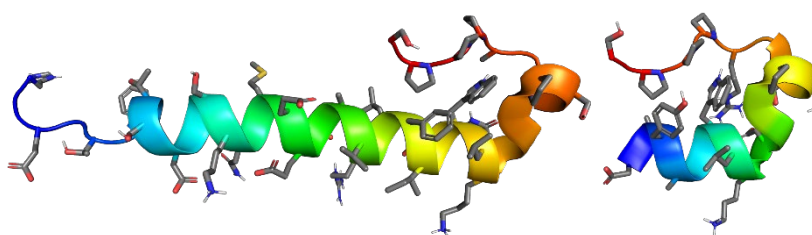


Figure 2: Alignment of sequences of exendin-4, TC5b, TC10b and E19 (top). NMR structures of exendin-4 (bottom, left) and the Trp-cage miniprotein (bottom, right). The NMR-derived structure (bottom, left; PDB entry 1jrj, 1/36) is based on NOE spectra recorded in the presence of 30% TFE to avoid aggregation. The NMR structure of the Trp-cage TC10b (bottom, right; PDB entry 2jof, 1/28) is based on measurements in water without TFE.

The original Trp-cage miniprotein variant Tc5b was created by truncating exendin-4 and mutating it at selected positions within the Trp-cage fold.^[46] The research group of Niels H. Andersen succeeded in stabilizing the Trp-cage fold and increasing its solubility in water to obtain a highly stable miniprotein ($T_m = 42^\circ\text{C}$) of only 20 residues.^[46] After the initial publication, several mutations have been published that increase the stability even further and of which TC10b is best characterized.^[47, 48] An NMR-derived structure (**Figure 2**) of this highly stable miniprotein ($T_m = (58 \pm 2)^\circ\text{C}$) illustrates how the W6 indole side chain is sandwiched by the dipeptide G11-P12 as well as P18.^[47] Due to strong ring current effects, protons located directly above (P18 H^{B3}) or below (G11 H^{A2}) the aromatic indole moiety are observed to have very large chemical shift deviations (CSDs).^[46, 47] The indole moiety is flanked by the side chains of L7 on one side and R16 on the other. The Y3 stabilizes the fold further by interactions with the central W6 indole side chain, but also by forming a “hydrophobic staple”^[47] with P19 thus keeping the N- and C-terminus in close proximity. The Trp-cage may achieve even higher stability than TC10b when a K8A mutation is implemented.^[47, 48]

Exendin-4 is prone to aggregation at NMR concentrations and its Trp-cage domain is not very stably folded.^[42] In order to increase the solubility, Petra Rovó, András Perczel and co-workers set out to stabilize the Trp-cage domain of exendin-4 by implementing most mutations of the first stably folded Trp-cage variant TC5b.^[49] The resulting peptide E19 was an analogue of exendin-4 with a stabilized Trp-cage domain. In comparison to exendin-4, E19 was shown to have a more stable α -helical conformation as observed by CD spectroscopy and has a slightly lower tendency to aggregate. However, stabilization of the Trp-cage domain slightly reduced the ability to stimulate insulin secretion in cultured INS-1E cells.^[49]

1. Introduction

1.3. Trp-cage grafting

1.3.1. A Trp-cage-based inhibitor of the E6 oncoprotein

Apart from their exceptionally stable fold, the Trp-cage variants optimized by Jonathan W. Neidigh *et al.*^[46–48] fulfill no biological function anymore. Therefore, the Trp-cage motif is an ideal scaffold for protein grafting. Shortly after the original publication the Trp-cage miniprotein, Yuqi Liu, James D. Baleja and co-workers grafted selected residues from a peptide inhibitor of the E6 protein of human papillomavirus (HPV) onto the scaffold of TC5b.^[50]

For its replication, the human papillomavirus requires the viral proteins E6 and E7.^[51, 52] The E7 protein is responsible for interfering with the cell cycle progression of the infected cell.^[52] Without E6 proteins, this would lead to an up regulation of the tumor suppressor protein p53 resulting in apoptosis.^[52] However, the E6 protein is able to prevent the induction of apoptosis by recruiting the E6-associated protein (E6AP), a cellular E3 ubiquitin ligase. E6AP binds to E6 *via* a short acidic motif with the sequence ELTLQELLGEER. The underlined residues of this motif are in an α -helical conformation in the bound state, as shown by the crystal structure of the E6AP-derived ligand bound to the E6 protein (**Figure 3**).^[53] Upon docking to the binding site of E6AP, E6 folds into the structure required to bind p53,^[54] which will then be ubiquitinated and targeted for degradation.^[52, 55] A potent binder of E6 at the E6-E6AP binding interface could prevent p53 degradation by competitive inhibition of the E6-E6AP complex formation and therefore be a potential therapeutic agent against HPV-derived cancers.

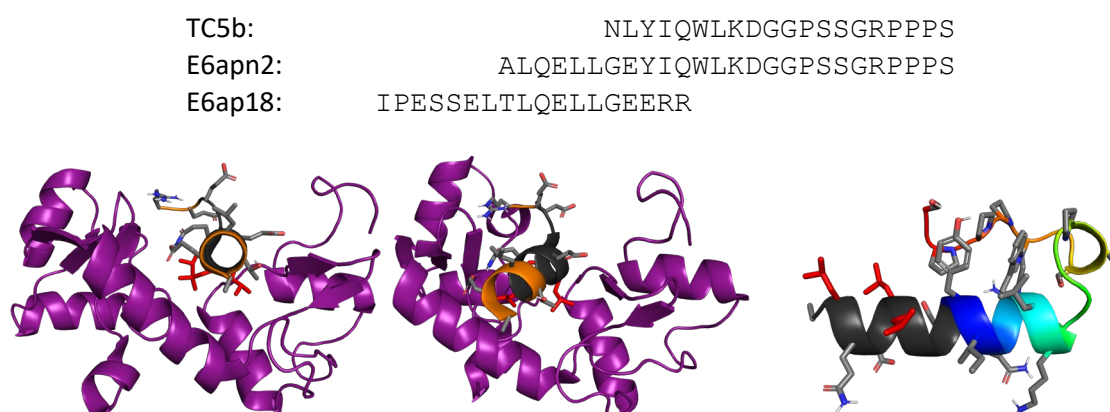


Figure 3: Top: Sequence alignment of TC5b, E6apn2 and E6ap18. Bottom: Crystal structure of the E6-E6AP complex (PDB entry 4giz; left and middle) and molecular model of E6apn2 (right). The E6-binding domain of E6AP (ribbon: black and orange) is shown from two perspectives (left and middle) in complex with the E6 protein. The N-terminus of the E6AP-derived peptide has α -helical structure, while its C-terminus is in an extended conformation. The three leucine side chains (red) of the recognition motif are deeply buried in hydrophobic pockets of the E6 surface. The ribbon of the LQELLGE motif that was grafted onto the Trp-cage protein is shown in black. The same elements are colored in black in the model of the grafted Trp-cage protein termed E6apn2 (right). This model demonstrates that the three leucine side chains (red) are at the same side of the α -helix as the Trp-cage domain. In consequence, E6apn2 can only bind the E6 pocket, when its helix is interrupted by a strong kink, or when the Trp-cage domain is unfolded.

When Yuqi Liu, James D. Baleja and co-workers set out to develop a Trp-cage-based E6-binding miniprotein,^[50] neither the crystal structure of the E6-E6AP complex^[53] nor that of the E6-E6AP-p53 complex^[54] had been resolved. From NMR and CD spectroscopic measurements, an 18-residue peptide inhibitor of E6 named E6ap18 was known to be partly α -helical in solution, but its structure when bound to E6 was unknown.^[56] The recognition motif LQELLGE of E6ap18 was grafted onto the helix of the Trp-cage TC5b.^[50] The resulting peptide E6apn2 (**Figure 3**) inhibited E6 ($IC_{50} = (26.2 \pm 4.8) \mu M$), but it was not as potent as E6ap18 ($IC_{50} = (10.5 \pm 1.4) \mu M$).^[50]

Unfortunately, the Trp-cage-derived variant E6apn2 was prone to aggregation at low millimolar concentrations precluding NMR-based structure determination.^[50] **Figure 3** depicts a molecular model of E6apn2 that was created based on the assumption that the Trp-cage induces a stable α -helix from L2 to K14. It demonstrates that the chosen Trp-cage grafting approach is not efficient because the leucine residues required for binding the E6 pocket are located at the same side of the helix as the Trp-cage domain. This precludes the formation of a continuous α -helix in the bound state and the strengths of the grafting approach, i.e. a preformed binding epitope, cannot be exploited with E6apn2. Nevertheless, in light of the difficulties to design a grafted protein without an elucidated structure of the target protein, it is remarkable that Yuqi Liu, James D. Baleja, and co-workers were able to create miniproteins that are almost as potent binders as the parent peptide E6ap18. Although in retrospect, Trp-cage grafting did not achieve optimal results here, the Trp-cage remains an interesting scaffold for other grafting applications.

1.3.2. Ice-binding Trp-cage proteins

The development of a Trp-cage with ice-binding and antifreeze properties was pursued by Matthias Lipfert^[57], Joana Gronow^[58], and Katrin Bamberg^[59] from the laboratory of Frank D. Sönnichsen. Antifreeze proteins (AFPs), also referred to as ice-binding proteins (IBPs), are a class of proteins present in organisms that are often exposed to temperatures below the freezing point of water.^[57, 58] These proteins are able to bind to the surface of ice crystals and kinetically inhibit their growth thus preventing the organism from freezing to death.^[58] The well characterized AFP termed type 1 isoform HPLC-6 (AFP1-6) is present in a single, continuous α -helix in water at low temperatures. It comprises three 11-residue repeats displaying the pattern TAXXAXAAAXX, where X can be alanine or a hydrophilic residue.^[57, 58] Due to the high alanine content, AFP1-6 is notoriously difficult to synthesize and purify. Truncation would facilitate the synthesis, but the activity of AFP1-6 fragments is highly dependent on their helicity,^[60, 61] which is typically reduced in truncated versions of AFP1-6. Therefore, Trp-cage grafting was successfully applied to stabilize the α -helix of short AFP1-6 fragments.^[57, 58] The resulting ice-binding Trp-cages (IBTCs) showed ice-structuring and ice growth retardation properties even though neither the Trp-cage nor the short AFP fragment alone showed these effects.^[57–59] The Trp-cage induces a helical secondary structure in the AFP-derived part, thus activating its antifreeze properties.

1.3.3. Photocontrol of the Trp-cage fold

Photoswitches are molecules that undergo a light-triggered reversible reaction between two isomeric states.^[62, 63] The activation energy to react from one isomer to the other is provided by light. As both isomers are able to absorb light, illumination triggers the photoisomerization in both directions resulting in a dynamic equilibrium termed photostationary state (PSS). Since the efficiency of converting one isomer to the other is dependent on the wavelength, light of different wavelengths may be used to shift the equilibrium towards one isomer or the other. In a pioneering study, Matthias Lipfert from the Sönnichsen laboratory intended to synthesize a Trp-cage equipped with a photoswitch allowing to unfold and refold the secondary and tertiary structure.^[57] Starting from the Trp-cage TC10b[K8A]^[47, 48] the mutations A2K and S20K as well as N-terminal acetylation were implemented.^[57] The resulting variant Ac-TC-KKA was cross-linked with an azobenzene moiety between the two lysine side chains *via* active ester functional groups resulting in a peptide termed Ac-TC-KKA-azo. Through irradiation with light the

1. Introduction

azobenzene moiety of Ac-TC-KKA-azo can isomerize reversibly between an extended, planar *trans*-state and a contracted, bent *cis*-state. As expected, the *cis*-isomer of the cross-linker supported the Trp-cage fold (**Figure 4**, left).^[57] When Ac-TC-KKA-azo was irradiated with blue light (450 nm), the azobenzene-moiety underwent an isomerization to the extended *trans*-isomer. Originally, this isomerization was intended to disrupt the fold by pushing the termini apart.^[57] Indeed, the Trp-cage loop (but not the α -helix) was unfolded in the *trans*-state of Ac-TC-KKA-azo (**Figure 4**, right).^[57] However, this was not an effect of the length increase of azobenzene - the highly flexible lysine side chains compensated the cross-linker's increase in length. Instead, the planar and highly hydrophobic *trans*-azobenzene moiety was shown to be interacting with Y3 and W6 thus efficiently competing with the hydrophobic cluster of the Trp-cage whilst keeping the helix intact.^[57] The isomerization was reversible by irradiation with ultraviolet (UV) light (350 nm) which produced a PSS of approximately 70% *cis*-isomer.^[57]

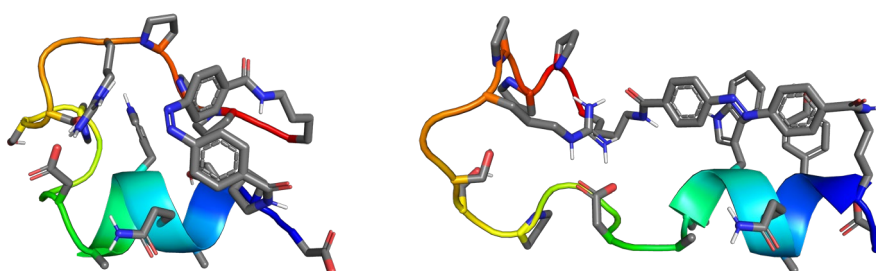


Figure 4: Ac-TC-KKA-azo is shown in its *cis*- (left) and *trans*-configuration (right). This figure is an adaption of Figure I.4.10 from ref.^[57] and was created with permission from Matthias Lipfert. The PDB files of both structures were created by Matthias Lipfert. Note that this figure shows the Trp-cage from the backside to show the cross-linker, while most depictions in this thesis show the Trp-cage from its frontside.

1.3.4. En route to photoswitchable ice-binding proteins

In an early study of the Sönnichsen group, implementation of photoswitchability in AFP1-6 by cross-linking the peptide with an azobenzene moiety was prevented by the high hydrophobicity of the azobenzene-peptide conjugate.^[57] In contrast, ice-binding Trp-cages (IBTCs) exhibit ice growth retardation properties and are highly soluble. If photoswitchability of the Trp-cage fold could be achieved, the photoresponsive folding or unfolding might encompass the entire α -helix (**Figure 5**) leading to switchable ice-binding properties.

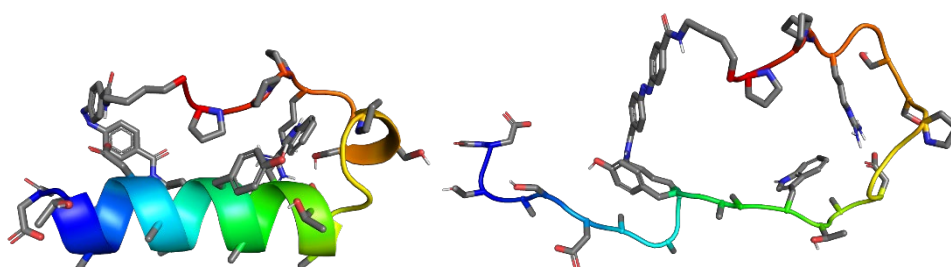


Figure 5: Models of AFP-TC-5c-azo in its *cis*-configuration (left) and *trans*-configuration (right). The ice-binding site of *cis*-AFP-TC-5c-azo is at the side of the helix opposite to the Trp-cage domain.

Incorporating the photoswitchable azobenzene cross-linker into the ice-binding Trp-cage resulted in the protein termed AFP-TC-5c-azo.^[59] Characterization of AFP-TC-5c-azo by NMR spectroscopy revealed multiple un- or misfolded by-forms many of which did not respond to irradiation. However, further investigation provided evidence of switchability of the Trp-cage, i.e. a folded Trp-cage domain was present in the main *cis*-state, but not in the main *trans*-state

of AFP-TC-5c-azo.^[59] Unfortunately, the large amount of uncharacterized by-forms complicated the correlation of NMR and CD spectroscopy results. Furthermore, the high hydrophobicity of AFP-TC-5c-azo not only resulted in slow aggregation, but also created strong artifacts in assays to determine the antifreeze activity preventing a meaningful comparison of the different photostationary states.^[59] In conclusion, future works need to address the high hydrophobicity of unfolded Trp-cage-azobenzene conjugates to facilitate applications in aqueous environments.

1.3.5. En route to antimicrobial Trp-cage proteins

In an approach analogous to designing the IBTC, one can envision to fuse a linear, α -helical antimicrobial peptide (α AMP) to a Trp-cage domain to form an antimicrobial Trp-cage (AMTC). α AMPs are a class of short peptides with the ability to kill bacteria or inhibit their growth. To estimate the feasibility and prospects of success of fusing an α AMP with a Trp-cage domain, two different AMTCs (**Table 2**) were designed in preliminary works with contributions from Matthias Lipfert, Nils Preußke, Andrea Ganesini, and Frank D. Sönnichsen. These AMTCs were based on the α AMPs KR-12^[64] and IsCT^[65, 66]. KR-12 is a 12-residue fragment of human cathelicidin LL-37,^[64] whereas IsCT is a 13-residue α AMP isolated from *Opisthacanthus madagascariensis* scorpion venom^[65]. *In silico*, KR-12 and IsCT were fused to the N-terminus of the Trp-cage TC-KKA to obtain models of the two desired AMTCs, i.e. AMTC31-6 (KR-12-derived) and AMTC33-2 (IsCT-derived). In the case of AMTC31-6, the C-terminal helix capping residue D1 of TC-KKA had to be deleted in order to align the hydrophobic face of the AMP with the hydrophobic side of the Trp-cage helix. In contrast, AMTC33-2 was designed without any additions to or deletions in the Trp-cage or the AMP part, as the hydrophobic faces of both helical parts were aligned upon simple fusion of both parts. The resulting antimicrobial Trp-cages were shown to have a stable α -helical structure at 1 °C as determined by CD spectroscopy, whereas their parent peptides, KR-12 and IsCT, were unstructured in solution under the same conditions (**Figure 6**).^[67]

Table 2: Sequence, length and charge of the AMTCs and their parent peptides.

Peptide	Sequence	Length	Charge
Ac-TC-KKA	Ac-DKYAQWLADGGPSSGRPPPK	20	0
KR-12	KRIVQRIKDFLR-NH ₂	12	+5
AMTC31-6	KRIVQRIKDFLRKYAQWLADGGPSSGRPPPK	31	+6
IsCT	ILGKIWEGIKSLF-NH ₂	13	+2
AMTC33-2	ILGKIWEGIKSLFDKYAQWLADGGPSSGRPPPK	33	+2

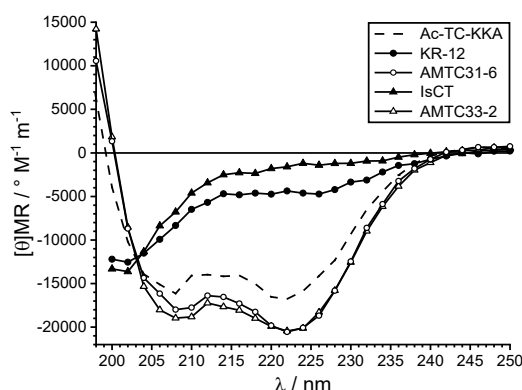


Figure 6: CD spectra of the AMTCs and their parent peptides. The mean residue molar ellipticity $[\theta]_{MR}$ is plotted over the wavelength λ . The spectra were recorded at 1 °C in 50 mM phosphate buffer at pH = 7.2 by accumulation of three measurements and with background subtraction. The data were acquired by Matthias Lipfert and are printed here with permission. © Matthias Lipfert, 2016, all rights reserved.

2. Objective

The pancreatic polypeptide (PP) fold has been used for more than 20 years as a scaffold to preorganize different α -helical binding epitopes or catalytic sites. In contrast, grafting of the Trp-cage miniprotein has not been widely applied, even though it is also characterized by a highly stable fold with an α -helix and a PPII helix. Using two independent examples, this thesis aims to explore and expand the potential of the Trp-cage as a scaffold for protein grafting.

The first example of Trp-cage grafting aims to provide a Trp-cage with antimicrobial activity by fusing it to an α -helical antimicrobial peptide (α AMP). Because of their activity against a broad range of pathogens, α AMPs are under investigation to develop peptide-based antibiotics. The chapter begins with a description of the mammalian and the bacterial cell envelope to understand the interactions of α AMPs with a cell. Subsequently, their mode of action and approaches to designing α AMPs will be reviewed. The review will conclude by summarizing which challenges still have to be resolved in order to develop α AMPs into an antibiotic drug. One of those challenges is the susceptibility to enzymatic degradation. As a stable fold may reduce the susceptibility to proteolytic cleavage, stabilizing the helical structure of an α AMP by fusing it with a Trp-cage domain may be a viable strategy to increase the bioavailability of α AMPs. This hypothesis will be tested in experimental studies using AMTC31-6 and AMTC33-2. An additional AMTC will be created by mutating and extending the α -helix of TC-KKA to achieve a shorter antimicrobial Trp-cage compared to AMTC31-6 and AMTC33-2. Overall, this work is intended to identify, whether the a stable Trp-cage fold can be maintained in the AMTCs and whether it may stabilize the α -helix sufficiently to decrease the susceptibility to cleavage by proteases compared to unstructured α AMPs in solution. For this reason, the AMTCs will be characterized with regard to their structure in solution and their resistance to enzymatic proteolysis. The activity of the peptides will be assessed in microdilution assays with Gram-positive and Gram-negative bacteria in order to determine the minimal inhibitory concentration (MIC) and minimal bactericidal concentration (MBC). As a first indicator regarding the toxicity of the peptides, a hemolysis assay will quantify the activity against human erythrocytes.

The second example of Trp-cage grafting will cover the targeted manipulation of peptide and protein structures using a photoresponsive cross-linker. The chapter will describe how α -helical peptides equipped with azobenzene-based cross-linkers can be switched between folded and disordered conformations using light of different wavelengths. In addition, applications of this approach will be reviewed, where the structural changes have been used to activate or inactivate binding of DNA, RNA or proteins. Furthermore, a discussion regarding the challenges of applying photoswitches *in vivo* will be provided. While the fold of simple helices can be efficiently controlled using azobenzene-based cross-linkers, it is unclear whether this approach also works in the context of a protein's tertiary structure and whether it may lead to reversible folding and unfolding of a (mini)protein. In experimental works, a diazocine, i.e. an azobenzene derivative, will be covalently attached to the α -helix of a Trp-cage protein. The two isomeric states of the Trp-cage-cross-linker conjugate will be analyzed by NMR spectroscopy and switching efficiencies will be determined. Characterization of the fold state by NMR and CD spectroscopy will identify, whether the Trp-cage fold can be reversibly unfolded and refolded upon irradiation with light of different wavelengths. If these experiments are successful, the concept may be applied to functional proteins in future studies to control their fold and thus their function.

3. Antimicrobial Trp-cage proteins

3.1. The antibiotic resistance crisis

Microbial resistances against antibiotics are occurring worldwide at an increasing pace. This development poses a serious threat to the therapeutic efficiency of various medical treatments.^[68] Since the discovery of penicillin by Sir Alexander Fleming in 1928, antibiotics have revolutionized modern medicine and are now indispensable for the treatment of bacterial infections and chronic diseases, for chemotherapies and for complex surgeries.^[68] Microbial resistances against penicillin have been known even before it was available for civic use in 1943. In the 1950s, microbial resistance to antibiotics became a clinical problem that was efficiently dealt with by developing new antibiotics until the late 1980s. Since the 1990s, multiresistant pathogens have been known that make bacterial infections life threatening again.^[68, 69] There are two general causes why the development of resistances in microbes is becoming a serious threat to our society. The first is the clinical and agricultural mis- or overuse of antibiotics that lead to evolutionary pressure among pathogens giving rise to resistances.^[68] As a result, antibiotics are losing their therapeutic effect. The second reason is that less new antibiotics are being developed.^[68] Resistances against existing antibiotics are unproblematic as long as new, potent drugs can replace compounds that have become ineffective. Since the 1980's, however, the number of approvals of new antibiotics is declining, while antibiotic resistant pathogens are on the rise.^[68]

Mis- and overuse of antibiotics not only pose a threat to our health, but also to the environment.^[70–72] Unfortunately, the persistence of antibiotics, especially of fluoroquinolones, in the environment is very high due to their limited biodegradability.^[73] For the potency of an antibiotic, chemical stability is an advantage because it contributes to a high bioavailability when no degradation of the compound occurs in the host. Once the substance is excreted, however, its stability is a major disadvantage if it precludes quantitative degradation and inactivation in the nature. Antibiotics used in veterinary medicine, as well as in animal husbandry find their way into the environment for example through the application of manure onto fields to fertilize soils.^[74–77] Although the use of antibiotic as growth promoters in livestock farming and aquaculture is banned in the European Union (EU) and many other countries, the global consumption of antibiotics in animal husbandry remains high and is predicted to increase on all continents.^[78] As a direct consequence, the emergence of antibiotic resistant bacteria in animals bred in low- and middle-income countries is increasing.^[79]

High concentrations of antibiotics can also be found in municipal wastewater, especially in the effluents of hospitals. Modern sewage treatment is able to drastically reduce the amount of antibiotics^[72, 80] and the residual antibiotics in the effluents of a sewage treatment plant were shown not to drive the evolution of antibiotic-resistant bacteria.^[81, 82] However, heavy rains may lead to sewer overflows resulting in pollution of the environment with antibiotics or antibiotic resistant bacteria.^[82] Furthermore, *in vitro* studies have shown that concentrations as low as 0.1 µg l⁻¹ of ciprofloxacin, a fluoroquinolone antibiotic, can induce resistance in bacteria.^[83] This concentration is well below its concentrations found in some surface waters or in the effluents of sewage treatment plants.^[84] Environmental pollution with antibiotics may change the microbiome of ecosystems and consequently affect the whole biotope.^[71] Thus, it may lead to a qualitative and quantitative change in the bacterial fauna resulting for instance in altered decomposition rates of organic matter.^[70, 71] Additionally, toxic effects on the living fauna and the aforementioned increased emergence of bacterial resistances are plausible.^[71]

3. Antimicrobial Trp-cage proteins

To combat the resistance problem, a drastic reduction of the overuse of antibiotics is necessary. This can mitigate the evolutionary pressure on non-resistant bacteria and slow down the emergence of new resistances. In addition, new antibiotics have to be developed to replace those that have become ineffective due to antibiotic resistance in pathogens.

While the first antibiotics, including penicillin or streptomycin, were natural products, modern antibiotics are either chemically modified natural compounds or synthetic drugs.^[84] One way of reducing the negative impact of drugs when released into the environment is the Benign by Design strategy. This concept implies the development of therapeutics that are sufficiently active in the host, but susceptible to degradation in the environment.^[85] For example, Christoph Leder, Klaus Kümmerer *et al.* developed the ciprofloxacin derivative CIP-Hemi that degrades in mildly acidic environments into less active compounds (**Figure 7**).^[86]

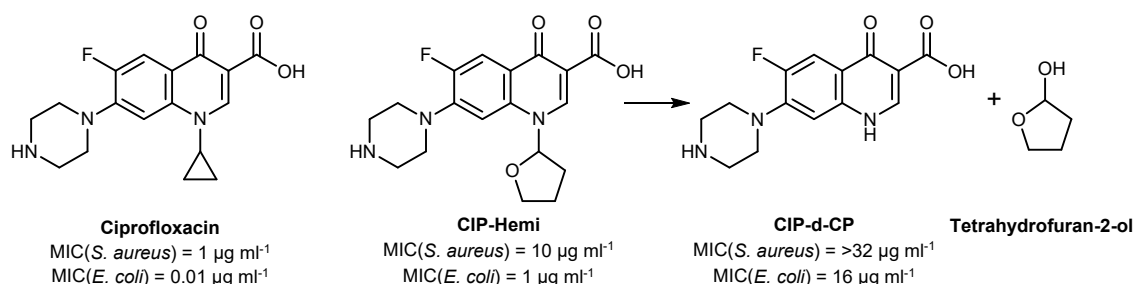


Figure 7: Chemical structures and minimal inhibitory concentrations of the fluoroquinolones ciprofloxacin and CIP-Hemi, as well as the primary degradation products of the latter.^[86] In acidic environments, CIP-Hemi is hydrolyzed to the less active CIP-d-CP and tetrahydrofuran-2-ol. Tetrahydrofuran-2-ol in turn is degraded into γ -hydroxybutyric acid, which subsequently degrades into CO_2 and H_2O . The minimal inhibitory concentration (MIC) is the concentration of a compound that inhibits the propagation of a microbial organism *in vitro*. MICs are provided for the bacteria *Staphylococcus aureus* (*S. aureus*) and *Escherichia coli* (*E. coli*).^[86]

A different class of compounds with high antimicrobial activity comprises antimicrobial peptides (AMPs). While conventional antibiotics are degraded very slowly, peptides are cleaved with high efficiency by any living organism on the planet. In consequence, bioavailability of AMPs is limited by their fast degradation and different strategies have been developed to increase their bioavailability. This chapter provides a review on α -helical AMPs (α AMPs; the largest class of AMPs) and presents a strategy, how a Trp-cage domain may be used to reduce their susceptibility to enzymatic degradation. The approach aims to improve their bioavailability to facilitate their use as therapeutic agents in the future.

3.2. Antimicrobial peptides

The multifunctional, fast, and microbicidal immune response of the innate immune system is in part affected by gene-encoded host defense peptides (HDPs) that are present in virtually every eukaryotic organism.^[87–91] Historically, the activity of those HDPs was entirely attributed to their direct inhibition or killing of pathogens,^[89] hence the original denomination as antimicrobial peptides (AMPs). Nowadays, both terms are often used synonymously. In this work, however, the term HDP will be used to describe peptides released by an organism to defend itself against infection. The mode of action of HDPs may therefore be immunomodulatory and/or directly antimicrobial.^[89, 92] Immunomodulatory peptides of synthetic origin will be termed innate defense regulators (IDRs),^[92] while the term AMP includes synthetic and natural peptides with direct antimicrobial activity, i.e. killing or growth inhibition

of bacteria evidenced *in vitro*. By those definitions, AMP and HDP are no synonyms, although many peptides can be assigned to both groups. The immunomodulatory effects of HDPs have been reviewed extensively^[88, 89, 92, 93] and are beyond the scope of this thesis.

There is a broad sequential and structural variety among AMPs. Based on their secondary structure, AMPs can be divided into four groups: α -helical, β -sheet, extended, and loop AMPs,^[94] the largest groups being α -helical and β -sheet peptides.^[95] Common features involve a positive net charge allowing them to interact with the negatively charged microbial cell surface, and amphipathicity to insert into the lipid membrane.^[95, 96] Perturbation and disruption of the bacterial membrane is a common reason for the antimicrobial activity of AMPs, but they may also attack intracellular targets – often after “self-promoted uptake”^[94] across the bacterial membranes. For instance, some AMPs have been shown to bind DNA or ribonucleic acid (RNA) or to inhibit RNA synthesis or protein synthesis. Regardless of the precise mode of action, knowledge about the cell envelope of mammalian and bacterial cells is crucial to understanding antimicrobial peptides.

3.2.1. Mammalian and bacterial cell envelopes

Once AMPs encounter a cell, they interact with the cell envelope. This interaction is dependent on both the AMP and the architecture of the cell envelope. The term cell envelope includes the plasma membrane (also referred to as cytoplasmic membrane) and any of the following components if present: the periplasm, the peptidoglycan, the outer membrane, the lipopolysaccharide (LPS) layer, the surface layer (S-layer), and the glycocalyx.

In general, plasma membranes of both, bacteria and mammals, are composed of lipids and contain membrane spanning integral proteins as well as peripheral proteins.^[97–99] The current understanding of cell membranes follows the fluid mosaic model^[97] which has been refined to include a higher complexity and organization, limited lateral diffusion of lipids and proteins, as well as the existence of lipid domains, e.g. lipid rafts.^[98] In detail, composition of the plasma membrane differs greatly between mammals and bacteria, providing a basis for AMP selectivity, because mammalian cell envelopes typically possess several features precluding or reducing harmful actions of AMPs. However, there are also differences in mammalian membrane composition between species, tissues, and cell types.^[100] The diversity in bacterial membrane composition is not only dependent on Gram-staining sensitivity or on the species, but also on the environment, as bacterial membranes are known to adapt to environmental challenges by changing the lipid composition.^[101] This kind of diversity is not only present in the membrane composition, but also in the other components of the cell envelope.^[102] However, to design a broadly potent α AMP it is necessary to use a less diverse and more general model of the cell envelope that displays the major differences between mammalian and bacterial cells. This subchapter provides insight into the structural composition of bacterial and mammalian cell envelopes starting from the innermost layer, the cytoplasmic membrane.

3.2.1.1. Mammalian cell envelopes

Mammalian cells have a relatively rigid plasma membrane as it has to compensate for the lack of a cell wall.^[103] To achieve this high stability, equimolar quantities of rigid cholesterol and more flexible phospholipids (**Figure 8**) are incorporated into the mammalian plasma membrane.^[103] The most abundant phospholipids in the membrane are zwitterionic, i.e. phosphatidylcholine, sphingomyelin, and phosphatidylethanolamine.^[103] Lipids with a net negative charge such as phosphatidylinositol and phosphatidylserine only make up circa

3. Antimicrobial Trp-cage proteins

10 mol% of all lipid compounds in the mammalian plasma membrane.^[103] The distribution of phospholipids differs between its inner leaflet and outer leaflet.^[103–108] Phosphatidylserine^[104] and phosphatidylethanolamine are mainly found in the cytosolic leaflet, whereas the outer leaflet is dominated by sphingomyelin and phosphatidylcholine.^[105–108] As a result, the plasma membrane of eukaryotic cells displays an overall neutral charge to the exterior of the cell.

The two leaflets of the mammalian cytoplasmic membrane are not only different regarding the distribution of the lipid head groups, but also in terms of acyl chain unsaturation.^[108] The exoplasmic leaflet is more ordered and less fluid because its lipids have a rather low degree of unsaturated acyl chains, whereas the lipids of the inner leaflet have a higher degree of unsaturation rendering the inner leaflet more diffusive.^[108]

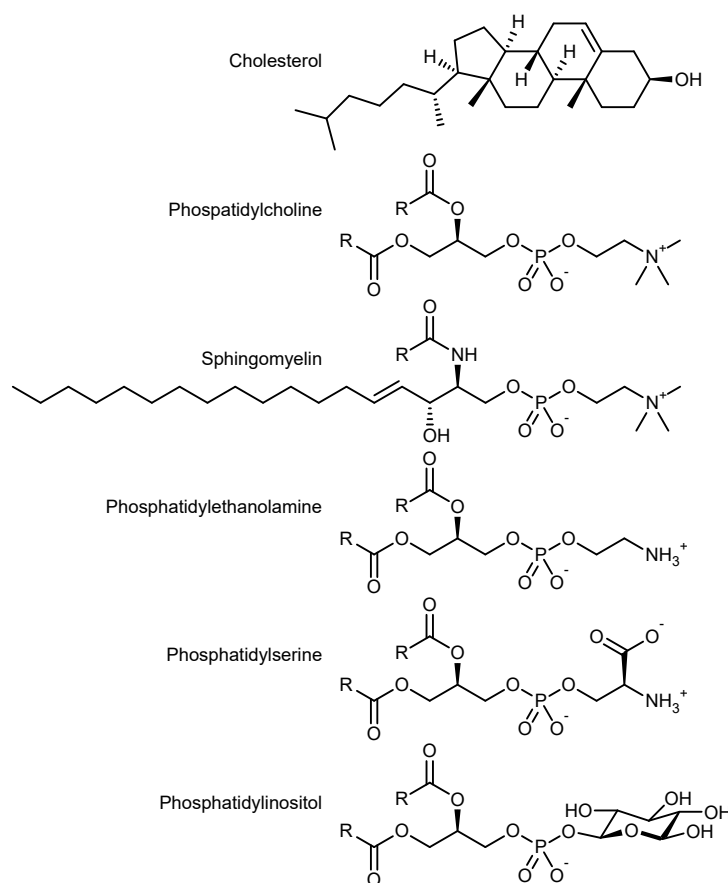


Figure 8: Chemical structures of lipid head groups found in eukaryotic cell membranes in the order of their abundance (top = most abundant).^[103] The residues R are not necessarily identical and may be saturated or partially unsaturated linear aliphatic chains.

In addition to the lipid fraction, eukaryotic plasma membranes are densely populated by proteins.^[109] A typical lipid-protein ratio by weight of roughly 1:1 can be found in most eukaryotic plasma membranes.^[99] However, lipids and proteins are not evenly distributed in the membrane but tend to form domains of specifically associated lipids and proteins.^[108, 109]

Due to the lipophilic nature of the lipid bilayer, the cytoplasmic membranes constitute a barrier for hydrophilic ions. This allows the build-up of an electrostatic gradient through the membrane, the so-called transmembrane potential. Ion pumps in the mammalian plasma membrane generate a high K^+ concentration and a low Na^+ concentration inside the cell.^[110] Especially the Na^+/K^+ -ATPase is involved in the generation of these concentration gradients. It transports three sodium ions from the cytoplasm to the extracellular medium in exchange for

the import of only two potassium ions resulting in the build-up of a negative transmembrane potential.^[111, 112] The potential is increased (i.e. more negative) by continuous conductance of K^+ along its concentration gradient through selective K^+ channels.^[110] In consequence, the resulting transmembrane potential is with values around $U_{eq} = -70 \text{ mV}$ ^[110, 113] close to the Nernstian equilibrium potential of K^+ .^[113, 114]

On the outside of the plasma membrane lies the glycocalyx,^[115] which is particularly well studied in endothelial cells.^[116] Covering every living cell in nature,^[115] the glycocalyx is a mesh of glycans, which are the carbohydrate portions of proteoglycans, glycoproteins, and glycolipids. In mammals, the glycocalyx is anchored to the plasma membrane *via* lipids or membrane proteins. The glycans usually are large, flexible, highly hydrated, and often anionic.^[117] Because these glycans are displayed at the cell surface, they constitute a major interface for the interaction with neighboring cells, symbionts, pathogens, and the environment in general.^[115, 117]

When assessing the activity of AMPs, their effects on bacteria as well as on mammalian cells are usually tested. While common bacteria such as *Escherichia coli* (*E. coli*), *Pseudomonas aeruginosa* (*P. aeruginosa*), and *Staphylococcus aureus* (*S. aureus*) are easily grown in liquid and on solid media, culturing primary cells derived from healthy tissues is very complex. Therefore, mammalian cell cultures mainly rely on tumor-derived cell lines.^[118] Unfortunately, tumor cells have a different membrane composition than healthy cells.^[119] In consequence, erythrocytes (also referred to as red blood cells, RBCs) are often used in studies to represent mammalian cells.^[120] They can be easily obtained through blood donations and their overall membrane composition and lipid distribution between the inner and outer leaflet is in fact similar to the prototypical mammalian cell envelope described above.^[121, 122] Another advantage of erythrocytes is the simple detectability of hemoglobin leakage upon membrane disruption by an AMP, which is exploited in so-called hemolysis assays.^[123, 124] These features qualify RBCs to represent mammalian cells in hemolysis assays as a first indicator of AMP toxicity. However, there are certain discrepancies between erythrocytes and other mammalian cell types, that limit the applicability of RBCs as a general model of mammalian cell. For instance, the transmembrane potential of human RBCs is with approximately $U_{eq} = -10 \text{ mV}$ ^[125–127] less negative than that of other mammalian cells. Presumably, this makes human erythrocytes more resistant against cationic AMPs because larger, i.e. more negative, transmembrane potentials facilitate the membrane disruption through cationic AMPs. Secondly, the RBC membrane is stabilized by a two-dimensional network of skeletal protein filaments, which is located inside the cell close to the membrane.^[122] The membrane skeleton is covalently attached to transmembrane proteins and non-covalently bound by anionic phospholipids of the inner leaflet.^[122] It confers the necessary stability and elasticity to the erythrocyte membrane enabling drastic deformations of RBCs.^[122] It appears plausible that this stabilization not only prevents membrane breakup, vesiculation, or cell fragmentation under mechanical stress, but also increases the resistance against cationic AMPs. A further drawback of using mammalian RBCs to assess the toxicity of AMPs to mammalian cells is their lack of a nucleus and cell organelles.^[121] Thus, hemolysis assays provide no or only limited insight how an AMP may affect internal targets of mammalian cells.

In conclusion, the absence of hemolytic behavior in AMPs does not necessarily imply low toxicity towards mammalian cells as hemolysis tests tend to underestimate the lytic potential of AMPs and do not report on how internal targets would be affected. Nonetheless, erythrocytes are well suited to serve as an inexpensive and easily obtainable model for the mammalian cell membrane and hemolysis assays may provide first insights into the lytic behavior of AMPs.

3. Antimicrobial Trp-cage proteins

3.2.1.2. Bacterial cell envelopes

Like eukaryotes, bacteria possess a lipid bilayer membrane bordering the cytoplasm,^[128] albeit with a different lipid composition. Main components of the bacterial cytoplasmic membrane are the zwitterionic phosphatidylethanolamine, as well as the anionic lipids phosphatidylglycerol and cardiolipin (**Figure 9**).^[129] Additionally, bacteria may incorporate phosphatidylcholine, phosphatidylserine, phosphatidylinositol or phosphate-lacking lipids into their membrane.^[101, 102, 129] As a result of the lipid composition, the surface of the bacterial plasma membrane is negatively charged, which is in contrast to the overall neutral outer leaflet of the mammalian cytoplasmic membrane.

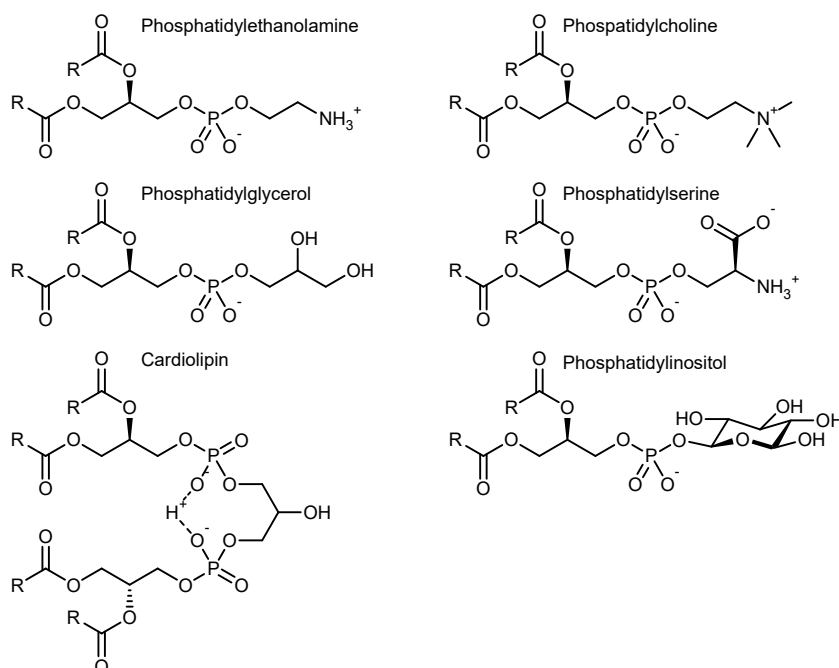


Figure 9: Chemical structures of lipid head groups found in bacterial cell membranes. Their abundance is highly dependent on the bacterial species as well as environmental factors. The residues R are not necessarily identical and may be saturated or partially unsaturated linear aliphatic chains.^[129]

Bacteria lack intracellular organelles and must incorporate many membrane proteins into the cytoplasmic membrane, the eukaryotic equivalents of which are associated with membranes of organelles.^[102] For instance, in eukaryotes the complexes of the respiratory chain are found in the inner membranes of mitochondria, where they produce a proton gradient and *ipso facto* an electrostatic gradient between the mitochondrial matrix (high pH) and the intermembrane space (low pH).^[130] This proton gradient is exploited by ATP synthase that uses the proton motive force to synthesize ATP from ADP and phosphate. In respiring bacteria, these functions are located in the cytoplasmic membrane pumping protons out of the bacterium.^[128] This leads to a larger transmembrane potential compared to eukaryotic cells. Typical transmembrane potentials of respiring, neutrophilic bacteria reach levels around $U_{eq} = -150$ mV.^[131]

Apart from these differences in membrane composition and transmembrane potential, the cell envelope of bacteria differs greatly from that of mammals because bacteria generally possess a cell wall (**Figure 10**). Most bacteria can be divided into being either Gram-positive or Gram-negative, depending on their sensitivity to the Gram-staining method.^[128] Typical representatives of Gram-positive bacteria and well-studied model organisms are *Micrococcus*

luteus (*M. luteus*), *Bacillus subtilis* (*B. subtilis*), and *S. aureus*.^[102] Gram-positive bacteria mainly incorporate phosphatidylglycerol, cardiolipin, and the lipid part of lipoteichoic acids into their plasma membrane.^[129] Outside the cytoplasmic membrane lies the cell wall composed of its main component peptidoglycan as well as teichoic acids.^[102, 128] Peptidoglycan is composed of alternating, β -(1,4)-linked *N*-acetylglucosamine (NAG) and *N*-acetylmuramic acid (NAM).^[128] The long strands are interconnected by short, overall negatively charged peptide chains containing proteinogenic and non-proteinogenic amino acids.^[128] Usually, the cell wall of Gram-positive bacteria is thick (circa 30 nm – 100 nm) and contains multiple layers of peptidoglycan.^[128, 129] Embedded in the peptidoglycan are teichoic acids, i.e. linear polymers of glycerol phosphate, glucosyl phosphate or ribitol phosphate.^[128, 102] There are D-alanine or D-glucose molecules attached to the glycerol or ribitol moieties of the teichoic acids.^[128] The strands of wall teichoic acids are covalently bound to the peptidoglycan, whereas lipoteichoic acids are connected to membrane lipids.^[102, 128] Due to their negative charge, teichoic acids bind divalent cations such as Ca^{2+} and Mg^{2+} .^[102, 128] Strands of wall teichoic acids are known to protrude through and beyond the peptidoglycan layers into the aqueous environment of the cell.^[102]

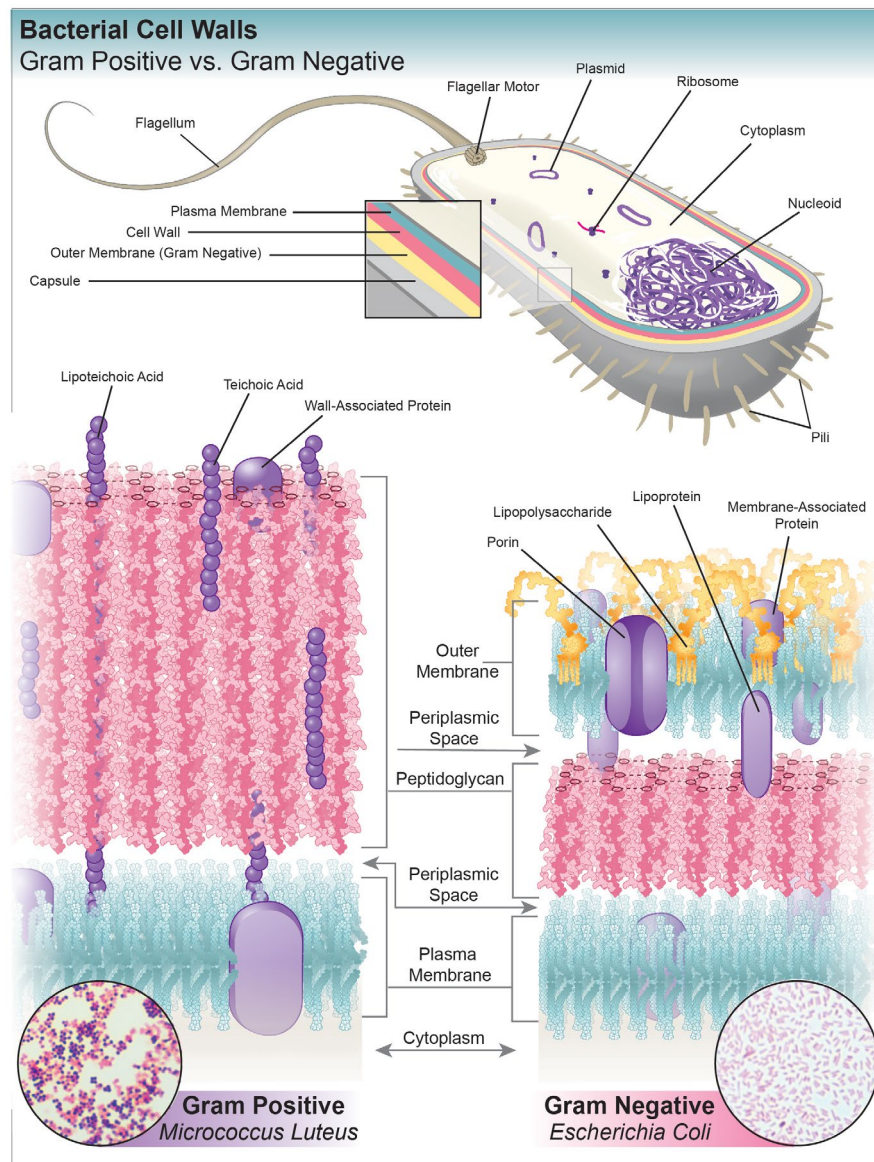


Figure 10: Cross-section of a Gram-negative bacterium (top). Cell wall and membrane(s) of Gram-positive and Gram-negative bacteria (bottom). © Rebekka M. Bamert, 2018, all rights reserved.

3. Antimicrobial Trp-cage proteins

The cell envelope of Gram-negative bacteria includes at least the cytoplasmic membrane, the periplasm, a thin peptidoglycan layer, a second membrane termed the outer membrane and the LPS layer.^[128] Most research on Gram-negative bacteria targeted *E. coli*,^[101, 102, 132] a common model organism in microbiology. Like the plasma membrane of Gram-positive bacteria, that of Gram-negative bacteria is mainly composed of lipids and embedded proteins. The lipid fraction typically contains phosphatidylethanolamine and phosphatidylglycerol, usually with higher amounts of phosphatidylethanolamine.^[129] Additionally, cardiolipin is also abundant with a typical share of 5 % – 10 % of all lipids.^[129] Phosphatidylserine and other lipids are less common.^[102] Outside of the cytoplasmic membrane lies the periplasm which is isolated from the exterior of the cell by the outer membrane.^[102] The periplasm is more viscous than the cytoplasm due to its high content of proteins and solutes.^[102, 128] Embedded into the periplasm with a gap to both neighboring membranes lies a thin layer of overall negatively charged peptidoglycan (circa 3 nm – 5 nm).^[128, 129] As opposed to the Gram-positive cell wall it contains no teichoic acids. The peptidoglycan is covalently attached to the inner leaflet of the outer membrane by the Braun lipoprotein, also termed Lpp.^[102, 128] The outer membrane differs significantly between its inner and outer leaflet. Whereas the inner leaflet of the outer membrane displays a similar lipid composition as the cytoplasmic membrane,^[129] the outer leaflet of the outer membrane is mainly composed of lipopolysaccharides (LPS).^[102] Although there is great variability in the components of LPS among different Gram-negative bacterial species, its overall structure is well preserved.^[128] The lipid part of LPS is lipid A, a phospholipid comprising a doubly phosphorylated glucosamine disaccharide head group equipped with six to seven acyl chains.^[102, 128] Attached to lipid A there is a branched and partly phosphorylated oligosaccharide core. Finally, the core is connected to the O-specific polysaccharide, also referred to as O-antigen, a long, highly variable polysaccharide strand.^[128] The protein fraction of the outer membrane includes many lipoproteins of unknown function attached to the inner leaflet.^[102] Further it contains porins and other transmembrane proteins that allow diffusion of small molecules across the outer membrane.^[102] Proteins, however, cannot pass these porins and remain located within the periplasm.^[128] The outer membrane contains only few embedded enzymes, but one of them, OmpT, is of particular importance. The active site of this protease is accessible from outside the cell. It is able to degrade peptides and may therefore confer resistance against AMPs and HDPs. Accordingly, it may facilitate the pathogenic colonialization of the human intestine by enterohemorrhagic and enteropathogenic *Escherichia coli* (EHEC and EPEC).^[133]

Some, but not all Gram-negative and Gram-positive bacteria possess a surface layer (S-layer).^[134] The bacterial S-layer is a paracrystalline monolayer of (glyco)proteins, typically 5 nm – 10 nm thick and generally composed of a single molecular species.^[134] The S-layer forms a sheath covering the entire bacterium. The monomers are arranged in a defined, two-dimensional lattice. In Gram-positive bacteria the S-layer is non-covalently attached to secondary cell wall polymers which in turn are covalently bound to the peptidoglycan,^[135] whereas in Gram-negative bacteria the S-layer adheres to the glycan of LPS.^[134] S-layers typically possess regularly distributed, uniform pores between 2 nm and 8 nm in diameter,^[134] which is large enough for the passage of peptides and small proteins. Despite these pores, the S-layer may provide enhanced resistance against AMPs in bacteria, possibly through electrostatic repulsion of the positively charged AMPs.^[136]

The outmost layer of each cell is the typically anionic and highly hydrated glycocalyx.^[137] The main components of the glycocalyx are polysaccharides and (glyco)proteins.^[137] For instance, teichoic acids, glycolipids, glycans of LPS, or glycans of S-layers belong to the glycocalyx if they

protrude into the extracellular medium. There are varying definitions of the glycocalyx^[128, 137] and the simplest^[128] distinguishes two categories. The term “capsule” describes a dense, definite network of biopolymers that is firmly bound to the cell envelope.^[128] A slime layer, in contrast, is less dense and easily deformed. It is rather loosely attached and may at least partly shed into the extracellular space.^[128, 137]

3.2.1.3. Selectivity of AMPs

The different cell envelopes of bacterial and mammalian cells allow for AMPs to display selectivity, i.e. to have a bactericidal or bacteriostatic effect while mammalian host cells are left unaffected. The ratio of minimal hemolytic concentration (MHC) and MIC is referred to as therapeutic index (TI) and is commonly used as a measure for the selectivity of AMPs.^[123] A higher therapeutic index indicates higher activity towards bacteria than towards erythrocytes. Three major differences between the plasma membrane of bacteria and mammals are mainly responsible for the selectivity of AMPs towards bacteria: the presence of anionic lipids at the bacterial outer leaflet, the absence of cholesterol in the bacterial membrane, and the increased (i.e. more negative) electrostatic potential across the bacterial plasma membrane.

Anionic lipids are abundant in the outer leaflet of the bacterial plasma membrane but scarce at the outer leaflet of mammalian plasma membranes. In consequence, cationic AMPs often show higher association constants with, and more efficient membrane permeabilization of bacterial membranes compared to mammalian ones.^[138] According to the currently accepted modes of action (described in detail in chapter **3.2.2 α -helical AMPs: Mode of action**) the first interaction between cationic AMPs and the envelope of any cell is mediated by electrostatics. Attracted by charge-charge interactions, cationic AMPs are able to diffuse into the negatively charged glycocalyx. In bacteria, a diffusion deeper into the cell envelope is facilitated, because not only the glycocalyx, but also LPS (in Gram-negative bacteria), peptidoglycan, and the plasma membrane display negative charges and diffusion of the AMPs to the cytoplasmic membrane proceeds primarily along a concentration gradient. In mammalian cells, however, the cytoplasmic membrane beneath the glycocalyx is neutral on the outside. Association with the membrane is therefore hampered by attractive forces between the glycocalyx and the peptides.^[139]

The second major difference between bacterial and mammalian plasma membranes is the presence of cholesterol. With equimolar quantities of cholesterol and phospholipids, cholesterol is highly abundant in the mammalian plasma membrane.^[103] Due to its rigid backbone, the presence of cholesterol has an ordering effect on the acyl chains of neighboring phospholipids leading to reduced density fluctuations, overall thickening, and decreased permeability of the membrane.^[140] Nonetheless, some liquid properties of the membrane, such as translational disorder and lateral diffusion of the lipids, are maintained in this cholesterol-induced, so-called liquid-ordered state.^[140] Cholesterol has a higher affinity for sphingomyelin or other phospholipids with saturated hydrocarbon tails than for unsaturated lipids which can result in the formation of two distinct phases referred to as membrane domains.^[141–143] Studies of model membranes showed that cholesterol influences the formation of lipid domains or lipid rafts, i.e. lateral structures with different membrane constituents (phospholipids, cholesterol, and peripheral or integral proteins).^[140–143] The highly stable liquid-ordered phase containing cholesterol and saturated lipids is relatively resistant to detergents^[141] or AMPs^[142, 143], whereas domains in a liquid-disordered state containing unsaturated phospholipids and low to no amounts of cholesterol are not.^[141–143] Some studies argue that cholesterol might have only a

3. Antimicrobial Trp-cage proteins

limited effect on the resistance of mammalian cells against AMPs, because domains exist that contain few or no cholesterol and which are therefore susceptible to disruption by antimicrobial peptides.^[142, 143] This interpretation is contrasted by a study assessing the effect of granulysin, a cationic pore-forming protein of 74 residues with a mode of action comparable to AMPs, on model membranes of different compositions.^[144] Membranes composed of lipid extracts from erythrocytes or different lipid mixtures containing cholesterol were completely resistant to pore formation by granulysin, whereas membranes lacking cholesterol were highly susceptible. It should be noted, that domain formation was not observed in these membranes, but only occurred upon heating the membranes above 50 °C.^[144] Cholesterol was also found to not only stabilize artificial membranes containing saturated lipids, but also those comprising mainly unsaturated phospholipids.^[143, 145] It appears plausible, that the high concentration of cholesterol in eukaryotic plasma membranes may result in a saturation of lipid rafts with cholesterol such that a fraction of the cholesterol partitions into domains with lower cholesterol affinity. There it may significantly improve the AMP resistance and hence increase the overall stability of the cell.

In addition to the presence of anionic lipids and the absence of cholesterol, the efficiency of AMPs against bacteria is increased by the more negative bacterial transmembrane potential. The bacterial transmembrane potential ranges around $U_{eq} = -150$ mV,^[131] whereas the typical transmembrane potential of mammalian cells is about $U_{eq} = -70$ mV^[110, 113]. In a study with bacterial membrane-mimicking planar lipid bilayers, highly negative transmembrane potentials (-180 mV) were required to initiate AMP-induced conductance across the membrane, i.e. membrane permeabilization. Subsequent reduction of the voltage to -80 mV often resulted in reduced activity of the peptides.^[146]

The presented differences are general observations and exceptions do occur. Nonetheless, these three differences are key factors for the specificity of many AMPs against bacteria.

3.2.2. α -helical AMPs: Mode of action

α -helical AMPs (α AMPs) are a large group of linear AMPs that display an α -helical structure in the membrane-associated state (**Figure 11**).^[95, 96] Sometimes, the entire molecule is helically structured when adsorbed to the membrane or a membrane mimic.^[147] More often, however, kinks within a helix^[64, 148–150] or disordered termini^[64, 149–152] are observed.

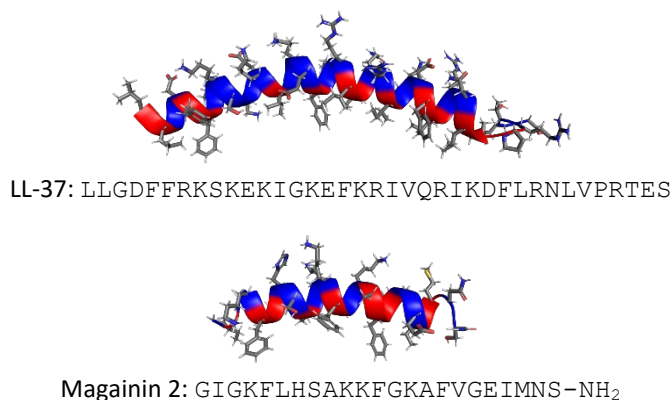


Figure 11: Structure of two representative α AMPs, LL-37 (top) and magainin 2 (bottom), when bound to sodium dodecyl sulfate (SDS) or dodecylphosphocholine (DPC) micelles, respectively. Hydrophilic residues are marked by a blue ribbon, while for hydrophobic residues the ribbon is colored in red. The hydrophobic residues are buried in the detergent micelles (not shown) driving the formation of the amphipathic α -helix. The depiction of LL-37 is derived from PDB entry 2k6o (1/4). The depiction of magainin 2 is derived from PDB entry 2mag (1/10).

The helical conformation in a membrane environment is a result of the amphipathicity of α AMPs. Typically, these peptides present a hydrophilic and a hydrophobic side of similar size when displayed in a helical wheel projection.^[96] The helical conformation is assumed, when the burial of the hydrophobic side of the helix into the membrane compensates for the entropic costs of helix formation. In aqueous solution, however, α AMPs often are highly flexible with little or no secondary structure.^[95, 96]

In vitro, α AMPs possess a high activity against many potential pathogens such as Gram-positive and Gram-negative bacteria, fungi, protozoa, or viruses.^[95, 96, 153] The following sub-chapters focus on the interactions of α AMPs with bacteria as those are well understood^[94–96, 154] and most important for this work. Early studies found α AMPs composed of only D-amino acids to have similar activities as their all-L-enantiomers, which precluded a receptor based mechanism.^[155, 156] Further investigations revealed two distinct modes of action by which α AMPs can act on bacteria.^[95, 96, 154] One of them is membrane permeabilization, which includes procedures that weaken and disrupt the bacterial membrane(s). This will eventually lead to loss of transmembrane potential, nutrients, and other essential cytosolic constituents ultimately resulting in growth inhibition (bacteriostatic effect) or cell death (bactericidal effect).^[95, 96] The other mode of action targets intracellular components and functions.^[95, 96] AMPs are able to reach the bacterial cytosol where they may associate with nucleic acids or proteins to block important cellular processes. It is possible that one α AMP exerts both mechanisms, depending on its structure and concentration as well as membrane architecture.^[96] Regardless of the mode of action, interaction with the cell envelope is crucial for the activity of α AMPs.

The interactions of cationic α AMPs with Gram-negative bacteria are well understood.^[94] First, the initially disordered peptides diffuse into the anionic glycocalyx attracted by charge-charge interactions. If present, an overall neutral S-layer is usually no significant barrier, as α AMPs are small enough to pass the pores. The first interaction harmful to the bacterium occurs when they encounter the LPS layer of the outer membrane. Divalent metal ions confer rigidity to the cell envelope by non-covalently cross-linking the polysaccharide chains of the LPS layer.^[94] Replacement of those metal ions by the much larger cationic α AMPs weakens the outer membrane and facilitates interaction with the lipid core of the outer membrane.^[94] Interaction with the lipid A moiety of LPS results in helix formation of α AMPs due to the burial of the hydrophobic site in the lipid bilayer.^[157, 158] Additionally, some α AMPs have been described to directly bind lipid A.^[158–161] This interaction counteracts the endotoxic activity of released lipid A and further destabilizes the outer membrane.^[94] Once sufficient AMPs are located at the outer membrane the formation of pores or even lysis of the outer membrane facilitates the uptake of more AMPs – a process aptly described as “self-promoted uptake”.^[94] After having passed the outer membrane, the peptides diffuse into the peptidoglycan layer until they reach the inner membrane.

With Gram-positive bacteria, diffusion into the glycocalyx and through the S-layer by α AMPs is a process similar to Gram-negative bacteria as these structures are alike in both bacterial types. The presence of negatively charged teichoic acids embedded in the peptidoglycan of Gram-positive bacteria facilitates the diffusion deep into the cell wall.^[96] However, the thick peptidoglycan layer of Gram-positive bacteria may also sequester the cationic peptides thus reducing their antimicrobial activity and slowing their bactericidal effect.^[162]

After having reached the cytoplasmic membrane, the further processes are again similar between Gram-negative and Gram-positive bacteria. Attracted by the anionic phospholipids,

3. Antimicrobial Trp-cage proteins

α AMPs accumulate at the surface of the cytoplasmic membrane.^[96] Hydrophobic residues partition into the lipophilic tail region of the outer leaflet of the membrane, while polar residues remain in the head group region. As a result, the peptide assumes an α -helical conformation while floating in the membrane at the interface to the periplasm. Its helical axis is oriented parallel to the membrane surface.^[96] Once a critical concentration is reached, membrane permeabilization may proceed according to one of several proposed mechanisms.

3.2.2.1. Barrel stave mechanism

The barrel stave mechanism was the first model to explain the mode of action of pore-forming peptides. It was proposed in 1974 to explain the voltage-, lipid-, and concentration-dependent conductance of membranes in the presence of alamethicin.^[163] Although the original model was based on an incorrect cyclic alamethicin structure,^[163] the general barrel stave mechanism was confirmed to apply to alamethicin in later studies.^[164, 165] Alamethicin is not cationic but highly hydrophobic and displays only one charged residue which is glutamic acid.^[166] Because of its hydrophobicity, alamethicin is largely unstructured and forms aggregates in solution (**Figure 12A**).^[167] The barrel stave mechanism is assumed to start with the accumulation of monomeric peptides in α -helical conformation at the membrane surface (**Figure 12B**).^[95] Lateral diffusion leads to the formation of peptide aggregates stabilized by peptide-peptide interactions, locally disturbing the membrane order (**Figure 12C**).^[95] This facilitates the insertion of the peptide aggregates into the membrane and the formation of the barrel stave pore.^[95] An alternative mechanism of barrel stave pore formation was proposed in which monomeric alamethicin inserts vertically into the membrane (**Figure 12D**) and lateral diffusion facilitates the assembly of transient pores.^[168] Regardless how they are formed in detail, the barrel stave pores (**Figure 12E**) comprise five to ten α -helices oriented perpendicular to the membrane surface.^[95, 169] Typically, the barrel stave mechanism therefore requires helices long enough to span the entire membrane.^[169] In the pore, neighboring peptides are directly in contact with each other. While hydrophilic residues are pointing inwards, the hydrophobic outside of the pore is surrounded by the lipid tails.^[169]

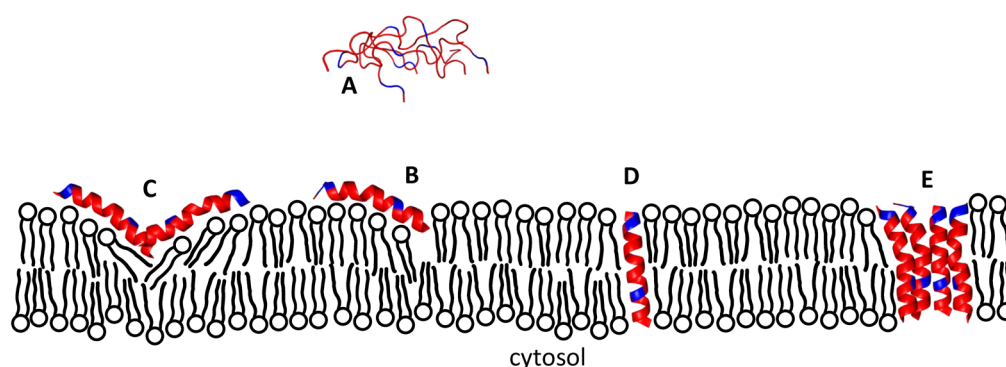


Figure 12: Barrel stave mechanism. Helical structures of alamethicin are taken from its crystal structure (pdb entry 1amt). Hydrophilic residues of the peptides are colored in blue, hydrophobic residues in red. The phospholipids of the membrane are represented by black circles (head groups) and two wavy black lines (hydrocarbon tails).

Initially, the barrel stave model was the only model to describe the characteristics of pore formation and was thought to apply to not only alamethicin but also cationic α AMPs such as melittin, cecropins or magainins.^[169] However, with the identification of other pore-forming mechanisms (described below), the applicability of the barrel stave model to cationic α AMPs

was increasingly doubted.^[165, 170–173] One reason was the strong electrostatic repulsion between heavily charged cationic helices, that would prevent the hydrophobicity-driven peptide-peptide interactions necessary to form the pore.^[172] Therefore, the barrel stave mechanism is limited to highly hydrophobic peptides with only limited net charge. Further, other mechanisms gave better explanation for rapid lipid flip-flopping that was observed with cationic α AMPs.^[170]

3.2.2.2. Carpet mechanism

Lack of evidence supporting the barrel stave mechanism led to the proposal of a different, much simpler mechanism, in which the peptides accumulate at the outer leaflet of the membrane, oriented in parallel to its surface.^[173, 174] This model was first proposed in 1988^[174] and subsequently named carpet-like mechanism^[172, 173, 175] or simply carpet mechanism^[139, 176]. According to the carpet mechanism, monomeric and unstructured α AMPs (**Figure 13A**) diffuse to the bacterial cytoplasmic membrane, where they accumulate attracted by electrostatic interactions (**Figure 13B**). While the polar residues remain in the head group region of the membrane, the hydrophobic residues interact with the lipid tails which results in the formation of an α -helical conformation (**Figure 13C**). Accumulation of α AMPs in the membrane takes place until the membrane is covered by a dense layer of α AMPs.^[139, 174, 175] Calculations based on partition constants and MIC values of several AMPs demonstrate that high membrane coverage is physiologically relevant.^[177] It leads to membrane thinning and weakening, as the embedded AMPs push apart the lipid head groups (**Figure 13C**).^[178, 179] Then, peptides diffuse through the membrane (**Figure 13D**), mainly driven by the high transmembrane potential of bacterial cells, effectively perturbing the membrane at the outer and the inner leaflet. With a weakened membrane, flip-flopping of lipids between the inner and outer leaflet of the membrane is facilitated leading to a reorganization of the membrane.^[139, 175, 180] Weakening of the membrane may also result in transient pores or ruptures (**Figure 13E**) which allow the passage of peptides into and cytosolic compounds out of the cell (**Figure 13F**). According to the carpet mechanism, membrane micellation or lysis is often the final result once a critical concentration of peptides is reached (**Figure 13G**).^[180]

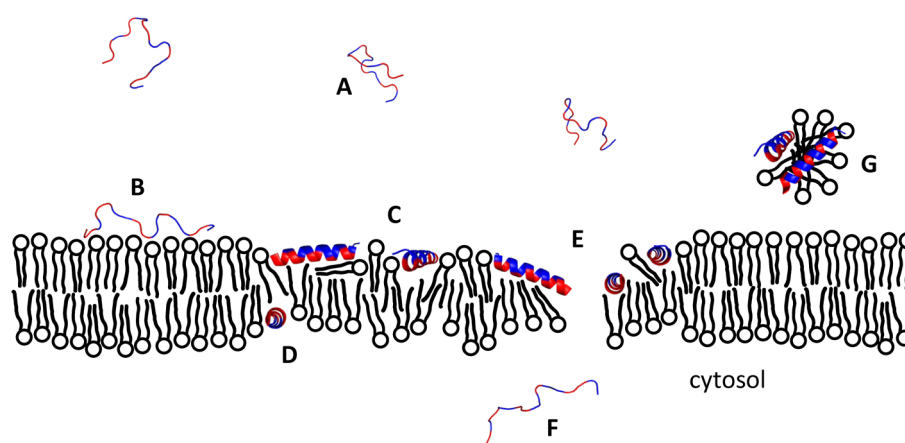


Figure 13: Carpet mechanism. Hydrophilic residues of the peptides are colored in blue, hydrophobic residues in red. The phospholipids of the membrane are represented by black circles (head groups) and two wavy black lines (hydrocarbon tails).

3.2.2.3. Toroidal pore mechanism

In 1996, the toroidal pore mechanism was independently proposed by two research groups for the cationic α AMP magainin 2.^[170, 171] This model delivered the explanation for the

3. Antimicrobial Trp-cage proteins

observation of cationic α AMPs to be oriented perpendicular to the membrane surface, forming large pores despite their electrostatic repulsion.^[171] Like the carpet mechanism, the toroidal pore mechanism is initialized by monomeric α AMPs accumulating at the outer leaflet of the cytoplasmic membrane assuming an α -helical structure oriented parallel to the membrane surface (**Figure 14A-C**).^[171, 181] At high peptide concentrations and subsequent to thinning of the membrane, α AMPs begin to insert vertically into the membrane.^[171, 181] This results in the formation of toroidal pores (**Figure 14D**), the walls of which are composed of the peptides oriented perpendicular to the surface and the lipid head groups between them.^[171] Consequently, the lipids in the toroidal pore connect the inner and outer leaflet forming a single surface (**Figure 14**, expansion). The supramolecular complex of anionic lipid head groups and cationic peptides is able to shield the electrostatic repulsion between the peptides. As a consequence, there are no or only limited peptide-peptide interactions in the toroidal pore, which is in contrast to the barrel stave model.^[171] Connection of the inner and outer membrane leaflet by the pore enables rapid lipid flip-flopping.^[170, 171] Further, the pore allows the passage of peptides into and cytosolic compounds out of the cell (**Figure 14E**). Peptides will diffuse to the inner membrane leaflet, effectively weakening the membrane at the outer and the inner leaflet (**Figure 14F**). The stability and size of the pores are influenced by various factors, such as the properties of the peptide, peptide concentration, the membrane composition, or the transmembrane potential.^[146, 182, 183] Pore stability and size, in turn, have a direct influence on the pore selectivity and peptide translocation across the membrane.^[183]

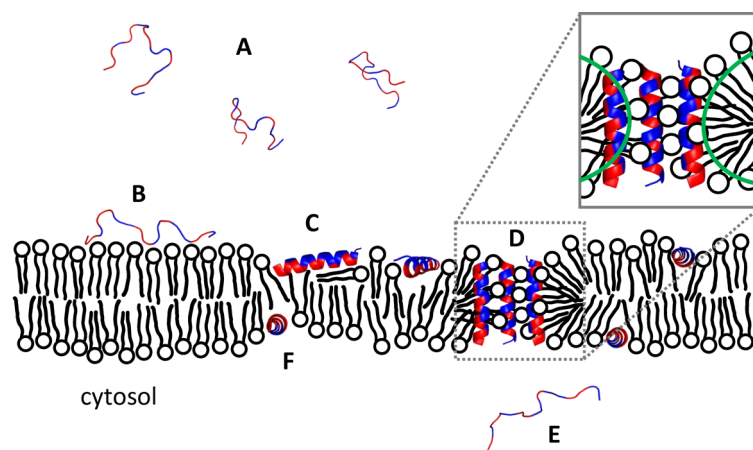


Figure 14: Toroidal pore mechanism. Hydrophilic residues of the peptides are colored in blue, hydrophobic residues in red. The phospholipids of the membrane are represented by black circles (head groups) and two wavy black lines (hydrocarbon tails). The expansion shows a cross-section of the toroidal pore. The green lines indicate the pore lining which connects the outer and the inner leaflet of the membrane.

3.2.2.4. Aggregate mechanism

Initially described as a refinement of the toroidal pore mechanism, the aggregate model was published in 1999 by Robert E. W. Hancock and co-workers to describe the mode of action of short AMPs that are not long enough to span entire the membrane and therefore cannot form an ordered toroidal pore as described above.^[146] The aggregate model describes a more disordered state of the lipid-peptide supramolecular complex, which is similar to the toroidal pore with respect to the arrangement of the lipids, but the peptides are not necessarily vertically aligned (**Figure 15D**).^[146] All other steps (**Figure 15A-C, E, F**) are identical to the toroidal pore model. The variability in size and stability of those aggregates explain the frequently observed fluctuations of conductance in planar bilayer studies, as well as rapid lipid flip-flop and passage

of AMPs across the membrane.^[146] A minireview by Hancock and Chapple revisits the aggregate model rephrasing the aggregate as a “micelle-like complex” spanning the membrane.^[184] The term “micelle-like complex” emphasizes the disorder of the aggregate and implies that a pore, i.e. an open channel crossing the membrane, is not necessarily present.

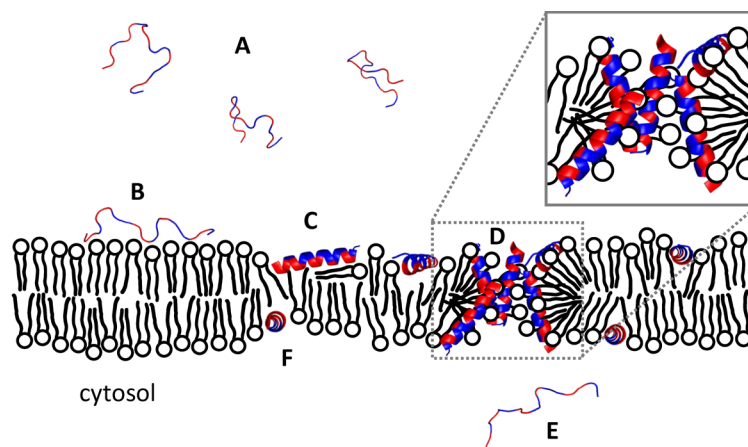


Figure 15: Aggregate mechanism. Hydrophilic residues of the peptides are colored in blue, hydrophobic residues in red. The phospholipids of the membrane are represented by black circles (head groups) and two wavy black lines (hydrocarbon tails). The expansion shows that the peptides in the aggregate are not all vertically aligned with respect to the membrane surface, which is in contrast to the toroidal pore model.

3.2.2.5. Detergent-like mechanism

Over time, the different models were refined and expanded to include new scientific evidence which led to their gradual assimilation and to inclusion of all the experimentally observed phenomena in comprehensive models.^[138, 139, 185–187] By proposing micelle-like complexes, the aggregate model uses analogies to detergents.^[184] However, detergent-like properties of α AMPs have more often been associated with the carpet model,^[95, 96, 139, 176, 185, 186, 188] because lysis of the membrane is the final step in this model. In their review from 2006, Burkhard Bechinger and Karl Lohner emphasize the detergent-like biophysical properties of linear, amphipathic, and cationic AMPs.^[187] Their proposed detergent-like model rationalizes the effect of those peptides on a lipid membrane on the basis of their molecular geometries and amphipathicity.^[187] For instance, the similar membrane-permeabilizing activity of the α AMP magainin 2 amide and the surfactants Triton X-100 and octyl glucoside was reported early.^[189] According to the detergent-like model, all three molecules have a more or less similar geometry^[187] simplistically described as cone-shaped with a short or shallow hydrophobic part and a large hydrophilic portion. Upon insertion into the membrane, they push apart the hydrophilic head groups of the lipids while being not able to fill the void space they create in the hydrophobic tail region. In consequence, they create a positive curvature strain on the membrane.^[187, 190–192]

The detergent-like model illustrates the complexity of intermolecular and supramolecular interactions in aqueous mixtures of peptides and lipids using phase diagrams.^[187, 192] An exemplary two-dimensional phase diagram with the variables “peptide concentration” (ordinate) and “lipid composition” (abscissa) is shown in **Figure 16**. Dependent on those two variables, peptide-lipid micellar aggregates, bicelles, lamellar bilayers or hexagonal phases may form.^[187] The toroidal pore, a carpet of peptides covering the membrane or peptide aggregates inside the membrane also each have their own regions in the phase diagram and are considered special cases that occur under distinct conditions.^[187, 192] Similarly, membrane micellation and

3. Antimicrobial Trp-cage proteins

fragmentation as described in the carpet model and its inhibition by cholesterol can be explained with detergent-like properties of AMPs.^[145, 192] Notably, the detergent-like mechanism is also able to rationalize transient membrane disruptions at low peptide-to-lipid ratios, which other models fail explain. When AMPs partition into the outer leaflet of the membrane they perturb the lipid order in a radius of a few nanometers around them. At low peptide-to-lipid concentration, lateral diffusion of the peptides may result in stochastic increases of the local concentration leading to an overlap of regions of reduced membrane stability and formation of transient membrane ruptures.^[187, 193] Another appealing feature of this model is its tunable complexity. In theory, more variables such as peptide composition, lipid concentration, temperature, pH or salinity can be added generating a multidimensional phase diagram in which each variable is represented in one dimension.

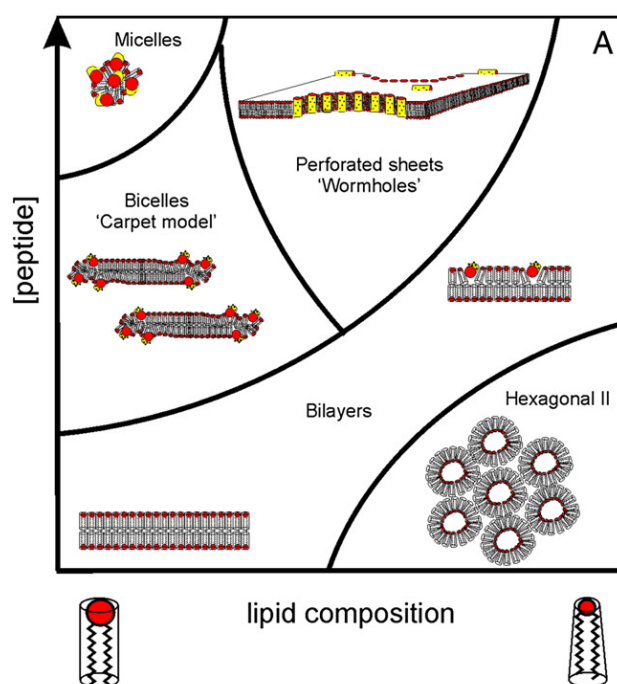


Figure 16: Two-dimensional phase diagram of a mixture of an α AMP with different lipid compositions.^[192] Peptides are depicted as yellow cylinders with red basal planes. Cylindrical lipids (i.e. with a large red head group) represent phosphatidylcholines, while inverted truncated cone-shaped lipids (i.e. with a smaller red head group) represent phosphatidylethanolamines. The term “wormholes” refers to toroidal pores.

Reprinted from Current Opinion in Colloid & Interface Science, volume 14, issue 5, Burkhard Bechinger, Rationalizing the membrane interactions of cationic amphipathic antimicrobial peptides by their molecular shape, pages 349-355, Copyright 2009, with permission from Elsevier.

3.2.2.6. Multi-target mechanism

A membrane-permeabilizing mode of action can be ascribed to almost any cationic AMP at high concentration^[194, 195] and extensive formation of pores or ruptures, regardless of the detailed mechanism, eventually leads to the collapse of the proton motive force, loss of cytosolic components and ultimately to growth inhibition or cell death. However, pore formation or - in extreme cases - lysis of the cell is not always the primary mode of action of an α AMP.^[185, 194] Many α AMPs have a bactericidal or bacteriostatic effect even at concentrations that are not sufficient for the formation of long-lived pores or ruptures. At these concentrations, the damage dealt to the membrane is not profound enough to explain the antimicrobial effect. However, these conditions do suffice to elicit short-lived membrane lesions that enable the peptides to

enter the bacterial cytoplasm. Once inside the cell, many α AMPs may disrupt intracellular processes resulting in the killing of the microbes, as the following examples demonstrate.

The analysis of four different α AMPs regarding their ability to dissipate the membrane potential of *E. coli* showed that membrane disruption does not necessarily coincide with the MIC.^[146] Depending on the peptide, membrane dissipation can occur well above or even below the MIC.^[146] The difference between MIC and membrane-depolarizing concentration is particularly large with the cationic, α -helical peptide P-Der, a chimera of pleurocidin and its homologue dermaseptin.^[195] Applied at concentrations well above its MIC, P-Der permeabilizes the cytoplasmic membrane of *E. coli* immediately and displays a killing efficiency of 99.8% after 10 min.^[195] At its MIC, however, P-Der translocates into the cytoplasm of *E. coli* without depolarizing the cytoplasmic membrane, where it is able to inhibit RNA synthesis.^[195] Additionally, in model membranes lipid flip-flopping was observed at concentrations that did not cause membrane permeabilization. Both effects, RNA synthesis inhibition and induction of lipid flip-flop, may contribute to its bacteriostatic effect on *E. coli* at P-Der's MIC, but other internal effects may also be involved.^[195]

The α AMP buforin II is particularly well characterized and highly active against Gram-positive and -negative bacteria as well as fungi.^[196, 197] Similar to P-Der, it does not lyse or perforate the cell membrane of *E. coli* or *B. subtilis* even at concentrations five times its MIC.^[197, 198] Supposedly, a kink in its helix^[149] induced by a proline residue is responsible for its non-pore-forming translocation across the cytoplasmic membrane.^[197, 199] In the cytoplasm, it is believed to act by binding to the negatively charged DNA and RNA.^[197–200]

Another well-studied α AMP with antimicrobial and anti-tumor activity but low hemolytic effect is NK-18.^[201, 202] It was shown to act on *E. coli* and *S. aureus* through a membrane-permeabilizing mechanism.^[202] In addition, high affinity to plasmid DNA was evidenced *in vitro*.^[202] Together, these findings indicate a double-action mechanism targeting the membrane and the DNA.

The α AMP SP1-1 has a unique mode of action as it targets the serine kinase RsbW with nanomolar affinity.^[203] Association of SP1-1 with this enzyme compromises RsbW's inhibition of the transcription factor SigB in *S. aureus*, leading to unregulated expression of downstream genes.^[203] In the cytoplasm, SP1-1 is also thought to bind bacterial plasmid DNA as *in vitro* DNA-binding assays suggest.^[203] Originally designed as an agent for plant protection, the non-hemolytic peptide SP1-1 was tested for pore-forming activity against the bacteria *Pseudomonas syringae* pv. *syringae* and *Clavibacter michiganensis* ssp. *michiganensis* resulting in concentration-dependent, but rather low membrane depolarization.^[204] Altogether, with some membrane activity, the ability to bind DNA, and high affinity to an important gene expression-regulating enzyme, the peptide SP1-1 makes a compelling case for a multi-target mechanism.

Indications for multi-target mechanisms of prototypical α AMPs were also found in a study analyzing the mode of action of α AMPs designed from a sequence template.^[205] The peptides elicit a membrane disruptive mode of action in *Staphylococcus simulans* (*S. simulans*), but hit *S. aureus* differently.^[205] Concentrations 10-fold the MIC against *S. aureus* had only little impact on the bacterium's transmembrane potential and did not evoke release of radioactively labeled glutamine from the cytosol. Active glutamine uptake, however, was largely inhibited after treatment with the peptides. Analysis of gene expression patterns before and after exposure to sublethal doses of one α AMP in a different *S. aureus* strain revealed that the peptide produced diverse stresses at the plasma membrane affecting cell wall synthesis, lipid metabolism and aerobic energy generation.^[205]

3. Antimicrobial Trp-cage proteins

These examples indicate that other targets than the cell membrane(s) may be as important for the mode of action of cationic α AMPs as their membrane disruptive function.^[185, 194, 205] At concentrations around the MIC α AMPs do not necessarily permeabilize the membrane, which indicates an intracellular mechanism. Even magainin 2, an α AMP with a high pore-forming activity^[170, 171] that was thought to act solely through membrane permeabilization,^[182] is able to translocate into the cytoplasm of *E. coli* at concentrations below its MIC.^[206] One may assume that cationic α AMPs reach the cytoplasm where they unspecifically bind to DNA or RNA through electrostatic interactions and thus interfere with macromolecule synthesis in the bacterium. Furthermore, non-membrane permeabilizing interactions of AMPs with the cytoplasmic membrane potentially influence lateral diffusion, disturb the organization of membrane domains or disorganize the leaflet asymmetry. Mounting evidence for multi-target modes of action lead to the conclusion that cationic α AMPs in general follow a mechanism aptly described as “sand in a gearbox”^[205] employing multiple low-affinity interactions with the microbial membrane(s) as well as internal targets.^[185, 194, 202, 205] Like a distributed denial of service attack, each individual interaction is harmless to the bacterium, but taken together the simultaneous attacks are overwhelming the bacterium’s defense mechanisms. Because many of these interactions may differ among bacterial species, a peptide may confer different mechanisms on different bacteria.^[205]

3.2.2.7. Fibrillary structures

The β -amyloid peptide, also referred to as amyloid- β ($A\beta$), is a peptide that is able to self-associate in a β -sheet conformation to form fibrillary structures found in brain plaques of patients with Alzheimer’s disease. Protofibrils of $A\beta$, i.e. short fibrillary aggregates with rather low molecular weights, were found to be cytotoxic.^[207] Recently, it was shown that these fibrillary aggregates have membrane-permeabilizing capacities.^[208] Moreover, antimicrobial properties have been demonstrated for a variety of amyloid peptides.^[209] The similarities between amyloid peptides and AMPs become even more obvious, when considering that certain β -sheet antimicrobial peptides are also capable of forming fibrillary structures.^[207, 210–212] More surprising, however, is the fact that β -sheet structure is not a prerequisite for fibril formation. The following examples show that even α AMPs may spontaneously form amyloid fibrils and raise the question whether the formation of fibrils is a mode of action of α AMPs.

The 17-residue α AMP uperin 3.5 (GVGDLIRKAVSVIKNIV-NH₂) was discovered in skin secretions of the Australian toadlet *Uperoleia mjobergii*. The peptide is prone to forming amyloid fibrils at neutral pH at concentrations of 0.5 μ M,^[213] which is well below its MIC against several Gram-positive bacteria^[214]. While pores were formed by uperin 3.5 in lipid bilayers mimicking mammalian cytoplasmic membranes, bacterial membrane mimics were disintegrated by uperin 3.5.^[215] The type of membrane activity of uperin 3.5 was independent from its aggregation state, although monomeric uperin 3.5 was observed to have faster kinetics^[215] and lower MICs^[214]. Incubation of uperin 3.5 in the presence of the Gram-positive bacterium *M. luteus* or small unilamellar vesicles (SUVs) mimicking a bacterial membrane induced fibril formation.^[214] Surprisingly, uperin 3.5 was found to form two kinds of fibrillary structures: cross- α and cross- β fibrils, which were composed of monomers in α -helix or β -sheet conformation, respectively.^[214] While the cross- β fibrils formed upon heating of uperin 3.5 and were relatively inactive, the formation of cross- α fibrils was induced not only from monomers, but also from β -fibrils, both in presence of a microbial membrane.^[214] The fibril formation was hypothesized to be of biological relevance for the toadlet. Possibly, monomeric uperin 3.5 is

secreted constantly and when no bacteria are present, the peptide may adopt its cross- β fibrillary structure to be stored safely. In the presence of bacteria, however, cross- β fibrils may be converted into active cross- α fibrils.^[214] It remains unknown whether the cross- α fibrils have direct antimicrobial activity, or whether they just facilitate the release of monomeric uperin 3.5 which then targets the bacterial membrane.

Similar to uperin 3.5, the α AMP human cathelicidin LL-37 was also shown to be able to form fibrillary structures. The presence of 10 μ M LL-37 drives the aggregation of liposomes composed of saturated phospholipids into tubular structures with a diameter of approximately 10 μ m.^[216] Analysis of the liposome-peptide interaction by transmission electron microscopy (TEM) showed fibrillary structures with a diameter of approximately 10 nm, i.e. thousand-fold smaller than the macroscopic tubular structures. Those fibrils formed only in the presence of saturated phospholipids and were assumed to drive the formation of the tubular superstructures from liposomes *via* an unknown mechanism.^[216] No nanoscale fibrils were formed when LL-37 was mixed with unsaturated phospholipids or lipid mixtures containing cholesterol.^[216]

Like uperin 3.5, the peptide LL-37₁₇₋₂₉ (FKRIVQRIKDFLR), a fragment of human LL-37, forms thermostable fibrils in the presence of the *M. luteus*. The fibrils aggregate into ribbons with a few hundred nanometers in width and several micrometers in length.^[217] It was even possible to obtain a crystal structure of the fibrils formed by LL-37₁₇₋₂₉. Surprisingly, the peptide assumes an α -helical conformation, when incorporated into the fibrils.^[217] Regular patterns of hydrophilic and hydrophobic patches at the surface of those fibrils are thought to be responsible for their ability to interact with bacterial membranes.^[217]

The ability to shift between α -helical and β -sheet structure has not only been observed in uperin 3.5, but also in the α AMP GL13K (GKI I K L K A S L K L L -NH₂).^[218] It was shown to form fibrils under basic conditions and during the process, its secondary structure was observed to shift in a pH-dependent manner from unstructured to β -sheet to α -helical.^[219] Although the bacterial susceptibility assays were performed in conditions that were too acidic to observe fibril formation, an impact of fibril formation on the MIC has been postulated by the authors.^[219] NMR^[218] and CD^[220] studies did reveal formation of β -sheet structures in the presence of biomembrane mimics, but did not inform about the aggregation state. In consequence, the importance of fibril formation for biological activity of GL13K remains inconclusive.

These examples show that fibril formation by AMPs is currently a topic of active research. There are several observations that argue against fibril formation being a mode of actions. In uperin 3.5 and its derivatives, for example, the propensity to form amyloid fibrils was shown to be inversely correlated with their membrane disrupting activity.^[215] Moreover, monomeric uperin 3.5 was observed to have faster membrane-permeabilizing kinetics^[215] and lower MICs^[214] than in the fibrillary state. Most importantly, formation of fibrils often requires hours, while other antimicrobial peptides have been reported to kill bacteria^[205, 221–223] or at least dissipate their membrane potential^[146] within minutes. Therefore, the formation of cross- α fibrils may plausibly also take place after the microbe was killed by the non-fibrillary uperin 3.5.

Other observations indicate that amyloid fibrils have direct antimicrobial activity. For instance, uperin 3.5 and LL-37 form fibrils which are nucleating at the microbial membrane surface. The direct interaction of the membrane and the fibril may plausibly negatively affect the bacterial membrane integrity. Most amyloid peptides are not cytotoxic in their monomeric state or when self-assembled into fibrils, but only in the protofibrillary state.^[207] Potentially, the formation of protofibrils nucleating at the bacterial membrane surface may have a bactericidal effect. Unfortunately, the causality between antimicrobial action and (proto)fibril formation is

3. Antimicrobial Trp-cage proteins

difficult to prove and future studies are required to determine whether formation of fibrils or protofibrils truly is a mode of action of AMPs or just a peculiar phenomenon.

3.2.3. α -helical AMPs: Peptide design

The goal of many AMP design studies is to provide highly active, non-toxic AMPs that have a high bioavailability, are cheap to produce, and able to kill antibiotic-resistant pathogens *in vivo*. Understanding which parameters affect an AMP's observable macroscopic properties including activity against different pathogens, hemolysis, toxicity against mammalian cells, or bioavailability is crucial for the design of active, peptide-based antibiotics. In general, the observable, macroscopic effects of AMPs result from intermolecular interactions dictated by molecular properties which in turn are determined by the sequence of amino acids. The intermolecular interactions imply phenomena as peptide-membrane interactions, peptide aggregation, enzymatic degradation, or peptide-DNA interactions. Molecular properties include among others hydrophobicity, amphipathicity, net charge, helical propensity, peptide length, and structural characteristics such as kinks or unfolded regions. While the molecular properties of α AMPs are relatively easy to deduce from a given short primary structure, the countless intermolecular interactions *in vivo* add such complexity to the system that the resulting macroscopic properties are much more difficult to understand in detail. A review article summarizing the most important computational and non-computational approaches to AMP design was recently provided by Marcelo D. T. Torres, César de la Fuente-Núñez and colleagues.^[224] This subchapter will reflect on the historic development of α AMP design.

3.2.3.1. Rational and heuristic design of α AMPs

Soon after the discoveries of HDPs in a variety of species, such as cecropins^[225] in hemolymph of cecropia moth (*Hyalophora cecropia*) pupae or magainins^[223] in the skin of African clawed frogs (*Xenopus laevis*), synthetic analogs were produced and compared to variants with point mutations or deletions in order to figure out what sequential characteristics determine antimicrobial activity.^[226–228] From first structure-activity relationship (SAR) studies like these in the 1980s it became apparent that cationicity, helicity, and amphipathicity are important determinants for the activity of α AMPs. With this knowledge, α AMPs were designed *de novo* from regular repeats of cationic and hydrophobic residues.^[229, 230] Other early α AMP design studies combined different parts of α HDPs creating chimeric peptides with improved properties, concluding that kinks or hinges between two helical stretches may be an important structural feature in cecropins and cecropin-derived peptides.^[161, 231] In the process of developing broadly potent α AMPs, Magainin Pharmaceuticals, Inc. produced over 200 substitution and deletion variants of magainin and PGLa. Their data set confirmed the importance of basicity and hydrophobicity for activity against a broad spectrum of pathogens, but indicated an increased hemolytic activity when the hydrophobicity was too pronounced.^[232]

In the 1990s new sources to inspire the design of α AMPs were exploited such as amphipathic and cationic helical segments derived from larger proteins.^[233, 234] The implementation of synthetic combinatorial libraries (SCLs) was another big innovation in α AMP design during that time.^[235, 236] SCL approaches can yield active and selective α AMPs^[236] but synthesis and screening of SCLs is a complex endeavor and extracting information from SCLs requires elaborate deconvolution techniques.^[235, 236] In consequence, this approach is not easily implemented in laboratories and has not been applied in many studies.

In the late 1990s and in the 2000s, more systematic attempts were made to quantitate the influence of molecular parameters on the antimicrobial activity and cell selectivity of α AMPs, such as hydrophobicity,^[237–239] hydrophobic moment,^[237, 238, 240] (inducible) helicity,^[237, 238, 241, 242] charge^[237] and angle subtended by hydrophobic or charged residues^[183, 238, 243]. For instance, a non-continuous hydrophobic face interrupted by a hydrophilic residue was shown to reduce the hemolytic effect of α AMPs.^[123, 244] Similar approaches to identify the influence of molecular parameters were conducted using data base-supported design of α AMPs,^[96, 162, 205, 245, 246] facilitated by the many sequences of α AMPs and α HDPs that had been identified and archived by that time. Notably, Alessandro Tossi and co-workers evaluated a data set of more than 150 natural α AMPs within the Antimicrobial Sequences Database (AMSDb; now offline) and gained empiric information on the typical ranges of the parameters net charge, content of hydrophobic residues, and amphipathicity.^[96, 162] They created a sequence template based on the first 20 N-terminal residues of each database entry (**Table 3**).^[96, 162] The N-terminal domain was chosen, as it “is generally essential and often sufficient for antimicrobial activity”.^[96]

Table 3: The sequence template by Alessandro Tossi and colleagues.^[96, 162]

1	2	3	4	5	6	7	8	9	10	11	12	13	14	15	16	17	18	19	20
G	⊕	⊕	±	+	⊕	X	±	X	⊕	±	+	⊕	⊕	+	+	⊕	X	±	G
			p	p		G	p			p	p		G	p				p	

This sequence template represents the average N-terminal stretch of more than 150 natural α AMPs of the AMSDb. Each position is marked by one or two symbols indicating the most common type of amino acid in the indicated position: Glycine (G), hydrophobic (⊕), positively charged (+), either positively or negatively charged (±), polar (p), no preference for any specific residue (X).

With this template a series of 20 systematically altered, short peptides was synthesized and characterized in order to determine the influence of the individual molecular parameters on the macroscopic properties.^[96, 162] Unfortunately, it is hardly possible to modify one molecular property without affecting others when using only the standard 20 amino acids. For example, an Ile→Lys mutation not only affects the net charge, but also the hydrophobicity, amphipathicity and helical propensity. Therefore, non-standard residues were incorporated to uncouple the different molecular properties from each other and to identify their individual importance for antimicrobial activity.^[96, 162]

3.2.3.2. Computational design of α AMPs

Since the turn of the millennium, increasing computing power combined with growing data bases collecting structural and activity data on AMPs and HDPs facilitated the development of computational approaches to α AMP design.^[224, 247] The discovery of AMPs in previously uncharted sequence space, i.e. design of AMPs with no or only limited sequence identity to known AMPs, is the goal of many computational design studies. Those *de novo* design strategies, also referred to as quantitative SAR (QSAR) studies, are commonly based on a set of AMPs that is statistically evaluated based on so-called descriptors, i.e. measurable or computable properties that are responsible for or at least co-occur with antimicrobial activity. Found correlations are then used to predict the activity of novel peptides. The accuracy of the prediction is highly dependent on the size (and accuracy) of the original dataset, the chosen descriptors, and the statistical method. To obtain a very large training dataset, two landmark articles^[248, 249] from 2009 reported the use of high-throughput methods^[250] to synthesize more than 1400 AMPs and to analyze them regarding their antimicrobial activity. The resulting dataset was used as the input for artificial neural networks (ANNs) to predict the antimicrobial activity of 100,000 hypothetical antimicrobial peptides that are each nine residues in length.^[248, 249] Two

3. Antimicrobial Trp-cage proteins

lead candidates, the α AMPs HHC-10 (KRWWKWIRW) and HHC-36 (KRWWKWRR),^[248] were synthesized and showed high *in vitro* activity against a variety of pathogenic bacteria. They were even successfully applied in a murine *S. aureus* infection model.^[248]

An important computational method is pattern recognition, which scans datasets of AMPs for common patterns in their sequences. For instance, the α -core formula, a sequence template similar to the one developed by Alessandro Tossi and co-workers (**Table 3**), was found by pattern recognition. The α -core formula was then used to screen protein sequences archived in data bases of the public domain in order to identify protein fragments with predicted antimicrobial activity.^[251] Pattern recognition was also involved in an early method of computational AMP design which has been introduced as a “linguistic model” because the detected patterns of residues in a set of natural AMPs resemble the grammatical rules of a language.^[252] A similar pattern recognition method was also used in a design algorithm called Joker. The Joker algorithm was used to convert inactive peptides into antimicrobial peptides by introducing mutations according patterns identified in a dataset of antimicrobial peptides.^[253] Similarly, patterns detected in AMPs have been used for the *de novo* design of α AMPs.^[254] A different study sought to design highly selective α AMPs based on a dataset comprising 73 frog-derived AMPs with published antimicrobial and hemolytic activities. In this study, pattern recognition was combined with other descriptors including the sequence moment.^[124] This descriptor is a vector representing the asymmetry of a peptide’s hydrophobicity along its sequence. The sequence moment was shown to be correlated with a peptide’s therapeutic index, i.e. its selectivity towards bacterial cell over erythrocytes. The algorithm produced the α AMP adeptanin 1 which was shown to exhibit high activity against Gram-negative bacteria and a low hemolytic behavior.^[124] Remarkably, although using only amphibian AMPs as input, adeptanin 1 does not resemble any natural AMP.^[124]

Genetic algorithms, also referred to as evolutionary algorithms, are peptide design methods inspired by Darwin’s theory of evolution. Computer-aided genetic algorithms have been applied already in the 1990’s,^[255] but more recent approaches are based on much larger datasets and more complex fitness functions.^[256, 257] In general, genetic algorithms are based on a peptide which is subject to mutation resulting in a set of mutated peptides. The peptides in this new set are evaluated with regard to a certain property, e.g. antimicrobial activity. The best peptides are selected for further mutation and peptides that do not fit the selection criteria are discarded. The mutation/selection cycle is repeated until a peptide has evolved that fits the required properties, e.g. high antimicrobial activity. The approach may be pursued entirely without computational aid, but this would imply the synthesis and testing of hundreds or thousands of peptides. To reduce time and expense, instead of introducing random mutations, mutations may be directed by a machine learning algorithm which increases the probability of obtaining peptides with the desired property. This principle was tested when the AMP temporin-Ali^[258] (FFPIVGKLLSGLL-NH₂) was subject to two almost identical genetic algorithms. Their only difference was that in only one of them the mutations were directed by a machine learning algorithm, that would use the previously synthesized and characterized generations of peptides as training input.^[256] When the mutations were selected by the machine learning algorithm, the average activity of each generation would improve and would finally converge at the third generation.^[256] In contrast, when mutations were implemented randomly, each generation contained only a few highly active peptides but also many peptides with low or no activity.^[256] It should be noted, however, that the most active peptides from either strategy were similarly active with MICs against *E. coli* ranging between 0.5 μ M and 2 μ M.^[256] This study showed, that

machine learning may be applied together with synthesis and testing to reduce the amount of inactive sequences resulting from evolutionary peptide design. However, computational methods may also be used for the *in silico* evaluation of randomized mutants to entirely replace the experimental synthesis and testing during each cycle, as was shown by a study starting from four fragments of the plant AMP Pg-AMP1.^[257] The mutation/selection cycles were performed entirely *in silico* using a so-called fitness function based on the hydrophobic moment and helical propensity.^[257] Starting from the same sequence, 100 independent simulations with 50 mutation/selection cycles each were performed resulting in a total of 100 final sequences. Peptides reflecting the 15 highest ranked sequences were synthesized and assayed *in vitro*.^[257] The best-performing candidate was guavanin 2, a 20-residue α AMP that primarily targets Gram-negative bacteria *in vitro* and in mouse models and acts through a membrane-permeabilizing mechanism.^[257]

With increasing datasets, it became apparent that there is no universal approach to design the most potent, least toxic antimicrobial peptide with broad-spectrum activity. Realizing the necessity for selectively active antibiotics, many researchers turned to developing α AMPs targeting only a specific group of pathogens. For instance, rational design by targeted mutation of a broadly potent, membrane-permeabilizing α AMP led to the discovery of a peptide targeting primarily Gram-negative bacteria.^[244] In a different case, the research group of Guangshun Wang, the developer and curator of the antimicrobial peptides database^[259] (APD), developed a computational database filtering technology to design a highly potent α AMP against methicillin-resistant *S. aureus* (MRSA).^[260] In this method, descriptor-based selection algorithms take into account the peptide length, charge, hydrophobicity, common residues and secondary structure of active AMPs to identify important residues to create an AMP with selectivity for Gram-positive bacteria. Subsequently, the identified residues were arranged into a peptide sequence according to a pattern analysis similar to a linguistic approach.^[260] Local sequence shuffling slightly increased the antibacterial activity, but more importantly drastically reduced the hemolytic effect, because of a non-continuous hydrophobic face of its α -helix.^[261] The resulting α AMPs DFT503 (GLSLLLSLGLKLL-NH₂) and DFT561 (GLKLLLSLGLKLL-NH₂) proved efficient in reducing the bacterial burden in neutropenic^a mice infected with MRSA.^[261] It was further shown that DFT503 would also enhance the immune reaction of non-neutropenic mice.^[261] Remarkably, DFT503 and DFT561 have a net charge of only +2 and +3, respectively, and increasing the net charge did not only increase the hemolytic effect but also resulted in a complete loss of efficiency *in vivo*.^[261]

3.2.3.3. α -helical AMPs: From bench to bedside?

Resistances of bacteria against AMPs occur less often than against conventional antibiotics because the mode of action of AMPs is not to block a certain receptor that may be altered as a consequence random mutations, but to disrupt the cell membrane and probably also employing a multi-target mechanism.^[262, 263] In consequence, those peptides have drawn the interest of academic research laboratories and of pharmaceutical companies.^[87, 91, 93, 153, 154] As early as 1987, Michael Zasloff, the discoverer of magainins, was one of the first researchers to recognize the “therapeutic potential [of antimicrobial peptides] in the treatment of bacterial, fungal, and

^a Neutropenic mice have a drastically reduced neutrophil count. Those mice are commonly used to assess the antibacterial activity of antibiotics without interference of neutrophils.

3. Antimicrobial Trp-cage proteins

protozoan infections in man".^[223] Indeed, there are many advantages of α AMPs that add to their benefit of eliciting only very few resistances in bacteria. Due to their small size and no requirement for post-synthetic modifications, α AMPs are easy to synthesize and characterize. They may be active against a wide spectrum of pathogens or designed to affect only specific targets. Finally, their peptidic nature renders them non-persistent if released into the environment. Opposing those advantages are several disadvantages that may include systemic or local toxicity, dependence of the activity on salinity or pH value, low bioavailability due to proteolysis or due to adsorption to components of body fluids and cells, development of sensitivities or allergies, as well as high production costs.^[87] The transfer from the laboratory (bench) into the clinic (bedside) is only possible, if those disadvantages are addressed and resolved.

Since the early 2000's, enzymatic degradation of α AMPs has been recognized to potentially limit the bioavailability *in vivo*^[154, 264–267] and strategies to avoid proteolysis of α AMPs are increasingly implemented in the design processes. Such strategies are based on amidation and acetylation of the C- and N-terminus^[153, 154, 268], incorporation of D-amino acids^[153, 268, 269] or other non-standard amino acids^[154, 269, 270], synthesis of peptides with sequences designed to avoid cleavage sites^[268, 271, 272], as well as stabilization of secondary structure through side chain cross-linking^[273, 274] (also referred to as peptide stapling). Protection of the N-terminus by acetylation and of the C-terminus by amidation is inexpensive when peptides are produced by solid phase peptide synthesis (SPPS). These measures provide protection against degradation by exopeptidases, but are inefficient with regard to endopeptidases. In contrast, all-D- α AMPs are not susceptible to enzymatic proteolysis at all.^[155, 156] Unfortunately, all-D-AMPs are very expensive to produce and their production cost will preclude their commercialization as therapeutics. However, α AMPs do not need to be composed entirely of D-amino acids to be resistant to proteases. Directed incorporation of only a few D- or other non-genetically encoded amino acids was also shown to provide resistance to enzymatic proteolysis,^[269, 270, 274] but these non-standard residues will also significantly increase the production costs compared to all-L-AMPs. An elegant and inexpensive way to increase the stability of α AMPs with regard to enzymatic proteolysis was achieved by arranging the residues in such a way that trypsin-, chymotrypsin-, and aureolysin-specific cleavage sites were avoided.^[272] The resulting peptide GNU7 (RLLRPLLQLLKQKLR) was highly active, short, composed of only gene-encoded L-amino acids, and nonetheless highly resistant to a selection of proteases.^[272]

Next to enzymatic degradation, toxicity is a potential weakness of α AMPs that needs to be addressed. Because a pore-forming or membrane-disrupting mode of action is assumed for most α AMPs, hemolysis is commonly used as an indicator for toxicity.^[120] However, hemolysis assays can at best report on the toxicity with regard to cell membrane permeabilization, but provide no information on the toxicity towards internal targets or immunomodulating effects (cf. chapter **3.2.1.1. Mammalian cell envelopes**). In addition to underestimating the toxicity, *in vitro* tests are not necessarily well-suited to predict the activity *in vivo*. For instance, the *in vivo* activity may be affected by a low bioavailability as a result of metabolism, degradation, or adsorption to tissues or serum components. Recognizing those point of concerns, more recent studies have evaluated the efficiency of α AMPs in animal models.^[248, 257, 261, 269, 274, 275]

Production costs have mainly been addressed by designing short antimicrobial peptides^[64, 276–278] – especially when techniques such as SCLs^[235] or high-throughput synthesis and screening^[248–250] are used. Longer peptides are more expensive to synthesize and recombinant production methods^[279–282] may become a cost-efficient alternative with increasing length. Of course, measures have to be taken to prevent the antimicrobial peptide from killing

the expression organism. Typically, AMPs are therefore produced as fusions with a protein to reduce the antimicrobial activity, increase the solubility, amplify the expression and facilitate the purification.^[280, 282] Cost-effective industrial scale production of AMPs by means of gene expression is currently restricted to the standard 20 gene-encoded amino acids.^[281, 282] Several strategies to prevent proteolytic degradation rely on D-amino acids or other non-standard residues and are therefore not compatible with recombinant AMP production. In addition, production costs for peptides or proteins produced by recombinant gene expression are still very high compared to standard antibiotics. Even if the costs for recombinant production of α AMPs could be brought down to the production costs of human insulin (approximately 25,000 US\$/kg)^[283], they would still by far exceed those of penicillin (20 US\$/kg).^[284] In conclusion, peptide antibiotics cannot compete with conventional antibiotics in terms of production costs, so far. Therefore, AMPs will most likely not be such mass products in the next 50 years, but will only be used in cases where cheaper antibiotics fail. In this niche, however, high production costs may be justified and accepted by the public.

Although most research regarding AMPs and HDPs is academic and/or pre-clinical, some of those compounds have already entered clinical stages.^[93] Of course, many compounds have failed to show efficiency in clinical studies, but many more are currently being developed or already in clinical trials.^[93] The majority of peptides are administered topically, while oral or intravenous administration is rare.^[93] Presumably, the relatively high concentrations required for antibiotic activity necessitate the administration of the active compound directly at the site of infection, e.g. in skin or wound infections by topical administration or in lung infections when administered by inhalation. As a positive side effect of the high costs and the limited cases where the use of AMPs may be indicated, however, their overuse in human medicine will be limited and their extensive use in veterinary medicine will be completely prohibited for economic reasons. Thus, mistakes that have been made in the past with conventional antibiotics may be prevented with AMPs. To conclude, many disadvantages of antimicrobial peptides hamper their development into therapeutics. Nonetheless, the hopes of finally obtaining an active antimicrobial drug that produces only few resistances in pathogens and beneficially modulates the immune response of the host continues to motivate researchers to find ways to circumvent those disadvantages and develop efficient peptide-based antibiotics.

3.3. Antimicrobial Trp-cage: Results

Peptide stapling is an approach to stabilize the α -helical structure of peptides by covalently cross-linking the side chains of two residues with $i, i+4$, $i, i+7$ or $i, i+11$ spacing and can be applied to α AMPs.^[273] Stapled α AMPs have been shown to be highly resistant to proteolytic degradation,^[274] presumably because of their stable α -helix. Proteases are known to cleave peptides only when they have the flexibility to assume an extended conformation. When constrained in an α -helical conformation, they cannot access the active site of any protease.^[285] Unfortunately, however, peptide stapling is not accessible through biosynthetic methods.

Stabilizing the α -helical structure of α AMPs in solution by introduction of a tertiary structure to protect them from enzymatic degradation is a new approach that has not been investigated yet. If an α AMP sequence is fused with a Trp-cage to form an antimicrobial Trp-cage (AMTC), the structural stability of the Trp-cage is expected to carry forward to the antimicrobial segment. This Trp-cage grafting approach should lead to a higher resistance against proteolysis, similar to the example of exendin-4. As in exendin-4, the increased proteolytic resistance is assumed to

3. Antimicrobial Trp-cage proteins

contribute to increased bioavailability *in vivo*. To this end, two AMTCs, i.e. KR-12-derived AMTC31-6 and IsCT-derived AMTC33-2, have been designed previously (cf. chapter 1.3.5. **En route to antimicrobial Trp-cage proteins**) and will be characterized here.

3.3.1. Unpublished results: AMTC33-2 and IsCT

The synthesis, purification, and biological activity of AMTC31-6 and KR-12 are reported and discussed in the original publication^[286], which is provided in the chapter 3.3.2. **Antimicrobial Trp-cage: Publication**. Here, they are listed merely for comparison with AMTC33-2 and IsCT.

Synthesis and purification of AMTC33-2 was performed by Sven Rothmund at the Faculty of Medicine, University of Leipzig. IsCT was synthesized by Andrea Ganesini analogous to the synthesis of KR-12 (cf. chapter 6.1.1. **Peptide synthesis**). I have purified the crude IsCT by means of HPLC using the Agilent PLRP-S column with the same gradient that was used for the purification of Helix19-6 (gradient 1; cf. chapter 6.1.2. **Peptide purification**).

3.3.1.1. Antibacterial activity of AMTC33-2 and IsCT

The antibacterial activity of AMTC33-2 and IsCT against *E. coli* and *Bacillus megaterium* (*B. megaterium*) was determined at pH = 7.5 and pH = 5.5, each with and without supplemented NaCl (150 mM). The assays were performed as described in the original publication.^[286]

With respect to *E. coli*, the antibacterial activity of AMTC33-2 and IsCT is similar, but both are drastically less active than AMTC31-6, regardless of pH or salinity (Table 4). Similar results are obtained from the antibacterial assays with *B. megaterium* (Table 5).

Table 4: MIC and MBC of AMTC31-6, KR-12, AMTC33-2 and IsCT against *E. coli*.

	<i>Escherichia coli</i>							
	pH = 7.5, 150 mM NaCl		pH = 7.5, 0 mM NaCl		pH = 5.5, 150 mM NaCl		pH = 5.5, 0 mM NaCl	
Peptide	MIC / μM	MBC / μM	MIC / μM	MBC / μM	MIC / μM	MBC / μM	MIC / μM	MBC / μM
AMTC31-6	0.313	0.313	0.313	0.313	0.039	0.039	0.078	0.078
KR-12	> 5		0.039	0.156	> 5		0.078	0.313
AMTC33-2	> 5		> 5		5	5	2.5	2.5
IsCT	5	> 5	2.5	> 5	> 5		2.5	2.5

X X is the average MIC or MBC, respectively, rounded to the nearest dilution level.

> X The respective MIC or MBC are above the concentration X in all measurements.

> X The average MIC or MBC, respectively, is above the concentration X, but individual measurements may be at or below X.

[empty] The MBC was not determined, because no activity was measured in the corresponding MIC assay.

Table 5: MIC and MBC of AMTC31-6, KR-12, AMTC33-2 and IsCT against *B. megaterium*.

	<i>Bacillus megaterium</i>							
	pH = 7.5, 150 mM NaCl		pH = 7.5, 0 mM NaCl		pH = 5.5, 150 mM NaCl		pH = 5.5, 0 mM NaCl	
Peptide	MIC / μM	MBC / μM	MIC / μM	MBC / μM	MIC / μM	MBC / μM	MIC / μM	MBC / μM
AMTC31-6	0.02	0.02	0.02	0.02	0.005	0.005	0.01	0.01
KR-12	0.02	0.02	≤ 0.002	≤ 0.002	0.078	0.078	0.002	0.005
AMTC33-2	1.25	1.25	0.625	1.25	0.313	0.625	0.156	0.156
IsCT	1.25	2.5	0.625	1.25	1.25	1.25	0.313	0.625

X X is the average MIC or MBC, respectively, rounded to the nearest dilution level.

$\leq X$ X is the lowest tested concentration and the peptide is active at that concentration.

IsCT was previously reported to be rather inactive against Gram-negative bacteria, although the activity against two different *E. coli* strains was in the range from 5 μM to 10 μM .^[65] Since the *E. coli* strain used here (*E. coli* K12 D31) has an LPS defect,^[287] the slightly lower MIC of IsCT detected here (2.5 μM – 5 μM) has been expected. The low activity of AMTC33-2 and IsCT against *B. megaterium*, however, is surprising, because this bacterium is known to be highly susceptible to antimicrobial peptides^[288] and IsCT has been reported^[65] to be more active against Gram-positive than Gram-negative bacteria.

Fusing the Trp-cage TC-KKA to IsCT did not have a large effect on the antibacterial activity. It slightly decreased the activity against *E. coli* at pH = 7.5, but not at pH = 5.5. In contrast, it slightly increased the activity against *B. megaterium* at pH = 5.5, but not at pH = 7.5.

3.3.1.2. Pore-forming activity of AMTC33-2 and IsCT

To assess whether a pore-forming mode of action is responsible for the antibacterial activity of the designed AMTCs, a liposome depolarization assay was performed. The method is described in the original publication.^[286] Briefly, a positively charged fluorescent dye is trapped in large multilamellar liposomes at concentrations sufficient for self-quenching of the fluorescence. An electrostatic gradient (negative inside, positive outside) keeps the dye inside the liposomes. Addition of pore-forming or membrane-disrupting peptides dissipates the membrane potential and releases the dye from the liposomes resulting in a measurable increase in fluorescence over time. The activity in $\text{U } \mu\text{M}^{-1}$ given in **Table 6** is a measure for the increase in fluorescence one minute after the addition of antimicrobial peptide. The liposomes are composed of soybean phospholipids containing zwitterionic and negatively charged head groups thus mimicking the bacterial plasma membrane.

Table 6: Pore forming activity of AMTC31-6, KR-12, AMTC33-2 and IsCT.

	AMTC31-6	KR-12	AMTC33-2	IsCT
Activity / $\text{U } \mu\text{M}^{-1}$	35.57	11.09	37.93	8.15
Standard deviation	12.39	9.35	7.75	6.65

The pore forming activity was determined for each peptide at a concentration of 0.1 μM .

Although AMTC33-2 and IsCT have similar activities against *E. coli* and *B. megaterium*, their performance in the liposome depolarization assay is very different (**Table 6**) and AMTC33-2 is able to dissipate the membrane potential much more efficiently than IsCT. Comparison with AMTC31-6 and KR-12 might indicate that a longer peptide probably forms more stable pores or disruptions in the membrane leading to a faster dissipation of the membrane potential.

3.3.1.3. Hemolytic activity of AMTC33-2 and IsCT

Since AMTC33-2 was shown to disrupt the membrane of liposomes, a hemolysis assay was performed to test whether it would also permeabilize the cell membrane of erythrocytes. The hemolysis assay was performed as described in the original publication.^[286]

IsCT is a toxin that was discovered in scorpion venom and its strong hemolytic effect has been described in the literature.^[65] In comparison to IsCT, AMTC33-2 is significantly less hemolytic (**Table 7**). Potentially, the Trp-cage domain of AMTC33-2 reduces the activity against human erythrocytes because it lowers the overall hydrophobicity compared to IsCT. Nonetheless, the hemolytic activity of AMTC33-2 is still rather strong compared to AMTC31-6 and KR-12.

Table 7: Hemolytic activity of AMTC31-6, KR-12, AMTC33-2 and IsCT in dependence of their concentration. The intensity of the red background coloring is proportional to the hemolytic activity.

c / μM	AMTC31-6	KR-12	AMTC33-2	IsCT
80	4	0	38	82
40	3	0	18	39
20	2	0	14	20
10	0	0	9	6
5	0	0	4	1
2.5	0	0	1	0
1.25	0	0	0	0

3. Antimicrobial Trp-cage proteins

The hemolytic activity of AMTC33-2 and IsCT is significant (i.e. larger than 1%) at concentrations of 5 μM and 10 μM , respectively, which is in the same range as their MIC against *E. coli*. Therefore, IsCT and AMTC33-2 were not considered further to be able to focus more on the characterization and development of the more promising AMTC31-6. Nonetheless, it is worth noting that fusion with a Trp-cage domain could mitigate the hemolytic potency of IsCT and was able to induce a stable α -helical structure at 1 $^{\circ}\text{C}$ (**Figure 6** in chapter **1.3.5. En route to antimicrobial Trp-cage proteins**), despite several helix disrupting residues (glycines and isoleucines; **Table 8**) in the sequence of IsCT.

Table 8: Sequence, length and charge of the AMTCs and their parent peptides. This table is identical to **Table 2**.

Peptide	Sequence	Length	Charge
Ac-TC-KKA	Ac-DKYAQWLADGGPSSGRPPPK	20	0
KR-12	KRIVQRIKDFLR-NH ₂	12	+5
AMTC31-6	KRIVQRIKDFLRKYAQWLADGGPSSGRPPPK	31	+6
IsCT	ILGKIWEGIKSLF-NH ₂	13	+2
AMTC33-2	ILGKIWEGIKSLFDKYAQWLADGGPSSGRPPPK	33	+2

3.3.2. Antimicrobial Trp-cage: Publication

Designed Trp-cage proteins with antimicrobial activity and enhanced stability

Nils Preußke, Matthias Lipfert, Sven Rothmund, Matthias Leippe and Frank D. Sönnichsen

Biochemistry **2021**, *60*, 3187-3199

DOI: [10.1021/acs.biochem.1c00567](https://doi.org/10.1021/acs.biochem.1c00567)

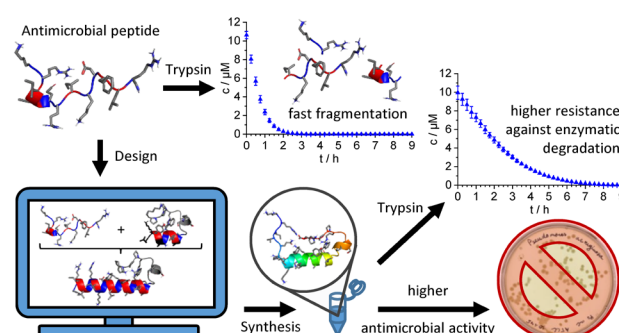


Figure 17: Graphical Abstract. A chimeric protein comprising an antimicrobial peptide fused to a Trp-cage domain displays not only increased antimicrobial activity compared to the parent antimicrobial peptide but also is digested significantly slower by trypsin or chymotrypsin.

Author contributions

Frank D. Sönnichsen, Matthias Lipfert, and Nils Preußke developed the concept. Matthias Lipfert, Nils Preußke, and Frank D. Sönnichsen designed AMTC31-6. Sven Rothmund synthesized and purified AMTC31-6. Nils Preußke designed, synthesized, and purified the other peptides. Nils Preußke performed the molecular dynamics (MD) simulations and structural characterizations. Matthias Leippe designed and Nils Preußke performed and evaluated the biological experiments. Nils Preußke designed, performed, and evaluated the digest experiments. Nils Preußke prepared the original draft. Nils Preußke, Matthias Lipfert, Matthias Leippe, and Frank D. Sönnichsen revised the manuscript. Matthias Leippe and Frank D. Sönnichsen supervised the work. Frank D. Sönnichsen, Matthias Leippe, and Nils Preußke acquired funding.

Designed Trp-Cage Proteins with Antimicrobial Activity and Enhanced Stability

Nils Preußke, Matthias Lipfert, Sven Rothmund, Matthias Leippe, and Frank D. Sönnichsen*



Cite This: *Biochemistry* 2021, 60, 3187–3199



Read Online

ACCESS |



Metrics & More

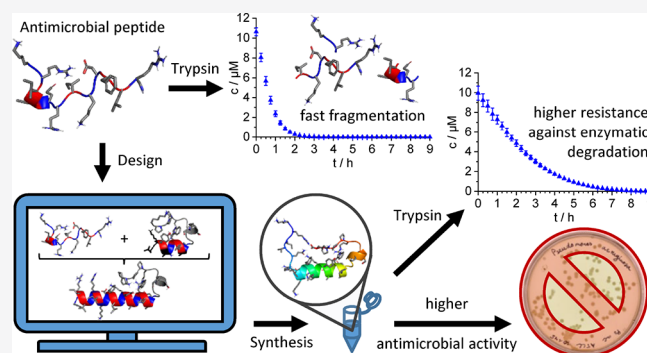


Article Recommendations



Supporting Information

ABSTRACT: α -Helical antimicrobial peptides (α AMPs) are among the potential candidates for new anti-infectives to tackle the global crisis in antibiotic resistance, but they suffer from low bioavailability due to high susceptibility to enzymatic degradation. Here, we describe a strategy to increase the resistance of α AMPs against proteases. Fusing the 12-residue α AMP KR-12 with a Trp-cage domain induces an α -helical structure in the otherwise unfolded KR-12 moiety in solution. The resulting antimicrobial Trp-cage exhibits higher proteolytic resistance due to its stable fold as evidenced by correlating sequence-resolved digest data with structural analyses. In addition, the antimicrobial Trp-cage displays increased activity against bacteria in the presence of physiologically relevant concentrations of NaCl, while the hemolytic activity remains negligible. In contrast to previous strategies, the presented approach is not reliant on artificial amino acids and is therefore applicable to biosynthetic procedures. Our study aims to improve the pharmacokinetics of α AMPs to facilitate their use as therapeutics.



1. INTRODUCTION

Antibiotic-resistant bacterial pathogens pose a serious threat to the efficiency of medical therapies that rely on antibiotics. The global economic consequences of antimicrobial resistance are estimated to compare to the effect of an average worldwide 2 °C temperature increase due to global warming.¹ The ongoing “crisis in antibiotic resistance”² is driving the investigation of antimicrobial peptides (AMPs) and host defense peptides (HDPs) as clinically applicable antibiotics.^{3,4} These peptides have a direct bactericidal mode of action, while HDPs often also comprise immunomodulatory functions and can potentially be used for the treatment of chronic inflammatory diseases.^{3,4}

Although their name might insinuate otherwise, α -helical AMPs (α AMPs) typically are disordered in aqueous solution. Upon insertion into the lipid membrane of their target organism, they assume the eponymous α -helical structure. Lack of a stable conformation in solution renders α AMPs susceptible to enzymatic proteolysis, which limits their bioavailability. LL-37, for instance, a drug candidate for the treatment of venous leg ulcers, is highly susceptible to degradation by ulcerous wound fluids^{5,6} and by proteases of bacterial^{6–9} or human^{8,9} origin. Strategies to slow the enzymatic degradation of α AMPs include N-terminal acetylation and C-terminal amidation,⁸ avoidance of cleavage sites by sequence design,^{8,10} incorporation of D-amino acids^{8,11,12} or other nonstandard amino acids,^{12,13} and intramolecular cross-linking.^{14,15}

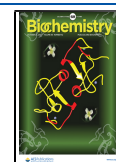
A different way to increase proteolytic resistance of peptides can be observed in exendin-4, an approved active agent for the treatment of diabetes mellitus type 2.¹⁶ The solution structure of exendin-4 is characterized by a unique folding pattern named the Trp-cage motif.¹⁷ The fold of exendin-4 is stabilized by clustering of hydrophobic side chains around a central tryptophan residue in an α -helix of five turns. At its N-terminus, the α -helix is gradually fraying and is preceded by a short disordered region.¹⁷ When incubated in human plasma, proteolytic cleavage of exendin-4 occurs in its unfolded N-terminal region only, indicating the role of the Trp-cage in exendin-4’s resistance to proteolytic degradation.¹⁸ Sequence optimizations and N-terminal shortening of exendin-4 yielded the Trp-cage miniprotein,^{19–21} a 20-residue protein that exhibits a stable fold but lacks biological activity.

Here, we present a strategy to design α AMPs with reduced susceptibility to enzymatic degradation. The approach relies on the stabilization of an α -helical structure in an α AMP directly fused to a Trp-cage domain. It exploits the fact that peptides

Received: August 20, 2021

Revised: September 17, 2021

Published: October 6, 2021



with a rigid structure are less susceptible to enzymatic degradation than those with a disordered conformation.

2. EXPERIMENTAL DETAILS

2.1. Peptide Design. Peptide design and molecular dynamics (MD) simulations were performed with Schrödinger Suite Release 2017-4 and 2020-4 (Schrödinger LLC, New York, NY, USA). The AMTCs were based on structure 1/28 of the Trp-cage variant TC10b (PDB: 2JOF). Additional residues of the AMTC's α -helix were added in an ideal α -helical conformation using Maestro (Schrödinger LLC, New York, NY, USA). Net charges were compensated by adding Cl^- , and the structures were geometrically relaxed by applying the force field OPLS3 with implicit water using MacroModel (Schrödinger LLC, New York, NY, USA). MD simulations were performed with the Desmond Molecular Dynamics System (D.E. Shaw Research, New York, NY, USA) and set up with the Maestro-Desmond Interoperability Tools (Schrödinger LLC, New York, NY, USA). The peptide was submerged in a cubic box ($125,000 \text{ \AA}^3$) of explicit water complying with the TIP4P-D water model.²² OPLS3e was the applied force field.²³ The temperature and pressure were set to 310 K and 1.01325 bar, respectively. MD simulations covered a period of 1000 ns with recording intervals of 1000 ps (trajectory) and 1.2 ps (energy). Depictions were created with Open-Source PyMOL Molecular Graphics System 1.9.0.0 (Schrödinger LLC, New York, NY, USA).

2.2. Peptide Synthesis. All peptides were synthesized using solid-phase peptide synthesis (SPPS) employing a fluorenylmethoxycarbonyl (Fmoc) protecting group strategy.²⁴ Apart from two dipeptides (DG and SS), standard Fmoc-protected amino acids with acid-labile side chain protecting groups were used. The DG-dipeptide Fmoc-Asp-(OtBu)-(DMB)Gly-OH (Novabiochem, Merck, Darmstadt, Germany) was used to avoid aspartimide formation during synthesis, and the SS-dipeptide was coupled as the pseudo-proline Fmoc-Ser(tBu)-Ser(psiMe,Mepro)-OH (Novabiochem, Merck, Darmstadt, Germany or Iris Biotech, Marktredwitz, Germany) to disrupt secondary structure effects during synthesis.

TC-KKA, KR-12, Helix19-6, AMTC26-4, AMTC27-6, and AMTC24-5 were synthesized on a microwave-assisted, semi-automated peptide synthesizer Initiator⁺ SP Wave (Biotage, Uppsala, Sweden). TC-KKA, AMTC26-4, AMTC27-6, and AMTC24-5 were synthesized on Wang resin (200–400 mesh, $860 \mu\text{mol g}^{-1}$, ChemPep, Wellington, FL, USA) on a 172 or 258 μmol scale. Helix19-6 and KR-12 were synthesized on Rink amide resin (100–200 mesh, $450 \mu\text{mol g}^{-1}$, ChemPep, Wellington, FL, USA) on a 90 μmol scale. Coupling was performed with 5 equiv of the corresponding amino acid or dipeptide using hexafluorophosphate azabenzotriazole tetramethyl uronium (HATU; 4.9 equiv) and *N,N*-diisopropylethylamine (DIPEA; 10 equiv) dissolved in DMF at 75 °C for 5 min. Capping was performed using a solution of DMF (50% v/v), pyridine (25% v/v), and acetic anhydride (25% v/v) at 75 °C for 5 min. Cleavage of the terminal Fmoc-protecting group was achieved with piperidine (25% v/v) in DMF at 75 °C for 5 or 9 min. Final cleavage and deprotection were achieved using a solution of trifluoroacetic acid (TFA; 90% v/v), 1,3-dimethoxybenzene (5% v/v), triisopropyl silane (TIS; 2.5% v/v), and water (2.5% v/v) for 3 ± 1 h at ambient temperature.

AMTC31-6 was synthesized on an automated peptide synthesizer MultiPep RS (Intavis, Köln, Germany) using

preloaded PHB-TentaGel resin (Rapp Polymere, Tübingen, Germany) on a 50 μmol scale. Standard Fmoc-protected residues (5 equiv) were coupled in a 1:1 mixture of DMF and *N*-methyl-2-pyrrolidone (NMP) at ambient temperature for 45 min using *O*-(1*H*-6-chlorobenzotriazole-1-yl)-1,1,3,3-tetramethyluronium hexafluorophosphate (HCTU; 5 equiv) and *N*-methylmorpholine (NMM; 10 equiv) as coupling agents. Each dipeptide (3 equiv) was coupled using DIPEA (6 equiv) and HATU (3 equiv) in DMF/NMP (1:1) at ambient temperature for 4 h. Removal of all protecting groups and cleavage from the resin occurred during the final reaction employing a mixture of TFA (94.8% v/v), TIS (2.6% v/v), and water (2.6% v/v) supplemented with phenol (2.5% m/m) for 4 h at room temperature.

The cleavage mixture was filtrated and the peptides were precipitated from the filtrate through addition of cold diethyl ether and were subsequently dried.

2.3. Peptide Purification. Purification of all peptides was achieved by means of reverse-phase (RP) high-performance liquid chromatography (HPLC) on a VWR-Hitachi LaChrom Elite instrument (VWR, Darmstadt, Germany) equipped with a VWR-Hitachi L2400 UV detector (VWR, Darmstadt, Germany) and a Foxy R1 fraction autocollector (Teledyne ISCO, Lincoln, NE, USA). The peptides were purified in small batches of approximately 10 to 100 mg of crude peptide. The preparative gradients were 90 min in length using water acidified with 0.1% (v/v) formic acid (FA) as solvent A and MeCN acidified with 0.1% (v/v) FA as solvent B. Peptides were prepurified on a semipreparative VP 250/32 Nucleosil 100-7 C18 column (dimensions: 250 mm \times 32 mm; pore diameter: 10 nm; particle size: 7 μm ; Macherey-Nagel, Düren, Germany) with a flow rate of 8 mL min^{-1} . A subsequent purification was performed using a PLRP-S column (dimensions: 325 mm \times 30 mm; pore diameter: 30 nm; particle size: 8 μm ; Agilent, Santa Clara, CA, USA) with a flow rate of 6 mL min^{-1} . Purified peptides were handled in a sterile environment to avoid contamination with microorganisms and other sources of proteases.

2.4. Analytical UHPLC. Ultrahigh-performance liquid chromatography (UHPLC) was performed with a Dionex Ultimate 3000 RS instrument comprising a solvent degasser, binary pump, autosampler, column compartment, and diode array detector (DAD) coupled to a QExactive Plus Hybrid Quadrupole-Orbitrap mass spectrometer (all instruments: Thermo Fisher Scientific, Waltham, MA, USA). The UHPLC device was equipped with an Accucore Polar Premium column (dimensions: 100 mm \times 2.1 mm; pore diameter: 15 nm; particle size: 2.6 μm) and precolumn (dimensions: 10 mm \times 2.1 mm; pore diameter: 15 nm; particle size: 2.6 μm ; column and precolumn: Thermo Fisher Scientific, Waltham, MA, USA).

The autosampler temperature and the column compartment temperature were set to 25.0 °C. LC-MS-grade water acidified with 0.1% (v/v) FA served as solvent A, while HPLC-grade MeCN acidified with 0.1% (v/v) FA served as solvent B. The flow rate was set to 0.4 mL min^{-1} , and the following gradient was applied: 0.0 min, 5% B; 1.0 min, 5% B; 9.0 min, 65% B; 9.5 min, 95% B; 11.0 min, 95% B; 11.5 min, 5.0% B; 13.3 min, 5% B. The DAD was set to detect signals at 220 and at 280 nm.

The daily calibrated mass spectrometer was equipped with a heated electrospray ionization (HESI) source and was set to operate in positive ion mode with a resolution power of 70,000

at full width at half maximum (FWHM) at $m/z = 200$ scanning an m/z range from 100 to 1500.

2.5. Creation of Peptide Stock Solutions. Lyophilized peptides were weighed on an AB135-S FACT analytical balance (Mettler-Toledo, Columbus, OH, USA) with a precision of 0.01 mg. Subsequently, they were dissolved in a defined amount of water to a concentration c_{weight} between 200 and 300 μM . The concentration c_{UV} of the peptides containing tyrosine and/or tryptophan (TC-KKA, Helix19-6, AMTC31-6, AMTC26-4, AMTC27-6, and AMTC24-5) was determined by ultraviolet and visible light (UV–Vis) spectroscopy using the method of Gill and von Hippel.²⁵ By averaging over all peptides and all measurements in which the concentration was determined with both methods ($n = 20$), the mean ratio of c_{UV} to c_{weight} was found to be $c_{\text{UV}}/c_{\text{weight}} = 0.79 \pm 0.08$. The concentration of KR-12 was determined by weight and corrected by multiplying it with the correction factor of 0.79

$$c(\text{KR-12}) = c_{\text{weight}}(\text{KR-12}) \cdot 0.79$$

Aliquots of each peptide with a known volume and concentration were lyophilized and stored at $-20\text{ }^{\circ}\text{C}$ until use. Prior to use, stock solutions of $(1.0 \pm 0.1)\text{ mM}$ in water were prepared from the aliquots, which were then diluted to the required concentration with the required buffer for the respective experiment. Even though the determination of concentration by UV–Vis spectroscopy is accurate, the subsequent lyophilization, creation, and dilution of stock solutions may lead to an error of approximately 10%.

2.6. pH Determination. The pH was determined using a pH meter 320 (Corning, Corning, NY, USA) equipped with a Spinrode pH electrode (Hamilton, Reno, NV, USA). The device was calibrated using two-point calibration at $\text{pH} = 4.01$ and $\text{pH} = 7.00$.

2.7. NMR Spectroscopy. NMR spectra were recorded on an AV II 600 Fourier transform–NMR spectrometer (Bruker, Billerica, MA, USA) at frequencies of 600.1 MHz for ^1H nuclei and 150.9 MHz for ^{13}C nuclei. The spectrometer was equipped with a triple-resonance cryoprobe (Bruker, Billerica, MA, USA). All samples were measured in Aldrich ColorSpec NMR tubes ($5 \times 178\text{ mm}$; precision: 500 MHz; Sigma-Aldrich, Merck KGaA, Darmstadt, Germany) at $25\text{ }^{\circ}\text{C}$. For every peptide, a solution in water with 8.3% (v/v) D_2O for locking was prepared from the stock solutions. The pH was adjusted to $\text{pH} = 5.5 \pm 0.1$ (not corrected for D_2O content) by addition of diluted aqueous NaOH, and the concentration was adjusted to $(400 \pm 40)\text{ }\mu\text{M}$. For referencing, each sample contained 7.6 μM sodium 4,4-dimethyl-4-silapentane-1-sulfonate (DSS) as an internal standard. The peptide concentration in each NMR sample (Table S8) was assessed by integrating the DSS reference signal and comparing its intensity to that of the peptide's high field aliphatic signals (in the range between 0.8 and 1.1 ppm) and to the intensity of the Trp $\text{H}^{\epsilon 1}$ signals (reduced signal intensity of the Trp $\text{H}^{\epsilon 1}$ due to exchange with deuterium was considered in the calculation).

^1H chemical shifts were identified using ^1H , ^1H -correlation spectroscopy (COSY), ^1H , ^1H -total correlation spectroscopy (TOCSY), and ^1H , ^1H -nuclear Overhauser enhancement spectroscopy (NOESY). ^{13}C chemical shifts were obtained from ^1H , ^{13}C -heteronuclear single quantum coherence (HSQC) spectroscopy. Assignments according to IUPAC recommendations²⁶ are given in Tables S9–S22. The sequence identity of every peptide was confirmed by sequential assignment using

$(i, i + 1)$ -NOE signals. To calculate the chemical shift deviation (CSD or $\Delta\delta$; $\Delta\delta = \delta_{\text{observed}} - \delta_{\text{random coil}}$), random coil shifts were taken from Wishart et al.²⁷ CSD plots (Figures S2 and S3) were analyzed to check for helicity according to Wishart and co-workers.^{28,29}

All homonuclear proton experiments used excitation sculpting with gradient pulses (ESGP) for water suppression.³⁰ For the HSQC spectra, water suppression was achieved using presaturation. The data were processed using TopSpin 4.0.6 (Bruker, Billerica, MA, USA) and analyzed using NMRviewJ 9.2.0-b24 with Java 1.8.0_192 amd64 (One Moon Scientific, Westfield, NJ, USA).

2.8. CD Spectroscopy. CD spectra were recorded on a J-720 spectropolarimeter (Jasco, Pfungstadt, Germany) equipped with a Haake WKL 26 thermostat (Thermo Electron Corporation, now Thermo Fisher Scientific, Waltham, MA, USA) and a PTC-423S Peltier element (Jasco, Pfungstadt, Germany). All measurements were performed with the same quartz glass cuvette with an optical path length of 1.00 mm. Samples for CD spectroscopy were prepared by diluting an aliquot of the NMR sample with a 10 mM aqueous buffer of sodium acetate adjusted to $\text{pH} = 5.5 \pm 0.1$ (Table S23). Full spectra were recorded at $25\text{ }^{\circ}\text{C}$ (Figure 2A) and at $37\text{ }^{\circ}\text{C}$ (Figure S4A) in the range from 200 to 250 nm with a data pitch of 1 nm and were averaged over 12 measurements. Each spectrum was background-corrected.

Thermal unfolding (Figure 2B) was observed at the wavelength of 222 nm in the range of 5 to $80\text{ }^{\circ}\text{C}$ or $90\text{ }^{\circ}\text{C}$ with a data pitch of $1\text{ }^{\circ}\text{C}$. Two consecutive cycles of heating and cooling were averaged for each melting curve. A heating and cooling rate of $1\text{ }^{\circ}\text{C min}^{-1}$ was applied. Prior to the measurement, the sample was equilibrated at the starting temperature for at least 5 min. Background subtraction was applied. Melting curves of the peptides TC-KKA, AMTC31-6, and AMTC26-4 were fitted with a sigmoidal Boltzmann function (Table S24).

2.9. Minimal Inhibitory Concentration Assay. The bacterial strains *Bacillus megaterium* ATCC 14581 as well as the LPS-impaired³¹ and streptomycin- and ampicillin-resistant^{32,33} *Escherichia coli* K12 D31 are rather susceptible to antimicrobial peptides,³⁴ and they were chosen to detect even minor antibacterial activities. To assess the antibacterial activity against clinically relevant strains, *Staphylococcus aureus* ATCC 12600 and *Pseudomonas aeruginosa* ATCC 10145 were used. Bacteria were grown in lysogeny broth (LB) medium (10 g L^{-1} tryptone, 5 g L^{-1} yeast extract, and 10 g L^{-1} NaCl dissolved in water) in a shaking incubator at $37\text{ }^{\circ}\text{C}$ under aerobic conditions to the mid-exponential phase. The bacterial suspension was diluted with fresh LB medium to a concentration of 10,000 cfu/mL immediately prior to use.

The serial microdilution assay was performed in sterile, transparent, and round-bottom polypropylene 96-well plates. To reduce the hydrophobicity of the wells' surfaces, they were incubated with a sterile solution (0.1% w/v) of bovine serum albumin (BSA) in water for 20 min (200 μL /well) and emptied so that only a thin film remained on the well walls. Each well was filled with 90 μL of serially diluted peptide (2-fold dilution per step) in sterile 10 mM sodium phosphate buffer adjusted to $\text{pH} = 5.5 \pm 0.5$ or $\text{pH} = 7.5 \pm 0.5$. For assays at higher salinity, the buffer was supplemented with 150 mM NaCl. Ten microliters of a 10,000 cfu mL^{-1} bacterial suspension was added to each well. Melittin (from honey bee venom, 91.8% purity by HPLC, Sigma-Aldrich, Merck,

Darmstadt, Germany) served as a positive control and buffer containing no peptide served as a negative control. Sterile LB medium served as a sterile control. The plates were incubated at 37 °C for (18 ± 2) h. After this period of incubation, the plates were centrifuged at 1800g for 3 min to enforce the formation of a bacterial pellet. Each peptide was analyzed in duplicate per assay, and each assay was performed at three different days ($n = 6$). The minimal inhibitory concentration (MIC) is the average lowest concentration of the peptide (rounded to the nearest dilution level) at which no bacterial growth is visible using binoculars after the incubation period.

2.10. Minimal Bactericidal Concentration Assay. The minimal bactericidal concentration (MBC) assay was performed immediately after the analysis of the MIC assay. Ten microliters was taken from the first well below the MIC (positive control), the well at the MIC, and the first one or two wells above the MIC of each row of the MIC assay and spread on separate sterile LB agar plates (LB medium gelled with 15 g L⁻¹ agar). As a negative control, sterile LB agar was spread on an agar plate. The agar plates were incubated at 37 °C for (18 ± 2) h. The MBC is the average lowest concentration of the peptide (rounded to the nearest dilution level) at which no bacterial colonies are apparent on the agar plates after the incubation period.

2.11. Liposome Depolarization Assay. The liposome depolarization assay was performed essentially as described³⁵ using large multilamellar liposomes. To prepare the liposomes,³⁶ 60 mg of crude extract of soybean phospholipids type II-S (P5638, Sigma-Aldrich, Merck, Darmstadt, Germany) was dissolved in 1.5 mL of chloroform in a 250 mL round-bottom flask. The solution was blow-dried with nitrogen while carefully spinning the flask to create an even and thin layer, which was dried in vacuo for (18 ± 2) h. The lipid film was reconstituted in 1.5 mL of liposome buffer (water, 50 mM tris(hydroxymethyl)aminomethane (Tris) maleate, 50 mM K₂SO₄, 0.5 mM ethylenediaminetetraacetic acid (EDTA), and 0.02% (m/v) sodium azide; adjusted to pH = 5.2 with KOH) by gently agitating it with a few glass beads. The mixture was transferred into a small glass vial and sonicated at 0 °C to gain a clear solution. The solution was subjected to three freeze-and-thaw cycles using dry ice and a water bath of 37 °C. Finally, it was sonicated for 15 s and stored at (6 ± 2) °C until use.

Two microliters of the liposome suspension and 8 μL of a 2 mM solution of the fluorescent dye 3,3'-diethylthiadicarbocyanine iodide in ethanol (final conc.: 2 μM) were mixed with 8 mL of cuvette buffer (water, 50 mM Tris maleate, 50 mM Na₂SO₄, and 0.5 mM EDTA; adjusted to pH = 5.2 with NaOH) through short and gentle agitation and equilibrated to 25 °C. Two milliliters of this suspension was filled into a polystyrene fluorescence cuvette. Fluorescence was measured with a fluorescence spectrophotometer LS50B (PerkinElmer, Waltham, MA, USA) using excitation wavelengths of 620 nm and emission wavelengths of 670 nm. Approximately 40 s into the measurement, the cuvette was taken out of the instrument, and 4 μL of a 0.5 μM valinomycin solution in ethanol was added to a final concentration of 1 nM. The cuvette was gently agitated and quickly placed back into the (still recording) spectrometer. Addition of valinomycin creates a K⁺ diffusion potential across the liposome membrane driving the dye into the liposomes, effectively quenching the fluorescence. Once a stable fluorescence level was reached, 4 μL of a 50 μM peptide solution in 10 mM HCl was added to the cuvette to a final

concentration of 0.1 μM in a process identical to the addition of valinomycin. The addition of a pore-forming peptide will dissipate the K⁺ diffusion potential, releasing the dye from the liposome and leading to restoration of fluorescence over time. A 5% restoration of fluorescence intensity 1 min after the peptide was added is defined as 1 U of activity. The assay was performed at three different days and at least in triplicate each time for each peptide ($n \geq 9$). The activity was averaged over all measurements and was corrected by subtracting the average activity of a blank sample (4 μL of 10 mM HCl in water). Four microliters of a 50 μM alamethicin (from *Trichoderma viride*, ≥ 98% purity by HPLC, Sigma-Aldrich, Merck, Darmstadt, Germany) solution in ethanol served as a positive control.

2.12. Hemolysis Assay. Human erythrocytes (blood group A, Rh(D)-positive) were obtained as a concentrate for infusion from the Institute of Transfusion Medicine of the University Clinic of Schleswig-Holstein (UKSH, Kiel, Germany). Twenty milliliters of erythrocyte concentrate was washed three times by addition of 30 mL of sterile hemolysis buffer (water, 50 mM Na₂HPO₄ and 150 mM NaCl adjusted to pH 7.4 with 6 M HCl), careful mixing, centrifugation (20 min, 500g), and removal of the supernatant. A total of 1.25 mL of the washed erythrocyte concentrate was diluted with 8.75 mL of hemolysis buffer to gain a 12.5% erythrocyte suspension.

The serial microdilution assay was performed in sterile, transparent, and V-bottom polypropylene 96-well plates. To reduce the hydrophobicity of the wells' surfaces, they were incubated with BSA as described for the MIC assay. Each serial dilution implied 12 different dilution levels with a twofold dilution per step. Each well was filled with 80 μL of serially diluted peptide in hemolysis buffer. Twenty microliters of the dilute (12.5%) erythrocyte suspension was added to each well. Melittin served as a positive control, and a blank sample containing no peptide served as a negative control. Osmolysis of erythrocytes, which was achieved by adding 20 μL of the 12.5% erythrocyte suspension to 80 μL of sterile deionized water, was defined as 100% lysis. The plates were incubated at 37 °C for 1 h. After this period of incubation, the plates were centrifuged at 550g for 1 min. Twenty microliters of the supernatant was transferred into a corresponding well of a flat-bottom transparent polypropylene 96-well plate already containing 180 μL of hemolysis buffer per well. The absorption at 405 nm of each well was measured with a LEDETECT96 microplate reader (Deelux Labortechnik, Gödenstorf, Germany). The hemolytic activity of each peptide concentration was expressed in % and calculated according to the following formula

$$\% \text{hemolytic activity} = \frac{A_{\text{sample}} - A_{\text{neg. control}}}{A_{100\% \text{ lysis}} - A_{\text{neg. control}}} \cdot 100$$

where the averaged absorption at 405 nm of the osmolysis wells was defined as $A_{100\% \text{ lysis}}$, A_{sample} is the absorption at 405 nm of the well of interest, and $A_{\text{neg. control}}$ is the average absorption of the negative control wells. Each peptide was analyzed in duplicate per assay, and each assay was performed at four different days ($n = 8$). Activity was considered significant when it was larger than 1%.

2.13. Enzymatic Degradation Monitoring. The enzymatic degradation monitoring assay was performed as described in detail in the Supporting Information. Briefly, a calibration curve of the parent peptide at 10, 8, 6, 4, and 2 μM was recorded. Subsequently, the parent peptide (10 μM) was

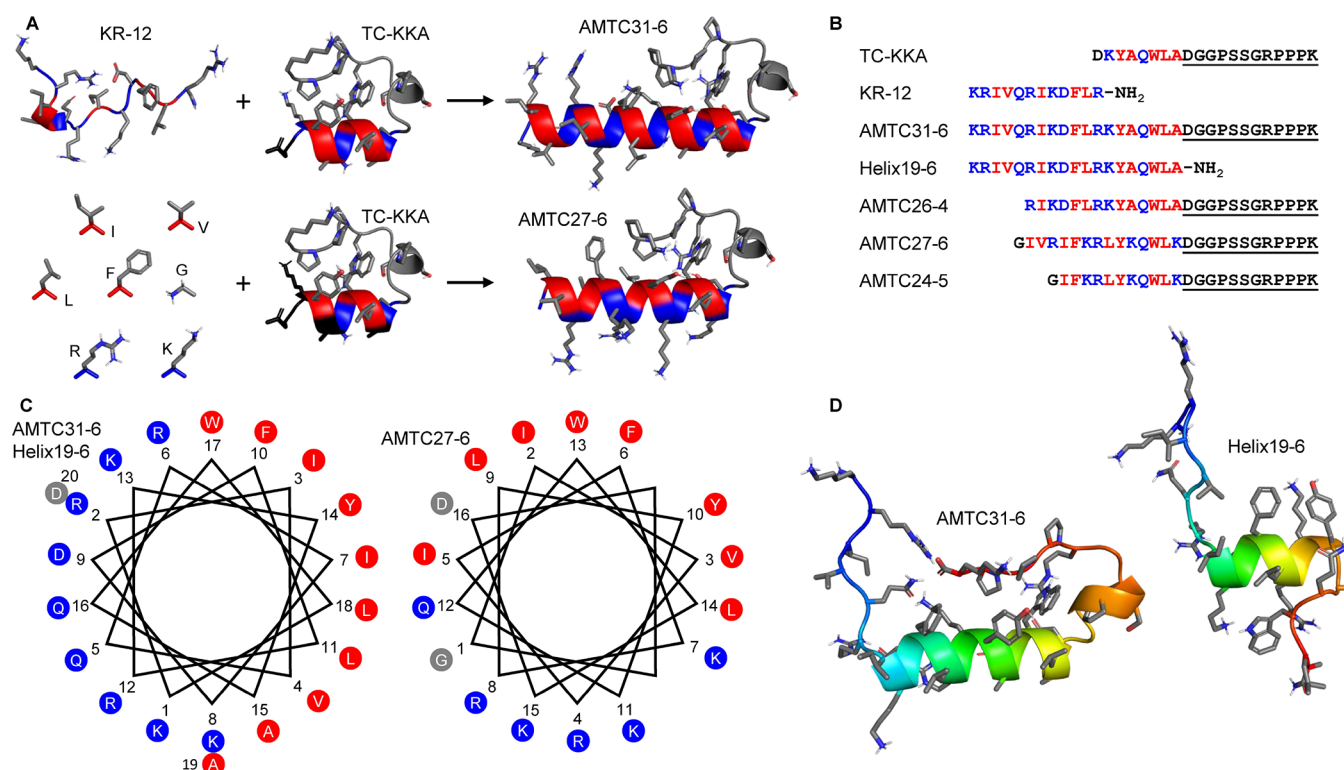


Figure 1. Design of AMTCs. Blue and red indicate hydrophilic or hydrophobic residues, respectively, of the α -helix. (A) Design concept of AMTC31-6 and AMTC27-6. While the model AMTC31-6 was obtained from fusing KR-12 and TC-KKA_{2–20} in silico, AMTC27-6 was designed de novo from TC-KKA and from bulky hydrophobic residues as well as basic residues. Glycine was chosen as the N-capping residue. Residues of TC-KKA depicted in black were replaced, and they are not part of the AMTC. The backbone of the Trp-cage loop is colored in gray. (B) The sequences of all peptides synthesized for this study are displayed. Colored residues are expected to form an α -helix in the membrane-associated state. Underlined residues form the Trp-cage loop in the solution state. (C) The helical wheel projections of the α -helix of AMTC31-6 (left) and AMTC27-6 (right) are oriented in the same way as in panel (A), i.e., with the tryptophan residue and the Trp-cage domain facing up. Helix-capping residues are colored in gray. The D20 of AMTC31-6 is not part of Helix19-6, but apart from this difference, their helical wheel projection is identical. (D) Representative structures of AMTC31-6 and Helix19-6 were obtained from molecular dynamics (MD) simulations of both peptides. The backbone is shown in cartoon style with rainbow coloring (N-terminus: blue; C-terminus: red). AMTC31-6 is oriented similar to its depiction in panel (A). In general accordance with NMR spectroscopic observations, its N-terminus is unfolded until R6, but the rest of the peptide is well structured. In this depiction, Helix19-6 is helical between residues I7 and Y14 but not across the whole peptide to indicate nascent helicity.

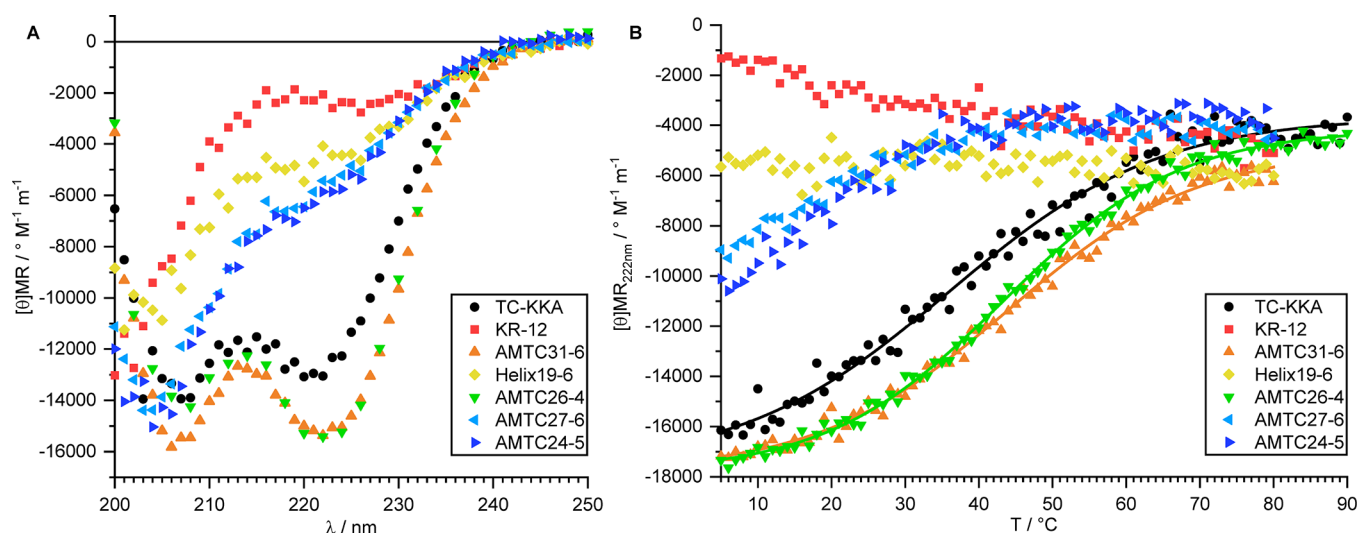


Figure 2. CD data. (A) CD data were recorded at 25 °C and at pH = 5.5. The mean residue molar ellipticity $[\theta]_{MR}$ is plotted over the wavelength λ . A negative band at 222 nm is indicative of helicity. (B) The mean residue molar ellipticity at 222 nm $[\theta]_{MR_{222\text{nm}}}$ was recorded at pH = 5.5 in a temperature range of up to 90 °C to monitor thermal unfolding. Two heating and cooling cycles were averaged for each peptide. Because of slight thermal degradations in TC-KKA and AMTC26-4 after two heating cycles to 90 °C, the other peptides were only heated to 80 °C. T_m 's obtained from sigmoidal Boltzmann fits are stated in Table 1, while the complete sets of fit parameters are given in Table S24.

Table 1. Structural Properties^a

peptide	$T_m/^\circ\text{C}$	sequence	solution structure at 25 °C
TC-KKA	35.9 ± 1.1	DKYAQLADGGPSSGRPPPK	D1: dynamic α -helix K2–A8: stable α -helix D9–K20: stable Trp-cage loop
KR-12	n.a.	KRIVQRIKDFLR-NH ₂	K1–R12: random coil
AMTC31-6	44.0 ± 0.5	KRIVQRIKDFLRKYAQLADGGPSSGRPPPK	K1–V4: random coil Q5–I7: dynamic α -helix K8–A19: stable α -helix D20–K31: stable Trp-cage loop
Helix19-6	n.a.	KRIVQRIKDFLRKYAQLA-NH ₂	K1–V4: random coil Q5–A19: nascent α -helix
AMTC26-4	43.3 ± 0.3	RIKDFLRKYAQLADGGPSSGRPPPK	R1–D4: dynamic α -helix F5–A14: stable α -helix D15–K26: stable Trp-cage loop
AMTC27-6	<10	GIVRIFKRLYKQWLKDGPPSSGRPPPK	G1–I5: random coil F6–K15: dynamic α -helix D16–K27: dynamic Trp-cage loop
AMTC24-5	<10	GIFKRLYKQWLKDGPPSSGRPPPK	G1–I2: random coil F3–K12: dynamic α -helix D13–K24: dynamic Trp-cage loop

^aThe T_m (\pm the standard deviation resulting from the fit) was determined by CD spectroscopy, and it reports the thermal stability of the peptides' α -helix. Melting point determination is not applicable (n.a.) for KR-12 and Helix19-6 as those peptides do not show melting behavior. The solution structure descriptions at 25 °C are based on the CSD (Figures S2 and S3) and NOE analyses (Tables S1–S7). The stability of a structural element in a protein is characterized as follows: unstructured = random coil < nascent < dynamic < stable.

placed in the temperature-controlled autosampler of a UHPLC-MS device and a chromatogram was recorded (t_0). One microliter of enzyme solution at a defined concentration was added, and the digest was monitored for 9 h by withdrawing and analyzing a sample every 15 min. The chromatograms were processed using TraceFinder 4.1 (Thermo Fisher Scientific, Waltham, MA, USA), considering multiple adducts and charge states for every parent peptide and fragment.

3. RESULTS

3.1. Design and Structure of the Antimicrobial Trp-cage. **3.1.1. Fusion Approach.** Because of its stable fold, the Trp-cage variant TC10b[K8A]²⁰ was the starting point for designing the first antimicrobial Trp-cage (AMTC). As a higher net charge is often beneficial for the membrane activity of AMPs,^{37,38} the net charge of TC10b[K8A] was increased from -1 to $+1$ through the mutations A2K and S20K, resulting in the Trp-cage TC-KKA (Figure 1). Characterization by circular dichroism (CD) and nuclear magnetic resonance (NMR) spectroscopy found TC-KKA to adopt the typical Trp-cage fold¹⁹ at 25 °C. However, the two mutations A2K and S20K led to a decrease in stability of the fold characterized by a midpoint of thermal unfolding at $T_m = (35.9 \pm 1.1)^\circ\text{C}$ (Figure 2 and Table 1) compared to $T_m(\text{TC10b}) = (45.4 \pm 0.9)^\circ\text{C}$ (cf. Supporting Information, p. 25) and to the presence of some un- or misfolded by-forms at 25 °C (12%; Supporting Information, p. 3, and Figure S1). TC-KKA possesses a short N-terminal α -helix as evidenced by CD spectroscopy (Figure 2), NMR chemical shift deviations (CSDs) of the H $^\alpha$ and C $^\alpha$ nuclei (Figure S2), and ($i, i + 3$) and ($i, i + 4$) nuclear Overhauser enhancement (NOE) signals (Table S1). With three bulky hydrophobic residues on one side (Y3, W6, and L7) and four polar residues that are located roughly on the opposite side (D1, K2, Q5, and D9), the α -helix of TC-KKA has amphipathic character (Figure 1).

The 12-residue peptide KR-12 served as the antimicrobial part of the first designed AMTC (Figure 1). As a fragment of LL-37, KR-12 is reported to be active against several bacteria while being short and nonhemolytic.^{39–41} According to CD spectroscopy (Figure 2), NOE analysis (Table S2), and H $^\alpha$ - and C $^\alpha$ -CSD evaluation (Figure S2), KR-12 is completely unstructured in solution.

When combining KR-12 and TC-KKA in silico, the D1 of the Trp-cage was eliminated to align the hydrophobic faces of the helices on the same side in the fused protein (Figure 1). Being a helix-capping residue, the D1 of TC-KKA was not required when the helix was elongated. Moreover, the elimination of its negative charge should be beneficial for the activity of the AMTC. The chimeric miniprotein resulting from the fusion of KR-12 and TC-KKA_{2–20} was termed as AMTC31-6, where 31 is the number of residues and 6 is the peptide's net positive charge. The stable α -helicity of the Trp-cage was expected to carry forward to the KR-12-derived part of AMTC31-6 in solution. Any antimicrobial activity of AMTC31-6 was presumed to come from its amphipathic α -helical part (residues K1–A19). Similar to exendin-4, whose Trp-cage loop unfolds completely upon association with dodecylphosphocholine micelles,¹⁷ the Trp-cage loop of AMTCs should be unstructured in the membrane-associated state. As unstructured termini are common in the membrane-associated state of AMPs,^{39,42–44} an unfolded Trp-cage loop of AMTC31-6 was not expected to have a severe effect on its biological activity.

The fusion of KR-12 and TC-KKA_{2–20} led to an increase in fold stability of AMTC31-6 ($T_m = (44.0 \pm 0.5)^\circ\text{C}$) compared to TC-KKA (Figure 2B and Table 1). A detailed NMR analysis of AMTC31-6 including CSDs (Figure S2) and NOEs (Table S3) indicated a random coil conformation between residues K1 and V4 with an onset of helicity at residue Q5 transitioning to a highly stable α -helix (Table 1). Presumably, the high density of positive charges (N-terminus, K1, R2, R7, and K8)

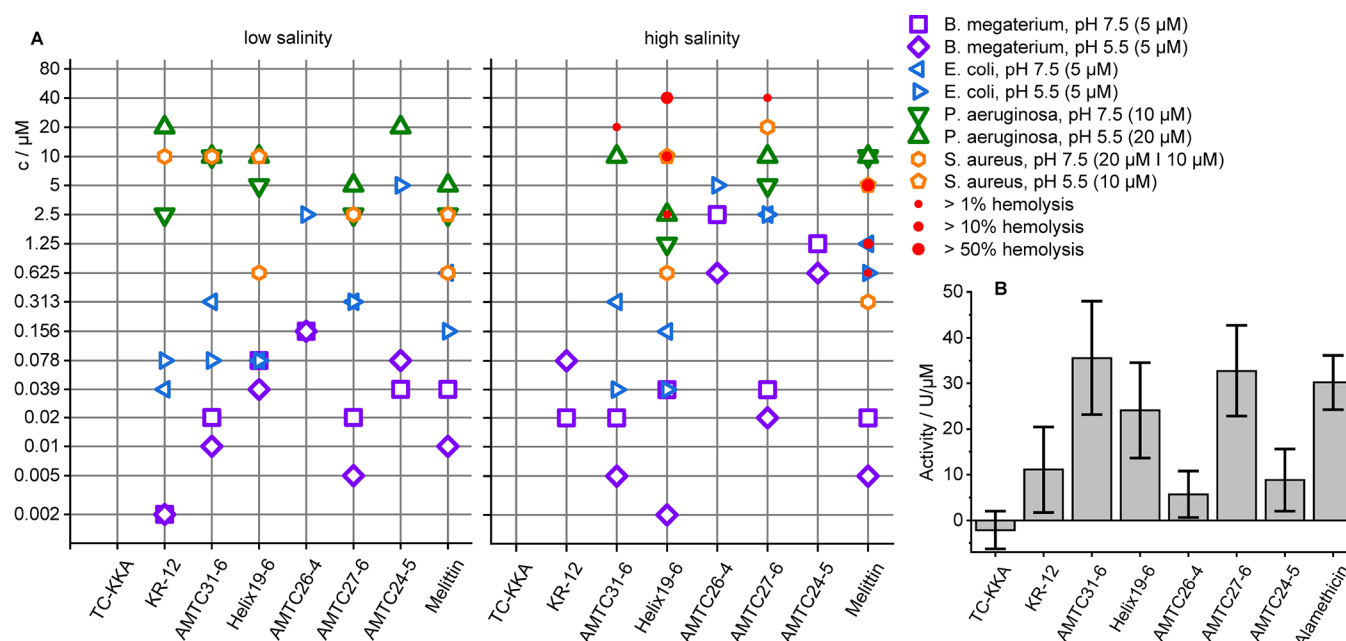


Figure 3. Antibacterial, hemolytic, and pore-forming activity. (A) The average ($n = 6$) minimal inhibitory concentration (MIC) against *B. megaterium*, *E. coli*, *P. aeruginosa*, and *S. aureus* is displayed for every peptide at pH = 5.5 and pH = 7.5 at low salinity (without addition of NaCl; left) and high salinity (addition of 150 mM NaCl; right). The error of measurement is within ± 1 dilution level. The hemolytic activity was assessed only at high salinity at pH = 7.4. The maximum concentration of each assay is stated in the panel legend in brackets. In the case of the assay with *S. aureus* at pH = 7.5, the maximum concentration was 20 μM at high salinity and 10 μM at low salinity. The highest tested concentration of the hemolysis assay was 80 μM . When no symbol of a certain assay is present in a column, the respective peptide was not active under these conditions in the tested concentration range. MICs, MBCs, and hemolytic activities including their standard deviation are given in Tables S25–S33. Values of every individual measurement are given in Data S1. (B) The pore-forming activity is displayed for every peptide in this study and for alamethicin. The peptide concentration was 0.1 μM . Each column represents an average of at least nine measurements (cf. Data S1); error bars represent the standard deviation. A graphical example how the pore-forming activity was determined is given in Figure S5.

and β -branched residues (I3, V4, and I7) within the first eight residues prevent helix formation in the first four residues. Nonetheless, the stable, amphipathic α -helix between residues K8 and A19 results in a large, solvent-exposed hydrophobic face in AMTC31-6 because only the residue W17 is completely shielded from the solvent by the Trp-cage loop.

To identify the impact of the Trp-cage loop on the structure, resistance against enzymatic proteolysis, or biological activity, the peptide Helix19-6 was included in this study. Comprising the 19 N-terminal residues of AMTC31-6 and a C-terminal amidation but lacking a Trp-cage loop, the structure of Helix19-6 is very dynamic in solution. Its four N-terminal residues assume a random coil conformation. The other residues of the peptide show characteristics of a nascent α -helix as evidenced by a weak, negative CD band at 222 nm (Figure 2A), weak CSDs (Figure S2), and weak ($i, i + 3$)-NOEs (Table S4).

To determine how truncation affects the stability and activity of AMTC31-6, residues 1–5 (KRIVQ) were eliminated, resulting in AMTC26-4. With a melting point at $T_m = (43.3 \pm 0.3)^\circ\text{C}$, this peptide is of similar stability as AMTC31-6 (Figure 2B and Table 1). The α -helix of AMTC26-4 is fraying in the first turn (R1–D4) but displays high stability in the following 2.5 turns (F5–A14) as indicated by CD spectroscopy (Figure 2), CSDs (Figure S2), and NOEs (Table S5).

3.1.2. De Novo Design. Contrary to AMTC31-6, the peptide AMTC27-6 was devised without using a known natural AMP motif (Figure 1). The Trp-cage loop of AMTC27-6 is identical to that in AMTC31-6, but the α -

helix was designed de novo. Being shorter and having a modified orientation of the hydrophobic face of the α -helix relative to the Trp-cage loop, AMTC27-6 was designed to have a smaller solvent-accessible hydrophobic surface in solution. This design was chosen because a large solvent-exposed hydrophobic face of a preformed α -helix has been associated with increased hemolytic activity¹⁴ or decreased antimicrobial activity.⁴⁵ When displaying the helix of AMTC27-6 in a helical wheel projection (Figure 1C), the essential tryptophan residue of the Trp-cage, W13, is located in the center of the hydrophobic sector. In consequence, the Trp-cage loop is covering the hydrophobic side of two helix turns (Figure 1A). Only upon association with a microbial membrane should the Trp-cage loop unfold, driven by insertion of the complete hydrophobic side of the helix into the membrane. Following this positioning, the hydrophilic face of the helix was devised using mainly R and K to reach a desired net charge of +6. To simplify the NMR analysis, the hydrophobic side comprises different large hydrophobic residues (V, I, L, and F). G was chosen as the N-capping residue because it had been identified as the most common first residue in α -helical AMPs.³⁷

The melting point of AMTC27-6 was estimated to be $T_m < 10^\circ\text{C}$ (Figure 2B and Table 1), and its solution structure was found to be dynamic at 25 $^\circ\text{C}$ as indicated by a shoulder rather than a minimum at 222 nm in the CD spectrum (Figure 2A) and by a significant number of un- or misfolded by-forms (23%; Supporting Information, p. 3, and Figure S1). The β -branched residues I2, V3, and I5 presumably reduce the helical propensity at the N-terminus. The main reason for the high flexibility of AMTC27-6 is, however, its high positive charge

density that counteracts helix formation through multiple repulsive interactions. AMTC27-6 displays a much higher helical propensity at high pH when the lysine charges are neutralized (Figure S4B). Still, CSDs (Figure S3) and NOEs (Table S6) indicate dynamic helicity in the region of F6–K15 of AMTC27-6 corresponding to 2.5 helical turns (Table 1). As a result of the dynamic α -helix, the stability of the Trp-cage loop is reduced compared to TC-KKA as evidenced by generally lower CSDs. Nonetheless, according to the CSDs, the stability of AMTC27-6 is higher than that of Helix19-6 (Figures S2 and S3).

To keep the Trp-cage intact, truncation of AMTC27-6 was restricted to residues near the N-terminus. Eliminating two β -branched residues (I2 and V3) and one charged residue (R4) in AMTC27-6 resulted in the peptide AMTC24-5 (Figure 1), which is only slightly more stable than AMTC27-6 (Figure 2 and Figure S3). Both peptides are very dynamic; nonetheless, characteristics of an α -helix and the Trp-cage fold are present.

3.2. Biological Activity. **3.2.1. Antibacterial Activity.** The peptides' antibacterial activity was tested by microdilution susceptibility assays in phosphate buffer at two different pH values (pH = 5.5 \pm 0.5, pH = 7.5 \pm 0.5), with or without the addition of 150 mM NaCl (Figure 3A and Tables S25–S32). Peptides that showed growth inhibition were subjected to a minimal bactericidal concentration (MBC) assay. Minimal inhibitory concentration (MIC) and MBC assays were performed with two rather susceptible bacteria (*B. megaterium* and *E. coli*) and two robust pathogenic bacteria (*S. aureus* and *P. aeruginosa*). With the exception of KR-12, the averaged MIC and MBC were mostly identical (occasionally deviating by one dilution step) for all peptides. With KR-12, however, the MBC was typically 4-fold (two dilution steps) higher than the MIC. Of the tested peptides, only TC-KKA expectedly was not active against any bacterium under any condition.

Comparison of the activities of KR-12 and AMTC31-6 provides insights into how the fusion with TC-KKA_{2–20} affects activity. At low salinity, both peptides show similar high to reasonable activity against the bacteria tested. However, while the activity of KR-12 is highly dependent on the NaCl concentration, the activity of AMTC31-6 against most bacteria is virtually independent of the salinity. AMTC31-6 outperforms KR-12 at high salinity with any of the four bacteria and at any tested pH.

The role of the Trp-cage loop of AMTC31-6 can be identified when comparing this peptide with Helix19-6 that lacks this loop. Against *E. coli*, both peptides are similarly effective in the submicromolar range at mildly acidic pH irrespective of the salinity. At neutral pH, however, Helix19-6 has an advantage of one or two dilution levels over AMTC31-6. Against *S. aureus*, Helix19-6 achieves submicromolar MICs and MBCs at neutral pH and both salinities, whereas AMTC31-6 exhibits drastically reduced activity at high and low NaCl concentrations. At mildly acidic pH and regardless of the NaCl concentration, i.e., conditions where *S. aureus* is very resistant against AMPs, Helix19-6 reaches an MIC and MBC of 10 μ M, but AMTC31-6 is inactive in the tested concentration range. The results with *P. aeruginosa* are similar but less pronounced. AMTC31-6 is active at concentrations of 10 μ M against this bacterium under all tested conditions except neutral pH and high salinity. Helix19-6, in contrast, is active at low micromolar concentration at high salinity (1.25–2.5 μ M) but displays slightly higher MICs (5–10 μ M) under conditions with no added NaCl.

Truncation of AMTC31-6 by elimination of its first five residues resulting in AMTC26-4 led to a drastic loss of activity under any tested condition. Apparently, the two positive charges and two bulky hydrophobic residues are very important for the activity of AMTC31-6.

Despite an identical net charge (+6) and a very similar amino acid composition, the antibacterial activity of the de novo-designed AMTC27-6 differs significantly from that of AMTC31-6. While both peptides are similar in activity against *B. megaterium*, AMTC27-6 is less active than AMTC31-6 against *E. coli* under most conditions but it is generally more active against *S. aureus* and *P. aeruginosa*. Generally, AMTC27-6 is more active at low rather than high salinity; this effect is especially pronounced with *E. coli* and *S. aureus*. Truncation of AMTC27-6 to AMTC24-5 led to a drastic loss in activity under all tested conditions, suggesting that the minimal hydrophobicity requirements for activity are not reached.

3.2.2. Pore-Forming Activity. With their amphipathic α -helix and highly positive net charge, the presented peptides were designed to have a pore-forming mode of action against negatively charged phospholipid membranes like those of bacteria. Their membrane-permeabilizing effect was tested in a liposome depolarization assay using asolectin vesicles to mimic cell membranes.^{46,47} Similar to bacterial membranes, asolectin liposomes display negative charges on the outer surface, and there is an electrostatic potential across their membrane. Pore formation by added peptides dissipates the transmembrane potential and releases a fluorescent dye from the liposomes, resulting in a fluorescence increase (Figure S5).

In general, the antibacterial activity of the peptides assayed in this study correlated well with their ability to dissipate the transmembrane potential of the liposomes (Figure 3B). Especially, the highly active bactericidal peptides AMTC31-6 and AMTC27-6 were shown to permeabilize the liposomes effectively. Consistent with their low antimicrobial activity, AMTC26-4 and AMTC24-5 showed only little liposome-permeabilizing activity, while TC-KKA showed no activity at all. Surprisingly, Helix19-6 dissipated the transmembrane potential of the liposomes slightly less than AMTC31-6 and AMTC27-6, even though it has the highest antibacterial activity.

3.2.3. Hemolysis. As membrane disruption is a likely mode of action for the AMTCs, it is of particular interest to determine whether they permeabilize mammalian cells as well. Human erythrocytes are commonly used to represent host cells in serial dilution assays,^{14,38,40} and they were employed here. The peptides TC-KKA, KR-12, AMTC26-4, and AMTC24-5 have no significant activity against erythrocytes at concentrations up to 80 μ M (Figure 3A and Table S33). These findings are not surprising as those peptides have very low activity against bacteria at high salt concentrations as well. Helix19-6, however, is highly hemolytic with significant hemolysis starting at 2.5 μ M. In comparison to Helix19-6, the activity of AMTC31-6 and AMTC27-6 is drastically reduced. Helix19-6 displays 3% hemolytic activity at 2.5 μ M, whereas this level of activity is only achieved at 40 μ M by AMTC31-6 and AMTC27-6 (Table S33). This comparison reveals that the Trp-cage loop of AMTC31-6 reduces the hemolytic activity up to 16-fold.

3.3. Enzymatic Degradation. Exposition of the peptides to trypsin (at 37 and 25 $^{\circ}$ C) and chymotrypsin (at 25 $^{\circ}$ C) was employed to assess whether and how the Trp-cage domain

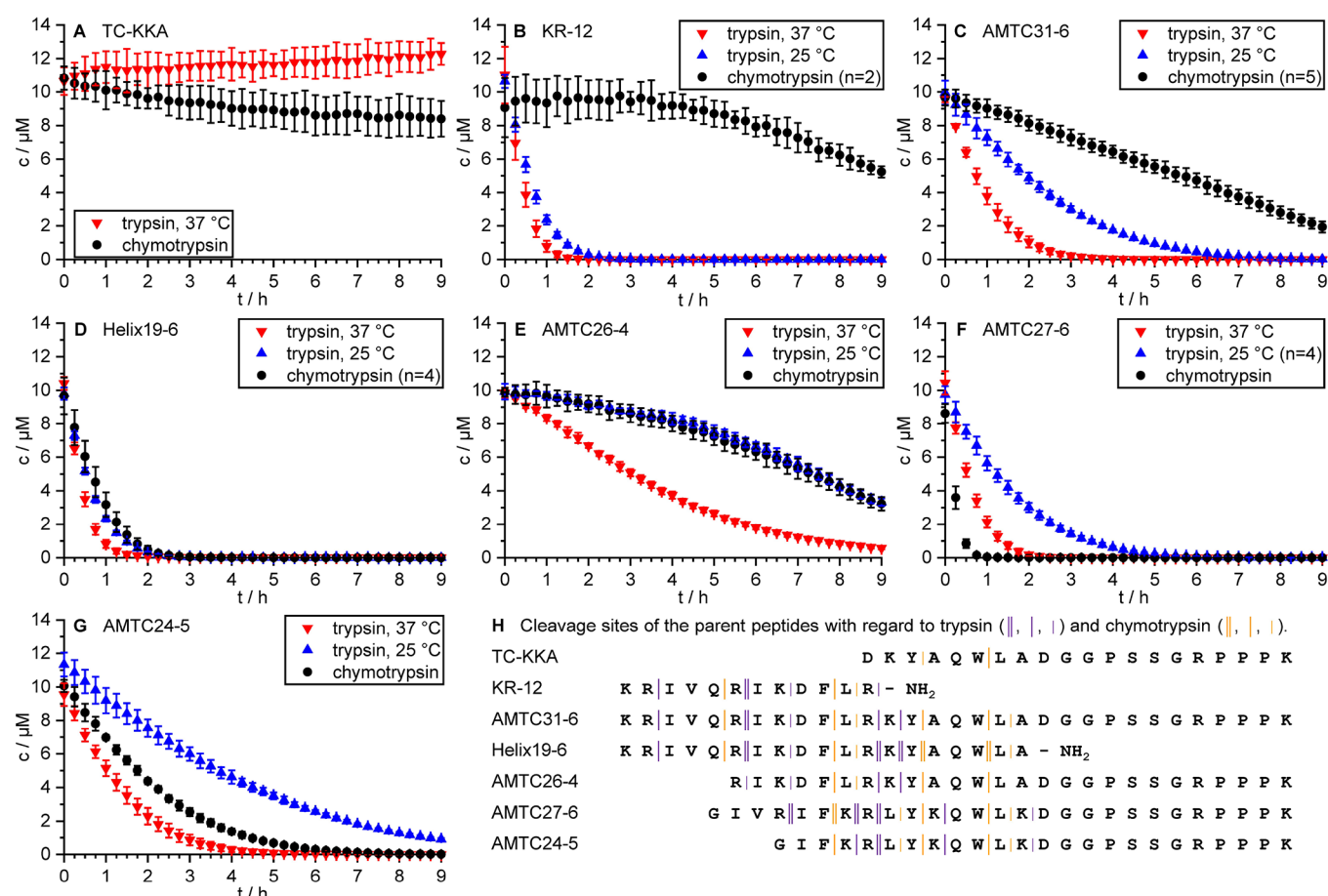


Figure 4. Quantitative digest of the parent peptide. The concentration of the parent peptide is plotted over the time. (A–G) The plots are an average of three individual digests; exceptions are stated in the panel legend. The error bars represent the standard deviation. Plots of all the individual digests can be found in [Figures S13–S15](#). (H) All identified cleavage sites for trypsin and chymotrypsin are indicated in the sequence of each peptide. Vertical lines indicate the cleavability of most scissile bonds (double vertical bar), frequently cleaved bonds (long single vertical bar), and rarely cleaved bonds (short vertical line). Plots of the emergence of fragments over time are given in [Figures S6–S12](#).

could increase the resistance against enzymatic proteolysis. The peptides in this study comprise multiple cleavage sites for trypsin (K-X and R-X) or chymotrypsin (W-X, Y-X, F-X, and L-X) positioned throughout their peptide chains. Both sequencing-grade enzymes have a high purity and low propensity to autoproteolysis at the applied temperatures, which guarantees all detected fragments to be AMP-derived. The enzymatic degradation assay was performed in a temperature-controlled autosampler of an ultrahigh-performance liquid chromatography device coupled to a high-resolution mass spectrometer. This setup allows one to record the progress of the digest by serially analyzing samples from the reaction mixture. In addition to quantitating the degradation of the parent peptide, the method allows identification of the cleavage sites and analysis of their cleavability by comparing the relative rates of fragment formation.

TC-KKA was not cleaved by trypsin under the conditions of the assay ([Figure 4A](#)). All residues K and R in TC-KKA are directly neighbored by P or D ([Figure 4H](#)), which are both known to reduce the cleavability.⁴⁸ Chymotrypsin diminished the concentration of TC-KKA by approximately only 15% after 9 h ([Figure 4A](#)), even though Y3–A4 and W6–L7 should be highly susceptible cleavage sites. Presumably, its stable fold

prevents TC-KKA from inserting into the active site of chymotrypsin.

In contrast to TC-KKA, KR-12 is cleaved very fast by trypsin ([Figure 4B](#)). The most scissile peptide bond of KR-12 for trypsin is R6–I7 followed by R2–I3 ([Figure 4H](#) and [Figure S8A](#)). Despite its conformational flexibility, KR-12 is rather resistant against degradation by chymotrypsin ([Figure 4B](#)). Its most susceptible residue F10 is N-terminally neighbored by a D, presumably reducing its cleavability ([Figure 4H](#) and [Figure S8B](#)).

The largely unstructured peptide Helix19-6 is highly susceptible to cleavage by trypsin and chymotrypsin ([Figure 4D](#)). The most scissile peptide bonds for trypsin are R6–I7, R12–K13, and K13–Y14, while the cleavability of the R2–I3 bond is somewhat lower ([Figure 4H](#) and [Figure S6B](#)). Incidentally, the C terminus of Helix19-6 presents no cleavage sites for trypsin but contains two highly susceptible bonds for cleavage by chymotrypsin (W17–L18 and Y14–A15). The Q5–R6 and F10–L11 bonds are less scissile for chymotrypsin and are therefore cleaved later in the digest ([Figure 4H](#) and [Figure S7B](#)).

As the Trp-cage loop has no cleavage sites for trypsin and chymotrypsin, the potential cleavage sites of AMTC31-6 and Helix19-6 are identical ([Figure 4H](#)). Toward the N-terminus, AMTC31-6 is increasingly dynamic, providing limited

structural protection against the trypsin digest. Therefore, the cleavage site R6–I7 is slightly affected by the stabilization, while R2–I3 is not affected at all. However, the peptide bonds R12–K13 and K13–Y14 of AMTC31-6 are significantly less efficiently cleaved than in Helix19-6 (Figure 4H and Figure S6). Consequently, AMTC31-6 is significantly more resistant to enzymatic degradation than Helix19-6 (Figure 4). This is quantifiable by comparing their average initial turnover frequency k (Table 2), i.e., the number of parent peptides

Table 2. Initial Turnover Frequencies k of the Peptides^a

peptide	trypsin (37 °C) (k/s^{-1})	trypsin (25 °C) (k/s^{-1})	chymotrypsin (k/s^{-1})
TC-KKA	0 ± 0	n.d.	0.026 ± 0.003
KR-12	9.00 ± 2.53	5.73 ± 0.74	0.045 ± 0.005
AMTC31-6	3.48 ± 0.16	1.47 ± 0.12	0.097 ± 0.001
Helix19-6	8.64 ± 0.66	5.61 ± 0.57	0.843 ± 0.338
AMTC26-4	0.89 ± 0.01	0.41 ± 0.01	0.085 ± 0.002
AMTC27-6	5.99 ± 1.00	2.27 ± 0.17	2.228 ± 0.225
AMTC24-5	2.47 ± 0.17	1.19 ± 0.27	0.320 ± 0.011

^aFor each digest, the initial turnover frequency k is given. k is the number of parent peptides that are cleaved by one enzyme molecule per second at the beginning of the assay, i.e., when the cleavage of the parent peptide is not perturbed by the presence of peptide fragments. The digest using chymotrypsin was performed at 25 °C.

that are cleaved by one enzyme molecule per second at the beginning of the assay. With regard to trypsin, AMTC31-6 is digested slower by factors of 2.5 at 37 °C and 3.8 at 25 °C. The resistance is increased at lower temperatures because the fold is more rigid under these conditions. With chymotrypsin, the resistance of AMTC31-6 against degradation increased even 8.7-fold compared to Helix19-6 because the main cleavage sites W17–L18 and Y14–A15 are part of the Trp-cage domain, i.e., constrained in an α -helical conformation. The F10–L11 bond is also less accessible for chymotrypsin than in Helix19-6. The Q5–R6 bond appears not to be affected by the structuring influence of the Trp-cage but is generally only slightly susceptible to chymotrypsin cleavage (Figure 4H and Figure S7).

Of the AMTCs, AMTC26-4 is the most resistant against trypsin and chymotrypsin (Figure 4E). The most susceptible cleavage sites for trypsin (R7–K8 and K8–Y9) are well protected by the stable α -helical structure, and the peptide bond R1–I2 is only of low importance for the digest (Figure 4H and Figure S9A). Similarly, the most susceptible cleavage sites for chymotrypsin (Y9–A10 and W12–L13; Figure 4H and Figure S9B) are also in the well-folded α -helical region. Additionally, there are no highly scissile cleavage sites in the fraying N-terminal helix turn of AMTC26-4.

AMTC27-6 is highly susceptible to degradation by trypsin and especially by chymotrypsin (Figure 4F). The main cleavage sites for trypsin are R8–L9, R4–I5, and K7–R8 (Figure 4H and Figure S10A). The rate of chymotrypsin digestion of AMTC27-6 exceeds the rates of all other parent peptides cleaved by chymotrypsin in this study owing to the highly scissile F6–K7 peptide bond, which is located in the unstructured part of AMTC27-6. All other cleavage sites in AMTC27-6 are hydrolyzed subsequently (Figure 4H and Figure S11A).

In contrast to AMTC27-6, its truncated derivative AMTC24-5 is more stable with regard to the trypsin and

chymotrypsin digest (Figure 4). With trypsin, the most scissile peptide bond is R5–L6, followed by K8–Q9 and K4–R5 (Figure 4H and Figure S10B). In the chymotrypsin digest, the cleavage site Y7–K8 is the most susceptible followed by W10–L11 and F3–K4 (Figure 4H and Figure S11B). Interestingly, cleavage at F3–K4 is not dominating the digest like the corresponding bond F6–K7 in AMTC27-6. Apparently, the remaining N-terminal region in AMTC24-5 is insufficient to facilitate an efficient cleavage of this bond by chymotrypsin.

4. DISCUSSION

Several studies have investigated the protease resistance of AMPs, mainly using SDS-PAGE^{5,6,8–10,12} but also HPLC-coupled^{6,13,14} or stand-alone mass spectrometry.^{5,7} Other reports document the reduction of antimicrobial activity after treatment of AMPs with proteases.^{6,7,11} An analysis of cleavage sites was performed in some of these studies,^{5–7,13} but the digest assay used here provides unrivaled temporal resolution. In addition, the unambiguous assignment of parent peptides and fragments is achieved by considering their retention time as well as multiple high-resolved MS peaks of different charge states and adducts. In consequence, this method facilitates the semiquantitative detection of all fragments that are larger than one residue and the quantification of the parent peptide leading to deeper insights into the progression of the digest. Comparison with structural data finally provided direct evidence on how Trp-cage-induced helicity affects the resistance against proteolytic degradation.

The fusion of KR-12 and TC-KKA_{2–20} effectively induced helicity in the KR-12-derived part of AMTC31-6 and thus provided significant resistance against degradation by trypsin, which is of pharmacological relevance as this enzyme is present in human epithelial cells.⁴⁹ Compared to the structurally dynamic Helix19-6, AMTC31-6 is 2.5- to 8.7-fold more resistant to proteolytic degradation, dependent on the temperature and enzyme. In fact, a helical conformation provides resistance to degradation by almost all proteases as the vast majority of proteases bind and cleave peptides in a stretched β -strand conformation only.⁵⁰

In addition to providing resistance to enzymatic proteolysis, the Trp-cage domain in AMTC31-6 significantly increased the antibacterial activity at high salinity compared to KR-12 while keeping the hemolytic activity very low. In contrast to the activity of AMTC31-6, the MIC of KR-12 is highly dependent on the salinity of the medium, which may explain why previous reports^{39–41} are stating different MICs of KR-12 against *E. coli* ranging from 4 μ M⁴⁰ to 64 μ M.⁴¹ Efficient depolarization of liposomes indicates a pore-forming mechanism of AMTC31-6. The Trp-cage loop reduces the hemolytic activity and increases the selectivity of AMTC31-6 compared to Helix19-6. With an MIC of 10 μ M, its moderate activity against *P. aeruginosa* is in the range of other LL-37-derived, nonhemolytic peptides¹² that resist degradation by chymotrypsin, but not trypsin, by virtue of incorporated D-amino acids and artificial residues.

AMTC27-6 shows the limitations of stabilizing an α -helix with the Trp-cage: A high net charge density may be beneficial for activity against Gram-negative bacteria but opposes the formation of a stable α -helix. Thus, the presented approach holds particular promise in the development of α AMPs against Gram-positive bacteria, as those require only low cationicity.⁵¹ As the fusion of an AMP with a Trp-cage protein increases the sequence length and thus the costs of production, truncated

AMTCs were produced and included in all assays. Truncation of AMTC31-6 and AMTC27-6 to AMTC26-4 and AMTC24-5, respectively, resulted in drastic losses in activity, showing that the N-terminal residues significantly contribute to their antimicrobial activity. On the other hand, truncation increased the resistance against enzymatic proteolysis. To harness this advantage and produce shorter AMTCs, the losses in activity have then to be compensated by further optimization.

Despite these limitations, the presented strategy to stabilize α AMPs has several advantages over established methods that aim to reduce enzymatic proteolysis in peptides. Protected termini, D-amino acids, or unnatural residues only protect neighboring residues from enzymatic degradation. In contrast, stabilizing peptides by introduction of a Trp-cage domain provides protection for a larger stretch. For instance, the Trp-cage domain is able to induce helicity in up to three to four helical turns in AMTC31-6, effectively reducing the cleavability in this region. While, in this study, the resistance of AMTC31-6 against enzymatic proteolysis was solely mediated by the Trp-cage to identify its potential in this regard, the presented approach may of course be combined with protected termini, artificial residues, nonpeptidic building blocks, or peptide stapling. However, these modifications are only accessible via chemical synthesis, while, by itself, the Trp-cage-mediated stabilizing approach is also compatible with biosynthetic methods because it relies only on the 20 standard gene-encoded amino acids.

The Trp-cage-induced α -helix stabilization is not limited to α AMPs but transferable to other peptides with α -helical propensity. Similar to the pancreatic polypeptide grafting approach,^{52–58} the Trp-cage may be used to stabilize protein- or DNA-binding α -helices in peptide drugs. For instance, an inhibitor of the E6 protein of human papillomavirus was developed based on Trp-cage grafting.⁵⁹ A different study focused on stabilizing the Trp-cage fold in exendin-4 to reduce aggregation and to increase helicity.⁶⁰ Our study suggests that, in addition to preorganizing an α -helical binding epitope, Trp-cage grafting may also reduce enzymatic proteolysis. Moreover, their composition of only natural amino acids renders Trp-cage-based peptide drugs compatible with drug discovery tools such as phage display libraries.^{53,55,56,61}

In conclusion, this study applies a universal approach to stabilize peptides with α -helical propensity, exemplified by α AMPs, against enzymatic degradation by fusing them to a Trp-cage domain. Compared to KR-12, its derivative AMTC31-6 demonstrated increased salt tolerance of its antimicrobial activity combined with negligible hemolysis. Moreover, a higher resistance against proteases paves the way for an increased bioavailability. These features render the Trp-cage-mediated stabilization approach a promising technique for future peptide drug development.

■ ASSOCIATED CONTENT

Supporting Information

The Supporting Information is available free of charge at <https://pubs.acs.org/doi/10.1021/acs.biochem.1c00567>.

Additional figures, tables, and text regarding NMR spectroscopy, CD spectroscopy, and enzymatic degradation monitoring and references (PDF)


Data S1: data regarding the MIC, MBC, liposome depolarization, and hemolysis assays (XLSX)

■ AUTHOR INFORMATION

Corresponding Author

Frank D. Sönnichsen – Otto Diels Institute for Organic Chemistry, Kiel University, 24118 Kiel, Germany;
 orcid.org/0000-0002-4539-3755; Email: fsönnichsen@oc.uni-kiel.de

Authors

Nils Preußke – Otto Diels Institute for Organic Chemistry, Kiel University, 24118 Kiel, Germany; Zoological Institute, Kiel University, 24118 Kiel, Germany; Present Address: Leibniz Institute for Natural Product Research and Infection Biology–Hans Knöll Institute, Beutenbergstraße 11a, 07745 Jena, Germany;
 orcid.org/0000-0001-7887-6203

Matthias Lipfert – Otto Diels Institute for Organic Chemistry, Kiel University, 24118 Kiel, Germany; Present Address: Lonza Group AG, Lonzastraße 2, 3930 Visp, Switzerland

Sven Rothemund – Faculty of Medicine, University of Leipzig, 04103 Leipzig, Germany

Matthias Leippe – Zoological Institute, Kiel University, 24118 Kiel, Germany

Complete contact information is available at:
<https://pubs.acs.org/10.1021/acs.biochem.1c00567>

Author Contributions

F.D.S., M. Lipfert, and N.P. developed the concept. M. Lipfert, N.P., and F.D.S. designed AMTC31-6. S.R. synthesized and purified AMTC31-6. N.P. designed, synthesized, and purified the other peptides. N.P. performed the MD simulations and structural characterizations. M. Leippe designed and N.P. performed and evaluated the biological experiments. N.P. designed, performed, and evaluated the digest experiments. N.P. prepared the original draft. N.P., M. Lipfert, M. Leippe, and F.D.S. revised the manuscript. M. Leippe and F.D.S. supervised the work. F.D.S., M. Leippe, and N.P. acquired funding.

Funding

This work was supported by a German Federal Environmental Foundation predoctoral fellowship awarded to N.P., grant 20017/473.

Notes

The authors declare no competing financial interest. The data supporting the findings of the study are available in this article and its Supporting Information files. The assigned chemical shifts are given in the Supporting Information and have been deposited in the BMRB database with the accession codes 50968 (KR-12), 50978 (TC-KKA), 50979 (Helix19-6), 50980 (AMTC31-6), 50981 (AMTC26-4), 50982 (AMTC27-6), and 50983 (AMTC24-5). The raw data of this study are available from the corresponding author upon request.

■ ACKNOWLEDGMENTS

We thank Heidrun Ließegang for technical assistance, Prof. Dr. Thisbe K. Lindhorst for access to the Schrödinger software, Prof. Dr. Joachim Grötzinger for access to the CD spectrometer, Prof. Dr. Andreas Tholey for advice regarding the digest assay, and Katrin Bamberg and Dr. Widukind Moormann for critical reading of the manuscript. N.P. is grateful to the German Federal Environmental Foundation

(Deutsche Bundesstiftung Umwelt, DBU) for a predoctoral fellowship (grant 20017/473).

■ REFERENCES

- (1) Roope, L. S. J.; Smith, R. D.; Pouwels, K. B.; Buchanan, J.; Abel, L.; Eibich, P.; Butler, C. C.; Tan, P. S.; Walker, A. S.; Robotham, J. V.; et al. The challenge of antimicrobial resistance: What economics can contribute. *Science* **2019**, *364*, eaau4679.
- (2) Neu, H. C. The crisis in antibiotic resistance. *Science* **1992**, *257*, 1064–1073.
- (3) Mookherjee, N.; Anderson, M. A.; Haagsman, H. P.; Davidson, D. J. Antimicrobial host defence peptides: Functions and clinical potential. *Nat. Rev. Drug Discov.* **2020**, 311.
- (4) Mansour, S. C.; Pena, O. M.; Hancock, R. E. W. Host defense peptides: Front-line immunomodulators. *Trends Immunol.* **2014**, *35*, 443–450.
- (5) McCrudden, M. T. C.; McLean, D. T. F.; Zhou, M.; Shaw, J.; Linden, G. J.; Irwin, C. R.; Lundy, F. T. The host defence peptide LL-37 is susceptible to proteolytic degradation by wound fluid isolated from foot ulcers of diabetic patients. *Int. J. Pept. Res. Ther.* **2014**, *20*, 457–464.
- (6) Schmidtchen, A.; Frick, I.-M.; Andersson, E.; Tapper, H.; Björck, L. Proteinases of common pathogenic bacteria degrade and inactivate the antibacterial peptide LL-37. *Mol. Microbiol.* **2002**, *46*, 157–168.
- (7) Sieprawska-Lupa, M.; Mydel, P.; Krawczyk, K.; Wójcik, K.; Puklo, M.; Lupa, B.; Suder, P.; Silberring, J.; Reed, M.; Pohl, J.; et al. Degradation of human antimicrobial peptide LL-37 by *Staphylococcus aureus*-derived proteinases. *Antimicrob. Agents Chemother.* **2004**, *48*, 4673–4679.
- (8) Strömstedt, A. A.; Pasupuleti, M.; Schmidtchen, A.; Malmsten, M. Evaluation of strategies for improving proteolytic resistance of antimicrobial peptides by using variants of EFK17, an internal segment of LL-37. *Antimicrob. Agents Chemother.* **2009**, *53*, 593–602.
- (9) Moncla, B. J.; Pryke, K.; Rohan, L. C.; Graebing, P. W. Degradation of naturally occurring and engineered antimicrobial peptides by proteases. *Adv. Biosci. Biotechnol.* **2011**, *02*, 404–408.
- (10) Kim, H.; Jang, J. H.; Kim, S. C.; Cho, J. H. *De novo* generation of short antimicrobial peptides with enhanced stability and cell specificity. *J. Antimicrob. Chemother.* **2014**, *69*, 121–132.
- (11) Hamamoto, K.; Kida, Y.; Zhang, Y.; Shimizu, T.; Kuwano, K. Antimicrobial activity and stability to proteolysis of small linear cationic peptides with D-amino acid substitutions. *Microbiol. Immunol.* **2002**, *46*, 741–749.
- (12) Wang, G.; Hanke, M. L.; Mishra, B.; Lushnikova, T.; Heim, C. E.; Chittesham Thomas, V.; Bayles, K. W.; Kielian, T. Transformation of human cathelicidin LL-37 into selective, stable, and potent antimicrobial compounds. *ACS Chem. Biol.* **2014**, *9*, 1997–2002.
- (13) Knappe, D.; Henklein, P.; Hoffmann, R.; Hilpert, K. Easy strategy to protect antimicrobial peptides from fast degradation in serum. *Antimicrob. Agents Chemother.* **2010**, *54*, 4003–4005.
- (14) Mourtada, R.; Herce, H. D.; Yin, D. J.; Moroco, J. A.; Wales, T. E.; Engen, J. R.; Walensky, L. D. Design of stapled antimicrobial peptides that are stable, nontoxic and kill antibiotic-resistant bacteria in mice. *Nat. Biotechnol.* **2019**, *37*, 1186–1197.
- (15) Migoń, D.; Neubauer, D.; Kamysz, W. Hydrocarbon stapled antimicrobial peptides. *Protein J.* **2018**, *37*, 2–12.
- (16) Bray, G. M. Exenatide. *Am. J. Health Syst. Pharm.* **2006**, *63*, 411–418.
- (17) Neidigh, J. W.; Fesinmeyer, R. M.; Prickett, K. S.; Andersen, N. H. Exendin-4 and glucagon-like-peptide-1: NMR Structural comparisons in the solution and micelle-associated states. *Biochemistry* **2001**, *40*, 13188–13200.
- (18) Chen, J.; Yu, L.; Wang, L.; Fang, X.; Li, L.; Li, W. Stability of synthetic exendin-4 in human plasma *in vitro*. *Protein Pept. Lett.* **2007**, *14*, 19–25.
- (19) Neidigh, J. W.; Fesinmeyer, R. M.; Andersen, N. H. Designing a 20-residue protein. *Nat. Struct. Biol.* **2002**, *9*, 425–430.
- (20) Barua, B.; Lin, J. C.; Williams, V. D.; Kummeler, P.; Neidigh, J. W.; Andersen, N. H. The Trp-cage: Optimizing the stability of a globular miniprotein. *Protein Eng., Des. Sel.* **2008**, *21*, 171–185.
- (21) Lin, J. C.; Barua, B.; Andersen, N. H. The helical alanine controversy: An (Ala)₆ insertion dramatically increases helicity. *J. Am. Chem. Soc.* **2004**, *126*, 13679–13684.
- (22) Piana, S.; Donchev, A. G.; Robustelli, P.; Shaw, D. E. Water dispersion interactions strongly influence simulated structural properties of disordered protein states. *J. Phys. Chem. B* **2015**, *119*, 5113–5123.
- (23) Roos, K.; Wu, C.; Damm, W.; Reboul, M.; Stevenson, J. M.; Lu, C.; Dahlgren, M. K.; Mondal, S.; Chen, W.; Wang, L.; et al. OPLS3e: Extending force field coverage for drug-like small molecules. *J. Chem. Theory Comput.* **2019**, *15*, 1863–1874.
- (24) *Fmoc solid phase peptide synthesis: A practical approach*; White, P. D.; Chan, W. C., Eds.; Oxford University Press: New York, 2000.
- (25) Gill, S. C.; von Hippel, P. H. Calculation of protein extinction coefficients from amino acid sequence data. *Anal. Biochem.* **1989**, *182*, 319–326.
- (26) Markley, J. L.; Bax, A.; Arata, Y.; Hilbers, C. W.; Kaptein, R.; Sykes, B. D.; Wright, P. E.; Wüthrich, K. Recommendations for the presentation of NMR structures of proteins and nucleic acids. (IUPAC Recommendations 1998). *Pure Appl. Chem.* **1998**, *70*, 117–142.
- (27) Wishart, D. S.; Bigam, C. G.; Holm, A.; Hodges, R. S.; Sykes, B. D. ¹H, ¹³C and ¹⁵N random coil NMR chemical shifts of the common amino acids. I. Investigations of nearest-neighbor effects. *J. Biomol. NMR* **1995**, *5*, 67–81.
- (28) Wishart, D. S.; Sykes, B. D.; Richards, F. M. The chemical shift index: A fast and simple method for the assignment of protein secondary structure through NMR spectroscopy. *Biochemistry* **1992**, *31*, 1647–1651.
- (29) Wishart, D. S.; Sykes, B. D. The ¹³C chemical-shift index: A simple method for the identification of protein secondary structure using ¹³C chemical-shift data. *J. Biomol. NMR* **1994**, *4*, 171–180.
- (30) Hwang, T.-L.; Shaka, A. J. Water suppression that works.: Excitation sculpting using arbitrary waveforms and pulsed field gradients. *J. Magn. Reson. A* **1995**, *112*, 275–279.
- (31) Monner, D. A.; Jonsson, S.; Boman, H. G. Ampicillin-resistant mutants of *Escherichia coli* K-12 with lipopolysaccharide alterations affecting mating ability and susceptibility to sex-specific bacteriophages. *J. Bacteriol.* **1971**, *107*, 420–432.
- (32) Boman, H. G.; Eriksson-Grennberg, K. G.; Normark, S.; Matsson, E. Resistance of *Escherichia coli* to penicillins: IV. Genetic study of mutants resistant to D,L-ampicillin concentrations of 100 µg/ml. *Genet. Res.* **1968**, *12*, 169–185.
- (33) Boman, H. G.; Nilsson-Faye, I.; Paul, K.; Rasmuson, T., Jr. Insect immunity: I. Characteristics of an inducible cell-free antibacterial reaction in hemolymph of *Samia cynthia* pupae. *Infect. Immun.* **1974**, *10*, 136–145.
- (34) Fedders, H.; Michalek, M.; Grötzinger, J.; Leippe, M. An exceptional salt-tolerant antimicrobial peptide derived from a novel gene family of haemocytes of the marine invertebrate *Ciona intestinalis*. *Biochem. J.* **2008**, *416*, 65–75.
- (35) Loew, L. M.; Rosenberg, I.; Bridge, M.; Gitler, C. Diffusion potential cascade. Convenient detection of transferable membrane pores. *Biochemistry* **1983**, *22*, 837–844.
- (36) Pick, U. Liposomes with a large trapping capacity prepared by freezing and thawing of sonicated phospholipid mixtures. *Arch. Biochem. Biophys.* **1981**, *212*, 186–194.
- (37) Tossi, A.; Sandri, L.; Giangaspero, A. Amphipathic, α -helical antimicrobial peptides. *Biopolymers* **2000**, *55*, 4–30.
- (38) Giangaspero, A.; Sandri, L.; Tossi, A. Amphipathic α helical antimicrobial peptides: A systematic study of the effects of structural and physical properties on biological activity. *Eur. J. Biochem.* **2001**, *268*, 5589–5600.
- (39) Wang, G. Structures of human host defense cathelicidin LL-37 and its smallest antimicrobial peptide KR-12 in lipid micelles. *J. Biol. Chem.* **2008**, *283*, 32637–32643.

- (40) Jacob, B.; Park, I.-S.; Bang, J.-K.; Shin, S. Y. Short KR-12 analogs designed from human cathelicidin LL-37 possessing both antimicrobial and antiendotoxic activities without mammalian cell toxicity. *J. Pept. Sci.* **2013**, *19*, 700–707.
- (41) Mishra, B.; Epand, R. F.; Epand, R. M.; Wang, G. Structural location determines functional roles of the basic amino acids of KR-12, the smallest antimicrobial peptide from human cathelicidin LL-37. *RSC Adv.* **2013**, *3*, 19560–19571.
- (42) Yi, G.-S.; Park, C. B.; Kim, S. C.; Cheong, C. Solution structure of an antimicrobial peptide buforin II. *FEBS Lett.* **1996**, *398*, 87–90.
- (43) Koo, Y. S.; Kim, J. M.; Park, I. Y.; Yu, B. J.; Jang, S. A.; Kim, K.-S.; Park, C. B.; Cho, J. H.; Kim, S. C. Structure-activity relations of parasin I, a histone H2A-derived antimicrobial peptide. *Peptides* **2008**, *29*, 1102–1108.
- (44) Wang, G.; Elliott, M.; Cogen, A. L.; Ezell, E. L.; Gallo, R. L.; Hancock, R. E. W. Structure, dynamics, and antimicrobial and immune modulatory activities of human LL-23 and its single-residue variants mutated on the basis of homologous primate cathelicidins. *Biochemistry* **2012**, *51*, 653–664.
- (45) Houston, M. E., Jr.; Kondejewski, L. H.; Karunaratne, D. N.; Gough, M.; Fidai, S.; Hodges, R. S.; Hancock, R. E. W. Influence of preformed α -helix and α -helix induction on the activity of cationic antimicrobial peptides. *J. Pept. Res.* **1998**, *52*, 81–88.
- (46) Leippe, M.; Ebel, S.; Schoenberger, O. L.; Horstmann, R. D.; Müller-Eberhard, H. J. Pore-forming peptide of pathogenic *Entamoeba histolytica*. *Proc. Natl. Acad. Sci. U. S. A.* **1991**, *88*, 7659–7663.
- (47) Andrä, J.; Herbst, R.; Leippe, M. Amoebapores, archaic effector peptides of protozoan origin, are discharged into phagosomes and kill bacteria by permeabilizing their membranes. *Dev. Comp. Immunol.* **2003**, *27*, 291–304.
- (48) Gershon, P. D. Cleaved and missed sites for trypsin, lys-C, and lys-N can be predicted with high confidence on the basis of sequence context. *J. Proteome Res.* **2014**, *13*, 702–709.
- (49) Koshikawa, N.; Hasegawa, S.; Nagashima, Y.; Mitsushashi, K.; Tsubota, Y.; Miyata, S.; Miyagi, Y.; Yasumitsu, H.; Miyazaki, K. Expression of trypsin by epithelial cells of various tissues, leukocytes, and neurons in human and mouse. *Am. J. Pathol.* **1998**, *153*, 937–944.
- (50) Tyndall, J. D. A.; Nall, T.; Fairlie, D. P. Proteases universally recognize beta strands in their active sites. *Chem. Rev.* **2005**, *105*, 973–1000.
- (51) Mishra, B.; Lakshmaiah Narayana, J.; Lushnikova, T.; Wang, X.; Wang, G. Low cationicity is important for systemic in vivo efficacy of database-derived peptides against drug-resistant Gram-positive pathogens. *Proc. Natl. Acad. Sci. U. S. A.* **2019**, *116*, 13517–13522.
- (52) Zondlo, N. J.; Schepartz, A. Highly specific DNA recognition by a designed miniature protein. *J. Am. Chem. Soc.* **1999**, *121*, 6938–6939.
- (53) Chin, J. W.; Schepartz, A. Design and evolution of a miniature Bcl-2 binding protein. *Angew. Chem., Int. Ed.* **2001**, *40*, 3806–3809.
- (54) Volkman, H. M.; Rutledge, S. E.; Schepartz, A. Binding mode and transcriptional activation potential of high affinity ligands for the CBP KIX domain. *J. Am. Chem. Soc.* **2005**, *127*, 4649–4658.
- (55) Chin, J. W.; Schepartz, A. Concerted evolution of structure and function in a miniature protein. *J. Am. Chem. Soc.* **2001**, *123*, 2929–2930.
- (56) Rutledge, S. E.; Volkman, H. M.; Schepartz, A. Molecular recognition of protein surfaces: High affinity ligands for the CBP KIX domain. *J. Am. Chem. Soc.* **2003**, *125*, 14336–14347.
- (57) Shimba, N.; Nomura, A. M.; Marnett, A. B.; Craik, C. S. Herpesvirus protease inhibition by dimer disruption. *J. Virol.* **2004**, *78*, 6657–6665.
- (58) Montclare, J. K.; Schepartz, A. Miniature homeodomains: High specificity without an N-terminal arm. *J. Am. Chem. Soc.* **2003**, *125*, 3416–3417.
- (59) Liu, Y.; Liu, Z.; Androphy, E.; Chen, J.; Baleja, J. D. Design and characterization of helical peptides that inhibit the E6 protein of papillomavirus. *Biochemistry* **2004**, *43*, 7421–7431.
- (60) Rovó, P.; Farkas, V.; Stráner, P.; Szabó, M.; Jermendy, Á.; Hegyi, O.; Tóth, G. K.; Perczel, A. Rational design of α -helix-stabilized exendin-4 analogues. *Biochemistry* **2014**, *53*, 3540–3552.
- (61) Herman, R. E.; Badders, D.; Fuller, M.; Makienko, E. G.; Houston, M. E.; Quay, S. C. J.; Johnson, P. H. The Trp cage motif as a scaffold for the display of a randomized peptide library on bacteriophage T7. *J. Biol. Chem.* **2007**, *282*, 9813–9824.

4. Switch cage

Photopharmacology is an emerging field of pharmacology seeking to understand the biochemical and physiological effects of light-responsive molecules on living cells, tissues, organs and organisms. In brief, photopharmacology aims to activate therapeutic compounds by irradiation with light to reduce unwanted side effects. This may be achieved by activating the compound at the target site in a non-invasive, non-toxic way. Thus, high concentrations of an active, but potentially toxic compound are only generated where needed. The activation is achieved by irradiation with light. When a photon of a certain wavelength is absorbed by a molecule, it may provide the activation energy for a chemical reaction changing the properties of the compound and in consequence modifying its therapeutic effect. A topic that has been covered comprehensively is the cleavage of a photoremovable protecting group (PPG) to irreversibly activate a therapeutic compound.^[289] More recent developments in photopharmacology focus on the investigation of molecular photoswitches. Photoswitches are small molecules that undergo a reversible isomerization reaction to a metastable isomer upon irradiation at a specific wavelength. The reaction back to the thermodynamically stable form may be activated thermally or by irradiation with light of a different wavelength. A thermal relaxation back to the inactive state may have the advantage that the compound relaxes spontaneously to its deactivated state when it diffuses away from the site of activation. A thorough analysis of the prospects and challenges of photopharmacology has been presented in a perspective written by Ben L. Feringa and co-workers.^[290] It should be noted that photopharmacology is still in its infancy. As summarized by Dirk Trauner and colleagues, most *in vivo* studies are analyzing the effects of photoswitchable compounds on cultured cells, while applications in higher organisms such as rodents are still scarce.^[291]

4.1. Azobenzenes

Several compound classes may serve as the photoswitchable chromophore for photopharmacological applications, but the most prominent photoswitches are azobenzene and its derivatives.^[291, 292] The next paragraph refers to the parent azobenzene (**Figure 18**, R^1 and $R^2 = H$) but the general principle also applies to its *para*-substituted derivatives.

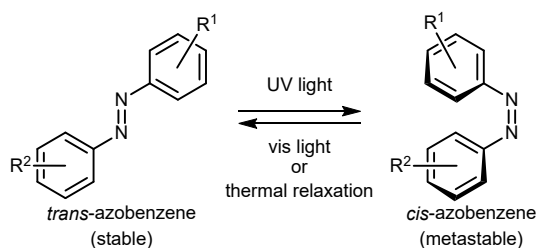


Figure 18: Isomerization of azobenzene derivatives.

Azobenzene exists in two isomeric states with profoundly different properties. The thermodynamically stable form of azobenzene is its planar *trans*-state.^[62] Because of its C_{2h} symmetry^[293] the dipole moment is zero. Its aromaticity and planarity render it prone to π - π stacking which also contributes to the high hydrophobicity of *trans*-azobenzene.^[292] *Cis*-azobenzene, in contrast, is not planar due to steric hindrance. The C-N=N-C dihedral angle of *cis*-azobenzene is circa 7° and the aromatic rings are twisted out of the N=N-C plane by approximately 54° .^[293, 294] With a dipole moment of about 3 D, *cis*-azobenzene is more polar and

has a higher solubility in water than its *trans*-isomer.^[292, 295] Probably the most important feature of *cis*-azobenzene, however, is its significantly reduced end-to-end distance compared to *trans*-azobenzene. The difference in length between both isomeric states is exploited in many switching applications, as examples given below will show.

The isomerization reaction of azobenzene is a complex physico-chemical process.^[62] The activation energy for the *trans*-to-*cis* isomerization is provided by a photon with a wavelength of approximately 320 nm that lifts a π electron to an excited π^* state. In contrast, the *cis*-isomer may be converted to the *trans*-state by irradiation into its $\pi\text{-}\pi^*$ band ($\lambda_{\text{max}} = 250$ nm) or its $n\text{-}\pi^*$ band ($\lambda_{\text{max}} = 450$ nm).^[62] However, the absorption bands are broad and the $\pi\text{-}\pi^*$ bands of the *cis*- and *trans*-isomer are partially overlapping. Therefore, illumination commonly triggers the photoisomerization in both directions, albeit with different conversion efficiencies. The resulting dynamic equilibrium is termed photostationary state (PSS) and light of different wavelengths may be used to shift the equilibrium towards one isomer or the other.^[62] The thermal relaxation back to the thermodynamically stable isomer proceeds usually with first-order kinetics and the temperature-dependent half-life is frequently used as a measure of the thermal stability of the metastable isomer.

Azobenzenes are common photoswitches in biological applications. This is not only because of their synthetic accessibility, but also due to their well-balanced photochemical properties (UV/Vis spectra, quantum yields, PSSs, half-life of the metastable state), which are tunable by derivatization.^[63, 296–298] Azobenzenes typically show high conversion yields upon switching and have a low susceptibility to photobleaching, i.e. they maintain their molecular integrity during exposure to UV light. The necessity of using UV-light to elicit the *trans*-to-*cis* isomerization, however, is a disadvantage in biological applications, as UV light is harmful to living cells. The search for so-called “red-shifted” azobenzenes that are switchable with visible light is therefore a topic of active research. Another advantage of red light is its much higher penetration depth in blood supported tissues compared to other visible or UV light. A red-shift may be achieved by incorporation of electron-donating groups in *ortho*- or *para*-position to the azo group or by implementing a push-pull system. Unfortunately, both approaches often come at the costs of drastic shortening of *cis*-to-*trans* isomerization half-lives precluding the application of those photoswitches.^[297] A different method to enable *trans*-to-*cis* isomerization with light of longer wavelengths is the introduction of four methoxy groups in all *ortho*-positions with respect to the azo moiety.^[299] With such a substitution pattern (**Figure 19**), steric clashes prevent the *trans*-isomer from adopting a planar geometry leading to an increase and red-shift of the $n\text{-}\pi^*$ band of the *trans*-state. While in planar *trans*-azobenzenes the UV-absorbing $\pi\text{-}\pi^*$ band is excited for *trans*-to-*cis* isomerization, the twisted *trans*-azobenzene may be converted to its *cis*-isomer by exciting the green-absorbing $n\text{-}\pi^*$ band with efficiencies of 70% *trans*-to-*cis* conversion in water.^[299]

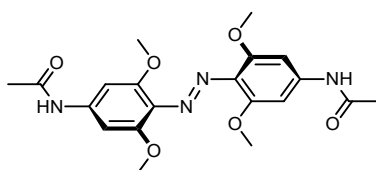


Figure 19: Structural formula of *trans*-tetra-*ortho*-methoxy azobenzene. The *trans*-to-*cis* isomerization of tetra-*ortho*-methoxy azobenzene can be triggered with green light.

4.2. Azobenzene-mediated photocontrol of peptides

A subsection of photopharmacology deals with photoswitchable peptides as bioactive compounds.^[296] In general, peptide drugs^[300] may combine the advantages of small molecule active agents and protein therapeutics. Like small molecules, peptides are synthetically accessible and may have cell-penetrating properties. However, a peptide may be designed to bind a protein with high affinity and specificity even at binding interfaces with shallow topologies, which is a typical trait of larger proteins, but not small molecules. The biologic activity of a peptide is often dependent on its three-dimensional structure. Therefore, it is a common strategy to combine a peptide with a photoswitch in order to manipulate the peptide's structure by triggering the isomerization of the photoswitch upon irradiation with light. For instance, the incorporation of an azobenzene moiety into a peptide's backbone to achieve a light-controlled function is applied frequently. Examples include a regulator of a guanylyl cyclase^[301], a derivative of the pharmaceutical compound liraglutide^[302], inhibitors of a methyltransferase^[303], and a cell-penetrating peptide^[304]. In these examples, isomerization of the photoswitch elicits a change of the peptide's backbone conformation, which affects its function.

A different study reports the effect of an azobenzene photoswitch on β -sheet formation in a syntrophin-binding peptide (SBP). The protein α -1-syntrophin plays a role in regulating the oxygen supply in murine muscles. An azobenzene moiety was attached to the N- and C-terminus of SBP effectively cyclizing it.^[305] The *cis*-isomer of the resulting azo-SBP supported β -sheet formation (**Figure 20**) and bound syntrophin with micromolar affinity effectively preventing muscle contraction.^[305, 306] In contrast, the *trans*-form disrupted this secondary structure and prevented binding of syntrophin.^[305, 306] Therefore, addition of *trans*-SBP to electrically stimulated murine muscles fibers had no effect on their contraction.^[306]

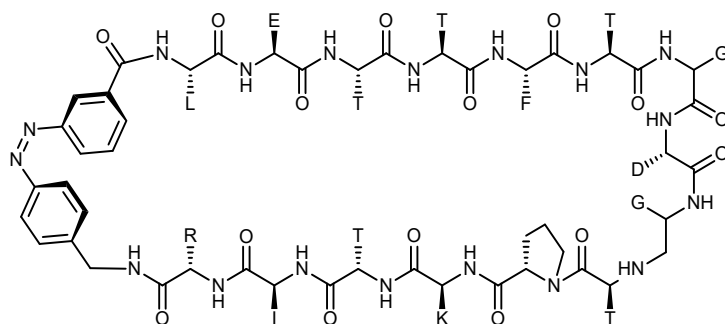


Figure 20: Structural formula of *cis*-azo-SBP. Side chains are abbreviated by the one letter code of their corresponding amino acid.

An azobenzene moiety may not only be introduced into the backbone or *via* the termini, but also *via* the peptide's side chains. While the Sönnichsen group focused on the conjugation *via* lysine residues,^[57, 59] other groups mainly rely on cysteine chemistry. A common strategy is the incorporation of an azobenzene via two attachment points positioned in *para* to the azo-moiety to make use of the maximal change in end-to-end distance upon isomerization. With two attachment points, the azobenzene moiety may be incorporated as an intermolecular^[307] or intramolecular^[308–313] cross-linker^[308–313].

4.2.1. Photoswitchable α -helical peptides

The use of azobenzenes as an intramolecular cross-linker to achieve photocontrol over α -helical peptides is particularly well explored. The strategy was invented by Janet R. Kumita, Oliver S. Smart and G. Andrew Woolley, who designed a cysteine-reactive cross-linker based on 4,4'-diaminobenzene which is amidated with iodoacetamide at both sides (**Figure 21**).^[308]

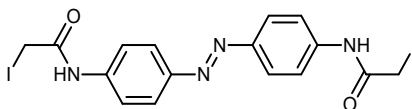


Figure 21: Woolley's cysteine-reactive standard azobenzene cross-linker in its *trans*-configuration.^[308]

Cross-linkers of this type are ideally connected to residues spaced one ($i, i+4$), two ($i, i+7$) or three ($i, i+11$) helical turns apart (**Figure 22**). When incorporated with an $i, i+7$ ^[308] or $i, i+4$ ^[309] spacing, the cross-linker stabilizes the helix in its *cis*-state. Switching to the *trans*-state, however, will increase the end-to-end distance of the azobenzene and it no longer supports a stably folded α -helix. In contrast, when attached to residues $i, i+11$ the cross-linker's *trans*-configuration does indeed support a folded α -helix, but the end-to-end distance of the *cis*-state is too short and it will prevent helix formation.^[309]

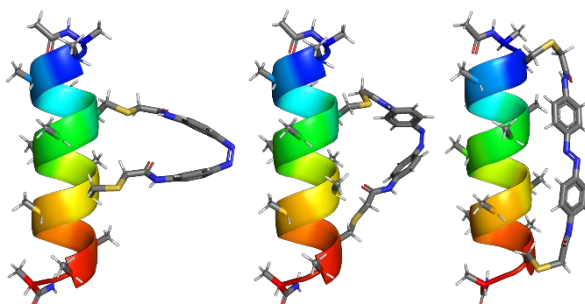


Figure 22: Strategies for cross-linker attachment in order to control helix content. The depiction shows three fictional peptides. Cysteines located in the positions $i, i+4$ (left), $i, i+7$ (middle) or $i, i+11$ (right) are covalently attached to Woolley's azobenzene cross-linker. The helix is stabilized by the *cis*-cross-linker, when it is attached with the spacing $i, i+4$ or $i, i+7$. Isomerization to the *trans*-state would destabilize the helix (not shown). However, when attached with the spacing $i, i+11$, the *trans*-configuration of the cross-linker stabilizes the helix, while helix formation is prevented in its *cis*-state (not shown).

Simple, non-functional peptides with helical propensity have served to demonstrate switching of a peptide's helicity as a proof of principle^[308, 309, 314] and to test an improved cross-linker designed for applications under aqueous conditions^[315]. This improved azobenzene derivative^[315, 316] is sulfonated in *meta*-position to the azo bond (**Figure 23**) to drastically increase its solubility in water. Importantly, these modifications do not significantly affect its photoswitching properties compared to the non-sulfonated azobenzene cross-linker.^[315]

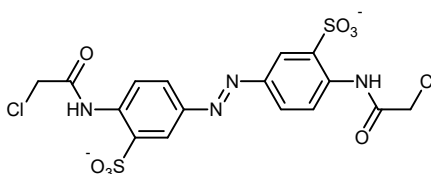


Figure 23: Woolley's cysteine-reactive bis-sulfonated azobenzene cross-linker in its *trans*-configuration.^[315]

4. Switch cage

α -Helices are common motifs in proteins and play an important role in many biological processes, including interactions between peptides, proteins and nucleic acids. Both azobenzene cross-linkers presented above may reversibly affect the helicity of peptides and thus switch their function. Therefore, it is not surprising that both cross-linkers have been applied in biological applications.

4.2.1.1. Photocontrol of peptide-protein interactions

A simple example for the interaction between an α -helical peptide and a protein is the ribonuclease S complex comprising the short fragment S-peptide and the larger fragment S-protein ($K_d \approx 130$ nM).^[317] When bound to the S-protein, the S-peptide assumes an α -helical conformation from residue A4 to residue H12.^[318] To achieve photoswitchable complex formation of RNase S, the S-peptide was cross-linked using Woolley's bis-sulfonated azobenzene with various spacings.^[319] The best results were achieved when the cross-linker was conjugated to cysteines at position 6 and 10 ($i, i+4$ spacing).^[319] The *trans*-state of the cross-linker did not support an α -helical conformation of the peptide and significantly reduced its affinity for the S-protein. Switching from the *trans*-state to the PSS at 370 nm (approximately 80% *cis*-isomer), however, restored the helicity of the S-peptide and increased its affinity approximately 20-fold reaching dissociation constants in the low micromolar range.^[319]

Photoswitchable peptides with pharmacological relevance were presented by Sabine Kneissl, Rudolf K. Allemann and co-workers, when they published their results on apoptosis-regulating peptides equipped with an azobenzene moiety.^[320] Erroneous regulation of apoptosis may promote the growth of tumors, which is why the interactions of apoptosis-regulating proteins including B-cell lymphoma 2 (Bcl-2) and its relatives have been the subject of intensive research.^[321–324] Important members of the Bcl-2 family of proteins are the anti-apoptotic proteins Bcl-2^[325, 326] and Bcl-x_L^[327–329] as well as the pro-apoptotic protein Bcl-2 homologous antagonist/killer (BAK)^[330–332]. Those proteins fold into the same globular structure and share four regions of homology termed Bcl-2 homology (BH) domains. A hydrophobic groove on their surface^[326–329] is able to recognize the α -helical BH3 domain of other Bcl-2 family proteins. For instance, the 16-residue BH3 domain of BAK (BAK_{72–87}) mediates binding of BAK to Bcl-2^[326] or Bcl-x_L^[328, 333] without the assistance of other binding epitopes and is therefore ideal for the introduction of an azobenzene cross-linker to investigate light-controlled apoptosis.

The pro-apoptotic peptide BAK_{72–87} was equipped with Woolley's bis-sulfonated azobenzene cross-linker with $i, i+7$ (BAK ^{$i, i+7$}) or $i, i+11$ (BAK ^{$i, i+11$}) spacing, respectively, in order to control their affinity to Bcl-x_L by irradiation with light. The active state of BAK ^{$i, i+11$} , i.e. in which the helix is supported by the *trans*-cross-linker (**Figure 24**), bound Bcl-x_L with a dissociation constant of $K_d = (21 \pm 1)$ nM.^[320] Switching to *cis*-BAK ^{$i, i+11$} was achieved with an efficiency of 69% at 360 nm, but it reduced the affinity only by a factor of approximately 2.3 ($K_d = (48 \pm 10)$ nM).^[320] In contrast to active *trans*-BAK ^{$i, i+11$} , active *cis*-BAK ^{$i, i+7$} ($K_d = (42 \pm 9)$ nM) had a slightly lower affinity to Bcl-x_L. The *cis*-state was obtained with an efficiency of 76% by irradiation at 360 nm. Remarkably, relaxation to the less active *trans*-states lowered its affinity approximately by a factor of 20 ($K_d(\text{trans-BAK}^{i, i+7}) = (825 \pm 157)$ nM),^[320] making this peptide an efficient photosensitive regulator of apoptosis.

Unfortunately, BAK ^{$i, i+7$} is not able to cross the cytoplasmic membrane of cells. In order to assess its apoptosis-inducing function in human lymphoma SU-DHL-4 cells they had to be treated with the cytotoxic membrane-permeabilizing agent digitonin.^[334] It was shown that 7.5 μ M of

BAK^{i, i+7} is relatively inactive in its dark-adapted *trans*-state, but irradiation at 360 nm produces approximately 70% *cis*-BAK^{i, i+7} which significantly reduces the mitochondrial outer membrane potential leading to cytochrome c release, which are two hallmarks of apoptosis initiation.^[334]

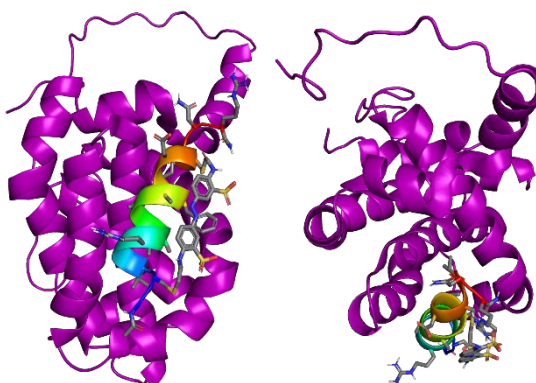


Figure 24: NMR-derived structure of *trans*-BAK^{i, i+11} (rainbow-colored ribbon, side chains colored by atom type) in complex with Bcl-x_L (purple). The depiction shows the complex from the side (left) and from the top (right). It was created from PDB entry 2lp8 (1/21).^[335]

Membrane permeabilization is a very harsh way to enforce the internalization of peptides. A natural way for a mammalian cell to internalize specific extracellular components is clathrin-mediated endocytosis (CME). This process is initiated by a complex machinery of proteins driving the formation of a shallow pit in the cell membrane.^[336] The adaptor protein 2 (AP2) complex is forming on the intracellular side of the pit. *Via* its appendage domains, AP2 binds accessory adaptor proteins that define which receptors are recruited to the pit.^[336] The β -appendage domain of AP2 (also referred to as β -adaptin), for instance, may bind an α -helical section of the accessory cargo adaptor β -arrestin.^[337] β -arrestin in turn recruits the transferrin-binding receptor (TfR), which binds the extracellular iron-transporting protein transferrin (Tf). In addition to organizing the receptors, the AP2 complex recruits clathrin proteins to the cytosolic side of the pit to promote further invagination and to stabilize the nascent vesicle.^[336] Finally, scission and maturation to an endocytic vesicle complete the cargo uptake.^[336]

Laura Nevola from Ernest Giralt's group, Andrés Martín-Quirós from Pau Gorostiza's group and co-workers reasoned that the α -helical β -arrestin-derived peptide (BAP) was a well-suited template for the design of a photoswitchable inhibitor of CME-mediated uptake of Tf.^[338] They created variants of BAP with cysteines in various positions for the introduction of Woolley's bis-sulfonated azobenzene cross-linker.^[338, 339] Depending on the position and configuration of their azobenzene moiety, the resulting photoswitchable inhibitors of CME aptly named traffic light (TL) peptides were able to affect the uptake of Tf.^[338] The peptide TL-2 (**Figure 25**) was cross-linked with *i, i+7* spacing, so its *trans*-state prevented the formation of an α -helix. Interestingly, the *cis*-azobenzene cross-linker did not directly induce folding of TL-2 into an α -helix in solution, but it allowed the formation of an α -helix upon binding to β -adaptin facilitating the β -adaptin-TL-2 complex formation.^[339] After irradiation to the PSS at 380 nm, TL-2 displayed an inhibition constant regarding the β -adaptin-BAP complex of $K_i = 19.0 \pm 0.3 \mu\text{M}$,^[338, 339] showing that *cis*-TL-2 is a 12.6-fold more potent inhibitor than the dark-adapted *trans*-state.^[338, 339]

The application of TL-2 in human cultured cells was facilitated by its ability to penetrate the cytoplasmic membrane.^[338] TL-2 was able to reach its target site, i.e. the cytoplasmic side of clathrin-coated pits (CCPs), upon simple incubation of the cells in TL-2-containing medium

4. Switch cage

(20 μM). While its *trans*-state showed no signs of inhibition of Tf uptake in live HeLa cells, irradiation at 380 nm led to a reduction of Tf uptake by approximately 70%.^[338] Unfortunately, no control experiments were pursued to exclude the effect of the UV radiation on cell viability and CME. Nonetheless, the response of CME activity to light may (at least partially) be ascribed to the photoisomerization of TL-2 by comparison with other TL peptides.

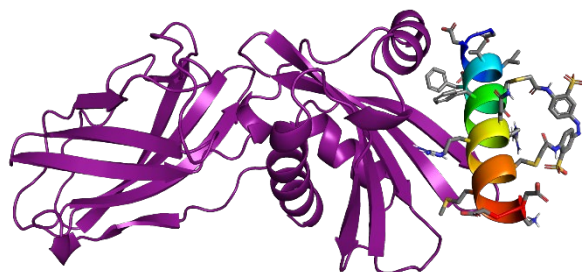


Figure 25: Model of TL-2 (rainbow-colored ribbon, side chains colored by atom type) bound to β -adaptin (purple). The structure was created based on the crystal structure of the β -adaptin-BAP complex^[337] (PDB entry 2iv8).

While the TL peptides are intrinsically cell-penetrating irrespective of their azobenzene configuration, an α -helical peptide termed Ab-LK has been designed to have a photoswitchable ability to traverse the cytoplasmic membrane of cells.^[340] Cell-penetrating peptides (CPPs) may transport even large, hydrophilic molecules such as proteins across the cytoplasmic membrane into the cytosol,^[40] where their cargo may exert a therapeutic function.^[341] Therefore, photoswitchable CPPs are an interesting subject of photopharmacology. The photoswitchable CPP Ab-LK is a 16-residue amphipathic peptide mainly composed of leucines and lysines. Photoswitchability was implemented by attaching Woolley's standard azobenzene cross-linker to cysteines with (*i*, *i*+4) spacing at the hydrophobic face of the peptide. When employed in an assay to determine the cell-penetrating properties using HeLa cells, irradiated Ab-LK (PSS at 357 nm, approximately 78% *cis*-Ab-LK) was twice as potent as its dark-adapted *trans*-state. Remarkably, the employed concentration was only 100 nM, which implies a high activity of Ab-LK compared to other cell-penetrating peptides such as Tat.^[340] CD spectroscopy indicated *cis*-Ab-LK to be only slightly more α -helical than the dark-adapted *trans*-state. Nonetheless, the change in azobenzene configuration and peptide conformation upon irradiation at 357 nm sufficed to induce self-association of *cis*-Ab-LK. It was reversible by inducing the *cis*-to-*trans* isomerization upon irradiation at 440 nm. While other azobenzene-cross-linked peptides have been reported to aggregate because of the high hydrophobicity of the *trans*-azobenzene,^[342–344] AB-LK self-associates only when the cross-linker assumes the more hydrophilic *cis*-state.^[340] Presumably, the slightly higher helical propensity in the *cis*-state drives the aggregation as it promotes the formation of a large hydrophobic face by the alignment of leucines in the α -helix. Aggregation has previously been described to be a prerequisite for some peptides to traverse a cytoplasmic membrane,^[345] so it might play a role in the mode of action of Ab-LK as well.^[340] However, more studies are needed to identify the precise molecular mechanism. In light of its high activity and low cytotoxicity,^[340] Ab-LK is an interesting subject for further development for applications in photopharmacology.

4.2.1.2. Photocontrol of DNA-binding peptides

The α -helix is not only a common element of secondary structure in peptide-protein interactions, but it is also an abundant DNA-binding motif of transcription factors. This is because the diameter of an α -helix has just the right size to fit into the major groove of the DNA

double helix. Two different photoswitchable DNA-binding peptides resulted from a collaboration of Rudolf K. Allemann's and G. Andrew Woolley's group.^[343, 346] In both designs, the bis-sulfonated azobenzene cross-linker was directly attached to the DNA-binding α -helix, at the side of the α -helix opposite to the DNA-binding interface. Therefore, isomerization of the cross-linker would directly affect the helicity of the DNA-binding helix and in consequence elicit changes in affinity of the peptide-DNA complex. The peptide photoMyoD^[343] (**Figure 26**) showed largest changes in affinity to DNA upon cross-linker isomerization. The azobenzene was attached to cysteines with *i, i+7* spacing,^[343] i.e. the *cis*-state of the cross-linker supported a stably folded α -helix, while the *trans*-state did not. Irradiation at 360 nm would result in a PSS of 61% *cis*-configuration of the azobenzene-peptide conjugate. Despite not quantitative conversion to the active *cis*-state, irradiation at 360 nm afforded a 60-fold increase in apparent affinity to specific DNA.^[343]

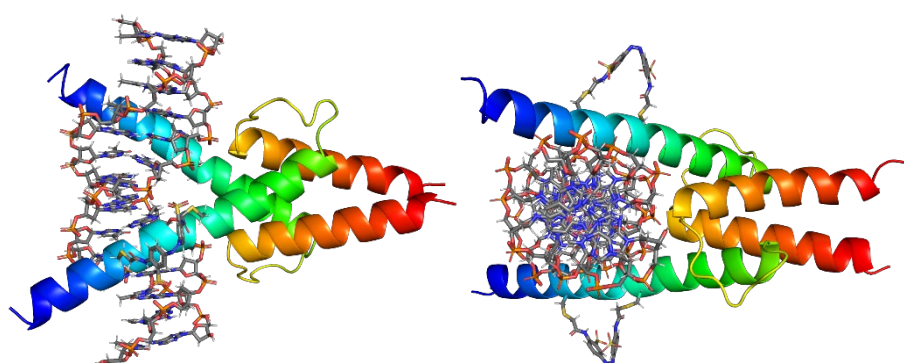


Figure 26: Model of homodimeric PhotoMyoD (rainbow-colored ribbon, cross-linker colored by atom type) in its *cis*-state bound to DNA. The structure (shown from two different angles) is adapted from the crystal structure of a complex comprising the homodimeric MyoD bHLH domain and a short double-stranded DNA (PDB entry 1mdy).^[347]

A different approach to gain photocontrol over a peptide's affinity to DNA makes use of the fact that many natural DNA-binding domains are only active in a dimeric form. A prototypical example of such a dimeric DNA-binding domain is the 56-residue basic region leucine zipper (bZIP) of the yeast transcription factor GCN4 (a photoswitchable version the GCN4 bZIP is shown in **Figure 27**).^[348, 349] The bZIP domain comprises two subdomains, namely the N-terminal basic region and the C-terminal leucine zipper. The leucine zipper region is responsible for homodimerization of GCN4 by forming a parallel α -helical coiled coil.^[348] The basic region is rich in Arg residues and only adopts a helical structure at low temperatures or upon DNA binding. When bound to DNA, the bZIP dimer embraces the double-stranded DNA in the major groove.^[348, 350, 351] The homodimeric bZIP domain achieves binding of specific DNA with nanomolar affinity ($K_d = 20$ nM, 23 °C, pH = 7.5).^[352]

Based on a pioneering study investigating switching of the dimerization state of a leucine zipper,^[342] G. Andrew Woolley and colleagues developed a GCN4 bZIP-derived photoswitchable DNA-binding peptide.^[353] While in previous approaches the photoswitchable cross-linker was directly attached at the opposite side of the DNA-binding face of an α -helix^[343, 346] (cf. **Figure 26**), photoswitchability of the bZIP-derived peptide termed AZO(*i, i+7*) GCN4-bZIP (**Figure 27**) was achieved by controlling the peptide's ability to homodimerize.^[353] The bis-sulfonated azobenzene cross-linker was incorporated into the leucine zipper region of the GCN4 bZIP domain. Depending on the isomeric state, the cross-linker effectively allowed or prevented the formation of the coiled coil and thus DNA binding. Remarkably, the isomerization had only little effect on the overall helicity, but the slight structural changes induced by *trans*-azobenzene had

4. Switch cage

nonetheless a strong impact on the dimerization. In the PSS at 370 nm (approximately 70% *cis*-state), the affinity of AZO(*i, i+7*) GCN4-bZIP to specific DNA was approximately an order of magnitude higher than in its dark-adapted state. It should be noted however, that the affinity of wild-type GCN4-bZIP to target DNA is yet ten-fold higher than that of irradiated (PSS_{370 nm}) AZO(*i, i+7*) GCN4-bZIP.^[353] The *trans*-to-*cis* photoisomerization was reported to be completely reversible by thermal relaxation at 37 °C within 1 h.^[353]

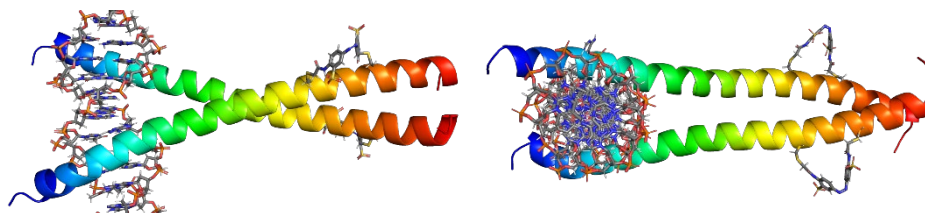


Figure 27: Model of *cis*-AZO(*i, i+7*) GCN4-bZIP (rainbow-colored ribbon, cross-linker colored by atom type) bound to DNA. The structure is shown from two different angles. It is based on the crystal structure of GCN4-bZIP bound to DNA (PDB entry 1ysa).

The concept of photoswitching DNA-binding peptides was subject to further investigations by the Woolley group and was even applied in human cell cultures.^[354] In consequence, the focus shifted from GCN4 found in yeasts to its mammalian homologues, i.e. the activator protein 1 (AP-1) family of transcription factors. Similar to GCN4, the dimerization and DNA-binding of AP-1 complexes is mediated by a bZIP domain.^[355] A big difference to GCN4 complexes is, however, that AP-1 complexes are not necessarily homodimeric, but may also be heterodimeric.^[355] A well-characterized AP-1 complex comprises a cJun and a cFos monomer. To achieve photoswitching of gene expression in human embryonic kidney 293T (HEK293T) cells, G. Andrew Woolley and colleagues devised a new strategy to reversibly prevent the c-Fos·c-Jun·DNA complex formation *in vivo*. They created a photoswitchable competitive inhibitor named XAFosW of this complex.^[354] AFosW is a cFos-derived peptide, in which the DNA-binding basic region was replaced by an acidic region to increase the affinity to cJun through electrostatic interactions.^[354] To introduce photoswitchability, the AFosW peptide was equipped with a bis-sulfonated azobenzene cross-linker with *i, i+7* spacing located in the middle of the leucine zipper region.^[354] In its *cis*-state, the cross-linker supports a folded α -helix of XAFosW and thus allows the formation of a coiled coil complex with c-Jun (**Figure 28**). The *cis*-XAFosW·cJun complex is not able to bind DNA. Moreover, it is more stable than the cFos·cJun·DNA complex. Therefore, the formation of the native AP-1 transcription factor is effectively inhibited by *cis*-XAFosW. Thermal ($t_{1/2} \approx 17$ min at 37 °C) or light-induced (460 nm) isomerization to the *trans*-configuration, however, interferes with the helical fold of the XAFosW leucine zipper region and lowers the affinity of XAFosW to c-Jun.^[354] As a result, monomeric cJun is released, binds cFos and thus induces transcription of genes bearing an AP-1 promoter. The photoswitchability of gene expression was demonstrated in live HEK293T cells transfected with XAFosW.^[354] Several control experiments confirmed that *cis-trans*-isomerization of the cross-linker was solely responsible for the activation or deactivation of genes bearing an AP-1 promoter. The concept of developing an acidic region leucine zipper (aZIP) to inhibit bZIP dimerization was also applied in a subsequent study aiming to optimize the position of the cross-linker and the length of the acidic region.^[344]

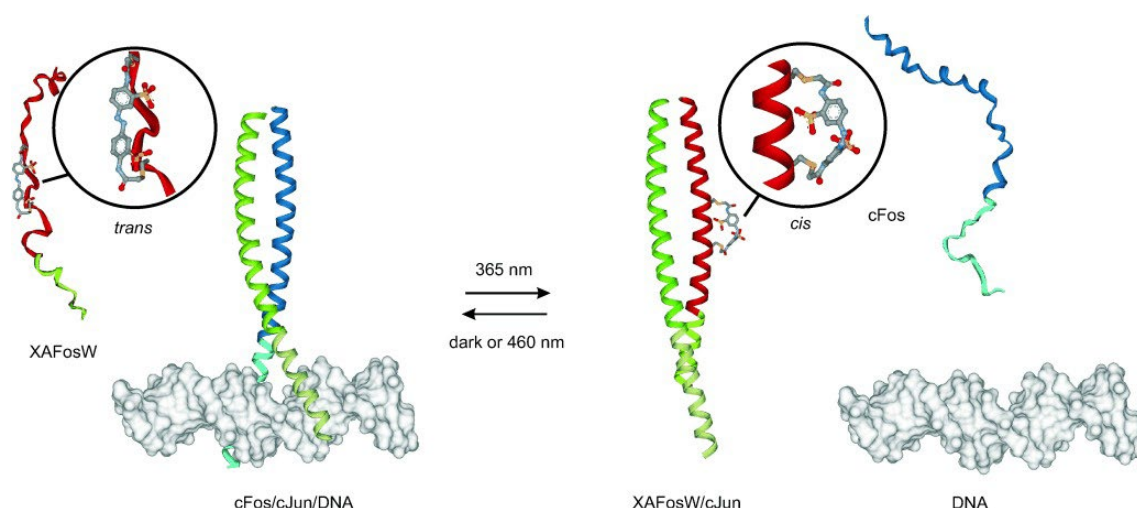


Figure 28: Concept of the photoswitchable inhibitor XAFosW. In its *trans*-state XAFosW is and not able to bind cJun. cJun forms a heterodimeric complex with cFos which is able to bind specific DNA and activate its transcription (left). Irradiation at 365 nm results in the formation of *cis*-XAFosW, which has a high affinity for cJun. *Cis*-XAFosW is therefore inhibiting the formation of the cFos-cJun-DNA complex, by tightly binding cJun (right). This prevents the DNA transcription.^[354]

Reprinted from *Angewandte Chemie International Edition*, volume 49, issue 23, Fuzhong Zhang, Katharina A. Timm, Katja M. Arndt, Andrew G. Woolley, Photocontrol of coiled-coil proteins in living cells, pages 3943-3946, Copyright 2010, with permission from John Wiley & Sons, Inc.

4.2.1.3. Photocontrol of peptide-RNA interactions

While the well-structured right-handed double helix of DNA can be recognized even by short peptides, RNA has a much greater conformational flexibility and is therefore very difficult to target. An exception is RNA containing the Rev response element (RRE). It assumes a helical structure that can be recognized by the protein Rev and by Rev-derived peptides.^[330, 331] The NMR-derived structure^[356] of a short α -helical Rev-derived peptide in complex with RRE-containing RNA served as the starting point for the design of a photoswitchable RNA-binding peptide.^[357] The first designs used Woolley's bis-sulfonated azobenzene, but had low or no affinity for RRE-containing RNA. Apparently, the sulfonate groups' caused steric clashes with the RNA backbone and their negative charges were interfering with the charge-charge interactions of the positively charged peptide with the negatively charged phosphates of RNA.^[357] In contrast, peptides cross-linked with the non-sulfonated standard azobenzene cross-linker displayed much higher affinities to RRE-containing RNA. With an affinity of $K_d = (24 \pm 9)$ nM, the dark-adapted peptide-cross-linker conjugate Rev^{i, i+11}-XL-H bound RRE-containing RNA with much higher affinity than all other photoswitchable Rev-derived peptides from this study (**Figure 29**).^[357] Although irradiation at 363 nm produced a PSS of approximately only 50% *cis*-state, the irradiated Rev^{i, i+11}-XL-H had a three-fold reduced affinity to RRE-containing RNA when compared to its dark-adapted state.^[357]

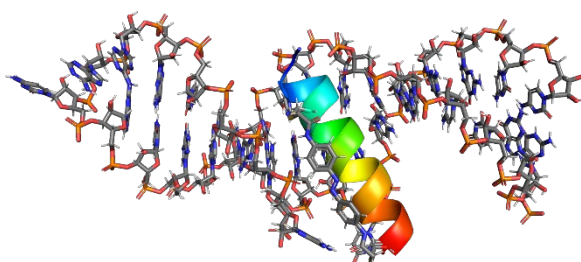


Figure 29: Model of Rev^{i, i+11}-XL-H (rainbow-colored ribbon, cross-linker colored by atom type) in complex with RRE-containing RNA. This depiction is derived from the NMR structure of a peptide-RNA complex (PDB entry 1etf).^[356]

4.3. Challenges of applying azobenzenes in *in vivo* applications

A general problem of highly hydrophilic drugs like peptides is their inability to diffuse through cell membranes. Cell-penetrating properties are required for active agents that are supposed to act on intracellular targets. A hydrophobic photoswitch like azobenzene attached to a hydrophilic peptide may even bestow it with membrane penetrating properties. While some peptides amended with azobenzene moieties show cell-penetrating properties,^[306, 338] others do not^[334, 354]. However, even those peptides that become internalized *via* endocytosis are not necessarily able to escape the endosome and reach the cytosol. The TL peptides used to regulate clathrin-mediated endocytosis by light, for instance, appear as puncta in images of cultured cells obtained by confocal microscopy.^[338] This may indicate that the majority of those peptides are trapped in or associated to endosomes. However, it is irrefutable that at least a fraction of the TL peptides does reach the cytosol, as they are inhibiting a complex formation at the cytosolic site of the plasma membrane.^[338]

Even though there are a few cases in which the high hydrophobicity of azobenzene promotes cell-penetrating properties, the hydrophobicity of azobenzenes is in many cases a major disadvantage for applications *in vivo*, i.e. in aqueous environments.^[292] Burial of the extended and flat hydrophobic surface of *trans*-azobenzene is a strong driving force of aggregation or precipitation, which has been encountered even in the context of peptides.^[342, 344] This problem has been solved by equipping the azobenzene with sulfonate moieties.^[315, 316] However, even peptides cross-linked with the bis-sulfonated azobenzene have shown signs of aggregation at high nanomolar concentrations.^[343] Moreover, sulfonates are known to form strong ion pairs with guanidinium moiety of arginines, which may lead to unintended interactions between the cross-linker and the peptide affecting the peptide's fold.^[357] Despite a reported incidence of aggregation or an altered peptide fold associated with the introduction of the bis-sulfonated azobenzene, the introduction of this cross-linker was successful in the majority of applications.^[319, 320, 334, 338, 339, 343, 346, 353, 354] While bis-sulfonated azobenzene is significantly less prone to aggregation than the standard azobenzene cross-linker, it still requires UV light for switching from the *trans*- to the *cis*-isomer, which harms cells by damaging their DNA. Therefore, special care should be taken to avoid long exposure of cells to UV light.^[354] This may require short irradiation pulses that do not suffice for reaching the PSS with the result that the full potential of the photoswitchable cross-linker cannot be exploited.^[354] Furthermore, the penetration depth of light in blood supported tissue is extremely short, with the exception of red light. With the current azobenzenes, activating a photoresponsive therapeutic agent at its target site would therefore require the use of minimal invasive surgery by inserting an optical fiber through the surrounding tissue all the way to the target site. However, this approach is impractical and the use of minimal invasive surgery contradicts the original promise of photopharmaceuticals to require only a light source and a drug for treatment. To really be applicable *in vivo*, the development of a photoswitch that is responsive to red light with high conversion yields is absolutely desirable.

The search for red-sensitive photoswitches has long been started and azobenzenes that may be switched with visible light have been produced. One example is the green-responsive tetra-*ortho*-methoxy azobenzene. Unfortunately, its azo moiety is highly susceptible to reduction to the corresponding hydrazine by glutathione (GSH).^[299] The cytosol of mammalian cells typically contains reduced GSH in concentrations of 0.5 mM to 10 mM.^[358] The redox potential is in many cases sufficient to reduce the azo group of many azobenzenes, especially under illuminated

conditions with the *cis*-isomer as the predominant form.^[359] As the redox potential of azobenzenes depends on their substitution pattern, the susceptibility to reduction by GSH should be tested prior to *in vivo* experiments.^[334, 306] Additionally, the presence of GSH may^[306] or may not^[360] significantly shorten the half-life of thermal relaxation from the metastable *cis*-isomer to the thermodynamically stable *trans*-state of an azobenzene.

An improved tetra-*ortho*-substituted azobenzene was developed by David Bléger, Stefan Hecht and colleagues.^[361] Like the methoxy-substituted version, their tetra-*ortho*-fluoro azobenzene isomerizes from the stable *trans*-state to the metastable *cis*-state upon excitation of the green-absorbing $n\text{-}\pi^*$ transition and the reverse reaction is achieved with violet light. However, unlike tetra-*ortho*-methoxy azobenzene the fluorinated azobenzene is not twisted but planar, because the fluorine atoms are less sterically demanding than the methoxy groups. The band separation of the $n\text{-}\pi^*$ bands of *trans*- and *cis*-tetra-*ortho*-fluoro azobenzene, which allows switching with visible light, is a result of the electron withdrawing properties of the fluorine atoms. The low electron density of the azobenzene is also the reason why tetra-*ortho*-fluoro azobenzene is not susceptible to reduction by GSH.^[362] A tetra-*ortho*-fluoro azobenzene (**Figure 30**) incorporated into the backbone of a protein-binding peptide achieved isomerization efficiencies in water above 85% in both directions.^[362] Unfortunately, the contraction and expansion motion of the azobenzene upon isomerization is partially compensated by the high flexibility of the 1,2-diaminoethane moiety. Therefore, the high isomerization efficiencies did not lead to high switching efficiencies of the peptide's function.^[362] In conclusion, it remains a very difficult and yet unsolved task to find a photoswitch that combines all the desired properties for individual *in vivo* applications like high switching efficiencies, switchability with red light, resistance to GSH, ideal thermal relaxation, large difference in length of the isomers and a low tendency to aggregate.

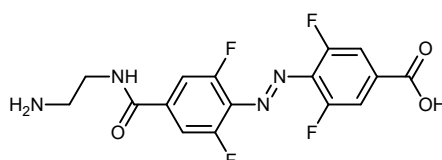


Figure 30: This tetra-*ortho*-fluoro azobenzene can be incorporated into a peptide's backbone.^[362]

4.4. Diazocines

The design of new photoswitches is pursued by many research groups. In 2009, the groups of Rainer Herges and Friedrich Temps reported the characterization of an azobenzene-related photoswitch termed bridged azobenzene or diazocine (**Figure 31**).^[363]

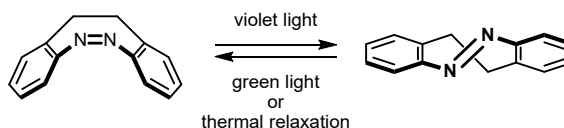


Figure 31: The *cis*-isomer (left) is the thermodynamically stable form of diazocine, while the *trans*-isomer (right) is metastable. This inverted switchability (with respect to azobenzene) is a result of the constraints imposed by the ethylene bridge.

Like other azobenzene-derived photoswitches, diazocine can be switched efficiently in both directions between a *cis*- and a *trans*-isomer with high efficiencies using visible light. More importantly, however, the diazocine is different from linear (i.e. non-bridged) azobenzenes

4. Switch cage

because its *cis*-isomer is the thermodynamically stable state while the *trans*-state is meta-stable. This inverted stability is a result of the ring strains evoked by the ethylene bridge.^[363] Switching to its elongated *trans*-isomer is achieved with visible violet light (385 nm) with conversion yields larger than 90% in unpolar organic solvents.^[363, 364] The reverse reaction is achieved quantitatively upon irradiation with green light or through thermal relaxation ($t_{1/2} \approx 3$ h at 20 °C).^[363] Diazocine is superior to the parent unsubstituted azobenzene in many photochemical aspects including separation of $n-\pi^*$ bands of both isomers, higher conversion efficiencies, and higher quantum yields.^[363] Unfortunately, synthesis and derivatization of diazocine is more complex, which is why it has not been applied in many biological applications yet.

Similar to the approaches cross-linking an α -helical peptide with an azobenzene, a peptide was conjugated to a diazocine-based cross-linker to assess the photoswitchability of the peptide's α -helical secondary structure.^[365] The free cross-linker (i.e. not in conjugation with a peptide, **Figure 32**) underwent *cis*-to-*trans* isomerization with an efficiency of 70% upon irradiation to the PSS at 407 nm in the solvent dimethyl sulfoxide (DMSO).^[365] The slightly reduced switching efficiency compared to the parent unsubstituted diazocine may be a result of the derivatization or the different solvent.

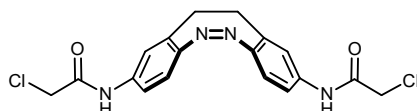


Figure 32: Woolley's cysteine-reactive diazocine-derived cross-linker in its *cis*-configuration.^[365]

The diazocine-based cross-linker was attached to the peptide *via* two cysteines with *i, i+11* spacing. Because the thermodynamically stable *cis*-isomer does not support the formation of an α -helix, the peptide displayed only nascent helicity in the dark-adapted state as indicated by CD spectroscopy. In contrast, the CD spectrum of the peptide-cross-linker conjugate irradiated to the PSS at 407 nm showed the typical characteristics of a well-defined α -helix.^[365] While the *cis*-cross-linker was inert to reduction by GSH in the dark, constant irradiation at 407 nm in the presence of GSH resulted in the reduction of the azo-moiety to the corresponding hydrazine derivative.^[365]

A different diazocine (**Figure 33**) was incorporated into a peptide's backbone to achieve photoswitchable peptide-protein interactions.^[362] When incorporated into the peptide, however, irradiation to the PSS at 405 nm achieved only 16% *cis*-to-*trans* isomerization.^[362] Apparently, the $\pi-\pi^*$ and the $n-\pi^*$ band of the *cis*-isomer are largely overlapping with the $\pi-\pi^*$ band of the *trans*-isomer thus preventing high *cis*-to-*trans* conversion. It is unclear, however, whether the derivatization or the aqueous environment is responsible for overlap of absorption bands of the *cis*- and the *trans*-state.

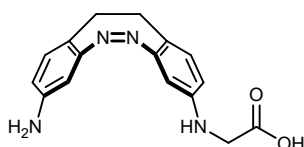


Figure 33: Diazocine for the incorporation into a peptide's backbone.^[362]

Studies on the application of other diazocine-derivatives in aqueous environments report *cis*-to-*trans* conversion of 50%-60% *trans*-state.^[366-368] At least in one instance, the compromised performance compared to the parent diazocine has been attributed to the derivatization.^[367]

The diazocine-derivative CLOGO (**Figure 34**) designed by Dirk Trauner and co-workers is a remarkable exception to the aforementioned diazocines because the π electrons of the substituent are not conjugated the π electron system of the diazocine.^[368] Therefore, the diazocine's electron density and photoswitching properties are hardly affected by the substituent. As a result, the *cis*-to-*trans* isomerization yield of CLOGO upon irradiation of at 390 nm is above 80% *trans*-state in a 1:1 mixture of DMSO and phosphate-buffered saline and increasing the DMSO content leads to even better switching efficiencies.^[368]

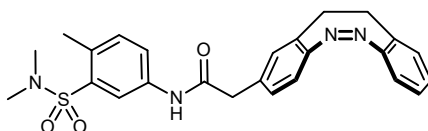


Figure 34: Structural formula of the diazocine-derivative CLOGO.

With CLOGO, Dirk Trauner and colleagues demonstrated that a diazocine with an unperturbed electron system may achieve nearly as high switching efficiencies in aqueous environments as the parent diazocine in unpolar solvents. A diazocine-based cross-linker with an unperturbed electron system like in CLOGO may therefore achieve visible-light-driven photocontrol of an α -helix with very high efficiencies in both directions. In addition, the twisted nature of the *trans*-diazocine potentially reduces π - π stacking and thus the tendency to aggregate compared to the planar *trans*-azobenzene.

4.5. Switch cage: Publication

While photoswitching of helicity in a peptide has been achieved in numerous cases, obtaining photocontrol over the tertiary structure of a small protein or protein domain is more difficult. Woolley's bis-sulfonated azobenzene cross-linker has been incorporated into a FynSH3 domain to allow photoswitching of its tertiary structure.^[310] The switching efficiencies that could be achieved in the context of the protein were 85% *cis*-state (PSS at 365 nm) and approximately 100% *trans*-state. While the *cis*-cross-linker stabilized the fold to such an extent that 95% of the FynSH3 domains were folded, only 40% of the population in the *trans*-state were properly folded. The remaining 60% of the population in the *trans*-state were reported to be entirely unfolded.^[310] Importantly, switching of the tertiary structure also modulated the peptide-binding ability of the cross-linked FynSH3 domain.^[310]

An azobenzene-derived cross-linker has also been conjugated to the restrictive endonuclease scPvuII to reversibly modulate its ability to cleave DNA.^[311] One or two azobenzene cross-linker per enzyme were attached at different locations, i.e. at connecting loops or β -strands near the active site or as a cross-linker within α -helices near the DNA-binding site. When the azobenzenes were introduced near the active site of the enzyme, changing their isomerization state led to up to 16-fold changes of the enzymatic activity.^[311] In contrast, introduction at the α -helices did not lead to efficient photoswitchability of the enzyme activity.^[311] Presumably, the α -helices were too far from the core of the enzyme and switching their structure would not result in significant changes of the overall fold, of the DNA-binding site or of the catalytic site.

Although switching of helicity did not substantially affect the enzymatic activity of scPvuII,^[311] the fold of many proteins or protein domains relies on central, partially solvent-exposed α -helices. Examples include the apoptosis-regulating Bcl-family of proteins^[326, 329], the engrailed homeodomain transcription factor^[369, 370], the KIX domain of CBP^[371], the ribonuclease T1^[372],

4. Switch cage

the villin headpiece subdomain^[373] or the Trp-cage^[46, 47]. Their tertiary structure is characterized by one or more α -helices that may be equipped with a photoswitchable cross-linker. Hypothetically, isomerization of the cross-linker could then lead to disruption of the fold. Thus, Woolley's approach to switching single helices^[308, 309] could not only be used to affect the structure and function of isolated α -helical peptide, but also to affect the tertiary structure and thus the function of proteins or protein domains. To test the hypothesis, this chapter reports the design, synthesis and characterization of a Trp-cage miniprotein equipped with a diazocine photoswitch. The diazocine cross-linker was synthesized by Widukind Moormann from Rainer Herges' research group. The substituents of this photoswitch are not affecting the π electron system of the diazocine, which should result in high efficiencies of photoisomerization.

Visible-light-driven photocontrol of the Trp-cage protein fold by a diazocine cross-linker

Nils Preußke, Widukind Moormann, Katrin Bamberg, Matthias Lipfert,
Rainer Herges and Frank D. Sönnichsen

Organic and Biomolecular Chemistry **2020**, *18*, 2650-2660

DOI: [10.1039/c9ob02442e](https://doi.org/10.1039/c9ob02442e)

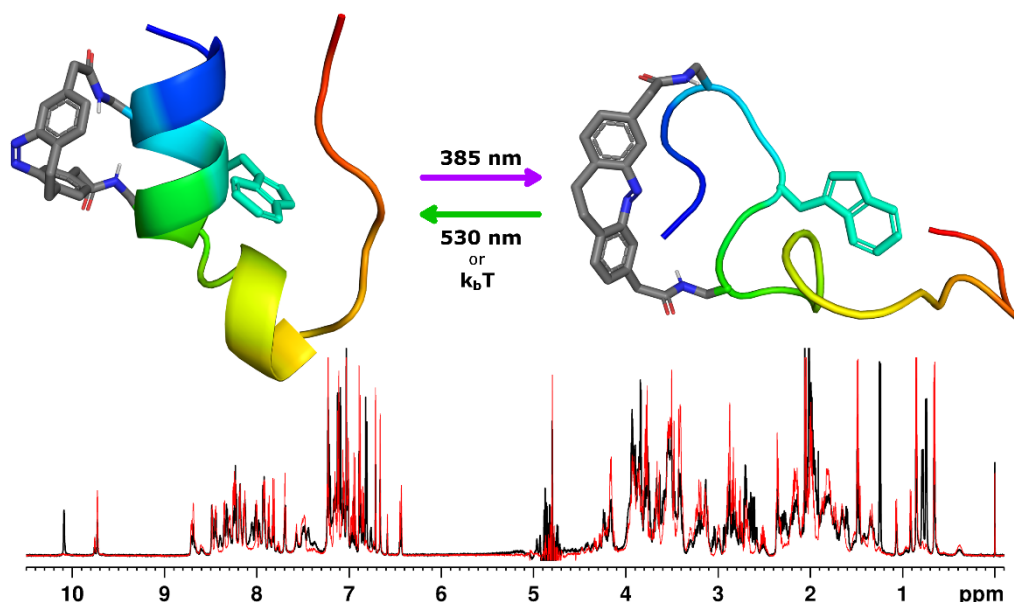


Figure 35: Graphical Abstract. A specifically designed diazocine cross-linker affords complete conformational control of a small, globular protein by the photoisomeric state.

Author contributions

Frank D. Sönnichsen, Matthias Lipfert, Nils Preußke, and Widukind Moormann developed the concept. Nils Preußke planned and performed all MD simulations as well as the synthesis and characterization of the Trp-cage and the switch cage. For his PhD thesis in organic chemistry, Widukind Moormann planned and performed the synthesis and characterization of the cross-linker. For his bachelor thesis in biochemistry, Widukind Moormann performed the MD-simulations as well as the synthesis and characterization of the Trp-cage and the switch cage under the guidance of Nils Preußke. Matthias Lipfert and Katrin Bamberg optimized the cross-linking reaction conditions. Nils Preußke and Widukind Moormann prepared the original draft. Nils Preußke, Widukind Moormann, Frank D. Sönnichsen, and Rainer Herges revised the manuscript. Frank D. Sönnichsen and Rainer Herges supervised the work. Nils Preußke, Frank D. Sönnichsen, Rainer Herges, and Katrin Bamberg acquired the funding.

PAPER

View Article Online
View Journal | View Issue



Cite this: *Org. Biomol. Chem.*, 2020, **18**, 2650

Visible-light-driven photocontrol of the Trp-cage protein fold by a diazocine cross-linker†

Nils Preußke, , Widukind Moormann, Katrin Bamberg, Matthias Lipfert, Rainer Herges * and Frank D. Sönnichsen *

Diazocines are characterized by extraordinary photochemical properties rendering them of particular interest for switching the conformation of biomolecules with visible light. Current developments afford synthetic access to unprecedented diazocine derivatives promising particular opportunities in photocontrol of proteins and biological systems. In this work, the well-established approach of photocontrolling the secondary structure of α -helices was exploited using a diazocine to reversibly fold and unfold the tertiary structure of a small protein. The protein of choice was the globular folded Trp-cage, a widely used model system for the elucidation of protein folding pathways. A specifically designed, short and rigid dicarboxy-functionalized diazocine-based cross-linker was attached to two solvent-exposed side chains at the α -helix of the miniprotein through the use of a primary amine-selective active ester. This cross-linking strategy is orthogonal to the common cysteine-based chemistry. The cross-linked Trp-cage was successfully photoisomerized and exhibited a strong correlation between protein fold and diazocine isomeric state. As determined by NMR spectroscopy, the *cis*-isomer stabilized the fold, while the *trans*-isomer led to complete protein unfolding. The successful switching of the protein fold in principle demonstrates the ability to control protein function, as the activity depends on their structural integrity.

Received 12th November 2019,
Accepted 19th December 2019

DOI: 10.1039/c9ob02442e

rscl.li/obc

Introduction

Biological systems comprise a complex network of biochemical interactions, *e.g.* signal transduction cascades, of very diverse compounds including small molecules (second messengers, metabolites), peptides (hormones), and proteins (enzymes, receptors). The ability to control the biological activities of peptides or proteins with high spatio-temporal resolution is a powerful tool to elucidate the mechanisms, kinetics and sequence of these biochemical pathways.^{1–4} Visible light is a perfect trigger as it transfers a desired amount of energy with the required spatial and temporal resolution, does not contaminate the sample, is non-toxic and has a high penetration depth (except through blood-supported tissue). Consequently, irradiation-induced configurational changes of incorporated light-sensitive chromophores have been used to control the three-dimensional structure of peptides and proteins.^{1–4}

By far the most frequently used photoswitches are azobenzenes.^{1–4} Upon irradiation, they undergo reversible isomerization between two states of significantly different geometry (Fig. 1, top). The thermodynamically stable extended *trans*-configuration can be converted to the shorter, bent *cis*-isomer with high yields upon irradiation with ultraviolet (UV) light. Due to its planarity, *trans*-azobenzene exhibits a tendency to aggregate when incorporated into peptides.^{5,6} Additionally, it may influence condensation and melting of DNA when equipped with positive charges.^{7–9} Therefore, most peptide or protein switching applications^{10–19} make use of a water soluble sulfonic acid-substituted azobenzene.²⁰ However, even this cross-linker may lead to aggregation when

tries (Fig. 1, top). The thermodynamically stable extended *trans*-configuration can be converted to the shorter, bent *cis*-isomer with high yields upon irradiation with ultraviolet (UV) light. Due to its planarity, *trans*-azobenzene exhibits a tendency to aggregate when incorporated into peptides.^{5,6} Additionally, it may influence condensation and melting of DNA when equipped with positive charges.^{7–9} Therefore, most peptide or protein switching applications^{10–19} make use of a water soluble sulfonic acid-substituted azobenzene.²⁰ However, even this cross-linker may lead to aggregation when

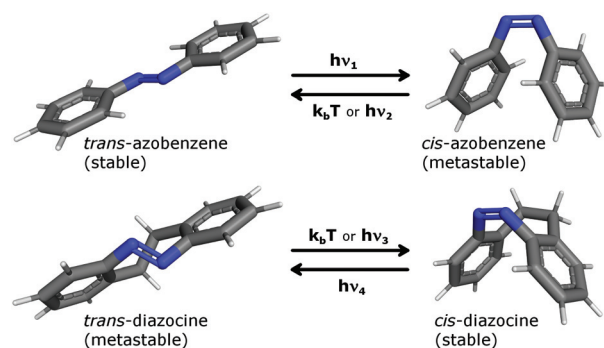


Fig. 1 *cis*–*trans*-isomerization of azobenzene (top) and diazocine (bottom).

Otto-Diels-Institute for Organic Chemistry, Christian-Albrechts-University of Kiel,
Otto-Hahn-Platz 4, 24118 Kiel, Germany. E-mail: rherges@oc.uni-kiel.de,
fsoennichsen@oc.uni-kiel.de

† Electronic supplementary information (ESI) available: Additional experimental procedures and spectroscopic data. See DOI: 10.1039/c9ob02442e



incorporated into a peptide¹⁰ or can unintentionally interfere with the protein fold due to interactions of the sulfonic acid moieties with guanidinium groups of arginine.¹⁵

Compared to azobenzenes, diazocines show a reversed switchability (Fig. 1, bottom): the ethylene bridge stabilizes the bent and bulky *cis*-configuration rendering it the thermodynamically stable isomer.^{21–24} *trans*-Diazocine is not planar, but adopts a twist or chair conformation. It is therefore not prone to π - π -stacking. Diazocines also display improved photochemical properties in organic solvents when compared to azobenzenes.^{21,22} These include a better separation of absorption bands and exceptionally high quantum yields resulting in higher switching efficiencies, *i.e.* better isomer ratios in the photostationary states (PSS).^{21,22,24} Importantly, switching in both directions can be achieved with visible light, which is essential for applications in biological systems. Recent developments in the synthesis of diazocines now render them almost as easily accessible as azobenzenes.^{25–27}

If carefully designed and attached to a protein, the relatively subtle structural change of the molecular switch affects the fold of the much larger biomacromolecule. Photocontrolling the biological function of α -helical peptides by reversibly allowing or preventing formation of their secondary structure is already well-established and has been applied to DNA recognition,^{10–12,14} protein–protein interactions^{5,6,12–14,16–19} or RNA binding.¹⁵ These examples make use of cross-linking the respective peptide using an azobenzene moiety with both attachment points at the same side of the α -helix. In contrast to azobenzene, a diazocine was applied only once to achieve photocontrol over a simple α -helical peptide in a study by Woolley *et al.*²⁸

The *cis*-configuration of an azobenzene or diazocine stabilizes the helical backbone conformation when the cross-linker is connected to residues $i, i + 4$ ^{13,19} or $i, i + 7$ ^{5,6,10,12–19} while switching to its *trans*-isomer prevents formation of the secondary structure. In contrast, connected to residues $i, i + 11$ the *trans*-cross-linker would stabilize the α -helical fold, which in turn adapts a disordered state upon isomerization to the contracted *cis*-state of the cross-linker.^{11,13,28}

Either of these approaches is useful to switch single, bio-active helices. A question of greater interest is whether they could be used to control the tertiary structure and thus function of cooperatively folded proteins. α -Helices are central and essential elements of the fold, particularly in small globular proteins or domains. Examples are the apoptosis-regulating Bcl-family of proteins,^{29,30} the engrailed homeodomain transcription factor,^{31,32} the KIX domain of CBP,³³ the ribonuclease T₁,³⁴ the villin headpiece subdomain³⁵ or the Trp-cage.^{36,37} In these, a solvent-exposed α -helix is of particular importance for establishing a network of tertiary contacts. Reversibly preventing the formation of secondary structure in these domains would be expected to result in their unfolding. This will perturb the integrity of the entire protein or protein complex which can be used as a tool to control their function.

The Trp-cage miniprotein^{36,37} displays typical protein properties³⁸ despite its length of only 20 residues. It comprises three elements of secondary structure, *i.e.* an N-terminal

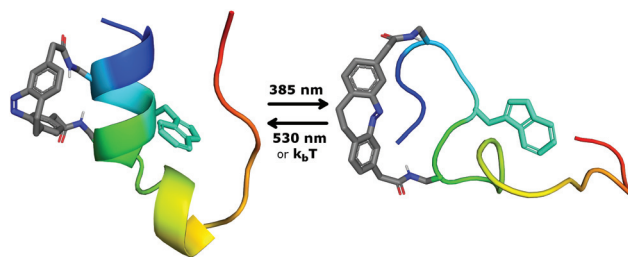


Fig. 2 The switchable Trp-cage (switch cage) was designed to exhibit a stable fold in the dark or under irradiation with green light (530 nm) when the diazocine cross-linker is present in its *cis*-configuration. Upon irradiation with violet light (385 nm) the diazocine is converted to the *trans*-isomer which prevents formation of the helix and in turn disrupts the tertiary structure.

α -helix, a short 3_{10} -helix and a polyproline II (PPII) helix. The eponymous encapsulation of a central tryptophan residue is driven by hydrophobic interactions and additionally stabilized by hydrogen bonds and a salt bridge. The highly stable and well characterized mutant 'TC10b' exhibits characteristics of folding cooperativity including reversible, sigmoidal thermal unfolding curves with a T_m above 55 °C.³⁷ Because of its protein-typical features yet small size the Trp-cage is a well-established model system for the experimental^{36,37,39–44} and theoretical^{37,40,45–48} elucidation of protein folding pathways with the aim to deduce general mechanisms applicable to larger proteins.

In this work, the Trp-cage was chosen to evaluate the hypothesis that folding of a surface-exposed α -helix reversibly influences the complete tertiary structure of a protein. Here, we describe the design, synthesis and characterization of a Trp-cage miniprotein conjugated with a diazocine-based cross-linker (Fig. 2). The cross-linker was conjugated with the protein through the use of an active ester which constitutes an adequate alternative to the common cysteine-based chemistry. We set out to reversibly fold and unfold the Trp-cage through visible-light-driven photocontrol of its α -helix. This approach explores the application of diazocines in aqueous environments and their use in achieving photocontrol of proteins.

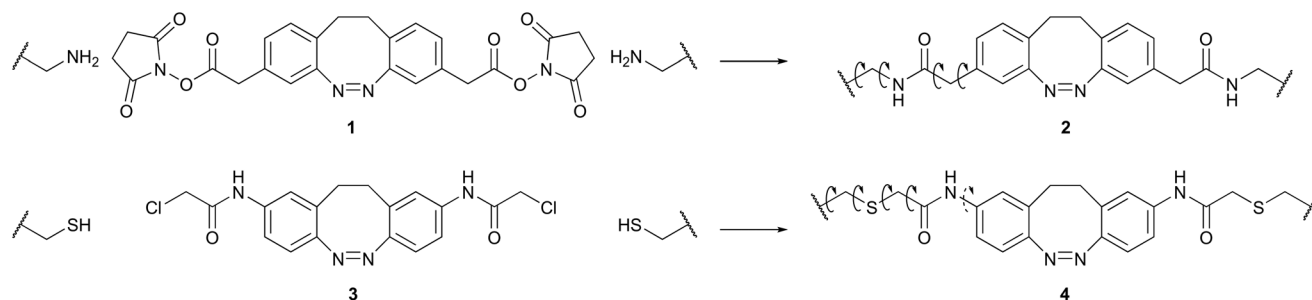
Results and discussion

The Trp-cage

Due to its small size, most residues in the Trp-cage significantly contribute to the fold stability which limits the options for attaching the cross-linker. Moreover, the short α -helix of the Trp-cage only allows cross-linking to residues $i, i + 4$ or $i, i + 7$. Residues 4 and 8 ($i, i + 4$) of TC10b seemed most suitable for conjugation because they are solvent exposed and contribute relatively little to the fold stability.³⁷ Incidentally, Markiewicz and co-workers came to the same conclusion when investigating the folding dynamics of the Trp-cage using a rigid, non-switchable cross-linker.⁴⁰

In our hands,⁴⁹ the use of primary-amine-selective active esters in peptide conjugation reactions has proven superior to





Scheme 1 Comparison of the primary amine-reactive cross-linker (1) presented in this work with the thiol-reactive cross-linker (3) by Woolley *et al.* Curved arrows indicate rotational degrees of freedom of single bonds of the cross-linker incorporated into a peptide or protein (2 and 4). The dashed arrow indicates reduced rotational freedom due to partial double bond character.

the usually employed cysteine-based cross-linking chemistry.^{1,3,28,40} In order to enable selective cross-linking, residues Ala4 and Lys8 of TC10b were mutated to L-2,3-diaminopropionic acid (Dpr, Γ)[‡] and the N-terminus was acetylated resulting in a Trp-cage named TC(4,8). Dpr was chosen over lysine because it has a drastically reduced side chain length and flexibility, which is necessary to efficiently couple the geometric properties of the diazocine with the fold state of the Trp-cage.

TC(4,8) was synthesized *via* Fmoc-based solid phase peptide synthesis. It was confirmed to exhibit the Trp-cage fold as evidenced by CD and two-dimensional (2D) ¹H-NMR spectroscopy. However, with a T_m of $(31.6 \pm 2.7)^\circ\text{C}$ the fold stability of TC(4,8) was reduced compared to TC10b ($\sim 55^\circ\text{C}$). This destabilization can be ascribed to the repulsion between the positively charged amines of Dpr4 and Dpr8. It leads to the presence of unfolded by-forms of the Trp-cage (Fig. S5†).

The cross-linking strategy

The diazocine-based cross-linker 1 (Scheme 1) was designed to match the distance between the amino side chains of Dpr4 and Dpr8 ($i, i + 4$) of the folded Trp-cage. The chosen design is based on an “unfolding-upon-extension/folding-upon-contraction” switching mechanism where the short, contracted *cis*-diazocine supports the stable fold of the protein. Upon switching to the extended *trans*-state of cross-linker formation of the Trp-cage fold is prevented (Fig. 2). This concept is in contrast to the diazocine-based photoswitchable α -helix by Woolley and co-workers, which relies on an $i, i + 11$ approach (folding-upon-extension/unfolding-upon-contraction).²⁸

When incorporated into the protein, advantages of cross-linkage 2 over the cysteine-dependent diazocine cross-linkage 4 by Woolley and co-workers²⁸ include reduced length and flexibility (decreased number of rotatable bonds) in the *cis*- as well as in the *trans*-configuration (Scheme 1). Furthermore, methylene groups in 2 serve as spacers between the diazocine moiety and the amide groups. This should preserve the excellent photochemical properties of the parent diazocine.²⁵

In order to validate the proposed cross-linking strategy, molecular dynamics (MD) simulations of the uncross-linked TC(4,8) and of the hypothetical amidated diazocine 5 (*cis*-5 and *trans*-5) were performed (Fig. 3). The distance between the cross-linker attachment points at TC(4,8), *i.e.* N^γ of Dpr4 and N^γ of Dpr8 was measured during the simulation. Similarly, the *cis*- and *trans*-isomer of the amidated diazocine 5 were constructed *in silico* to assess the accessible N–N'-distance of the cross-linker during the simulations.

The side chain amines (N^γ) of TC(4,8) are always less than 9.8 Å apart. With an accessible distance range of 9.8 Å to 15.2 Å *trans*-5 does not match this distance. On the other hand, *cis*-5 displays a large variance in its N–N'-distance covering a range between 3.3 Å and 13.1 Å that largely overlaps with the attachment point distances in TC(4,8). Finally, a model of the peptide-cross-linker-conjugate (*cis*-SC_a, Fig. 3) was constructed and its MD simulation resulted in a narrow distribution of $N^\gamma_{\text{Dpr4}}-N^\gamma_{\text{Dpr8}}$ -distances between 5.6 Å and 7.0 Å.

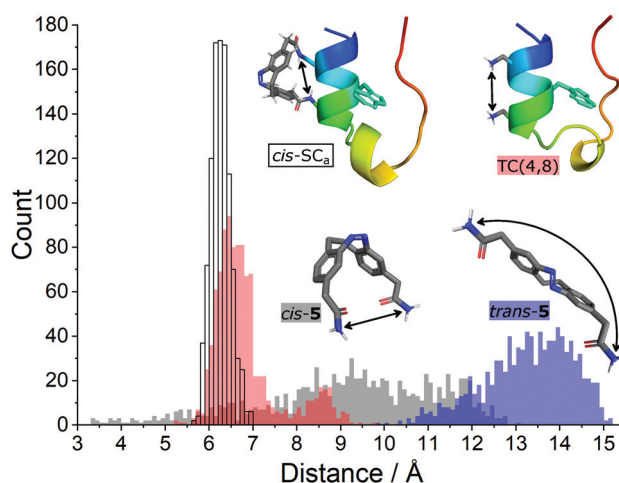


Fig. 3 The histograms of the switchable Trp-cage '*cis*-SC_a' (open), the uncross-linked Trp-cage 'TC(4,8)' (red), as well as the diazocines *cis*-5 (gray) and *trans*-5 (blue) result from an MD simulation over a period of 100 ns for each displayed molecule. Each simulation resulted in 1000 structures from which the indicated N–N'-distances were measured and plotted with a bin-size of 0.1 Å.

[‡] IUPAC did not define any one-letter code for the artificial amino acid L-2,3-diaminopropionic acid. Therefore, in this work we assigned it the greek letter Γ .



Thus, MD simulations indicated that the *trans*-cross-linker would prevent a stable fold when conjugated with the Trp-cage while the *cis*-diazocine supports a stable fold. Importantly, both observations confirm the concept.

The linear five step synthesis of the cross-linker **1** (Scheme 2) was based on a previously published oxidative C–C coupling and reductive azo cyclization.^{25,26} Initially, the carboxylic acid functional group of 3-nitro-4-methyl-phenylacetic acid (**6**) was protected with an 4-methyl-2,6,7-trioxabicyclo [2.2.2]octane-1-yl (OBO) protecting group. This protection according to Corey and Raju⁵⁰ started with an esterification with 3-methyl-3-oxetanemethanol (**7**) followed by a BF₃·Et₂O-catalysed rearrangement yielding the desired orthoester **9**. Potassium butoxide was used as a non-nucleophilic base to selectively deprotonate the toluene α protons of **9**. By addition of bromine as an oxidizing agent, the anions were converted into radicals and C–C-bond formation led to the desired dinitro dimer **10**. In the ensuing reductive azo cyclization, **10** was reduced with Ba(OH)₂/Zn to a hydrazine intermediate and subsequently oxidized with CuCl₂ and air. During work-up, the orthoester was hydrolysed to the open ester **11**, which was cleaved with Cs₂CO₃. Without purification, the resulting free carboxylic acid was converted with 1-ethyl-3-(3-dimethylaminopropyl)carbodiimide (EDC) and *N*-hydroxysuccinimide (NHS) into the active ester **1**.

The PSS of diazocine **11** was determined at 385 nm in MeOH or MeCN at 298 K (Fig. S23†). With 78% and 82% *trans*-isomer, respectively, **11** largely retains the outstanding properties of the parent diazocine (87% *trans*-isomer²⁵ at 385 nm in MeCN). In addition to its use in bio- and organic chemistry the dicarboxy-diazocine can therefore be applied as a monomer of polyamides or polyesters in photo- and mechano-responsive materials.

The folded *cis*-switch cage

Conjugation of TC(4,8) with cross-linker **1** was carried out in high dilution in dimethylsulfoxide (DMSO) by means of a

double syringe pump and resulted in the photo-switchable Trp-cage that we designate 'switch cage' (SC; Fig. 2).

Dark-adapted *cis*-SC shows all characteristics of a stable Trp-cage fold as evidenced by NMR chemical shift deviations (CSDs; Table S4†), number and intensity of nuclear Overhauser enhancement (NOE) cross-peaks and CD spectroscopy (Fig. 4). As expected, conjugation with the *cis*-diazocine markedly increases the stability of the fold reaching a *T*_m of (48.5 ± 1.4) °C compared to TC(4,8) ((31.6 ± 2.7) °C; Fig. 4a).

The Trp6 indole NH proton (H^{ε1}) is a particularly valuable indicator for the existence of the hydrophobic cluster, as its resonance frequency is not overlapping with other signals. Most importantly, it lies in the centre of the fold and its chemical shift deviation from the random coil chemical shift (~10.2 ppm^{51,52}) correlates with the stability of the Trp-cage. Interestingly, the indole region of the ¹H-NMR spectrum indicates two folded species of *cis*-SC (*cis*-SC_a: 9.728 ppm,

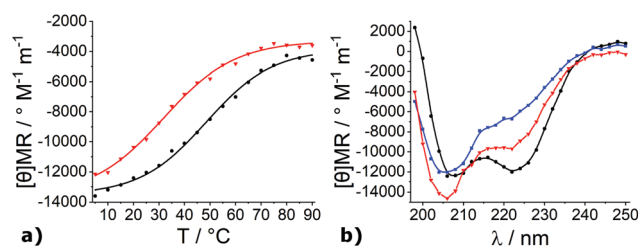
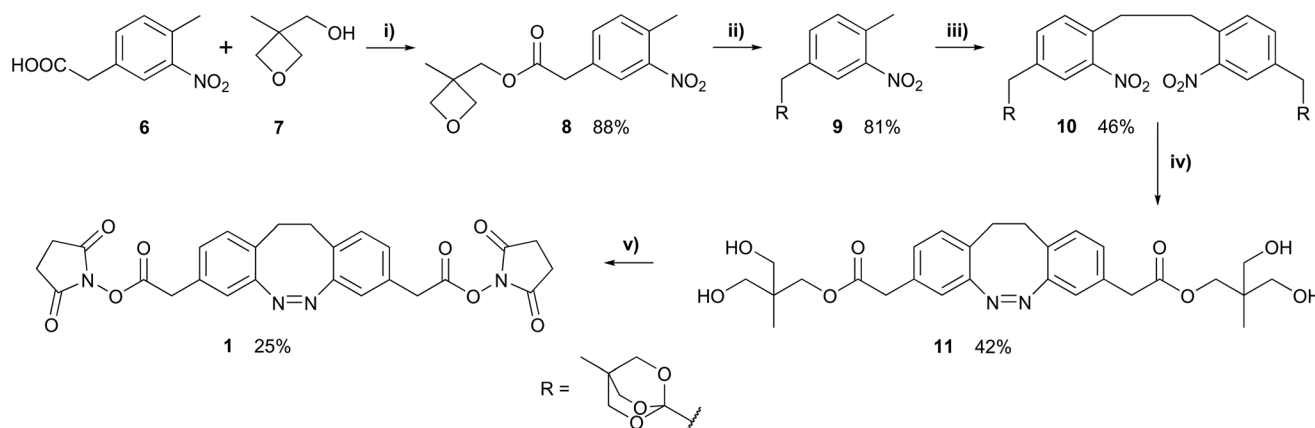


Fig. 4 (a) The mean residue molar ellipticity $[\theta]_{MR}$ at 222 nm of TC(4,8) (red triangles) and *cis*-SC (black circles) is plotted over the temperature. A sigmoidal Boltzman function was fitted to each plot to obtain the mid-point of thermal unfolding (melting temperature, *T*_m). Details regarding the fitted function can be obtained from the ESI.† (b) The CD spectrum of *cis*-SC (black circles) displays two minima at 206 nm and 222 nm indicative of an α -helix. TC(4,8) (red triangles) appears to have a lower helical propensity as the minimum at 222 nm is less pronounced. Compared to the spectrum of *cis*-SC, the spectrum of the switch cage after having reached the PSS at 385 nm (blue squares) indicates significantly reduced helical propensity.



Scheme 2 Reaction conditions: (i) *N,N'*-Dicyclohexylcarbodiimide (DCC), 4-dimethylaminopyridine (DMAP), dichloromethane (DCM); (ii) BF₃·Et₂O, triethylamine (TEA), DCM; (iii) *t*BuOK, Br₂, tetrahydrofuran (THF); (iv) 1. Zn, Ba(OH)₂ H₂O/EtOH; 2. CuCl₂/O₂, NaOH/MeOH; (v) 1. Cs₂CO₃, MeOH, H₂O; 2. 1-ethyl-3-(3-dimethylaminopropyl)carbodiimide (EDC), *N*-hydroxysuccinimide (NHS), *N,N'*-dimethylformamide (DMF).



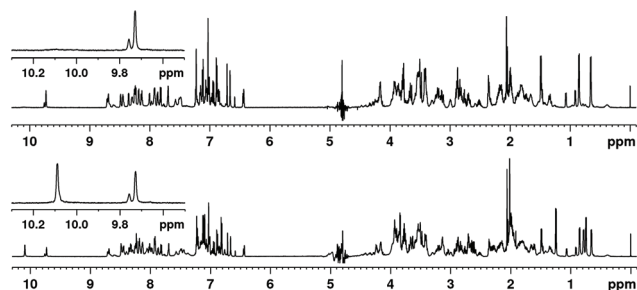


Fig. 5 The 1D ^1H -NMR spectra of *cis*-SC in its dark adapted state (top) and after having reached the PSS at 385 nm (bottom) are shown. In the expansion of the spectrum at the top the two folded species *cis*-SC_a and *cis*-SC_b are indicated by the two singlets of the Trp6 H $^{\epsilon 1}$ at 9.728 ppm and 9.757 ppm. The expansion of the important indole region between 10.3 ppm and 9.5 ppm clearly shows the rise of an unfolded species indicated by the intense singlet at 10.089 nm (bottom).

cis-SC_b: 9.757 ppm; Fig. 5, top). In fact, there is a second set of resonances for the spin systems of many, but not all residues and the diazocine moiety. NMR chemical shifts and NOE cross-peaks confirm that the major (*cis*-SC_a) and the minor (*cis*-SC_b) form both comprise the correctly folded protein and differ only in the orientation of the cross-linker (Fig. 6). The two diastereomers are the result of conjugating the prochiral diazocine moiety with the chiral protein. The *cis*-cross-linker is incorporated so that either its ethylene bridge (*cis*-SC_a, Fig. 6, left) or its azo-group (*cis*-SC_b, Fig. 6, right) is oriented towards residue Leu7. NOE spectroscopy (NOESY) indicates that the ethylene bridge side of the diazocine is in close vicinity to H $^{\beta 2/\beta 3}$ and H $^{\delta 1/\delta 2}$ of Leu7 in *cis*-SC_a. Similarly, the orientation of the cross-linker in *cis*-SC_b was also derived from the NOESY data. Notably, *cis*-SC_a is the main form with an approximately 3-fold higher population than its diastereomer *cis*-SC_b.

Switching from *cis*-SC to *trans*-SC

Irradiation with light at the wavelength of 385 nm produces a photo stationary state (PSS) with approximately 46% *trans*-SC and 54% *cis*-SC (Table S6†). At first glance, this ratio appears to be low for a diazocine, but few conversion ratios of diazo-

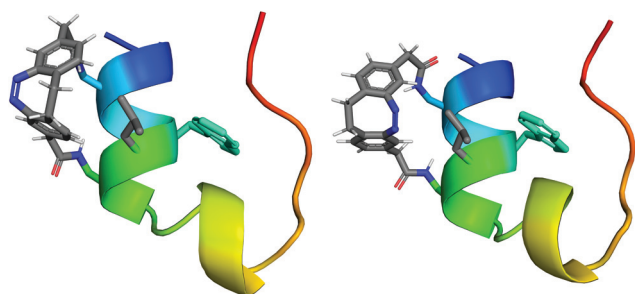


Fig. 6 The two different possible orientations of the cross-linker produce the two diastereomers *cis*-SC_a (left) and *cis*-SC_b (right). Structural models of the Trp-cage are shown in cartoon mode with the Trp6 side chain in the center of the molecule. The side chain of Leu7 is shown in grey in stick representation omitting hydrogens for clarity.

cines in water have been published. For instance, Woolley and colleagues²⁸ provided information on the PSS of their diazocine only in DMSO. In fact, the PSS of the switch cage compares well with the few published PSSs of diazocine derivatives in aqueous solution that range between 16% and 60% of *trans*-isomer.^{53–56} Although the conditions differ in pH, buffer and DMSO content, it appears that the PSSs of ethylene bridged diazocines§ in aqueous environment are generally lower than the PSS of the parent diazocine^{21,22} in organic solvents (>90% *trans*-species in *n*-hexane). In addition to the solvent effect, in *cis*-SC the folding free energy of the Trp-cage has to be overcome in order to unfold the miniprotein upon *cis* → *trans*-isomerization which also may lower the PSS.

After irradiation with light at 385 nm, new resonances are observed in the NMR spectra (Fig. 5) belonging to the *trans*-species of the switch cage (*trans*-SC). It was not possible to assign many atoms of *trans*-SC, as their resonances overlap with those of *cis*-SC_a and *cis*-SC_b. Moreover, the unfolded nature of *trans*-SC prohibits the assignment due to overlap of intramolecular proton signals and resulting equivocal inter-residual NOEs. Despite these difficulties it was possible to determine the folding state of *trans*-SC.

A first evidence, that *trans*-SC is unfolded and assumes a random coil conformation is provided by the chemical shift of its Trp6 indole NH proton (H $^{\epsilon 1}$) at 10.089 ppm (Fig. 5, bottom). This is very close to the random coil shift (~10.2 ppm^{51,52}) indicating the absence of the hydrophobic cluster of the folded state. Moreover, at 298 K the Trp6 H $^{\epsilon 1}$ of *cis*-SC_a shows coupling through space to H $^{\beta 2}$, H $^{\beta 3}$, H $^{\gamma}$ and the backbone H N of Arg16 as well as H $^{\alpha}$ and H $^{\delta}$ of Pro18 and H $^{\delta 2/\delta 3}$ of Pro19 (Fig. 7). In contrast, the Trp6 H $^{\epsilon 1}$ of *trans*-SC displays only one extremely weak NOE cross-peak (3.498 ppm). Even at 278 K, a temperature that favours folding and which enables long measurements due to slow *trans* → *cis* isomerization, no further NOE cross-peaks are observable in the *trans*-SC NOE spectrum.

In addition to NMR spectroscopy, CD spectroscopy also provides evidence that *trans*-SC is completely unfolded. The mean residue molar ellipticity [θMR] at 222 nm in the dark-adapted state amounts to −12 017° M^{−1} m^{−1}, which is reduced to −6725° M^{−1} m^{−1} in the PSS at 385 nm (Fig. 4b). This corresponds to a reduction by 44% which is in the same range as the *cis* → *trans*-conversion ratio in the PSS indicating complete unfolding of the α-helix and thus absence of secondary and tertiary structure in *trans*-SC.

The lack of α-helicity as evidenced by CD-spectroscopy, the Trp6 H $^{\epsilon 1}$ chemical shift and the disappearance of inter-residual NOE cross-peaks upon switching to the *trans*-state unambiguously demonstrate that the switch cage is entirely unfolded in its *trans*-state. Conversely, the switch cage is nearly

§The recently developed N-bridged diazocines are a remarkable exception to that rule because of their nitrogen-atom incorporated into the bridge. This feature distinguishes them from 'standard' diazocines bearing an ethylene bridge. The NAc-CH₂-bridged diazocine shows *cis* → *trans* conversion rates of 78% *trans*-isomer in D₂O : MeOH-d₄ (80 : 20) at 405 nm.²⁴



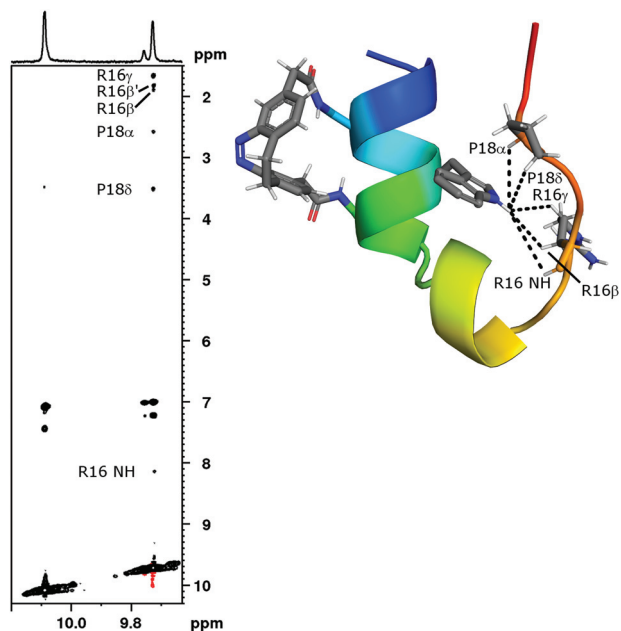


Fig. 7 The ^1H , ^1H -NOESY of the switch cage after irradiation to the PSS at 385 nm was recorded at 298 K. The expansion shows the indole region of *cis*-SC_a (F2: 9.728 ppm), *cis*-SC_b (F2: 9.757 ppm) and *trans*-SC (F2: 10.089 ppm). The six inter-residual cross-peaks in the vertical direction of *cis*-SC_a evidence a stable tertiary structure. The NOE signals highlighted in the expansion are depicted in the model structure of *cis*-SC_a. In contrast to *cis*-SC_a, only one unassigned cross-peak is observed for the indole proton of *trans*-SC (F2: 10.098 ppm, F1: 3.485 ppm). The NOEs between 7.0 ppm and 7.5 ppm are intra-residual cross-peaks with the neighbouring aromatic protons. For *cis*-SC_b inter-residual NOEs are not visible in this depiction due to low population.

quantitatively folded in the presence of the *cis*-linker. Thus, the folding state of the protein is completely coupled to the isomeric state of the cross-linker.

Switching from *trans*-SC to *cis*-SC

Irradiation with light at the wavelength of 530 nm provides almost complete conversion to *cis*-SC (Fig. S16†). Moreover, the NMR-spectrum of *cis*-SC recorded immediately after irradiation to its PSS at 530 nm is indistinguishable from that of dark-adapted *cis*-SC.

The thermal *trans* → *cis* relaxation process of the switch cage was observed by ^1H -NMR spectroscopy and quantified by integration of selected peaks of the protein or the diazocine moiety (Table S5 and Fig. S14, S15†) after irradiation to the PSS at 385 nm. At 298 K in the dark, this process requires 39 h after which *trans*-SC is not quantifiable anymore (Fig. S16†). It follows first order kinetics with a half-life of (6.2 ± 0.3) h (Table S6†). Within the error of measurement, differences in the determined relaxation rates for diazocine signals and protein signals (Trp6 H^{e1}) are insignificant. Further, the relaxation of *trans*-SC to *cis*-SC_a and to *cis*-SC_b is equally fast. Together, this is an additional demonstration of the strict coupling between the isomeric state of the diazocine and the folding state of the Trp-cage.

Throughout the entire study, the same sample was used for all spectroscopic measurements. In consequence, it was subjected to multiple switching cycles without showing any sign of photobleaching or other material fatigue. Furthermore, aggregation was never observed, not even in the PSS at 385 nm, when approximately half of the population of the switch cage was unfolded exposing the hydrophobic core and the *trans*-diazocine to the solvent. This emphasizes the reversibility of the switching process and the photochemical stability of the switch cage.

The relationship between *cis*-SC_a and *cis*-SC_b

Regardless of the wavelength or intensity of incident light (day-light-adapted, dark-adapted, PSS at 385 nm, PSS at 530 nm), the two diastereomers *cis*-SC_a and *cis*-SC_b have always been observed in a ratio of 3 : 1. While often indicative of a thermodynamic reaction control, the apparently constant ratio of *cis*-SC_a to *cis*-SC_b in photoreactions appears surprising at first. The parent *cis*-diazocine **1** is prochiral and converts upon radiation at 385 nm equally fast into two enantiomeric *trans*-forms, that are believed to comprise an equilibrium of twist- and chair-conformations.⁵⁷ These forms convert back to *cis*-diazocine equally well.

In the chiral context of the protein, however, irradiation results in multiple possible *cis*-*trans*-isomerizations (Scheme S1†) between diastereomeric states. Unhindered inter-conversion would lead to the expectation of a 1 : 1 product ratio of *cis*-SC_a and *cis*-SC_b. The observed uneven *cis*-SC_a/*cis*-SC_b ratio thus suggest that the conversion rates between the states differ between diastereomers implying a form of chiral induction by the protein moiety.

Although it is possible that the conversion from either *trans*-diastereomer occurs faster to the *cis*-SC_a diastereomer, a chiral induction in the *trans*-state appears unlikely since the protein moiety is unfolded and should have very limited influence on the conversion kinetics. In the *cis*-states, however, the environment of the chromophore differs significantly for example with closer protein-diazocine contacts in *cis*-SC_a. These structural differences might slow the photoconversion of *cis*-SC_a sterically or energetically whereas *cis*-SC_b more rapidly isomerizes to either *trans*-isomer. Accordingly, this chiral induction could lead to the observed bias in the photo-stationary states.

Conclusions

The present study aimed to reversibly fold and unfold the Trp-cage upon irradiation with visible light of different wavelengths. Since the elongation of the diazocine during *cis* → *trans*-isomerization induces unfolding, the switching approach presented in this work is described as “unfolding-upon-extension/folding-upon-contraction”. This goal was achieved through the conjugation of an N-terminally acetylated Trp-cage mutant ‘TC(4,8)’ bearing L-2,3-diaminopropionic acid (Dpr, Γ)‡ in positions 4 and 8. A diazocine-based, primary amine-selec-



tive cross-linker (**1**) was designed to match the distance between the N^γ of both Dpr-residues in its *cis*-state. Upon cross-linking, the fold of the resulting photoswitchable Trp-cage (switch cage, SC) is stabilized significantly compared to the uncross-linked peptide. Irradiation with light of the wavelength 385 nm produces a PSS of approximately 46% *trans*-SC. This isomerization is completely reversed upon irradiation with light at 530 nm or through thermal relaxation. Most importantly, in the *trans*-state, secondary and tertiary structuring is completely abolished. As predicted, pulling apart only one helical turn between residues 4 and 8 destroys the entire helical structure and in consequence unfolds the hydrophobic cluster.

With these features, the switch cage may serve as a valuable tool for the analysis of the Trp-cage folding pathway adding visible light as an alternative trigger to the previously used T-jump^{39,41} in IR or fluorescence spectroscopy. The reversibility of the switching process enables multiple switching cycles and thus facilitates multiple and repeated observations of folding and unfolding kinetics.

In this study, a dicarboxy-functionalized diazocine was furnished with selective reactivity towards primary amines by introduction of NHS-active ester moieties. This cross-linking strategy adds a valuable alternative to current methods to conjugate the chromophore with the protein. The NHS-ester cross-linking chemistry is orthogonal to the common cysteine-based chemistry.⁵⁸ When incorporated into the protein (*cf.* Scheme 1), the presented diazocine cross-linker is shorter and more rigid than the chloroacetamide-functionalized diazocine.²⁸

The active ester cross-linking strategy is especially interesting for synthetic peptides and proteins, as next to lysine several amino group-bearing homologues exist that can be used to tailor length and flexibility of the cyclized product. Particularly short and rigid cross-linkages are obtained when the shortest lysine-homologue Dpr is utilized. The cross-linker **1** may also be incorporated *via* naturally occurring lysine residues or a free N-terminus, but this would limit its application to “folding-upon-extension/unfolding-upon-contraction”-approaches due to the high flexibility of the lysine side chains.

In conclusion, we were able to reversibly fold and unfold the secondary and tertiary structure of the Trp-cage miniprotein upon irradiation with visible light. Most importantly the present study shows that it is generally possible to reversibly fold and unfold a single, solvent-exposed α -helix in a small, but stable protein resulting in photocontrol of the entire fold. This strengthens our beliefs that this approach is applicable to larger proteins or protein domains.

Experimental

Trp-cage synthesis

TC(4,8) (Ac-DAYΓQWLΓDGGPSSGRPPPS) \ddagger was synthesized using Fmoc-based solid phase peptide synthesis with a microwave-assisted, semi-automated peptide synthesizer Initiator⁺

SP Wave (Biotage, Uppsala, Sweden) on Wang-resin (200–400 mesh, 0.86 mmol g^{−1}; 200 mg, 1 eq.; ChemPep, Wellington, FL, USA) at a 0.172 mmol scale. To avoid aspartimide formation during synthesis the dipeptide Fmoc-Asp(OtBu)-(DMB)Gly-OH (Novabiochem, Merck, Darmstadt, Germany) was used. Moreover, the two consecutive serines were coupled as the pseudo-proline dipeptide Fmoc-Ser(*t*Bu)-Ser(ψ Me,Mepro)-OH (Novabiochem, Merck, Darmstadt, Germany). In general, the peptide was synthesised using repetitive cycles of coupling, capping (*i.e.* acetylating unreacted peptide chains) and deprotection. Each coupling, capping or deprotection step was followed by draining the liquid and washing the resin with *N,N*-dimethylformamide (DMF; 2 ml) four times. Coupling of amino acids was achieved using the corresponding amino acid (860 μ mol, 5 eq.), hexafluorophosphate azabenzotriazole tetramethyl uronium (HATU; 320 mg, 843 μ mol 4.9 eq.) and *N,N*-diisopropylethylamine (DIPEA; 300 μ l, 1.72 mmol, 10 eq.) dissolved in DMF (2 ml). The reaction solution was heated to 75 °C and vortexed at 600 rpm for 5 min. The coupling step was performed twice (double coupling) for the following amino acids: Fmoc-Ser(*t*Bu)-OH, Fmoc-Arg(Pbf)-OH, Fmoc-Gly-OH, Fmoc-Dpr(Boc)-OH, Fmoc-Gln(Trt)-OH and Fmoc-Ala-OH. (Double) coupling was followed by a capping step using a solution (2 ml) of pyridine (25% v/v), and acetic anhydride (25% v/v) in DMF at 75 °C at 600 rpm for 5 min. Removal of the Fmoc-group was achieved in three consecutive steps (1 min, 4 min, 4 min). Each step used a solution (2 ml) of piperidine (25% v/v) in DMF at 75 °C at 600 rpm which was drained afterwards. After the final deprotection, the peptide was N-terminally acetylated using the capping reagents and conditions. The peptide was cleaved off the resin using a mixture of trifluoroacetic acid (TFA; 90% v/v), *m*-dimethoxybenzene (DMB; 5% v/v), triisopropylsilane (TIPS; 2.5% v/v) and water (2.5% v/v). The cleavage reaction was completed after gently agitating it for 3 h at room temperature. The peptide was precipitated using cold diethyl ether and centrifuged. The supernatant was decanted. The pellet was dissolved in water and lyophilized.

Trp-cage purification

The peptide was purified in four batches by high performance liquid chromatography (HPLC) on a VWR-Hitachi LaChrom Elite instrument (VWR, Darmstadt, Germany) equipped with a semi-preparative PLRP-S column (325 mm \times 30 mm, 30 nm pore diameter, 8 μ m particle size; Agilent, Santa Clara, CA, USA), a VWR-Hitachi L2400 UV detector (VWR, Darmstadt, Germany) and a Foxy R1 fraction collector (Teledyne ISCO, Lincoln, NE, USA). A flow rate of 6 mL min^{−1} and the following gradient (solvent A: water, 0.1% formic acid (FA), solvent B: acetonitrile, 0.1% FA) was applied: 0 min: 5% B, 5 min: 5% B, 25 min: 15% B, 55 min: 25% B, 65 min: 95% B, 75 min: 95% B, 80 min: 5% B, 90 min: 5% B. Fractions of 3 ml were collected between 45 min and 75 min. TC(4,8) eluted after retention time of t_R = 55.5 min. A dead time of 20 min was observed.

Collected fractions were analysed by HPLC-mass spectrometry (HPLC-MS) using the same VWR-Hitachi LaChrom



Elite instrument (VWR, Darmstadt, Germany) equipped with a 717 plus autosampler (Waters, Milford, MA, USA), an analytical PLRP-S column (150 mm \times 4.6 mm, 30 nm pore diameter, 8 μ m particle size; Agilent, Santa Clara, CA, USA), a VWR-Hitachi L2400 UV detector (VWR, Darmstadt, Germany) and an expressionL cms MS device (Advion, Harlow, UK). A flow rate of 1 mL min⁻¹ and the following gradient (solvent A: water, 0.1% FA, solvent B: acetonitrile, 0.1% FA) was applied: 0.0 min: 5% B, 2.5 min: 5% B, 12.5 min: 60% B, 13.5 min: 95% B, 16.0 min: 95% B, 17.0 min: 5% B, 18.5 min: 5% B. A dead time of 2.0 min was observed. TC(4,8) eluted after retention time of t_R = 9.8 min. Fractions deemed sufficiently pure were combined and lyophilized. The peptide was obtained as a white fluffy solid (17.8 mg, 8.65 μ mol, 5%).

Cross-linker synthesis and purification

Details regarding the cross-linker synthesis, purification and characterization can be found in the ESI.†

Cross-linking reaction and purification

DIPEA (33 μ L, 190 μ mol, 100 eq.) and DMSO (1.5 ml) were added to a 50 ml polypropylene (PP) centrifuge tube equipped with a magnetic stir bar. A solution of TC(4,8) (4.0 mg, 1.9 μ mol, 1 eq.) in DMSO (1.5 mL) supplemented with DIPEA (33 μ L, 190 μ mol, 100 eq.) was transferred into a 2 mL syringe. A second 2 mL syringe was filled with a solution of the NHS-functionalized cross-linker **1** (1 mg, 2.1 μ mol, 1.1 eq.) in DMSO (1.81 mL). The two reactants were slowly added to the centrifuge tube, each at a speed of 2 μ L min⁻¹ under continuous stirring at room temperature. After complete addition, the reaction was stirred for 2 d. Subsequently, the solution was flash-frozen with liquid nitrogen and lyophilized. The crude product was dissolved in 2.5 mL of water by briefly sonicating it in the centrifuge tube using an ultrasonic bath. The switch cage was purified in ten small batches *via* HPLC using the VWR-Hitachi LaChrom Elite instrument (VWR, Darmstadt, Germany) equipped with a 717 plus autosampler (Waters, Milford, MA, USA), an analytical PLRP-S column (150 mm \times 4.6 mm, 30 nm pore diameter, 8 μ m particle size; Agilent, Santa Clara, CA, USA), a VWR-Hitachi L2400 UV detector (VWR, Darmstadt, Germany) and a Foxy R1 fraction collector (Teledyne ISCO, Lincoln, NE, USA). A flow rate of 1 mL min⁻¹ and the following gradient (solvent A: water, 0.1% FA, solvent B: acetonitrile, 0.1% FA) was applied: 0.0 min: 5% B, 2.5 min: 5% B, 10 min: 27% B, 20 min: 29% B, 25 min: 95% B, 29 min: 95% B, 31 min: 5% B, 35 min: 5% B. The switch cage eluted after a retention time of t_R = 18.2 min. A dead time of 2.0 min was observed. Fractions of the ten different batches with identical retention times were collected into the same containers. Fractions were analysed using the same HPLC-MS set-up as described in the chapter Trp-cage purification. The switch cage eluted after a retention time of t_R = 12.0 min. Fractions deemed sufficiently pure were combined and lyophilized which afforded the switch cage as a yellowish solid (0.8 mg, 330 nmol, 17%).

Ultrahigh performance liquid chromatography – high resolution mass spectrometry

TC(4,8) and the switch cage analysed by ultrahigh performance liquid chromatography – high resolution mass spectrometry (UHPLC-HRMS) using an Ultimate 3000 RS instrument coupled to a QExactive Plus Hybrid Quadrupole-Orbitrap MS device (both Thermo Fisher Scientific, Waltham, MA, USA). A Zorbax RRHD Eclipse Plus C18 column with a length of 100 mm and a diameter of 3 mm (Agilent, Santa Clara, CA, USA) was used. The MS was set to detect positive ions and the resolution was set to FWHM = 70 000 at m/z = 200. The Full MS method was applied covering an m/z range between 200 and 3000. A flow rate of 0.4 mL min⁻¹ and the following gradient (solvent A: water, 0.1% FA, solvent B: acetonitrile, 0.1% FA) was applied: 0.0 min: 5% B, 1.0 min: 5% B, 9.0 min: 80% B, 9.5 min: 95% B, 11.0 min: 95% B, 11.5 min: 5% B, 13.2 min: 5% B. A dead time of 1.23 min was observed. The TC(4,8) eluted after retention time of t_R = 4.92 min. Chromatograms and the corresponding mass spectra of TC(4,8) can be found in the ESI (Fig. S1–S3†). The switch cage eluted after retention time of t_R = 6.19 min. Chromatograms and the corresponding mass spectra of the switch cage can be found in the ESI (Fig. S5–S8†).

Molecular modelling and molecular dynamics simulations

All computational studies were performed using the Schrödinger Suite Release 2017-4 (Schrödinger LLC, New York, NY, USA). The amidated cross-linkers *cis*-5 and *trans*-5 were built *in silico* using Maestro (Schrödinger LLC, New York, NY, USA). The structures were geometrically relaxed using MacroModel (Schrödinger LLC, New York, NY, USA) by applying the OPLS3 force field with implicit water. Charges were compensated by the addition of Na⁺ or Cl⁻. To avoid isomerization during conformational energy minimization, constraints were applied to the CNNC torsion angle (*cis*-5: 0°, force constant (FC) = 200 kJ mol⁻¹ Å⁻²; *trans*-5: 147°, FC = 300 kJ mol⁻¹ Å⁻²) and to the NNC bond angles (*cis*-5: 121°, FC = 200 kJ mol⁻¹ Å⁻²; *trans*-5: 112°, FC = 200 kJ mol⁻¹ Å⁻²).

The model of TC(4,8) was built from the first structure of the NMR-derived structure ensemble of TC10b (RCSB PDB accession code 2JOF) using Maestro. Energy minimization was achieved in the same way as for *cis*-5 and *trans*-5, but without any constraints.

The model of *cis*-SC was built from the relaxed model of TC (4,8). The relaxed *cis*-5 cross-linker was incorporated into the peptide using Maestro resulting in the diastereomer *cis*-SC_a. Relaxation was achieved in the same way as for *cis*-5 applying the same constraints to the cross-linker.

MD simulations were performed using the Desmond Molecular Dynamics System (D. E. Shaw Research, New York, NY, USA) and set up with the Maestro-Desmond Interoperability Tools (Schrödinger LLC, New York, NY, USA). The molecule was submerged in an orthorhombic box of explicit water complying with the SPC water model using the OPLS3 force field. The size of the box was adjusted to a minimal



volume with at least 10 Å distance between the molecule and each side of the box. The temperature was set to 300 K and the pressure was set to 1.01325 bar. MD simulations covered a period of 100 ns with recording intervals of 100 ps (trajectory) and 1.2 ps (energy). The starting geometry of each molecule was the result of the previous minimization using MacroModel. In order to avoid isomerization of the cross-linkers during MD simulations, the central eight-membered ring of the cross-linker was restrained to its starting geometry with a FC of 300 kJ mol⁻¹ Å⁻². Distances between atoms were measured and exported using the simulation event analysis panel of the Schrödinger Suite. The structures created with the Schrödinger Suite were exported as PDB files to create the molecule depictions for the figures using the PyMOL Molecular Graphics System Version 1.9.0.0. (Schrödinger LLC, New York, NY, USA).

CD spectroscopy

CD spectra were recorded on a Jasco J-720 spectropolarimeter (Jasco, Pfungstadt, Germany) equipped with a Haake WKL 26 thermostat (Thermo Electron Corporation, now Thermo Fisher Scientific, Waltham, MA, USA) and a Jasco PTC-423S peltier element (Jasco, Pfungstadt, Germany). For all measurements the same Quartz glass cuvette with an optical path length of 1.00 mm was used. All spectra were obtained in water at concentrations of 36 µM. The pH was adjusted to 5.4 ± 0.2 using 0.1 M solutions of NaOH and/or HCl. The concentration of TC (4,8) was determined by the UV absorption of Tyr and Trp according to Gill and von Hippel.⁵⁹ This method was not applicable to the switch cage because of the unknown extinction coefficient of the diazocine in water. Therefore, the concentration of the switch cage was determined by recording a 1D-¹H-NMR spectrum of the sample with a known amount of DSS and correlating the integrals of the DSS signal and the Leu7δ-methyl groups of *cis*-SC_a and *cis*-SC_b, which do not exchange and are not overlapping with other signals.

Full spectra are averaged over six measurements and were recorded at 25 °C. In order to obtain the spectra of the switch cage in its PSS, the sample was irradiated at 385 nm for 10 s prior to each of the six measurements.

Thermal unfolding and folding was observed between 5 °C and 90 °C at a wavelength of 222 nm. A heating and cooling rate of 1 °C min⁻¹ was applied. Before starting the temperature gradient, the sample was equilibrated for 5 min at the starting temperature. Two consecutive heating and cooling cycles were averaged for each spectrum. This repetition indicated full reversibility of thermal unfolding and folding of *cis*-SC and TC (4,8). For determination of the melting point the spectra were fitted with a sigmoidal Boltzmann fit. The fitting results are given in the ESI.†

NMR spectroscopy

The NMR spectra of TC(4,8) and of the switch cage were obtained on a AV III 600 Fourier transform-NMR spectrometer (Bruker, Billerica, MA, USA) at frequencies of 600.1 MHz for ¹H-nuclei. The spectrometer was equipped with a triple reso-

nance cryo probe. All samples were dissolved in a solution of 90% H₂O and 10% D₂O. 4,4-Dimethyl-4-silapentane-1-sulfonic acid (DSS) served as the internal standard for referencing. Water suppression was achieved by excitation sculpting⁶⁰ using standard bruker pulse sequences.

Chemical shifts were assigned using 2D-NMR techniques including ¹H,¹H-correlated spectroscopy (COSY), ¹H,¹H-total correlation spectroscopy (TOCSY) and ¹H,¹H-nuclear Overhauser enhancement spectroscopy (NOESY). Except for the spectra of the switch cage after having reached the PSS at 385 nm, all 2D-NMR spectra were recorded with the following parameters: COSY spectra were recorded with a size of free induction decay (FID) of 4096 (F2) by 1024 (F1) data points and a spectral width of 14.0261 ppm (F2) by 14.0000 ppm (F1). TOCSY data were acquired with a size of FID of 4096 (F2) by 512 (F1), a spectral width of 14.0261 ppm (F2) by 14.0261 ppm (F1) and a mixing time of 60 ms. NOESY data were recorded with a size of FID of 4096 (F2) by 512 (F1), a spectral width of 14.0261 ppm (F2) by 14.0261 ppm (F1) and using a mixing time of 200 ms.

All measurements were performed at 298 K if not stated otherwise. Spectra of TC(4,8) were recorded at concentrations of 3.3 mg ml⁻¹ (1.6 mM) at pH = 5.3 ± 0.1. Each data point of each spectrum was an accumulation of 8 scans. Spectra of the switch cage were recorded at concentrations of 1.2 mg ml⁻¹ (0.5 mM) at pH = 5.5 ± 0.1. Each data point of each spectrum was an accumulation of 16 scans.

In order to obtain spectra of the Trp-cage after having reached its PSS at 385 nm the sample was irradiated for 10 s immediately before each experiment. Due to the relatively fast *trans* → *cis* relaxation the 2D-NMR experiments were recorded with a reduced amount of scans and a reduced size of FID in the F1 dimension but otherwise identical parameters as stated above. The COSY, TOCSY and NOESY were recorded with an F1 FID of 512 and 8 scans per data point.

Irradiation

Irradiation was performed immediately prior to the measurements outside the spectrometer (NMR, CD, UV/vis) with samples already inside their container for the respective spectroscopic measurement. Samples were irradiated using light emitting diodes (LEDs) emitting at 385 nm or 530 nm (Sahlmann Photochemical Solutions, Kiel, Germany). Irradiation at 385 nm was performed from four sides by a total of twelve Nichia NCSU034A LEDs with the following specifications: FWHM = 9 nm, *P*(opt) = 12 × 340 mW. Irradiation at 530 nm was performed from four sides by a total of 16 Luxeon LXML-PM01-0080 LEDs with the following specifications: FWHM = 33 nm, *P*(opt) = 16 × 200 mW. Regardless of the container and the wavelength the PSS was reached within 10 s of irradiation.

Author contributions

F. D. S., M. L., N. P. and W. M. developed the concept. N. P. planned and performed all MD simulations as well as the syn-



thesis and characterization of the Trp-cage and the switch-cage. For his PhD thesis in organic chemistry, W. M. planned and performed the synthesis and characterization of the cross-linker. For his bachelor thesis in biochemistry, W. M. performed the MD-simulations as well as the synthesis and characterization of the Trp-cage and the switch-cage under the guidance of N. P. M. L. and K. B. optimized the cross-linking reaction conditions. N. P. and W. M. prepared the original draft. N. P., W. M., F. D. S. and R. H. revised the manuscript. F. D. S. and R. H. supervised the work. N. P., F. D. S., R. H. and K. B. acquired the funding.

Conflicts of interest

There are no conflicts to declare.

Acknowledgements

The authors gratefully acknowledge financial support by the Deutsche Forschungsgesellschaft (DFG) within the Collaborative Research Center SFB 677, "Function by Switching". N. P. thanks the Deutsche Bundesstiftung Umwelt (German Federal Environmental Foundation) for a predoctoral fellowship. K. B. thanks the Studienstiftung des deutschen Volkes (German Academic Scholarship Foundation) for a predoctoral fellowship. The authors thank Prof. Joachim Gröttinger for granting access to and use of his CD spectrometer.

Notes and references

- 1 A. A. Beharry and G. A. Woolley, *Chem. Soc. Rev.*, 2011, **40**(8), 4422.
- 2 W. Szymański, J. M. Beierle, H. A. V. Kistemaker, W. A. Velema and B. L. Feringa, *Chem. Rev.*, 2013, **113**(8), 6114.
- 3 R. J. Mart and R. K. Allemann, *Chem. Commun.*, 2016, **52**(83), 12262.
- 4 L. Albert and O. Vázquez, *Chem. Commun.*, 2019, **55**(69), 10192.
- 5 J. R. Kumita, D. G. Flint, G. A. Woolley and O. S. Smart, *Faraday Discuss.*, 2002, **122**, 89–103; discussion 171–190.
- 6 A. M. Ali, M. W. Forbes and G. A. Woolley, *ChemBioChem*, 2015, **16**(12), 1757.
- 7 A. Bergen, S. Rudiuk, M. Morel, T. Le Saux, H. Ihmels and D. Baigl, *Nano Lett.*, 2016, **16**(1), 773.
- 8 A. Estévez-Torres, C. Crozatier, A. Diguët, T. Hara, H. Saito, K. Yoshikawa and D. Baigl, *Proc. Natl. Acad. Sci. U. S. A.*, 2009, **106**(30), 12219.
- 9 A.-L. M. Le Ny and C. T. Lee Jr., *J. Am. Chem. Soc.*, 2006, **128**(19), 6400.
- 10 L. Guerrero, O. S. Smart, C. J. Weston, D. C. Burns, G. A. Woolley and R. K. Allemann, *Angew. Chem., Int. Ed.*, 2005, **44**(47), 7778.
- 11 L. Guerrero, O. S. Smart, G. A. Woolley and R. K. Allemann, *J. Am. Chem. Soc.*, 2005, **127**(44), 15624.
- 12 G. A. Woolley, A. S. I. Jaikaran, M. Berezovski, J. P. Calarco, S. N. Krylov, O. S. Smart and J. R. Kumita, *Biochemistry*, 2006, **45**(19), 6075.
- 13 S. Kneissl, E. J. Loveridge, C. Williams, M. P. Crump and R. K. Allemann, *ChemBioChem*, 2008, **9**(18), 3046.
- 14 F. Zhang, K. A. Timm, K. M. Arndt and G. A. Woolley, *Angew. Chem., Int. Ed.*, 2010, **49**(23), 3943.
- 15 R. J. Mart, P. Wysoczański, S. Kneissl, A. Ricci, A. Brancale and R. K. Allemann, *ChemBioChem*, 2012, **13**(4), 515.
- 16 R. J. Mart, R. J. Errington, C. L. Watkins, S. C. Chappell, M. Wiltshire, A. T. Jones, P. J. Smith and R. K. Allemann, *Mol. Biosyst.*, 2013, **9**(11), 2597.
- 17 L. Nevola, A. Martín-Quirós, K. Eckelt, N. Camarero, S. Tosi, A. Llobet, E. Giralt and P. Gorostiza, *Angew. Chem., Int. Ed.*, 2013, **52**(30), 7704.
- 18 A. Martín-Quirós, L. Nevola, K. Eckelt, S. Madurga, P. Gorostiza and E. Giralt, *Chem. Biol.*, 2015, **22**(1), 31.
- 19 B. Jankovic, A. Gulzar, C. Zanobini, O. Bozovic, S. Wolf, G. Stock and P. Hamm, *J. Am. Chem. Soc.*, 2019, **141**(27), 10702.
- 20 Z. Zhang, D. C. Burns, J. R. Kumita, O. S. Smart and G. A. Woolley, *Bioconjugate Chem.*, 2003, **14**(4), 824.
- 21 R. Siewertsen, H. Neumann, B. Buchheim-Stehn, R. Herges, C. Näther, F. Renth and F. Temps, *J. Am. Chem. Soc.*, 2009, **131**(43), 15594.
- 22 R. Siewertsen, J. B. Schönborn, B. Hartke, F. Renth and F. Temps, *Phys. Chem. Chem. Phys.*, 2011, **13**(3), 1054.
- 23 M. Hammerich, C. Schütt, C. Stähler, P. Lentès, F. Röhricht, R. Höppner and R. Herges, *J. Am. Chem. Soc.*, 2016, **138**(40), 13111.
- 24 P. Lentès, E. Stadler, F. Röhricht, A. Brahms, J. Gröbner, F. D. Sönnichsen, G. Gescheidt and R. Herges, *J. Am. Chem. Soc.*, 2019, **141**(34), 13592.
- 25 W. Moormann, D. Langbehn and R. Herges, *Beilstein J. Org. Chem.*, 2019, **15**, 727.
- 26 W. Moormann, D. Langbehn and R. Herges, *Synthesis*, 2017, (15), 3471.
- 27 M. S. Maier, K. Hüll, M. Reynders, B. S. Matsuura, P. Leippe, T. Ko, L. Schäffer and D. Trauner, *J. Am. Chem. Soc.*, 2019, **141**(43), 17295.
- 28 S. Samanta, C. Qin, A. J. Lough and G. A. Woolley, *Angew. Chem., Int. Ed.*, 2012, **51**(26), 6452.
- 29 A. M. Petros, A. Medek, D. G. Nettesheim, D. H. Kim, H. S. Yoon, K. Swift, E. D. Matayoshi, T. Oltersdorf and S. W. Fesik, *Proc. Natl. Acad. Sci. U. S. A.*, 2001, **98**(6), 3012.
- 30 S. W. Muchmore, M. Sattler, H. Liang, R. P. Meadows, J. E. Harlan, H. S. Yoon, D. Nettesheim, B. S. Chang, C. B. Thompson, S.-L. Wong, S.-C. Ng and S. W. Fesik, *Nature*, 1996, **381**(6580), 335.
- 31 C. R. Kissinger, B. Liu, E. Martin-Blanco, T. B. Kornberg and C. O. Pabo, *Cell*, 1990, **63**(3), 579.
- 32 N. D. Clarke, C. R. Kissinger, J. Desjarlais, G. L. Gilliland and C. O. Pabo, *Protein Sci.*, 1994, **3**(10), 1779.



- 33 I. Radhakrishnan, G. C. Pérez-Alvarado, D. Parker, H. J. Dyson, M. R. Montminy and P. E. Wright, *Cell*, 1997, **91**(6), 741.
- 34 J. Martinez-Oyanedel, H.-W. Choe, U. Heinemann and W. Saenger, *J. Mol. Biol.*, 1991, **222**(2), 335.
- 35 C. J. McKnight, P. T. Matsudaira and P. S. Kim, *Nat. Struct. Biol.*, 1997, **4**(3), 180.
- 36 J. W. Neidigh, R. M. Fesinmeyer and N. H. Andersen, *Nat. Struct. Biol.*, 2002, **9**(6), 425.
- 37 B. Barua, J. C. Lin, V. D. Williams, P. Kummeler, J. W. Neidigh and N. H. Andersen, *Protein Eng., Des. Sel.*, 2008, **21**(3), 171.
- 38 S. H. Gellman and D. N. Woolfson, *Nat. Struct. Biol.*, 2002, **9**(6), 408.
- 39 H. Meuzelaar, K. A. Marino, A. Huerta-Viga, M. R. Panman, L. E. J. Smeenk, A. J. Kettelarij, J. H. van Maarseveen, P. Timmerman, P. G. Bolhuis and S. Woutersen, *J. Phys. Chem. B*, 2013, **117**(39), 11490.
- 40 B. N. Markiewicz, H. Jo, R. M. Culik, W. F. DeGrado and F. Gai, *J. Phys. Chem. B*, 2013, **117**(47), 14688.
- 41 L. Qiu, S. A. Pabit, A. E. Roitberg and S. J. Hagen, *J. Am. Chem. Soc.*, 2002, **124**(44), 12952.
- 42 A. Byrne, D. V. Williams, B. Barua, S. J. Hagen, B. L. Kier and N. H. Andersen, *Biochemistry*, 2014, **53**(38), 6011.
- 43 M. Scian, J. C. Lin, I. Le Trong, G. I. Makhatadze, R. E. Stenkamp and N. H. Andersen, *Proc. Natl. Acad. Sci. U. S. A.*, 2012, **109**(31), 12521.
- 44 W. W. Streicher and G. I. Makhatadze, *Biochemistry*, 2007, **46**(10), 2876.
- 45 C. Simmerling, B. Strockbine and A. E. Roitberg, *J. Am. Chem. Soc.*, 2002, **124**(38), 11258.
- 46 S. Kannan and M. Zacharias, *PLoS One*, 2014, **9**(2), e88383.
- 47 J. Juraszek and P. G. Bolhuis, *Proc. Natl. Acad. Sci. U. S. A.*, 2006, **103**(43), 15859.
- 48 R. Day, D. Paschek and A. E. Garcia, *Proteins*, 2010, **78**(8), 1889.
- 49 Matthias Lipfert, *Design of a Stabilizing and Switching Module for α -Helical Peptides*, Dissertation, Kiel, 2017.
- 50 E. J. Corey and N. Raju, *Tetrahedron Lett.*, 1983, **24**(50), 5571.
- 51 A. Bundi and K. Wüthrich, *Biopolymers*, 1979, **18**(2), 285.
- 52 G. Merutka, H. J. Dyson and P. E. Wright, *J. Biomol. NMR*, 1995, **5**(1), 14.
- 53 G. Cabré, A. Garrido-Charles, À. González-Lafont, W. Moormann, D. Langbehn, D. Egea, J. M. Lluch, R. Herges, R. Alibés, F. Busqué, P. Gorostiza and J. Hernando, *Org. Lett.*, 2019, **21**(10), 3780.
- 54 E. R. Thapaliya, J. Zhao and G. C. R. Ellis-Davies, *ACS Chem. Neurosci.*, 2019, **10**(5), 2481.
- 55 J. B. Trads, K. Hüll, B. S. Matsuura, L. Laprell, T. Fehrentz, N. Görltdt, K. A. Kozek, C. D. Weaver, N. Klöcker, D. M. Barber and D. Trauner, *Angew. Chem., Int. Ed.*, 2019, **58**(43), 15421.
- 56 L. Albert, A. Peñalver, N. Djokovic, L. Werel, M. Hoffarth, D. Ruzic, J. Xu, L.-O. Essen, K. Nikolic, Y. Dou and O. Vázquez, *ChemBioChem*, 2019, **20**(11), 1417.
- 57 H. Sell, C. Näther and R. Herges, *Beilstein J. Org. Chem.*, 2013, **9**, 1.
- 58 S. S. Wong, *Chemistry of protein conjugation and cross-linking*, CRC Press, Boca Raton, FL, USA, 1991.
- 59 S. C. Gill and P. H. von Hippel, *Anal. Biochem.*, 1989, **182**(2), 319.
- 60 T.-L. Hwang and A. J. Shaka, *J. Magn. Reson., Ser. A*, 1995, **112**(2), 275.



5. Discussion and Conclusion

Miniprotein grafting, and in particular that of PP family peptides, is a versatile approach. It exploits the stable fold of PP family peptides to preorganize a binding epitope or catalytic site. So far, no grafted PP family peptide has made it into clinical trials, but in many cases they contributed to the discovery of new therapeutic possibilities. For instance, the aPP-derived KSDD was the first allosteric inhibitor of the oncogenic herpesvirus protease KSHV Pr,^[20] providing a proof of principle. It paved the way for the development of small molecules capable of inhibiting KSHV Pr.^[36–39] Similarly, the grafted miniprotein aPP5.3 demonstrated proof of concept that miniproteins can be designed to have cell-penetrating properties, even when covalently bound to hydrophilic small molecules or whole proteins. This way, highly hydrophilic active agents that would not be able to cross the cell membrane alone might be fused to a cell-permeant miniprotein to reach their intracellular target. The development aPP5.3 finally led to the creation of the highly cell-permeant miniprotein ZF5.3,^[11, 40] which has already been applied in animal studies.^[341]

In analogy to PP grafting, one can envision the potential of Trp-cage grafting in the search for new applications. The Trp-cage provides a scaffold containing an α -helix and a PPII helix and therefore can be subject to the same protein grafting methods as PP family peptides. Whereas aPP is a 36-residue peptide, the Trp-cage contains only 20 residues. This is an advantage over the aPP grafting approach, as it principally enables the design of smaller functional peptides compared to aPP. Nevertheless, some grafting applications of the Trp-cage may necessitate the elongation of its sequence in order to provide sufficient residues required to gain the desired function. Fortunately, the small size of the Trp-cage enables the fusion of short peptide sequences to the helical N-terminus of the Trp-cage in order to induce helicity in the added peptide fragment, as has been shown with AMTC31-6. Elongation of the Trp-cage's α -helix by ten additional residues would result in a grafted Trp-cage comprising 30 residues – the same size as the smallest aPP-derived functional peptides (KSDD^[20] and pGolemi^[19, 26]). Such a grafted Trp-cage would then have an α -helix of 18 residues, i.e. five helical turns, which is the same length as the α -helix in PP family peptides. In contrast to the Trp-cage, extending PP family peptides with additional residues would make a production by SPPS very costly. Another advantage of the Trp-cage is that it is monomeric in solution independent of its concentration, whereas aPP and bPP form homodimers at micromolar concentrations.

Despite the differences of PP family peptides and the Trp-cage outlined above, their similarities are significant and both scaffolds can be used to stabilize α -helical peptides. In fact, PP grafting and Trp-cage grafting can even be viewed as two complementary approaches, because the PP fold stabilizes an α -helix from its N-terminus, while the α -helix of the Trp-cage is stabilized from the C-terminus.

An example how Trp-cage grafting might be of benefit for peptide drug development was provided with the design, synthesis, and characterization of the AMTCs.^[286] The Trp-cage domain was fused to the α AMPs KR-12 and IsCT, respectively. Even though the Trp-cage domain itself has no antimicrobial activity and has almost twice as many residues as KR-12 and IsCT, the AMP-Trp-cage chimeras generally showed comparable antibacterial activity as the respective α AMP alone. Notably, the activity of AMTC31-6 was much higher than that of KR-12, when assessed in environments containing physiologically relevant salt concentrations. AMTC31-6 was significantly active against *E. coli* (pH = 7.5 and pH = 5.5) and *P. aeruginosa* (pH = 5.5) in the

presence of 150 mM NaCl, while the related KR-12 showed no activity under the same conditions. In this case, fusion with the Trp-cage domain brings an advantage that is relevant for potential *in vivo* applications.

Many attempts to increase the antimicrobial activity of an α AMP also result in increased hemolytic activity and thus increased toxicity.^[238–240, 243] In the study presented here,^[286] however, the strong increase in antimicrobial activity of AMTC31-6 in the presence of 150 mM NaCl was not concomitant with a pronounced increase the hemolytic activity compared to KR-12. In the case of IsCT, fusion with a Trp-cage domain even produced a peptide (AMTC33-2) that was significantly less hemolytic than IsCT.

The most important benefit of grafting a Trp-cage with an α AMP is the stable fold in solution which was shown to drastically reduce the susceptibility to enzymatic proteolysis. Compared to α AMPs that are protected from fast degradation by introduction of hydrocarbon staples, D-amino acids, and other non-gene-encoded residues or building blocks, AMTCs have the advantage of comprising only gene-encoded residues. AMTCs are therefore producible by cost-efficient biosynthetic procedures. As recombinant production was shown to cost-efficiently produce AMPs regardless of their length,^[279–282] the increased length of AMTCs compared to other α AMPs is not necessarily a disadvantage.

In conclusion, Trp-cage grafting is a new design approach to optimize the activity and resistance to enzymatic degradation of α AMPs and its applicability has been proven with the rational design of the AMTCs described in the original publication^[286]. Optimization using sophisticated computer-aided design approaches^[224, 261, 274] may potentially produce AMTCs with even higher stability and antimicrobial potency while maintaining their low hemolytic activity. Future studies may also investigate whether the specificity towards Gram-positive pathogens like *S. aureus* can be increased by reducing the net cationic charge.^[261] To this end, a Trp-cage domain might be fused with the short and highly potent α AMPs developed by Guangshun Wang and colleagues.^[261]

The second project of this thesis aimed to create a Trp-cage protein equipped with a photosensitive cross-linker. The photoswitch, a visible-light-responsive diazocine moiety, was introduced at the Trp-cage's α -helix affording the so-called switch cage. The design of the diazocine cross-linker intendedly avoided conjugation of its π electron system with electron lone pairs or π electrons of the substituents to preserve the extraordinary *cis*-to-*trans* conversion yields of the parent diazocine. Unexpectedly, however, the isomerization to the *trans*-state could only be achieved in yields close to 50%. The rather low photoconversion can mainly be attributed to the negative influence of water on the diazocine's switching efficiency, which was reported^[374] a few months after publication of the switch cage. Accordingly, highly polar solvents such as water lower the yields of the *cis*-to-*trans* isomerization of diazocines by stabilizing the *cis*-isomer and destabilizing the *trans*-isomer. Moreover, a polar environment results in a hypsochromic shift of the $n\text{-}\pi^*$ band of a diazocine narrowing the band separation between the *cis*- and the *trans*-state and thus additionally decreases the photoconversion yields.^[374] Despite these unforeseen difficulties, thorough investigation of the switch cage demonstrated that the cross-linker affected the formation or disruption of the α -helix and in consequence influenced the entire fold depending on its isomeric state.^[375] CD and NMR spectroscopy provided evidence that the diazocine stabilized the fold of the switch cage in the *cis*-state, but prevented proper folding of the *trans*-switch cage. Switching the fold state by irradiation with violet (*cis*-to-*trans* isomerization, 46% yield) or green (*trans*-to-*cis* isomerization, nearly 100% yield) light was

5. Discussion and Conclusion

completely reversible and did not require UV light. Notably, unfolding of the switch cage's hydrophobic cluster did not result in aggregation or precipitation despite the presence of the unpolar *trans*-diazocine.

In conclusion, tertiary structures of proteins can be reversibly disrupted preventing or allowing the formation of an α -helix that is a central part of said tertiary structure. With this proof of principle at hand, the method can be transferred to other small proteins or protein domains. The fact that the diazocine cross-linker can be switched in both directions with visible light is an advantage over azobenzene. However, further improvements of the *cis*-to-*trans* conversion efficiencies are desirable. Higher switching efficiencies could be obtained by employing the water-soluble NAc-diazocine^[374, 376] (**Figure 36**). Future cross-linkers could make use of this water-soluble diazocine-derived chromophore, which achieves *cis*-to-*trans* conversion yields of 72% at 393 nm in water. However, NAc-diazocine derivatives with reactive moieties for cross-linking of peptides still need to be developed.

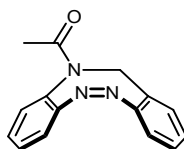


Figure 36: *Cis*-isomer of the NAc-diazocine.

The switch cage designed in our proof of concept study was not intended to be directly compatible with other Trp-cage grafting approaches. In fact, combining the switch cage and the AMTC, i.e. designing a photoswitchable AMTC, is not straight forward but would necessitate extensive modifications. First of all, the hydrophobic nature of the diazocine moiety would require the incorporation at the hydrophobic side of the helix in order to keep the well-balanced amphipathicity intact. Incorporation of the photoswitchable cross-linker at the hydrophilic side cannot be recommended, as it would drastically increase hydrophobicity and would most likely result in an insoluble or even cytotoxic peptide. For the same reason, an azobenzene moiety was incorporated at the hydrophobic face of the helix, when an amphipathic photoswitchable cell-penetrating peptide was designed.^[340] In the AMTC, however, the hydrophobic side is partially blocked by the Trp-cage loop which significantly reduces the available options to install the photoswitch.

Secondly, the AMTCs presented in this thesis possess many lysines and a free N-terminus, which are able to react with the NHS-moieties of the diazocine cross-linker preventing a site-selective conjugation. In order to make use of the primary amine-reactive cross-linker, all lysines had to be substituted for arginines and the peptide's N-terminus had to be protected, e.g. by acetylation. Both measures could affect the antimicrobial and hemolytic activity. If lysines and a free N-terminus are important for a grafted Trp-cage, one could employ the well-known cysteine-based chemistry to incorporate a cross-linker.

Combination of the switch cage and the AMTC would, in conclusion, require extensive redesign and it remains uncertain whether the incorporation of a photoswitchable cross-linker would really result in photoswitchable antimicrobial activity.

To conclude, PP grafting and Trp-cage grafting are two similar approaches that may be used to stabilize functional peptides that depend on an α -helical secondary structure. Two applications how the Trp-cage may be enhanced with new functions were presented in this

thesis. AMTCs are antimicrobial peptides with a higher resistance to enzymatic proteolysis that are accessible through methods of gene expression and the Trp-cage may therefore be an important scaffold for the design of peptide antibiotics in the future. Moreover, Trp-cage grafting may also be applied to stabilize binding epitopes in order to design α -helical peptide drugs (other than antibiotics) with enhanced stability against enzymatic degradation.

The switch cage provides a proof of concept how Woolley's approach to switching a peptide's helicity may be applied to control the tertiary structure of folded proteins. As a protein's function is usually dependent on a correct and unperturbed fold, controlling a protein's tertiary structure could result in the ability to manipulate its function. With these two new examples of Trp-cage grafting, this work successfully contributed to advancing the field of protein and peptide engineering and showed how the Trp-cage can be of use in peptide drug design.

6. Detailed methods and supplementary information

6.1. Detailed description of methods regarding the AMTC

While the methods as described in the original publication^[286] (cf. chapter **3.3.2. Antimicrobial Trp-cage: Publication**) are written as concise as possible, the following description provides sufficient detail to allow an exact replication of the procedures.

6.1.1. Peptide synthesis

All peptides were synthesized using SPPS employing a fluorenylmethoxycarbonyl (Fmoc) protecting group strategy.^[377] TC-KKA, KR-12, Helix19-6, AMTC26-4, AMTC27-6, and AMTC24-5 were synthesized on a microwave-assisted, semi-automated peptide synthesizer Initiator⁺ SP Wave (Biotage, Uppsala, Sweden). TC-KKA, AMTC27-6, and AMTC24-5 were synthesized on Wang resin (200-400 mesh, 860 $\mu\text{mol g}^{-1}$, ChemPep, Wellington, FL, USA) at a 172 μmol (200 mg resin) scale in a 5 ml reaction vessel. AMTC26-4 was synthesized on Wang resin at a 258 μmol (300 mg resin) scale in a 10 ml reaction vessel. The C-terminally amidated peptides Helix19-6 and KR-12 were synthesized on Rink amide resin (100-200 mesh, 450 $\mu\text{mol g}^{-1}$, ChemPep, Wellington, FL, USA) at a 90 μmol scale (200 mg resin) in a 5 ml reaction vessel. Apart from two dipeptides (DG and SS), standard Fmoc-protected amino acids with acid-labile side chain protecting groups were used. The DG dipeptide Fmoc-Asp-(OtBu)-(DMB)Gly-OH (Novabiochem, Merck, Darmstadt, Germany) was used to avoid aspartimide formation during synthesis and the SS dipeptide was coupled as the pseudo-proline variant Fmoc-Ser(*t*Bu)-Ser(ψ Me, Mepro)-OH (Novabiochem, Merck, Darmstadt, Germany) to disrupt secondary structure effects during synthesis. In the following text, 1 equivalent (eq.) of reagents corresponds to either 90 μmol (KR-12 and Helix19-6), 172 μmol (TC-KKA, AMTC27-6 and AMTC24-5), or 258 μmol (AMTC26-4). Whenever two different values separated by a vertical line ($x|y$) are stated, the first value x corresponds to a 5 ml reaction vessel synthesis (TC-KKA, KR-12, Helix19-6, AMTC27-6, and AMTC24-5), whereas the second value y corresponds to a 10 ml reaction vessel synthesis (AMTC26-4).

6.1.1.1. Swelling

The resin was prepared for the synthesis by letting it swell in dichloromethane (DCM) or *N,N*-dimethylformamide (DMF) for at least 30 min at ambient temperature. When DCM was used for swelling, four washes with acetonitrile (MeCN; 2 ml|4 ml) for at least 30 s each, while vortexing at 600 rpm at ambient temperature were applied after the DCM was drained. The solvent was drained and the resin was washed four times with DMF (2 ml|4 ml) for at least 30 s at 600 rpm at ambient temperature. The solvent was drained. In case of Rink amide resin, the extended deprotection procedure (*vide infra*) was performed prior to coupling the first residue.

6.1.1.2. Coupling

Peptide synthesis was performed as a repetitive cycle of (double) coupling, capping, and (extended) deprotection for each residue of the peptide. Coupling was performed with 5 eq. of the corresponding amino acid and 4.9 eq. of hexafluorophosphate azabenzotriazole tetramethyl uronium (HATU) dissolved in DMF (2 ml|4 ml). 10 eq. of *N,N*-diisopropylethylamine (DIPEA) were added to the solution to activate the amino acid immediately prior to the addition to the resin. The reaction mixture was vortexed at 600 rpm at 75 °C for 5 min and the solution was

drained. Depending on the peptide and residue, an additional coupling step (i.e. double coupling) with fresh reaction solution was performed. Finally, the resin was washed with DMF (2 ml | 4 ml) by vortexing the suspended resin at 600 rpm at ambient temperature for (30 s | 45 s) and the wash solution was drained. The washing step was performed four times in a row.

6.1.1.3. Capping

A capping step was performed after the coupling procedure by adding a solution (2 ml | 4 ml) of DMF (50% v/v), pyridine (25% v/v), and acetic anhydride (25% v/v) to the resin and vortexing it at 600 rpm at 75 °C for 5 min. The solution was drained and four wash steps with DMF (2 ml | 4 ml) were performed at the end of the capping procedure.

6.1.1.4. Deprotection of the Fmoc protecting group

Cleavage of the terminal Fmoc protecting group was achieved by adding a solution (2 ml | 4 ml) of piperidine (25% v/v) in DMF to the resin and vortexing it at 600 rpm at 75 °C for 1 min. The solvent was drained and fresh deprotection mixture (2 ml | 4 ml) was added to react for another 4 min at 600 rpm at 75 °C. Extended deprotection included a third reaction step with fresh reaction mixture to react for another 4 min at 600 rpm at 75 °C. The solution was drained and four wash steps with DMF (2 ml | 4 ml) were performed at the end of the Fmoc cleavage procedure. Specifications which residue of which peptide was subjected to double coupling and/or extended deprotection can be found in **Table 9** to **Table 14**.

6.1.1.5. Final cleavage

When all residues were coupled and the N-terminus was deprotected, the resin was washed four times with DMF (2 ml | 4 ml) for 30 s at 600 rpm at ambient temperature and the solvent was drained. This procedure was followed by four identical washing steps but using MeCN instead of DMF and another four identical washing steps using DCM. Finally, the resin was drained for 60 min to dry the resin completely.

Cleavage of all side chain protecting groups and release of the peptide from the resin was achieved by treating the peptide-bearing resin with a solution of trifluoroacetic acid (TFA; 90% v/v), 1,3-dimethoxybenzene (5% v/v), triisopropyl silane (TIS; 2.5% v/v) and water (2.5% v/v) by gently agitating the suspension for (3 ± 1) h at ambient temperature. 1 ml of this solution was applied per 100 mg of dried peptide-bearing resin. After the treatment, the solution was filtered through a syringe filter and the beads in the filter were washed with approximately 1 ml TFA. The filtrates were combined and the peptide was precipitated by adding cold diethyl ether (min. five times the volume of the filtrate) to the filtrate. After centrifugation, the supernatant was decanted and discarded. The pellet was dissolved in a few ml of water and lyophilized.

The following tables list the details of the SPPS of all peptides synthesized by Nils Preußke. The vial size refers to the size of the reaction vessel in which the microwave-assisted synthesis was performed. The peptide amount and mass state how much peptide one would obtain if all couplings and deprotections were achieved in yields of 100%. The stated peptide amount in µmol corresponds to 1 equivalent (1 eq.). Coupling and deprotection conditions are given for each amino acid. If a field in these columns is left blank, standard conditions (i.e. single coupling or standard deprotection) apply. If the synthesis could not be completed within one day, the loaded resin was stored at 6 °C at night and the synthesis was continued the next day.

6. Detailed methods and supplementary information

Table 9: Synthesis sheet of TC-KKA.

peptide name	TC-KKA	
peptide molecular mass / g mol ⁻¹	2127.32	
vial size	5 ml	
resin mass / mg	200	
resin capacity / μmol g ⁻¹	860	Wang resin
peptide amount / μmol	172	
peptide mass / mg	366	
4.9 eq HATU / mg	320	
10 eq DIPEA / μL	300	

Day	amino acid	m / mg	coupling	deprotection
1	K	403	double	extended
1	P	290		extended
1	P	290		extended
1	P	290		extended
2	R	558	double	extended
2	G	256	double	extended
2	SS	439		extended
2	P	290		extended
2	G	256	double	extended
2	DG	532		extended
2	A	268	double	extended
2	L	304		extended
2	W	453		extended
3	Q	525	double	extended
3	A	268	double	extended
3	Y	395		extended
3	K	403	double	extended
3	D	354		extended

Table 10: Synthesis sheet of KR-12.

peptide name	KR-12	
peptide molecular mass / g mol ⁻¹	1570.93	
vial size	5 ml	
resin mass / mg	200	
resin capacity / μmol g ⁻¹	450	Rink amide resin
peptide amount / μmol	90	
peptide mass / mg	141	
4.9 eq HATU / mg	168	
10 eq DIPEA / μL	157	

Day	amino acid	m / mg	coupling	deprotection
1	Resin deprotection		none	
1	R	292		
1	L	159		
1	F	174		
1	D	185		
1	K	211		
1	I	159		
1	R	292		
1	Q	275		
1	V	153		
1	I	159		
1	R	292		
1	K	211		

6.1. Detailed description of methods regarding the AMTC

Table 11: Synthesis sheet of Helix19-6.

peptide name	Helix19-6	
peptide molecular mass / g mol ⁻¹	2431.93	
vial size	5 ml	
resin mass / mg	200	
resin capacity / μmol g ⁻¹	450	Rink amide resin
peptide amount / μmol	90	
peptide mass / mg	219	
4.9 eq HATU / mg	168	
10 eq DIPEA / μL	157	

Day	amino acid	m / mg	coupling	deprotection
1	Resin deprotection		none	extended
1	A	140	double	extended
1	L	159		extended
1	W	237		extended
2	Q	275	double	extended
2	A	140	double	extended
2	Y	207		extended
2	K	211	double	extended
2	R	292	double	extended
2	L	159		extended
2	F	174		extended
2	D	185		extended
2	K	211	double	extended
3	I	159	double	extended
3	R	292	double	extended
3	Q	275	double	extended
3	V	153		extended
3	I	159		extended
3	R	292	double	extended
3	K	211	double	extended

Table 12: Synthesis sheet of AMTC26-4.

peptide name	AMTC26-4	
peptide molecular mass / g mol ⁻¹	2941.35	
vial size	10 ml	
resin mass / mg	300	
resin capacity / μmol g ⁻¹	860	Wang resin
peptide amount / μmol	258	
peptide mass / mg	759	
4.9 eq HATU / mg	480	
10 eq DIPEA / μL	449	

Day	amino acid	m / mg	coupling	deprotection
1	K	604	double	extended
1	P	435		extended
1	P	435		extended
1	P	435		extended
1	R	837	double	extended
1	G	384	double	extended
1	SS	659		extended
2	P	435	double	extended
2	G	384	double	extended
2	DG	798	double	extended
2	A	402	double	extended
2	L	456		extended
2	W	679		extended
2	Q	557		extended
2	A	402	double	extended
2	Y	593		extended
2	K	604		extended
3	R	837		extended
3	L	456		extended
3	F	500		extended
3	D	531		extended
3	K	604		extended
3	I	456		extended
3	R	837		extended

6. Detailed methods and supplementary information

Table 13: Synthesis sheet of AMTC27-6.

peptide name	AMTC27-6				
peptide molecular mass / g mol ⁻¹	3053.6				
vial size	5 mL				
resin mass / mg	200				
resin capacity / μmol g ⁻¹	860				
peptide amount / μmol	172				
peptide mass / mg	525				
4.9 eq HATU / mg	320				
10 eq DIPEA / μL	300				
			Wang resin		
Day	amino acid	m / mg	coupling	deprotection	
1	K	403	double	extended	
1	P	290		extended	
1	P	290		extended	
1	P	290		extended	
1	R	558	double	extended	
2	G	256	double	extended	
2	SS	439		extended	
2	P	290		extended	
2	G	256	double	extended	
2	DG	532		extended	
2	K	403	double	extended	
2	L	304		extended	
2	W	453		extended	
2	Q	525	double	extended	
3	K	403	double	extended	
3	Y	395		extended	
3	L	304		extended	
3	R	558	double	extended	
3	K	403	double	extended	
3	F	333		extended	
3	I	304	double	extended	
3	R	558	double	extended	
3	V	292	double	extended	
4	I	304	double	extended	
4	G	256	double	extended	

Table 14: Synthesis sheet of AMTC24-5.

peptide name	AMTC24-5				
peptide molecular mass / g mol ⁻¹	2713.14				
vial size	5 ml				
resin mass / mg	200				
resin capacity / μmol g ⁻¹	860				
peptide amount / μmol	172				
peptide mass / mg	467				
4.9 eq HATU / mg	320				
10 eq DIPEA / μL	300				
			Wang resin		
Day	amino acid	m / mg	coupling	deprotection	
1	K	403	double	extended	
1	P	290		extended	
1	P	290		extended	
1	P	290		extended	
1	R	558	double	extended	
1	G	256	double	extended	
1	SS	439		extended	
1	P	290		extended	
2	G	256	double	extended	
2	DG	532		extended	
2	K	403	double	extended	
2	L	304		extended	
2	W	453		extended	
2	Q	525	double	extended	
2	K	403	double	extended	
2	Y	395		extended	
2	L	304		extended	
2	R	558	double	extended	
3	K	403	double	extended	
3	F	333		extended	
3	I	304		extended	
3	G	256		extended	

6.1.2. Peptide purification

Purification of all peptides was achieved by means of reverse phase (RP) high-performance liquid chromatography (HPLC) on a VWR-Hitachi LaChrom Elite instrument (VWR, Darmstadt, Germany) equipped with a VWR-Hitachi L2400 UV detector (VWR, Darmstadt, Germany) and a Foxy R1 fraction autocollector (Teledyne ISCO, Lincoln, NE, USA). The peptides were purified in small batches of approximately 10 mg to 100 mg crude peptide. The preparative gradients used water acidified with 0.1% v/v formic acid (FA) as solvent A and MeCN acidified with 0.1% v/v FA as solvent B. Peptides were pre-purified on a semi-preparative VP 250/32 Nucleosil 100-7 C18 column (dimensions: 250 mm x 32 mm, pore diameter: 10 nm, particle size: 7 µm; Macherey-Nagel, Düren, Germany). A subsequent purification was performed using a PLRP-S column (dimensions: 325 mm x 30 mm, pore diameter: 30 nm, particle size: 8 µm; Agilent, Santa Clara, CA, USA).

The crude AMTC31-6 was purified by Sven Rothmund to >95% purity using preparative HPLC (Gilson, Middleton, WI, USA) equipped with a PLRP-S column (dimensions: 300 mm x 25 mm, pore diameter: 30 nm, particle size: 5 µm; Agilent, Santa Clara, CA, USA) at room temperature. The mobile phases were water (A) and acetonitrile (B), respectively, each containing 0.1% TFA. Detection was accomplished at 220 nm. Samples were eluted with a linear gradient from 10% B to 70% B in 90 min for preparative runs. Pure fractions were lyophilized. Dissolution of the pure peptide in 10 mM HCl and subsequent lyophilization was performed three times to exchange the TFA anions for chloride anions. Partial deamidation of AMTC31-6 at the glutamine residues over time required re-purification using the equipment that was used to purify the other peptides.

For each purification method the applied column, gradient, flow rate, dead time, retention time t_R and time range of fraction collection (FC) are given in **Table 15** to **Table 21**. Purified peptides were handled in a sterile environment to avoid contamination with microorganisms and other sources of proteases.

Table 15: Purification of TC-KKA.

Macherey-Nagel column								
Flow rate: 8 ml/min				Dead time: 16 min				
$t_R = (56 \pm 2)$ min				FC: 40 min – 70 min, 4 ml/vial				
Time / min	0	5	25	55	65	75	80	90
% A	95	95	84	74	5	5	95	95
% B	5	5	16	26	95	95	5	5

Agilent column								
Flow rate: 6 ml/min				Dead time: 20 min				
$t_R = (60 \pm 2)$ min				FC: 45 min – 75 min, 3 ml/vial				
Time / min	0	5	25	55	65	75	80	90
% A	95	95	87	77	5	5	95	95
% B	5	5	13	23	95	95	5	5

Table 16: Purification of KR-12.

Macherey-Nagel column								
Flow rate: 8 ml/min				Dead time: 16 min				
$t_R = (49 \pm 2)$ min				FC: 40 min – 70 min, 4 ml/vial				
Time / min	0	5	25	55	65	75	80	90
% A	95	95	80	70	5	5	95	95
% B	5	5	20	30	95	95	5	5

Agilent column								
Flow rate: 6 ml/min				Dead time: 20 min				
$t_R = (60 \pm 2)$ min				FC: 45 min – 75 min, 3 ml/vial				
Time / min	0	5	25	55	65	75	80	90
% A	95	95	87	77	5	5	95	95
% B	5	5	13	23	95	95	5	5

6. Detailed methods and supplementary information

Table 17: Purification of AMTC31-6.

Agilent column								
Flow rate: 6 ml/min				Dead time: 20 min				
$t_R = (55 \pm 2)$ min				FC: 45 min – 75 min, 3 ml/vial				
Time / min	0	5	25	55	65	75	80	90
% A	95	95	87	77	5	5	95	95
% B	5	5	13	23	95	95	5	5

Table 18: Purification of Helix19-6.

Macherey-Nagel column								
Flow rate: 8 ml/min				$t_R = (55 \pm 2)$ min				
$t_R = (49 \pm 2)$ min				Dead time: 16 min				
				FC: 40 min – 70 min, 4 ml/vial				
Time / min	0	5	25	55	65	75	80	90
% A	95	95	70	60	5	5	95	95
% B	5	5	30	40	95	95	5	5

Agilent column (gradient 1)								
Flow rate: 6 ml/min				Dead time: 20 min				
$t_R = (60 \pm 2)$ min				FC: 40 min – 70 min, 3 ml/vial				
Time / min	0	5	25	25	65	75	80	90
% A	95	95	75	65	5	5	95	95
% B	5	5	25	35	95	95	5	5

Agilent column (gradient 2)								
Flow rate: 8 ml/min				Dead time: 15 min				
$t_R = (59 \pm 2)$ min				FC: 51 min – 61 min, 2 ml/vial				
Time / min	0	5	25	55	65	75	80	90
% A	95	95	78	68	5	5	95	95
% B	5	5	22	32	95	95	5	5

Table 19: Purification of AMTC26-4.

Macherey-Nagel column								
Flow rate: 8 ml/min				Dead time: 16 min				
$t_R = (60 \pm 2)$ min				FC: 40 min – 70 min, 4 ml/vial				
Time / min	0	5	25	55	65	75	80	90
% A	95	95	77	67	5	5	95	95
% B	5	5	23	33	95	95	5	5

Agilent column								
Flow rate: 6 ml/min				Dead time: 20 min				
$t_R = (61 \pm 2)$ min				FC: 42 min – 72 min, 3 ml/vial				
Time / min	0	5	25	55	65	75	80	90
% A	95	95	80	70	5	5	95	95
% B	5	5	20	30	95	95	5	5

Table 20: Purification of AMTC27-6.

Macherey-Nagel column								
Flow rate: 8 ml/min				Dead time: 16 min				
$t_R = (59 \pm 2)$ min				FC: 40 min – 70 min, 4 ml/vial				
Time / min	0	5	25	55	65	75	80	90
% A	95	95	75	65	5	5	95	95
% B	5	5	25	35	95	95	5	5

Agilent column								
Flow rate: 6 ml/min				Dead time: 20 min				
$t_R = (60 \pm 2)$ min				FC: 45 min – 75 min, 3 ml/vial				
Time / min	0	5	25	55	65	75	80	90
% A	95	95	78	68	5	5	95	95
% B	5	5	22	32	95	95	5	5

6.1. Detailed description of methods regarding the AMTC

Table 21: Purification of AMTC24-5.

Macherey-Nagel column								
Flow rate: 8 ml/min			Dead time: 16 min					
$t_R = (54 \pm 2)$ min			FC: 40 min – 70 min, 4 ml/vial					
Time / min	0	5	25	55	65	75	80	90
% A	95	95	80	70	5	5	95	95
% B	5	5	20	30	95	95	5	5

Agilent column								
Flow rate: 6 ml/min			Dead time: 20 min					
$t_R = (60 \pm 2)$ min			FC: 45 min – 75 min, 3 ml/vial					
Time / min	0	5	25	55	65	75	80	90
% A	95	95	83	73	5	5	95	95
% B	5	5	17	27	95	95	5	5

6.1.3. Analytical UHPLC: Settings of the mass spectrometer

The mass spectrometer was equipped with a heated electrospray ionization (HESI) source using the following parameters: spray voltage: 3.5 kV, capillary temperature: 250 °C, sheath gas flow rate: 40, auxiliary gas flow: 15, sweep gas: 0, probe heater temperature: 300 °C, S-lens RF level: 50.00. The mass spectrometer was set to operate in positive ion mode with a resolution power of 70,000 at full width at half maximum (FWHM) at $m/z = 200$ scanning an m/z -range from 100 to 1,500. The automated gain control (AGC) target was set to 1,000,000 and the maximum inject time was adjusted to 100 ms.

In addition to full spectra, data-dependent tandem mass spectrometry (dd-MS²) data were recorded using the m/z -range from 200 to 2,000 with a resolution power of 17,500 at FWHM at $m/z = 200$. The AGC target was set to 100,000 and the maximum inject time was adjusted to 50 ms. The minimum AGC target was set to 8,000 and the intensity threshold was adjusted to 160,000. The normalized collision energy (NCE) was set to 30. Only the isotope with the highest intensity of each parent peptide was on the inclusion list for dd-MS² and no other molecules were subjected to dd-MS² (setting: “if idle do not pick others”). The dynamic exclusion was set to 4.0 s.

The spectrometer was calibrated once a day and no lock masses were used. All chromatograms and dd-MS² data were recorded in profile mode.

6.1.4. NMR spectroscopy: number of scans, size of FID and mixing times

One-dimensional ¹H-NMR spectra were recorded by accumulating 32 scans with a spectral width of 16.0221 ppm. TOCSY spectra were recorded using decoupling in the presence of scalar interactions (DIPS12) with a mixing time of 60 ms.^[378] The size of free induction decay (FID) was 4096 (F2) by 512 (F1) data points and the spectral width was 14.0261 ppm by 14.0261 ppm. 8 scans were accumulated during data acquisition. COSY spectra were recorded by accumulating 8 scans with an FID of 4096 (F2) by 1024 (F1) data points and a spectral width of 14.0261 ppm by 14.0000 ppm. NOESY spectra were recorded by accumulating 16 scans with an FID of 4096 (F2) by 1024 (F1) data points and a spectral width of 14.0261 ppm by 14.0261 ppm using a mixing time of 200 ms. HSQC spectra were recorded by accumulating 128 scans with an FID of 1024 (F2) by 128 (F1) data points and a spectral width of 12.0166 ppm by 160.0000 ppm.

6.1.5. MIC assay: Bacterial growth and preparation of the serial dilution

3 ml sterile lysogeny broth (LB) medium (10 g l⁻¹ tryptone, 5 g l⁻¹ yeast extract, 10 g l⁻¹ NaCl dissolved in water) were inoculated with bacteria from a deep-frozen glycerin stock. After an incubation period of 14 h to 18 h at 37 °C under agitation, 100 µl of the then turbid broth were

6. Detailed methods and supplementary information

diluted to 100 mL with fresh sterile LB medium and grown in a shaking incubator at 37 °C under aerobic conditions to mid-exponential growth phase ($OD_{600} = 0.2 \pm 0.1$). Depending on the type of bacterium, a bacterial suspension with an optical density of 0.1 at the wavelength of $\lambda = 600$ nm ($OD_{600} = 0.1$) corresponded to the following concentrations: *B. megaterium* – $2.8 \cdot 10^6$ colony forming units per ml (cfu ml⁻¹), *E. coli* – $2.5 \cdot 10^7$ cfu ml⁻¹, *S. aureus* – $2.5 \cdot 10^7$ cfu ml⁻¹, *P. aeruginosa* – $2.5 \cdot 10^7$ cfu ml⁻¹. The bacterial suspension was diluted with fresh LB medium to a concentration of 10,000 cfu/ml immediately prior to use.

The serial microdilution assay was performed in sterile, transparent, round-bottomed polypropylene 96-well plates. To reduce the hydrophobicity of the wells' surfaces, they were incubated with a sterile solution (0.1% w/v) of bovine serum albumin (BSA) in water for 20 min (200 µl/well), emptied and vigorously shaken (upside-down) so that only a thin film remained on the well walls. Each well was filled with 90 µl of sterile 10 mM sodium phosphate buffer adjusted to pH = 5.5 ± 0.5 or to pH = 7.5 ± 0.5. The tests were also performed with higher salinity; in this case the 10 mM phosphate buffer was supplemented with 150 mM NaCl. Depending on the desired highest concentration, 5 µl, 10 µl or 20 µl of a peptide stock solution (200 µM in 10 mM HCl) were added to the first well of each row of the 96-well plate. The well was filled to 180 µl by the addition of the same phosphate buffer (85 µl, 80 µl or 70 µl) and the solution was thoroughly mixed. The peptide was serially diluted by taking 90 µl from the first well, adding it to the next well to the right and mixing it thoroughly, then transferring 90 µl of that solution to the next well and so forth until the whole row of the 96-well plate was filled with a serial dilution of the peptide. The 90 µl that were taken out of the last well of the row were discarded. 10 µl of a bacterial suspension containing 10,000 cfu ml⁻¹ were added to each well. Melittin, a pore-forming peptide from bee venom, served as positive control and 10 mM HCl served as negative control. Additionally, two rows of each 96-well plate were not supplemented with peptide and bacterial suspension but only with sterile LB medium to serve as sterile control. The plates were closed with a lid and placed in an incubator at 37 °C with high humidity for (18 ± 2) h.

6.1.6. Hemolysis assay: preparation of the serial dilution

The serial microdilution assay was performed in sterile, transparent, V-bottomed polypropylene 96-well plates. To reduce the hydrophobicity of the wells' surfaces, they were incubated with a sterile solution of BSA in water (0.1% w/v) for 20 min (200 µl/well), emptied and vigorously shaken so that only a thin film remained on the well walls. 80 µl of hemolysis buffer was filled into each well, except for the first well of each row. The first well of each row was filled with 80 µl of double-concentrated hemolysis buffer (water, 100 mM Na₂HPO₄, 300 mM NaCl, adjusted to pH 7.4 using 6 M HCl) and 80 µl of a 160 µM peptide solution in 2 mM HCl. The content of the first well was mixed thoroughly. The peptide was serially diluted by transferring 80 µl from the first well to the second well of the row, mixing it thoroughly, transferring 80 µl of that solution to the next well and so forth. The 80 µl of the last well were discarded so that every well contained 80 µl of serially diluted peptide with a peptide concentration of 80 µM in the first well. 20 µl of the 12.5% erythrocyte suspension were added to each well. Melittin served as a positive control and 2 mM HCl served as a negative control. Two rows of a 96-well plate were not used for the serial dilution, but for osmolysis of erythrocytes, which was achieved by adding 20 µl of the 12.5% erythrocyte suspension to 80 µl of sterile, deionized water. The plates were closed with a lid and placed in an incubator at 37 °C with high humidity for 1 h.

6.2. Supporting information on the AMTC publication

Supporting information on the publication “Designed Trp-cage proteins with antimicrobial activity and enhanced stability” (cf. chapter **3.3.2. Antimicrobial Trp-cage: Publication**) can be found on pages S1-S54.

6.3. Supplementary information on the switch cage publication

Supporting information on the publication “Visible-light-driven photocontrol of the Trp-cage protein fold by a diazocine cross-linker” (cf. chapter **4.5. Switch cage: Publication**) can be found after the supporting information on the AMTC publication.

Supporting Information for

Designed Trp-cage proteins with antimicrobial activity and enhanced stability

Nils Preußke^{a,b,#}, Matthias Lipfert^{a,§}, Sven Rothmund^c, Matthias Leippe^b, Frank D. Sönnichsen^{a*}

^a Otto Diels Institute for Organic Chemistry, Kiel University, Otto-Hahn-Platz 3-5, 24118 Kiel, Germany

^b Zoological Institute, Kiel University, Am Botanischen Garten 3-9, 24118 Kiel, Germany

^c Faculty of Medicine, University of Leipzig, Liebigstraße 21, 04103 Leipzig, Germany

[#] Present address: Leibniz Institute for Natural Product Research and Infection Biology – Hans Knöll Institute, Beutenbergstraße 11a, 07745 Jena, Germany

[§] Present address: Lonza Group AG, Lonzastraße 2, 3930 Visp, Switzerland

*Corresponding author. Email: fsoennichsen@oc.uni-kiel.de

This PDF file includes:

NMR analysis	S3
Figure S1. 1D- ¹ H-NMR spectra	S4
Figure S2. ¹ H- and ¹³ C-chemical shift deviation (CSD or $\Delta\delta$) plots	S5
Figure S3. ¹ H- and ¹³ C-chemical shift deviation (CSD or $\Delta\delta$) plots	S6
Table S1. NOE signals of TC-KKA indicative of helicity	S7
Table S2. NOE signals of KR-12 indicative of helicity	S8
Table S3. NOE signals of AMTC31-6 indicative of helicity	S9
Table S4. NOE signals of Helix19-6 indicative of helicity	S10
Table S5. NOE signals of AMTC26-4 indicative of helicity	S11
Table S6. NOE signals of AMTC27-6 indicative of helicity	S12
Table S7. NOE signals of AMTC24-5 indicative of helicity	S13
Table S8. Concentrations of the NMR samples	S13
Table S9. ¹ H chemical shifts of TC-KKA	S14
Table S10. ¹³ C chemical shifts of TC-KKA	S14
Table S11. ¹ H chemical shifts of KR-12	S15
Table S12. ¹³ C chemical shifts of KR-12	S15
Table S13. ¹ H chemical shifts of AMTC31-6	S16
Table S14. ¹³ C chemical shifts of AMTC31-6	S17
Table S15. ¹ H chemical shifts of Helix19-6	S18
Table S16. ¹³ C chemical shifts of Helix19-6	S18
Table S17. ¹ H chemical shifts of AMTC26-4	S19
Table S18. ¹³ C chemical shifts of AMTC26-4	S20
Table S19. ¹ H chemical shifts of AMTC27-6	S21
Table S20. ¹³ C chemical shifts of AMTC27-6	S22
Table S21. ¹ H chemical shifts of AMTC24-5	S23
Table S22. ¹³ C chemical shifts of AMTC24-5	S24
CD analysis	S25
Figure S4. CD data	S25
Table S23. Concentration of the CD samples	S25
Table S24. Parameters of the melting curve fits of TC-KKA, AMTC31-6 and AMTC26-6	S25
MIC and MBC results	S26
Table S25: Averaged MIC results and their standard deviation regarding <i>E. coli</i>	S26
Table S26: Averaged MBC results and their standard deviation regarding <i>E. coli</i>	S26
Table S27: Averaged MIC results and their standard deviation regarding <i>B. megaterium</i>	S27

Table S28: Averaged MBC results and their standard deviation regarding <i>B. megaterium</i> .	S27
Table S29: Averaged MIC results and their standard deviation regarding <i>S. aureus</i> .	S28
Table S30: Averaged MBC results and their standard deviation regarding <i>S. aureus</i> .	S28
Table S31: Averaged MIC results and their standard deviation regarding <i>P. aeruginosa</i> .	S29
Table S32: Averaged MBC results and their standard deviation regarding <i>P. aeruginosa</i> .	S29
Hemolysis assay .	S30
Table S33: Hemolysis results	S30
Liposome depolarization assay	S30
Figure S5. Liposome depolarization assay.	S30
Enzymatic degradation analysis	S31
Figure S6: Fragment analysis of the trypsin digests of AMTC31-6 and Helix19-6 at 25 °C.	S32
Figure S7: Fragment analysis of the chymotrypsin digests of AMTC31-6 and Helix19-6.	S33
Figure S8. Fragment analysis of KR-12.	S34
Figure S9. Fragment analysis of AMTC26-4.	S35
Figure S10. Fragment analysis of the trypsin digests of AMTC27-6 and AMTC24-5 at 25 °C.	S36
Figure S11. Fragment analysis of the chymotrypsin digests of AMTC27-6 and AMTC24-5.	S37
Figure S12. Fragment analysis of the chymotrypsin digest of TC-KKA.	S38
Table S34. Linear region and resulting <i>k</i> obtained from the trypsin digest at 25 °C.	S39
Table S35. Linear region and resulting <i>k</i> obtained from the chymotrypsin digest.	S39
Figure S13. Quantitative trypsin digests of the parent peptides at 25 °C.	S40
Figure S14. Quantitative chymotrypsin digests of the parent peptides.	S41
Table S36: Linear region and resulting <i>k</i> obtained from the trypsin digest at 37 °C.	S42
Figure S15. Quantitative trypsin digests of the parent peptides at 37 °C.	S43
Figure S16. Fragment analysis of the trypsin digest of KR-12 at 37 °C.	S44
Figure S17. Fragment analysis of the trypsin digest of AMTC31-6 at 37 °C.	S45
Figure S18. Fragment analysis of the trypsin digest of Helix19-6 at 37 °C.	S46
Figure S19. Fragment analysis of the trypsin digest of AMTC26-4 at 37 °C.	S47
Figure S20. Fragment analysis of the trypsin digest of AMTC27-6 at 37 °C.	S48
Figure S21. Fragment analysis of the trypsin digest of AMTC24-5 at 37 °C.	S49
Detailed Procedure: Enzymatic degradation monitoring and analysis .	S50
Figure S22. Analytical chromatograms.	S53
Figure S23. Analytical chromatograms.	S54
References	S54

Other Supporting Information for this manuscript include the following:

Data S1.xlsx (Data of the individual measurements of the MIC, MBC, liposome depolarization and hemolysis assays)

NMR analysis

Un- or misfolded by-forms in slow equilibrium with the folded state

With a folding rate of approximately $0.25 \mu\text{s}^{-1}$ (62) the folding of a stable Trp-cage variant is fast compared to the NMR time scale. In consequence, there should be only one resonance for each nucleus of the Trp-cage and the chemical shift of any resonance would directly reflect the amount of folded and unfolded proteins in the sample at a certain temperature. However, Trp-cage variants with low stability and even highly stable Trp-cages at elevated temperatures have multiple resonances for some nuclei. Especially the indole-NH proton of the Trp side chain (Trp H^{ε1}) often displays multiple resonances in Trp-cages. These multiple resonances of the Trp-indole NH proton indicate un- or misfolded states of the Trp-cage in slow equilibrium with the folded state (63). A possible explanation may be isomerizations of Xxx-Pro peptide bonds between the *cis*- and the *trans*-state. Those isomerizations are slow on the NMR time scale and are more likely to occur in proteins of low stability or at elevated temperatures. In consequence, the amount and intensity of resonances in the indole-NH proton region of a Trp-cage ¹H-NMR spectrum may indicate how much of the Trp-cage is present in a folded, misfolded or unfolded state in a pure sample. Since the indole-NH proton resonance of those by-forms is often located at or near its random coil shift, it can be assumed that the Trp-cage loop is at least partially unfolded in those by-forms. Occasionally occurring broad line shapes of those resonances may also indicate aggregation. In this paper, all NMR-based evaluations refer to the folded main population if not stated otherwise. The main population of every peptide is characterized by sharp resonances and does not show signs of aggregation or formation of multimers.

TC-KKA

Folded: **88%** (two resonances at 9.751 ppm (77%) and 9.707 ppm (11%))
Unfolded or misfolded: **12%** (minimum of four resonances between 10.18 ppm and 10.08 ppm)

KR-12

There are no by-forms of KR-12. Lacking a Trp-cage, KR-12 is present in a random coil conformation in aqueous solution.

AMTC31-6

Folded: **93%** (at 9.714 ppm)
Unfolded or misfolded: **7%** (broad resonances between 10.2 ppm and 10.0 ppm)

Helix19-6

There are no by-forms of Helix19-6. Lacking a Trp-cage, Helix19-6 is present in a dynamic state with some helical propensity in aqueous solution.

AMTC26-4

Folded: **92%** (at 9.725 ppm)
Unfolded or misfolded: **8%** (broad resonances between 10.2 ppm and 10.0 ppm)

AMTC27-6

Folded: **77%** (at 9.956 ppm)
Unfolded or misfolded: **23%** (two sharp resonances at 10.170 ppm (7%) and 10.157 ppm (13%)
one broad resonance at 10.093 ppm (3%))

AMTC24-5

Folded: **79%** (at 9.949 ppm)
Unfolded or misfolded: **21%** (two sharp resonances at 10.171 ppm (6%) and 10.156 ppm (13%)
one broad resonance at 10.098 ppm (2%))

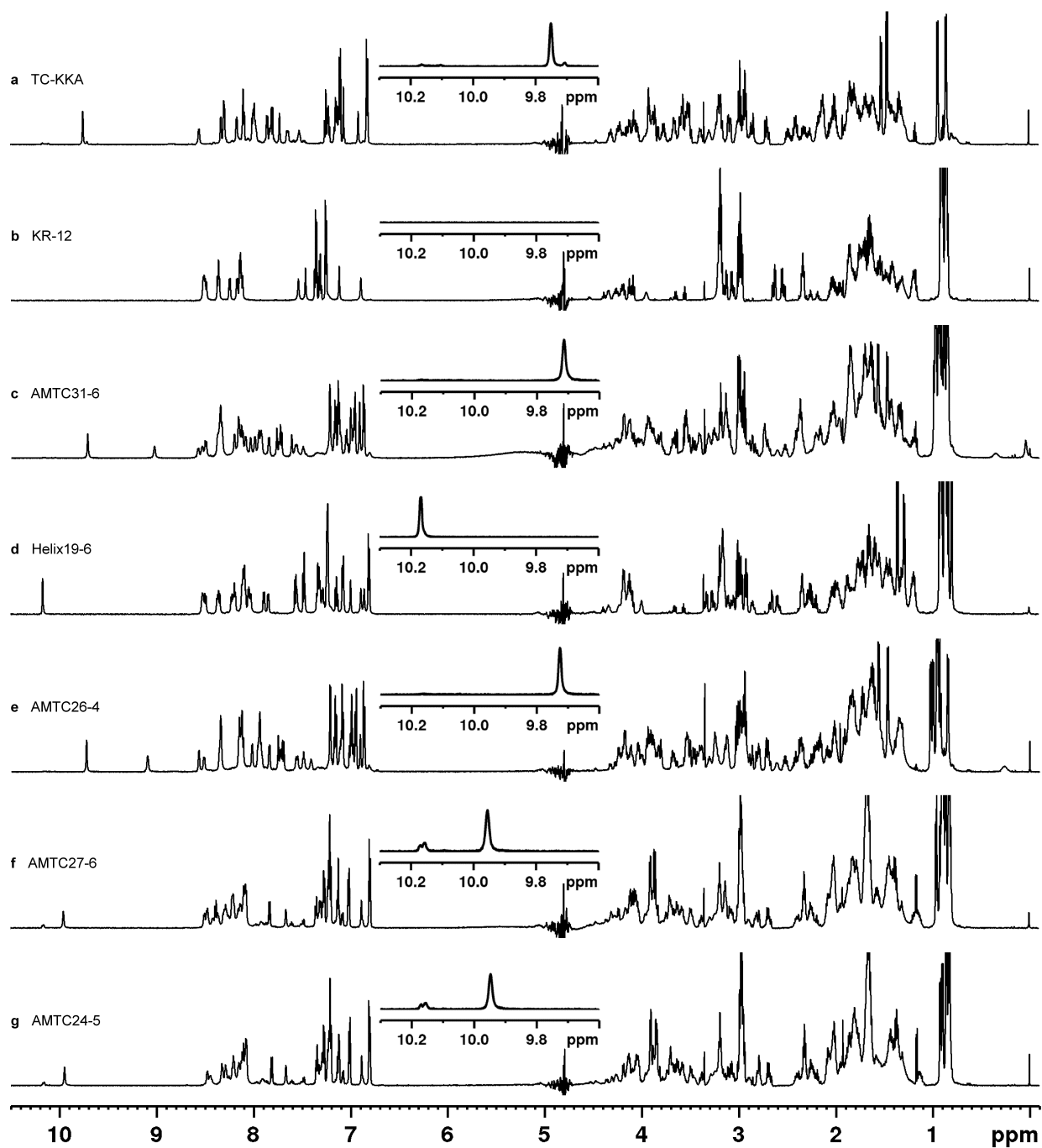


Figure S1. 1D- ^1H -NMR spectra.

1D- ^1H -NMR spectra of TC-KKA (a), KR-12 (b), AMTC31-6 (c), Helix19-6 (d), AMTC26-4 (e), AMTC27-6 (f) and AMTC24-5 (g). The inserts show an expansion of the region between 10.3 ppm and 9.7 ppm, i.e. the region of the tryptophan $\text{H}^{\epsilon 1}$ (indole NH). Trp-cage variants of low stability show mis- or unfolded by-forms whose W $\text{H}^{\epsilon 1}$ resonance is close to the tryptophan random coil shift at 10.2 ppm. These by-forms are relatively highly populated in AMTC27-6 (f) and AMTC24-5 (g).

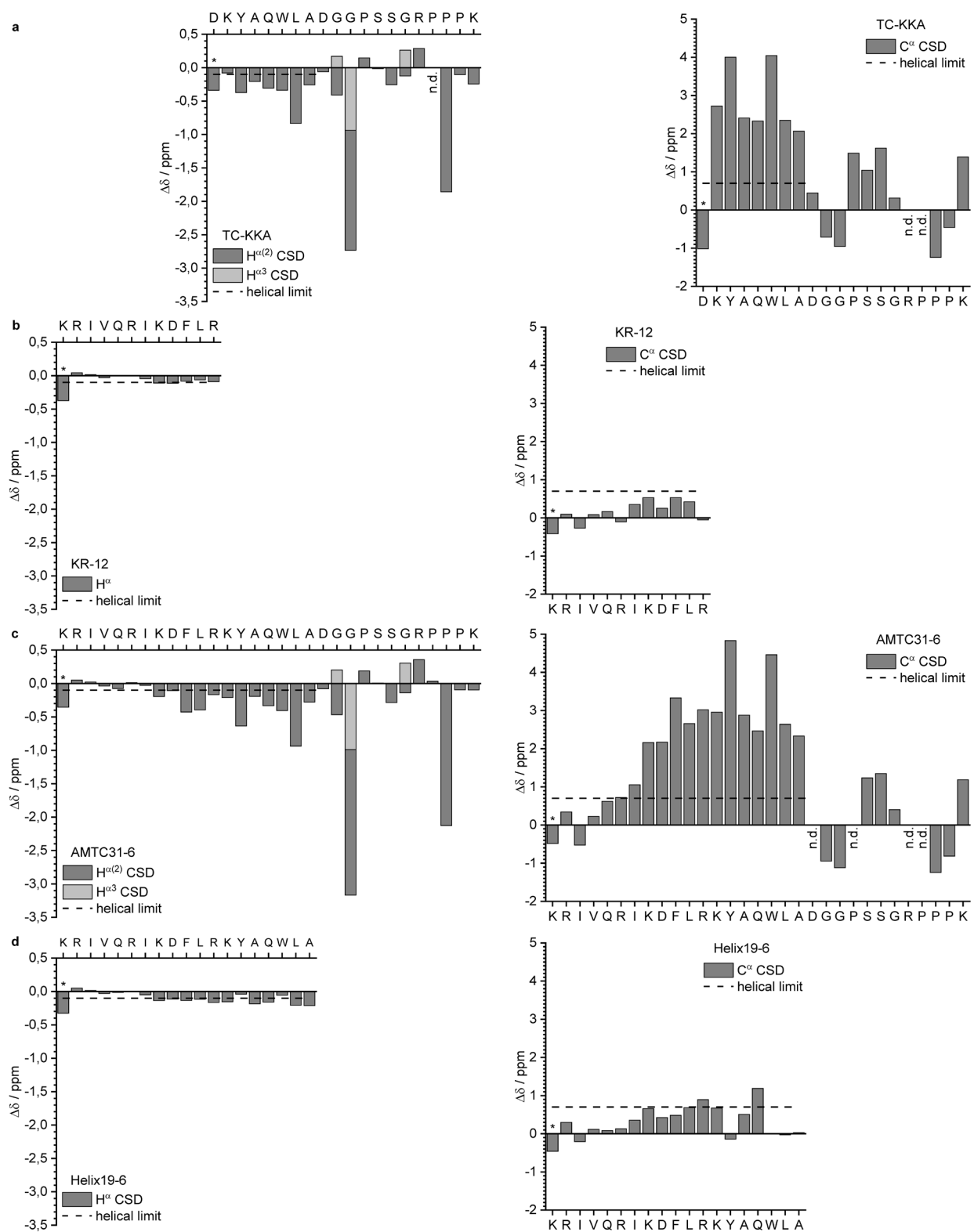


Figure S2. ^1H - and ^{13}C -chemical shift deviation (CSD or $\Delta\delta$) plots.

The description of Figure S2 is provided together with the description Figure S3 on the next page.

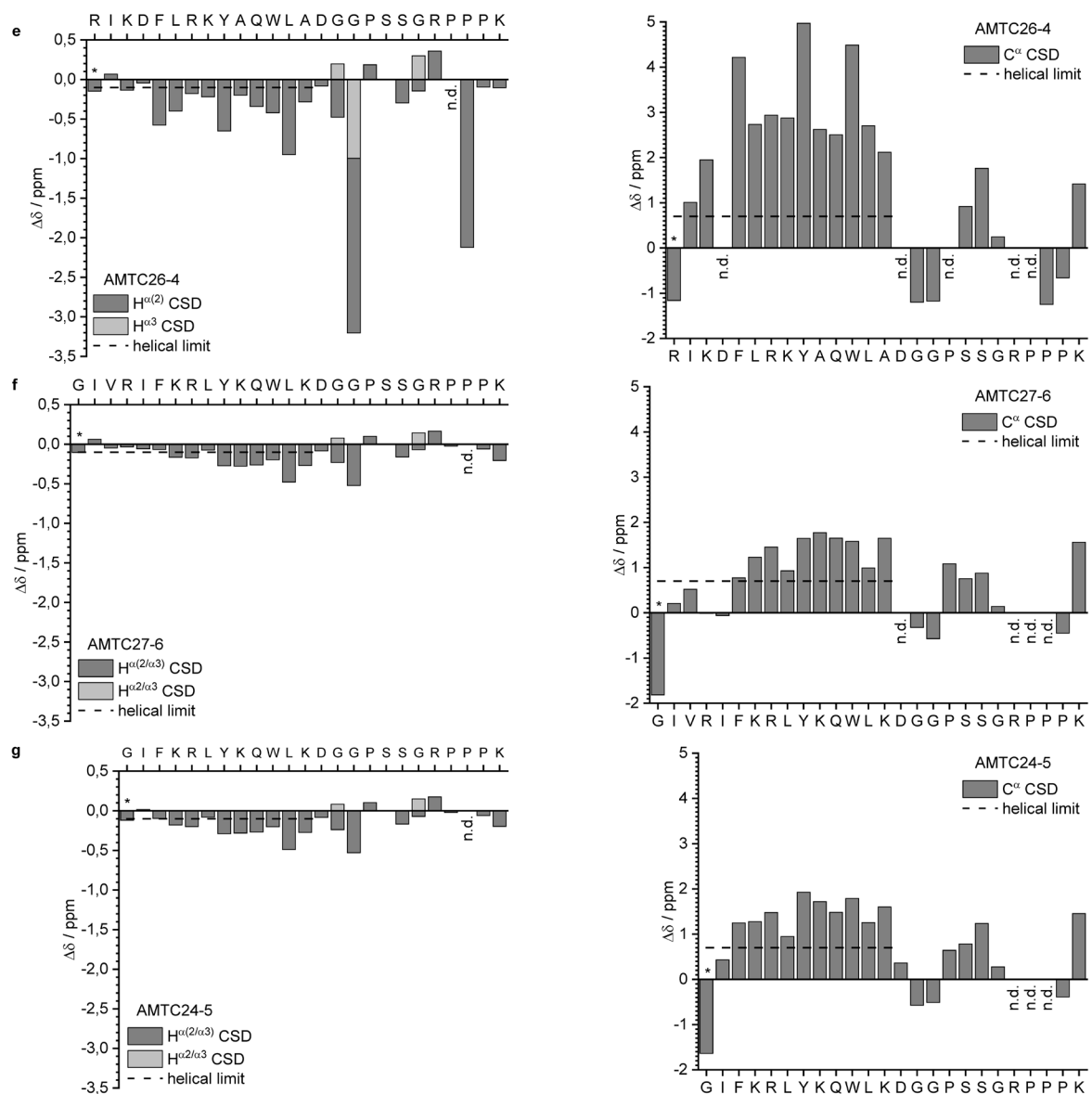


Figure S3. ^1H - and ^{13}C -chemical shift deviation (CSD or $\Delta\delta$) plots.

The $^1\text{H}^\alpha$ -CSDs (left) and $^{13}\text{C}^\alpha$ -CSDs (right) of TC-KKA (**a**), KR-12 (**b**), AMTC31-6 (**c**), Helix19-6 (**d**), AMTC26-4 (**e**), AMTC27-6 (**f**) and AMTC24-5 (**g**) are plotted over the respective sequence. Plots are arranged such that identical residues are vertically aligned. If four of five consecutive residues exceed the helical limit, this stretch is considered to have a helical conformation (53, 54). A more stable helix induces a larger chemical shift deviation. The N-terminal residue is marked by an asterisk, because a free N-terminus produces an upfield chemical shift of the α nuclei of the first residue. Therefore, the $\Delta\delta$ of the first residue in these peptides will always be negative and provides no information regarding the helicity of that residue. Some signals were not detected (n.d.), mainly because they were obstructed by the water artifact or because of excessive line broadening (see chemical shift tables S9-S22 for individual reasons a certain shift was not detected). The H^α nuclei of glycine were stereo-chemically assigned in **a – e**, but not in **f** and **g**. The Gly11 $\text{H}^{\alpha 2}$ and Pro18 H^α nuclei in TC-KKA and the corresponding nuclei in the AMTCs display a large negative CSD which is typical for the Trp-cage fold (19, 20). These nuclei are located directly below and above the Trp indole side chain and their CSDs result from the Trp indole ring current.

NOESY evaluation to identify helicity

($i, i+3$)- or ($i, i+4$)-NOEs are indicators of a stable α -helix between the respective residues. Especially, $H^{\alpha}_i, H^{\beta}_{i+3}$ -NOEs and H^{α}_i, H^N_{i+3} -NOEs are commonly observed in an α -helix. Furthermore, significant H^N_i, H^N_{i+1} -NOEs are often of medium or high intensity in an α -helix, because both NH-groups point in the same direction when in an α -helical conformation. In contrast, strong H^{α}_i, H^N_{i+1} -NOEs are typical for random coil conformations or less stable α -helices.

Table S1. NOE signals of TC-KKA indicative of helicity.

Residue i	H^N_i, H^N_{i+1} -NOE	H^{α}_i, H^N_{i+1} -NOE	H^{α}_i, H^N_{i+3} -NOE	$H^{\alpha}_i, H^{\beta}_{i+3}$ -NOE	H^{α}_i, H^N_{i+4} -NOE
01 D	exch.	exch.	-	-	-
02 K	exch.	++	++	++	o
03 Y	++	++	++	o	-
04 A	++	++	++	++	+
05 Q	o	++	++	++	o
06 W	++	++	++	+++	-
07 L	++	++	-	n.a.	o
08 A	++	++	-	n.a.	n.a.
09 D	+++	+	n.a.	o	o
10 G	+++	o	-	o	-
11 G	n.a.	n.a.	-	-	o
12 P	n.a.	++	-	n.a.	-
13 S	++	++	-	-	n.a.
14 S	++	o	n.a.	o	n.a.
15 G	++	++	n.a.	-	n.a.
16 R	n.a.	n.a.	n.a.	-	-
17 P	n.a.	n.a.	-	-	n.a.
18 P	n.a.	n.a.	n.a.	n.a.	n.a.
19 P	n.a.	+++	n.a.	n.a.	n.a.
20 K	n.a.	n.a.	n.a.	n.a.	n.a.

n.a. = Not applicable because one or both of the protons are not existent in the peptide.

exch. = Not applicable because one or both of the protons are not visible in the spectrum due to exchange.

- = No observed NOE.

o = Potential signal, but cannot be unambiguously assigned and/or quantified due to overlap.

+ = NOE of low intensity

++ = NOE of medium intensity

+++ = NOE of high intensity

Table S2. NOE signals of KR-12 indicative of helicity.

Residue <i>i</i>	H^N_i, H^N_{i+1} -NOE	H^α_i, H^N_{i+1} -NOE	H^α_i, H^N_{i+3} -NOE	$H^\alpha_i, H^\beta_{i+3}$ -NOE	H^α_i, H^N_{i+4} -NOE
01 K	exch.	exch.	-	-	-
02 R	exch.	++	o	-	o
03 I	+	+++	-	-	-
04 V	-	++	-	-	o
05 Q	o	o	-	o	-
06 R	-	+++	-	-	-
07 I	+	+++	-	-	-
08 K	+	++	-	-	-
09 D	o	o	o	-	n.a.
10 F	o	o	n.a.	n.a.	n.a.
11 L	o	o	n.a.	n.a.	n.a.
12 R	n.a.	n.a.	n.a.	n.a.	n.a.

n.a. = Not applicable because one or both of the protons are not existent in the peptide.

exch. = Not applicable because one or both of the protons are not visible in the spectrum due to exchange.

- = No observed NOE.

o = Potential signal, but cannot be unambiguously assigned and/or quantified due to overlap.

+= NOE of low intensity

++ = NOE of medium intensity

+++ = NOE of high intensity

Table S3. NOE signals of AMTC31-6 indicative of helicity.

Residue <i>i</i>	H^N_i, H^N_{i+1} -NOE	H^α_i, H^N_{i+1} -NOE	H^α_i, H^N_{i+3} -NOE	$H^\alpha_i, H^\beta_{i+3}$ -NOE	H^α_i, H^N_{i+4} -NOE
01 K	exch.	exch.	-	-	-
02 R	exch.	+++	-	-	-
03 I	o	+++	-	o	o
04 V	-	++	-	o	o
05 Q	o	++	+	+	o
06 R	+	++	+	+	-
07 I	+	+++	++	+	o
08 K	o	+++	++	o	+
09 D	+	++	++	+	+
10 F	++	++	++	o	+
11 L	++	++	o	+	o
12 R	++	++	++	++	+
13 K	++	++	o	+	+
14 Y	++	++	++	++	+
15 A	++	++	o	+	o
16 Q	o	++	o	++	o
17 W	+++	++	++	+	-
18 L	+++	++	+	n.a.	o
19 A	+++	++	-	n.a.	n.a.
20 D	++	++	n.a.	-	-
21 G	+++	o	-	o	o
22 G	n.a.	n.a.	o	-	o
23 P	n.a.	++	+	n.a.	+
24 S	++	++	+	-	n.a.
25 S	++	o	n.a.	o	n.a.
26 G	++	++	n.a.	-	n.a.
27 R	n.a.	n.a.	n.a.	-	-
28 P	n.a.	n.a.	-	-	n.a.
29 P	n.a.	n.a.	n.a.	n.a.	n.a.
30 P	n.a.	+++	n.a.	n.a.	n.a.
31 K	n.a.	n.a.	n.a.	n.a.	n.a.

n.a. = Not applicable because one or both of the protons are not existent in the peptide.

exch. = Not applicable because one or both of the protons are not visible in the spectrum due to exchange.

- = No observed NOE.

o = Potential signal, but cannot be unambiguously assigned and/or quantified due to overlap.

+= NOE of low intensity

++ = NOE of medium intensity

+++ = NOE of high intensity

Table S4. NOE signals of Helix19-6 indicative of helicity.

Residue <i>i</i>	H^N_i, H^N_{i+1} -NOE	H^α_i, H^N_{i+1} -NOE	H^α_i, H^N_{i+3} -NOE	$H^\alpha_i, H^\beta_{i+3}$ -NOE	H^α_i, H^N_{i+4} -NOE
01 K	exch.	exch.	-	-	-
02 R	exch.	+++	o	-	o
03 I	+	+++	-	o	o
04 V	+	++	-	-	o
05 Q	o	o	+	o	o
06 R	+	+++	+	+	-
07 I	+	+++	o	+	o
08 K	+	++	o	o	o
09 D	+	o	+	+	o
10 F	o	++	o	+	o
11 L	+	++	o	+	o
12 R	+	o	o	o	o
13 K	o	o	o	o	o
14 Y	o	++	+	+	-
15 A	+	++	o	o	o
16 Q	+	++	+	o	n.a.
17 W	++	++	n.a.	n.a.	n.a.
18 L	+	o	n.a.	n.a.	n.a.
19 A	n.a.	n.a.	n.a.	n.a.	n.a.

n.a. = Not applicable because one or both of the protons are not existent in the peptide.

exch. = Not applicable because one or both of the protons are not visible in the spectrum due to exchange.

- = No observed NOE.

o = Potential signal, but cannot be unambiguously assigned and/or quantified due to overlap.

+= NOE of low intensity

++ = NOE of medium intensity

+++ = NOE of high intensity

Table S5. NOE signals of AMTC26-4 indicative of helicity.

Residue <i>i</i>	H ^N _{<i>i</i>} ,H ^N _{<i>i</i>+1} -NOE	H ^α _{<i>i</i>} ,H ^N _{<i>i</i>+1} -NOE	H ^α _{<i>i</i>} ,H ^N _{<i>i</i>+3} -NOE	H ^α _{<i>i</i>} ,H ^β _{<i>i</i>+3} -NOE	H ^α _{<i>i</i>} ,H ^N _{<i>i</i>+4} -NOE
01 R	exch.	exch.	o	-	o
02 I	exch.	+++	o	+	o
03 K	o	++	o	o	o
04 D	++	++	o	+	-
05 F	o	++	o	+	+
06 L	o	++	o	++	o
07 R	++	o	o	++	o
08 K	++	+	o	+	+
09 Y	++	++	++	++	o
10 A	++	++	++	++	o
11 Q	++	o	o	++	o
12 W	o	o	+	++	-
13 L	+++	++	+	n.a.	o
14 A	+++	+	o	n.a.	n.a.
15 D	++	+	n.a.	-	-
16 G	+++	o	o	o	o
17 G	n.a.	n.a.	o	-	o
18 P	n.a.	+	o	n.a.	-
19 S	++	++	-	-	n.a.
20 S	++	o	n.a.	o	n.a.
21 G	++	+	n.a.	-	n.a.
22 R	n.a.	n.a.	n.a.	o	-
23 P	n.a.	n.a.	br.	o	n.a.
24 P	n.a.	n.a.	n.a.	n.a.	n.a.
25 P	n.a.	+++	n.a.	n.a.	n.a.
26 K	n.a.	n.a.	n.a.	n.a.	n.a.

n.a. = Not applicable because one or both of the protons are not existent in the peptide.

exch. = Not applicable because one or both of the protons are not visible in the spectrum due to exchange.

br. = Not applicable because one or both of the protons are too broad to be visible.

- = No observed NOE.

o = Potential signal, but cannot be unambiguously assigned and/or quantified due to overlap.

+ = NOE of low intensity

++ = NOE of medium intensity

+++ = NOE of high intensity

Table S6. NOE signals of AMTC27-6 indicative of helicity.

Residue <i>i</i>	H ^N _{<i>i</i>} ,H ^N _{<i>i</i>+1} -NOE	H ^α _{<i>i</i>} ,H ^N _{<i>i</i>+1} -NOE	H ^α _{<i>i</i>} ,H ^N _{<i>i</i>+3} -NOE	H ^α _{<i>i</i>} ,H ^β _{<i>i</i>+3} -NOE	H ^α _{<i>i</i>} ,H ^N _{<i>i</i>+4} -NOE
01 G	exch.	exch.	-	o	-
02 I	exch.	+++	-	-	-
03 V	+	+++	o	o	-
04 R	o	o	-	-	o
05 I	+	+++	o	o	-
06 F	+	++	+	+	-
07 K	+	o	+	+	o
08 R	o	+++	o	o	o
09 L	++	o	o	++	o
10 Y	+	o	o	++	o
11 K	++	o	o	o	o
12 Q	o	o	o	o	o
13 W	o	+++	o	++	-
14 L	o	+++	-	n.a.	++
15 K	o	+++	o	n.a.	n.a.
16 D	++	++	n.a.	-	o
17 G	++	++	o	o	-
18 G	n.a.	n.a.	-	o	-
19 P	n.a.	o	o	n.a.	o
20 S	o	++	o	-	n.a.
21 S	o	++	n.a.	o	n.a.
22 G	o	o	n.a.	o	n.a.
23 R	n.a.	n.a.	n.a.	o	-
24 P	n.a.	n.a.	-	br.	n.a.
25 P	n.a.	n.a.	n.a.	n.a.	n.a.
26 P	n.a.	+++	n.a.	n.a.	n.a.
27 K	n.a.	n.a.	n.a.	n.a.	n.a.

n.a. = Not applicable because one or both of the protons are not existent in the peptide.

exch. = Not applicable because one or both of the protons are not visible in the spectrum due to exchange.

br. = Not applicable because one or both of the protons are too broad to be visible.

- = No observed NOE.

o = Potential signal, but cannot be unambiguously assigned and/or quantified due to overlap.

+= NOE of low intensity

++ = NOE of medium intensity

+++ = NOE of high intensity

Table S7. NOE signals of AMTC24-5 indicative of helicity.

Residue <i>i</i>	H^N_i, H^N_{i+1} -NOE	H^α_i, H^N_{i+1} -NOE	H^α_i, H^N_{i+3} -NOE	$H^\alpha_i, H^\beta_{i+3}$ -NOE	H^α_i, H^N_{i+4} -NOE
01 G	exch.	exch.	-	o	-
02 I	exch.	+++	o	o	-
03 F	o	++	o	o	-
04 K	o	o	+	o	o
05 R	o	o	o	o	++
06 L	++	o	o	++	o
07 Y	+	+++	o	++	o
08 K	++	o	o	o	o
09 Q	o	o	o	o	o
10 W	o	o	o	++	-
11 L	o	+++	-	n.a.	++
12 K	o	+++	o	n.a.	n.a.
13 D	++	++	n.a.	o	o
14 G	+++	o	o	o	o
15 G	n.a.	n.a.	-	o	-
16 P	n.a.	o	-	n.a.	o
17 S	o	++	o	-	n.a.
18 S	o	++	n.a.	-	n.a.
19 G	o	++	n.a.	-	n.a.
20 R	n.a.	n.a.	n.a.	-	-
21 P	n.a.	n.a.	-	-	n.a.
22 P	n.a.	n.a.	n.a.	n.a.	n.a.
23 P	n.a.	+++	n.a.	n.a.	n.a.
24 K	n.a.	n.a.	n.a.	n.a.	n.a.

n.a. = Not applicable because one or both of the protons are not existent in the peptide.

exch. = Not applicable because one or both of the protons are not visible in the spectrum due to exchange.

- = No observed NOE.

o = Potential signal, but cannot be unambiguously assigned and/or quantified due to overlap.

+ = NOE of low intensity

++ = NOE of medium intensity

+++ = NOE of high intensity

Table S8. Concentrations of the NMR samples.

Peptide	TC-KKA	KR-12	AMTC31-6	Helix19-6	AMTC26-4	AMTC27-6	AMTC24-5
<i>c</i> / μM	383	401	400 ^a	404	376	384	370

The stated concentration is an average of the results of two methods: concentration determination by UV/vis spectroscopy with subsequent lyophilization, reconstitution and dilution and concentration determination by NMR.

^a) The concentration of the peptide AMTC31-6 was not corrected by NMR integration, as the DSS signal was not baseline separated.

Chemical shift tables

Table S9. ¹H chemical shifts of TC-KKA.

#	AA	Proton: Shift / ppm
01	D	H ^N : Exch., H ^α : 4.301, H ^{β2/β3} : 3.088/2.930
02	K	H ^N : Exch., H ^α : 4.241, H ^{β2/β3} : 1.845/1.790, H ^{γ2/γ3} : 1.438, H ^{δ2/δ3} : 1.687, H ^{ε2/ε3} : 2.977
03	Y	H ^N : 8.554, H ^α : 4.178, H ^{β2/β3} : 3.175/3.086, H ^δ : 7.102, H ^ε : 6.819
04	A	H ^N : 8.328, H ^α : 4.114, H ^β : 1.522
05	Q	H ^N : 8.002, H ^α : 4.034, H ^{β2/β3} : 2.141, H ^{γ2/γ3} : 2.405, H ^{ε21/ε22} : 7.723/6.911
06	W	H ^N : 7.986, H ^α : 4.323, H ^{β2} : 3.178, H ^{β3} : 3.496, H ^{δ1} : 7.064, H ^{ε1} : 9.751, H ^{ζ2} : 7.249, H ^{η2} : 7.218, H ^{ε3} : 7.148, H ^{ζ3} : 7.126
07	L	H ^N : 8.293, H ^α : 3.507, H ^{β2} : 1.777, H ^{β3} : 1.414, H ^γ : 1.584, H ^{δ1} : 0.940, H ^{δ2} : 0.854
08	A	H ^N : 8.100, H ^α : 4.064, H ^β : 1.462
09	D	H ^N : 7.851, H ^α : 4.579, H ^{β2/β3} : 2.852/2.697
10	G	H ^N : 7.640, H ^{α2} : 3.552, H ^{α3} : 4.131
11	G	H ^N : 8.297, H ^{α2} : 1.397, H ^{α3} : 3.193
12	P	H ^α : 4.565, H ^{β2} : 2.044, H ^{β3} : 2.478, H ^{γ2/γ3} : 2.121, H ^{δ2} : 3.764, H ^{δ3} : 3.385
13	S	H ^N : 7.820, H ^α : 4.457, H ^{β2/β3} : 3.919
14	S	H ^N : 8.165, H ^α : 4.215, H ^{β2/β3} : 3.890/3.590
15	G	H ^N : 7.972, H ^{α2} : 3.836, H ^{α3} : 4.222
16	R	H ^N : 8.091, H ^α : 4.940, H ^{β2/β3} : 1.850, H ^{γ2/γ3} : 1.753/1.670, H ^{δ2/δ3} : 3.297/3.220, H ^ε : 7.519
17	P	H ^α : 4.732, H ^{β2/β3} : 2.319/1.807, H ^{γ2/γ3} : 2.004, H ^{δ2/δ3} : 3.862/3.654
18	P	H ^α : 2.873, H ^{β2} : 1.393, H ^{β3} : 0.752, H ^{γ2/γ3} : 1.794/1.706, H ^{δ2} : 3.516, H ^{δ3} : 3.566
19	P	H ^α : 4.315, H ^{β2/β3} : 2.154/1.893, H ^{γ2/γ3} : 1.844, H ^{δ2/δ3} : 3.199/3.005
20	K	H ^N : 7.799, H ^α : 4.077, H ^{β2/β3} : 1.740/1.631, H ^{γ2/γ3} : 1.337, H ^{δ2/δ3} : 1.613, H ^{ε2/ε3} : 2.925

Exch. = The signal is not detectable due to exchange with solvent protons.

Table S10. ¹³C chemical shifts of TC-KKA.

#	AA	Proton: Shift / ppm
01	D	C ^α : 53.2, C ^β : 40.2
02	K	C ^α : 58.9, C ^β : 32.7, C ^γ : 25.0, C ^δ : 29.3, C ^ε : 42.1
03	Y	C ^α : 61.9, C ^β : 38.1, C ^δ : 133.0, C ^ε : 118.4
04	A	C ^α : 54.9, C ^β : 18.3
05	Q	C ^α : 58.0, C ^β : 28.9, C ^γ : 33.8
06	W	C ^α : 61.5, C ^β : 28.1, C ^{δ1} : 127.5, C ^{ζ2} : 114.4, C ^{η2} : 124.0, C ^{ε3} : 120.7, C ^{ζ3} : 122.7
07	L	C ^α : 57.4, C ^β : 42.1, C ^γ : 26.5, C ^{δ1} : 25.6, C ^{δ2} : 23.3
08	A	C ^α : 54.6, C ^β : 17.8
09	D	C ^α : 54.6, C ^β : 41.0
10	G	C ^α : 44.4
11	G	C ^α : 43.5
12	P	C ^α : 64.8, C ^β : 32.0, C ^γ : 27.4, C ^δ : 50.9
13	S	C ^α : 59.3, C ^β : 63.2
14	S	C ^α : 59.9, C ^β : 64.9
15	G	C ^α : 45.4
16	R	C ^α : n.d., C ^β : 30.7, C ^γ : 26.9, C ^δ : 43.6
17	P	C ^α : n.d., C ^β : 30.6, C ^γ : 27.1, C ^δ : 50.7
18	P	C ^α : 60.3, C ^β : 29.5, C ^γ : 26.9, C ^δ : 49.8
19	P	C ^α : 62.8, C ^β : 31.7, C ^γ : 27.2, C ^δ : 49.9
20	K	C ^α : 57.6, C ^β : 33.9, C ^γ : 24.7, C ^δ : 29.1, C ^ε : 42.2

n.d. = The signal is obstructed by the water artifact.

Table S11. ¹H chemical shifts of KR-12.

#	AA	Proton: Shift / ppm
01	K	H ^N : Exch., H ^α : 3.946, H ^{β2/β3} : 1.861, H ^{γ2/γ3} : 1.416, H ^{δ2/δ3} : 1.696, H ^{ε2/ε3} : 2.993
02	R	H ^N : Exch., H ^α : 4.383, H ^{β2/β3} : 1.762, H ^{γ2/γ3} : 1.637/1.555, H ^{δ2/δ3} : 3.192
03	I	H ^N : 8.490, H ^α : 4.184, H ^β : 1.826, H ^{γ12/γ13} : 1.488/1.190, H ^{δ1} : 0.849, H ^{γ2} : 0.866
04	V	H ^N : 8.366, H ^α : 4.089, H ^β : 2.007, H ^{γx} : 0.918, H ^{γy} : 0.896
05	Q	H ^N : 8.512, H ^α : 4.341, H ^{β2/β3} : 2.047/1.952, H ^{γ2/γ3} : 2.337, H ^{ε21/ε22} : 7.537/6.892
06	R	H ^N : 8.515, H ^α : 4.339, H ^{β2/β3} : 1.809/1.736, H ^{γ2/γ3} : 1.603, H ^{δ2/δ3} : 3.176
07	I	H ^N : 8.245, H ^α : 4.124, H ^β : 1.851, H ^{γ12/γ13} : 1.463/1.198, H ^{δ1} : 0.863, H ^{γ2} : 0.907
08	K	H ^N : 8.356, H ^α : 4.209, H ^{β2/β3} : 1.716, H ^{γ2/γ3} : 1.365, H ^{δ2/δ3} : 1.660, H ^{ε2/ε3} : 2.969
09	D	H ^N : 8.170, H ^α : 4.527, H ^{β2/β3} : 2.633/2.542
10	F	H ^N : 8.137, H ^α : 4.538, H ^{β2/β3} : 3.133/3.061, H ^δ : 7.254, H ^ε : 7.361, H ^ζ : 7.311
11	L	H ^N : 8.141, H ^α : 4.277, H ^{β2/β3} : 1.630/1.546, H ^γ : 1.514, H ^{δx} : 0.902, H ^{δy} : 0.858
12	R	H ^N : 8.117, H ^α : 4.249, H ^{β2/β3} : 1.866/1.752, H ^{γ2/γ3} : 1.629, H ^{δ2/δ3} : 3.202, H ^ε : 7.230
	NH ₂	H ^{N1/N2} : 7.463/7.116

Exch. = The signal is not detectable due to exchange with solvent protons.

Table S12. ¹³C chemical shifts of KR-12.

#	AA	Proton: Shift / ppm
01	K	C ^α : 55.8, C ^β : 33.6, C ^γ : 24.1, C ^δ : 29.4, C ^ε : 42.0
02	R	C ^α : 56.1, C ^β : 30.9, C ^γ : 27.3, C ^δ : 43.4
03	I	C ^α : 60.8, C ^β : 38.7, C ^{γ1} : 27.2, C ^{δ1} : 12.7, C ^{γ2} : 17.4
04	V	C ^α : 62.3, C ^β : 32.9, C ^{γx} : 20.7, C ^{γy} : 21.0
05	Q	C ^α : 55.9, C ^β : 29.8, C ^γ : 33.7
06	R	C ^α : 55.9, C ^β : 30.8, C ^γ : 27.4, C ^δ : 43.2
07	I	C ^α : 61.5, C ^β : 38.8, C ^{γ1} : 27.4, C ^{δ1} : 12.8, C ^{γ2} : 17.5
08	K	C ^α : 56.7, C ^β : 32.9, C ^γ : 24.7, C ^δ : 29.2, C ^ε : 42.2
09	D	C ^α : 54.5, C ^β : 41.3
10	F	C ^α : 58.2, C ^β : 39.4, C ^δ : 131.9, C ^ε : 131.6, C ^ζ : 130.0
11	L	C ^α : 55.5, C ^β : 42.2, C ^γ : 27.1, C ^{δx} : 24.9, C ^{δy} : 23.6
12	R	C ^α : 55.9, C ^β : 30.7, C ^γ : 27.3, C ^δ : 43.4

Table S13. ¹H chemical shifts of AMTC31-6.

#	AA	Proton: Shift / ppm
01	K	H ^N : Exch., H ^α : 3.965, H ^{β2/β3} : 1.869, H ^{γ2/γ3} : 1.434, H ^{δ2/δ3} : 1.697, H ^{ε2/ε3} : 2.998
02	R	H ^N : Exch., H ^α : 4.391, H ^{β2/β3} : 1.765, H ^{γ2/γ3} : 1.636/1.565, H ^{δ2/δ3} : 3.187, H ^ε : 7.182
03	I	H ^N : 8.496, H ^α : 4.191, H ^β : 1.832, H ^{γ12/γ13} : 1.491/1.197, H ^{δ1} : 0.850, H ^{γ2} : 0.882
04	V	H ^N : 8.335, H ^α : 4.081, H ^β : 2.047, H ^{γx} : 0.938, H ^{γy} : 0.918
05	Q	H ^N : 8.573, H ^α : 4.265, H ^{β2/β3} : 2.054/2.018, H ^{γ2/γ3} : 2.367, H ^{ε21/ε22} : 7.610/6.911
06	R	H ^N : 8.532, H ^α : 4.351, H ^{β2/β3} : 1.830, H ^{γ2/γ3} : 1.629, H ^{δ2/δ3} : 3.136, H ^ε : 7.224
07	I	H ^N : 8.134, H ^α : 4.141, H ^β : 1.969, H ^{γ12/γ13} : 1.527/1.273, H ^{δ1} : 0.890, H ^{γ2} : 0.986
08	K	H ^N : 8.325, H ^α : 4.125, H ^{β2/β3} : 1.849, H ^{γ2/γ3} : 1.536/1.423, H ^{δ2/δ3} : 1.710, H ^{ε2/ε3} : 3.006
09	D	H ^N : 8.347, H ^α : 4.534, H ^{β2/β3} : 2.738
10	F	H ^N : 8.034, H ^α : 4.194, H ^{β2/β3} : 3.320/3.091, H ^δ : 7.124, H ^ε : 7.164, H ^ζ : 7.042
11	L	H ^N : 8.375, H ^α : 3.943, H ^{β2/β3} : 1.874/1.571, H ^γ : 1.854, H ^{δx} : 0.973, H ^{δy} : 0.942
12	R	H ^N : 7.920, H ^α : 4.172, H ^{β2/β3} : 1.963, H ^{γ2/γ3} : 1.767/1.651, H ^{δ2/δ3} : 3.259, H ^ε : 7.361
13	K	H ^N : 8.084, H ^α : 4.111, H ^{β2/β3} : 1.843/1.716, H ^{γ2/γ3} : 1.435, H ^{δ2/δ3} : 1.638, H ^{ε2/ε3} : 2.972
14	Y	H ^N : 9.024, H ^α : 3.914, H ^{β2/β3} : 2.833/2.408, H ^δ : 6.962, H ^ε : 6.866
15	A	H ^N : 8.200, H ^α : 4.127, H ^β : 1.566
16	Q	H ^N : 7.989, H ^α : 4.007, H ^{β2/β3} : 2.208/2.115, H ^{γ2/γ3} : 2.417/2.381, H ^{ε21/ε22} : 7.764/6.909
17	W	H ^N : 7.950, H ^α : 4.255, H ^{β2} : 3.125, H ^{β3} : 3.453, H ^{δ1} : 7.003, H ^{ε1} : 9.714, H ^{ε2} : 7.216, H ^{η2} : 7.217, H ^{ε3} : 6.987, H ^{ζ3} : 7.109
18	L	H ^N : 8.343, H ^α : 3.402, H ^{β2} : 1.836, H ^{β3} : 1.380, H ^γ : 1.631, H ^{δ1} : 0.968, H ^{δ2} : 0.847
19	A	H ^N : 8.158, H ^α : 4.042, H ^β : 1.471
20	D	H ^N : 7.845, H ^α : 4.562, H ^{β2} : 2.700, H ^{β3} : 2.875
21	G	H ^N : 7.564, H ^{α2} : 3.493, H ^{α3} : 4.162
22	G	H ^N : 8.356, H ^{α2} : 0.963, H ^{α3} : 3.141
23	P	H ^α : 4.608, H ^{β2} : 2.072, H ^{β3} : 2.522, H ^{γ2/γ3} : 2.159, H ^{δ2} : 3.811, H ^{δ3} : 3.405
24	S	H ^N : 7.736, H ^α : 4.476, H ^{β2/β3} : 3.924
25	S	H ^N : 8.154, H ^α : 4.184, H ^{β2/β3} : 3.867/3.522
26	G	H ^N : 7.934, H ^{α2} : 3.820, H ^{α3} : 4.266
27	R	H ^N : 8.121, H ^α : 5.006, H ^{β2/β3} : 1.861, H ^{γ2/γ3} : 1.793/1.670, H ^{δ2/δ3} : 3.310/3.225, H ^ε : 7.491
28	P	H ^α : 4.763, H ^{β2} : 1.823, H ^{β3} : 2.350, H ^{γ2/γ3} : 2.022, H ^{δ2} : 3.678, H ^{δ3} : 3.888
29	P	H ^α : 2.604, H ^{β2} : 1.339, H ^{β3} : 0.352, H ^{γ2/γ3} : 1.699, H ^{δ2/δ3} : 3.542
30	P	H ^α : 4.325, H ^{β2} : 1.898, H ^{β3} : 2.203, H ^{γ2/γ3} : 1.741/1.664, H ^{δ2} : 2.905, H ^{δ3} : 3.102
31	K	H ^N : 7.719, H ^α : 4.223, H ^{β2/β3} : 1.747/1.635, H ^{γ2/γ3} : 1.347, H ^{δ2/δ3} : 1.623, H ^{ε2/ε3} : 2.943

Exch. = The signal is not detectable due to exchange with solvent protons.

Table S14. ¹³C chemical shifts of AMTC31-6.

#	AA	Proton: Shift / ppm
01	K	C ^α : 55.7, C ^β : 33.5, C ^γ : 24.3, C ^δ : 29.3, C ^ε : 42.1
02	R	C ^α : 56.3, C ^β : 30.9, C ^γ : 27.1, C ^δ : 43.4
03	I	C ^α : 60.6, C ^β : 38.8, C ^{γ1} : 27.4, C ^{δ1} : 12.7, C ^{γ2} : 17.6
04	V	C ^α : 62.4, C ^β : 32.7, C ^{γx} : 20.5, C ^{γy} : 21.1
05	Q	C ^α : 56.3, C ^β : 29.4, C ^γ : 33.7
06	R	C ^α : 56.7, C ^β : 30.7, C ^γ : 27.0, C ^δ : 43.3
07	I	C ^α : 62.2, C ^β : 38.6, C ^{γ1} : 27.8, C ^{δ1} : 12.9, C ^{γ2} : 17.7
08	K	C ^α : 58.4, C ^β : 32.8, C ^γ : 25.4, C ^δ : 29.3, C ^ε : 42.0
09	D	C ^α : 56.4, C ^β : 40.9
10	F	C ^α : 61.0, C ^β : 39.2, C ^δ : 131.7, C ^ε : 131.4, C ^ζ : 130.1
11	L	C ^α : 57.8, C ^β : 41.6, C ^γ : 27.1, C ^{δx} : 25.6, C ^{δy} : 22.8
12	R	C ^α : 59.0, C ^β : 30.0, C ^γ : 27.1, C ^δ : 43.3
13	K	C ^α : 59.2, C ^β : 32.5, C ^γ : 24.4, C ^δ : 29.3, C ^ε : 42.2
14	Y	C ^α : 62.7, C ^β : 38.3, C ^δ : 132.8, C ^ε : 118.4
15	A	C ^α : 55.4, C ^β : 18.0
16	Q	C ^α : 58.2, C ^β : 28.5, C ^γ : 33.7
17	W	C ^α : 62.0, C ^β : 27.6, C ^{δ1} : 127.5, C ^{ζ2} : 114.3, C ^{η2} : 123.9, C ^{ε3} : 120.5, C ^{ζ3} : 122.9
18	L	C ^α : 57.7, C ^β : 42.0, C ^γ : 25.3, C ^{δ1} : 25.6, C ^{δ2} : 23.1
19	A	C ^α : 54.8, C ^β : 17.7
20	D	C ^α : n.d., C ^β : 41.0
21	G	C ^α : 44.2
22	G	C ^α : 43.4
23	P	C ^α : n.d., C ^β : 32.0, C ^γ : 27.4, C ^δ : 50.9
24	S	C ^α : 59.5, C ^β : 63.1
25	S	C ^α : 59.6, C ^β : 65.0
26	G	C ^α : 45.5
27	R	C ^α : n.d., C ^β : 31.0, C ^γ : 27.0, C ^δ : 46.0
28	P	C ^α : n.d., C ^β : 30.6, C ^γ : 27.2, C ^δ : 50.6
29	P	C ^α : 60.3, C ^β : 29.2, C ^γ : 26.7, C ^δ : 49.8
30	P	C ^α : 62.5, C ^β : 31.9, C ^γ : 27.0, C ^δ : 49.5
31	K	C ^α : 57.4, C ^β : 34.7, C ^γ : 24.7, C ^δ : 29.3, C ^ε : 42.2

n.d. = The signal is obstructed by the water artifact.

Table S15. ¹H chemical shifts of Helix19-6.

#	AA	Proton: Shift / ppm
01	K	H ^N : Exch., H ^α : 3.994, H ^{β2/β3} : 1.880, H ^{γ2/γ3} : 1.435, H ^{δ2/δ3} : 1.705, H ^{ε2/ε3} : 3.002
02	R	H ^N : Exch., H ^α : 4.390, H ^{β2/β3} : 1.771, H ^{γ2/γ3} : 1.646/1.580, H ^{δ2/δ3} : 3.190
03	I	H ^N : 8.491, H ^α : 4.185, H ^β : 1.831, H ^{γ12/γ13} : 1.493/1.193, H ^{δ1} : 0.855, H ^{γ2} : 0.872
04	V	H ^N : 8.348, H ^α : 4.089, H ^β : 2.016, H ^{γx} : 0.923, H ^{γy} : 0.901
05	Q	H ^N : 8.516, H ^α : 4.326, H ^{β2/β3} : 2.045/1.962, H ^{γ2/γ3} : 2.340, H ^{ε21/ε22} : 7.548/6.887
06	R	H ^N : 8.523, H ^α : 4.342, H ^{β2/β3} : 1.811/1.744, H ^{γ2/γ3} : 1.604, H ^{δ2/δ3} : 3.160
07	I	H ^N : 8.220, H ^α : 4.120, H ^β : 1.865, H ^{γ12/γ13} : 1.472/1.202, H ^{δ1} : 0.858, H ^{γ2} : 0.911
08	K	H ^N : 8.367, H ^α : 4.183, H ^{β2/β3} : 1.728, H ^{γ2/γ3} : 1.415/1.361, H ^{δ2/δ3} : 1.666, H ^{ε2/ε3} : 2.970
09	D	H ^N : 8.199, H ^α : 4.527, H ^{β2/β3} : 2.660/2.586
10	F	H ^N : 8.092, H ^α : 4.484, H ^{β2/β3} : 3.152/3.094, H ^δ : 7.234, H ^ε : 7.334, H ^ζ : 7.278
11	L	H ^N : 8.110, H ^α : 4.224, H ^{β2/β3} : 1.660, H ^γ : 1.541, H ^{δx} : 0.912, H ^{δy} : 0.866
12	R	H ^N : 8.027, H ^α : 4.176, H ^{β2/β3} : 1.766, H ^{γ2/γ3} : 1.604/1.545, H ^{δ2/δ3} : 3.157, H ^ε : 7.202
13	K	H ^N : 8.111, H ^α : 4.166, H ^{β2/β3} : 1.654, H ^{γ2/γ3} : 1.293/1.195, H ^{δ2/δ3} : 1.592, H ^{ε2/ε3} : 2.918
14	Y	H ^N : 8.095, H ^α : 4.508, H ^{β2/β3} : 3.056/2.846, H ^δ : 7.074, H ^ε : 6.805
15	A	H ^N : 8.080, H ^α : 4.135, H ^β : 1.288
16	Q	H ^N : 8.186, H ^α : 4.180, H ^{β2/β3} : 1.981, H ^{γ2/γ3} : 2.260, H ^{ε21/ε22} : 7.467/6.853
17	W	H ^N : 8.047, H ^α : 4.604, H ^{β2} : 3.333, H ^{β3} : 3.259, H ^{δ1} : 7.231, H ^{ε1} : 10.170, H ^{ζ2} : 7.479, H ^{η2} : 7.235, H ^{ε3} : 7.564, H ^{ζ3} : 7.139
18	L	H ^N : 7.888, H ^α : 4.133, H ^{β2/β3} : 1.479, H ^γ : 1.397, H ^{δx} : 0.836, H ^{δy} : 0.798
19	A	H ^N : 7.843, H ^α : 4.109, H ^β : 1.359
NH ₂		H ^{N1/N2} : 7.309/6.994

Exch. = The signal is not detectable due to exchange with solvent protons.

Table S16. ¹³C chemical shifts of Helix19-6.

#	AA	Proton: Shift / ppm
01	K	C ^α : 55.7, C ^β : 33.6, C ^γ : 24.2, C ^δ : 29.3, C ^ε : 42.0
02	R	C ^α : 56.3, C ^β : 30.7, C ^γ : 27.2, C ^δ : 43.4
03	I	C ^α : 60.9, C ^β : 38.8, C ^{γ1} : 27.4, C ^{δ1} : 12.7, C ^{γ2} : 17.5
04	V	C ^α : 62.3, C ^β : 32.8, C ^{γx} : 20.7, C ^{γ2} : 21.0
05	Q	C ^α : 55.8, C ^β : 29.7, C ^γ : 33.8
06	R	C ^α : 56.1, C ^β : 30.8, C ^γ : 27.3, C ^δ : 43.4
07	I	C ^α : 61.5, C ^β : 38.7, C ^{γ1} : 27.4, C ^{δ1} : 12.7, C ^{γ2} : 17.6
08	K	C ^α : 56.9, C ^β : 33.0, C ^γ : 24.7, C ^δ : 29.3, C ^ε : 42.2
09	D	C ^α : 54.6, C ^β : 41.2
10	F	C ^α : 58.2, C ^β : 39.4, C ^δ : 131.9, C ^ε : 131.6, C ^ζ : 130.0
11	L	C ^α : 55.8, C ^β : 42.2, C ^γ : 26.9, C ^{δx} : 25.1, C ^{δy} : 23.4
12	R	C ^α : 56.9, C ^β : 30.7, C ^γ : 27.3, C ^δ : 43.4
13	K	C ^α : 56.9, C ^β : 32.8, C ^γ : 24.8, C ^δ : 29.2, C ^ε : 42.2
14	Y	C ^α : 57.8, C ^β : 38.8, C ^δ : 133.2, C ^ε : 118.2
15	A	C ^α : 53.0, C ^β : 19.0
16	Q	C ^α : 56.9, C ^β : 29.2, C ^γ : 33.9
17	W	C ^α : 57.5, C ^β : 29.2, C ^{δ1} : 127.1, C ^{ζ2} : 114.6, C ^{η2} : 124.7, C ^{ε3} : 120.8, C ^{ζ3} : 122.2
18	L	C ^α : 55.1, C ^β : 42.6, C ^γ : 26.7, C ^{δx} : 25.0, C ^{δy} : 23.5
19	A	C ^α : 52.5, C ^β : 19.3

Table S17. ¹H chemical shifts of AMTC26-4.

#	AA	Proton: Shift / ppm
01	R	H ^N : Exch., H ^α : 4.193, H ^{β2/β3} : 1.861, H ^{γ2/γ3} : 1.624, H ^{δ2/δ3} : 2.957, H ^ε : 7.158
02	I	H ^N : Exch., H ^α : 4.238, H ^β : 1.998, H ^{γ12/γ13} : 1.538/1.369, H ^{δ1} : 0.928, H ^{γ2} : 1.023
03	K	H ^N : 8.567, H ^α : 4.185, H ^{β2/β3} : 1.824, H ^{γ2/γ3} : 1.527/1.451, H ^{δ2/δ3} : 1.723, H ^{ε2/ε3} : 3.018
04	D	H ^N : 8.513, H ^α : 4.595, H ^{β2/β3} : 2.803/2.708
05	F	H ^N : 7.940, H ^α : 4.043, H ^{β2/β3} : 3.367/2.962, H ^δ : 7.086, H ^ε : 7.161, H ^ζ : 7.005
06	L	H ^N : 8.337, H ^α : 3.941, H ^{β2/β3} : 1.816/1.577, H ^γ : 1.794, H ^{δx} : 0.997, H ^{δy} : 0.953
07	R	H ^N : 7.953, H ^α : 4.161, H ^{β2/β3} : 1.914, H ^{γ2/γ3} : 1.747/1.640, H ^{δ2/δ3} : 3.245, H ^ε : 7.408
08	K	H ^N : 8.130, H ^α : 4.101, H ^{β2/β3} : 1.793/1.695, H ^{γ2/γ3} : 1.571, H ^{δ2/δ3} : 1.679, H ^{ε2/ε3} : 2.991
09	Y	H ^N : 9.094, H ^α : 3.899, H ^{β2/β3} : 2.801/2.348, H ^δ : 6.950, H ^ε : 6.862
10	A	H ^N : 8.125, H ^α : 4.120, H ^β : 1.559
11	Q	H ^N : 8.018, H ^α : 3.998, H ^{β2/β3} : 2.198/2.096, H ^{γ2/γ3} : 2.392, H ^{ε21/ε22} : 7.747/6.902
12	W	H ^N : 7.939, H ^α : 4.239, H ^{β2} : 3.122, H ^{β3} : 3.451, H ^{δ1} : 6.993, H ^{ε1} : 9.725, H ^{ε2} : 7.213, H ^{η2} : 7.214, H ^{ε3} : 6.980, H ^ζ : 7.108
13	L	H ^N : 8.340, H ^α : 3.390, H ^{β2/β3} : 1.827/1.373, H ^γ : 1.612, H ^{δ1} : 0.959, H ^{δ2} : 0.845
14	A	H ^N : 8.147, H ^α : 4.037, H ^β : 1.464
15	D	H ^N : 7.841, H ^α : 4.558, H ^{β2/β3} : 2.872/2.695
16	G	H ^N : 7.556, H ^{α2} : 3.484, H ^{α3} : 4.157
17	G	H ^N : 8.351, H ^{α2} : 0.925, H ^{α3} : 3.133
18	P	H ^α : 4.605, H ^{β2} : 2.069, H ^{β3} : 2.518, H ^{γ2/γ3} : 2.158, H ^{δ2} : 3.811, H ^{δ3} : 3.412
19	S	H ^N : 7.723, H ^α : 4.471, H ^{β2/β3} : 3.923
20	S	H ^N : 8.152, H ^α : 4.174, H ^{β2/β3} : 3.859/3.513
21	G	H ^N : 7.925, H ^{α2} : 3.814, H ^{α3} : 4.259
22	R	H ^N : 8.114, H ^α : 5.009, H ^{β2/β3} : 1.856, H ^{γ2/γ3} : 1.801/1.660, H ^{δ2/δ3} : 3.304/3.220, H ^ε : 7.486
23	P	H ^α : n.d., H ^{β2/β3} : 1.820/2.346, H ^{γ2/γ3} : 2.017, H ^{δ2/δ3} : 3.676/3.882
24	P	H ^α : 2.607, H ^{β2} : 1.329, H ^{β3} : 0.263, H ^{γ2/γ3} : 1.679, H ^{δ2/δ3} : 3.537
25	P	H ^α : 4.324, H ^{β2} : 1.860, H ^{β3} : 2.197, H ^{γ2} : 1.723, H ^{γ3} : 1.653, H ^{δ2} : 2.914, H ^{δ3} : 3.119
26	K	H ^N : 7.697, H ^α : 4.215, H ^{β2/β3} : 1.738/1.632, H ^{γ2/γ3} : 1.340, H ^{δ2/δ3} : 1.621, H ^{ε2/ε3} : 2.939

Exch. = The signal is not detectable due to exchange with solvent protons.

n.d. = The signal is obstructed by the water artifact.

Table S18. ^{13}C chemical shifts of AMTC26-4.

#	AA	Proton: Shift / ppm
01	R	C^α : 54.8, C^β : 31.2, C^γ : 26.4, C^δ : 42.8
02	I	C^α : 62.1, C^β : 39.1, C^{γ^1} : 27.3, C^{δ^1} : 13.7, C^{γ^2} : 17.7
03	K	C^α : 58.1, C^β : 32.8, C^γ : 25.2, C^δ : 29.4, C^ϵ : 42.2
04	D	C^α : n.d., C^β : 40.6
05	F	C^α : 61.9, C^β : 39.7, C^δ : 131.7, C^ϵ : 131.4, C^ζ : 130.1
06	L	C^α : 57.8, C^β : 41.5, C^γ : 27.0, C^{δ^x} : 25.3, C^{δ^y} : 23.1
07	R	C^α : 58.9, C^β : 30.3, C^γ : 27.1, C^δ : 43.3
08	K	C^α : 59.1, C^β : 32.5, C^γ : 25.9, C^δ : 29.3, C^ϵ : 42.5
09	Y	C^α : 62.9, C^β : 38.1, C^δ : 132.9, C^ϵ : 118.4
10	A	C^α : 55.1, C^β : 17.9
11	Q	C^α : 58.2, C^β : 28.3, C^γ : 33.8
12	W	C^α : 62.0, C^β : 27.6, C^{δ^1} : 127.4, C^{ζ^2} : 114.2, C^{η^2} : 123.7, C^{ϵ^3} : 120.6, C^{ζ^3} : 122.8
13	L	C^α : 57.8, C^β : 42.0, C^γ : 26.2, C^{δ^1} : 25.9, C^{δ^2} : 23.2
14	A	C^α : 54.6, C^β : 17.7
15	D	C^α : n.d., C^β : 40.7
16	G	C^α : 43.9
17	G	C^α : 43.3
18	P	C^α : n.d., C^β : 32.0, C^γ : 27.4, C^δ : 50.9
19	S	C^α : 59.2, C^β : 63.1
20	S	C^α : 60.1, C^β : 65.1
21	G	C^α : 45.3
22	R	C^α : n.d., C^β : 31.0, C^γ : 27.0, C^δ : 43.4
23	P	C^α : n.d., C^β : 30.6, C^γ : 27.2, C^δ : 50.6
24	P	C^α : 60.3, C^β : 28.9, C^γ : 26.7, C^δ : 49.7
25	P	C^α : 62.6, C^β : 32.1, C^γ : 26.7, C^δ : 49.5
26	K	C^α : 57.6, C^β : 34.9, C^γ : 24.7, C^δ : 29.3, C^ϵ : 42.5

n.d. = The signal is obstructed by the water artifact.

Table S19. ¹H chemical shifts of AMTC27-6.

#	AA	Proton: Shift / ppm
01	G	H ^N : exch., H ^{α2/α3} : 3.856
02	I	H ^N : exch., H ^α : 4.232, H ^β : 1.826, H ^{γ12/γ13} : 1.463/1.178, H ^{δ1} : 0.864, H ^{γ2} : 0.889
03	V	H ^N : 8.387, H ^α : 4.072, H ^β : 2.016, H ^{γx} : 0.958, H ^{γy} : 0.899
04	R	H ^N : 8.473, H ^α : 4.306, H ^{β2/β3} : 1.687, H ^{γ2/γ3} : 1.561/1.464, H ^{δ2/δ3} : 3.131, H ^ε : 7.168
05	I	H ^N : 8.209, H ^α : 4.113, H ^β : 1.783, H ^{γ12/γ13} : 1.413/1.137, H ^{δ1} : 0.822, H ^{γ2} : 0.826
06	F	H ^N : 8.502, H ^α : 4.553, H ^{β2/β3} : 3.083/3.061, H ^δ : 7.203, H ^ε : 7.274, H ^ζ : 7.208
07	K	H ^N : 8.357, H ^α : 4.156, H ^{β2/β3} : 1.822/1.776, H ^{γ2/γ3} : 1.469/1.389, H ^{δ2/δ3} : 1.684, H ^{ε2/ε3} : 2.977
08	R	H ^N : 8.216, H ^α : 4.167, H ^{β2/β3} : 1.818, H ^{γ2/γ3} : 1.650/1.575, H ^{δ2/δ3} : 3.190, H ^ε : 7.178
09	L	H ^N : 8.304, H ^α : 4.267, H ^{β2/β3} : 1.690/1.443, H ^γ : 1.646, H ^{δx} : 0.917, H ^{δy} : 0.860
10	Y	H ^N : 8.415, H ^α : 4.279, H ^{β2/β3} : 2.991/2.816, H ^δ : 7.016, H ^ε : 6.796
11	K	H ^N : 8.197, H ^α : 4.043, H ^{β2/β3} : 1.778, H ^{γ2/γ3} : 1.448/1.366, H ^{δ2/δ3} : 1.666, H ^{ε2/ε3} : 2.950
12	Q	H ^N : 8.085, H ^α : 4.079, H ^{β2/β3} : 2.045, H ^{γ2/γ3} : 2.320, H ^{ε21/ε22} : 7.661/6.882
13	W	H ^N : 8.073, H ^α : 4.463, H ^{β2} : 3.177, H ^{β3} : 3.380, H ^{δ1} : 7.121, H ^{ε1} : 9.956, H ^{ε2} : 7.352, H ^{η2} : 7.222, H ^{ε3} : 7.311, H ^{ζ3} : 7.121
14	L	H ^N : 8.102, H ^α : 3.862, H ^{β2/β3} : 1.677/1.420, H ^γ : 1.510, H ^{δx} : 0.897, H ^{δy} : 0.827
15	K	H ^N : 8.072, H ^α : 4.051, H ^{β2/β3} : 1.861/1.792, H ^{γ2/γ3} : 1.428, H ^{δ2/δ3} : 1.663, H ^{ε2/ε3} : 2.977
16	D	H ^N : 8.128, H ^α : 4.557, H ^{β2/β3} : 2.795/2.682
17	G	H ^N : 7.915, H ^{α2/α3} : 4.039/3.729
18	G	H ^N : 8.281, H ^{α2/α3} : 3.609
19	P	H ^α : 4.520, H ^{β2/β3} : 2.393/2.016, H ^{γ2/γ3} : 2.077, H ^{δ2/δ3} : 3.703/3.490
20	S	H ^N : 8.125, H ^α : 4.465, H ^{β2/β3} : 3.904
21	S	H ^N : 8.216, H ^α : 4.308, H ^{β2/β3} : 3.892/3.697
22	G	H ^N : 8.153, H ^{α2/α3} : 4.103/3.892
23	R	H ^N : 8.093, H ^α : 4.816, H ^{β2/β3} : 1.804, H ^{γ2/γ3} : 1.682, H ^{δ2/δ3} : 3.221, H ^ε : 7.331
24	P	H ^α : 4.706, H ^{β2/β3} : 2.324/1.839, H ^{γ2/γ3} : 2.015, H ^{δ2/δ3} : 3.842/3.624
25	P	H ^α : br., H ^{β2/β3} : 1.632/1.377, H ^{γ2/γ3} : 1.877, H ^{δ2/δ3} : 3.672/3.576
26	P	H ^α : 4.360, H ^{β2/β3} : 2.237/1.943, H ^{γ2/γ3} : 1.918/1.877, H ^{δ2/δ3} : 3.473/3.293
27	K	H ^N : 7.830, H ^α : 4.114, H ^{β2/β3} : 1.772/1.673, H ^{γ2/γ3} : 1.383, H ^{δ2/δ3} : 1.675, H ^{ε2/ε3} : 2.974

Exch. = The signal is not detectable due to exchange with solvent protons.

br. = The signal is not detectable due to excessive line broadening.

Table S20. ^{13}C chemical shifts of AMTC27-6.

AA Proton: Shift / ppm

01	G	C^α : 43.3
02	I	C^α : 61.3, C^β : 39.0, $\text{C}^{\gamma 1}$: 27.3, $\text{C}^{\delta 1}$: 13.0, $\text{C}^{\gamma 2}$: 17.6
03	V	C^α : 62.7, C^β : 32.5, $\text{C}^{\gamma x}$: 21.0, $\text{C}^{\gamma y}$: 21.1
04	R	C^α : 56.0, C^β : 31.1, C^γ : 27.2, C^δ : 43.4
05	I	C^α : 61.0, C^β : 38.9, $\text{C}^{\gamma 1}$: 27.2, $\text{C}^{\delta 1}$: 12.6, $\text{C}^{\gamma 2}$: 17.5
06	F	C^α : 58.5, C^β : 39.7, C^δ : 131.8, C^ϵ : 131.5, C^ζ : 129.9
07	K	C^α : 57.4, C^β : 32.9, C^γ : 25.0, C^δ : 29.3, C^ϵ : 42.2
08	R	C^α : 57.5, C^β : 30.5, C^γ : 27.3, C^δ : 43.5
09	L	C^α : 56.0, C^β : 42.4, C^γ : 27.0, $\text{C}^{\delta x}$: 25.2, $\text{C}^{\delta y}$: 23.1
10	Y	C^α : 59.5, C^β : 38.8, C^δ : 133.1, C^ϵ : 118.3
11	K	C^α : 58.0, C^β : 32.9, C^γ : 24.9, C^δ : 29.3, C^ϵ : 42.2
12	Q	C^α : 57.3, C^β : 29.1, C^γ : 33.7
13	W	C^α : 59.1, C^β : 28.7, $\text{C}^{\delta 1}$: 127.4, $\text{C}^{\zeta 2}$: 114.6, $\text{C}^{\eta 2}$: 124.4, $\text{C}^{\epsilon 3}$: 120.8, $\text{C}^{\zeta 3}$: 122.4
14	L	C^α : 56.1, C^β : 42.3, C^γ : 26.9, $\text{C}^{\delta x}$: 25.3, $\text{C}^{\delta y}$: 23.4
15	K	C^α : 57.8, C^β : 32.6, C^γ : 24.8, C^δ : 29.3, C^ϵ : 42.2
16	D	C^α : n.d., C^β : 41.1
17	G	C^α : 44.8
18	G	C^α : 43.9
19	P	C^α : 64.4, C^β : 32.1, C^γ : 27.4, C^δ : 50.3
20	S	C^α : 59.1, C^β : 63.7
21	S	C^α : 59.2, C^β : 64.5
22	G	C^α : 45.2
23	R	C^α : n.d., C^β : 30.5, C^γ : 26.9, C^δ : 43.5
24	P	C^α : n.d., C^β : 30.7, C^γ : 27.3, C^δ : 50.6
25	P	C^α : br., C^β : 29.3, C^γ : 27.2, C^δ : 50.3
26	P	C^α : 62.9, C^β : 32.0, C^γ : 27.2, C^δ : 50.1
27	K	C^α : 57.8, C^β : 33.8, C^γ : 24.8, C^δ : 29.3, C^ϵ : 42.2

n.d. = The signal is obstructed by the water artifact.

br. = The signal is not detectable due to excessive line broadening.

Table S21. ¹H chemical shifts of AMTC24-5.

#	AA	Proton: Shift / ppm
01	G	H ^N : exch., H ^{a2/a3} : 3.841
02	I	H ^N : exch., H ^a : 4.184, H ^β : 1.807, H ^{γ12/γ13} : 1.351/1.131, H ^{δ1} : 0.840, H ^{γ2} : 0.857
03	F	H ^N : 8.476, H ^a : 4.525, H ^{β2/β3} : 3.103/3.076, H ^δ : 7.205, H ^ε : 7.280, H ^ζ : 7.205
04	K	H ^N : 8.328, H ^a : 4.142, H ^{β2/β3} : 1.810/1.755, H ^{γ2/γ3} : 1.464/1.370, H ^{δ2/δ3} : 1.680, H ^{ε2/ε3} : 2.976
05	R	H ^N : 8.153, H ^a : 4.142, H ^{β2/β3} : 1.810, H ^{γ2/γ3} : 1.651/1.566, H ^{δ2/δ3} : 3.189, H ^ε : 7.167
06	L	H ^N : 8.321, H ^a : 4.260, H ^{β2/β3} : 1.681/1.434, H ^γ : 1.648, H ^{δx} : 0.921, H ^{δy} : 0.859
07	Y	H ^N : 8.449, H ^a : 4.261, H ^{β2/β3} : 2.969/2.785, H ^δ : 7.011, H ^ε : 6.805
08	K	H ^N : 8.202, H ^a : 4.040, H ^{β2/β3} : 1.774, H ^{γ2/γ3} : 1.445/1.364, H ^{δ2/δ3} : 1.666, H ^{ε2/ε3} : 2.949
09	Q	H ^N : 8.073, H ^a : 4.073, H ^{β2/β3} : 2.048, H ^{γ2/γ3} : 2.321, H ^{ε21/ε22} : 7.666/6.884
10	W	H ^N : 8.074, H ^a : 4.460, H ^{β2} : 3.176, H ^{β3} : 3.380, H ^{δ1} : 7.117, H ^{ε1} : 9.949, H ^{ε2} : 7.349, H ^{η2} : 7.223, H ^{ε3} : 7.305, H ^{ε3} : 7.123
11	L	H ^N : 8.109, H ^a : 3.852, H ^{β2/β3} : 1.678/1.422, H ^γ : 1.510, H ^{δx} : 0.898, H ^{δy} : 0.826
12	K	H ^N : 8.076, H ^a : 4.047, H ^{β2/β3} : 1.861/1.799, H ^{γ2/γ3} : 1.424, H ^{δ2/δ3} : 1.662, H ^{ε2/ε3} : 2.977
13	D	H ^N : 8.123, H ^a : 4.557, H ^{β2/β3} : 2.798/2.682
14	G	H ^N : 7.905, H ^{a2/a3} : 4.042/3.722
15	G	H ^N : 8.288, H ^{a2/a3} : 3.601
16	P	H ^a : 4.522, H ^{β2/β3} : 2.395/2.016, H ^{γ2/γ3} : 2.080, H ^{δ2/δ3} : 3.706/3.490
17	S	H ^N : 8.115, H ^a : 4.467, H ^{β2/β3} : 3.906
18	S	H ^N : 8.212, H ^a : 4.304, H ^{β2/β3} : 3.889/3.690
19	G	H ^N : 8.150, H ^{a2/a3} : 4.109/3.889
20	R	H ^N : 8.096, H ^a : 4.825, H ^{β2/β3} : 1.807, H ^{γ2/γ3} : 1.689, H ^{δ2/δ3} : 3.218, H ^ε : 7.337
21	P	H ^a : 4.709, H ^{β2/β3} : 2.326/1.840, H ^{γ2/γ3} : 2.015, H ^{δ2/δ3} : 3.842/3.626
22	P	H ^a : br., H ^{β2/β3} : 1.628/1.360, H ^{γ2/γ3} : 1.872, H ^{δ2/δ3} : 3.669/3.576
23	P	H ^a : 4.359, H ^{β2/β3} : 2.188/1.938, H ^{γ2/γ3} : 1.864, H ^{δ2/δ3} : 3.455/3.281
24	K	H ^N : 7.812, H ^a : 4.124, H ^{β2/β3} : 1.759/1.666, H ^{γ2/γ3} : 1.376, H ^{δ2/δ3} : 1.662, H ^{ε2/ε3} : 2.968

Exch. = The signal is not detectable due to exchange with solvent protons.

br. = The signal is not detectable due to excessive line broadening.

Table S22. ^{13}C chemical shifts of AMTC24-5.

AA Proton: Shift / ppm

01	G	C^α : 43.5
02	I	C^α : 61.5, C^β : 38.9, C^γ : 27.2, $\text{C}^{\delta 1}$: 13.2, $\text{C}^{\gamma 2}$: 17.5
03	F	C^α : 58.9, C^β : 39.5, C^δ : 131.8, C^ϵ : 131.5, C^ζ : 129.9
04	K	C^α : 57.5, C^β : 32.8, C^γ : 25.0, C^δ : 29.3, C^ϵ : 42.2
05	R	C^α : 57.5, C^β : 30.4, C^γ : 27.2, C^δ : 43.5
06	L	C^α : 56.0, C^β : 42.5, C^γ : 26.6, $\text{C}^{\delta x}$: 25.2, $\text{C}^{\delta y}$: 23.1
07	Y	C^α : 59.8, C^β : 38.8, C^δ : 133.1, C^ϵ : 118.3
08	K	C^α : 57.9, C^β : 32.8, C^γ : 24.9, C^δ : 29.3, C^ϵ : 42.2
09	Q	C^α : 57.2, C^β : 28.9, C^γ : 33.6
10	W	C^α : 59.3, C^β : 28.6, $\text{C}^{\delta 1}$: 127.4, $\text{C}^{\zeta 2}$: 114.5, $\text{C}^{\eta 2}$: 124.4, $\text{C}^{\epsilon 3}$: 120.8, $\text{C}^{\zeta 3}$: 122.4
11	L	C^α : 56.4, C^β : 42.3, C^γ : 26.8, $\text{C}^{\delta x}$: 25.4, $\text{C}^{\delta y}$: 23.4
12	K	C^α : 57.8, C^β : 32.4, C^γ : 24.8, C^δ : 29.3, C^ϵ : 42.2
13	D	C^α : 54.6, C^β : 41.1
14	G	C^α : 44.5
15	G	C^α : 44.0
16	P	C^α : 63.9, C^β : 32.1, C^γ : 27.4, C^δ : 50.5
17	S	C^α : 59.1, C^β : 63.6
18	S	C^α : 59.5, C^β : 64.6
19	G	C^α : 45.4
20	R	C^α : n.d., C^β : 30.4, C^γ : 26.8, C^δ : 43.6
21	P	C^α : n.d., C^β : 30.7, C^γ : 27.3, C^δ : 50.8
22	P	C^α : br., C^β : 29.3, C^γ : 27.1, C^δ : 50.1
23	P	C^α : 62.9, C^β : 32.0, C^γ : 27.1, C^δ : 50.2
24	K	C^α : 57.7, C^β : 33.9, C^γ : 24.8, C^δ : 29.3, C^ϵ : 42.2

n.d. = The signal is obstructed by the water artifact.

br. = The signal is not detectable due to excessive line broadening.

CD analysis

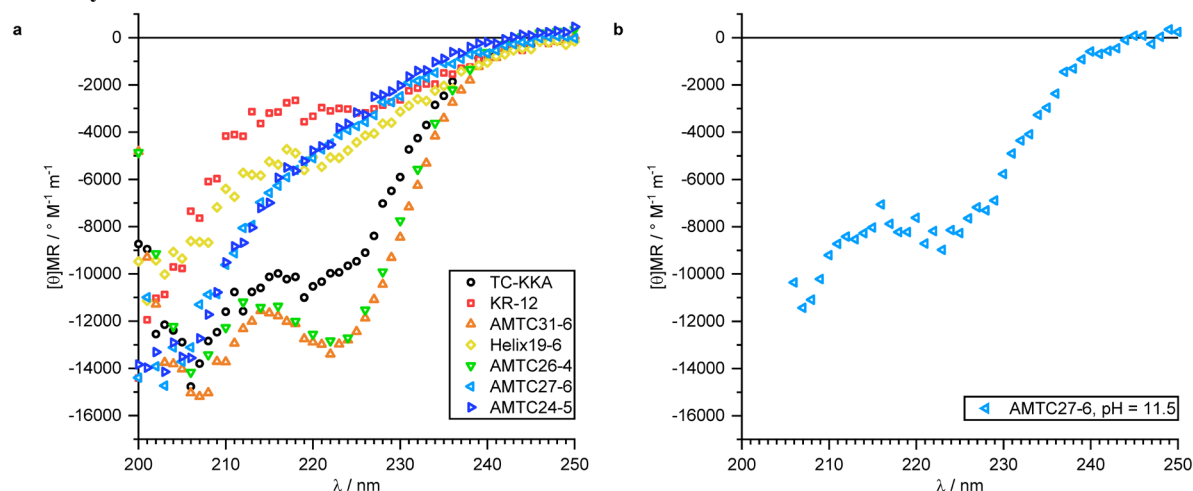


Figure S4. CD data.

(a) CD data were recorded at 37 °C and at pH = 5.5. The mean residue molar ellipticity $[\theta]_{MR}$ is plotted over the wavelength λ . A negative band at 222 nm is indicative of helicity. (b) The CD sample of AMTC27-6 was adjusted to pH = 11.5 \pm 1 by the addition of 7 μ l 1 M NaOH in water. The CD spectrum was recorded with the same setting as stated in the Methods section, chapter CD spectroscopy.

Table S23. Concentration of the CD samples.

Peptide	TC-KKA	KR-12	AMTC31-6	Helix19-6	AMTC26-4	AMTC27-6	AMTC24-5
$c / \mu\text{M}$	19.2	40.1	20.0 ^a	20.2	37.6	19.2	18.5

Table S24. Parameters of the melting curve fits of TC-KKA, AMTC31-6 and AMTC26-6.

Melting curves of the peptides TC-KKA, AMTC31-6 and AMTC26-4 were fitted with a sigmoidal Boltzmann function

$$f(T) = A_2 + \frac{A_1 - A_2}{1 + e^{\frac{T - T_m}{dT}}},$$

where A_1 corresponds to the mean residue molar ellipticity $[\theta]_{MR}$ of the 100% folded state, A_2 corresponds to $[\theta]_{MR}$ of the 0% folded state, T is the temperature and T_m is the midpoint of thermal unfolding. The fitted functions were characterized by the following values:

Parameter	TC-KKA	AMTC31-6	AMTC26-4
A_1	-17623.48837 \pm 505.60069	-17801.1158 \pm 190.73718	-17854.42811 \pm 119.95453
A_2	-3639.07054 \pm 210.16976	-4914.96338 \pm 215.83775	-4145.78212 \pm 88.46835
T_m	35.93098 \pm 1.12521	43.95979 \pm 0.52144	43.29814 \pm 0.29648
dT	14.21237 \pm 1.06117	12.94653 \pm 0.64696	11.96078 \pm 0.32063

The midpoint of thermal unfolding (also referred to as melting temperature, T_m) of TC-KKA was determined to be $T_m = (35.9 \pm 1.1) ^{\circ}\text{C}$ at pH = 5.5 \pm 0.1 which seems significantly lower than that of TC10b[K8A] ($T_m = (64 \pm 2) ^{\circ}\text{C}$) or TC10b ($T_m = (58 \pm 2) ^{\circ}\text{C}$) at pH = 7 (20). Comparison of this T_m to the melting points reported by Barua and co-workers (20), however, is compounded by a difference in T_m calculations. Using the data points of TC10b, our method affords a melting point of $T_m = (45.4 \pm 0.9) ^{\circ}\text{C}$ which is an underestimation of approximately 10 $^{\circ}\text{C}$ compared to Barua *et al.* (20).

MIC and MBC results

Table S25: Averaged MIC results and their standard deviation regarding *E. coli*.

Peptide	<i>Escherichia coli</i>							
	pH = 7.5, 150 mM NaCl		pH = 7.5, 0 mM NaCl		pH = 5.5, 150 mM NaCl		pH = 5.5, 0 mM NaCl	
	MIC / μ M	StdDev / μ M	MIC / μ M	StdDev / μ M	MIC / μ M	StdDev / μ M	MIC / μ M	StdDev / μ M
TC-KKA	>5	0	>5	0	>5	0	>5	0
KR-12	>5	0	0.039	0.0184	>5	0	0.078	0.0184
AMTC31-6	0.313	0.059	0.313	0.074	0.039	0.0095	0.078	0.0184
Helix19-6	0.156	0	0.078	0.0368	0.039	0.0145	0.078	0
AMTC26-4	>5	0	>5	0	5	0	2.5	1.18
AMTC27-6	2.5	0.59	0.313	0	2.5	1.25	0.313	0.074
AMTC24-5	>5	0	>5	2.5	>5	0	5	2.4
Melittin	1.25	0.295	0.625	0.147	0.625	0	0.156	0
solvent	>5	0	>5	0	>5	0	>5	2.4

Table S26: Averaged MBC results and their standard deviation regarding *E. coli*.

Peptide	<i>Escherichia coli</i>							
	pH = 7.5, 150 mM NaCl		pH = 7.5, 0 mM NaCl		pH = 5.5, 150 mM NaCl		pH = 5.5, 0 mM NaCl	
	MBC / μ M	StdDev / μ M	MBC / μ M	StdDev / μ M	MBC / μ M	StdDev / μ M	MBC / μ M	StdDev / μ M
TC-KKA								
KR-12			0.156	0.039			0.313	0.102
AMTC31-6	0.313	0	0.313	0.074	0.039	0.0206	0.078	0
Helix19-6	0.156	0.068	0.078	0	0.039	0.0169	0.078	0.0338
AMTC26-4					5	1.9	5	0.9
AMTC27-6	2.5	0.47	0.625	0.153	2.5	1.25	0.313	0
AMTC24-5			>5	2.5			>5	2.4

Legend

- X X is the average MIC or MBC, respectively, rounded to the nearest dilution level.
- >X All measurements of the respective MIC or MBC are above the concentration X.
- >X The average of the respective MIC or MBC is above the concentration X, but individual measurements may be at or below X.
- ≤X X is the lowest tested concentration and the peptide is active at that concentration.
- [empty] The MBC was not determined, because no activity was measured in the corresponding MIC assay. In case of melittin and solvent, the MBC was never determined.

Table S27: Averaged MIC results and their standard deviation regarding *B. megaterium*.

Peptide	<i>Bacillus megaterium</i>							
	pH = 7.5, 150 mM NaCl		pH = 7.5, 0 mM NaCl		pH = 5.5, 150 mM NaCl		pH = 5.5, 0 mM NaCl	
	MIC / μ M	StdDev / μ M	MIC / μ M	StdDev / μ M	MIC / μ M	StdDev / μ M	MIC / μ M	StdDev / μ M
TC-KKA	>5	0	>5	0	>5	1.9	>5	0
KR-12	0.02	0	≤ 0.002	0	0.078	0.0291	0.002	0.0014
AMTC31-6	0.02	0.0097	0.02	0.0090	0.005	0.0014	0.01	0.0050
Helix19-6	0.039	0	0.078	0.0195	0.002	0.0014	0.039	0.0193
AMTC26-4	2.5	0.47	0.156	0.029	0.625	0.280	0.156	0.074
AMTC27-6	0.039	0.0095	0.02	0.0114	0.02	0.0071	0.005	0.0029
AMTC24-5	1.25	0	0.039	0.0145	0.625	0.233	0.078	0.0291
Melittin	0.02	0.0090	0.039	0.0206	0.005	0.0029	0.01	
solvent	>5	0	>5	0	5	0	5	2.4

Table S28: Averaged MBC results and their standard deviation regarding *B. megaterium*.

Peptide	<i>Bacillus megaterium</i>							
	pH = 7.5, 150 mM NaCl		pH = 7.5, 0 mM NaCl		pH = 5.5, 150 mM NaCl		pH = 5.5, 0 mM NaCl	
	MBC / μ M	StdDev / μ M	MBC / μ M	StdDev / μ M	MBC / μ M	StdDev / μ M	MBC / μ M	StdDev / μ M
TC-KKA								
KR-12	0.02	0	≤ 0.002	0	0.078	0.0338	0.005	0.0015
AMTC31-6	0.02	0.0097	0.02	0.0090	0.005	0.0014	0.01	0.0045
Helix19-6	0.039	0	0.078	0.0169	0.002	0.0013	0.039	0.0169
AMTC26-4	2.5	0	0.156	0.070	0.625	0.280	0.156	0.074
AMTC27-6	0.039	0.0095	0.02	0.0144	0.02	0.0071	0.005	0.0029
AMTC24-5	1.25	0.589	0.039	0.0145	1.25	0.313	0.078	0.0368

Legend

- X X is the average MIC or MBC, respectively, rounded to the nearest dilution level.
- >X All measurements of the respective MIC or MBC are above the concentration X.
- >X The average of the respective MIC or MBC is above the concentration X, but individual measurements may be at or below X.
- $\leq X$ X is the lowest tested concentration and the peptide is active at that concentration.
- [empty] The MBC was not determined, because no activity was measured in the corresponding MIC assay. In case of melittin and solvent, the MBC was never determined.

Table S29: Averaged MIC results and their standard deviation regarding *S. aureus*.

Peptide	<i>Staphylococcus aureus</i>							
	pH = 7.5, 150 mM NaCl		pH = 7.5, 0 mM NaCl		pH = 5.5, 150 mM NaCl		pH = 5.5, 0 mM NaCl	
	MIC / μ M	StdDev / μ M	MIC / μ M	StdDev / μ M	MIC / μ M	StdDev / μ M	MIC / μ M	StdDev / μ M
TC-KKA	>20	0	>10	0	>10	0	>10	0
KR-12	>20	0	10	0	>10	0	>10	0
AMTC31-6	>20	0	10	2.4	>10	0	>10	0
Helix19-6	0.625	0.116	0.625	0	10	2.5	10	0
AMTC26-4	>20	0	>10	0	>10	0	>10	0
AMTC27-6	20	13.4	2.5	0	>10	0	>10	0
AMTC24-5	>20	0	>10	0	>10	0	>10	0
Melittin	0.313	0.147	0.625	0.190	5	1.3	2.5	0.59
solvent	>20	0	>10	0	>10	0	>10	0

Table S30: Averaged MBC results and their standard deviation regarding *S. aureus*.

Peptide	<i>Staphylococcus aureus</i>							
	pH = 7.5, 150 mM NaCl		pH = 7.5, 0 mM NaCl		pH = 5.5, 150 mM NaCl		pH = 5.5, 0 mM NaCl	
	MBC / μ M	StdDev / μ M	MBC / μ M	StdDev / μ M	MBC / μ M	StdDev / μ M	MBC / μ M	StdDev / μ M
TC-KKA								
KR-12			10	4.7				
AMTC31-6			10	1.9				
Helix19-6	0.625	0.116	0.625	0	10	0	10	0
AMTC26-4								
AMTC27-6	>20	0	2.5	0				
AMTC24-5								

Legend

- X X is the average MIC or MBC, respectively, rounded to the nearest dilution level.
- >X All measurements of the respective MIC or MBC are above the concentration X.
- >X The average of the respective MIC or MBC is above the concentration X, but individual measurements may be at or below X.
- ≤X X is the lowest tested concentration and the peptide is active at that concentration.
- [empty] The MBC was not determined, because no activity was measured in the corresponding MIC assay. In case of melittin and solvent, the MBC was never determined.

Table S31: Averaged MIC results and their standard deviation regarding *P. aeruginosa*.

Peptide	<i>Pseudomonas aeruginosa</i>							
	pH = 7.5, 150 mM NaCl		pH = 7.5, 0 mM NaCl		pH = 5.5, 150 mM NaCl		pH = 5.5, 0 mM NaCl	
	MIC / μ M	StdDev / μ M	MIC / μ M	StdDev / μ M	MIC / μ M	StdDev / μ M	MIC / μ M	StdDev / μ M
TC-KKA	>10	0	>10	0	>20	0	>20	0
KR-12	>10	0	2.5	3.54	>20	0	20	0
AMTC31-6	>10	0	10	2.5	10	0	10	0
Helix19-6	1.25	0.466	5	4.0	2.5	0.59	10	2.5
AMTC26-4	>10	0	>10	0	>20	0	>20	10
AMTC27-6	5	2.8	2.5	0.93	10	4.5	5	1.2
AMTC24-5	>10	0	>10	5	>20	9.4	20	10
Melittin	>5	2.5	2.5	2.76	10	1.9	5	0
solvent	>10	0	>10	0	>20	0	>20	0

Table S32: Averaged MBC results and their standard deviation regarding *P. aeruginosa*.

Peptide	<i>Pseudomonas aeruginosa</i>							
	pH = 7.5, 150 mM NaCl		pH = 7.5, 0 mM NaCl		pH = 5.5, 150 mM NaCl		pH = 5.5, 0 mM NaCl	
	MBC / μ M	StdDev / μ M	MBC / μ M	StdDev / μ M	MBC / μ M	StdDev / μ M	MBC / μ M	StdDev / μ M
TC-KKA							>20	0
KR-12			10	6.1	>20	0	>20	7.5
AMTC31-6	>10	0	>10	3.7	20	10	10	3.7
Helix19-6	2.5	0.54	5	2.7	2.5	1.18	10	2.4
AMTC26-4							>20	10
AMTC27-6	>10	5.6	5	5.7	10	4.7	5	13.3
AMTC24-5			>10	3.7	>20	0	20	12.1

Legend

- X X is the average MIC or MBC, respectively, rounded to the nearest dilution level.
- >X All measurements of the respective MIC or MBC are above the concentration X.
- >X The average of the respective MIC or MBC is above the concentration X, but individual measurements may be at or below X.
- ≤X X is the lowest tested concentration and the peptide is active at that concentration.
- [empty] The MBC was not determined, because no activity was measured in the corresponding MIC assay. In case of melittin and solvent, the MBC was never determined.

Hemolysis assay

Table S33: Hemolysis results.

$c / \mu\text{M}$	TC-KKA	KR-12	AMTC31-6	Helix19-6	AMTC26-4	AMTC27-6	AMTC24-5	Melittin
80	0	0	4	117	1	9	0	
40	0	0	3	61	0	3	0	
20	0	0	2	30	0	1	0	118
10	0	0	0	15	0	0	0	110
5	0	0	0	8	0	0	0	82
2.5	0	0	0	3	0	0	0	38
1.25	0	0	0	1	0	0	0	18
0.625	0	0	0	0	0	0	0	6
0.313	0	0	0	0	0	0	0	1
0.156	0	0	0	0	0	0	0	0
0.078	0	0	0	0	0	0	0	0
0.039	0	0	0	0	0	0	0	0

The hemolytic activity of all peptides at different concentrations is given in %. Osmolysis of erythrocytes is defined as 100% activity.

Liposome depolarization assay

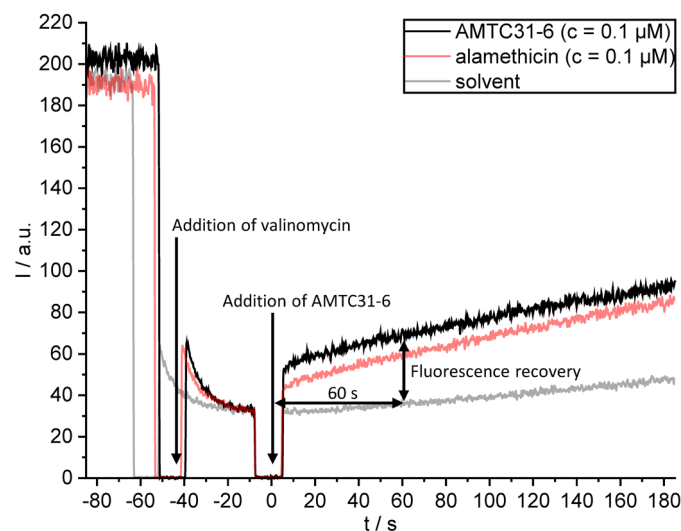


Figure S5. Liposome depolarization assay.

Fluorescence intensity I is plotted over the time t for AMTC31-6, for the control alamethicin and for the solvent (10 mM HCl in water). At first, a cationic fluorescent dye is dissolved freely resulting in high fluorescence ($I \approx 200$ a.u.). The fluorescence drops to zero every time the cuvette is taken out of the spectrometer, e.g. for the addition of valinomycin. Valinomycin-mediated K^+ -transport across the liposome membrane along the K^+ concentration gradient leads to the build-up of an electrostatic potential across the membrane driving the cationic dye into the liposomes where the fluorescence is quenched ($I \approx 40$ a.u.). Addition of a pore-forming peptide such as AMTC31-6 (at $t = 0$) dissipates the diffusion potential resulting in a fluorescence recovery compared to mere addition of solvent. 5% recovery after 60 s are defined as 1 U.

Enzymatic degradation analysis

Detailed trypsin and chymotrypsin fragment analyses at 25 °C

Analysis of the cleavability of peptide bonds was achieved by comparison of identical fragments between different peptides, as well as by analyzing the relative rates of fragment formation and degradation e.g. by correlating the time at which the parent peptide was completely degraded with the time points at which certain fragments reach their maximum concentration. Note that the ion counts of different fragments are not directly comparable (An example is given in Figure S6b) because some fragments may be ionized (and therefore detected) at a higher ratio than others and because only the most common proton-adducts, but no adducts with metal ions (Na^+ , K^+ , Ca^{++}) were included in the compound database.

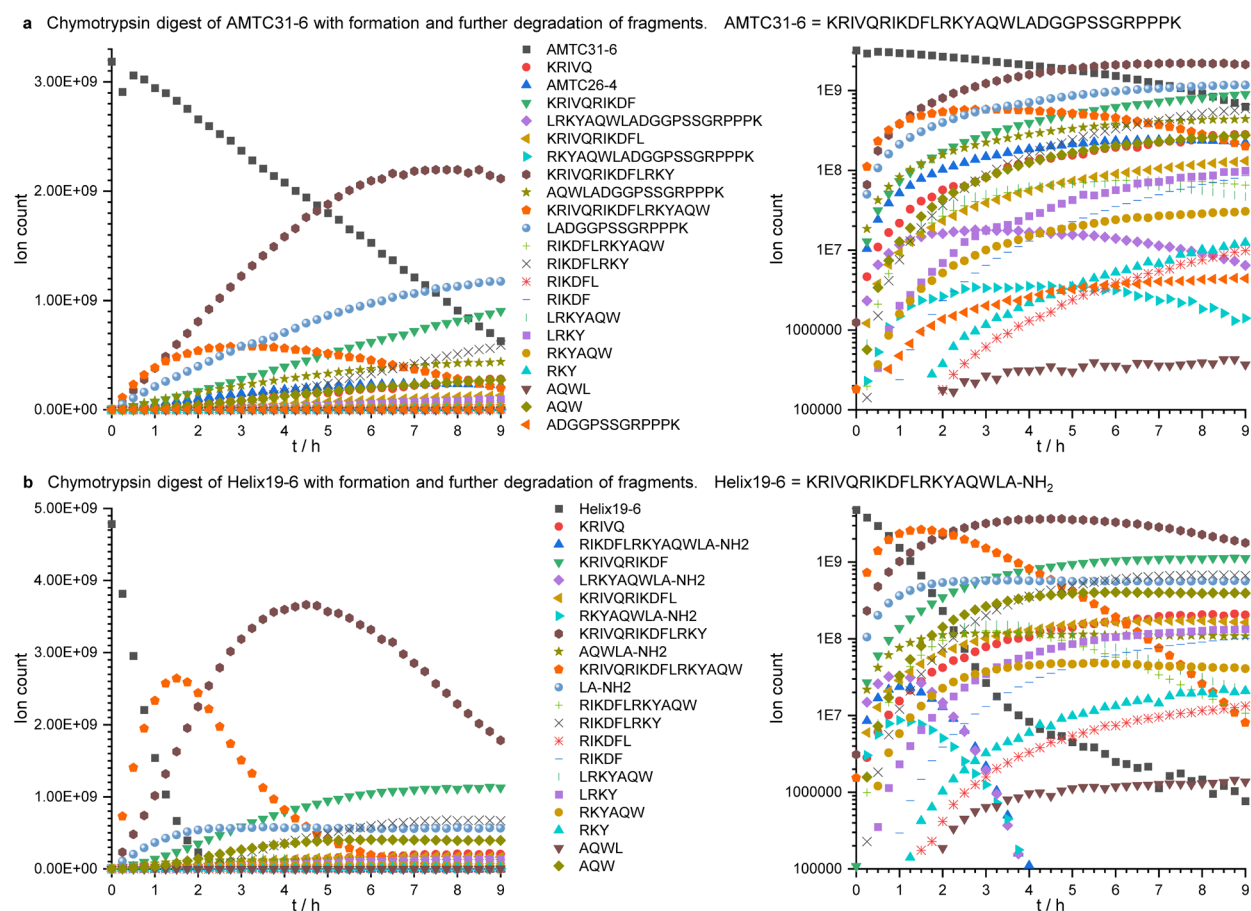


Figure S7: Fragment analysis of the chymotrypsin digests of AMTC31-6 and Helix19-6.

The average formation and further degradation of fragments of AMTC31-6 (**a**) and Helix19-6 (**b**) resulting from the chymotrypsin digest is shown on a linear scale (left) and on a logarithmic scale (right). The average ion count of the proton adducts of the parent and of each fragment is plotted over the time.

The formation of KRIVQ (●) is equally fast in AMTC31-6 and Helix19-6 and the cleavage site Q5-R6 is therefore not stabilized in AMTC31-6. The fragment KRIVQRIKDF (▼), however, is formed a little faster in Helix19-6 than in AMTC31-6. The cleavage sites W17-L18 is cleaved much faster in Helix19-6 than in AMTC31-6, as evidenced by the extremely fast formation of the fragment LA-NH₂ (●, panel **b**) reaching its maximum after 2 h compared to the slow increase of its counterpart LADGGPSSGRPPPK (●, panel **a**). Further evidence is provided by the rapid formation of the fragment KRIVQRIKDFLRKYAQL (●) in panel **b** compared to its slow increase in panel **a**. Similar to the W17-L18 bond, the Y14-A15 bond is also cleaved faster in Helix19-6. For instance, the fragment KRIVQRIKDFLRKY (●) is formed faster in panel **b** than in panel **a**.

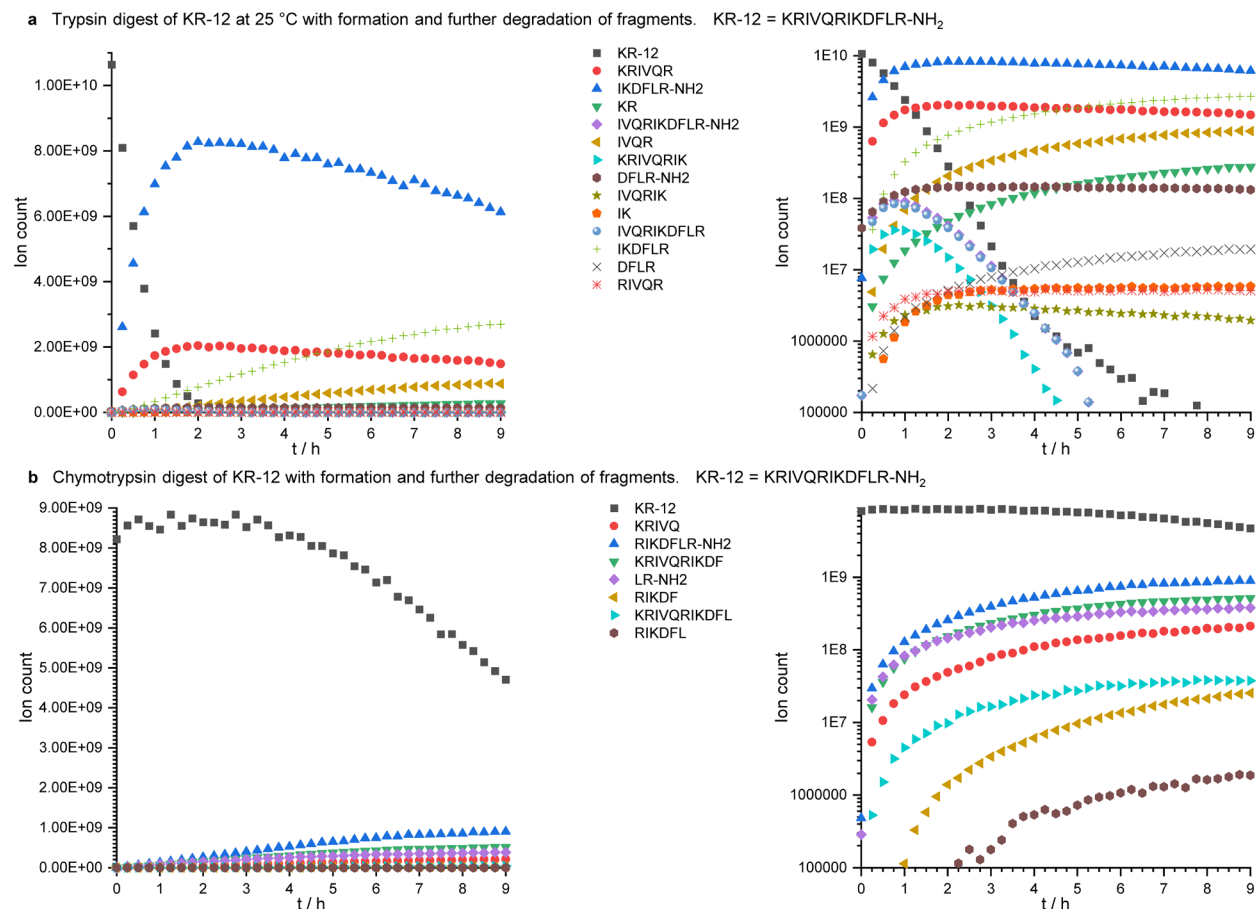


Figure S8. Fragment analysis of KR-12.

The average formation and further degradation of fragments of KR-12 resulting from the trypsin digest at 25 °C (a) and from the chymotrypsin digest (b) is plotted on a linear scale (left) and on a logarithmic scale (right). (a) The cleavage site R6-I7 is the most scissile cleavage site. The maximum ion count of the fragments resulting from that cleavage, i.e. KRIVQR (●) and IKDFLR-NH₂ (▲), is reached after approximately two hours, which is equal to the digest of Helix19-6 (Figure 5c). Subsequently, the KRIVQR (●) fragment is digested into KR (▼) and IVQR (◄), while the IKDFLR-NH₂ (▲) fragment is deamidated into IKDFLR (+). (b) The cleavage of KR-12 by chymotrypsin is very low, as indicated by the low increase of fragments. Nonetheless, the parent peptide ion count is dropping relatively fast in the second half of the digest. If this was due to a higher cleavage rate by chymotrypsin, the rate of fragment formation should increase at the same time. However, the rate of fragment formation seems to be slowed in the second half of the digest as well. This implies a methodical error probably resulting from an inhomogeneity, i.e. a concentration gradient of the peptide or enzyme in the sample. This methodical error has no impact on the evaluability of the digest, as all fragments are equally affected.

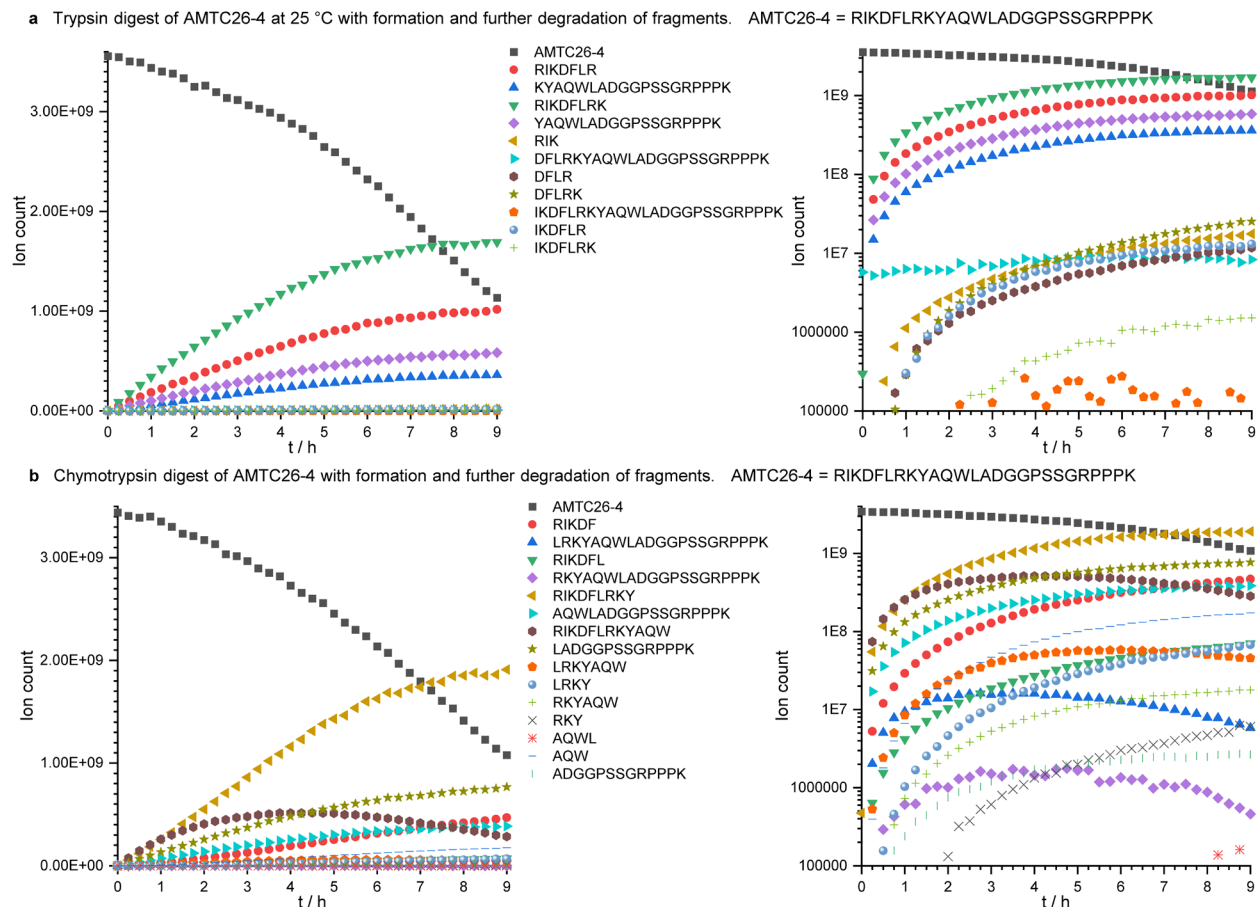


Figure S9. Fragment analysis of AMTC26-4.

The average formation and further degradation of fragments of AMTC26-4 resulting from the trypsin digest at 25 °C (a) and from the chymotrypsin digest (b) is plotted on a linear scale (left) and on a logarithmic scale (right). (a) Both fragments resulting from the K8-Y9 cleavage, i.e. RIKDFLRK (green triangles pointing down) and YAQLADGGPSSGRPPPK (purple diamonds), have higher ion counts than their counterparts resulting from the R7-K8 cleavage, i.e. RIKDFLR (red circles) and KYAQLADGGPSSGRPPPK (blue triangles). This indicates that the K8-Y9 cleavage is somewhat more favorable. The digest of the parent peptide is very slow because both cleavage sites are constrained in an α -helical conformation. (b) The cleavage of AMTC26-4 by chymotrypsin similarly slow due to its high fold stability. The Y9-A10 and W12-L13 peptide bonds seem most scissile. Compared to RIKDFLRKY (yellow triangles pointing up) the RIKDFLRKYAQLADGGPSSGRPPPK (brown diamonds) is rising first and then dropping after approximately 4 h because it is degraded primarily to RIKDFLRKY and AQLADGGPSSGRPPPK (blue triangles). In contrast, the constantly rising ion count of RIKDFLRKY (yellow triangles pointing up) shows that this fragment is degraded much slower than it is formed. This implies a lower cleavability of the F5-L6 peptide bond compared to Y9-A10 and W12-L13.

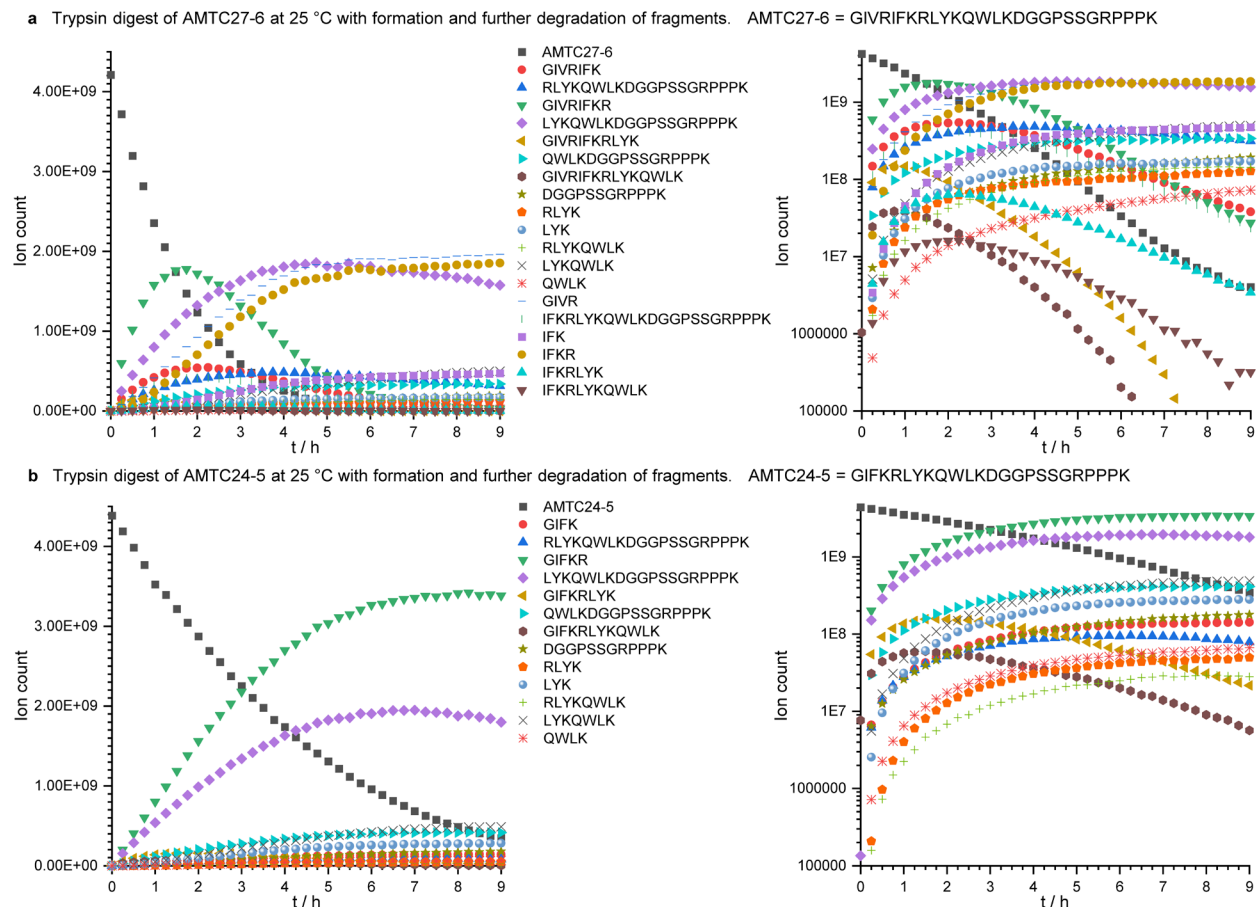


Figure S10. Fragment analysis of the trypsin digests of AMTC27-6 and AMTC24-5 at 25 °C.

The average formation and further degradation of fragments of AMTC27-6 (**a**) and AMTC24-5 (**b**) resulting from the trypsin digest at 25 °C is shown on a linear scale (left) and on a logarithmic scale (right). (**a**) AMTC27-6 presents four highly cleavable peptide bonds to trypsin, i.e. R8-L9, R4-I5, K7-R8, and K11-Q12, resulting in many different fragments compounding the identification of the most susceptible cleavage site. The small fragments GIVR (—) and IFKR (●) are end products of the digest and reach their maximum after approximately 5 h. The fact that fragments of the K7-R8 cleavage sites GIVRIFK (●), RLYKQWLKDGGPSSGRPPPK (▲), RLYK (●) and IFK (■) have all lower ion counts than their analogs of the cleavage site R8-L9 GIVRIFKR (▼), LYKQWLKDGGPSSGRPPPK (◆), LYK (●) and IFKR (●) is a strong indicator, that the R8-L9 cleavage site is more scissile. The fact that GIVRIFKR (▼) and GIVRIFK (●) are both reaching their maximum very early suggest that they are directly formed from the parent peptide. Subsequently, they are both cleaved at the R4-I5 bond. The fact that GIVRIFKR (▼) decreases faster than GIVRIFK (●) might indicate that some of the GIVRIFKR (▼) is cleaved at the K7-R8 bond instead. Since all fragments derived from the K11-Q12 cleavage have low ion counts, this cleavage seems to be of lower cleavability. (**b**) The degradation of the parent peptide AMTC24-5 (■, panel **b**) is much slower than that of AMTC27-6 (■, panel **a**). Similar to the digestion of AMTC27-6, AMTC24-5 is most frequently cleaved at the R5-L6 peptide bond (corresponding to R8-L9 in AMTC27-6). However, the ion counts of the fragment RLYKQWLKDGGPSSGRPPPK (▲) are much lower in panel **b** indicating a reduced cleavability of the K4-R5 cleavage site compared to its equivalent K7-R8 in AMTC27-6.

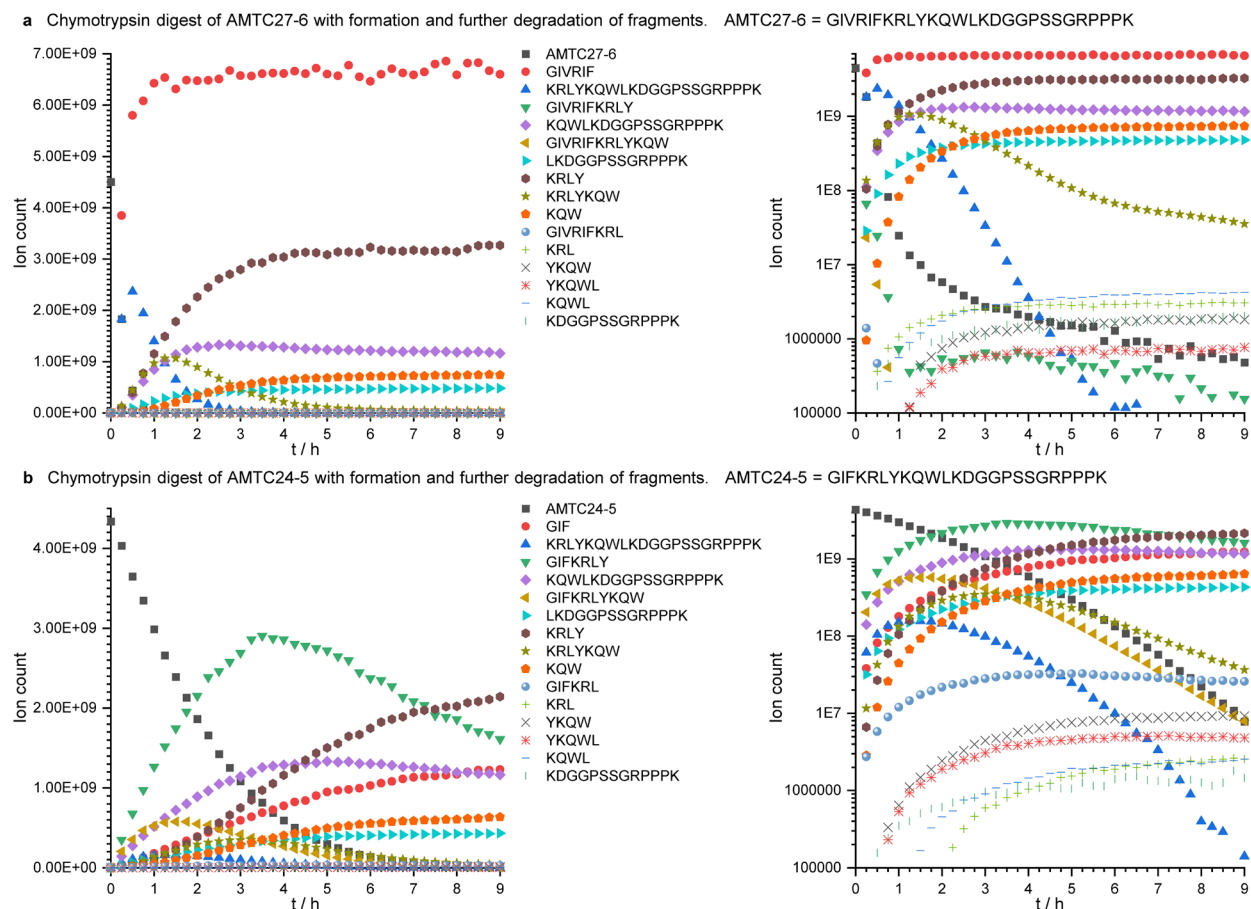


Figure S11. Fragment analysis of the chymotrypsin digests of AMTC27-6 and AMTC24-5.

The average formation and further degradation of fragments of AMTC27-6 (**a**) and AMTC24-5 (**b**) resulting from the chymotrypsin digest at 25 °C is shown on a linear scale (left) and on a logarithmic scale (right). (**a**) Since the fragment GIVRIF (●) reaches its maximum just as fast as the parent peptide AMTC27-6 (■, panel **a**) is degraded, this cleavage is mainly responsible for the immediate degradation of AMTC27-6. The resulting fragment KRLYKQWLKDGGPSSGRPPPK (▲) is subsequently cleaved into KRLY (●) and KQWLKDGGPSSGRPPPK (◆) and to a lower extent into KRLYKQW (★) and LKDGGPSSGRPPPK (▶). (**b**) The F3-K4 cleavage site in AMTC24-5 is characterized by drastically lower cleavability compared to its counterpart in AMTC27-6 (F6-K7) leading to a higher proteolytic resilience of AMTC24-5 (■, panel **b**). Moreover, also the Y7-K8 (corresponding to Y10-K11 in AMTC27-6) seems to have a somewhat reduced cleavability since the fragment KQWLKDGGPSSGRPPPK (◆) reaches its maximum later in panel **b** compared to panel **a**.

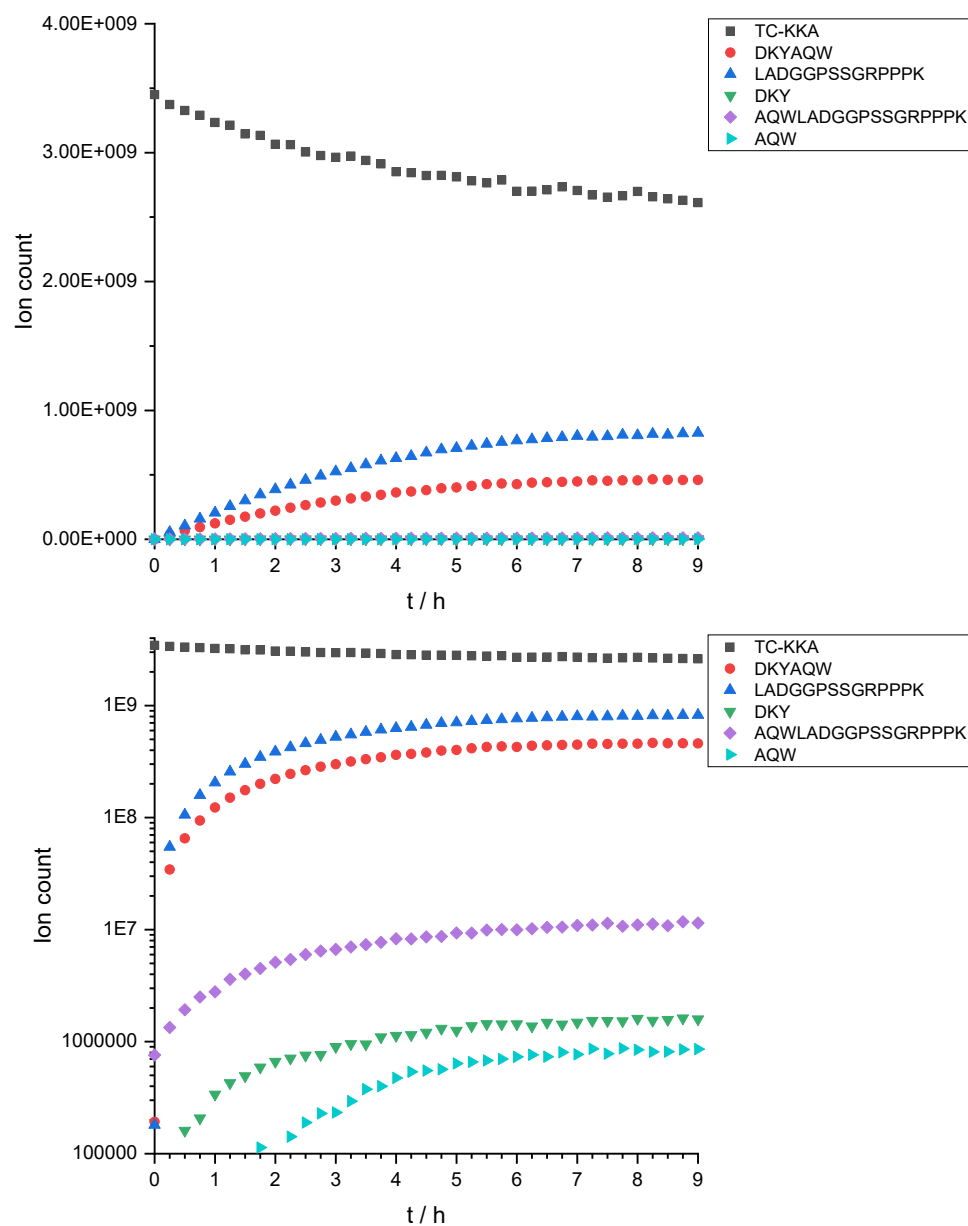


Figure S12. Fragment analysis of the chymotrypsin digest of TC-KKA.

The average formation and further degradation of fragments of TC-KKA resulting from the chymotrypsin digest at 25 °C is shown on a linear scale (top) and on a logarithmic scale (bottom). The sequence of the parent peptide TC-KKA is DKYAQLADGGPSSGRPPPK.

Table S34. Linear region and resulting k obtained from the trypsin digest at 25 °C.

Peptide	linear region	slope / $\mu\text{M}/\text{h}$	StdErr slope / $\mu\text{M}/\text{h}$	k / s^{-1}	StdErr k / s^{-1}		
TC-KKA ^a		n.d.					
KR-12 ^b	exp	-10.32	±	1.34	5.73	±	0.74
AMTC31-6	1.5 h	-2.65	±	0.21	1.47	±	0.12
Helix19-6 ^b	exp	-10.10	±	1.02	5.61	±	0.57
AMTC26-4	9 h	-0.74	±	0.02	0.41	±	0.01
AMTC27-6	1 h	-4.08	±	0.30	2.27	±	0.17
AMTC24-5	1 h	-2.14	±	0.48	1.19	±	0.27

The **linear region** is the time when the decrease of the parent peptide concentration is linear. “exp” marks an exponential decay with no apparent linear region. In this case the linear region was approximated by using the data points at t_0 and $t = 0.25$. The initial turnover frequency k was calculated from the **slope** of the function that was fitted to all data points in the linear region. k (\pm the standard deviation resulting from the fit) is the number of parent peptides that are cleaved by one enzyme molecule per second at the beginning of the assay.

a) TC-KKA was not digested by trypsin at 37 °C, therefore it was not included in trypsin digests at 25 °C.

b) KR-12 and Helix19-6 show only exponential degradation. The linear region can only be approximated by using the data points of $t = 0$ and $t = 0.25$ h.

Table S35. Linear region and resulting k obtained from the chymotrypsin digest.

Peptide	linear region	slope / $\mu\text{M}/\text{h}$	StdErr slope / $\mu\text{M}/\text{h}$	k / s^{-1}	StdErr k / s^{-1}
TC-KKA	9 h	-0.24	± 0.03	0.026	± 0.003
KR-12 ^a	9 h	-0.41	± 0.04	0.045	± 0.005
AMTC31-6	9 h	-0.87	± 0.01	0.097	± 0.001
Helix19-6 ^b	exp	-7.59	± 3.04	0.843	± 0.338
AMTC26-4 ^a	9 h	-0.76	± 0.02	0.085	± 0.002
AMTC27-6 ^b	exp	-20.05	± 2.02	2.228	± 0.225
AMTC24-5	2 h	-2.88	± 0.10	0.320	± 0.011

The **linear region** is the time when the decrease of the parent peptide concentration is linear. “exp” marks an exponential decay with no apparent linear region. In this case the linear region was approximated by using the data points at t_0 and $t = 0.25$. The initial turnover frequency k was calculated from the **slope** of the function that was fitted to all data points in the linear region. k (\pm the standard deviation resulting from the fit) is the number of parent peptides that are cleaved by one enzyme molecule per second at the beginning of the assay.

a) KR-12 and AMTC26-4 show peculiar digest curves with increasing digest rates over time. The linear function was therefore fitted to all data points to get an average degradation rate.

b) Helix19-6 and AMTC27-6 show only exponential degradation. The linear region can only be approximated by using the data points of $t = 0$ and $t = 0.25$ h.

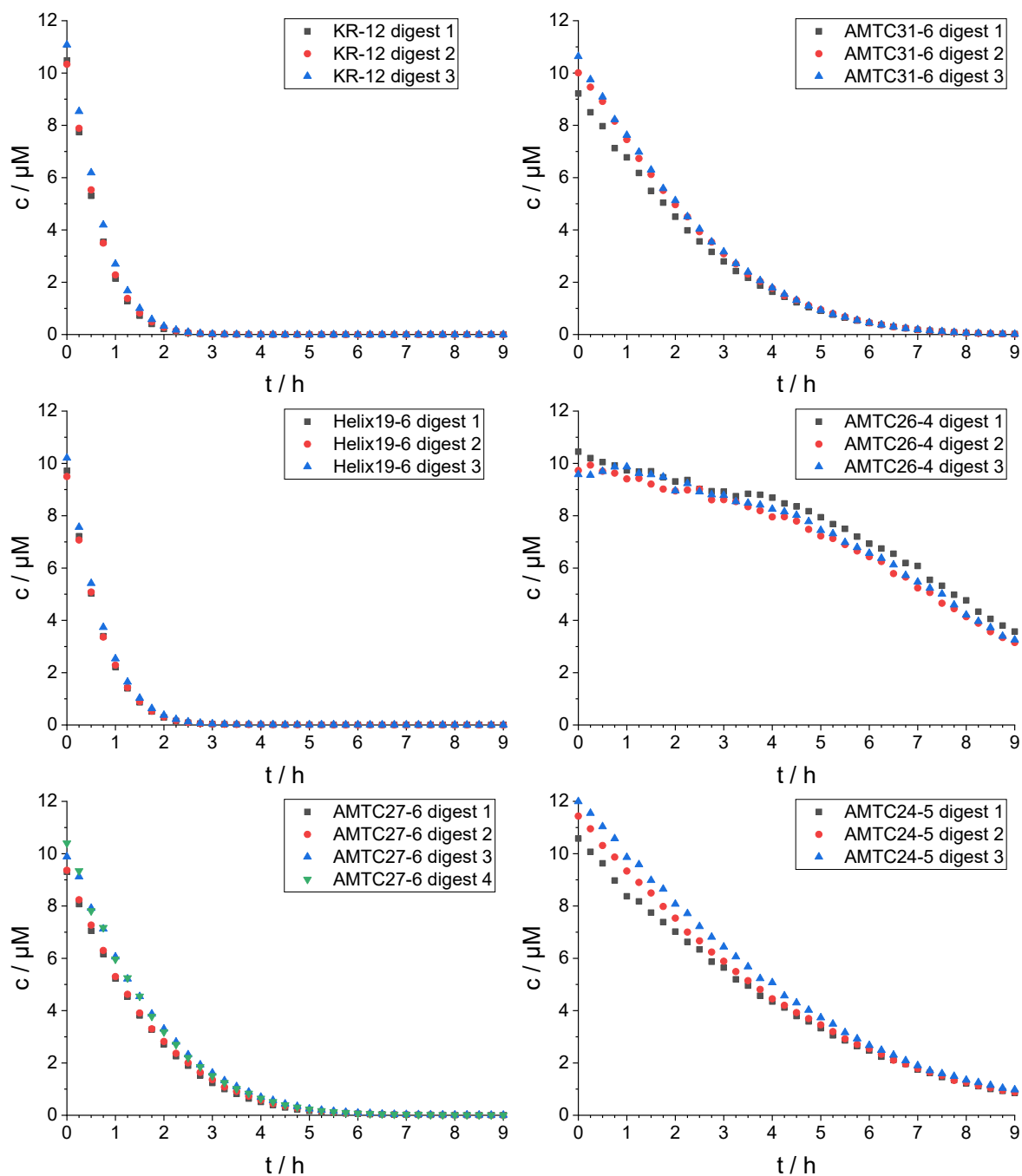


Figure S13. Quantitative trypsin digests of the parent peptides at 25 °C.

Each digest was performed in triplicate except the digest of AMTC27-6 which was performed four times. The concentrations of the parent peptide are plotted over the time.

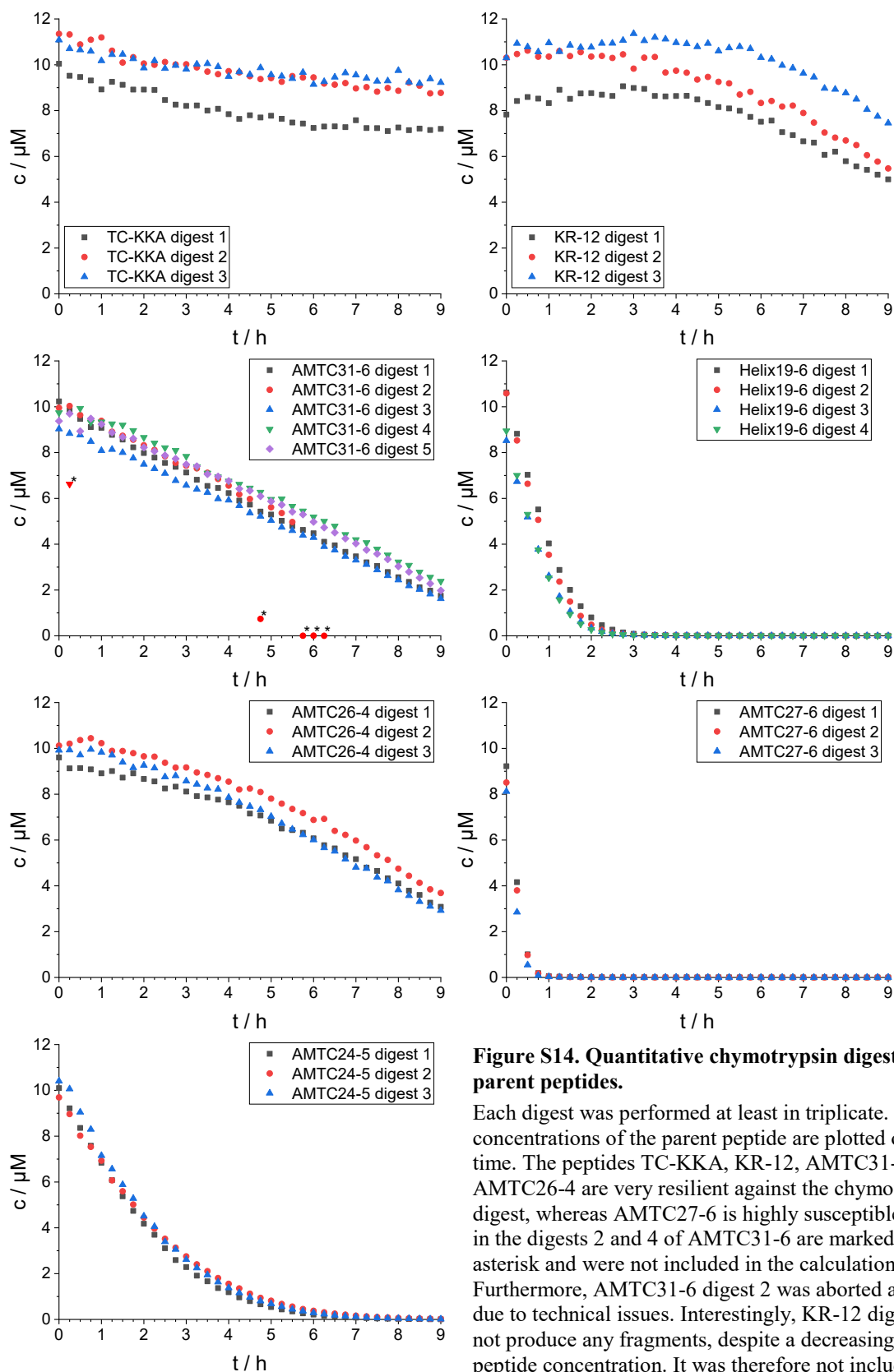


Figure S14. Quantitative chymotrypsin digests of the parent peptides.

Each digest was performed at least in triplicate. The concentrations of the parent peptide are plotted over the time. The peptides TC-KKA, KR-12, AMTC31-6 and AMTC26-4 are very resilient against the chymotrypsin digest, whereas AMTC27-6 is highly susceptible. Outliers in the digests 2 and 4 of AMTC31-6 are marked by an asterisk and were not included in the calculations of k . Furthermore, AMTC31-6 digest 2 was aborted after 6.25 h due to technical issues. Interestingly, KR-12 digest 3 did not produce any fragments, despite a decreasing parent peptide concentration. It was therefore not included in the calculation of k .

Trypsin digest at 37 °C

Table S36: Linear region and resulting k obtained from the trypsin digest at 37 °C.

Peptide	linear region	slope / $\mu\text{M}/\text{h}$		StdErr slope / $\mu\text{M}/\text{h}$	k / s^{-1}		StdErr k / s^{-1}
TC-KKA ^a	9 h	0.13	\pm	0.03	0 (-0.07)	\pm	0 (0.02)
KR-12 ^b	exp	-16.20	\pm	4.56	9.00	\pm	2.53
AMTC31-6	0.5 h	-6.27	\pm	0.29	3.48	\pm	0.16
Helix19-6 ^b	exp	-15.56	\pm	1.20	8.64	\pm	0.66
AMTC26-4	3.75 h	-1.60	\pm	0.02	0.89	\pm	0.01
AMTC27-6 ^b	exp	-10.78	\pm	1.79	5.99	\pm	1.00
AMTC24-5	1 h	-4.45	\pm	0.31	2.47	\pm	0.17

The **linear region** is the time when the decrease of the parent peptide concentration is linear. “exp” marks an exponential decay with no apparent linear region. In this case the linear region was approximated by using the data points at t_0 and $t = 0.25$. The initial turnover frequency k was calculated from the **slope** of the function that was fitted to all data points in the linear region. k (\pm the standard deviation resulting from the fit) is the number of parent peptides that are cleaved by one enzyme molecule per second at the beginning of the assay.

a) TC-KKA was not digested by trypsin, but the concentration was slightly increasing over time (probably due to evaporation, cf. **Figure S15**). Therefore, the slope is positive, but k is given as 0. The apparent k one would get from the slope of the fitted function is given in parentheses.

b) KR-12, Helix19-6 and AMTC27-6 show only exponential degradation. The linear region can only be approximated by using the data points of $t = 0$ and $t = 0.25$ h.

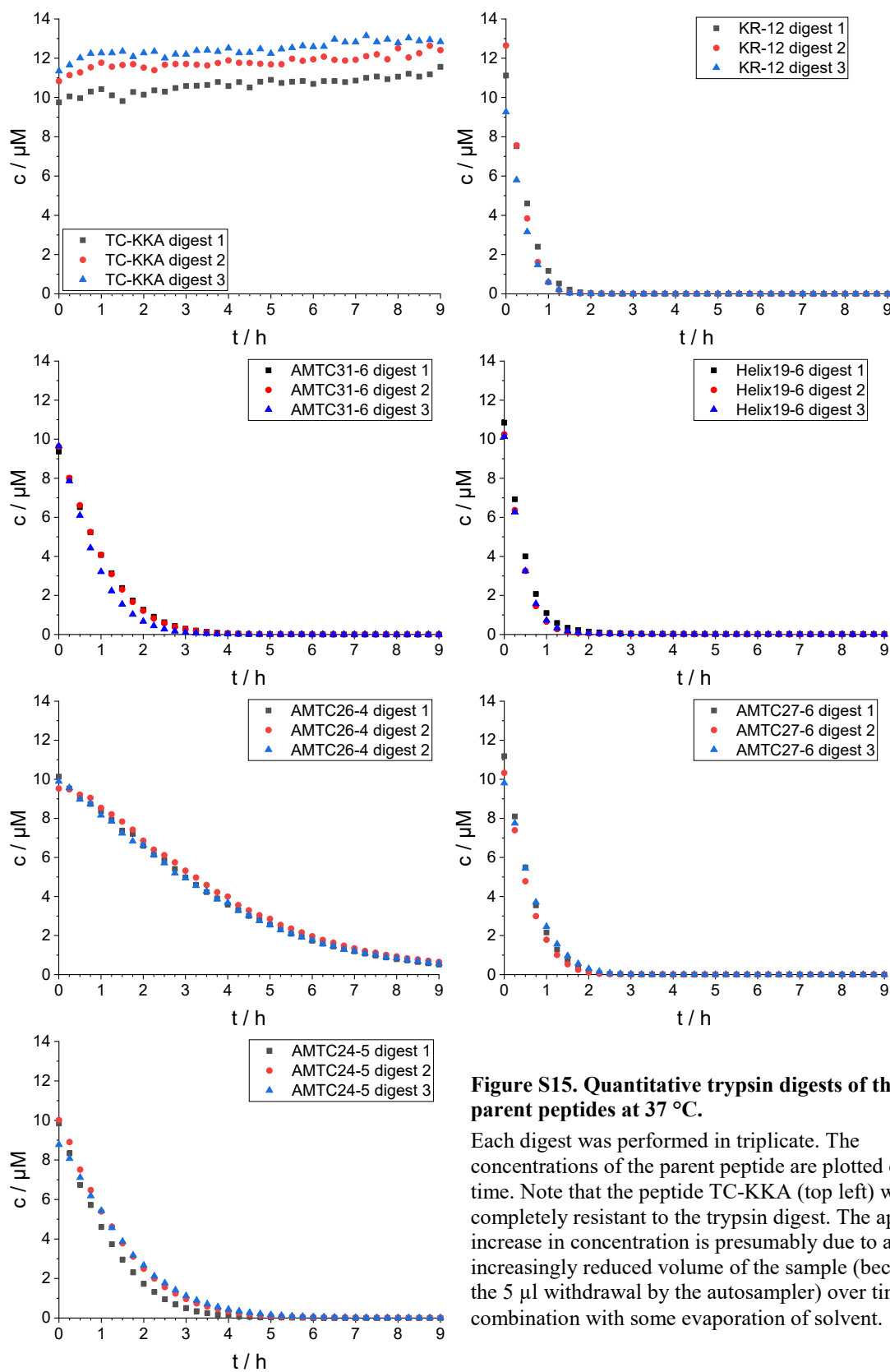


Figure S15. Quantitative trypsin digests of the parent peptides at 37°C .

Each digest was performed in triplicate. The concentrations of the parent peptide are plotted over the time. Note that the peptide TC-KKA (top left) was completely resistant to the trypsin digest. The apparent increase in concentration is presumably due to an increasingly reduced volume of the sample (because of the $5 \mu\text{l}$ withdrawal by the autosampler) over time in combination with some evaporation of solvent.

Analysis of trypsin cleavage sites at 37 °C

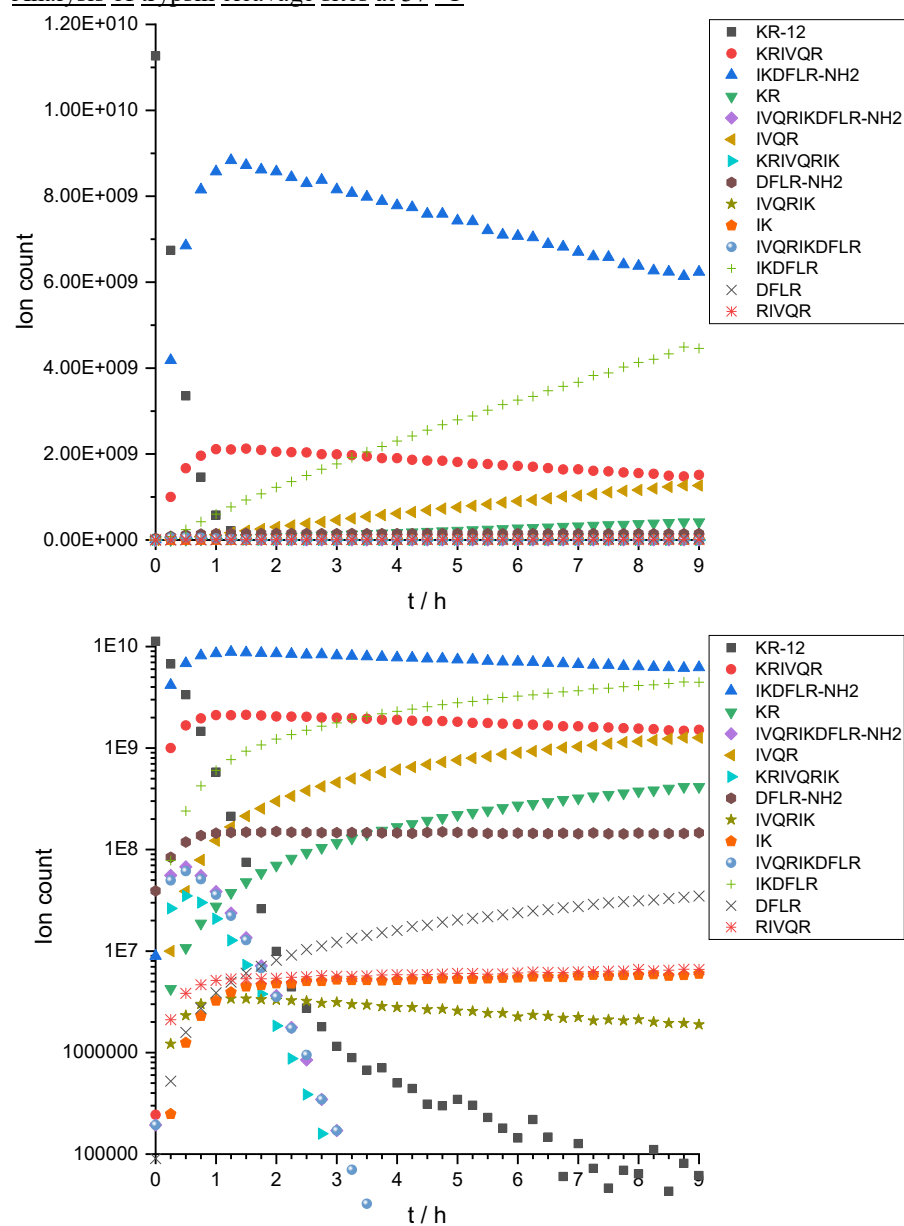


Figure S16. Fragment analysis of the trypsin digest of KR-12 at 37 °C.

The average formation and further degradation of fragments of KR-12 resulting from the trypsin digest at 37 °C is shown on a linear scale (top) and on a logarithmic scale (bottom). The sequence of the parent peptide KR-12 is KRIVQRIKDFLR-NH₂.

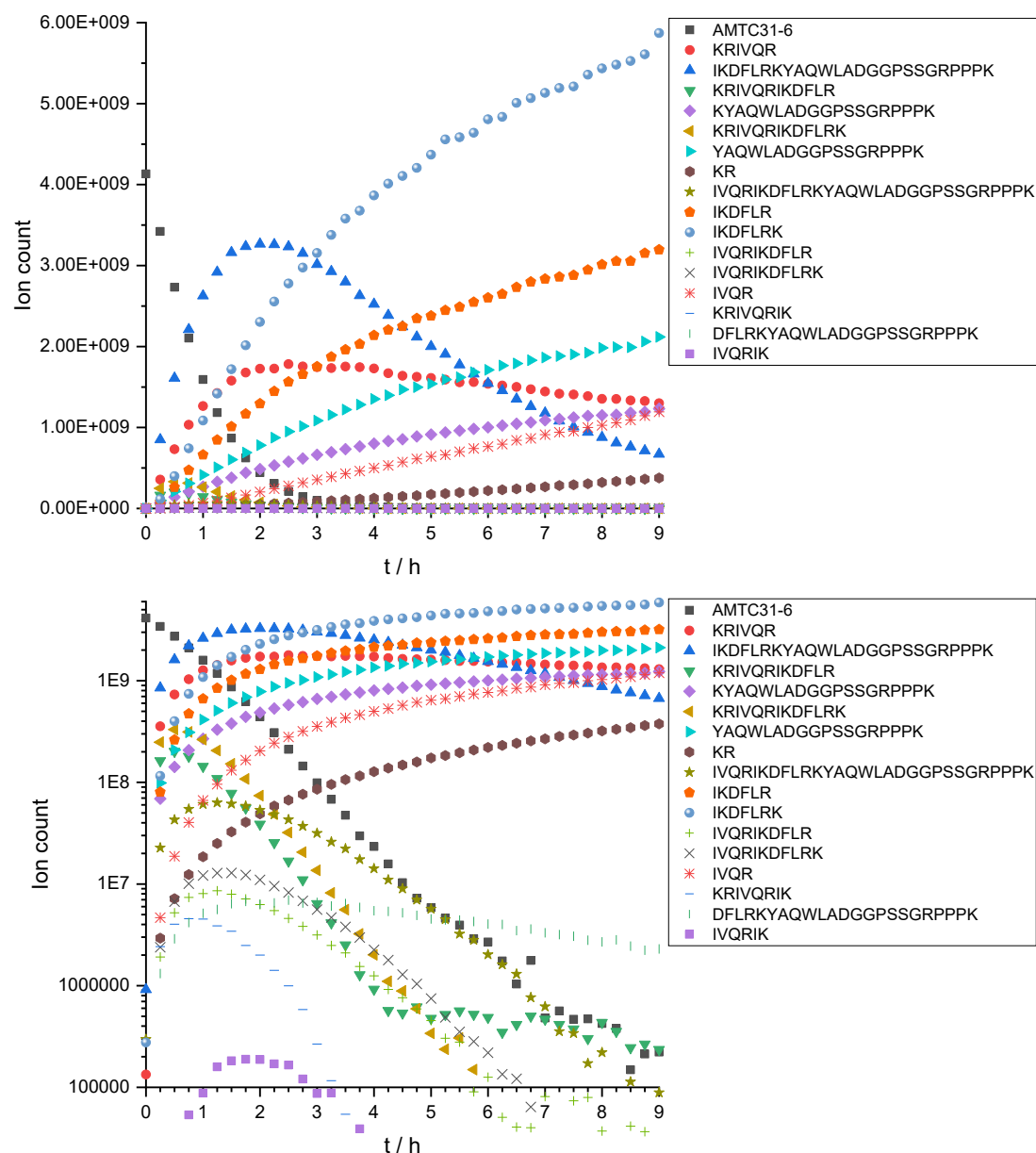


Figure S17. Fragment analysis of the trypsin digest of AMTC31-6 at 37 °C.

The average formation and further degradation of fragments of AMTC31-6 resulting from the trypsin digest at 37 °C is shown on a linear scale (top) and on a logarithmic scale (bottom). The sequence of the parent peptide AMTC31-6 is KRIVQRIKDFLRKYAQLADGGPSSGRPPPK.

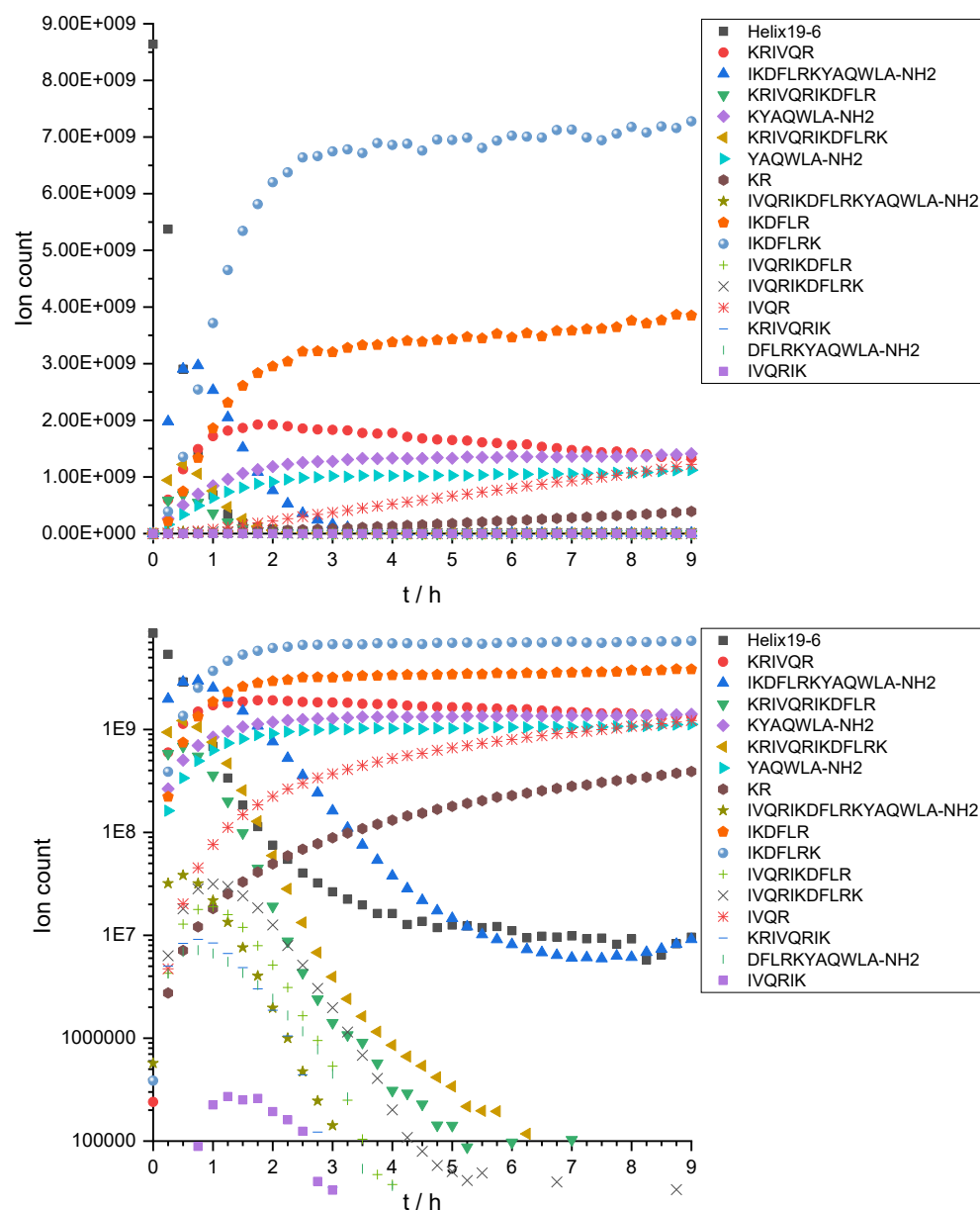


Figure S18. Fragment analysis of the trypsin digest of Helix19-6 at 37 °C.

The average formation and further degradation of fragments of Helix19-6 resulting from the trypsin digest at 37 °C is shown on a linear scale (top) and on a logarithmic scale (bottom). The sequence of the parent peptide Helix19-6 is KRIVQRIKDFLRKYAQLA-NH₂.

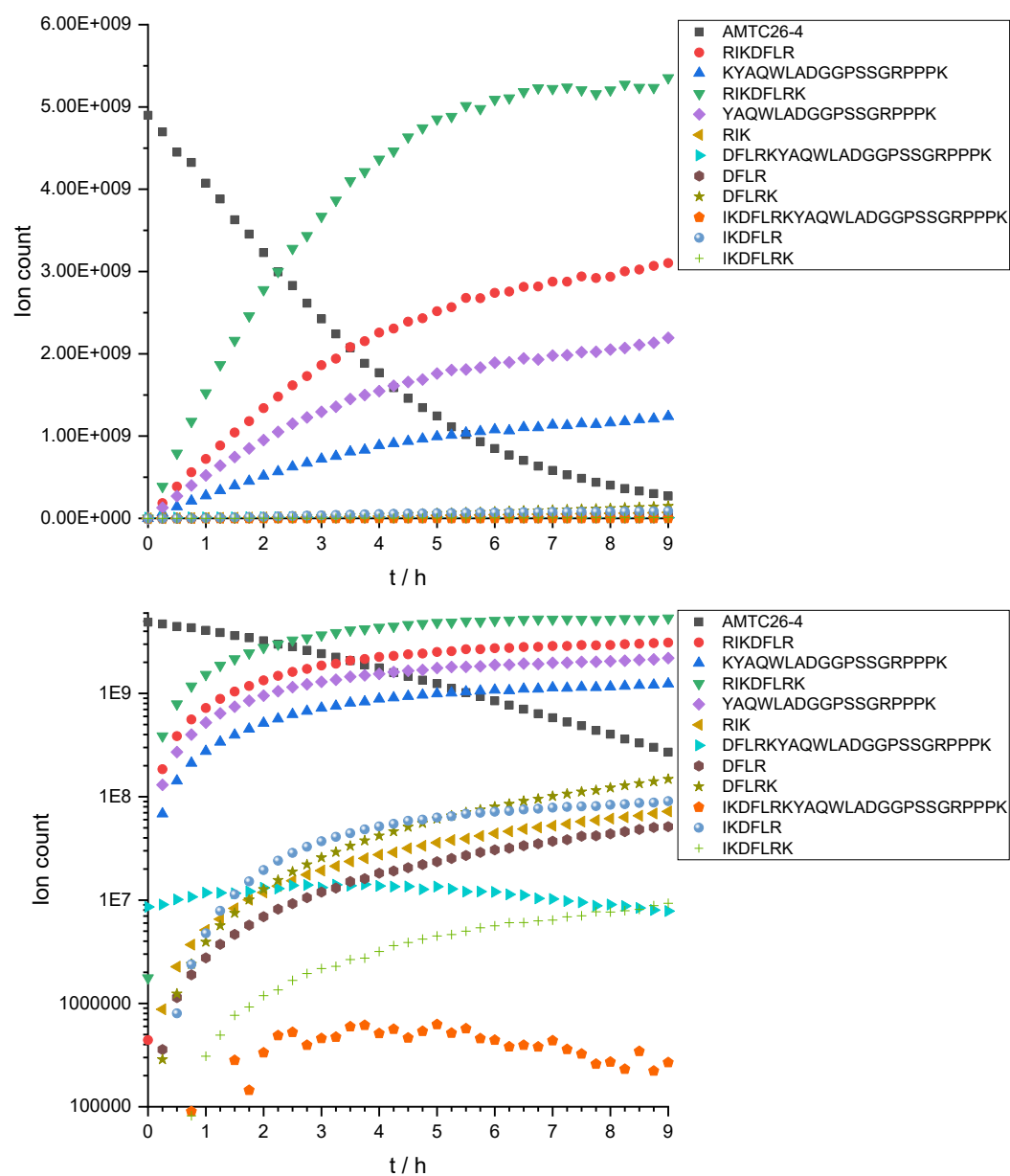


Figure S19. Fragment analysis of the trypsin digest of AMTC26-4 at 37 °C.

The average formation and further degradation of fragments of AMTC26-4 resulting from the trypsin digest at 37 °C is shown on a linear scale (top) and on a logarithmic scale (bottom). The sequence of the parent peptide AMTC26-4 is RIKDFLRKYAQLADGGPSSGRPPPK.

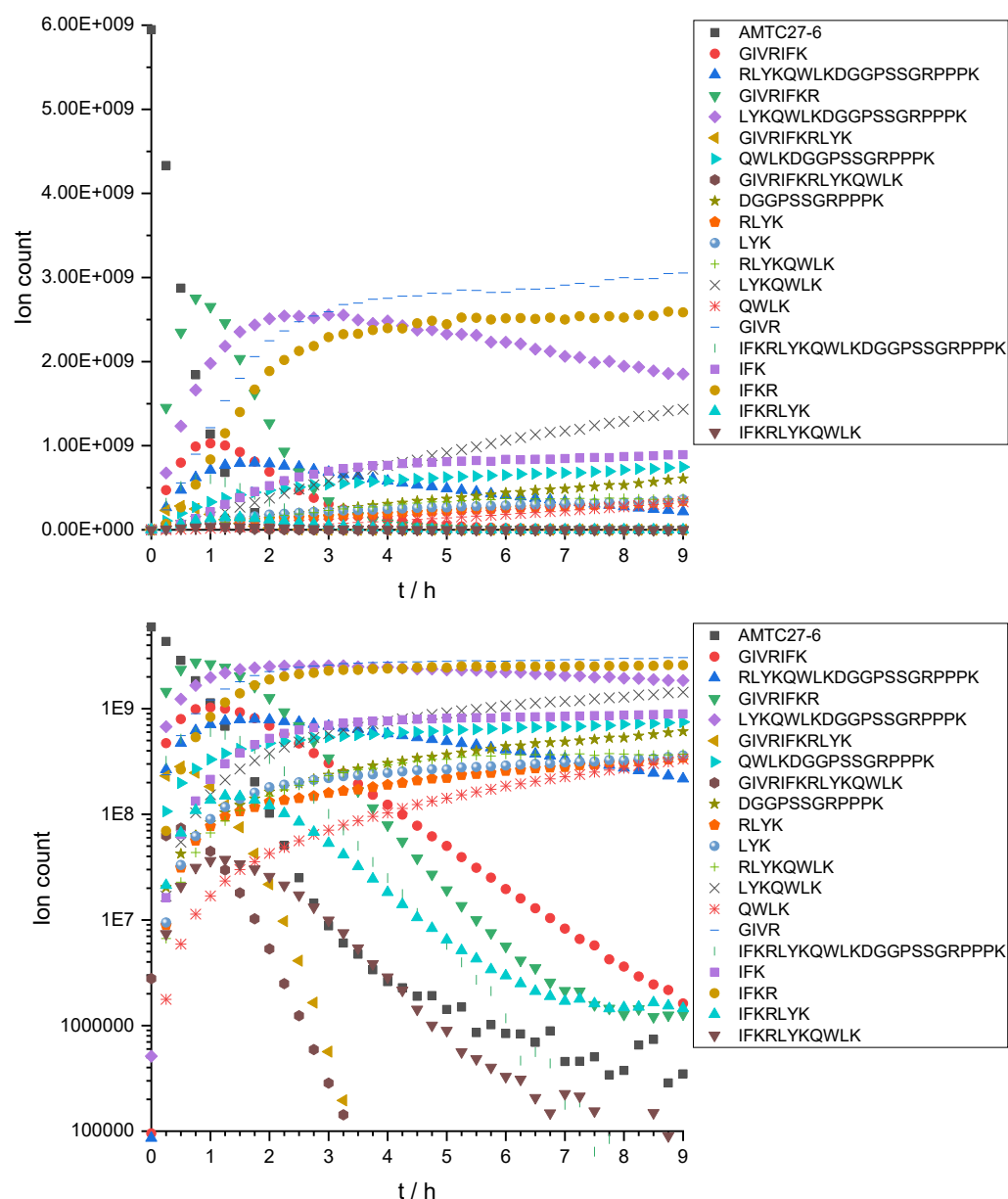


Figure S20. Fragment analysis of the trypsin digest of AMTC27-6 at 37 °C.

The average formation and further degradation of fragments of AMTC27-6 resulting from the trypsin digest at 37 °C is shown on a linear scale (top) and on a logarithmic scale (bottom). The sequence of the parent peptide AMTC27-6 is GIVRIFKRLYKQWLKDGGPSSGRPPPK.

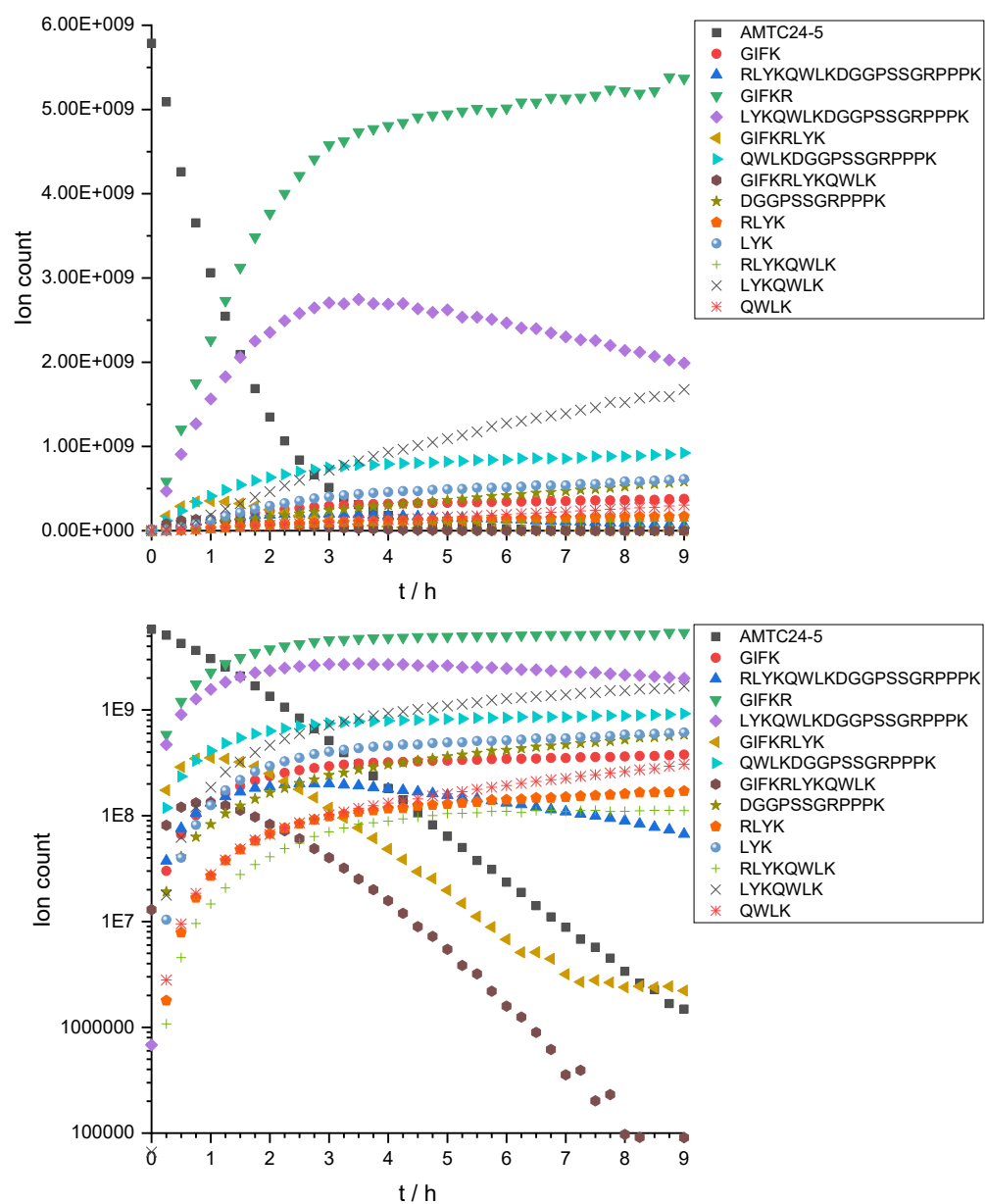


Figure S21. Fragment analysis of the trypsin digest of AMTC24-5 at 37 °C.

The average formation and further degradation of fragments of AMTC24-5 resulting from the trypsin digest at 37 °C is shown on a linear scale (top) and on a logarithmic scale (bottom). The sequence of the parent peptide AMTC24-5 is GIFKRLYKQWLKDGGPSSGRPPPK.

Detailed Procedure: Enzymatic degradation monitoring and analysis

The enzymatic degradation monitoring assay was performed in a Protein LoBind 0.5 ml tube placed in the autosampler of a UHPLC for the entire duration of the reaction to provide a temperature-controlled environment, occasional shaking of the vial and the possibility to withdraw a sample from the vial and directly analyze it by UHPLC-MS to monitor the progress of the reaction.

The UHPLC-MS was configured as described in the experimental procedures. The autosampler was adjusted to the temperature required for the digest. Chymotrypsin digests were performed only at 25 °C as higher temperatures would increase the risk of autoproteolysis according to the manufacturer. Trypsin digests were performed at 37 °C and at 25 °C. The tray shake function was set to shake the tray three times prior to sample withdrawal. Each individual run takes 15 min including tray shake, needle wash, sample withdrawal, sample injection and chromatogram recording. 5 µl of sample were injected for every measurement.

To reduce the adsorption of peptides to the surface of standard HPLC vials (64), Protein LoBind tubes with a volume of 0.5 ml (Eppendorf, Hamburg, Germany) served as reaction vessels. To protect the digest from contamination and to prevent excessive evaporation of buffer, the tubes needed to be sealed with a lid that could be pierced by the autosampler needle. Incidentally, each well of a sealing mat for 500 µl-deep well plates (Eppendorf, Hamburg, Germany) fits perfectly onto one 0.5 ml Eppendorf tube. The sealing mat is easily pierced with a needle and due to its elasticity the puncture site is readily resealed. To produce pierceable lids for the Eppendorf tubes, sealing mats were cut into 96 equal pieces in a sterile environment. The original lids of the tubes were removed. A droplet of water was found under the vial lid after each digest indicative of solvent evaporation during the assay, emphasizing the need of a pierceable lid for this assay. A vortexer (Select BioProducts) and a Sprout mini centrifuge (2000 g; HeathrowScientific, Vernon Hills, IL, USA) for six 0.5 ml Eppendorf tubes were placed directly next to the UHPLC-MS. Preparation of buffers, stock solutions, controls and samples was performed with gloves in a sterile environment to avoid contamination with microorganisms or proteases from other sources (e.g. from the skin). Buffers and solutions written in *italic* differ between trypsin and chymotrypsin digests; recipes for buffers and solvents are given below. All buffers and solvents were sterilized by 0.2 µm microfiltration.

Trypsin digest – buffers and solutions.

Reconstitution solution: 50 mM AcOH in water

Reaction buffer: 10 mM NH₄HCO₃ in water (pH = 7.8)

Trypsin stock solutions: 840 µL of reconstitution solution were added to one glass vial of sequencing grade modified trypsin (20 µg, 840 pmol; Promega, Madison, WI, USA) to yield a trypsin stock solution of 1 pmol µl⁻¹. 10 µl single-use aliquots of this trypsin stock solution were filled into 0.5 ml Eppendorf Protein LoBind tubes and stored at -20 °C until use.

Diluted trypsin solution: Immediately prior to use, a frozen aliquot (10 µl) of trypsin stock solution was thawed and diluted with 90 µl of trypsin reconstitution solution to a concentration of 0.1 pmol µl⁻¹.

Chymotrypsin digest – buffers and solutions.

Reconstitution solution: 1 mM HCl in water

Reaction buffer: 10 mM NH₄HCO₃ and 1 mM CaCl₂ in water (pH = 7.8)

Chymotrypsin stock solutions: 500 µL of reconstitution solution were added to one glass vial of sequencing grade chymotrypsin (25 µg, 1 nmol; Promega, Madison, WI, USA) to yield a chymotrypsin stock solution of 2 pmol µl⁻¹. 10 µl single-use aliquots of this trypsin stock solution were filled into 0.5 ml Eppendorf Protein LoBind tubes and stored at -20 °C until use.

Diluted chymotrypsin solution: Immediately prior to use, a frozen aliquot (10 µl) of chymotrypsin stock solution was thawed and diluted with 30 µl of chymotrypsin reconstitution solution to a concentration of 0.5 pmol µl⁻¹.

Calibration curves of the parent peptides. Prior to sample preparation, the UHPLC-MS was prepared to be started immediately. Calibration samples were prepared at the following concentrations of the parent peptide: 10 µM, 8 µM, 6 µM, 4 µM, 2 µM and a blank sample containing no peptide. Initially, three calibration samples at 10 mM peptide concentration were prepared by adding 1 µl of *reconstitution solution* and 2 µl of (1 ± 0.1) mM peptide stock solution to 197 µl of *reaction buffer*. Moreover, a blank sample was created by adding 3 µl of *reconstitution solution* to 597 µl of *reaction buffer*. Calibration samples 8 µM and 2 µM were produced by splitting one of the 10 µM calibration samples into two fractions of 160 µl and 40 µl and diluting them to 200 µl with 40 µl and 160 µl, respectively, from the blank sample. Likewise, calibration samples 6 µM and 4 µM were created. The calibration samples were vortexed twice for 10 s each, centrifuged for 10 s and placed into the autosampler. The sequence was started and the first sample to be measured was the blank sample. Two minutes before the end of the first

measurement, all the samples were taken out of the autosampler, vortexed for 10 s, centrifuged for 10 s and immediately reinserted into the autosampler before the end of the blank run. Afterwards each sample was measured in the following order: 10 μ M, 8 μ M, 6 μ M, 4 μ M, 2 μ M, blank. This sequence of measurements was performed a total of six times in a row.

Digest sample preparation and measurement. Prior to sample preparation, the UHPLC-MS was prepared to be started immediately. A blank sample was created by adding 1 μ l of *reconstitution solution* to 199 μ l of *reaction buffer*. Preparation of the control sample was achieved by adding 2 μ l of the peptide stock solution and 1 μ l of *reconstitution solution* to 197 μ l of *reaction buffer*. The digest sample was prepared by adding 2.05 μ l of the (1 ± 0.1) mM peptide stock solution to 201.95 μ l of *reaction buffer*.

The blank sample and the control sample were vortexed for 10 s twice, centrifuged for 10 s, placed in the autosampler and the sequence was started.

While the first measurement (blank sample) was running, a single-use aliquot of *enzyme stock solution* (10 μ l) was diluted with *reconstitution solution* to gain a *diluted enzyme solution*, vortexed for 10 s twice and centrifuged for 10 s. Two minutes before the end of the first measurement, the control sample was taken out of the autosampler, vortexed for 10 s, centrifuged for 10 s and immediately reinserted into the autosampler before the end of the blank run. One minute before the end of the first measurement, the digest sample was vortexed for 10 s, centrifuged for 10 s and placed into the autosampler before the end of the blank run.

Two minutes before the end of the second measurement (control sample), the digest sample was taken out of the autosampler, vortexed for 10 s, centrifuged for 10 s and immediately reinserted into the autosampler before the end of the control sample run. One minute before the end of the control sample run, the *diluted enzyme solution* was vortexed for 10 s and centrifuged for 10 s.

The first measurement of the digest sample was performed before any enzyme was added to it ($t = 0$). Immediately after the first injection of the digest sample it was taken out of the autosampler and 1 μ l of the *diluted enzyme solution* is added to it. It was vortexed for 10 s, centrifuged for 10 s and placed back into the autosampler. The final concentration of trypsin and chymotrypsin in the digest sample was 0.5 nM and 2.5 nM, respectively. Another 36 measurements of the same digest sample were performed in a row (without any further interference). After the 37 injections of the digest sample, the control sample was measured a second time. The digest was only considered valid and successful, when the control sample showed no traces of digestion, i.e. it was not contaminated with proteases. The last sample of the sequence was again a blank measurement. Each digest was performed in three independent measurements. However, the second and the third time, no control sample was used.

Quantitative parent peptide degradation analysis. All chromatograms of the calibration samples as well as those of the blank, control and digest samples of one parent peptide at the same temperature and with the same enzyme were processed in the same batch using TraceFinder 4.1 (Thermo Fisher Scientific, Waltham, MA, USA). The compound library included only the parent peptide, but in multiple adducts (including H^+ , Na^+ , K^+ , Ca^{2+}) and charge states (between M^{2+} and M^{8+} , depending on the parent peptide). The following adducts with up to three alkali metals (sodium and/or potassium) were included for all peptides except KR-12: $[M + a \cdot H + b \cdot Na + c \cdot K]^{n+}$ where $a, b, c \in \mathbb{N}_0$ and $a + b + c = n$ with $b + c \leq 3$. However, the possible charge states n vary with each parent peptide (see list below).

Peptide	$n \in$
TC-KKA	{2, 3, 4, 5}
AMTC31-6	{3, 4 ... 8}
Helix19-6	{2, 3 ... 6}
AMTC26-4	{2, 3 ... 7}
AMTC27-6	{3, 4 ... 8}
AMTC24-5	{2, 3, ... 7}

For large analytes (i.e. all parent peptides except KR-12), the difference between $[M + H + K]^{2+}$ and $[M + Ca]^{2+}$ is below 5 ppm and therefore in the range of the precision of mass detection (≤ 5 ppm). Therefore, adducts including $H^+ + K^+$ or Ca^{2+} are not discernable. To prevent TraceFinder from counting the same peak twice (i.e. as an adduct with $H^+ + K^+$ and as an adduct with Ca^{2+}), only the $H^+ + K^+$ adducts were included in the compound database, but the tolerance was adjusted high enough to include Ca^{2+} adducts as well, resulting in the following mass tolerances: TC-KKA: 9.13 ppm, AMTC31-6: 7.49 ppm, Helix19-6: 8.61 ppm, AMTC26-4: 8.00 ppm, AMTC27-6: 7.87 ppm, AMTC24-5: 8.25 ppm.

In the case of KR-12, the difference between adducts of $H^+ + K^+$ and of Ca^{2+} is larger than 5 ppm, so those adducts are discernable. In consequence, Ca^{2+} adducts were also included in the compound database of KR-12, which

comprised the following adducts: $[KR-12 + a \cdot H + b \cdot Na + c \cdot K + d \cdot Ca]^{n+}$ where $a, b, c, d \in \mathbb{N}_0$ and $a + b + c + 2d = n$ with $n \in \{2, 3, 4, 5\}$ and $b + c + 2d \leq 3$.

The retention time of the parent peptide was determined prior to TraceFinder analysis. A deviation of the retention time of ± 15 s (i.e. retention time window = 30 s) was allowed for the analysis. The peak area threshold was set to 100,000. The genesis algorithm was applied using the “highest peak” strategy to identify peaks within an extraction window of 3 min around the retention time. The minimum peak height (S/N) was 3 and the peak S/N cutoff was set to 10,000. Ratios, Isotopes and Suitability analysis was not enabled. Calibration levels were 10 μM , 8 μM , 6 μM , 4 μM and 2 μM . Blank samples were not used to represent 0 μM , instead the linear calibration curve was forced to go through the origin (0 | 0). All calibration levels and measurements were weighted equally. The analysis results were exported as MS Excel sheets. The data of each replicate was plotted and analyzed with Origin 2021 (Additive, Friedrichsdorf, Germany). The plots are depicted in Figure 4 (averaged) and in Figures S11-S13 (individual digests). To compare the resistance against enzymatic degradation of each parent peptide, the initial turnover frequency k was determined for each assay. k was calculated from the initial slope of the digest when the influence of the fragments on the digest is low. When the plot displays a linear region, the slope of the parent peptide concentration was determined by fitting a linear function to linear region of the digest plot. When the digest plots had no linear region, but an exponential appearance, the linear function was fitted only to the data points at $t_0 = t = 0$ h and $t = 0.25$ h to determine the initial rate and to approximate k . k in $[\text{s}^{-1}]$ was calculated from the slope in $[\mu\text{M h}^{-1}]$ of the linear region with the formula

$$k = \frac{-\left(\frac{\text{slope}}{3600}\right)}{c(\text{enzyme})},$$

where $c(\text{enzyme})$ is the concentration of the respective enzyme in $[\mu\text{M}]$. Note that k is most likely lower than the turnover number k_{cat} which is by definition determined at v_{max} i.e. when the enzyme is saturated with substrate; presumably an unmet condition in this assay.

Analysis of cleavage sites. All fragments that might theoretically occur during the digest were identified based on the sequence of the parent peptide and based on the enzyme’s cleavage ability as reported by the manufacturer. The raw data of the digests were manually searched for all the identified theoretical fragments with Freestyle 1.3 SP2 build 22 (Thermo Fisher Scientific, Waltham, MA, USA) to check which charge states of each fragment are the most common and to identify their retention time. One to four different proton adducts with high peak intensities of each fragment $[M + n \cdot H]^n$ were included in the compound database of TraceFinder 4.1 (Thermo Fisher Scientific, Waltham, MA, USA). To monitor the formation and further degradation of the fragments over time, the digest data were processed with TraceFinder similar to the method described in the chapter Quantitative parent peptide degradation analysis, i.e. including the peak integration but without the quantitation step as no calibration samples were available for the fragments. The ion counts for each fragment were averaged over all replicates of the respective assay. Analysis of the cleavability of peptide bonds was achieved by comparison of identical fragments between different peptides, as well as by analyzing the relative rates of fragment formation and degradation e.g. by correlating the time at which the parent peptide was completely degraded with the time points at which certain fragments reach their maximum concentration. Especially terminal fragments that require only one cleavage to be formed are very informative in this regard. Note that the ion counts (i.e. peak intensities) of different fragments are not directly comparable because some fragments may be ionized (and therefore detected) at a higher ratio than others and because only the most common proton-adducts, but no adducts with metal ions (Na^+ , K^+ , Ca^{++}) were included in the compound database. This is exemplified in Figure S6B.

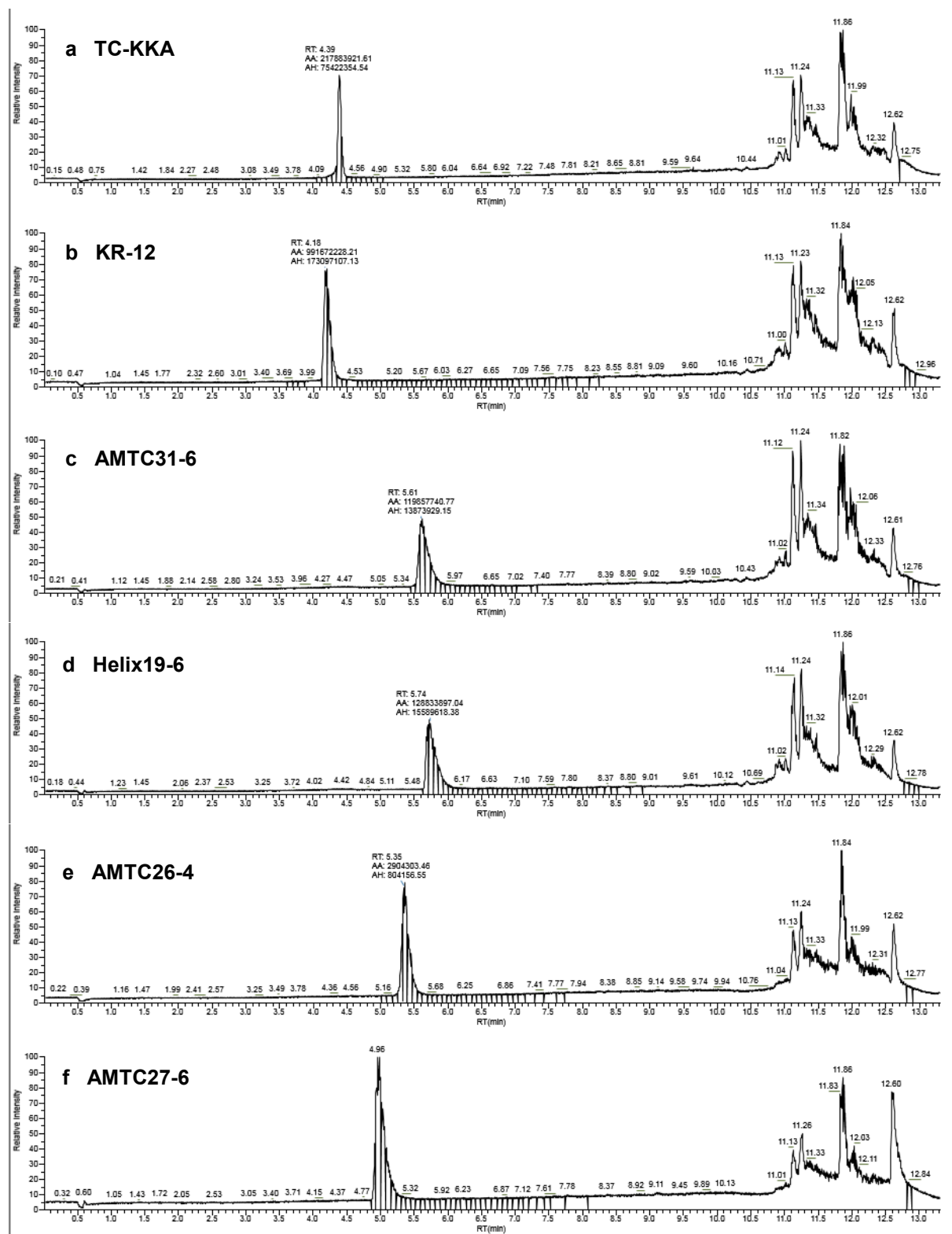


Figure S22. Analytical chromatograms.

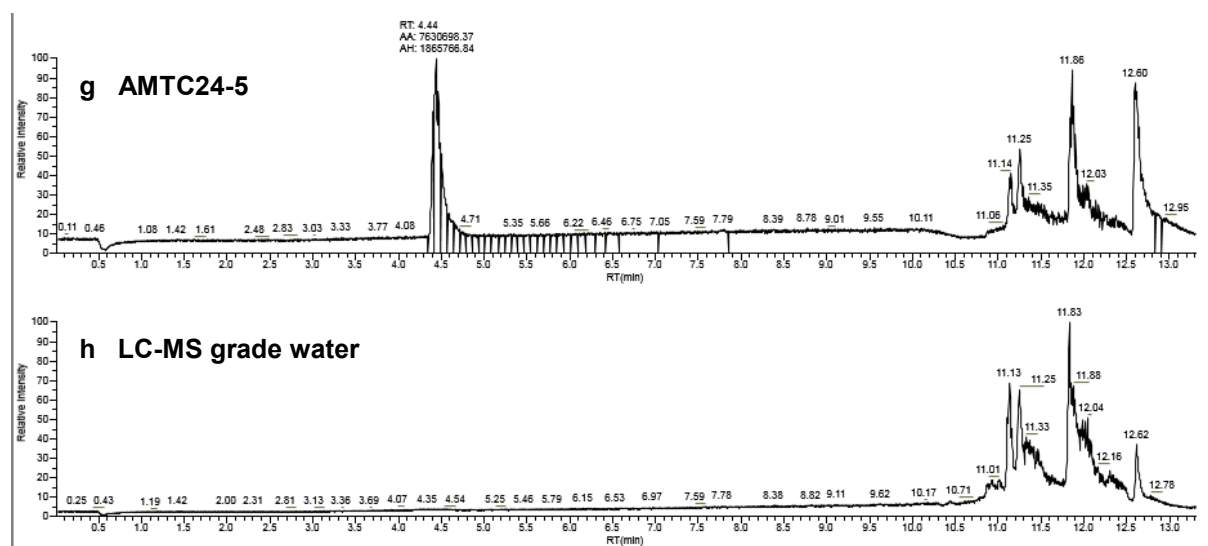


Figure S23. Analytical chromatograms.

References

- (19) Neidigh, J. W.; Fesinmeyer, R. M.; Andersen, N. H. Designing a 20-residue protein. *Nat. Struct. Biol.* **2002**, *9*, 425–430.
- (20) Barua, B.; Lin, J. C.; Williams, V. D.; Kummeler, P.; Neidigh, J. W.; Andersen, N. H. The Trp-cage: Optimizing the stability of a globular miniprotein. *Protein Eng. Des. Sel.* **2008**, *21*, 171–185.
- (28) Wishart, D. S.; Sykes, B. D.; Richards, F. M. The chemical shift index: A fast and simple method for the assignment of protein secondary structure through NMR spectroscopy. *Biochemistry* **1992**, *31*, 1647–1651.
- (29) Wishart, D. S.; Sykes, B. D. The ^{13}C chemical-shift index: A simple method for the identification of protein secondary structure using ^{13}C chemical-shift data. *J. Biomol. NMR* **1994**, *4*, 171–180.
- (62) Qiu, L.; Pabit, S. A.; Roitberg, A. E.; Hagen, S. J. Smaller and faster: The 20-residue Trp-cage protein folds in 4 μs . *J. Am. Chem. Soc.* **2002**, *124*, 12952–12953.
- (63) Preußke, N.; Moormann, W.; Bamberg, K.; Lipfert, M.; Herges, R.; Sönnichsen, F. D. Visible-light-driven photocontrol of the Trp-cage protein fold by a diazocine cross-linker. *Org. Biomol. Chem.* **2020**, *18*, 2650–2660.
- (64) Kristensen, K.; Henriksen, J. R.; Andresen, T. L. Adsorption of cationic peptides to solid surfaces of glass and plastic. *PloS one* **2015**, *10*, e0122419.

Supplementary Information

Visible-Light-Driven Photocontrol of the Trp-cage Protein Fold by a Diazocine Cross-Linker

Nils Preußke, Widukind Moormann, Katrin Bamberg, Matthias Lipfert, Rainer Herges, Frank D. Sönnichsen

Otto Diels-Institute for Organic Chemistry, Christian-Albrechts-University of Kiel, 24119 Kiel, Germany

Contents

1.	Distance Computation	3
2.	Characterization of TC(4,8).....	3
2.1.	UHPLC-HRMS.....	3
2.2.	NMR data.....	4
2.2.1.	Trp-cage by-forms	5
2.3.	Determination of midpoint of thermal unfolding of TC(4,8)	5
3.	Characterization of the folded <i>cis</i> -switch-cage	6
3.1.	UHPLC-HRMS.....	6
3.2.	NMR data.....	8
3.2.1.	Chemical shifts.....	8
3.2.2.	Chemical shift deviations.....	9
3.3.	Determination of midpoint of thermal unfolding of the switch cage	11
4.	Switching properties of the switch cage	11
4.1.	UV/vis spectroscopy	11
4.2.	Photostationary state at 385 nm and relaxation rates	12
4.2.1.	Experimental setup.....	12
4.2.2.	Selecting the nuclei for the determination of the PSS at 385 nm and the relaxation rate	12
4.2.3.	Determination of the PSS at 385 nm.....	13
4.2.4.	Determination of the relaxation rate	14

4.2.5.	Results	14
4.3.	Photostationary state at 530 nm.....	16
4.4.	Mechanism of interconversion between <i>cis</i> -SC _a and <i>cis</i> -SC _b	17
5.	Cross-linker synthesis and characterization	17
5.1.	Devices.....	17
5.1.1.	Chromatography stationary phases	17
5.1.2.	Melting point determination.....	17
5.1.3.	NMR spectroscopy.....	18
5.1.4.	IR spectroscopy	18
5.1.5.	Mass spectrometry.....	18
5.2.	Synthetic procedures and analysis results	19
5.2.1.	Synthesis of (3-methyloxetan-3-yl)methyl 2-(4-methyl-3-nitrophenyl)acetate (8)	19
5.2.2.	Synthesis of 4-methyl-1-(4-methyl-3-nitrobenzyl)-2,6,7-trioxabicyclo[2.2.2]octane (9)	21
5.2.3.	Synthesis of 1,2-bis(4-((4-methyl-2,6,7-trioxabicyclo[2.2.2]octan-1-yl)methyl)-2-nitrophenyl)ethane (10)	23
5.2.4.	Synthesis of (Z)-bis(3-hydroxy-2-(hydroxymethyl)-2-methylpropyl) 2,2'-(11,12-dihydrodibenzo[c,g][1,2]diazocine-3,8-diyl)diacetate (11)	25
5.2.4.1.	Determination of the PSS of diazocine 11	27
5.2.5.	Synthesis of (Z)-bis(2,5-dioxopyrrolidin-1-yl) 2,2'-(11,12-dihydrodibenzo[c,g][1,2]diazocine-3,8-diyl)diacetate (1)	28
6.	References.....	30

1. Distance Computation

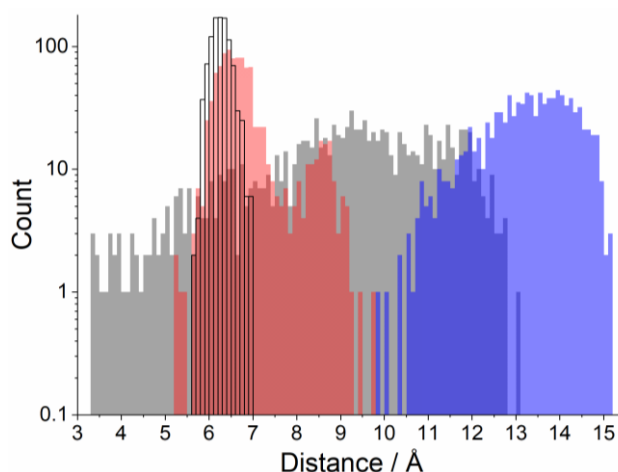


Fig. S 1: The same computed distances of the switchable Trp-cage ‘cis-SCa’ (open), the uncross-linked Trp-cage ‘TC(4,8)’ (red), as well as the diazocines *cis*-5 (gray) and *trans*-5 (blue) as in **Fig. 3** (in the paper) are here displayed on a logarithmic scale.

2. Characterization of TC(4,8)

2.1. UHPLC-HRMS

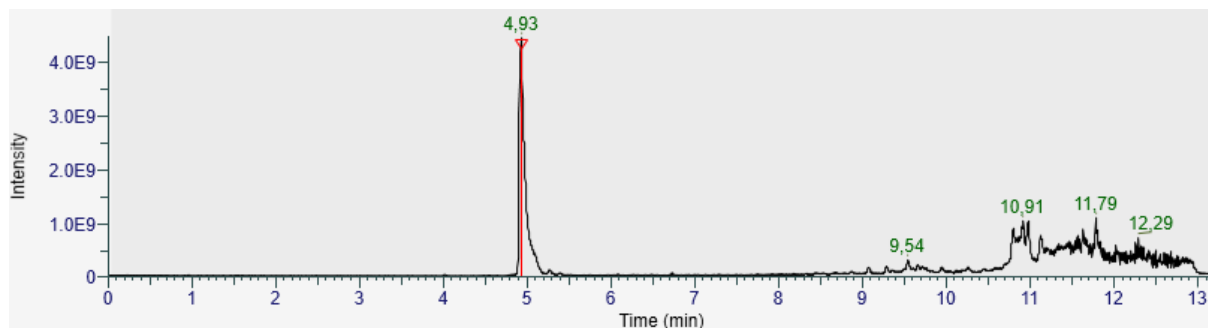


Fig. S 2: Chromatogram of TC(4,8). Peaks after 9 min are background noise.

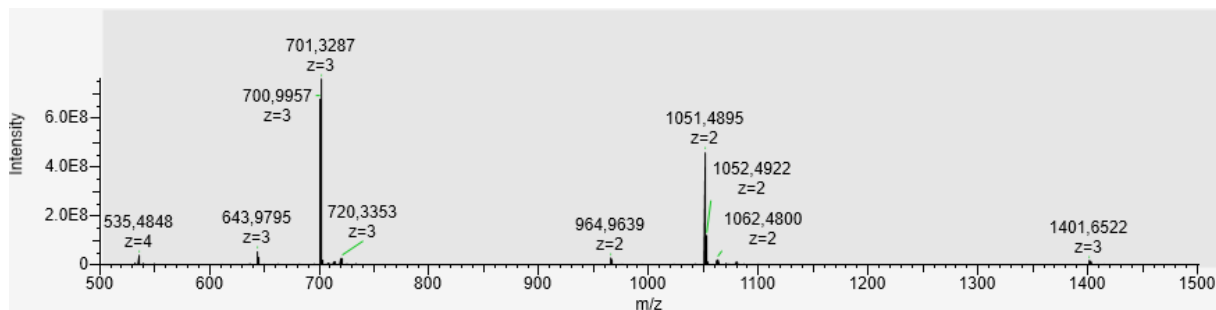


Fig. S 3: Mass spectrum of TC(4,8) at a retention time of 4.93 min. The peaks at 535, 701 and 1051 result from different charged states of TC(4,8). The small peaks immediately to the right of peak 701 and peak 1051 correspond to adducts of TC(4,8) with Na⁺ and/or K⁺. The peak at 1402 corresponds to the non-covalent homodimer of TC(4,8) [2M + 3H]³⁺. The peaks at 644 and 965 belong to a side product from solid phase synthesis of TC(4,8) that possesses a similar retention time as TC(4,8). Based on the MS-detected chromatogram the sample is at least 80% pure.

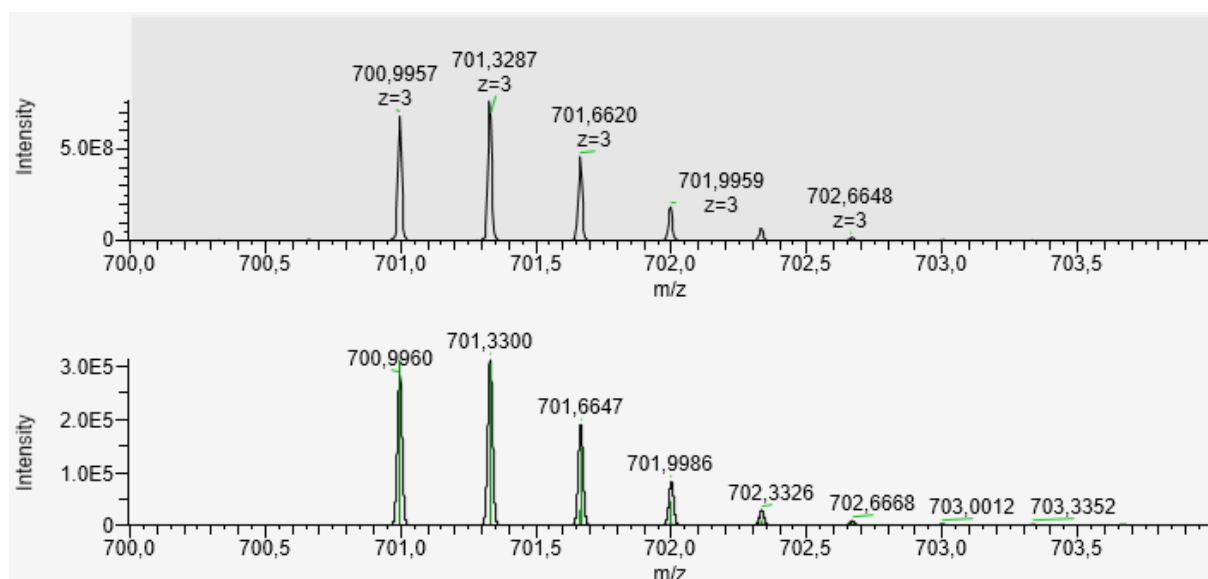


Fig. S 4: The expansion of the mass spectrum in **Fig. S 3** in the range between 700 and 704 demonstrates that the isotopic pattern of TC(4,8) (top) is identical with the isotopic pattern calculated based on its sum formula $[\text{C}_{91}\text{H}_{133}\text{N}_{27}\text{O}_{31} + 3\text{H}]^{3+}$ (bottom).

2.2. NMR data

Tab. S 1: Proton chemical shifts of the folded main form of TC(4,8).

No. Res. Proton: Shift / ppm

00	Ac	Me: 2.074
01	D	H^{N} : 8.245, H^{α} : 4.565, $\text{H}^{\beta 2/\beta 3}$: 2.828/2.726
02	A	H^{N} : 8.658, H^{α} : 4.185, H^{β} : 1.389
03	Y	H^{N} : 8.771, H^{α} : 4.248, H^{β} : 3.093, H^{δ} : 7.098, H^{ϵ} : 6.832
04	Γ	H^{N} : 8.622, H^{α} : 4.473, H^{β} : 3.470
05	Q	H^{N} : 8.465, H^{α} : 4.019, H^{β} : 2.114, H^{γ} : 2.311, $\text{H}^{\epsilon 21/\epsilon 22}$: 7.618/6.870
06	W	H^{N} : 8.228, H^{α} : 4.396, $\text{H}^{\beta 2/\beta 3}$: 3.394/3.204, $\text{H}^{\delta 1}$: 7.091, $\text{H}^{\epsilon 1}$: 9.873, $\text{H}^{\zeta 2}$: 7.308, $\text{H}^{\eta 2}$: 7.221, $\text{H}^{\epsilon 3}$: 7.135, $\text{H}^{\zeta 3}$: 7.226
07	L	H^{N} : 8.415, H^{α} : 3.696, $\text{H}^{\beta 2/\beta 3}$: 1.721/1.472, H^{γ} : 1.547, $\text{H}^{\delta 1/\delta 2}$: 0.937/0.854
08	Γ	H^{N} : 8.276, H^{α} : 4.467, $\text{H}^{\beta 2/\beta 3}$: 3.490/3.418
09	D	H^{N} : 8.055, H^{α} : 4.628, $\text{H}^{\beta 2/\beta 3}$: 2.840/2.699
10	G	H^{N} : 7.773, $\text{H}^{\alpha 2/\alpha 3}$: 4.100/3.657
11	G	H^{N} : 8.201, $\text{H}^{\alpha 2/\alpha 3}$: 3.420/1.983
12	P	H^{α} : 4.551, $\text{H}^{\beta 2/\beta 3}$: 2.440/2.040, H^{γ} : 2.102, $\text{H}^{\delta 2/\delta 3}$: 3.740/3.471
13	S	H^{N} : 7.963, H^{α} : 4.468, H^{β} : 3.906
14	S	H^{N} : 8.207, H^{α} : 4.260, $\text{H}^{\beta 2/\beta 3}$: 3.885/3.635
15	G	H^{N} : 8.071, $\text{H}^{\alpha 2/\alpha 3}$: 4.163/3.861
16	R	H^{N} : 8.096, H^{α} : 4.878, H^{β} : 1.819, $\text{H}^{\gamma 2/\gamma 3}$: 1.727/1.657, H^{δ} : 3.228, H^{ϵ} : 7.425
17	P	H^{α} : 4.708, $\text{H}^{\beta 2/\beta 3}$: 2.317/1.816, H^{γ} : 1.997, $\text{H}^{\delta 2/\delta 3}$: 3.837/3.634
18	P	H^{α} : 3.254, $\text{H}^{\beta 2/\beta 3}$: 1.547/1.046, H^{γ} : 1.816, $\text{H}^{\delta 2/\delta 3}$: 3.602/3.531
19	P	H^{α} : 4.376, $\text{H}^{\beta 2/\beta 3}$: 2.228/1.984, H^{γ} : 1.890, $\text{H}^{\delta 2/\delta 3}$: 3.369/3.180
20	S	H^{N} : 7.871, H^{α} : 4.191, H^{β} : 3.801

Assignments are according to IUPAC nomenclature.¹

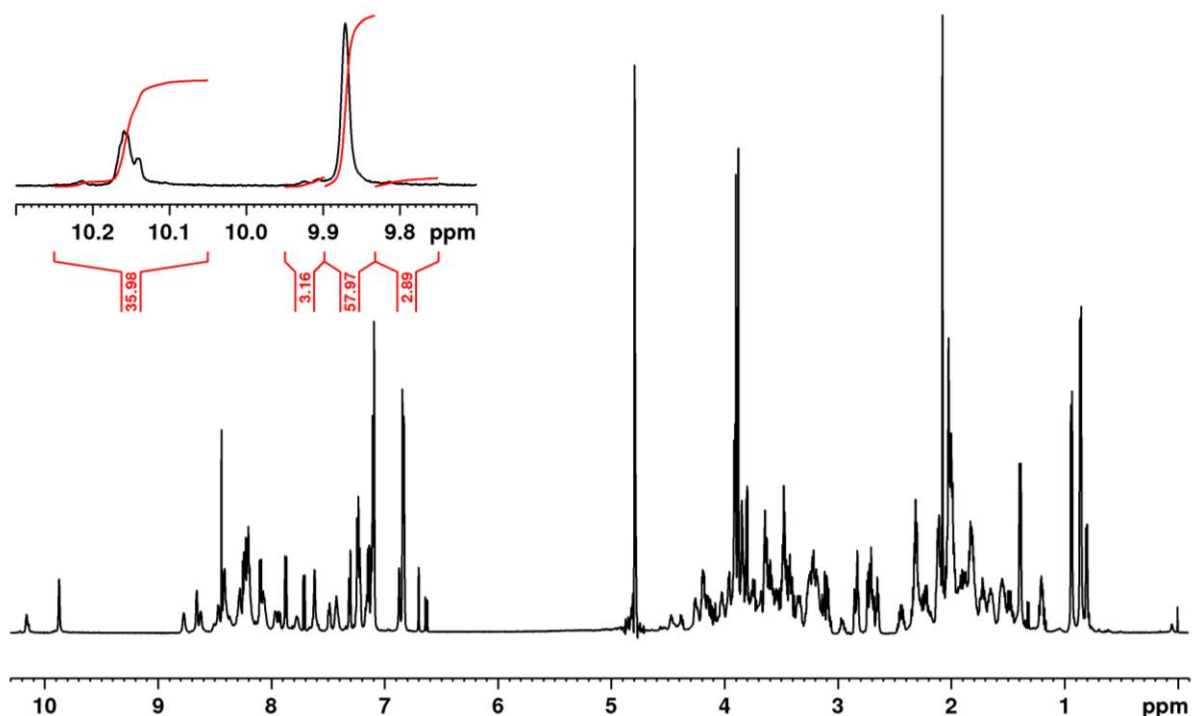


Fig. S 5: 1D ^1H -NMR spectrum of TC(4,8) in water with 10% D_2O at pH = 5.3, 298 K and a concentration of 1.6 mM. The expansion between 10.3 ppm and 9.7 ppm highlights the indole region. The highest peak (9.873 ppm) belongs to the Trp6 indole proton (H^{E1}) of the folded main form. Additional peaks in the indole region indicate unfolded by-forms of the Trp-cage with chemical shifts of the Trp6 indole proton (H^{E1}) around 10.15 ppm.

2.2.1. Trp-cage by-forms

Apart from the folded main-form described above, several by-forms of the Trp-cage are apparent in the indole NH-region in the ^1H -NMR spectrum (resonances between 9.7 ppm and 10.3 ppm). These by-forms belong to TC(4,8). They make up approximately 36% of the sample as determined by integration of the indole region (**Fig. S 5**) while ultra-high performance liquid chromatography coupled to high resolution mass spectrometry (UHPLC-HRMS) determined the amount of impurities of the sample to be <20% (**Fig. S 2** and **Fig. S 3**). These unfolded by-forms are detectable in NMR spectroscopy as separate resonances, because they are in slow equilibrium with the folded main population on the NMR chemical shift time scale.

In this paper, all NMR-based evaluations refer to the folded main population if not stated otherwise. In contrast, CD spectroscopy is averaged over every structure (including the folded and unfolded by-forms) weighted with respect to their population

2.3. Determination of midpoint of thermal unfolding of TC(4,8)

Fig 4a (in the paper) displays data of thermal unfolding of TC(4,8) (red triangles). The following function was fitted to the data

$$y = A_2 + \frac{A_1 - A_2}{1 + \exp\left(\frac{x - x_0}{dx}\right)}$$

yielding the following values: $A_1 = -13585.51999 \pm 850.58255$
 $A_2 = -3298.40652 \pm 135.41215$
 $x_0 = 31.62031 \pm 2.69452$ (in this case $x_0 = T_m$)
 $dx = 13.99868 \pm 1.57008$

3. Characterization of the folded *cis*-switch-cage

3.1. UHPLC-HRMS

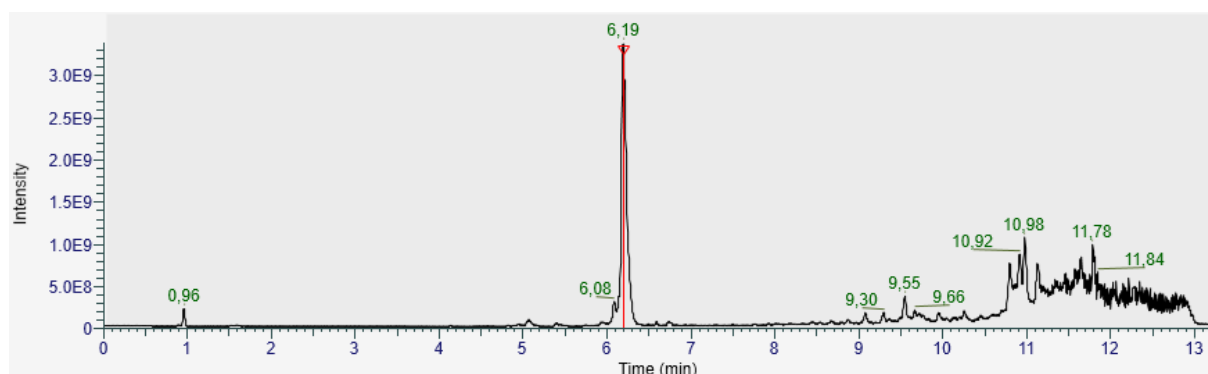


Fig. S 6: Chromatogram of the switch cage. An aliquot of the NMR sample (contains 10% D₂O) was subjected to UHPLC-HRMS analysis. Peaks after 9 min are background noise.

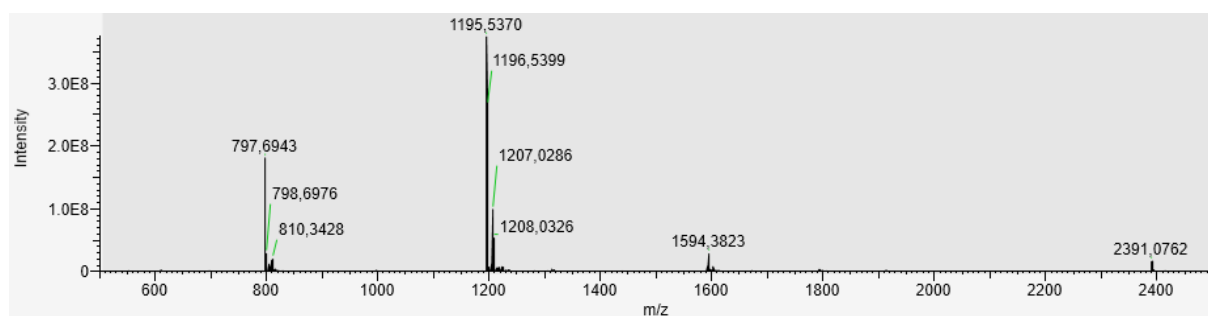


Fig. S 7: Mass spectrum of the switch cage at a retention time of 6.19 min. The peaks around 798, 1196 and 2391 result from different charged states of TC(4,8). The smaller peaks to the right of the product peaks correspond to adducts of the switch cage with Na⁺ and/or K⁺. The peak around 2391 can be assigned to singly charged switch cage $[M + H]^+$ overlaid the doubly charged non-covalent homodimer of the switch cage $[2M + 2H]^{2+}$. The peak around 1594 belongs to the triply charged non-covalent homodimer $[2M + 3H]^{3+}$. Based on the MS-detected chromatogram the sample is at least 85% pure.

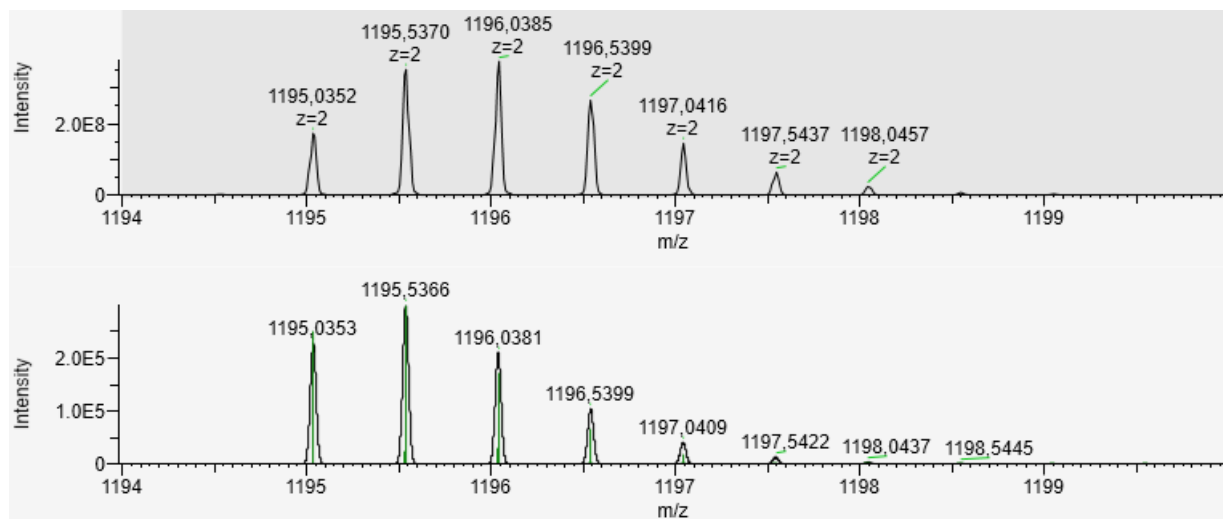


Fig. S 8: The expansion of the mass spectrum in **Fig. S 7** in the range between 1194 and 1200 demonstrates that the isotopic pattern of the switch cage (top) is almost identical with the isotopic pattern calculated based on its sum formula $[C_{109}H_{145}N_{29}O_{33} + 2H]^{2+}$ (bottom). The slight deviation is a result of exchanged protons for deuterons due to the D_2O content of the solvent (cf. **Fig. S 9**).

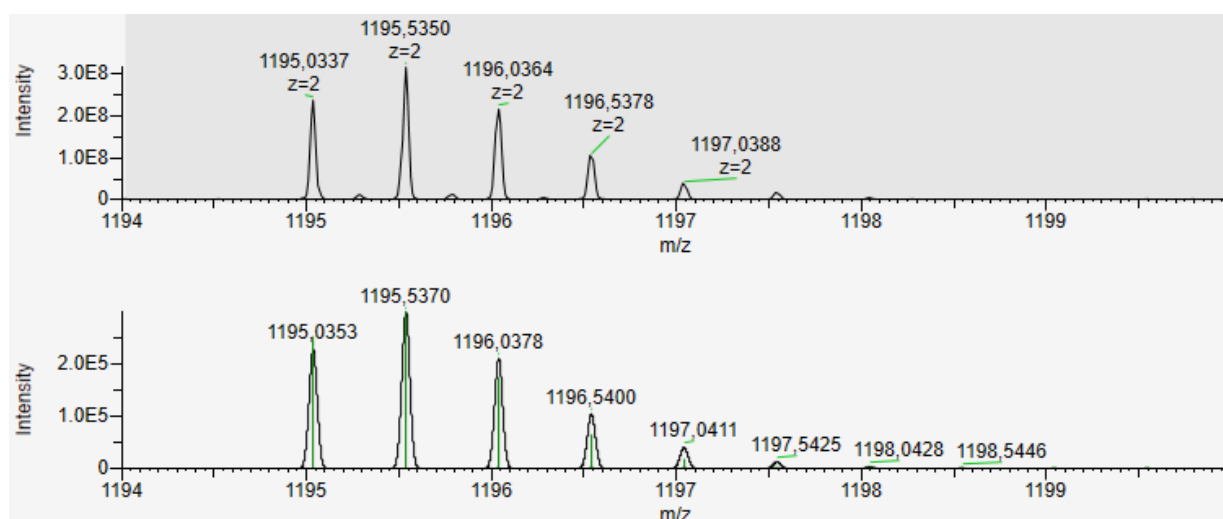


Fig. S 9: The sample from **Fig. S 6**, **Fig. S 7** and **Fig. S 8** was lyophilized and reconstituted with H_2O to exchange all deuterons in the protein with protons. The resulting isotopic pattern of the $[M + 2H]^{2+}$ species exactly matches the predicted pattern. The small peaks in between the isotopic pattern of $[M + 2H]^{2+}$ correspond to the non-covalent homodimer $[2M + 4H]^{4+}$.

3.2. NMR data

3.2.1. Chemical shifts

Tab. S 2: Proton chemical shifts of *cis*-SCa.

No. Res. Proton: shift / ppm

00	Ac	Me: 2.060
01	D	H ^N : 8.236, H ^α : 4.622, H ^{β2/β3} : 2.881/2.714
02	A	H ^N : 8.688, H ^α : 4.201, H ^β : 1.483
03	Y	H ^N : 8.709, H ^α : 4.156, H ^{β2/β3} : 3.203/3.128, H ^δ : 7.118, H ^ε : 6.888
04	Γ	H ^N : 8.446, H ^α : 3.543, H ^β : 3.543, H ^γ : 7.506, H ^{ε2/ε3} : 3.654/3.418, H ² : 6.714, H ^{4,5} : 7.030, H ^{br} : 2.83 ± 0.07
05	Q	H ^N : 8.353, H ^α : 3.923, H ^β : 2.173, H ^γ : 2.360, H ^{ε21/ε22} : 7.693/6.867
06	W	H ^N : 8.004, H ^α : 4.238, H ^{β2/β3} : 3.501/3.195, H ^{δ1} : 7.009, H ^{ε1} : 9.728, H ^{ζ2} : 7.229, H ^{η2} : 7.153, H ^{ε3} : 7.063, H ^{ζ3} : 7.148
07	L	H ^N : 8.487, H ^α : 3.414, H ^{β2/β3} : 1.724/1.335, H ^γ : 1.525, H ^{δ1/δ2} : 0.853/0.655
08	Γ	H ^N : 8.252, H ^α : 4.412, H ^{β2/β3} : 3.960/3.403, H ^γ : 7.917, H ^{ε2/ε3} : 3.488/3.400, H ² : 6.662, H ⁴ : 6.442, H ⁵ : 6.942, H ^{br} : 2.83 ± 0.07
09	D	H ^N : 7.871, H ^α : 4.624, H ^{β2/β3} : 2.892/2.683
10	G	H ^N : 7.484, H ^{α2/α3} : 4.148/3.497
11	G	H ^N : 8.295, H ^{α2/α3} : 3.123/0.969
12	P	H ^α : 4.594, H ^{β2/β3} : 2.516/2.069, H ^γ : 2.144, H ^{δ2/δ3} : 3.799/3.416
13	S	H ^N : 7.698, H ^α : 4.474, H ^β : 3.920
14	S	H ^N : 8.185, H ^α : 4.166, H ^{β2/β3} : 3.869/3.528
15	G	H ^N : 7.926, H ^{α2/α3} : 4.270/3.812
16	R	H ^N : 8.138, H ^α : 5.019, H ^{β2/β3} : 1.888/1.818, H ^γ : 1.658, H ^δ : 3.269, H ^ε : 7.563
17	P	H ^α : 4.748, H ^{β2/β3} : 2.339/1.798, H ^γ : 2.000, H ^{δ2/δ3} : 3.866/3.672
18	P	H ^α : 2.580, H ^{β2/β3} : 1.351/0.385, H ^{γ2/γ3} : 1.736/1.651, H ^δ : 3.519
19	P	H ^α : 4.331, H ^{β2/β3} : 2.199/1.981, H ^γ : 1.857, H ^{δ2/δ3} : 3.163/2.992
20	S	H ^N : 7.819, H ^α : 4.164, H ^β : 3.775

The assignments are according to IUPAC nomenclature.¹ The nomenclature of the cross-linker assignments is shown in **Fig. S 10**.

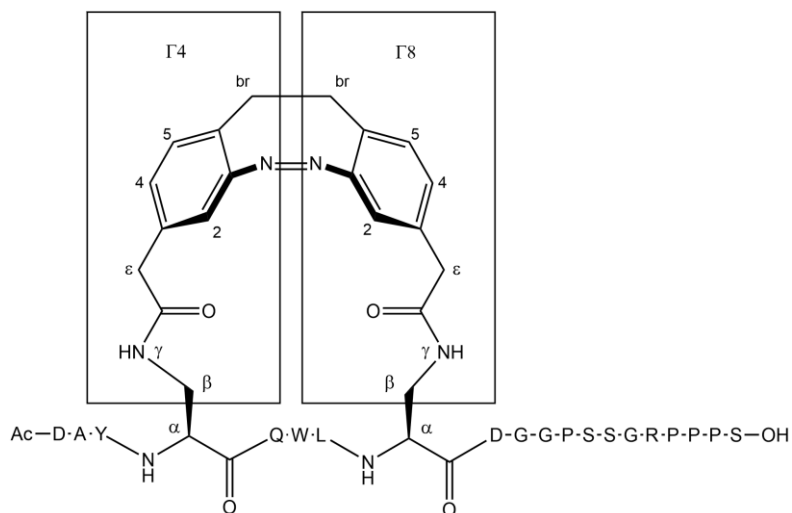


Fig. S 10: The nomenclature of the cross-linker assignments.

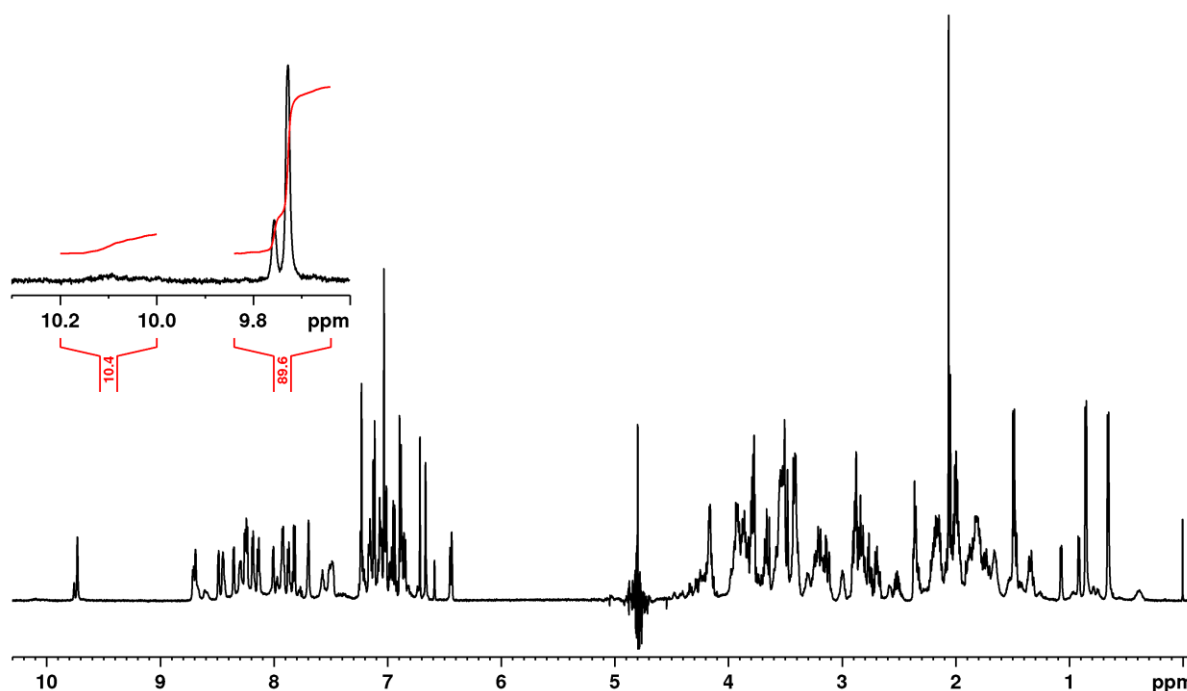


Fig. S 11: 1D ^1H -NMR spectrum of the dark-adapted switch cage in water with 10% D_2O at pH = 5.5, 298 K and a concentration of 0.5 mM. The expansion of the region between 10.3 ppm and 9.6 ppm shows that the amount of unfolded by-forms with chemical shifts of the Trp6 indole proton ($\text{H}^{\text{E}1}$) around 10.1 ppm adds up to approximately 10%, which is significantly reduced compared to TC(4,8) (cf. **Fig. S 5**). With approximately 10%, the amount of unfolded species lies within the range of impurity determined by UHPLC-MS. The broad signals may therefore also correspond to unfolded Trp-containing side-products from the synthesis and not necessarily belong to unfolded switch-cage species.

3.2.2. Chemical shift deviations

The chemical shift deviation (CSD, also referred to as $\Delta\delta$) is typically employed to assess the stability of the fold of a Trp-cage mutant.^{2,3} The CSD is the difference between the observed chemical shift of a certain nucleus in a peptide and the corresponding nucleus in an unstructured random coil peptide:

$$\text{CSD} = \Delta\delta = \delta_{\text{obs.}} - \delta_{\text{random coil}}$$

Unfortunately, we were unable to find a comprehensive list of random coil shifts used by Andersen *et al.*^{2,3}. Therefore, random coil shifts were taken from Wishart *et al.* and are listed in **Tab. S 3**.⁴ The random coil value of the Trp indole proton was taken from Bundi and Wüthrich.⁵ The random coil shifts by Wishart *et al.* are non-stereospecifically assigned. When two β -protons ($\text{H}^{\beta2/\beta3}$) from the same residue display different random coil shifts, their CSD was calculated by subtracting the larger random coil shift from the larger observed shift and the smaller random coil shift from the smaller observed shift.

Example from Asp1:	Observed shift:	$\text{H}^{\beta2/\beta3}$: 2.881/2.714 ppm
	Random coil shift:	$\text{H}^{\beta2/\beta3}$: 2.72/2.65 ppm
	CSD:	$\text{H}^{\beta2/\beta3}$: 0.16/0.06 ppm

No CSDs are given for the acetyl moiety of the N-terminus and for residues Dpr4 and Dpr8 as no random coil values are available for their nuclei.

Tab. S 3: Random coil shifts used for the calculation of CSDs.**No. Res. Proton: CSD / ppm**

00	Ac	Me: n.d.
01	D	H ^N : 8.34, H ^α : 4.64, H ^{β2/β3} : 2.72/2.65
02	A	H ^N : 8.24, H ^α : 4.32, H ^β : 1.39
03	Y	H ^N : 8.12, H ^α : 4.55, H ^{β2/β3} : 3.03/2.98, H ^δ : 7.14, H ^ε : 6.84
04	Γ	n.d.
05	Q	H ^N : 8.32, H ^α : 4.34, H ^{β2/β3} : 2.12/1.99, H ^γ : 2.360, H ^{ε21/ε22} : 7.52/6.85
06	W	H ^N : 8.25, H ^α : 4.66, H ^{β2/β3} : 3.29/3.27, H ^{δ1} : 7.27, H ^{ε1} : 10.22, H ^{ζ2} : 7.50, H ^{η2} : 7.25, H ^{ε3} : 7.65, H ^{ζ3} : 7.18
07	L	H ^N : 8.16, H ^α : 4.34, H ^β : 1.62, H ^γ : 1.59, H ^{δ1/δ2} : 0.92/0.87
08	Γ	n.d.
09	D	H ^N : 8.34, H ^α : 4.64, H ^{β2/β3} : 2.72/2.65
10	G	H ^N : 8.33, H ^α : 3.96
11	G	H ^N : 8.21, H ^α : 4.13
12	P	H ^α : 4.42, H ^{β2/β3} : 2.29/1.94, H ^γ : 2.02, H ^δ : 3.63
13	S	H ^N : 8.31, H ^α : 4.47, H ^{β2/β3} : 3.89/3.87
14	S	H ^N : 8.31, H ^α : 4.47, H ^{β2/β3} : 3.89/3.87
15	G	H ^N : 8.33, H ^α : 3.96
16	R	H ^N : 8.20, H ^α : 4.65, H ^β : 1.81, H ^γ : 1.67, H ^δ : 3.21, H ^ε : 8.07
17	P	H ^α : 4.73, H ^{β2/β3} : 2.31/1.91, H ^γ : 2.01, H ^δ : 3.60
18	P	H ^α : 4.73, H ^{β2/β3} : 2.31/1.91, H ^γ : 2.01, H ^δ : 3.60
19	P	H ^α : 4.42, H ^{β2/β3} : 2.29/1.94, H ^γ : 2.02, H ^δ : 3.63
20	S	H ^N : 8.31, H ^α : 4.47, H ^{β2/β3} : 3.89/3.87

Tab. S 4: Chemical shift deviations of *cis*-SCa.**No. Res. Proton: CSD / ppm**

00	Ac	n.d.
01	D	H ^N : -0.10, H ^α : -0.02, H ^{β2/β3} : 0.16/0.06
02	A	H ^N : 0.45, H ^α : -0.12, H ^β : 0.09
03	Y	H ^N : 0.59, H ^α : -0.39, H ^{β2/β3} : 0.17/0.15, H ^δ : -0.02, H ^ε : -0.05
04	Γ	n.d.
05	Q	H ^N : 0.03, H ^α : -0.42, H ^{β2/β3} : 0.05/0.18, H ^γ : 0.00, H ^{ε21/ε22} : 0.17/0.02
06	W	H ^N : -0.25, H ^α : -0.42, H ^{β2/β3} : 0.21/-0.08, H ^{δ1} : -0.26, H^{ε1}: -0.49 , H ^{ζ2} : -0.27, H ^{η2} : -0.10, H ^{ε3} : -0.59, H ^{ζ3} : -0.03
07	L	H ^N : 0.33, H^α: -0.93 , H ^{β2/β3} : 0.10/-0.28, H ^γ : -0.07, H ^{δ1/δ2} : -0.07/-0.22
08	Γ	n.d.
09	D	H ^N : -0.47, H ^α : -0.02, H ^{β2/β3} : 0.17/0.03
10	G	H ^N : -0.85, H ^{α2/α3} : 0.19/-0.46
11	G	H ^N : 0.08, H^{α2/α3}: -1.01/-3.16
12	P	H ^α : 0.17, H ^{β2/β3} : 0.23/0.13, H ^γ : 0.12, H ^{δ2/δ3} : 0.17/-0.21
13	S	H ^N : -0.61, H ^α : 0.00, H ^{β2/β3} : 0.03/0.05
14	S	H ^N : -0.13, H ^α : -0.30, H ^{β2/β3} : -0.02/-0.34
15	G	H ^N : -0.40, H ^{α2/α3} : 0.31/-0.15
16	R	H ^N : -0.06, H ^α : 0.37, H ^{β2/β3} : 0.08/0.01, H ^γ : -0.01, H ^δ : 0.06, H ^ε : -0.51
17	P	H ^α : 0.02, H ^{β2/β3} : 0.03/-0.11, H ^γ : -0.01, H ^{δ2/δ3} : 0.27/0.07
18	P	H^α: -2.15 , H^{β2/β3}: -0.96/-1.52 , H ^{γ2/γ3} : -0.27/-0.36, H ^δ : -0.08
19	P	H ^α : -0.09, H ^{β2/β3} : -0.09/0.04, H ^γ : -0.16, H ^{δ2/δ3} : -0.47/-0.64
20	S	H ^N : -0.49, H ^α : -0.31, H ^{β2/β3} : -0.12/-0.10

Large CSDs which are a result of and an indicator for the stable Trp-cage fold are highlighted in bold.

3.3. Determination of midpoint of thermal unfolding of the switch cage

Fig 4a (in the paper) displays data of thermal unfolding of the switch cage (black circles). The following function was fitted to the data

$$y = A_2 + \frac{A_1 - A_2}{1 + \exp\left(\frac{x - x_0}{dx}\right)}$$

yielding the following values: $A_1 = -13518.25883 \pm 404.28719$
 $A_2 = -3855.61105 \pm 228.37507$
 $x_0 = 48.50329 \pm 1.42176$ (in this case $x_0 = T_m$)
 $dx = 12.95674 \pm 1.42566$

4. Switching properties of the switch cage

4.1. UV/vis spectroscopy

UV/vis spectra were recorded at 25 °C on a Lambda 14 spectrometer (PerkinElmer, Waltham, MA, USA) equipped with a ecoline E100 thermostat mounted on an ecoline 003 water bath (Lauda, Lauda-Königshofen, Germany). Measurements were performed using low-volume (700 µL) Quartz cuvettes with an optical path length of 10 mm (Hellma, Müllheim, Germany) and water as a solvent at pH = 5.5 ± 0.1.

UV/vis spectroscopy was used to determine the which of the available light sources produces the largest *cis*→*trans*-conversion ratio (**Fig. S 12**). From the tested wavelengths, the highest conversion to *trans*-SC was achieved at 385 nm.

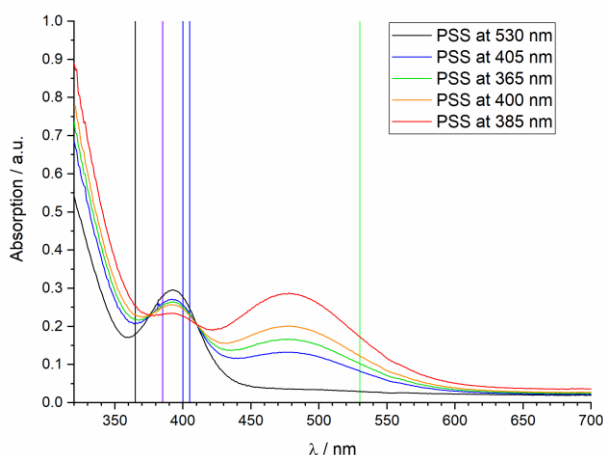


Fig. S 12: UV/vis spectra of the switch cage irradiated with light of different wavelengths (365 nm, 385 nm, 400 nm, 405 nm and 530 nm). The irradiation wavelengths are indicated by a vertical line. The baseline displays a small offset which is an artifact resulting from the narrow low-volume cuvettes.

4.2. Photostationary state at 385 nm and relaxation rates

4.2.1. Experimental setup

The photostationary state (PSS) and relaxation rate were determined by NMR spectroscopy. The sample with the switch cage was irradiated to the PSS at 385 nm and immediately afterwards a 1D- ^1H -NMR spectrum was recorded (**Fig. S 13**). The NMR spectrometer had previously been calibrated to a temperature of 298 °C. The sample remained in the spectrometer in the dark for the entire time of the relaxation measurements. After the first spectrum (representing the PSS, recorded at $t = 2$ min after irradiation), a new spectrum was recorded every 30 min for the next 21 h. The last spectrum was recorded at $t = 39$ h.

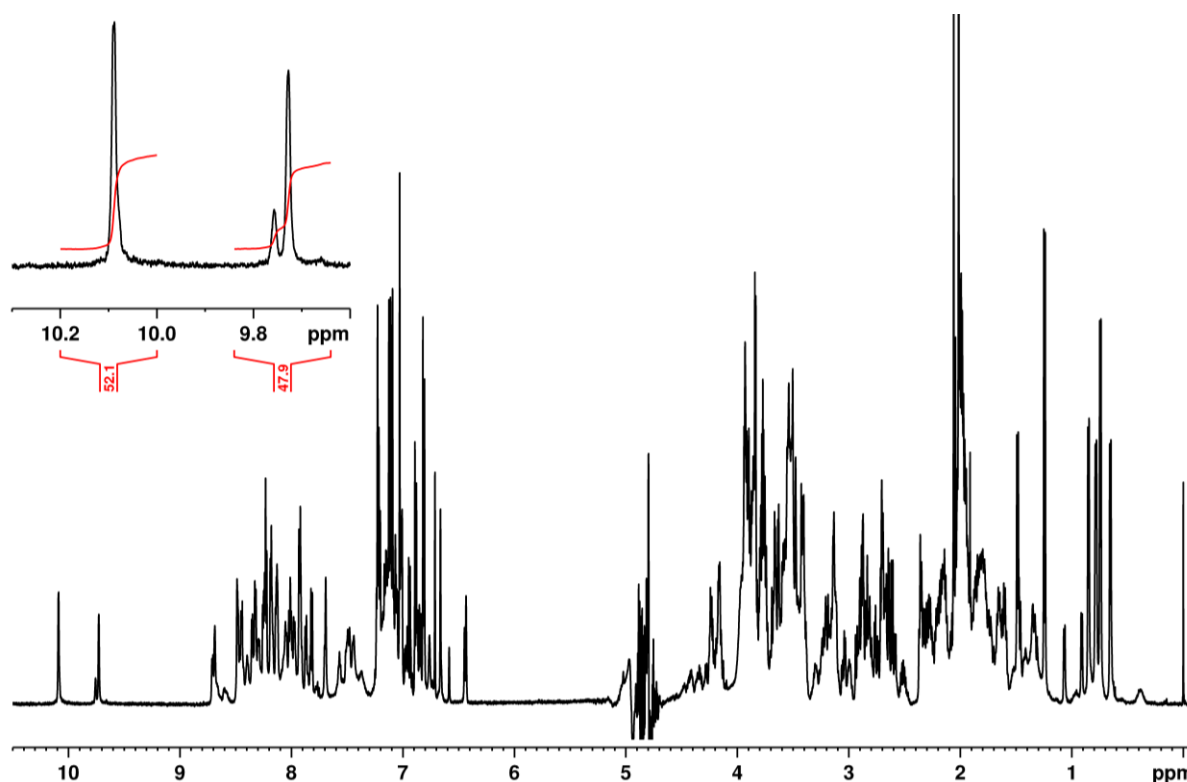


Fig. S 13: 1D- ^1H -NMR spectrum of the switch cage after irradiation to the PSS at 385 nm in water with 10% D_2O at pH = 5.5, 298 K and a concentration of 0.5 mM. The same regions as in **Fig. S 11** are integrated in the expansion.

4.2.2. Selecting the nuclei for the determination of the PSS at 385 nm and the relaxation rate

Accurate determination of photostationary states and relaxation rates ideally requires baseline-separated signals of the *cis*- and the *trans* diazocine to allow for integration. Unfortunately, all signals of the *trans*-diazocine overlap with other aromatic signals of *trans*-SC, *cis*-SC_a or *cis*-SC_b. In consequence, six largely separated signals of *cis*-SC (signals b) – g)) and one signal (signal a)) of *trans*-SC were used to quantify the *cis*- and *trans*-populations and determine the relaxation rate (**Tab. S 5**, **Fig. S 14**).

The six chosen *cis*-SC-signals (b) – g)) represent either the switching state of the diazocine cross-linker or the fold state of the switch cage (**Tab. S 5**). This facilitates the discrimination between the state of the linker and the fold and it also allows for the determination of the PSS and relaxation rates for each

individual species, i.e. *cis*-SC_a and *cis*-SC_b. Signal a) was chosen to calculate the relaxation rate by monitoring a fold-indicating proton of *trans*-SC.

Tab. S 5: List of signals that were chosen to calculate the PSS and/or the relaxation rate of the switch cage.

Entry	Species	Proton	Integr. Region / ppm	Representing
a)	<i>trans</i> -SC	Trp6 indole NH	10.105 – 10.065	fold
b)	<i>cis</i> -SC _b	Trp6 indole NH	9.780 – 9.744	fold
c)	<i>cis</i> -SC _a	Trp6 indole NH	9.744 – 9.700	fold
d)	<i>cis</i> -SC _a	Dpr4 H ²	6.725 – 6.699	diazocine
e)	<i>cis</i> -SC _a	Dpr8 H ²	6.692 – 6.632	diazocine
f)	<i>cis</i> -SC _b	DprX H ^{2*}	6.600 – 6.570	diazocine
g)	<i>cis</i> -SC _a : Dpr8 H ⁴ ; <i>cis</i> -SC _b : Dpr H ^{2**}		6.473 – 6.413	diazocine

*) It was not possible to unequivocally assign the two protons, Dpr4 H² and Dpr8 H² of *cis*-SC_b, to their corresponding residue in the sequence. **) These two signals are overlapping and treated as one.

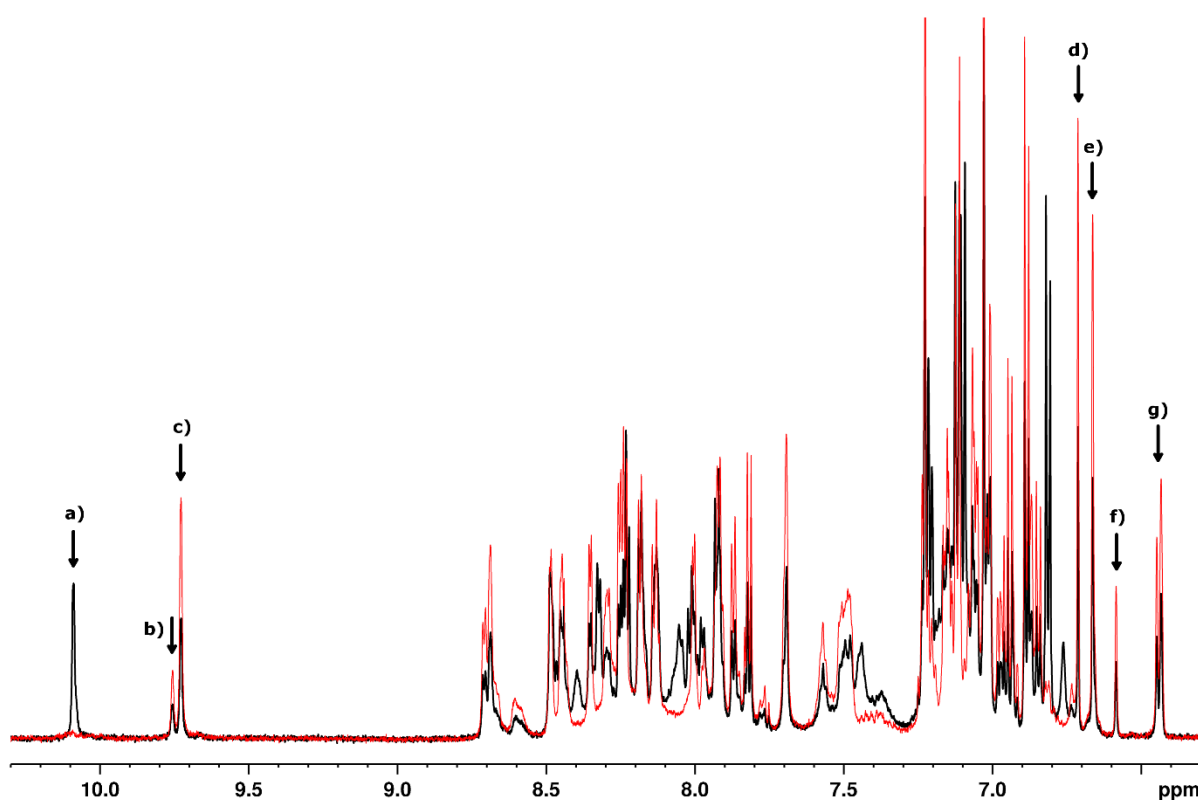


Fig. S 14: The indole, amide and aromatic region of the 1D-¹H-NMR spectra of the switch cage after irradiation to the PSS at 385 nm (red) and relaxation in the dark at 298 K for 39 h (black) are shown. The full spectra are depicted in **Fig. S 13** (PSS at 385 nm) and **Fig. S 11** (dark-adapted). The signals marked a) – g) were chosen for determination of the PSS and relaxation rates as they are more or less baseline-separated.

4.2.3. Determination of the PSS at 385 nm

The PSS at 385 nm was determined *via* the six signals of *cis*-SC (Signals b) – g) of **Tab. S 5** and **Fig. S 14**). The ratio of their intensity after irradiation to the PSS at 385 nm ($I_{385\text{ nm}}$) and their intensity in the dark-adapted state ($I_{\text{dark-adapted}}$) is correlated to the *cis*→*trans*-conversion ratio in the PSS according to the following formula:

$$1 - \frac{I_{385\text{ nm}}}{I_{\text{dark-adapted}}} = \text{cis} \rightarrow \text{trans-conversion ratio}$$

Note that this method can only be applied with signals of *cis*-SC, as signals of *trans*-SC are essentially zero in the dark-adapted state.

The first (recorded at $t = 2$ min after irradiation) and the last spectrum ($t = 39$ h) of the relaxation measurements were chosen to represent the PSS and the dark-adapted state, respectively. In order to determine the PSS, the intensity of signals b) – g) (**Tab. S 5, Fig. S 14**) was measured by integration. Their integrals were calibrated relative to the DSS integral which was arbitrarily set to 1. The obtained intensities were inserted in the formula to obtain the approximate fraction of *trans*-SC in the PSS listed in **Tab. S 6**.

4.2.4. Determination of the relaxation rate

In order to determine the relaxation rate, every 1D-¹H-NMR spectrum of the relaxation measurements was integrated within the ranges listed in **Tab. S 5** (signals a) – g)). These integrals were calibrated relative to the DSS signal, which was arbitrarily set to 1. The signal intensity was plotted over the time (**Fig. S 15**) and the following function of exponential decay was fitted to the data:

$$y = A_1 \cdot e^{\left(\frac{-x}{t_1}\right)} + y_0$$

In this formula, x is the time, y_0 is the offset to which the function approaches asymptotically, t_1 is the time constant of the decay and A_1 is the initial decaying quantity. The sum of y_0 and A_1 ($y_0 + A_1$) give the y-intercept (initial total quantity). The half-life $t_{1/2}$ was calculated by the following relationship:

$$t_{1/2} = t_1 \cdot \ln(2)$$

The results of the fitted data are listed in the table included in **Fig. S 15**, the final results are listed in **Tab. S 6**.

4.2.5. Results

Tab. S 6: Resulting PSS and relaxation rate from each signal a) – g).

Entry	Species	Representing	PSS _{385 nm} / % <i>trans</i> -state	$t_{1/2}$ / h
a)	<i>trans</i> -SC	fold	n.d.	6.7 ± 0.1
b)	<i>cis</i> -SC _b	fold	43	5.6 ± 0.3
c)	<i>cis</i> -SC _a	fold	49	6.1 ± 0.1
d)	<i>cis</i> -SC _a	diazocine	46	6.5 ± 0.1
e)	<i>cis</i> -SC _a	diazocine	45	6.3 ± 0.2
f)	<i>cis</i> -SC _b	diazocine	46	6.5 ± 0.3
g)	<i>cis</i> -SC _a / <i>cis</i> -SC _b	diazocine	47	6.0 ± 0.2
Average:			46 ± 2	6.2 ± 0.3

There is no significant discrepancy in the PSS or half-life of either species, i.e. *cis*-SC_a, *cis*-SC_b or *trans*-SC, nor is there any significant deviation between the behavior of the fold and the diazocine. This implies a direct coupling of the fold and the photoswitchable cross-linker.

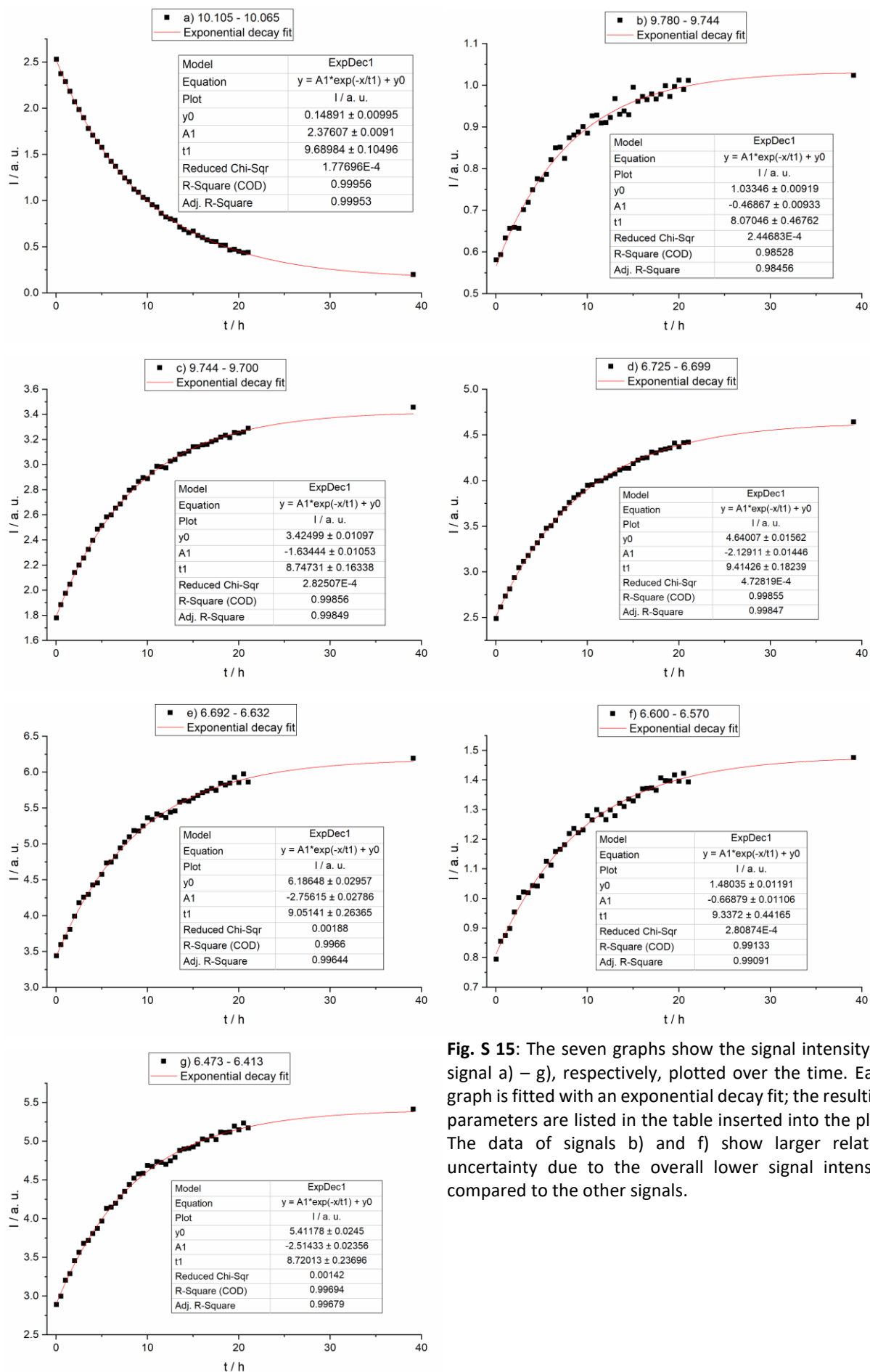


Fig. S 15: The seven graphs show the signal intensity of signal a) – g), respectively, plotted over the time. Each graph is fitted with an exponential decay fit; the resulting parameters are listed in the table inserted into the plot. The data of signals b) and f) show larger relative uncertainty due to the overall lower signal intensity compared to the other signals.

4.3. Photostationary state at 530 nm

The $1\text{D-}^1\text{H-NMR}$ spectrum of the switch-cage recorded immediately after irradiation to the PSS at 530 nm is virtually identical the spectra of the dark-adapted switch-cage (**Fig. S 16**). Therefore, irradiation with light of the wavelength 530 nm affords nearly complete conversion to the *cis*-switch cage.

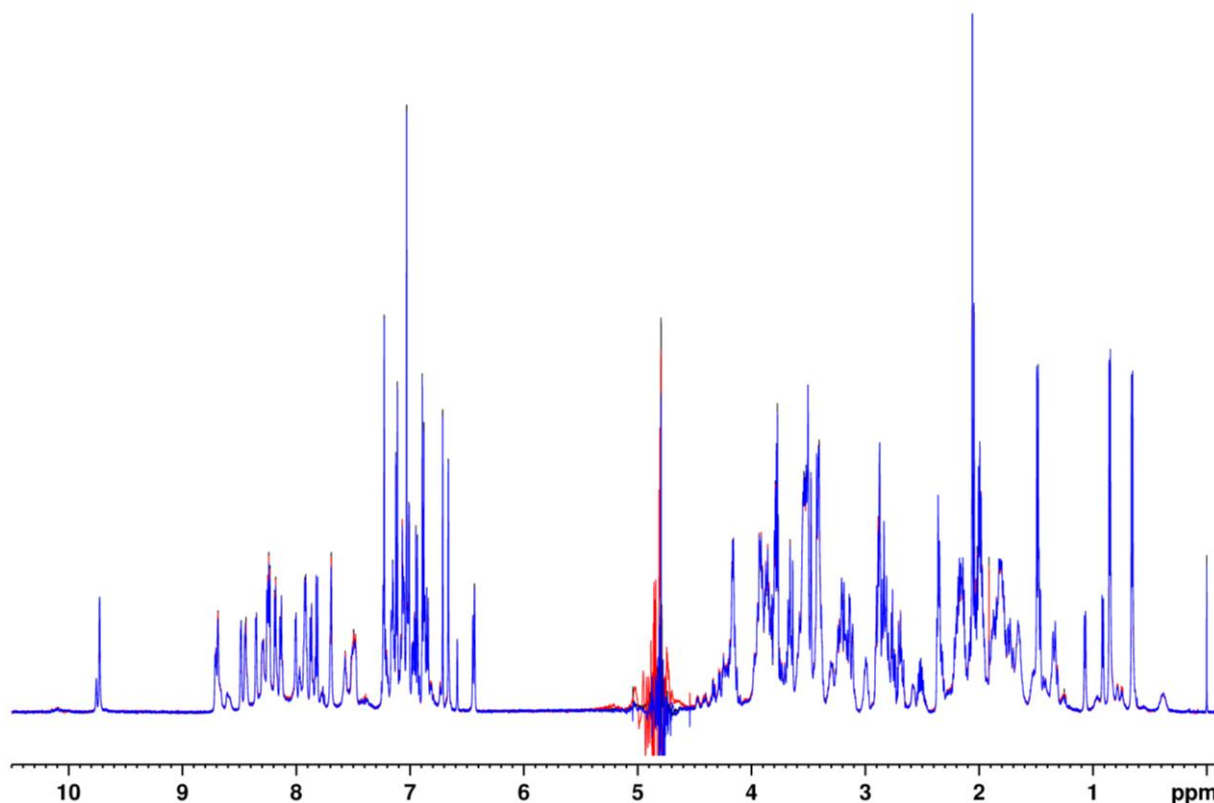
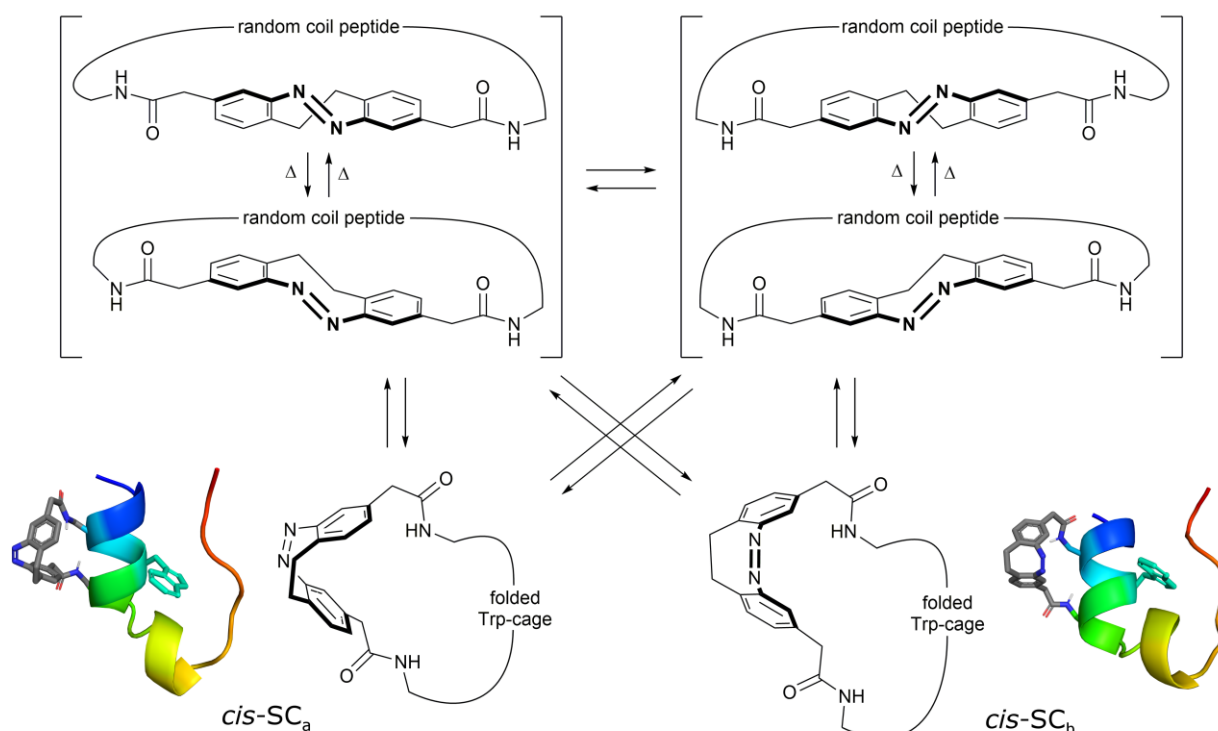


Fig. S 16: Overlay of the $1\text{D-}^1\text{H-NMR}$ spectra of dark-adapted *cis*-SC as obtained after purification (black), *cis*-SC immediately after irradiation to the PSS at 530 nm (red), and *cis*-SC after irradiation to the PSS at 385 nm and subsequent relaxation in the dark at 298 K (24.85 °C) for 39 h (blue). Apart from the water suppression artifact around 4.9 ppm, the three spectra are virtually identical.

4.4. Mechanism of interconversion between *cis*-SC_a and *cis*-SC_b



Scheme S 1: Mechanism of interconversion between *cis*-SC_a, *cis*-SC_b and the two diastereomers of *trans*-SC in the twist and chair conformation. Deltas (Δ) indicate thermal interconversion at ambient temperature. The other indicated equilibria are significantly slower and require higher temperatures or irradiation with light.

5. Cross-linker synthesis and characterization

5.1. Devices

5.1.1. Chromatography stationary phases

Flash column chromatography purifications were performed on a Biotage Isolera one with Biotage Ultra cartridges (HP-Sphere, particle diameter: 25 μ m, cartridge sizes: 10 g, 25 g, 50 g and 100 g; Biotage, Uppsala, Sweden). R_f values were determined by thin layer chromatography on Polygram SiLG/UV₂₅₄ (0.2 mm particle size; Macherey-Nagel, Düren, Germany) and ALUGRAM Xtra SIL G/UV₂₅₄ (0.2 mm particle size; Macherey-Nagel, Düren, Germany).

5.1.2. Melting point determination

Melting points were measured with a B-560 Melting Point Apparatus (Büchi, Essen, Germany) in melting point tubes.

5.1.3. NMR spectroscopy

NMR measurements of the cross-linker and its precursors were performed with a Bruker DRX 500 FT-NMR spectrometer (^1H -NMR: 500.1 MHz, ^{13}C -NMR: 125.8 MHz; Bruker, Billerica, MA, USA).

NMR spectra were measured in deuterated solvents (Deutero, Kastellaun, Germany). Spectra were referenced to TMS when acetone, acetonitrile or chloroform was the solvent. Otherwise the following solvent signals were used for referencing:

Tab. S 7: List of deuterated solvents.

Solvent	Degree of deuteration	^1H signal	^{13}C signal
Acetone- d_6	99.8%	2.05 (quintet)	29.84 (septet)
Acetonitrile- d_3	99.8%	1.94 (quintet)	118.26 (septet)
Chloroform- d_1	99.8%	7.26 (s)	77.16 (triplet)
DMSO- d_6	99.8%	2.50 (s)	39.52 (septet)
Methanol- d_4	99.8%	3.34 (s)	49.86 (septet)

5.1.4. IR spectroscopy

Infrared spectra were measured on a PerkinElmer 1600 Series FT-IR spectrometer with an A531-G Golden-Gate-Diamond-ATR-unit (PerkinElmer, Waltham, MA, USA). Signals were abbreviated with w for weak, m for medium and s for strong signal intensity.

5.1.5. Mass spectrometry

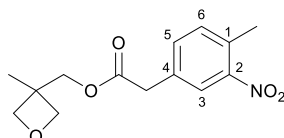
The high resolution-electron ionization (HR-EI) mass spectra were measured with an AccuTOF GCv 4G (Jeol Germany, Freising, Germany) with ionization energy of 70 eV and the high resolution-electrospray ionization (HR-ESI) mass spectra were measured with a Q Exactive Plus MS, Hybrid Quadrupol-Orbitrap (Thermo Fisher Scientific, Waltham, MA, USA).

5.2. Synthetic procedures and analysis results

General remark:

The 4-methyl-2,6,7-trioxabicyclo[2.2.2]octane-1-yl (OBO) protecting group that was employed during the cross-linker synthesis is highly labile against acids and a fraction may unintentionally be hydrolyzed to the open ester during the work-up of reaction ii) or iii) of **Scheme 2** in the paper.

5.2.1. Synthesis of (3-methyloxetan-3-yl)methyl 2-(4-methyl-3-nitrophenyl)acetate (**8**)



At 0 °C and under N₂ atmosphere 2-(4-methyl-3-nitrophenyl)acetic acid (**6**; 3.9 g, 20 mmol), 4-dimethylaminopyridine (DMAP; 244 mg, 2 mmol) and *N,N'*-dicyclohexylcarbodiimide (DCC; 4.13 g, 20 mmol) were dissolved in 30 ml dry dichloromethane (DCM). Immediately afterwards 3-methyl-3-oxetanemethanol (**7**; 1.98 ml, 20 mmol) was added. The reaction was stirred for 1 h at room temperature. The formed solid was filtered and washed with 100 ml DCM. The solvent was evaporated in vacuo and the crude product was purified by flash column chromatography (cyclohexane/ethyl acetate) to afford the product as a yellow oil (4.91 g, 17.6 mmol, 88%).

R_f: 0.29 (cyclohexane/ethyl acetate, 2:1).

¹H-NMR (500.1 MHz, Acetone-d₆, 300 K): δ = 7.96 (d, ⁴*J* = 1.8 Hz, 1 H, *H*-3), 7.58 (dd, ³*J* = 8.0 Hz, ⁴*J* = 1.7 Hz, 1 H, *H*-5), 7.44 (d, ³*J* = 7.8 Hz, 1 H, *H*-6), 4.41 (d, ⁴*J* = 5.8 Hz, 2 H, C-CH₂-O-), 4.25 (d, ⁴*J* = 5.8 Hz, 2 H, C-CH'₂-O-), 4.21 (s, 2 H, C-CH₂-OOC), 3.87 (s, 2 H, OOC-CH₂-C₄), 2.54 (s, 3H, C₁-CH₃), 1.29 (s, 3H, C-CH₃) ppm.

¹³C-NMR (125.8 MHz, Acetone-d₆, 300 K): δ = 171.4 (COO), 150.1 (C-2), 135.2 (C-5), 135.1 (C-4), 133.6 (C-6), 132.4 (C-1), 126.1 (C-3), 79.6 (C-CH₂-O-), 70.0 (C-CH₂-OOC), 40.2 (OOC-CH₂-C₄), 21.2 (C-CH₃), 19.7 (C₁-CH₃) ppm.

IR (ATR): $\tilde{\nu}$ = 2963 (w), 2872 (w), 1735 (s), 1526 (s), 1498 (w), 1454 (w), 1346 (s), 1298 (w), 1246 (m), 1223 (m), 1152 (s), 1031 (w), 977 (s), 833 (m), 815 (s), 751 (w), 732 (w), 678 (w) cm⁻¹.

MS (EI, 70 eV): *m/z* (%) = 279 (7), 262 (5), 196 (5), 177 (13), 150 (100).

HRMS (EI, 70 eV): [C₁₄H₁₇N₁O₅]⁺, calc.: *m/z* = 279.11067, found: *m/z* = 279.11046.

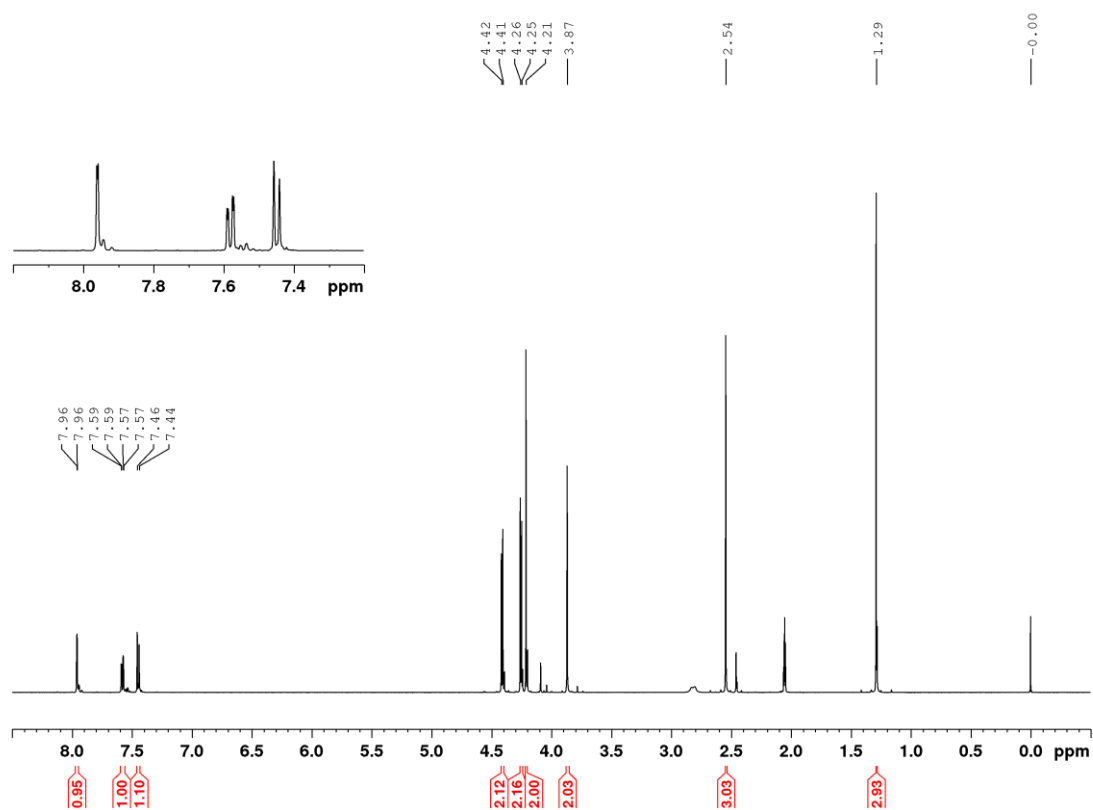


Fig. S 17: ¹H-NMR spectrum of compound **8** measured in deuterated acetone at 300 K.

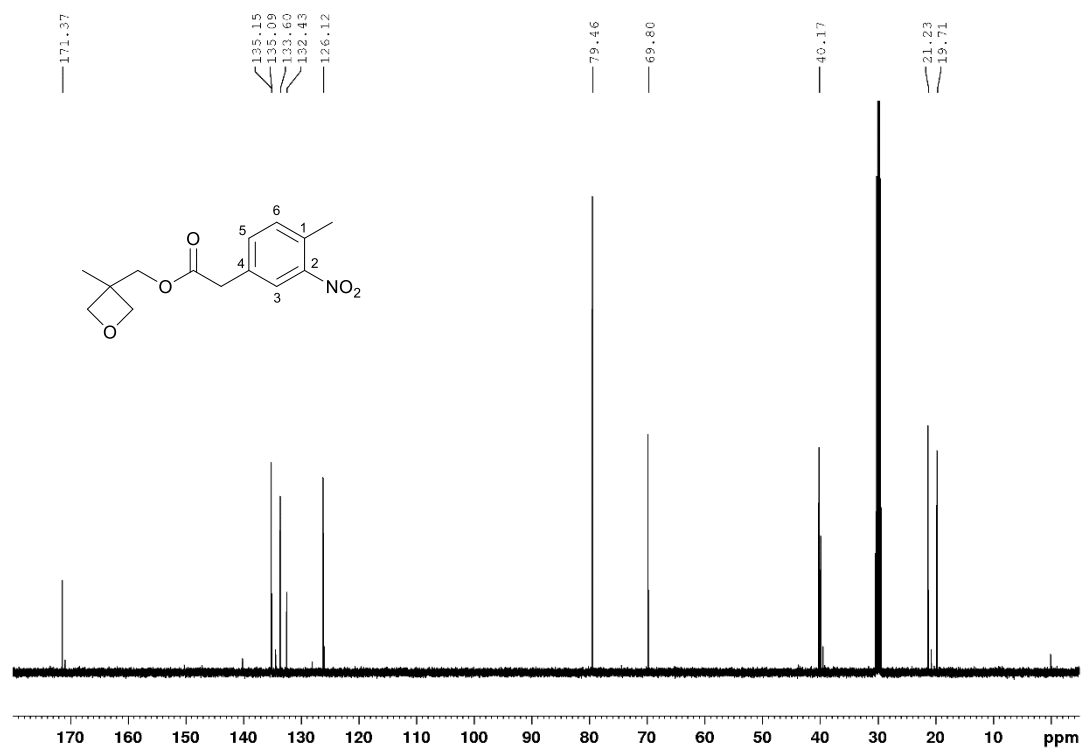
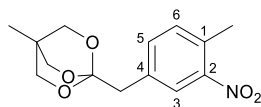


Fig. S 18: ¹³C-NMR spectrum of compound **8** measured in deuterated acetone at 300 K.

5.2.2. Synthesis of 4-methyl-1-(4-methyl-3-nitrobenzyl)-2,6,7-trioxabicyclo[2.2.2]octane (9)



Under N_2 atmosphere (3-methyloxetan-3-yl)methyl 2-(4-methyl-3-nitrophenyl)acetate (**8**; 2.00 g, 7.16 mmol) was dissolved in 20 ml dry DCM, cooled to $-10\text{ }^{\circ}\text{C}$ and 48% $\text{BF}_3\cdot\text{Et}_2\text{O}$ solution (200 μl , 716 μmol) was added dropwise. The reaction was stirred at room temperature for 2 h and stopped with trimethylamine (TEA; 1.00 ml, 7.16 mmol). The solvent was evaporated in vacuo and the residue was dissolved in ethyl acetate. The organic layer was washed with 5% ammonium chloride solution (150 ml), H_2O (2 x 100 ml), saturated sodium bicarbonate solution (2 x 100 ml), saturated sodium chloride solution (100 ml) and dried over magnesium sulfate. The solvent was evaporated in vacuo and the crude product was purified by flash column chromatography (cyclohexane/ethyl acetate, 1:2) to afford the product as colourless crystals (1.61 g, 5.79 mmol, 81%).

R_f : 0.48 (cyclohexane/ethyl acetate, 2:1).

T_m : $118\text{ }^{\circ}\text{C}$

$^1\text{H-NMR}$ (500.1 MHz, Acetone- d_6 , 300 K): δ = 7.85 (d, 4J = 1.7 Hz, 1 H, H -3), 7.47 (dd, 3J = 7.9 Hz, 4J = 1.78 Hz, 1 H, H -5), 7.34 (d, 3J = 7.9 Hz, 1 H, H -6), 3.86 (s, 6 H, C- CH_2 -O-), 2.98 (s, 2 H, C- CH_2 -C₄), 2.52 (s, 3H, C₁-CH₃), 0.79 (s, 3H, C-CH₃) ppm.

$^{13}\text{C-NMR}$ (125.8 MHz, Acetone- d_6 , 300 K): δ = 149.8 (C-2), 136.3 (C-5), 136.1 (C-4), 132.8 (C-6), 132.4 (C-1), 127.0 (C-3), 108.9 (O-C-CH₂), 73.1 (C-CH₂-O-), 42.5 (C-CH₂-C₄), 31.1 (C-CH₃), 19.7 (C₁-CH₃), 14.3 (C-CH₃).

IR (ATR): $\tilde{\nu}$ = 2966 (w), 2935 (w), 2886 (w), 1733 (m), 1526 (s), 1472 (w), 1464 (w), 1453 (w), 1440 (w), 1397 (w), 1384 (w), 1340 (w), 1309 (m), 1282 (m), 1264 (m), 1207 (m), 1190 (m), 1153 (m), 1043 (s), 1025 (s), 1011 (s), 984 (s), 928 (m), 923 (m), 895 (m), 886 (m), 851 (m), 837 (m), 818 (m), 768 (w), 755 (w), 718 (s), 688 (w), 675 (w) cm^{-1} .

MS (EI, 70 eV): m/z (%) = 279 (3), 249 (37), 179 (20), 150 (100).

HRMS (EI, 70 eV): $[\text{C}_{14}\text{H}_{17}\text{N}_1\text{O}_5]^+$, calc.: m/z = 279.11067, found: m/z = 279.11090.

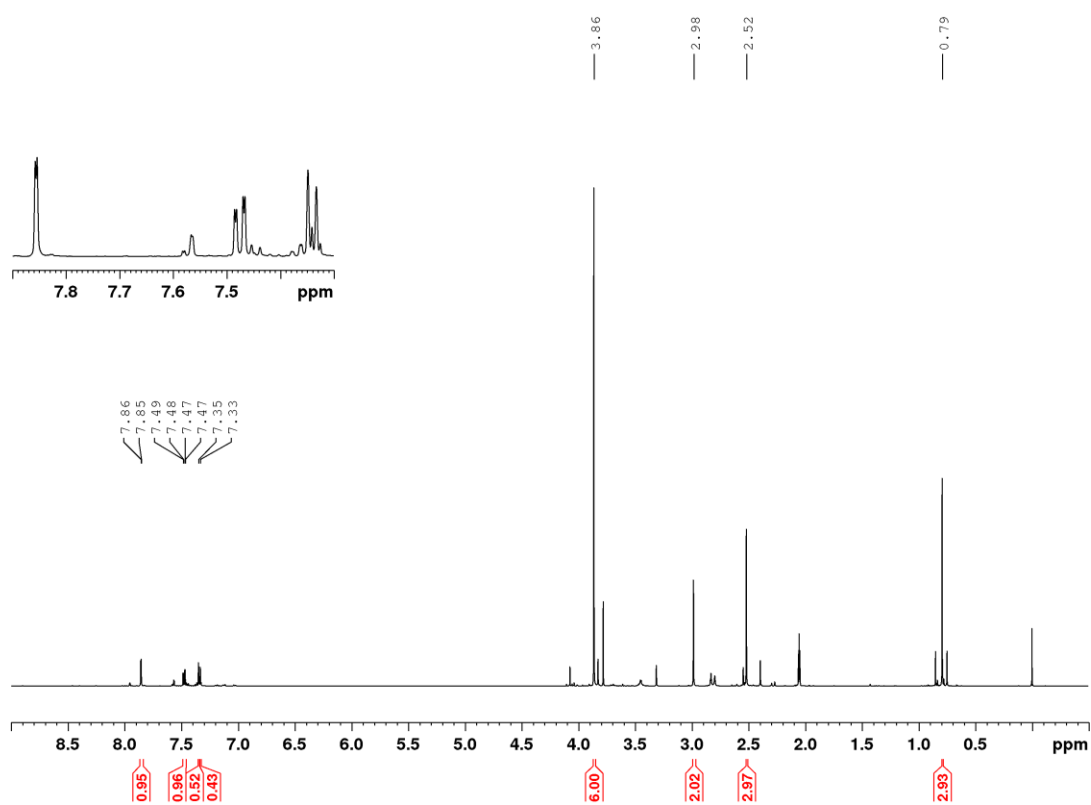


Fig. S 19: ¹H-NMR spectrum of compound **9** measured in deuterated acetone at 300 K.

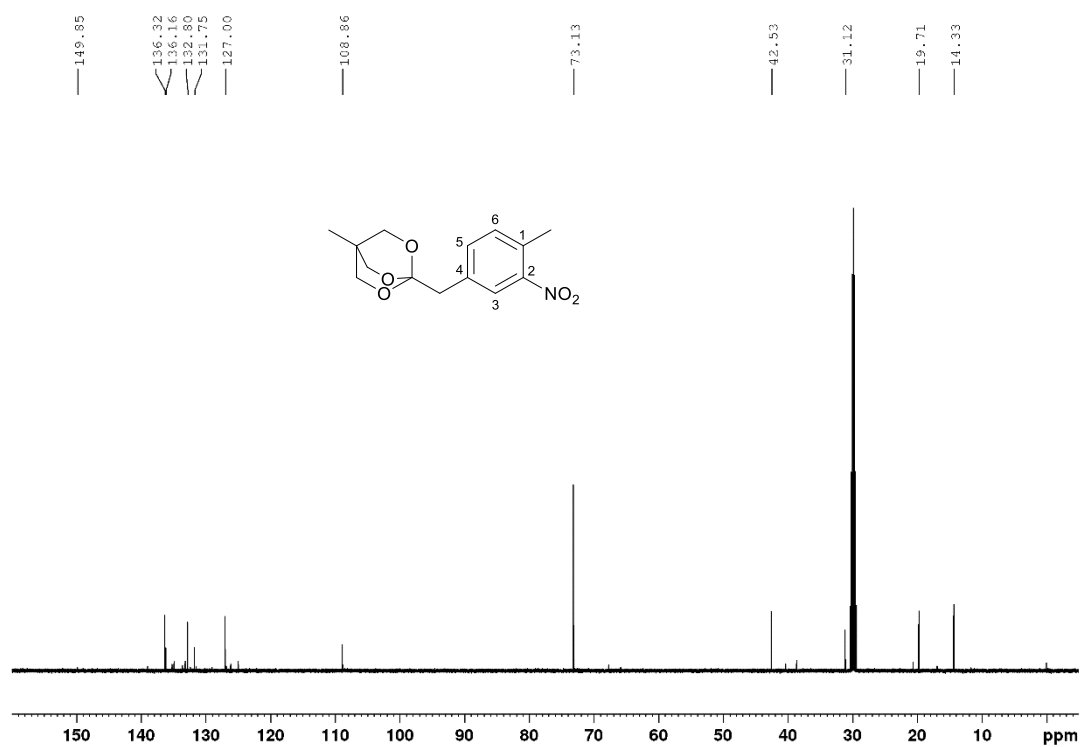
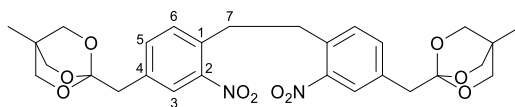


Fig. S 20: ¹³C-NMR spectrum of compound **9** measured in deuterated acetone at 300 K.

5.2.3. Synthesis of 1,2-bis(4-((4-methyl-2,6,7-trioxabicyclo[2.2.2]octan-1-yl)methyl)-2-nitrophenyl)-ethane (10)



Under N_2 atmosphere 4-methyl-1-(4-methyl-3-nitrobenzyl)-2,6,7-trioxabicyclo[2.2.2]octane (**9**; 1.50 g, 5.37 mmol) was dissolved in 30 ml dry tetrahydrofuran (THF) and cooled to $-5\text{ }^{\circ}\text{C}$, followed by addition of potassium butoxide (1.02 g, 9.13 mmol). The reaction was stirred for 40 s before addition of bromine (274 μl , 5.37 mmol). After further stirring for 10 min at room temperature the reaction mixture was added to a saturated sodium bicarbonate solution and extracted with ethyl acetate (3 x 100 ml). The combined organic layers were washed with 100 ml saturated sodium thiosulfate solution and dried over magnesium sulfate. The solvent was evaporated in vacuo and the crude product was purified by flash column chromatography (cyclohexane/ethyl acetate, 2:1) to afford the product as colourless crystals (680 mg, 2.44 mmol, 46%).

R_f : 0.28 (cyclohexane/ethyl acetate, 2:1).

T_m : $116\text{ }^{\circ}\text{C}$

$^1\text{H-NMR}$ (500.1 MHz, Acetone- d_6 , 300 K): δ = 7.86 (d, 4J = 1.7 Hz, 2 H, H -3), 7.55 (dd, 3J = 7.9 Hz, 4J = 1.8 Hz, 2 H, H -5), 7.42 (d, 3J = 7.9 Hz, 2 H, H -6), 3.87 (s, 12 H, C- CH_2 -O-), 3.20 (s, 4 H, C- CH_2 -C $_4$), 3.01 (s, 4H, H -7), 0.80 (s, 6H, C- CH_3) ppm.

$^{13}\text{C-NMR}^*$ (125.8 MHz, Acetone- d_6 , 300 K): δ = 149.8 (C-2), 136.5 (C-5), 136.8 (C-4), 134.5 (C-1), 132.1 (C-6), 127.2 (C-3), 108.9 (O-C- CH_2), 73.1 (C- CH_2 -O-), 42.6 (C- CH_2 -C $_4$), 34.2 (C-7), 31.1 (C- CH_3), 14.3 (C- CH_3).

IR (ATR): $\tilde{\nu}$ = 3310 (w), 2883 (w), 1726 (s), 1526 (w), 1525 (s), 1458 (w), 1341 (s), 1227 (m), 1169 (s), 1038 (s), 1002 (s), 924 (s), 846 (s), 817 (m), 764 (w), 732 (w), 679 (m) cm^{-1} .

MS (EI, 70 eV): m/z (%) = 556(8), 539 (9), 294 (32), 278 (100).

HRMS (EI, 70 eV): $[\text{C}_{28}\text{H}_{32}\text{N}_2\text{O}_{10}]^+$, calc.: m/z = 556.20569, found: m/z = 556.20124.

*Frequencies were determined from the carbon dimension of the HMBC spectrum.

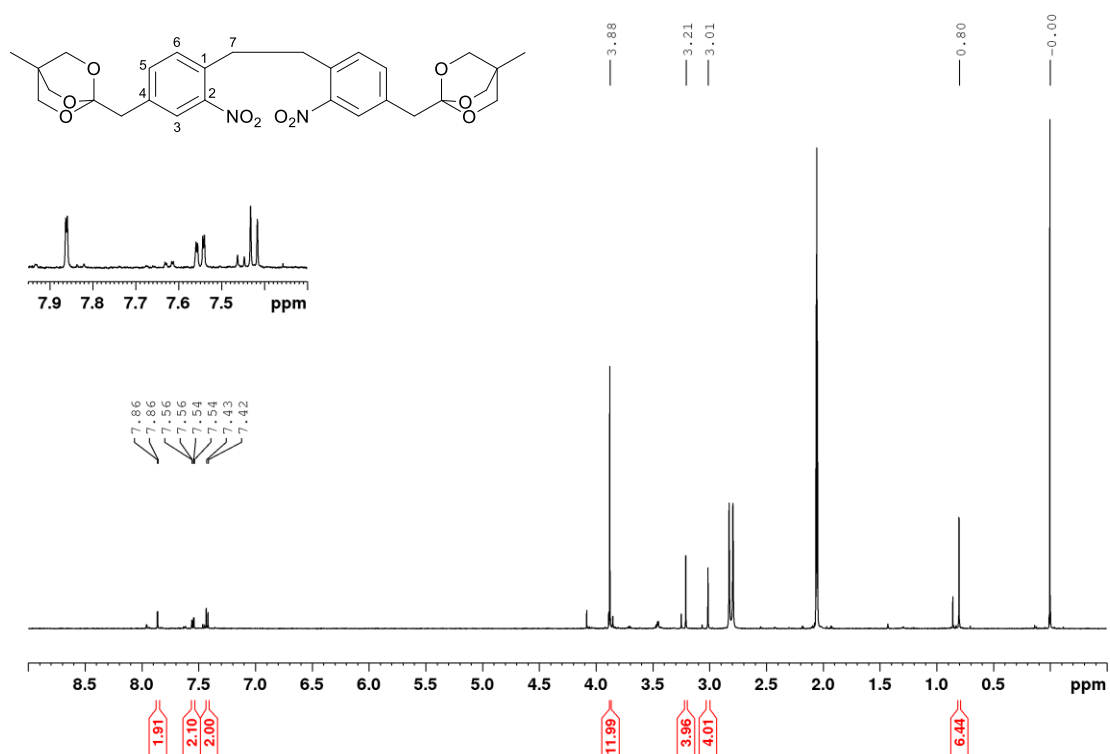


Fig. S 21: ^1H -NMR spectrum of compound **10** measured in deuterated acetone at 300 K.

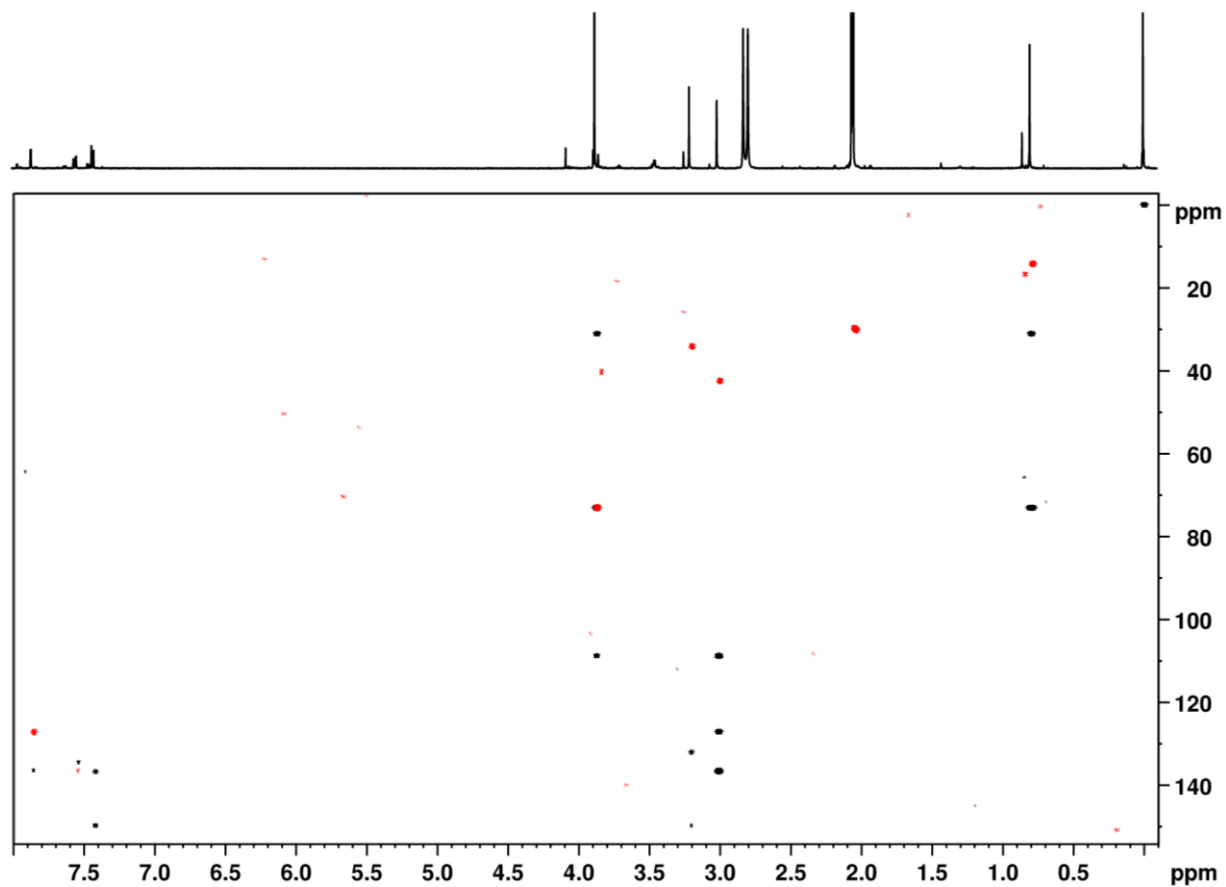
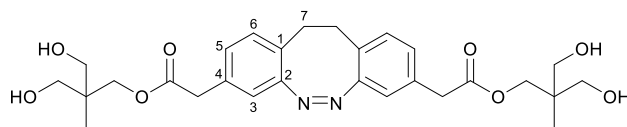


Fig. S 22: Overlay of the ^1H , ^{13}C -HSQC (red) and the ^1H , ^{13}C -HMBC (black) of compound **10** measured in deuterated acetone at 300 K.

5.2.4. Synthesis of (Z)-bis(3-hydroxy-2-(hydroxymethyl)-2-methylpropyl) 2,2'-(11,12-dihydrodibenzo[c,g][1,2]diazocine-3,8-diyl)diacetate (11)



A mixture of 1,2-bis(4-((4-methyl-2,6,7-trioxabicyclo[2.2.2]octan-1-yl)methyl)-2-nitrophenyl)ethane (**10**; 431 mg, 775 μmol), $\text{Ba}(\text{OH})_2 \cdot 8 \text{H}_2\text{O}$ (732 mg, 2.33 mmol) and zinc powder (811 mg, 12.4 mmol) were dissolved in an ethanol-water mixture (60 ml, 2:1) and stirred for 5 h under reflux. After filtration through Celite and evaporation of the solvent under reduced pressure, the crude product was dissolved in 90 ml 0.1 M methanolic NaOH solution, CuCl_2 (20 mg, 149 μmol) was added, and air was blown through the solution for 4 h. The reaction was added to a saturated sodium bicarbonate solution, neutralized with 1 M HCl solution and extracted with DCM (3 x 75 ml). The combined organic layers were washed with a saturated sodium chloride solution and dried over magnesium sulfate. The solvent was evaporated in vacuo and the crude product was purified by flash column chromatography (cyclohexane/ethyl acetate, 2:1) to afford the product as a yellow solid (161 mg, 326 μmol , 42%).

R_f : 0.22 (cyclohexane/ethyl acetate, 2:1).

T_m : 132 $^{\circ}\text{C}$

$^1\text{H-NMR}$ (500.1 MHz, CDCl_3 , 300 K): δ = 6.96 (s, 4 H, *H*-5, *H*-6), 6.79 (d, 3J = 7.9 Hz, 2 H, *H*-3), 4.13 (s, 4 H, $\text{COO-CH}_2\text{-C}$), 3.57 (s, 4 H, $\text{COO-CH}_2\text{-C}_4$), 3.44 (d, 3J = 11.4 Hz, 4 H, $\text{CH}_2\text{-OH}$), 3.36 (d, 3J = 11.4 Hz, 4 H, $\text{CH}'_2\text{-OH}$), 2.85 (s, 4 H, *H*-7), 2.41 (s, 4H, $\text{CH}_2\text{-OH}$), 0.71 (s, 6H, C-CH_3) ppm.

$^{13}\text{C-NMR}$ (125.8 MHz, CDCl_3 , 300 K): δ = 172.0 (COO), 155.3 (*C*-2), 132.5 (*C*-4), 130.0 (*C*-5), 128.1 (*C*-5), 127.0 (*C*-1), 125.6 (*C*-5), 119.8 (*C*-3), 67.5 ($\text{CH}_3\text{-C-(CH}_2\text{)}_3$) 67.4 ($\text{CH}_2\text{-OH}$) 66.9 ($\text{COO-CH}_2\text{-C}$), 40. ($\text{COO-CH}_2\text{-C}_4$), 31.4 (*C*-7), 16.7(C-CH_3) ppm.

IR (ATR): $\tilde{\nu}$ = 3312 (w), 2933 (w), 2880 (w), 1730 (s), 1458 (w), 1396 (w), 1334 (m), 1303 (m), 1253 (m), 1191 (m), 1151 (w), 1038 (s), 990 (s), 892 (w), 835 (w), 702 (w) cm^{-1} .

HRMS (HR-ESI): $[\text{C}_{28}\text{H}_{36}\text{O}_8\text{N}_2 + \text{NH}_4]^+$, calc.: m/z = 546.2806, found: m/z = 546.28099.

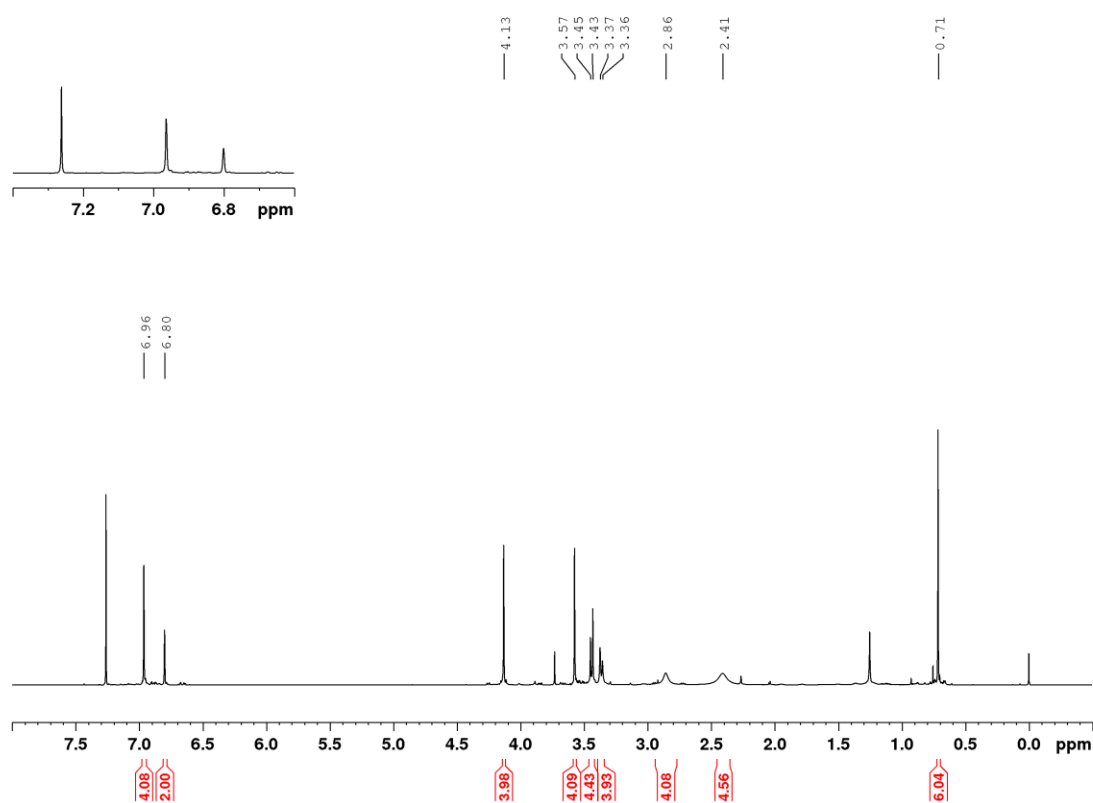


Fig. S 23: ¹H-NMR spectrum of compound **11** measured in deuterated chloroform at 300 K.

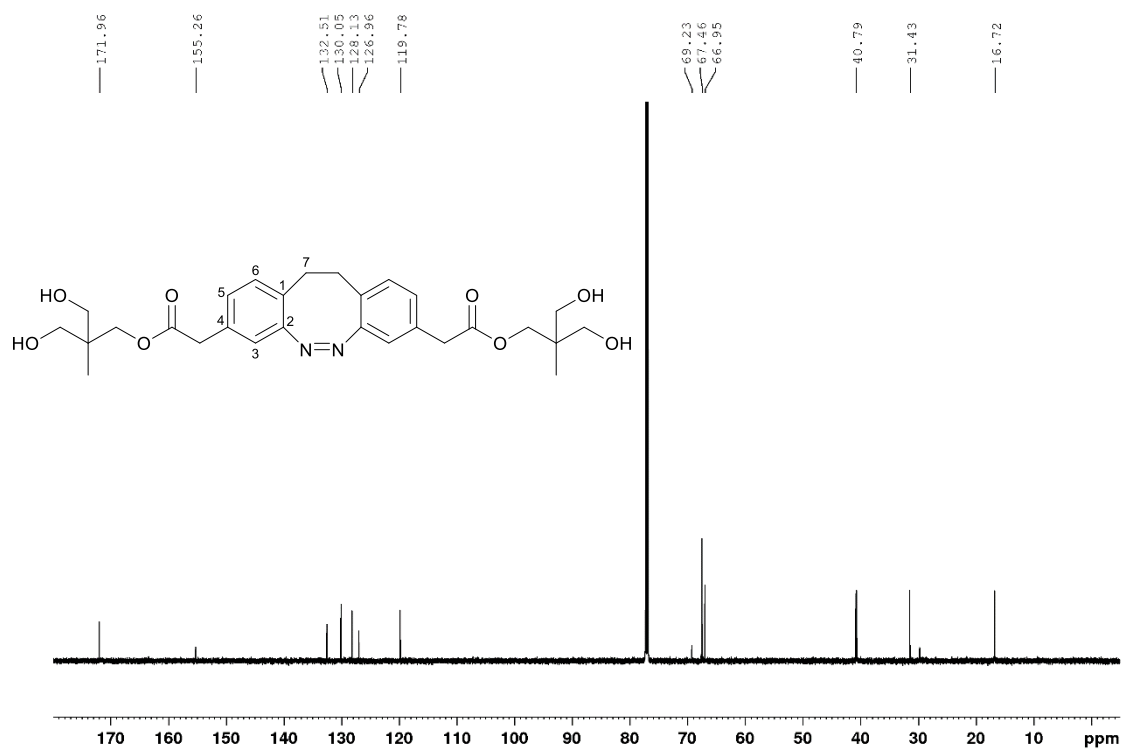


Fig. S 24: ¹³C-NMR spectrum of compound **11** measured in chloroform at 300 K.

5.2.4.1. Determination of the PSS of diazocine **11**

The PSS at 385 nm of diazocine **11** was determined in MeCN by integration of the *H*-3 signals of the *cis*- and the *trans*- isomer in the 1D-¹H-NMR spectrum of the PSS at 385 nm (Fig. S 25, red).

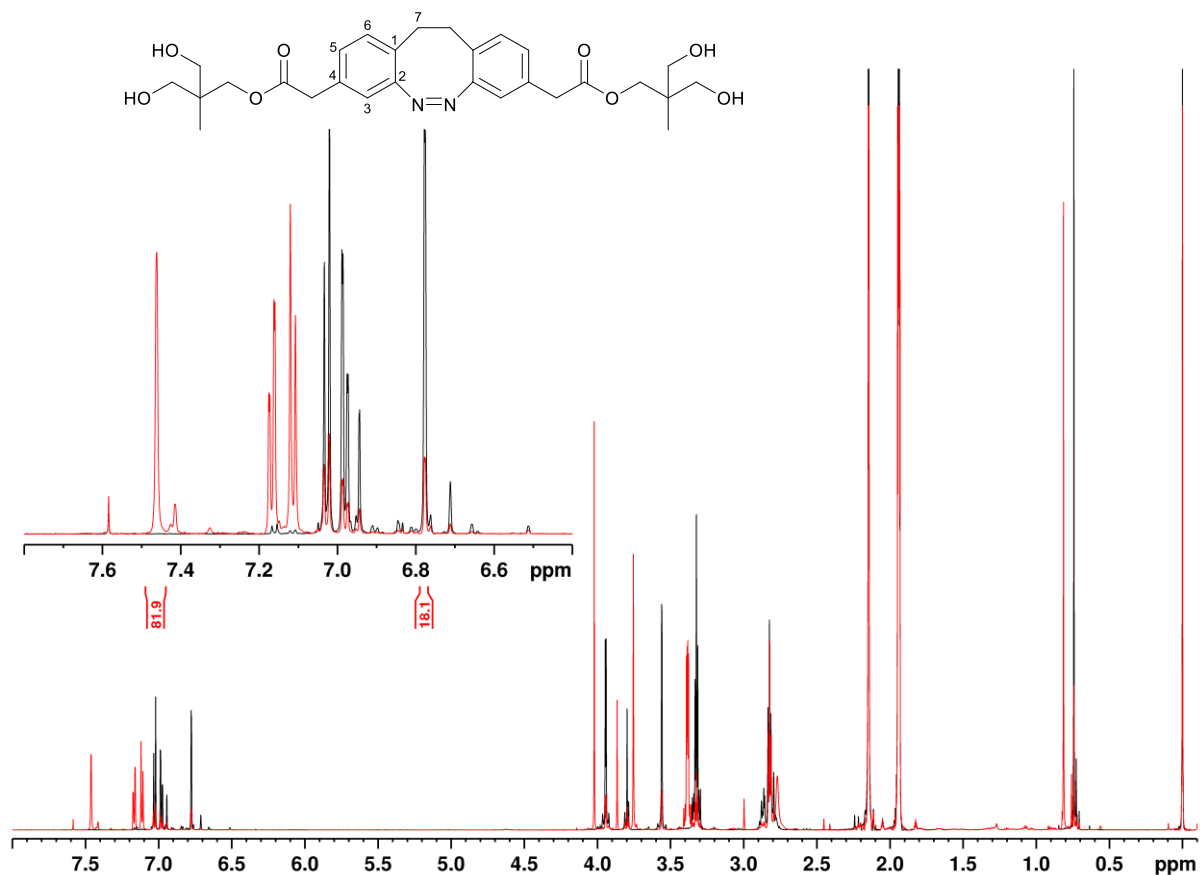


Fig. S 25: Overlay of the 1D-¹H-NMR spectra of diazocine **11** dissolved in MeCN-d₃. The spectrum displayed in black was recorded immediately after irradiation to the PSS at 530 nm, whereas the red spectrum represents the PSS at 385 nm. The expansion shows the aromatic region from which the PSS at 385 nm was determined by integration of the doublet at 7.46 ppm which represents the *trans*-species and at 6.78 ppm which represents the *cis*-isomer.

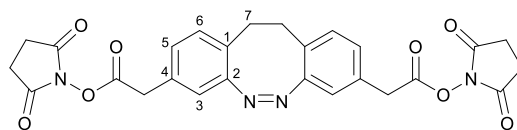
cis-diazocine **11** (black)

¹H-NMR (500.1 MHz, MeCN-d₃, 298 K): δ = 7.03 (d, ³*J* = 7.9 Hz, 2 H, *H*-6), 6.98 (dd, ³*J* = 7.9 Hz, ⁴*J* = 1.6 Hz, 2 H, *H*-5), 6.79 (d, ⁴*J* = 1.4 Hz, 2 H, *H*-3), 3.98-3.92 (m, 4 H, COO-CH₂-C), 3.56 (s, 4 H, COO-CH₂-C₄), 3.32 (m_c, 8 H, CH₂-OH, CH'₂-OH), 2.88-2.76 (m, 8 H, *H*-7, CH₂-OH), 0.74 (s, 6H, C-CH₃) ppm.

trans-diazocine **11** (red)

¹H-NMR (500.1 MHz, MeCN-d₃, 298 K): δ = 7.46 (s, 2 H, *H*-3), 7.17 (dd, ³*J* = 7.8 Hz, ⁴*J* = 1.6 Hz, 2 H, *H*-5), 7.11 (d, ³*J* = 7.8 Hz, 2 H, *H*-6), 4.02 (s, 4 H, COO-CH₂-C), 3.75 (s, 4 H, COO-CH₂-C₄), 3.38 (m_c, 8 H, CH₂-OH, CH'₂-OH), 2.86-2.72 (m, 8 H, *H*-7, CH₂-OH), 0.81 (s, 6H, C-CH₃) ppm.

5.2.5. Synthesis of (Z)-bis(2,5-dioxopyrrolidin-1-yl) 2,2'-(11,12-dihydrodibenzo[c,g][1,2]diazocine-3,8-diyl)diacetate (1)



(Z)-bis(3-hydroxy-2-(hydroxymethyl)-2-methylpropyl) 2,2'-(11,12-dihydrodibenzo[c,g][1,2]diazocine-3,8-diyl)diacetate (**11**; 182 mg, 345 μ mol) was dissolved in 5 ml MeOH/H₂O (4:1) and 5.5 ml 10% calcium carbonate solution was added. The reaction was stirred over night at room temperature. Afterwards the reaction was acidified to pH = 2 with 1 M hydrogen chloride solution and extracted with ethyl acetate (3 x 10 ml). The combined organic layers were washed with saturated sodium chloride solution, dried over magnesium sulfate and the solvent was evaporated in vacuo. Under N₂ atmosphere the crude product was dissolved in 5 ml DMF. 1-Ethyl-3-(3-dimethylaminopropyl)carbodiimide (EDC; 661 mg, 3.45 mmol) and *N*-hydroxysuccinimide (NHS; 199 mg, 1.73 mmol) were added at room temperature and the reaction stirred for 1 h. The reaction was added to 50 ml H₂O and extracted with (2 x 30 ml) DCM. The combined organic layers were washed with 10 % sodium bicarbonate solution, (2 x 50 ml) 0.1 M hydrogen chloride solution, 50 ml sodium chloride solution and dried over magnesium sulfate. The solvent was evaporated in vacuo and the crude product was purified by flash column chromatography (cyclohexane/ethyl acetate, 1:2) to afford the product as a yellow solid (45 mg, 87 μ mol, 25%).

R_f: 0.43 (cyclohexane/ethyl acetate, 1:2)

T_m: 190 °C

¹H-NMR (500.1 MHz, DMSO-d₆, 300 K): δ = 7.12 (d, ³*J* = 7.9 Hz, 2 H, *H*-6), 7.06 (dd, ³*J* = 7.9 Hz, ⁴*J* = 1.5 Hz 2 H, *H*-5), 6.89 (d, ⁴*J* = 1.4 Hz, 2 H, *H*-3), 4.05 (s, 4 H, COO-CH₂-C₄), 2.82-2.81 (m, 12 H, *H*-7, CH₂-CH'₂) ppm.

¹³C-NMR (125.8 MHz, DMSO-d₆, 300 K): δ = 170.0 (CO), 167.0 (COO), 154.7 (C-2), 130.9 (C-1) 130.0 (C-6), 128.1 (C-5), 127 (C-4) 119.87 (C-3), 35.7 (COO-CH₂-C₄), 30.5 (C-7), 25.4 (CH₂-C'₂) ppm.

IR (ATR): $\tilde{\nu}$ = 2925 (w), 1812 (w), 1781 (w), 1745 (s), 1727 (s), 1522 (w), 1497 (w), 1457 (w), 1426 (w), 1355 (m), 1205 (s), 1109 (m), 1062 (s), 991 (m), 963 (m), 892 (w), 877 (w), 846 (w), 807 (s), 758 (w), 738 (w), 646 (s) cm⁻¹.

HRMS (HR-ESI): [C₂₈H₃₆O₈N₂ + NH₄]⁺, *m/z* = calc.: 536.1772, found 536.17759.

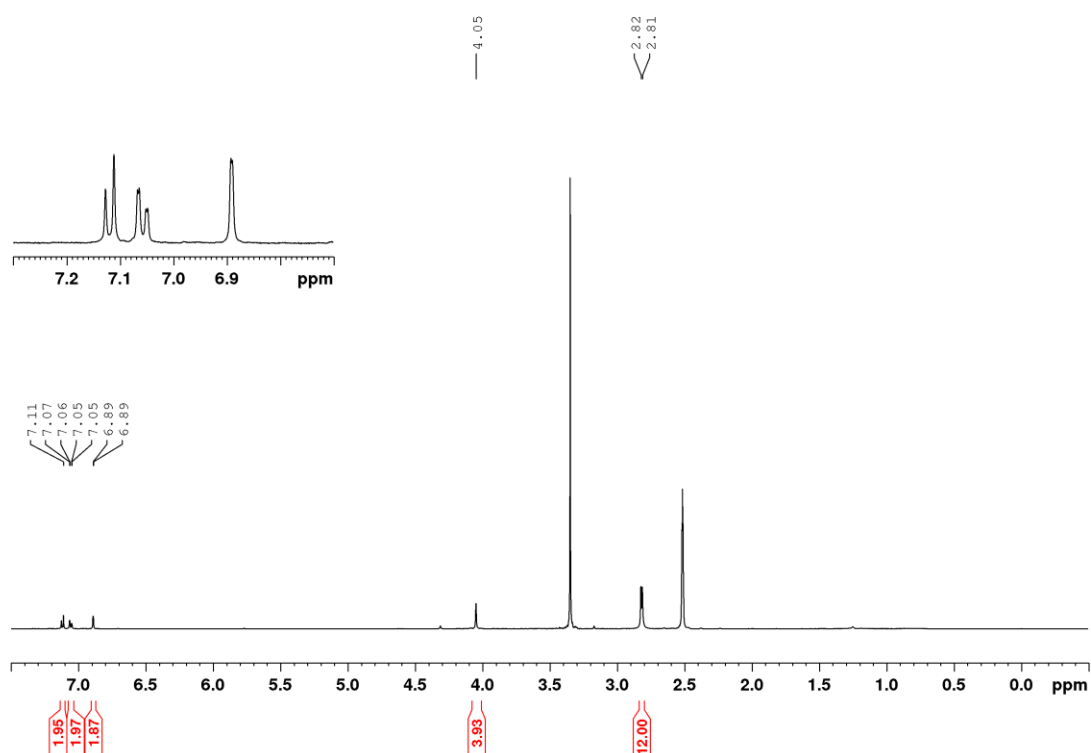


Fig. S 26: ¹H-NMR spectrum of compound **1** measured in deuterated DMSO at 300 K.

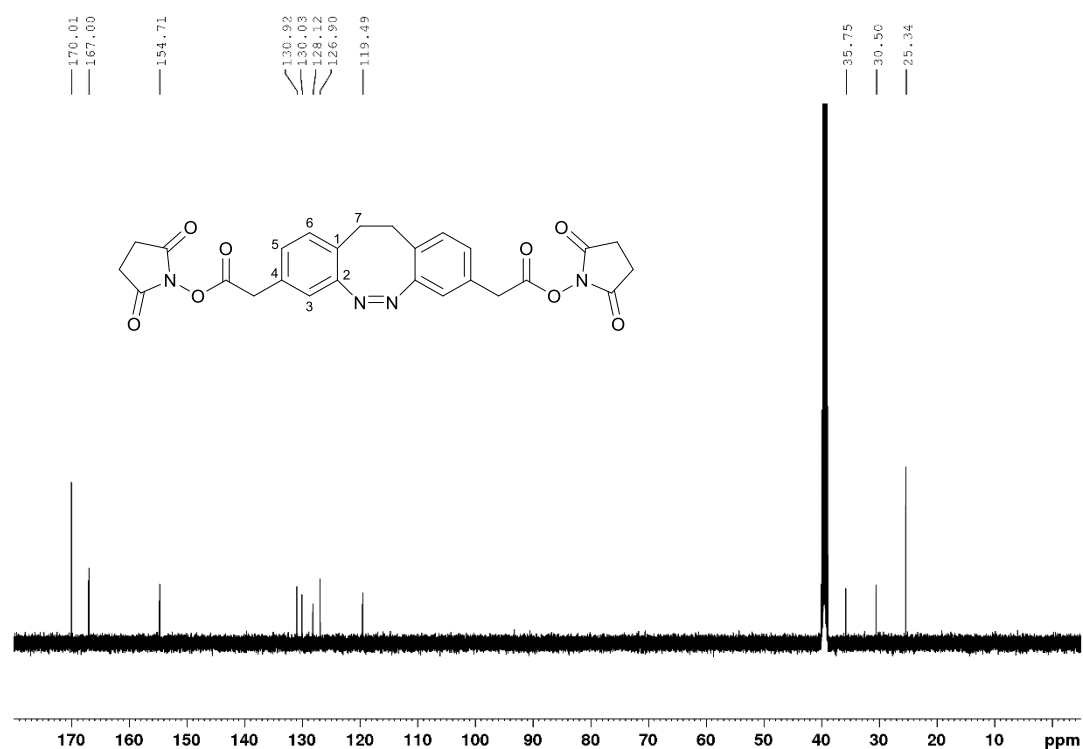


Fig. S 27: ¹³C-NMR spectrum of compound **1** measured in deuterated DMSO at 300 K.

6. References

1. J. L. Markley, A. Bax, Y. Arata, C. W. Hilbers, R. Kaptein, B. D. Sykes, P. E. Wright and K. Wüthrich, *Pure and Applied Chemistry*, 1998, **70**(1), 117.
2. J. W. Neidigh, R. M. Fesinmeyer and N. H. Andersen, *Nat. Struct. Biol.*, 2002, **9**(6), 425.
3. B. Barua, J. C. Lin, V. D. Williams, P. Kummier, J. W. Neidigh and N. H. Andersen, *Protein Eng. Des. Sel.*, 2008, **21**(3), 171.
4. D. S. Wishart, C. G. Bigam, A. Holm, R. S. Hodges and B. D. Sykes, *J. Biomol. NMR*, 1995, **5**(1), 67.
5. A. Bundi and K. Wüthrich, *Biopolymers*, 1979, **18**(2), 285.

7. Bibliography

- [001] T. L. Blundell, J. E. Pitts, I. J. Tickle, S. P. Wood, C. W. Wu, X-ray analysis (1.4-Å resolution) of avian pancreatic polypeptide: Small globular protein hormone, *Proc. Natl. Acad. Sci. USA* **1981**, *7*, 4175–4179. DOI: 10.1073/pnas.78.7.4175.
- [002] Rie Nygaard, Steen Nielbo, Thue W. Schwartz, Flemming M. Poulsen, The PP-fold solution structure of human polypeptide YY and human PYY3-36 as determined by NMR, *Biochemistry* **2006**, *27*, 8350–8357. DOI: 10.1021/bi060359l.
- [003] Xiang Li, Michael J. Sutcliffe, Thue W. Schwartz, Christopher M. Dobson, Sequence-specific proton NMR assignments and solution structure of bovine pancreatic polypeptide, *Biochemistry* **1992**, *4*, 1245–1253. DOI: 10.1021/bi00119a038.
- [004] David A. Keire, Mitsuo Kobayashi, Travis E. Solomon, Joseph R. Reeve, Jr., Solution structure of monomeric peptide YY supports the functional significance of the PP-fold, *Biochemistry* **2000**, *32*, 9935–9942. DOI: 10.1021/bi992576a.
- [005] Ian Glover, Illyas Haneef, Jim Pitts, Steve Wood, David Moss, Ian Tickle, Tom Blundell, Conformational flexibility in a small globular hormone: X-ray analysis of avian pancreatic polypeptide at 0.98-Å resolution, *Biopolymers (Pept. Sci.)* **1983**, *1*, 293–304. DOI: 10.1002/bip.360220138.
- [006] Mirjam Lerch, Margot Mayrhofer, Oliver Zerbe, Structural similarities of micelle-bound peptide YY (PYY) and neuropeptide Y (NPY) are related to their affinity profiles at the Y receptors, *J. Mol. Biol.* **2004**, *5*, 1153–1168. DOI: 10.1016/j.jmb.2004.04.032.
- [007] Milton E. Noelken, Paul J. Chang, Joe R. Kimmel, Conformation and association of pancreatic polypeptide from three species, *Biochemistry* **1980**, *9*, 1838–1843. DOI: 10.1021/bi00550a017.
- [008] Paul J. Chang, Milton E. Noelken, Joe R. Kimmel, Reversible dimerization of avian pancreatic polypeptide, *Biochemistry* **1980**, *9*, 1844–1849. DOI: 10.1021/bi00550a018.
- [009] Alexey Neumoin, Jiri Mares, Mirjam Lerch-Bader, Reto Bader, Oliver Zerbe, Probing the formation of stable tertiary structure in a model miniprotein at atomic resolution: Determinants of stability of a helical hairpin, *J. Am. Chem. Soc.* **2007**, *28*, 8811–8817. DOI: 10.1021/ja0716960.
- [010] David A. Keire, Peter Mannon, Mitsuo Kobayashi, John H. Walsh, Travis E. Solomon, Joseph R. Reeve, Jr., Primary structures of PYY, [Pro³⁴]PYY, and PYY-(3-36) confer different conformations and receptor selectivity, *Am. J. Physiol. Gastrointest. Liver Physiol.* **2000**, *1*, G126–G131. DOI: 10.1152/ajpgi.2000.279.1.G126.
- [011] Jacob S. Appelbaum, Jonathan R. LaRochelle, Betsy A. Smith, Daniel M. Balkin, Justin M. Holub, Alanna Schepartz, Arginine topology controls escape of minimally cationic proteins from early endosomes to the cytoplasm, *Chem. Biol.* **2012**, *7*, 819–830. DOI: 10.1016/j.chembiol.2012.05.022.
- [012] Eva S. Cobos, M. T. Pisabarro, M. C. Vega, Emmanuel Lacroix, Luis Serrano, Javier Ruiz-Sanz, Jose C. Martinez, A miniprotein scaffold used to assemble the polyproline II binding epitope recognized by SH3 domains, *J. Mol. Biol.* **2004**, *1*, 355–365. DOI: 10.1016/j.jmb.2004.06.078.
- [013] Neal J. Zondlo, Alanna Schepartz, Highly specific DNA recognition by a designed miniature protein, *J. Am. Chem. Soc.* **1999**, *29*, 6938–6939. DOI: 10.1021/ja990968z.
- [014] Jason W. Chin, Alanna Schepartz, Concerted evolution of structure and function in a miniature protein, *J. Am. Chem. Soc.* **2001**, *12*, 2929–2930. DOI: 10.1021/ja0056668.
- [015] Jin K. Montclare, Alanna Schepartz, Miniature homeodomains: High specificity without an N-terminal arm, *J. Am. Chem. Soc.* **2003**, *12*, 3416–3417. DOI: 10.1021/ja028628s.
- [016] Loretta Yang, Alanna Schepartz, Relationship between folding and function in a sequence-specific miniature DNA-binding protein, *Biochemistry* **2005**, *20*, 7469–7478. DOI: 10.1021/bi050121h.
- [017] Jason W. Chin, Alanna Schepartz, Design and evolution of a miniature Bcl-2 binding protein, *Angew. Chem. Int. Ed.* **2001**, *20*, 3806–3809. DOI: 10.1002/1521-3773(20011015)40:20<3806::AID-ANIE3806>3.0.CO;2-B.
- [018] Stacey E. Rutledge, Heather M. Volkman, Alanna Schepartz, Molecular recognition of protein surfaces: High affinity ligands for the CBP KIX domain, *J. Am. Chem. Soc.* **2003**, *47*, 14336–14347. DOI: 10.1021/ja034508o.
- [019] Dasantila Golemi-Kotra, Rachel Mahaffy, Matthew J. Footer, Jennifer H. Holtzman, Thomas D. Pollard, Julie A. Theriot, Alanna Schepartz, High affinity, paralog-specific recognition of the Mena EVH1 domain by a miniature protein, *J. Am. Chem. Soc.* **2004**, *1*, 4–5. DOI: 10.1021/ja037954k.
- [020] Nobuhisa Shimba, Anson M. Nomura, Alan B. Marnett, Charles S. Craik, Herpesvirus protease inhibition by dimer disruption, *J. Virol.* **2004**, *12*, 6657–6665. DOI: 10.1128/JVI.78.12.6657–6665.2004.
- [021] Anja C. Gemperli, Stacey E. Rutledge, Abby Maranda, Alanna Schepartz, Paralog-selective ligands for Bcl-2 proteins, *J. Am. Chem. Soc.* **2005**, *6*, 1596–1597. DOI: 10.1021/ja0441211.

- [022] Tanya L. Schneider, Rebecca S. Mathew, Kevin P. Rice, Kazuhiko Tamaki, John L. Wood, Alanna Schepartz, Increasing the kinase specificity of k252a by protein surface recognition, *Org. Lett.* **2005**, *9*, 1695–1698. DOI: 10.1021/ol050179o.
- [023] Heather M. Volkman, Stacey E. Rutledge, Alanna Schepartz, Binding mode and transcriptional activation potential of high affinity ligands for the CBP KIX domain, *J. Am. Chem. Soc.* **2005**, *127*, 4649–4658. DOI: 10.1021/ja042761y.
- [024] Joshua A. Kritzer, Reena Zutshi, Mingtatt Cheah, F. A. Ran, Rachel Webman, Taritree M. Wongjirad, Alanna Schepartz, Miniature protein inhibitors of the p53-hDM2 interaction, *ChemBioChem* **2006**, *7*, 29–31. DOI: 10.1002/cbic.200500324.
- [025] Crystal D. Zellefrow, Jennifer S. Griffiths, Sarmistha Saha, Abby M. Hodges, Jessica L. Goodman, Joshiawa Paulk, Joshua A. Kritzer, Alanna Schepartz, Encodable activators of SRC family kinases, *J. Am. Chem. Soc.* **2006**, *128*, 16506–16507. DOI: 10.1021/ja0672977.
- [026] Jennifer H. Holtzman, Kamil Woronowicz, Dasantila Golemi-Kotra, Alanna Schepartz, Miniature protein ligands for EVH1 domains: Interplay between affinity, specificity, and cell motility, *Biochemistry* **2007**, *46*, 13541–13553. DOI: 10.1021/bi700975f.
- [027] Nina M. Link, Cornelia Hunke, Jonathan W. Mueller, Jutta Eichler, Peter Bayer, The solution structure of pGolemi, a high affinity Mena EVH1 binding miniature protein, suggests explanations for paralog-specific binding to Ena/VASP homology (EVH) 1 domains, *Biological chemistry* **2009**, *380*, 417–426. DOI: 10.1515/BC.2009.045.
- [028] Elissa M. Hobert, Alanna Schepartz, Rewiring kinase specificity with a synthetic adaptor protein, *J. Am. Chem. Soc.* **2012**, *134*, 3976–3978. DOI: 10.1021/ja211089v.
- [029] Susan E. Taylor, Trevor J. Rutherford, Rudolf K. Allemann, Design, synthesis and characterisation of a peptide with oxaloacetate decarboxylase activity, *Bioorg. Med. Chem. Lett.* **2001**, *12*, 2631–2635. DOI: 10.1016/S0960-894X(01)00519-4.
- [030] Susan E. Taylor, Trevor J. Rutherford, Rudolf K. Allemann, Design of a folded, conformationally stable oxaloacetate decarboxylase, *J. Chem. Soc., Perkin Trans. 2* **2002**, *4*, 751–755. DOI: 10.1039/B200057C.
- [031] Andrew J. Nicoll, Rudolf K. Allemann, Nucleophilic and general acid catalysis at physiological pH by a designed miniature esterase, *Org. Biomol. Chem.* **2004**, *2*, 2175–2180. DOI: 10.1039/B404730C.
- [032] Simon Jurt, Andreas Aemissegger, Peter Güntert, Oliver Zerbe, Donald Hilvert, A photoswitchable miniprotein based on the sequence of avian pancreatic polypeptide, *Angew. Chem. Int. Ed.* **2006**, *45*, 6297–6300. DOI: 10.1002/anie.200602084.
- [033] Douglas S. Daniels, Alanna Schepartz, Intrinsically cell-permeable miniature proteins based on a minimal cationic PPII motif, *J. Am. Chem. Soc.* **2007**, *129*, 14578–14579. DOI: 10.1021/ja0772445.
- [034] Betsy A. Smith, Douglas S. Daniels, Abigail E. Coplin, Gregory E. Jordan, Lynn M. McGregor, Alanna Schepartz, Minimally cationic cell-permeable miniature proteins via alpha-helical arginine display, *J. Am. Chem. Soc.* **2008**, *130*, 2948–2949. DOI: 10.1021/ja800074v.
- [035] Jason W. Chin, Robert M. Grotzfeld, Miles A. Fabian, Alanna Schepartz, Methodology for optimizing functional miniature proteins based on avian pancreatic polypeptide using phage display, *Bioorg. Med. Chem. Lett.* **2001**, *12*, 1501–1505. DOI: 10.1016/S0960-894X(01)00139-1.
- [036] Tina Shahian, Gregory M. Lee, Ana Lazic, Leggy A. Arnold, Priya Velusamy, Christina M. Roels, R. K. Guy, Charles S. Craik, Inhibition of a viral enzyme by a small-molecule dimer disruptor, *Nat. Chem. Biol.* **2009**, *5*, 640–646. DOI: 10.1038/nchembio.192.
- [037] Gregory M. Lee, Tina Shahian, Aida Baharuddin, Jonathan E. Gable, Charles S. Craik, Enzyme inhibition by allosteric capture of an inactive conformation, *J. Mol. Biol.* **2011**, *410*, 999–1016. DOI: 10.1016/j.jmb.2011.06.032.
- [038] Jonathan E. Gable, Gregory M. Lee, Priyadarshini Jaishankar, Brian R. Hearn, Christopher A. Waddling, Adam R. Renslo, Charles S. Craik, Broad-spectrum allosteric inhibition of herpesvirus proteases, *Biochemistry* **2014**, *53*, 4648–4660. DOI: 10.1021/bi5003234.
- [039] Timothy M. Acker, Jonathan E. Gable, Markus-Frederik Bohn, Priyadarshini Jaishankar, Michael C. Thompson, James S. Fraser, Adam R. Renslo, Charles S. Craik, Allosteric Inhibitors, Crystallography, and Comparative Analysis Reveal Network of Coordinated Movement across Human Herpesvirus Proteases, *J. Am. Chem. Soc.* **2017**, *139*, 11650–11653. DOI: 10.1021/jacs.7b04030.
- [040] Rebecca F. Wissner, Angela Steinauer, Susan L. Knox, Alexander D. Thompson, Alanna Schepartz, Fluorescence correlation spectroscopy reveals efficient cytosolic delivery of protein cargo by cell-permeant miniature proteins, *ACS central science* **2018**, *4*, 1379–1393. DOI: 10.1021/acscentsci.8b00446.
- [041] Justin M. Holub, Small scaffolds, big potential: Developing miniature proteins as therapeutic agents, *Drug Dev. Res.* **2017**, *78*, 268–282. DOI: 10.1002/ddr.21408.

7. Bibliography

- [042] Jonathan W. Neidigh, R. M. Fesinmeyer, Kathryn S. Prickett, Niels H. Andersen, Exendin-4 and glucagon-like-peptide-1: NMR Structural comparisons in the solution and micelle-associated states, *Biochemistry* **2001**, *44*, 13188–13200. DOI: 10.1021/bi010902s.
- [043] Grant M. Bray, Exenatide, *Am. J. Health Syst. Pharm.* **2006**, *5*, 411–418. DOI: 10.2146/ajhp050459.
- [044] Jens J. Holst, The physiology of glucagon-like peptide 1, *Physiol. Rev.* **2007**, *4*, 1409–1439. DOI: 10.1152/physrev.00034.2006.
- [045] Jie Chen, Ling Yu, Liping Wang, Xuexun Fang, Li Li, Wei Li, Stability of synthetic exendin-4 in human plasma *in vitro*, *Protein Pept. Lett.* **2007**, *1*, 19–25. DOI: 10.2174/092986607779117272.
- [046] Jonathan W. Neidigh, R. M. Fesinmeyer, Niels H. Andersen, Designing a 20-residue protein, *Nat. Struct. Biol.* **2002**, *6*, 425–430. DOI: 10.1038/nsb798.
- [047] Bipasha Barua, Jasper C. Lin, Victoria D. Williams, Phillip Kummeler, Jonathan W. Neidigh, Niels H. Andersen, The Trp-cage: Optimizing the stability of a globular miniprotein, *Protein Eng. Des. Sel.* **2008**, *3*, 171–185. DOI: 10.1093/protein/gzm082.
- [048] Jasper C. Lin, Bipasha Barua, Niels H. Andersen, The helical alanine controversy: An (Ala)₆ insertion dramatically increases helicity, *J. Am. Chem. Soc.* **2004**, *42*, 13679–13684. DOI: 10.1021/ja047265o.
- [049] Petra Rovó, Viktor Farkas, Pál Stráner, Mária Szabó, Ágnes Jermendy, Orsolya Hegyi, Gábor K. Tóth, András Perczel, Rational design of α -helix-stabilized exendin-4 analogues, *Biochemistry* **2014**, *22*, 3540–3552. DOI: 10.1021/bi500033c.
- [050] Yuqi Liu, Zhiguo Liu, Elliot Androphy, Jason Chen, James D. Baleja, Design and characterization of helical peptides that inhibit the E6 protein of papillomavirus, *Biochemistry* **2004**, *23*, 7421–7431. DOI: 10.1021/bi049552a.
- [051] Emma J. Crosbie, Mark H. Einstein, Silvia Franceschi, Henry C. Kitchener, Human papillomavirus and cervical cancer, *The Lancet* **2013**, *9895*, 889–899. DOI: 10.1016/S0140-6736(13)60022-7.
- [052] Cary A. Moody, Laimonis A. Laimins, Human papillomavirus oncoproteins: Pathways to transformation, *Nat. Rev. Cancer* **2010**, *8*, 550–560. DOI: 10.1038/nrc2886.
- [053] Katia Zanier, Sebastian Charbonnier, Abdellahi O. M.'h. O. Sidi, Alastair G. McEwen, Maria G. Ferrario, Pierre Poussin-Courmontagne, Vincent Cura, Nicole Brimer, Khaled O. Babah, Tina Ansari, Isabelle Muller, Roland H. Stote, Jean Cavarelli, Scott Vande Pol, Gilles Travé, Structural basis for hijacking of cellular LxxLL motifs by papillomavirus E6 oncoproteins, *Science* **2013**, *6120*, 694–698. DOI: 10.1126/science.1229934.
- [054] Denise Martinez-Zapien, Francesc X. Ruiz, Juline Poirson, André Mitschler, Juan Ramirez, Anne Forster, Alexandra Cousido-Siah, Murielle Masson, Scott Vande Pol, Alberto Podjarny, Gilles Travé, Katia Zanier, Structure of the E6/E6AP/p53 complex required for HPV-mediated degradation of p53, *Nature* **2016**, *7587*, 541–545. DOI: 10.1038/nature16481.
- [055] Massimo Tommasino, Rosita Accardi, Sandra Caldeira, Wen Dong, Ilaria Malanchi, Anouk Smet, Ingeborg Zehbe, The role of TP53 in cervical carcinogenesis, *Hum. Mutat.* **2003**, *3*, 307–312. DOI: 10.1002/humu.10178.
- [056] Xiaobing Be, Yihui Hong, Julia Wei, Elliot J. Androphy, Jason J. Chen, James D. Baleja, Solution structure determination and mutational analysis of the papillomavirus E6 interacting peptide of E6AP, *Biochemistry* **2001**, *5*, 1293–1299. DOI: 10.1021/bi0019592.
- [057] Matthias Lipfert, *Dissertation*, Design of a stabilizing and switching module for α -helical peptides. Christian-Albrechts-Universität zu Kiel, Kiel **2017**.
- [058] Joana Gronow, *Dissertation*, Structural stabilization of α -helical antifreeze protein variants using the Trp-cage protein. Christian-Albrechts-Universität zu Kiel, Kiel **2019**.
- [059] Katrin Bamberg, *Masterarbeit*, Untersuchungen zur Photoschaltbarkeit von Trp-cage-Proteinen und eines AFP-Trp-cage Fusionsproteins. Christian-Albrechts-Universität zu Kiel, Kiel **2017**.
- [060] Michael E. Houston, Jr., Heman Chao, Robert S. Hodges, Brian D. Sykes, Cyril M. Kay, Frank D. Sönnichsen, Michèle C. Loewen, Peter L. Davies, Binding of an oligopeptide to a specific plane of ice, *J. Biol. Chem.* **1998**, *19*, 11714–11718. DOI: 10.1074/jbc.273.19.11714.
- [061] Hagit Kun, Yitzhak Mastai, Activity of short segments of Type I antifreeze protein, *Biopolymers (Pept. Sci.)* **2007**, *6*, 807–814. DOI: 10.1002/bip.20844.
- [062] H. M. D. Bandara, Shawn C. Burdette, Photoisomerization in different classes of azobenzene, *Chem. Soc. Rev.* **2012**, *5*, 1809–1825. DOI: 10.1039/c1cs15179g.
- [063] Wiktor Szymański, John M. Beierle, Hans A. V. Kistemaker, Willem A. Velema, Ben L. Feringa, Reversible photocontrol of biological systems by the incorporation of molecular photoswitches, *Chem. Rev.* **2013**, *8*, 6114–6178. DOI: 10.1021/cr300179f.
- [064] Guangshun Wang, Structures of human host defense cathelicidin LL-37 and its smallest antimicrobial peptide KR-12 in lipid micelles, *J. Biol. Chem.* **2008**, *47*, 32637–32643. DOI: 10.1074/jbc.M805533200.

- [065] Li Dai, Akikazu Yasuda, Hideo Naoki, Gerardo Corzo, Marta Andriantsiferana, Terumi Nakajima, IsCT, a novel cytotoxic linear peptide from scorpion *Opisthacanthus madagascariensis*, *Biochem. Biophys. Res. Commun.* **2001**, *4*, 820–825. DOI: 10.1006/bbrc.2001.5472.
- [066] Kyungik Lee, Song Y. Shin, Kyoungho Kim, Shin S. Lim, Kyung-Soo Hahm, Yangmee Kim, Antibiotic activity and structural analysis of the scorpion-derived antimicrobial peptide IsCT and its analogs, *Biochem. Biophys. Res. Commun.* **2004**, *2*, 712–719. DOI: 10.1016/j.bbrc.2004.08.144.
- [067] Matthias Lipfert, Andrea Giansini, Frank D. Sönnichsen, *personal communication*, Kiel, Germany (**09.09.2016**).
- [068] C. L. Ventola, The antibiotic resistance crisis: Part 1: causes and threats, *P & T* **2015**, *4*, 277–283.
- [069] Harold C. Neu, The crisis in antibiotic resistance, *Science* **1992**, *5073*, 1064–1073. DOI: 10.1126/science.257.5073.1064.
- [070] Jose L. Martinez, Environmental pollution by antibiotics and by antibiotic resistance determinants, *Environ. Pollut.* **2009**, *11*, 2893–2902. DOI: 10.1016/j.envpol.2009.05.051.
- [071] K. Nygaard, Bjørn T. Lunestad, Halvor Hektoen, John A. Berge, V. Hormazabal, Resistance to oxytetracycline, oxolinic acid and furazolidone in bacteria from marine sediments, *Aquaculture* **1992**, *1-2*, 31–36. DOI: 10.1016/0044-8486(92)90135-8.
- [072] Irene Michael, Luigi Rizzo, Christa S. McArdell, Célia M. Manaia, Christophe Merlin, Thomas Schwartz, Christophe Dagot, Despo Fatta-Kassinos, Urban wastewater treatment plants as hotspots for the release of antibiotics in the environment: A review, *Water Res.* **2013**, *3*, 957–995. DOI: 10.1016/j.watres.2012.11.027.
- [073] Klaus Kümmerer, Ali Al-Ahmad, Volker H. Mersch-Sundermann, Biodegradability of some antibiotics, elimination of the genotoxicity and affection of wastewater bacteria in a simple test, *Chemosphere* **2000**, *7*, 701–710. DOI: 10.1016/S0045-6535(99)00439-7.
- [074] Klaus Kümmerer, Significance of antibiotics in the environment, *J. Antimicrob. Chemother.* **2003**, *1*, 5–7. DOI: 10.1093/jac/dkg293.
- [075] Xiangang Hu, Qixing Zhou, Yi Luo, Occurrence and source analysis of typical veterinary antibiotics in manure, soil, vegetables and groundwater from organic vegetable bases, northern China, *Environ. Pollut.* **2010**, *9*, 2992–2998. DOI: 10.1016/j.envpol.2010.05.023.
- [076] W.-Y. Xie, Q. Shen, F. J. Zhao, Antibiotics and antibiotic resistance from animal manures to soil: A review, *Eur. J. Soil Sci.* **2018**, *1*, 181–195. DOI: 10.1111/ejss.12494.
- [077] Xian Zhou, Jian Wang, Chao Lu, Qihang Liao, Fredrick O. Gudda, Wanting Ling, Antibiotics in animal manure and manure-based fertilizers: Occurrence and ecological risk assessment, *Chemosphere* **2020**, 127006. DOI: 10.1016/j.chemosphere.2020.127006.
- [078] Katie Tiseo, Laura Huber, Marius Gilbert, Timothy P. Robinson, Thomas P. van Boeckel, Global Trends in Antimicrobial Use in Food Animals from 2017 to 2030, *Antibiotics* **2020**, *12*. DOI: 10.3390/antibiotics9120918.
- [079] Thomas P. van Boeckel, João Pires, Reshma Silvester, Cheng Zhao, Julia Song, Nicola G. Criscuolo, Marius Gilbert, Sebastian Bonhoeffer, Ramanan Laxminarayan, Global trends in antimicrobial resistance in animals in low- and middle-income countries, *Science* **2019**, *6459*, 1266. DOI: 10.1126/science.aaw1944.
- [080] Marcus Östman, Berndt Björleinius, Jerker Fick, Mats Tysklind, Effect of full-scale ozonation and pilot-scale granular activated carbon on the removal of biocides, antimycotics and antibiotics in a sewage treatment plant, *Sci. Total Environ.* **2019**, 1117–1123. DOI: 10.1016/j.scitotenv.2018.08.382.
- [081] Carl-Fredrik Flach, Maja Genheden, Jerker Fick, D. G. Joakim Larsson, A comprehensive screening of *Escherichia coli* isolates from scandinavia's largest sewage treatment plant indicates no selection for antibiotic resistance, *Environ. Sci. Technol.* **2018**, *19*, 11419–11428. DOI: 10.1021/acs.est.8b03354.
- [082] Alexander M. Voigt, Patrick Ciorba, Manuel Döhla, Martin Exner, Carsten Felder, Franziska Lenz-Plet, Esther Sib, Dirk Skutlarek, Ricarda M. Schmuthausen, Harald A. Färber, The investigation of antibiotic residues, antibiotic resistance genes and antibiotic-resistant organisms in a drinking water reservoir system in Germany, *Int. J. Hyg. Environ. Health* **2020**, 113449. DOI: 10.1016/j.ijheh.2020.113449.
- [083] Erik Gullberg, Sha Cao, Otto G. Berg, Carolina Ilbäck, Linus Sandegren, Diarmaid Hughes, Dan I. Andersson, Selection of resistant bacteria at very low antibiotic concentrations, *PLoS pathogens* **2011**, *7*, e1002158. DOI: 10.1371/journal.ppat.1002158.
- [084] Klaus Kümmerer, Antibiotics in the aquatic environment: A review - Part I, *Chemosphere* **2009**, *4*, 417–434. DOI: 10.1016/j.chemosphere.2008.11.086.
- [085] Stefanie Lorenz, Ann-Kathrin Amsel, Neele Puhlmann, Marco Reich, Oliver Olsson, Klaus Kümmerer, Toward Application and Implementation of in Silico Tools and Workflows within Benign by Design Approaches, *ACS Sustainable Chem. Eng.* **2021**, *37*, 12461–12475. DOI: 10.1021/acssuschemeng.1c03070.

7. Bibliography

- [086] Christoph Leder, Morten Suk, Stefanie Lorenz, Tushar Rastogi, Christian Peifer, Manfred Kietzmann, Daniel Jonas, Marion Buck, Axel Pahl, Klaus Kümmerer, Reducing environmental pollution by antibiotics through design for environmental degradation, *ACS Sustainable Chem. Eng.* **2021**, 28, 9358–9368. DOI: 10.1021/acssuschemeng.1c02243.
- [087] Y. J. Gordon, Eric G. Romanowski, Alison M. McDermott, A review of antimicrobial peptides and their therapeutic potential as anti-infective drugs, *Curr. Eye Res.* **2005**, 7, 505–515. DOI: 10.1080/02713680590968637.
- [088] Joseph B. McPhee, Monisha G. Scott, Robert E. W. Hancock, Design of Host Defence Peptides for Antimicrobial and Immunity Enhancing Activities, *Comb. Chem. High Throughput Screen.* **2005**, 3, 257–272. DOI: 10.2174/1386207053764558.
- [089] Anastasia Nijnik, Robert E. W. Hancock, Host defence peptides: Antimicrobial and immunomodulatory activity and potential applications for tackling antibiotic-resistant infections, *Emerg. Health Threats J.* **2009**, e1-e7. DOI: 10.3134/ehthj.09.001.
- [090] David A. Phoenix, Sarah R. Dennison, Frederick Harris, Antimicrobial Peptides, Wiley-VCH Verlag GmbH & Co. KGaA, Weinheim, Germany **2013**. ISBN: 9783527652853.
- [091] Paulina Kosikowska, Adam Lesner, Antimicrobial peptides (AMPs) as drug candidates: A patent review (2003-2015), *Expert Opin. Ther. Pat.* **2016**, 6, 689–702. DOI: 10.1080/13543776.2016.1176149.
- [092] Sarah C. Mansour, Olga M. Pena, Robert E. W. Hancock, Host defense peptides: Front-line immunomodulators, *Trends Immunol.* **2014**, 9, 443–450. DOI: 10.1016/j.it.2014.07.004.
- [093] Neeloffer Mookherjee, Marilyn A. Anderson, Henk P. Haagsman, Donald J. Davidson, Antimicrobial host defence peptides: Functions and clinical potential, *Nat. Rev. Drug Discov.* **2020**, 311–332. DOI: 10.1038/s41573-019-0058-8.
- [094] Robert E. W. Hancock, Peptide antibiotics, *The Lancet* **1997**, 9049, 418–422. DOI: 10.1016/S0140-6736(97)80051-7.
- [095] Michael R. Yeaman, Nannette Y. Yount, Mechanisms of antimicrobial peptide action and resistance, *Pharmacol. Rev.* **2003**, 1, 27–55. DOI: 10.1124/pr.55.1.2.
- [096] Alessandro Tossi, Luca Sandri, Anna Giangaspero, Amphipathic, α -helical antimicrobial peptides, *Biopolymers (Pept. Sci.)* **2000**, 1, 4–30. DOI: 10.1002/1097-0282(2000)55:1<4::AID-BIP30>3.0.CO;2-M.
- [097] Seymour J. Singer, Garth L. Nicolson, The Fluid Mosaic Model of the Structure of Cell Membranes, *Science* **1972**, 4023, 720–731. DOI: 10.1126/science.175.4023.720.
- [098] Henrik Strahl, Jeff Errington, Bacterial Membranes: Structure, Domains, and Function, *Annu. Rev. Microbiol.* **2017**, 519–538. DOI: 10.1146/annurev-micro-102215-095630.
- [099] Daniel J. Müller, Nan Wu, Krzysztof Palczewski, Vertebrate membrane proteins: Structure, function, and insights from biophysical approaches, *Pharmacol. Rev.* **2008**, 1, 43–78. DOI: 10.1124/pr.107.07111.
- [100] Takeshi Harayama, Howard Riezman, Understanding the diversity of membrane lipid composition, *Nat. Rev. Mol. Cell Biol.* **2018**, 5, 281–296. DOI: 10.1038/nrm.2017.138.
- [101] Christian Sohlenkamp, Otto Geiger, Bacterial membrane lipids: Diversity in structures and pathways, *FEMS Microbiol. Rev.* **2016**, 1, 133–159. DOI: 10.1093/femsre/fuv008.
- [102] Thomas J. Silhavy, Daniel Kahne, Suzanne Walker, The bacterial cell envelope, *Cold Spring Harb. Perspect. Biol.* **2010**, 5. DOI: 10.1101/cshperspect.a000414.
- [103] Gerrit van Meer, Dennis R. Voelker, Gerald W. Feigenson, Membrane lipids: Where they are and how they behave, *Nat. Rev. Mol. Cell Biol.* **2008**, 2, 112–124. DOI: 10.1038/nrm2330.
- [104] Bret Verhoven, Robert A. Schlegel, Patrick Williamson, Mechanisms of phosphatidylserine exposure, a phagocyte recognition signal, on apoptotic T lymphocytes, *J. Exp. Med.* **1995**, 5, 1597–1601. DOI: 10.1084/jem.182.5.1597.
- [105] Jos A. F. Op den Kamp, Lipid asymmetry in membranes, *Annu. Rev. Biochem.* **1979**, 47–71. DOI: 10.1146/annurev.bi.48.070179.000403.
- [106] Philippe F. Devaux, Roger Morris, Transmembrane asymmetry and lateral domains in biological membranes, *Traffic* **2004**, 4, 241–246. DOI: 10.1111/j.1600-0854.2004.0170.x.
- [107] David L. Daleke, Phospholipid flippases, *J. Biol. Chem.* **2007**, 2, 821–825. DOI: 10.1074/jbc.R600035200.
- [108] J. H. Lorent, K. R. Levental, L. Ganesan, G. Rivera-Longworth, E. Sezgin, M. Doktorova, E. Lyman, I. Levental, Plasma membranes are asymmetric in lipid unsaturation, packing and protein shape, *Nat. Chem. Biol.* **2020**, 6, 644–652. DOI: 10.1038/s41589-020-0529-6.
- [109] Ken Jacobson, Ole G. Mouritsen, Richard G. W. Anderson, Lipid rafts: At a crossroad between cell biology and physics, *Nat. Cell Biol.* **2007**, 1, 7–14. DOI: 10.1038/ncb0107-7.

- [110] R. Franco, C. D. Bortner, J. A. Cidlowski, Potential roles of electrogenic ion transport and plasma membrane depolarization in apoptosis, *J. Membr. Biol.* **2006**, *1*, 43–58. DOI: 10.1007/s00232-005-0837-5.
- [111] Hanne Poulsen, Himanshu Khandelia, J. P. Morth, Maike Bubltz, Ole G. Mouritsen, Jan Egebjerg, Poul Nissen, Neurological disease mutations compromise a C-terminal ion pathway in the Na⁺/K⁺-ATPase, *Nature* **2010**, *7311*, 99–102. DOI: 10.1038/nature09309.
- [112] Michael V. Clausen, Florian Hilbers, Hanne Poulsen, The Structure and Function of the Na,K-ATPase Isoforms in Health and Disease, *Front. Physiol.* **2017**, *371*. DOI: 10.3389/fphys.2017.00371.
- [113] Benjamin Ehrenberg, Valerie Montana, Mei-De Wei, Joseph P. Wuskell, Leslie M. Loew, Membrane potential can be determined in individual cells from the nernstian distribution of cationic dyes, *Biophys. J.* **1988**, *5*, 785–794. DOI: 10.1016/S0006-3495(88)83158-8.
- [114] Stephen H. Wright, Generation of resting membrane potential, *Adv. Physiol. Educ.* **2004**, *4*, 139–142. DOI: 10.1152/advan.00029.2004.
- [115] Ajit Varki, Evolutionary forces shaping the Golgi glycosylation machinery: Why cell surface glycans are universal to living cells, *Cold Spring Harb. Perspect. Biol.* **2011**, *6*. DOI: 10.1101/cshperspect.a005462.
- [116] Sietze Reitsma, Dick W. Slaaf, Hans Vink, Marc A. M. J. van Zandvoort, Mirjam G. A. oude Egbrink, The endothelial glycocalyx: Composition, functions, and visualization, *Pflugers Arch. - Eur. J. Physiol.* **2007**, *3*, 345–359. DOI: 10.1007/s00424-007-0212-8.
- [117] Ronald L. Schnaar, Rita Gerardy-Schahn, Herbert Hildebrandt, Sialic acids in the brain: Gangliosides and polysialic acid in nervous system development, stability, disease, and regeneration, *Physiol. Rev.* **2014**, *2*, 461–518. DOI: 10.1152/physrev.00033.2013.
- [118] Sónia Troeira Henriques, Nicole Lawrence, Stephanie Chaouis, Anjaneya S. Ravipati, Olivier Cheneval, Aurélie H. Benfield, Alysha G. Elliott, Angela M. Kavanagh, Matthew A. Cooper, Lai Y. Chan, Yen-Hua Huang, David J. Craik, Redesigned spider peptide with improved antimicrobial and anticancer properties, *ACS Chem. Biol.* **2017**, *9*, 2324–2334. DOI: 10.1021/acscchembio.7b00459.
- [119] Diana Gaspar, A. S. Veiga, Miguel A. R. B. Castanho, From antimicrobial to anticancer peptides. A review, *Front. Microbiol.* **2013**, *294*. DOI: 10.3389/fmicb.2013.00294.
- [120] Davor Juretić, Juraj Simunić, Design of α -helical antimicrobial peptides with a high selectivity index, *Expert Opin. Drug Discov.* **2019**, *10*, 1053–1063. DOI: 10.1080/17460441.2019.1642322.
- [121] P. M. Rodi, V. M. Trucco, A. M. Gennaro, Factors determining detergent resistance of erythrocyte membranes, *Biophysical chemistry* **2008**, *1-3*, 14–18. DOI: 10.1016/j.bpc.2008.02.015.
- [122] Narla Mohandas, Patrick G. Gallagher, Red cell membrane: Past, present, and future, *Blood* **2008**, *10*, 3939–3948. DOI: 10.1182/blood-2008-07-161166.
- [123] Yuxin Chen, Colin T. Mant, Susan W. Farmer, Robert E. W. Hancock, Michael L. Vasil, Robert S. Hodges, Rational design of α -helical antimicrobial peptides with enhanced activities and specificity/therapeutic index, *J. Biol. Chem.* **2005**, *13*, 12316–12329. DOI: 10.1074/jbc.M413406200.
- [124] Davor Juretić, Damir Vukicević, Nada Ilić, Nikolinka Antcheva, Alessandro Tossi, Computational design of highly selective antimicrobial peptides, *J. Chem. Inf. Model.* **2009**, *12*, 2873–2882. DOI: 10.1021/ci900327a.
- [125] Kang Cheng, Howard C. Haspel, Mary L. Vallano, Babatunde Osotimehin, Martin Sonenberg, Measurement of membrane potentials (ψ) of erythrocytes and white adipocytes by the accumulation of triphenylmethylphosphonium cation, *J. Membr. Biol.* **1980**, *3*, 191–201. DOI: 10.1007/bf01869476.
- [126] Margaret M. Gedde, Wray H. Huestis, Membrane potential and human erythrocyte shape, *Biophys. J.* **1997**, *3*, 1220–1233. DOI: 10.1016/S0006-3495(97)78769-1.
- [127] Iveta Waczulíková, Libuša Šikurová, Maria Bryszewska, Rękawiecka Katarzyna, Josef Čársky, Olĝa Uličná, Impaired erythrocyte transmembrane potential in diabetes mellitus and its possible improvement by resorcyldiene aminoguanidine, *Bioelectrochemistry* **2000**, *2*, 251–256. DOI: 10.1016/S0302-4598(00)00107-0.
- [128] Michael T. Madigan, Kelly S. Bender, Daniel H. Buckley, W. Matthew Sattley, David A. Stahl, Brock Biology of Microorganisms, 15th edition, global edition, Pearson, New York, NY **2019**. ISBN: 1-292-23510-1.
- [129] Ti-Yu Lin, Douglas B. Weibel, Organization and function of anionic phospholipids in bacteria, *Appl. Microbiol. Biotechnol.* **2016**, *10*, 4255–4267. DOI: 10.1007/s00253-016-7468-x.
- [130] Peter R. Rich, Amandine Maréchal, The mitochondrial respiratory chain, *Essays Biochem.* **2010**, *1–23*. DOI: 10.1042/BSE0470001.

7. Bibliography

- [131] Eva R. Kashket, The proton motive force in bacteria: A critical assessment of methods, *Annu. Rev. Microbiol.* **1985**, 219–242. DOI: 10.1146/annurev.mi.39.100185.001251.
- [132] Jennifer Gidden, Jackie Denson, Rohana Liyanage, D. M. Ivey, Jackson O. Lay, Lipid Compositions in *Escherichia coli* and *Bacillus subtilis* During Growth as Determined by MALDI-TOF and TOF/TOF Mass Spectrometry, *Int. J. Mass Spectrom.* **2009**, 1-3, 178–184. DOI: 10.1016/j.ijms.2009.03.005.
- [133] Jenny-Lee Thomassin, John R. Brannon, Bernard F. Gibbs, Samantha Gruenheid, Hervé Le Moual, OmpT outer membrane proteases of enterohemorrhagic and enteropathogenic *Escherichia coli* contribute differently to the degradation of human LL-37, *Infect. Immun.* **2012**, 2, 483–492. DOI: 10.1128/IAI.05674-11.
- [134] Uwe B. Sleytr, Bernhard Schuster, Eva-Maria Egelseer, Dietmar Pum, S-layers: Principles and applications, *FEMS Microbiol. Rev.* **2014**, 5, 823–864. DOI: 10.1111/1574-6976.12063.
- [135] Christina Schäffer, Paul Messner, The structure of secondary cell wall polymers: How Gram-positive bacteria stick their cell walls together, *Microbiology* **2005**, Pt 3, 643–651. DOI: 10.1099/mic.0.27749-0.
- [136] César de la Fuente-Núñez, Jan Mertens, John Smit, Robert E. W. Hancock, The bacterial surface layer provides protection against antimicrobial peptides, *Appl. Environ. Microbiol.* **2012**, 15, 5452–5456. DOI: 10.1128/AEM.01493-12.
- [137] John W. Costerton, Randall T. Irvin, K.-J. Cheng, The bacterial glycocalyx in nature and disease, *Annu. Rev. Microbiol.* **1981**, 299–324. DOI: 10.1146/annurev.mi.35.100181.001503.
- [138] Adam A. Strömstedt, Lovisa Ringstad, Artur Schmidtchen, Martin Malmsten, Interaction between amphiphilic peptides and phospholipid membranes, *Curr. Opin. Colloid Interface Sci.* **2010**, 6, 467–478. DOI: 10.1016/j.cocis.2010.05.006.
- [139] Yechiel Shai, Mode of action of membrane active antimicrobial peptides, *Biopolymers (Pept. Sci.)* **2002**, 4, 236–248. DOI: 10.1002/bip.10260.
- [140] Ole G. Mouritsen, Martin J. Zuckermann, What's so special about cholesterol?, *Lipids* **2004**, 11, 1101–1113. DOI: 10.1007/s11745-004-1336-x.
- [141] Hilde A. Rinia, Margot M.E. Snel, Jan P.J.M. van der Eerden, Ben de Kruijff, Visualizing detergent resistant domains in model membranes with atomic force microscopy, *FEBS Lett.* **2001**, 1, 92–96. DOI: 10.1016/S0014-5793(01)02636-9.
- [142] Jeffrey R. Brender, Austin J. McHenry, Ayyalusamy Ramamoorthy, Does cholesterol play a role in the bacterial selectivity of antimicrobial peptides?, *Front. Immunol.* **2012**, 195. DOI: 10.3389/fimmu.2012.00195.
- [143] Austin J. McHenry, Michele F. M. Sciacca, Jeffrey R. Brender, Ayyalusamy Ramamoorthy, Does cholesterol suppress the antimicrobial peptide induced disruption of lipid raft containing membranes?, *Biochim. Biophys. Acta - Biomembranes* **2012**, 12, 3019–3024. DOI: 10.1016/j.bbamem.2012.07.021.
- [144] Hanna Barman, Michael Walch, Sonja Latinovic-Golic, Claudia Dumrese, Max Dolder, Peter Groscurth, Urs Ziegler, Cholesterol in negatively charged lipid bilayers modulates the effect of the antimicrobial protein granulysin, *J. Membr. Biol.* **2006**, 1, 29–39. DOI: 10.1007/s00232-006-0040-3.
- [145] Dong-Kuk Lee, Anirban Bhunia, Samuel A. Kotler, Ayyalusamy Ramamoorthy, Detergent-type membrane fragmentation by MSI-78, MSI-367, MSI-594, and MSI-843 antimicrobial peptides and inhibition by cholesterol: A solid-state nuclear magnetic resonance study, *Biochemistry* **2015**, 10, 1897–1907. DOI: 10.1021/bi501418m.
- [146] Manhong Wu, Elke Maier, Roland Benz, Robert E. W. Hancock, Mechanism of interaction of different classes of cationic antimicrobial peptides with planar bilayers and with the cytoplasmic membrane of *Escherichia coli*, *Biochemistry* **1999**, 22, 7235–7242. DOI: 10.1021/bi9826299.
- [147] Jennifer Gesell, Micheal Zasloff, Stanley J. Opella, Two-dimensional ^1H NMR experiments show that the 23-residue magainin antibiotic peptide is an α -helix in dodecylphosphocholine micelles, sodium dodecylsulfate micelles, and trifluoroethanol/water solution, *J. Biomol. NMR* **1997**, 2, 127–135. DOI: 10.1023/A:1018698002314.
- [148] Teikichi Ikura, Nobuhiro Gō, Fuyuhiko Inagaki, Refined structure of melittin bound to perdeuterated dodecylphosphocholine micelles as studied by 2D-NMR and distance geometry calculation, *Proteins* **1991**, 2, 81–89. DOI: 10.1002/prot.340090202.
- [149] Gwan-Su Yi, Chan B. Park, Sun C. Kim, Chaejoon Cheong, Solution structure of an antimicrobial peptide buforin II, *FEBS Lett.* **1996**, 1, 87–90. DOI: 10.1016/S0014-5793(96)01193-3.
- [150] Fernando Porcelli, Raffaello Verardi, Lei Shi, Katherine A. Henzler-Wildman, Ayyalusamy Ramamoorthy, Gianluigi Veglia, NMR structure of the cathelicidin-derived human antimicrobial peptide LL-37 in dodecylphosphocholine micelles, *Biochemistry* **2008**, 20, 5565–5572. DOI: 10.1021/bi702036s.
- [151] Young S. Koo, Jung M. Kim, In Y. Park, Byung J. Yu, Su A. Jang, Key-Sun Kim, Chan B. Park, Ju H. Cho, Sun C. Kim, Structure-activity relations of parasin I, a histone H2A-derived antimicrobial peptide, *Peptides* **2008**, 7, 1102–1108. DOI: 10.1016/j.peptides.2008.02.019.

- [152] Guangshun Wang, Melissa Elliott, Anna L. Cogen, Edward L. Ezell, Richard L. Gallo, Robert E. W. Hancock, Structure, dynamics, and antimicrobial and immune modulatory activities of human LL-23 and its single-residue variants mutated on the basis of homologous primate cathelicidins, *Biochemistry* **2012**, *2*, 653–664. DOI: 10.1021/bi2016266.
- [153] Min-Duk Seo, Hyung-Sik Won, Ji-Hun Kim, Tsogbadrakh Mishig-Ochir, Bong-Jin Lee, Antimicrobial peptides for therapeutic applications: A review, *Molecules* **2012**, *10*, 12276–12286. DOI: 10.3390/molecules171012276.
- [154] Andrea Giuliani, Giovanna Pirri, Silvia F. Nicoletto, Antimicrobial peptides: An overview of a promising class of therapeutics, *Cent. Eur. J. Biol.* **2007**, *1*, 1–33. DOI: 10.2478/s11535-007-0010-5.
- [155] David Wade, Anita Boman, Birgitta Wåhlin, C. M. Drain, David Andreu, Hans G. Boman, Robert B. Merrifield, All-D amino acid-containing channel-forming antibiotic peptides, *Proc. Natl. Acad. Sci. USA* **1990**, *12*, 4761–4765. DOI: 10.1073/pnas.87.12.4761.
- [156] Roberto Bessalle, Aviva Kapitkovsky, Alfred Gorea, Itamar Shalit, Mati Friedkin, All-D-magainin: Chirality, antimicrobial activity and proteolytic resistance, *FEBS Lett.* **1990**, *1-2*, 151–155. DOI: 10.1016/0014-5793(90)81351-N.
- [157] Katsumi Matsuzaki, Ken-ichi Sugishita, Koichiro Miyajima, Interactions of an antimicrobial peptide, magainin 2, with lipopolysaccharide-containing liposomes as a model for outer membranes of Gram-negative bacteria, *FEBS Lett.* **1999**, *2-3*, 221–224. DOI: 10.1016/S0014-5793(99)00443-3.
- [158] Jeffrey Turner, Yoon Cho, Nhu-Nguyen Dinh, Alan J. Waring, Robert I. Lehrer, Activities of LL-37, a cathelin-associated antimicrobial peptide of human neutrophils, *Antimicrob. Agents Chemother.* **1998**, *9*, 2206–2214.
- [159] Fazale R. Rana, Catherine M. Sultany, Jack Blazys, Interactions between Salmonella typhimurium lipopolysaccharide and the antimicrobial peptide, magainin 2 amide, *FEBS Lett.* **1990**, *2*, 464–467. DOI: 10.1016/0014-5793(90)80616-Q.
- [160] S. A. David, V. I. Mathan, P. Balaram, Interaction of melittin with endotoxin lipid A, *Biochim. Biophys. Acta - Lipids and Lipid Metabolism* **1992**, *3*, 269–274. DOI: 10.1016/0005-2760(92)90006-H.
- [161] Kevin L. Piers, Melissa H. Brown, Robert E. Hancock, Improvement of outer membrane-permeabilizing and lipopolysaccharide-binding activities of an antimicrobial cationic peptide by C-terminal modification, *Antimicrob. Agents Chemother.* **1994**, *10*, 2311–2316. DOI: 10.1128/AAC.38.10.2311.
- [162] Anna Giangaspero, Luca Sandri, Alessandro Tossi, Amphipathic alpha helical antimicrobial peptides: A systematic study of the effects of structural and physical properties on biological activity, *Eur. J. Biochem.* **2001**, *21*, 5589–5600. DOI: 10.1046/j.0014-2956.2001.02494.x.
- [163] Gilbert Baumann, Peter Mueller, A molecular model of membrane excitability, *J. Supramol. Struct.* **1974**, *5-6*, 538–557. DOI: 10.1002/jss.400020504.
- [164] Shuo Qian, Wangchen Wang, Lin Yang, Huey W. Huang, Structure of the alamethicin pore reconstructed by x-ray diffraction analysis, *Biophys. J.* **2008**, *9*, 3512–3522. DOI: 10.1529/biophysj.107.126474.
- [165] Lin Yang, Thad A. Harroun, Thomas M. Weiss, Lai Ding, Huey W. Huang, Barrel-Stave Model or Toroidal Model? A Case Study on Melittin Pores, *Biophys. J.* **2001**, *3*, 1475–1485. DOI: 10.1016/S0006-3495(01)75802-X.
- [166] Robert O. Fox, Frederic M. Richards, A voltage-gated ion channel model inferred from the crystal structure of alamethicin at 1.5-Å resolution, *Nature* **1982**, *5890*, 325–330. DOI: 10.1038/300325a0.
- [167] Günther Jung, Norbert Dubischar, Dieter Liebfritz, Conformational changes of alamethicin induced by solvent and temperature: A ¹³C-NMR and circular-dichroism study, *Eur. J. Biochem.* **1975**, *2*, 395–409. DOI: 10.1111/j.1432-1033.1975.tb04150.x.
- [168] Derek Marsh, Orientation and peptide–lipid interactions of alamethicin incorporated in phospholipid membranes: Polarized infrared and spin-label EPR spectroscopy, *Biochemistry* **2009**, *4*, 729–737. DOI: 10.1021/bi801279n.
- [169] Mark S. P. Sansom, The biophysics of peptide models of ion channels, *Prog. Biophys. molec. Biol.* **1991**, *3*, 139–235. DOI: 10.1016/0079-6107(91)90004-C.
- [170] Katsumi Matsuzaki, Osamu Murase, Nobutaka Fujii, Koichiro Miyajima, An antimicrobial peptide, magainin 2, induced rapid flip-flop of phospholipids coupled with pore formation and peptide translocation, *Biochemistry* **1996**, *35*, 11361–11368. DOI: 10.1021/bi960016v.
- [171] S. J. Ludtke, K. He, W. T. Heller, T. A. Harroun, L. Yang, H. W. Huang, Membrane pores induced by magainin, *Biochemistry* **1996**, *43*, 13723–13728. DOI: 10.1021/bi9620621.
- [172] Yehonathan Pouny, Doron Rapaport, Amram Mor, Pierre Nicolas, Yechiel Shai, Interaction of antimicrobial dermaseptin and its fluorescently labeled analogs with phospholipid membranes, *Biochemistry* **1992**, *49*, 12416–12423. DOI: 10.1021/bi00164a017.
- [173] Yechiel Shai, Molecular recognition between membrane-spanning polypeptides, *Trends Biochem. Sci.* **1995**, *11*, 460–464. DOI: 10.1016/S0968-0004(00)89101-X.

7. Bibliography

- [174] Håkan Steiner, David Andreu, R. B. Merrifield, Binding and action of cecropin and cecropin analogues: Antibacterial peptides from insects, *Biochim. Biophys. Acta - Biomembranes* **1988**, 2, 260–266. DOI: 10.1016/0005-2736(88)90069-7.
- [175] Ehud Gazit, Anita Boman, Hans G. Boman, Yechiel Shai, Interaction of the Mammalian Antibacterial Peptide Cecropin P1 with Phospholipid Vesicles, *Biochemistry* **1995**, 36, 11479–11488. DOI: 10.1021/bi00036a021.
- [176] Yechiel Shai, Ziv Oren, From “carpet” mechanism to de-novo designed diastereomeric cell-selective antimicrobial peptides, *Peptides* **2001**, 10, 1629–1641. DOI: 10.1016/S0196-9781(01)00498-3.
- [177] Manuel N. Melo, Rafael Ferre, Miguel A. R. B. Castanho, Antimicrobial peptides: Linking partition, activity and high membrane-bound concentrations, *Nat. Rev. Microbiol.* **2009**, 3, 245–250. DOI: 10.1038/nrmicro2095.
- [178] Steve Ludtke, Ke He, Huey Huang, Membrane thinning caused by magainin 2, *Biochemistry* **1995**, 51, 16764–16769. DOI: 10.1021/bi00051a026.
- [179] Almut Mecke, Dong-Kuk Lee, Ayyalusamy Ramamoorthy, Bradford G. Orr, Mark M. Banaszak Holl, Membrane thinning due to antimicrobial peptide binding: An atomic force microscopy study of MSI-78 in lipid bilayers, *Biophys. J.* **2005**, 6, 4043–4050. DOI: 10.1529/biophysj.105.062596.
- [180] Ziv Oren, Yechiel Shai, Mode of action of linear amphipathic α -helical antimicrobial peptides, *Biopolymers (Pept. Sci.)* **1998**, 6, 451–463. DOI: 10.1002/(SICI)1097-0282(1998)47:6<451::AID-BIP4>3.0.CO;2-F.
- [181] Fang-Yu Chen, Ming-Tao Lee, Huey W. Huang, Evidence for Membrane Thinning Effect as the Mechanism for Peptide-Induced Pore Formation, *Biophys. J.* **2003**, 6, 3751–3758. DOI: 10.1016/S0006-3495(03)75103-0.
- [182] Katsumi Matsuzaki, Magainins as paradigm for the mode of action of pore forming polypeptides, *Biochim. Biophys. Acta - Reviews on Biomembranes* **1998**, 3, 391–400. DOI: 10.1016/S0304-4157(98)00014-8.
- [183] Natsuko Uematsu, Katsumi Matsuzaki, Polar Angle as a Determinant of Amphipathic α -Helix-Lipid Interactions: A Model Peptide Study, *Biophys. J.* **2000**, 4, 2075–2083. DOI: 10.1016/S0006-3495(00)76455-1.
- [184] Robert E. W. Hancock, Daniel S. Chapple, Peptide antibiotics, *Antimicrob. Agents Chemother.* **1999**, 6, 1317–1323.
- [185] Kim A. Brogden, Antimicrobial peptides: Pore formers or metabolic inhibitors in bacteria?, *Nat. Rev. Microbiol.* **2005**, 3, 238–250. DOI: 10.1038/nrmicro1098.
- [186] Evelyn Sun, Corrie R. Belanger, Evan F. Haney, Robert E. W. Hancock, Host defense (antimicrobial) peptides, 253–285. In: *Peptide Applications in Biomedicine, Biotechnology and Bioengineering*, Elsevier **2018**. ISBN: 9780081007365. DOI: 10.1016/B978-0-08-100736-5.00010-7.
- [187] Burkhard Bechinger, Karl Lohner, Detergent-like actions of linear amphipathic cationic antimicrobial peptides, *Biochim. Biophys. Acta - Biomembranes* **2006**, 9, 1529–1539. DOI: 10.1016/j.bbamem.2006.07.001.
- [188] Ali A. Bahar, Dacheng Ren, Antimicrobial peptides, *Pharmaceuticals* **2013**, 12, 1543–1575. DOI: 10.3390/ph6121543.
- [189] Earl Grant, Troy J. Beeler, Kenneth M. P. Taylor, Kenneth Gable, Mark A. Roseman, Mechanism of magainin 2a induced permeabilization of phospholipid vesicles, *Biochemistry* **1992**, 41, 9912–9918. DOI: 10.1021/bi00156a008.
- [190] P. R. Cullis, B. de Kruijff, Lipid polymorphism and the functional roles of lipids in biological membranes, *Biochim. Biophys. Acta - Reviews on Biomembranes* **1979**, 4, 399–420. DOI: 10.1016/0304-4157(79)90012-1.
- [191] Katsumi Matsuzaki, Ken-ichi Sugishita, Noriko Ishibe, Mayu Ueha, Saori Nakata, Koichiro Miyajima, Richard M. Epand, Relationship of membrane curvature to the formation of pores by magainin 2, *Biochemistry* **1998**, 34, 11856–11863. DOI: 10.1021/bi980539y.
- [192] Burkhard Bechinger, Rationalizing the membrane interactions of cationic amphipathic antimicrobial peptides by their molecular shape, *Curr. Opin. Colloid Interface Sci.* **2009**, 5, 349–355. DOI: 10.1016/j.cocis.2009.02.004.
- [193] Burkhard Bechinger, The structure, dynamics and orientation of antimicrobial peptides in membranes by multidimensional solid-state NMR spectroscopy, *Biochim. Biophys. Acta - Biomembranes* **1999**, 1-2, 157–183. DOI: 10.1016/S0005-2736(99)00205-9.
- [194] John D. F. Hale, Robert E. W. Hancock, Alternative mechanisms of action of cationic antimicrobial peptides on bacteria, *Expert Rev. Anti-Infect. Ther.* **2007**, 6, 951–959. DOI: 10.1586/14787210.5.6.951.
- [195] Aleksander Patrzykat, Carol L. Friedrich, Lijuan Zhang, Valentina Mendoza, Robert E. W. Hancock, Sublethal Concentrations of Pleurocidin-Derived Antimicrobial Peptides Inhibit Macromolecular Synthesis in *Escherichia coli*, *Antimicrob. Agents Chemother.* **2002**, 3, 605–614. DOI: 10.1128/AAC.46.3.605–614.2002.
- [196] Chan B. Park, Mi S. Kim, Sun C. Kim, A novel antimicrobial peptide from *Bufo bufo* gargarizans, *Biochem. Biophys. Res. Commun.* **1996**, 1, 408–413. DOI: 10.1006/bbrc.1996.0071.

- [197] Chan B. Park, Kwan-Su Yi, Katsumi Matsuzaki, Mi S. Kim, Sun C. Kim, Structure-activity analysis of buforin II, a histone H2A-derived antimicrobial peptide: The proline hinge is responsible for the cell-penetrating ability of buforin II, *Proc. Natl. Acad. Sci. USA* **2000**, *15*, 8245–8250. DOI: 10.1073/pnas.150518097.
- [198] Chan B. Park, Hun S. Kim, Sun C. Kim, Mechanism of action of the antimicrobial peptide buforin II: Buforin II kills microorganisms by penetrating the cell membrane and inhibiting cellular functions, *Biochem. Biophys. Res. Commun.* **1998**, *1*, 253–257. DOI: 10.1006/bbrc.1998.8159.
- [199] Yang Xie, Eleanor Fleming, Jessica L. Chen, Donald E. Elmore, Effect of proline position on the antimicrobial mechanism of buforin II, *Peptides* **2011**, *4*, 677–682. DOI: 10.1016/j.peptides.2011.01.010.
- [200] Erika T. Uytendoeven, Chase H. Butler, Danette Ko, Donald E. Elmore, Investigating the nucleic acid interactions and antimicrobial mechanism of buforin II, *FEBS Lett.* **2008**, *12*, 1715–1718. DOI: 10.1016/j.febslet.2008.04.036.
- [201] Jie-xi Yan, Kai-rong Wang, Ru Chen, Jing-jing Song, Bang-zhi Zhang, Wen Dang, Wei Zhang, Rui Wang, Membrane active antitumor activity of NK-18, a mammalian NK-lysin-derived cationic antimicrobial peptide, *Biochimie* **2012**, *1*, 184–191. DOI: 10.1016/j.biochi.2011.10.005.
- [202] Jiexi Yan, Kairong Wang, Wen Dang, Ru Chen, Junqiu Xie, Bangzhi Zhang, Jingjing Song, Rui Wang, Two hits are better than one: Membrane-active and DNA binding-related double-action mechanism of NK-18, a novel antimicrobial peptide derived from mammalian NK-lysin, *Antimicrob. Agents Chemother.* **2013**, *1*, 220–228. DOI: 10.1128/AAC.01619-12.
- [203] Alexandra Dangel, Nikolaus Ackermann, Omar Abdel-Hadi, Richard Maier, Kamil Önder, Patrice Francois, Carsten W. Müller, Jan Pané-Farré, Susanne Engelmann, Jacques Schrenzel, Jürgen Heesemann, Christian Lindermayr, A de novo-designed antimicrobial peptide with activity against multiresistant *Staphylococcus aureus* acting on RsbW kinase, *FASEB J.* **2013**, *11*, 4476–4488. DOI: 10.1096/fj.13-234575.
- [204] Benjamin Zeitler, Areli Herrera Diaz, Alexandra Dangel, Martha Thellmann, Helge Meyer, Michael Sattler, Christian Lindermayr, De-novo design of antimicrobial peptides for plant protection, *PloS one* **2013**, *8*, e71687. DOI: 10.1371/journal.pone.0071687.
- [205] Ulrike Pag, Marion Oedenkoven, Vera Sass, Yechiel Shai, Olga Shamova, Nikolinka Antcheva, Alessandro Tossi, Hans-Georg Sahl, Analysis of in vitro activities and modes of action of synthetic antimicrobial peptides derived from an alpha-helical 'sequence template', *J. Antimicrob. Chemother.* **2008**, *2*, 341–352. DOI: 10.1093/jac/dkm479.
- [206] H. H. Haukland, H. Ulvatne, K. Sandvik, L. H. Vorland, The antimicrobial peptides lactoferricin B and magainin 2 cross over the bacterial cytoplasmic membrane and reside in the cytoplasm, *FEBS Lett.* **2001**, *3*, 389–393. DOI: 10.1016/S0014-5793(01)03100-3.
- [207] Bruce L. Kagan, Antimicrobial amyloids?, *Biophys. J.* **2011**, *7*, 1597–1598. DOI: 10.1016/j.bpj.2011.02.023.
- [208] Patrick Flagmeier, Suman De, David C. Wirthensohn, Steven F. Lee, Cécile Vincke, Serge Muyldermans, Thomas P. J. Knowles, Sonia Gandhi, Christopher M. Dobson, David Klenerman, Ultrasensitive measurement of Ca²⁺ influx into lipid vesicles induced by protein aggregates, *Angewandte Chemie (International ed. in English)* **2017**, *27*, 7750–7754. DOI: 10.1002/anie.201700966.
- [209] Bruce L. Kagan, Hyunbum Jang, Ricardo Capone, Fernando Teran Arce, Srinivasan Ramachandran, Ratnesh Lal, Ruth Nussinov, Antimicrobial properties of amyloid peptides, *Mol. Pharmaceutics* **2012**, *4*, 708–717. DOI: 10.1021/mp200419b.
- [210] Hyunbum Jang, Fernando T. Arce, Mirela Mustata, Srinivasan Ramachandran, Ricardo Capone, Ruth Nussinov, Ratnesh Lal, Antimicrobial protegrin-1 forms amyloid-like fibrils with rapid kinetics suggesting a functional link, *Biophys. J.* **2011**, *7*, 1775–1783. DOI: 10.1016/j.bpj.2011.01.072.
- [211] Shalini Gour, Vibha Kaushik, Vijay Kumar, Priyanka Bhat, Subhash C. Yadav, Jay K. Yadav, Antimicrobial peptide (Cn-AMP2) from liquid endosperm of *Cocos nucifera* forms amyloid-like fibrillar structure, *J. Pept. Sci.* **2016**, *4*, 201–207. DOI: 10.1002/psc.2860.
- [212] Shalini Gour, Vijay Kumar, Ashutosh Singh, Kundlik Gadhave, Pankaj Goyal, Janmejay Pandey, Rajanish Giri, Jay K. Yadav, Mammalian antimicrobial peptide protegrin-4 self assembles and forms amyloid-like aggregates: Assessment of its functional relevance, *J. Pept. Sci.* **2019**, *3*, e3151. DOI: 10.1002/psc.3151.
- [213] Antonio N. Calabrese, Yanqin Liu, Tianfang Wang, Ian F. Musgrave, Tara L. Pukala, Rico F. Tabor, Lisandra L. Martin, John A. Carver, John H. Bowie, The amyloid fibril-forming properties of the amphibian antimicrobial peptide Uperin 3.5, *ChemBioChem* **2016**, *3*, 239–246. DOI: 10.1002/cbic.201500518.
- [214] Nir Salinas, Einav Tayeb-Fligelman, Massimo D. Sammito, Daniel Bloch, Raz Jelinek, Dror Noy, Isabel Usón, Meytal Landau, The amphibian antimicrobial peptide uperin 3.5 is a cross- α /cross- β chameleon functional amyloid, *Proc. Natl. Acad. Sci. USA* **2021**, *3*. DOI: 10.1073/pnas.2014442118.
- [215] Lisandra L. Martin, Clemens Kubeil, Stefania Piantavigna, Tarun Tikkoo, Nicholas P. Gray, Torsten John, Antonio N. Calabrese, Yanqin Liu, Yuning Hong, Mohammed A. Hossain, Nitin Patil, Bernd Abel, Ralf Hoffmann, John H. Bowie, John A. Carver,

7. Bibliography

- Amyloid aggregation and membrane activity of the antimicrobial peptide uperin 3.5, *Peptide Science* **2018**, *3*, e24052. DOI: 10.1002/pep2.24052.
- [216] Mahdi Shahmiri, Marta Enciso, Christopher G. Adda, Brian J. Smith, Matthew A. Perugini, Adam Mechler, Membrane core-specific antimicrobial action of cathelicidin LL-37 peptide switches between pore and nanofibre formation, *Sci. Rep.* **2016**, 38184. DOI: 10.1038/srep38184.
- [217] Yizhaq Engelberg, Meytal Landau, The Human LL-37(17-29) antimicrobial peptide reveals a functional supramolecular structure, *Nat. Commun.* **2020**, *1*, 3894. DOI: 10.1038/s41467-020-17736-x.
- [218] Nicole Harmouche, Christopher Aisenbrey, Fernando Porcelli, Youlin Xia, Sarah E. D. Nelson, Xi Chen, Jesus Raya, Louic Vermeer, Conrado Aparicio, Gianluigi Veglia, Sven-Ulrik Gorr, Burkhard Bechinger, Solution and solid-state nuclear magnetic resonance structural investigations of the antimicrobial designer peptide GL13K in membranes, *Biochemistry* **2017**, *32*, 4269–4278. DOI: 10.1021/acs.biochem.7b00526.
- [219] Zhou Ye, Xiao Zhu, Sergio Acosta, Dhiraj Kumar, Ting Sang, Conrado Aparicio, Self-assembly dynamics and antimicrobial activity of all L- and D-amino acid enantiomers of a designer peptide, *Nanoscale* **2019**, *1*, 266–275. DOI: 10.1039/C8NR07334A.
- [220] Vinod Balhara, Rolf Schmidt, Sven-Ulrik Gorr, Christine Dewolf, Membrane selectivity and biophysical studies of the antimicrobial peptide GL13K, *Biochim. Biophys. Acta* **2013**, *9*, 2193–2203. DOI: 10.1016/j.bbamem.2013.05.027.
- [221] Christopher W. Kaplan, Jee H. Sim, Kevin R. Shah, Aida Kolesnikova-Kaplan, Wen Yuan Shi, Randal Eckert, Selective membrane disruption: Mode of action of C16G2, a specifically targeted antimicrobial peptide, *Antimicrob. Agents Chemother.* **2011**, *7*, 3446–3452. DOI: 10.1128/AAC.00342-11.
- [222] Hans G. Boman, Birgitta Agerberth, Anita Boman, Mechanisms of action on *Escherichia coli* of cecropin P1 and PR-39, two antibacterial peptides from pig intestine, *Infect. Immun.* **1993**, *7*, 2978–2984.
- [223] Micheal Zasloff, Magainins, a class of antimicrobial peptides from *Xenopus* skin: Isolation, characterization of two active forms, and partial cDNA sequence of a precursor, *Proc. Natl. Acad. Sci. USA* **1987**, *15*, 5449–5453. DOI: 10.1073/pnas.84.15.5449.
- [224] Marcelo D. T. Torres, Jicong Cao, Octavio L. Franco, Timothy K. Lu, César de la Fuente-Núñez, Synthetic Biology and Computer-Based Frameworks for Antimicrobial Peptide Discovery, *ACS nano* **2021**, *2*, 2143–2164. DOI: 10.1021/acsnano.0c09509.
- [225] Håkan Steiner, D. Hultmark, Å. Engström, H. Bennich, Hans G. Boman, Sequence and specificity of two antibacterial proteins involved in insect immunity, *Nature* **1981**, *5820*, 246–248. DOI: 10.1038/292246a0.
- [226] David Andreu, Robert B. Merrifield, Håkan Steiner, Hans G. Boman, Solid-phase synthesis of cecropin A and related peptides, *Proc. Natl. Acad. Sci. USA* **1983**, *21*, 6475–6479. DOI: 10.1073/pnas.80.21.6475.
- [227] David Andreu, Robert B. Merrifield, Håkan Steiner, Hans G. Boman, N-terminal analogues of cecropin A: Synthesis, antibacterial activity, and conformational properties, *Biochemistry* **1985**, *7*, 1683–1688. DOI: 10.1021/bi00328a017.
- [228] Hao-Chia Chen, Judith H. Brown, John L. Morell, C. M. Huang, Synthetic magainin analogues with improved antimicrobial activity, *FEBS Lett.* **1988**, *2*, 462–466. DOI: 10.1016/0014-5793(88)80077-2.
- [229] Sannamu Lee, Hisakazu Mihara, Haruhiko Aoyagi, Tetsuo Kato, Nobuo Izumiya, Nobuyuki Yamasaki, Relationship between antimicrobial activity and amphiphilic property of basic model peptides, *Biochim. Biophys. Acta - Biomembranes* **1986**, *1*, 211–219. DOI: 10.1016/0005-2736(86)90485-2.
- [230] Sylvie E. Blondelle, Richard A. Houghten, Design of model amphipathic peptides having potent antimicrobial activities, *Biochemistry* **1992**, *50*, 12688–12694. DOI: 10.1021/bi00165a020.
- [231] David Wade, David Andreu, S. A. Mitchell, A. M. V. Silveira, Anita Boman, Hans G. Boman, Robert B. Merrifield, Antibacterial peptides designed as analogs or hybrids of cecropins and melittin, *Int. J. Pept. Protein Res.* **1992**, *5*, 429–436. DOI: 10.1111/j.1399-3011.1992.tb00321.x.
- [232] W. L. Maloy, U. P. Kari, Structure-activity studies on magainins and other host defense peptides, *Biopolymers (Pept. Sci.)* **1995**, *2*, 105–122. DOI: 10.1002/bip.360370206.
- [233] Lingxiu Zhong, Rebecca J. Putnam, W. C. Johnson, A. G. Rao, Design and synthesis of amphipathic antimicrobial peptides, *Int. J. Pept. Protein Res.* **1995**, *4*, 337–347. DOI: 10.1111/j.1399-3011.1995.tb01047.x.
- [234] Jörg Andrä, Otto Berninghausen, Jan Wülfken, Matthias Leippe, Shortened amoebapore analogs with enhanced antibacterial and cytolytic activity, *FEBS Lett.* **1996**, *1-2*, 96–100. DOI: 10.1016/0014-5793(96)00359-6.
- [235] Sylvie E. Blondelle, Richard A. Houghten, Novel antimicrobial compounds identified using synthetic combinatorial library technology, *Trends Biotechnol.* **1996**, *2*, 60–65. DOI: 10.1016/0167-7799(96)80922-X.

- [236] Sylvie E. Blondelle, Karl Lohner, Combinatorial libraries: A tool to design antimicrobial and antifungal peptide analogues having lytic specificities for structure-activity relationship studies, *Biopolymers (Pept. Sci.)* **2000**, *1*, 74–87. DOI: 10.1002/1097-0282(2000)55:1<74::AID-BIP70>3.0.CO;2-S.
- [237] Margitta Dathe, Michael Schümann, Torsten Wieprecht, Anett Winkler, Michael Beyermann, Eberhard Krause, Katsumi Matsuzaki, Osamu Murase, Michael Bienert, Peptide helicity and membrane surface charge modulate the balance of electrostatic and hydrophobic interactions with lipid bilayers and biological membranes, *Biochemistry* **1996**, *38*, 12612–12622. DOI: 10.1021/bi960835f.
- [238] Margitta Dathe, Torsten Wieprecht, Heike Nikolenko, Liselotte Handel, W. L. Maloy, Dorothy L. MacDonald, Michael Beyermann, Michael Bienert, Hydrophobicity, hydrophobic moment and angle subtended by charged residues modulate antibacterial and haemolytic activity of amphipathic helical peptides, *FEBS Lett.* **1997**, *2*, 208–212. DOI: 10.1016/S0014-5793(97)00055-0.
- [239] Torsten Wieprecht, Margitta Dathe, Michael Beyermann, Eberhard Krause, W. L. Maloy, Dorothy L. MacDonald, Michael Bienert, Peptide hydrophobicity controls the activity and selectivity of magainin 2 amide in interaction with membranes, *Biochemistry* **1997**, *20*, 6124–6132. DOI: 10.1021/bi9619987.
- [240] Torsten Wieprecht, Margitta Dathe, Eberhard Krause, Michael Beyermann, W. Lee Maloy, Dorothy L. MacDonald, Michael Bienert, Modulation of membrane activity of amphipathic, antibacterial peptides by slight modifications of the hydrophobic moment, *FEBS Lett.* **1997**, *1*, 135–140. DOI: 10.1016/S0014-5793(97)01266-0.
- [241] M. E. Houston, Jr., L. H. Kondejewski, D. N. Karunaratne, M. Gough, S. Fidai, R. S. Hodges, R. E. W. Hancock, Influence of preformed α -helix and α -helix induction on the activity of cationic antimicrobial peptides, *J. Pept. Res.* **1998**, *2*, 81–88. DOI: 10.1111/j.1399-3011.1998.tb01361.x.
- [242] Lijuan Zhang, Roland Benz, Robert E. W. Hancock, Influence of proline residues on the antibacterial and synergistic activities of alpha-helical peptides, *Biochemistry* **1999**, *25*, 8102–8111. DOI: 10.1021/bi9904104.
- [243] Torsten Wieprecht, Margitta Dathe, Richard M. Epand, Michael Beyermann, Eberhard Krause, W. L. Maloy, Dorothy L. MacDonald, Michael Bienert, Influence of the angle subtended by the positively charged helix face on the membrane activity of amphipathic, antibacterial peptides, *Biochemistry* **1997**, *42*, 12869–12880. DOI: 10.1021/bi971398n.
- [244] Ziqing Jiang, Adriana I. Vasil, Lajos Gera, Michael L. Vasil, Robert S. Hodges, Rational design of α -helical antimicrobial peptides to target Gram-negative pathogens, *Acinetobacter baumannii* and *Pseudomonas aeruginosa*: Utilization of charge, 'specificity determinants,' total hydrophobicity, hydrophobe type and location as design parameters to improve the therapeutic ratio, *Chem. Biol. Drug Des.* **2011**, *4*, 225–240. DOI: 10.1111/j.1747-0285.2011.01086.x.
- [245] Alessandro Tossi, Chiara Tarantino, Domenico Romeo, Design of synthetic antimicrobial peptides based on sequence analogy and amphipathicity, *Eur. J. Biochem.* **1997**, *2*, 549–558. DOI: 10.1111/j.1432-1033.1997.0549a.x.
- [246] Igor Zelezetsky, Sabrina Pacor, Ulrike Pag, Niv Papo, Yechiel Shai, Hans-Georg Sahl, Alessandro Tossi, Controlled alteration of the shape and conformational stability of α -helical cell-lytic peptides: Effect on mode of action and cell specificity, *Biochem. J.* **2005**, *1*, 177–188. DOI: 10.1042/BJ20042138.
- [247] Christopher D. Fjell, Jan A. Hiss, Robert E. W. Hancock, Gisbert Schneider, Designing antimicrobial peptides: Form follows function, *Nat. Rev. Drug Discov.* **2011**, *1*, 37–51. DOI: 10.1038/nrd3591.
- [248] Artem Cherkasov, Kai Hilpert, Håvard Jenssen, Christopher D. Fjell, Matt Waldbrook, Sarah C. Mullaly, Rudolf Volkmer, Robert E. W. Hancock, Use of artificial intelligence in the design of small peptide antibiotics effective against a broad spectrum of highly antibiotic-resistant superbugs, *ACS Chem. Biol.* **2009**, *1*, 65–74. DOI: 10.1021/cb800240j.
- [249] Christopher D. Fjell, Håvard Jenssen, Kai Hilpert, Warren A. Cheung, Nelly Panté, Robert E. W. Hancock, Artem Cherkasov, Identification of novel antibacterial peptides by chemoinformatics and machine learning, *J. Med. Chem.* **2009**, *7*, 2006–2015. DOI: 10.1021/jm8015365.
- [250] Kai Hilpert, Rudolf Volkmer-Engert, Tess Walter, Robert E. W. Hancock, High-throughput generation of small antibacterial peptides with improved activity, *Nat. Biotechnol.* **2005**, *8*, 1008–1012. DOI: 10.1038/nbt1113.
- [251] Nannette Y. Yount, David C. Weaver, Ernest Y. Lee, Michelle W. Lee, Huiyuan Wang, Liana C. Chan, Gerard C. L. Wong, Michael R. Yeaman, Unifying structural signature of eukaryotic α -helical host defense peptides, *Proc. Natl. Acad. Sci. USA* **2019**, *14*, 6944–6953. DOI: 10.1073/pnas.1819250116.
- [252] Christopher Loose, Kyle Jensen, Isidore Rigoutsos, Gregory Stephanopoulos, A linguistic model for the rational design of antimicrobial peptides, *Nature* **2006**, *7113*, 867–869. DOI: 10.1038/nature05233.
- [253] William F. Porto, Isabel C. M. Fensterseifer, Suzana M. Ribeiro, Octavio L. Franco, Joker: An algorithm to insert patterns into sequences for designing antimicrobial peptides, *Biochim. Biophys. Acta Gen. Subj.* **2018**, *9*, 2043–2052. DOI: 10.1016/j.bbagen.2018.06.011.

7. Bibliography

- [254] Igor E. Eliseev, Ivan N. Terterov, Anna N. Yudenko, Olga V. Shamova, Linking sequence patterns and functionality of alpha-helical antimicrobial peptides, *Bioinformatics (Oxford, England)* **2019**, *16*, 2713–2717. DOI: 10.1093/bioinformatics/bty1048.
- [255] Shail Patel, Ian P. Stott, Manmohan Bhakoo, Peter Elliott, Patenting computer-designed peptides, *J. Comput. Aided Mol. Des.* **1998**, *6*, 543–556. DOI: 10.1023/A:1008095802767.
- [256] Mari Yoshida, Trevor Hinkley, Soichiro Tsuda, Yousef M. Abul-Haija, Roy T. McBurney, Vladislav Kulikov, Jennifer S. Mathieson, Sabrina Galiñanes Reyes, Maria D. Castro, Leroy Cronin, Using evolutionary algorithms and machine learning to explore sequence space for the discovery of antimicrobial peptides, *Chem* **2018**, *3*, 533–543. DOI: 10.1016/j.chempr.2018.01.005.
- [257] William F. Porto, Luz Irazazabal, Eliane S. F. Alves, Suzana M. Ribeiro, Carolina O. Matos, Állan S. Pires, Isabel C. M. Fensterseifer, Vivian J. Miranda, Evan F. Haney, Vincent Humblot, Marcelo D. T. Torres, Robert E. W. Hancock, Luciano M. Liao, Ali Ladram, Timothy K. Lu, César d. La Fuente-Núñez, Octavio L. Franco, In silico optimization of a guava antimicrobial peptide enables combinatorial exploration for peptide design, *Nat. Commun.* **2018**, *1*, 1490. DOI: 10.1038/s41467-018-03746-3.
- [258] Meijuan Wang, Ying Wang, Aili Wang, Yuzhu Song, Dongying Ma, Hailong Yang, Yufang Ma, Ren Lai, Five novel antimicrobial peptides from skin secretions of the frog, *Amolops loloensis*, *Comp. Biochem. Physiol. B* **2010**, *1*, 72–76. DOI: 10.1016/j.cbpb.2009.10.003.
- [259] Guangshun Wang, Xia Li, Zhe Wang, APD3: The antimicrobial peptide database as a tool for research and education, *Nucleic Acids Res.* **2016**, *D1*, D1087–D1093. DOI: 10.1093/nar/gkv1278.
- [260] Biswajit Mishra, Guangshun Wang, *Ab initio* design of potent anti-MRSA peptides based on database filtering technology, *J. Am. Chem. Soc.* **2012**, *30*, 12426–12429. DOI: 10.1021/ja305644e.
- [261] Biswajit Mishra, Jayaram Lakshmaiah Narayana, Tamara Lushnikova, Xiuqing Wang, Guangshun Wang, Low cationicity is important for systemic in vivo efficacy of database-derived peptides against drug-resistant Gram-positive pathogens, *Proc. Natl. Acad. Sci. USA* **2019**, *27*, 13517–13522. DOI: 10.1073/pnas.1821410116.
- [262] José L. Anaya-López, Joel E. López-Meza, Alejandra Ochoa-Zarzosa, Bacterial resistance to cationic antimicrobial peptides, *Crit. Rev. Microbiol.* **2013**, *2*, 180–195. DOI: 10.3109/1040841X.2012.699025.
- [263] Réka Spohn, Lejla Daruka, Viktória Lázár, Ana Martins, Fanni Vidovics, Gábor Grézel, Orsolya Méhi, Bálint Kintszes, Mónika Számel, Pramod K. Jangir, Bálint Csörgő, Ádám Györkei, Zoltán Bódi, Anikó Faragó, László Bodai, Imre Földesi, Diána Kata, Gergely Maróti, Bernadett Pap, Roland Wirth, Balázs Papp, Csaba Pál, Integrated evolutionary analysis reveals antimicrobial peptides with limited resistance, *Nat. Commun.* **2019**, *1*, 4538. DOI: 10.1038/s41467-019-12364-6.
- [264] Bernard J. Moncla, Kara Pryke, Lisa C. Rohan, Phillip W. Graebing, Degradation of naturally occurring and engineered antimicrobial peptides by proteases, *Adv. Biosci. Biotechnol.* **2011**, *6*, 404–408. DOI: 10.4236/abb.2011.26059.
- [265] Maelíosa T. C. McCrudden, Denise T. F. McLean, Mei Zhou, Julia Shaw, Gerard J. Linden, Chris R. Irwin, Fionnuala T. Lundy, The host defence peptide LL-37 is susceptible to proteolytic degradation by wound fluid isolated from foot ulcers of diabetic patients, *Int. J. Pept. Res. Ther.* **2014**, *4*, 457–464. DOI: 10.1007/s10989-014-9410-3.
- [266] Artur Schmidtchen, Inga-Maria Frick, Emma Andersson, Hans Tapper, Lars Björck, Proteinases of common pathogenic bacteria degrade and inactivate the antibacterial peptide LL-37, *Mol. Microbiol.* **2002**, *1*, 157–168. DOI: 10.1046/j.1365-2958.2002.03146.x.
- [267] Magdalena Sieprawska-Lupa, Piotr Mydel, Katarzyna Krawczyk, Kinga Wójcik, Magdalena Puklo, Bogusław Lupa, Piotr Suder, Jerzy Silberring, Matthew Reed, Jan Pohl, William Shafer, Fionnuala McAleese, Timothy Foster, Jim Travis, Jan Potempa, Degradation of human antimicrobial peptide LL-37 by *Staphylococcus aureus*-derived proteinases, *Antimicrob. Agents Chemother.* **2004**, *12*, 4673–4679. DOI: 10.1128/AAC.48.12.4673–4679.2004.
- [268] Adam A. Strömstedt, Mukesh Pasupuleti, Artur Schmidtchen, Martin Malmsten, Evaluation of strategies for improving proteolytic resistance of antimicrobial peptides by using variants of EFK17, an internal segment of LL-37, *Antimicrob. Agents Chemother.* **2009**, *2*, 593–602. DOI: 10.1128/AAC.00477-08.
- [269] Guangshun Wang, Mark L. Hanke, Biswajit Mishra, Tamara Lushnikova, Courtney E. Heim, Vinai Chittiezham Thomas, Kenneth W. Bayles, Tammy Kielian, Transformation of human cathelicidin LL-37 into selective, stable, and potent antimicrobial compounds, *ACS Chem. Biol.* **2014**, *9*, 1997–2002. DOI: 10.1021/cb500475y.
- [270] Daniel Knappe, Petra Henklein, Ralf Hoffmann, Kai Hilpert, Easy strategy to protect antimicrobial peptides from fast degradation in serum, *Antimicrob. Agents Chemother.* **2010**, *9*, 4003–4005. DOI: 10.1128/AAC.00300-10.
- [271] Ann E. Shinnar, Kathryn L. Butler, Hyon J. Park, Cathelicidin family of antimicrobial peptides: Proteolytic processing and protease resistance, *Bioorg. Chem.* **2003**, *6*, 425–436. DOI: 10.1016/S0045-2068(03)00080-4.
- [272] Hyun Kim, Ju H. Jang, Sun C. Kim, Ju H. Cho, *De novo* generation of short antimicrobial peptides with enhanced stability and cell specificity, *J. Antimicrob. Chemother.* **2014**, *1*, 121–132. DOI: 10.1093/jac/dkt322.

- [273] Dorian Migoń, Damian Neubauer, Wojciech Kamysz, Hydrocarbon stapled antimicrobial peptides, *Protein J.* **2018**, *1*, 2–12. DOI: 10.1007/s10930-018-9755-0.
- [274] Rida Mourtada, Henry D. Herce, Daniel J. Yin, Jamie A. Moroco, Thomas E. Wales, John R. Engen, Loren D. Walensky, Design of stapled antimicrobial peptides that are stable, nontoxic and kill antibiotic-resistant bacteria in mice, *Nat. Biotechnol.* **2019**, *10*, 1186–1197. DOI: 10.1038/s41587-019-0222-z.
- [275] Marcelo D. T. Torres, Cibele N. Pedron, Yasutomi Higashikuni, Robin M. Kramer, Marlon H. Cardoso, Karen G. N. Oshiro, Octávio L. Franco, Pedro I. Silva Junior, Fernanda D. Silva, Vani X. Oliveira Junior, Timothy K. Lu, César de la Fuente-Núñez, Structure-function-guided exploration of the antimicrobial peptide polybia-CP identifies activity determinants and generates synthetic therapeutic candidates, *Commun. Biol.* **2018**, *221*. DOI: 10.1038/s42003-018-0224-2.
- [276] Berthony Deslouches, Shruti M. Phadke, Vanja Lazarevic, Michael Cascio, Kazi Islam, Ronald C. Montelaro, Timothy A. Mietzner, De novo generation of cationic antimicrobial peptides: Influence of length and tryptophan substitution on antimicrobial activity, *Antimicrob. Agents Chemother.* **2005**, *1*, 316–322. DOI: 10.1128/AAC.49.1.316-322.2005.
- [277] Xia Li, Yifeng Li, Huiyun Han, Donald W. Miller, Guangshun Wang, Solution structures of human LL-37 fragments and NMR-based identification of a minimal membrane-targeting antimicrobial and anticancer region, *J. Am. Chem. Soc.* **2006**, *17*, 5776–5785. DOI: 10.1021/ja0584875.
- [278] Binu Jacob, Il-Seon Park, Jeong-Kyu Bang, Song Y. Shin, Short KR-12 analogs designed from human cathelicidin LL-37 possessing both antimicrobial and antiendotoxic activities without mammalian cell toxicity, *J. Pept. Sci.* **2013**, *11*, 700–707. DOI: 10.1002/psc.2552.
- [279] Lijuan Zhang, T. Falla, Manhong Wu, S. Fidai, J. Burian, W. Kay, Robert E. W. Hancock, Determinants of recombinant production of antimicrobial cationic peptides and creation of peptide variants in bacteria, *Biochem. Biophys. Res. Commun.* **1998**, *3*, 674–680. DOI: 10.1006/bbrc.1998.8848.
- [280] Aaron B. Ingham, Robert J. Moore, Recombinant production of antimicrobial peptides in heterologous microbial systems, *Biotechnol. Appl. Biochem.* **2007**, *1*, 1–9. DOI: 10.1042/BA20060207.
- [281] B. Bommarius, H. Jenssen, M. Elliott, J. Kindrachuk, Mukesh Pasupuleti, H. Gieren, K.-E. Jaeger, R. E. W. Hancock, D. Kalman, Cost-effective expression and purification of antimicrobial and host defense peptides in *Escherichia coli*, *Peptides* **2010**, *11*, 1957–1965. DOI: 10.1016/j.peptides.2010.08.008.
- [282] David Wibowo, Chun-Xia Zhao, Recent achievements and perspectives for large-scale recombinant production of antimicrobial peptides, *Appl. Microbiol. Biotechnol.* **2019**, *2*, 659–671. DOI: 10.1007/s00253-018-9524-1.
- [283] Dzintars Gotham, Melissa J. Barber, Andrew Hill, Production costs and potential prices for biosimilars of human insulin and insulin analogues, *BMJ Glob. Health* **2018**, *5*, e000850. DOI: 10.1136/bmjgh-2018-000850.
- [284] R. P. Elander, Industrial production of beta-lactam antibiotics, *Appl. Microbiol. Biotechnol.* **2003**, *5-6*, 385–392. DOI: 10.1007/s00253-003-1274-y.
- [285] Joel D. A. Tyndall, Tessa Nall, David P. Fairlie, Proteases universally recognize beta strands in their active sites, *Chem. Rev.* **2005**, *3*, 973–999. DOI: 10.1021/cr040669e.
- [286] Nils Preußke, Matthias Lipfert, Sven Rothmund, Matthias Leippe, Frank D. Sönnichsen, Designed Trp-cage proteins with antimicrobial activity and enhanced stability, *Biochemistry* **2021**, *42*, 3187–3199. DOI: 10.1021/acs.biochem.1c00567.
- [287] David A. Monner, Staffan Jonsson, Hans G. Boman, Ampicillin-resistant mutants of *Escherichia coli* K-12 with lipopolysaccharide alterations affecting mating ability and susceptibility to sex-specific bacteriophages, *J. Bacteriol.* **1971**, *2*, 420–432. DOI: 10.1128/JB.107.2.420-432.1971.
- [288] Henning Fedders, Matthias Michalek, Joachim Grötzinger, Matthias Leippe, An exceptional salt-tolerant antimicrobial peptide derived from a novel gene family of haemocytes of the marine invertebrate *Ciona intestinalis*, *Biochem. J.* **2008**, *1*, 65–75. DOI: 10.1042/BJ20080398.
- [289] Petr Klán, Tomáš Šolomek, Christian G. Bochet, Aurélien Blanc, Richard Givens, Marina Rubina, Vladimir Popik, Alexey Kostikov, Jakob Wirz, Photoremovable protecting groups in chemistry and biology: Reaction mechanisms and efficacy, *Chem. Rev.* **2013**, *1*, 119–191. DOI: 10.1021/cr300177k.
- [290] Willem A. Velema, Wiktor Szymanski, Ben L. Feringa, Photopharmacology: Beyond proof of principle, *J. Am. Chem. Soc.* **2014**, *6*, 2178–2191. DOI: 10.1021/ja413063e.
- [291] Katharina Hüll, Johannes Morstein, Dirk Trauner, *In Vivo* Photopharmacology, *Chem. Rev.* **2018**, *21*, 10710–10747. DOI: 10.1021/acs.chemrev.8b00037.
- [292] Jana Volarić, Wiktor Szymanski, Nadja A. Simeth, Ben L. Feringa, Molecular photoswitches in aqueous environments, *Chem. Soc. Rev.* **2021**. DOI: 10.1039/D0CS00547A.
- [293] Heike Fliegl, Andreas Köhn, Christof Hättig, Reinhart Ahlrichs, Ab initio calculation of the vibrational and electronic spectra of *trans*- and *cis*-azobenzene, *J. Am. Chem. Soc.* **2003**, *32*, 9821–9827. DOI: 10.1021/ja034433o.

7. Bibliography

- [294] Asbjørn Mostad, Chr. Rømming, A refinement of the crystal structure of *cis*-azobenzene, *Acta Chem. Scand.* **1971**, 3561–3568. DOI: 10.3891/acta.chem.scand.25-3561.
- [295] G. S. Hartley, The *cis*-form of azobenzene, *Nature* **1937**, 3537, 281. DOI: 10.1038/140281a0.
- [296] Lea Albert, Olalla Vázquez, Photoswitchable peptides for spatiotemporal control of biological functions, *Chem. Commun.* **2019**, 69, 10192–10213. DOI: 10.1039/c9cc03346g.
- [297] Andrew A. Beharry, G. A. Woolley, Azobenzene photoswitches for biomolecules, *Chem. Soc. Rev.* **2011**, 8, 4422–4437. DOI: 10.1039/c1cs15023e.
- [298] Robert J. Mart, Rudolf K. Allemann, Azobenzene photocontrol of peptides and proteins, *Chem. Commun.* **2016**, 83, 12262–12277. DOI: 10.1039/c6cc04004g.
- [299] Andrew A. Beharry, Oleg Sadovski, G. A. Woolley, Azobenzene photoswitching without ultraviolet light, *J. Am. Chem. Soc.* **2011**, 49, 19684–19687. DOI: 10.1021/ja209239m.
- [300] Keld Fosgerau, Torsten Hoffmann, Peptide therapeutics: Current status and future directions, *Drug Discov. Today* **2015**, 1, 122–128. DOI: 10.1016/j.drudis.2014.10.003.
- [301] Tom Podewin, Johannes Broichhagen, Christina Frost, Dieter Groneberg, Julia Ast, Helena Meyer-Berg, Nicholas H. F. Fine, Andreas Friebe, Martin Zacharias, David J. Hodson, Dirk Trauner, Anja Hoffmann-Röder, Optical control of a receptor-linked guanylyl cyclase using a photoswitchable peptidic hormone, *Chem. Sci.* **2017**, 6, 4644–4653. DOI: 10.1039/C6SC05044A.
- [302] Johannes Broichhagen, Tom Podewin, Helena Meyer-Berg, Yorrick von Ohlen, Natalie R. Johnston, Ben J. Jones, Stephen R. Bloom, Guy A. Rutter, Anja Hoffmann-Röder, David J. Hodson, Dirk Trauner, Optical Control of Insulin Secretion Using an Incretin Switch, *Angew. Chem. Int. Ed.* **2015**, 51, 15565–15569. DOI: 10.1002/anie.201506384.
- [303] Lea Albert, Jing Xu, Ruiwei Wan, Vasundara Srinivasan, Yali Dou, Olalla Vázquez, Controlled inhibition of methyltransferases using photoswitchable peptidomimetics: Towards an epigenetic regulation of leukemia, *Chem. Sci.* **2017**, 6, 4612–4618. DOI: 10.1039/c7sc00137a.
- [304] Andreas Prestel, Heiko M. Möller, Spatio-temporal control of cellular uptake achieved by photoswitchable cell-penetrating peptides, *Chem. Commun.* **2016**, 4, 701–704. DOI: 10.1039/c5cc06848g.
- [305] Christian Hoppmann, Sabine Seedorff, Anja Richter, Heinz Fabian, Peter Schmieder, Karola Rück-Braun, Michael Beyermann, Light-directed protein binding of a biologically relevant beta-sheet, *Angew. Chem. Int. Ed.* **2009**, 36, 6636–6639. DOI: 10.1002/anie.200901933.
- [306] Christian Hoppmann, Peter Schmieder, Petra Domaing, Gabriela Vogelreiter, Jenny Eichhorst, Burkhard Wiesner, Ingo Morano, Karola Rück-Braun, Michael Beyermann, Photocontrol of contracting muscle fibers, *Angew. Chem. Int. Ed.* **2011**, 33, 7699–7702. DOI: 10.1002/anie.201101398.
- [307] Ana M. Caamaño, M. E. Vázquez, José Martínez-Costas, Luis Castedo, José L. Mascareñas, A light-modulated sequence-specific DNA-binding peptide, *Angew. Chem. Int. Ed.* **2000**, 17, 3104–3107. DOI: 10.1002/1521-3773(20000901)39:17<3104::AID-ANIE3104>3.0.CO;2-O.
- [308] Janet R. Kumita, Oliver S. Smart, G. A. Woolley, Photo-control of helix content in a short peptide, *Proc. Natl. Acad. Sci. USA* **2000**, 8, 3803–3808. DOI: 10.1073/pnas.97.8.3803.
- [309] Daniel G. Flint, Janet R. Kumita, Oliver S. Smart, G. A. Woolley, Using an Azobenzene Cross-Linker to Either Increase or Decrease Peptide Helix Content upon Trans-to-Cis Photoisomerization, *Chem. Biol.* **2002**, 3, 391–397. DOI: 10.1016/S1074-5521(02)00109-6.
- [310] Fuzhong Zhang, Arash Zarrine-Afsar, M. S. Al-Abdul-Wahid, R. S. Prosser, Alan R. Davidson, G. A. Woolley, Structure-based approach to the photocontrol of protein folding, *J. Am. Chem. Soc.* **2009**, 6, 2283–2289. DOI: 10.1021/ja807938v.
- [311] Benno Schierling, Ann-Josée Noël, Wolfgang Wende, Le T. Hien, Eugeny Volkov, Elena Kubareva, Tatiana Oretskaya, Michael Kokkinidis, Andreas Römpf, Bernhard Spengler, Alfred Pingoud, Controlling the enzymatic activity of a restriction enzyme by light, *Proc. Natl. Acad. Sci. USA* **2010**, 4, 1361–1366. DOI: 10.1073/pnas.0909444107.
- [312] Silvia Bellotto, Shiyu Chen, Inmaculada Rentero Rebollo, Hermann A. Wegner, Christian Heinis, Phage selection of photoswitchable peptide ligands, *J. Am. Chem. Soc.* **2014**, 16, 5880–5883. DOI: 10.1021/ja501861m.
- [313] Mohammad R. Jafari, Lu Deng, Pavel I. Kitov, Simon Ng, Wadim L. Matochko, Katrina F. Tjhung, Anthony Zeberoff, Anastasia Elias, John S. Klassen, Ratmir Derda, Discovery of light-responsive ligands through screening of a light-responsive genetically encoded library, *ACS Chem. Biol.* **2014**, 2, 443–450. DOI: 10.1021/cb4006722.
- [314] Darcy C. Burns, Daniel G. Flint, Janet R. Kumita, Howard J. Feldman, Luis Serrano, Zhihua Zhang, Oliver S. Smart, G. A. Woolley, Origins of helix-coil switching in a light-sensitive peptide, *Biochemistry* **2004**, 49, 15329–15338. DOI: 10.1021/bi048152k.

- [315] Zhihua Zhang, Darcy C. Burns, Janet R. Kumita, Oliver S. Smart, G. A. Woolley, A water-soluble azobenzene cross-linker for photocontrol of peptide conformation, *Bioconjugate Chem.* **2003**, *4*, 824–829. DOI: 10.1021/bc0340161.
- [316] Darcy C. Burns, Fuzhong Zhang, G. A. Woolley, Synthesis of 3,3'-bis(sulfonato)-4,4'-bis(chloroacetamido)azobenzene and cysteine cross-linking for photo-control of protein conformation and activity, *Nat. Protoc.* **2007**, *2*, 251–258. DOI: 10.1038/nprot.2007.21.
- [317] Frederic M. Richards, Paul J. Vithayathil, The Preparation of Subtilisin-modified Ribonuclease and the Separation of the Peptide and Protein Components, *J. Biol. Chem.* **1959**, *6*, 1459–1465. DOI: 10.1016/S0021-9258(18)70031-8.
- [318] Eunice E. Kim, Raghavan Varadarajan, Harold W. Wyckoff, Frederic M. Richards, Refinement of the crystal structure of ribonuclease S: Comparison with and between the various ribonuclease A structures, *Biochemistry* **1992**, *49*, 12304–12314. DOI: 10.1021/bi00164a004.
- [319] Brankica Jankovic, Adnan Gulzar, Claudio Zanobini, Olga Bozovic, Steffen Wolf, Gerhard Stock, Peter Hamm, Photocontrolling Protein-Peptide Interactions: From Minimal Perturbation to Complete Unbinding, *J. Am. Chem. Soc.* **2019**, *27*, 10702–10710. DOI: 10.1021/jacs.9b03222.
- [320] Sabine Kneissl, E. J. Loveridge, Christopher Williams, Matthew P. Crump, Rudolf K. Allemann, Photocontrollable peptide-based switches target the anti-apoptotic protein Bcl-x_L, *ChemBioChem* **2008**, *18*, 3046–3054. DOI: 10.1002/cbic.200800502.
- [321] M. G. Vander Heiden, C. B. Thompson, Bcl-2 proteins: Regulators of apoptosis or of mitochondrial homeostasis?, *Nat. Cell Biol.* **1999**, *8*, E209–E216. DOI: 10.1038/70237.
- [322] Judith Michels, Oliver Kepp, Laura Senovilla, Delphine Lissa, Maria Castedo, Guido Kroemer, Lorenzo Galluzzi, Functions of BCL-X L at the Interface between Cell Death and Metabolism, *Int. J. Cell Biol.* **2013**, 705294. DOI: 10.1155/2013/705294.
- [323] Peter E. Czabotar, Guillaume Lessene, Andreas Strasser, Jerry M. Adams, Control of apoptosis by the BCL-2 protein family: Implications for physiology and therapy, *Nat. Rev. Mol. Cell Biol.* **2014**, *1*, 49–63. DOI: 10.1038/nrm3722.
- [324] Jerry M. Adams, Suzanne Cory, The BCL-2 arbiters of apoptosis and their growing role as cancer targets, *Cell Death Differ.* **2018**, *1*, 27–36. DOI: 10.1038/cdd.2017.161.
- [325] David L. Vaux, Suzanne Cory, Jerry M. Adams, Bcl-2 gene promotes haemopoietic cell survival and cooperates with c-myc to immortalize pre-B cells, *Nature* **1988**, *6189*, 440–442. DOI: 10.1038/335440a0.
- [326] Andrew M. Petros, Ales Medek, David G. Nettesheim, Daniel H. Kim, Ho S. Yoon, Kerry Swift, Edmund D. Matayoshi, Tilman Oltersdorf, Stephen W. Fesik, Solution structure of the antiapoptotic protein bcl-2, *Proc. Natl. Acad. Sci. USA* **2001**, *6*, 3012–3017. DOI: 10.1073/pnas.041619798.
- [327] Motoshi Suzuki, Richard J. Youle, Nico Tjandra, Structure of Bax: Coregulation of Dimer Formation and Intracellular Localization, *Cell* **2000**, *4*, 645–654. DOI: 10.1016/S0092-8674(00)00167-7.
- [328] Michael Sattler, Heng Liang, David Nettesheim, Robert P. Meadows, John E. Harlan, Matthias Eberstadt, Ho S. Yoon, Suzanne B. Shuker, Brian S. Chang, Andy J. Minn, Craig B. Thompson, Stephen W. Fesik, Structure of Bcl-x_L-Bak Peptide Complex: Recognition Between Regulators of Apoptosis, *Science* **1997**, *5302*, 983–986. DOI: 10.1126/science.275.5302.983.
- [329] Steven W. Muchmore, Micheal Sattler, Heng Liang, Robert P. Meadows, John E. Harlan, Ho S. Yoon, David Nettesheim, Brian S. Chang, Craig B. Thompson, Sui-Lam Wong, Shi-Chung Ng, Stephen W. Fesik, X-ray and NMR structure of human Bcl-x_L, an inhibitor of programmed cell death, *Nature* **1996**, *6580*, 335–341. DOI: 10.1038/381335a0.
- [330] Michael C. Kiefer, Matthew J. Brauer, Virginia C. Powers, Jason J. Wu, Samuil R. Umansky, L. D. Tomei, Philip J. Barr, Modulation of apoptosis by the widely distributed Bcl-2 homologue Bak, *Nature* **1995**, *6524*, 736–739. DOI: 10.1038/374736a0.
- [331] Thomas Chittenden, Elizabeth A. Harrington, Rosemary O'Connor, Cathy Flemington, Robert J. Lutz, Gerard I. Evan, Braydon C. Guild, Induction of apoptosis by the Bcl-2 homologue Bak, *Nature* **1995**, *6524*, 733–736. DOI: 10.1038/374733a0.
- [332] Stuart N. Farrow, Julia H. White, Isabelle Martinou, Thomas Raven, Kwok-Tao Pun, Christine J. Grinham, Jean-Claude Martinou, Robin Brown, Cloning of a bcl-2 homologue by interaction with adenovirus E1B 19K, *Nature* **1995**, *6524*, 731–733. DOI: 10.1038/374731a0.
- [333] Eric P. Holinger, Thomas Chittenden, Robert J. Lutz, Bak BH3 Peptides Antagonize Bcl-x_L Function and Induce Apoptosis through Cytochrome c-independent Activation of Caspases, *J. Biol. Chem.* **1999**, *19*, 13298–13304. DOI: 10.1074/jbc.274.19.13298.
- [334] Robert J. Mart, Rachel J. Errington, Catherine L. Watkins, Sally C. Chappell, Marie Wiltshire, Arwyn T. Jones, Paul J. Smith, Rudolf K. Allemann, BH3 helix-derived biophotonic nanoswitches regulate cytochrome c release in permeabilised cells, *Mol. Biosyst.* **2013**, *11*, 2597–2603. DOI: 10.1039/c3mb70246d.

7. Bibliography

- [335] Piotr Wysoczanski, Robert J. Mart, E. J. Loveridge, Christopher Williams, Sara B.-M. Whittaker, Matthew P. Crump, Rudolf K. Allemann, NMR solution structure of a photoswitchable apoptosis activating Bak peptide bound to Bcl-x_L, *J. Am. Chem. Soc.* **2012**, *134*, 7644–7647. DOI: 10.1021/ja302390a.
- [336] Harvey T. McMahon, Emmanuel Boucrot, Molecular mechanism and physiological functions of clathrin-mediated endocytosis, *Nat. Rev. Mol. Cell Biol.* **2011**, *12*, 517–533. DOI: 10.1038/nrm3151.
- [337] Eva M. Schmid, Marijn G. J. Ford, Anne Burtsey, Gerrit J. K. Praefcke, Sew-Yeu Peak-Chew, Ian G. Mills, Alexandre Benmerah, Harvey T. McMahon, Role of the AP2 β -appendage hub in recruiting partners for clathrin-coated vesicle assembly, *PLoS biology* **2006**, *4*, e262. DOI: 10.1371/journal.pbio.0040262.
- [338] Laura Nevola, Andrés Martín-Quirós, Kay Eckelt, Núria Camarero, Sébastien Tosi, Artur Llobet, Ernest Giralt, Pau Gorostiza, Light-regulated stapled peptides to inhibit protein-protein interactions involved in clathrin-mediated endocytosis, *Angew. Chem. Int. Ed.* **2013**, *52*, 7704–7708. DOI: 10.1002/anie.201303324.
- [339] Andrés Martín-Quirós, Laura Nevola, Kay Eckelt, Sergio Madurga, Pau Gorostiza, Ernest Giralt, Absence of a stable secondary structure is not a limitation for photoswitchable inhibitors of β -arrestin/ β -Adaptin 2 protein-protein interaction, *Chem. Biol.* **2015**, *24*, 31–37. DOI: 10.1016/j.chembiol.2014.10.022.
- [340] Gyu C. Kim, Joon H. Ahn, Jae H. Oh, Sohee Nam, Soonsil Hyun, Jaehoon Yu, Yan Lee, Photoswitching of cell penetration of amphipathic peptides by control of α -helical conformation, *Biomacromolecules* **2018**, *19*, 2863–2869. DOI: 10.1021/acs.biomac.8b00428.
- [341] Susan L. Knox, Rebecca Wissner, Samantha Piskiewicz, Alanna Schepartz, Cytosolic delivery of argininosuccinate synthetase using a cell-permeant miniature protein, *ACS central science* **2021**, *7*, 641–649. DOI: 10.1021/acscentsci.0c01603.
- [342] Janet R. Kumita, Daniel G. Flint, G. A. Woolley, Oliver S. Smart, Achieving photo-control of protein conformation and activity: Producing a photo-controlled leucine zipper, *Faraday Discuss.* **2002**, 89-103; Discussion: 171-190. DOI: 10.1039/b200897a.
- [343] Lucia Guerrero, Oliver S. Smart, Chris J. Weston, Darcy C. Burns, G. A. Woolley, Rudolf K. Allemann, Photochemical regulation of DNA-binding specificity of MyoD, *Angew. Chem. Int. Ed.* **2005**, *44*, 7778–7782. DOI: 10.1002/anie.200502666.
- [344] Ahmed M. Ali, Matthew W. Forbes, G. A. Woolley, Optimizing the Photocontrol of bZIP Coiled Coils with Azobenzene Crosslinkers: Role of the Crosslinking Site, *ChemBioChem* **2015**, *16*, 1757–1763. DOI: 10.1002/cbic.201500191.
- [345] W. B. Kauffman, Taylor Fuselier, Jing He, William C. Wimley, Mechanism matters: A Taxonomy of cell penetrating peptides, *Trends Biochem. Sci.* **2015**, *40*, 749–764. DOI: 10.1016/j.tibs.2015.10.004.
- [346] Lucia Guerrero, Oliver S. Smart, G. A. Woolley, Rudolf K. Allemann, Photocontrol of DNA binding specificity of a miniature engrailed homeodomain, *J. Am. Chem. Soc.* **2005**, *127*, 15624–15629. DOI: 10.1021/ja0550428.
- [347] Philip C. M. Ma, Mark A. Rould, Harold Weintraub, Carl O. Pabo, Crystal structure of MyoD bHLH domain-DNA complex: Perspectives on DNA recognition and implications for transcriptional activation, *Cell* **1994**, *77*, 451–459. DOI: 10.1016/0092-8674(94)90159-7.
- [348] Tom Ellenberger, Christopher J. Brandl, Kevin Struhl, Stephen C. Harrison, The GCN4 basic region leucine zipper binds DNA as a dimer of uninterrupted α -helices: Crystal structure of the protein-DNA complex, *Cell* **1992**, *70*, 1223–1237. DOI: 10.1016/S0092-8674(05)80070-4.
- [349] Tom Ellenberger, Getting a grip on DNA recognition: Structures of the basic region leucine zipper, and the basic region helix-loop-helix DNA-binding domains, *Curr. Opin. Struct. Biol.* **1994**, *4*, 12–21. DOI: 10.1016/S0959-440X(94)90054-X.
- [350] Peter König, Timothy J. Richmond, The X-ray structure of the GCN4-bZIP bound to ATF/CREB site DNA shows the complex depends on DNA flexibility, *J. Mol. Biol.* **1993**, *231*, 139–154. DOI: 10.1006/jmbi.1993.1490.
- [351] Walter Keller, Peter König, Timothy J. Richmond, Crystal structure of a bZIP/DNA complex at 2.2 Å: Determinants of DNA specific recognition, *J. Mol. Biol.* **1995**, *250*, 657–667. DOI: 10.1006/jmbi.1995.0645.
- [352] Michael A. Weiss, Tom Ellenberger, C. R. Wobbe, Jonathan P. Lee, Stephen C. Harrison, Kevin Struhl, Folding transition in the DNA-binding domain of GCN4 on specific binding to DNA, *Nature* **1990**, *347*, 575–578. DOI: 10.1038/347575a0.
- [353] G. A. Woolley, Anna S. I. Jaikaran, Maxim Berezovski, Joseph P. Calarco, Sergey N. Krylov, Oliver S. Smart, Janet R. Kumita, Reversible photocontrol of DNA binding by a designed GCN4-bZIP protein, *Biochemistry* **2006**, *45*, 6075–6084. DOI: 10.1021/bi060142r.
- [354] Fuzhong Zhang, Katharina A. Timm, Katja M. Arndt, G. A. Woolley, Photocontrol of coiled-coil proteins in living cells, *Angew. Chem. Int. Ed.* **2010**, *49*, 3943–3946. DOI: 10.1002/anie.201000909.
- [355] Robert Eferl, Erwin F. Wagner, AP-1: A double-edged sword in tumorigenesis, *Nat. Rev. Cancer* **2003**, *3*, 859–868. DOI: 10.1038/nrc1209.

- [356] John L. Battiste, Hongyuan Mao, N. S. Rao, Ruoying Tan, D. R. Muhandiram, Lewis E. Kay, Alan D. Frankel, James R. Williamson, α -Helix-RNA major groove recognition in an HIV-1 REV peptide-RRE RNA complex, *Science* **1996**, 5281, 1547–1551. DOI: 10.1126/science.273.5281.1547.
- [357] Robert J. Mart, Piotr Wysoczański, Sabine Kneissl, Antonio Ricci, Andrea Brancale, Rudolf K. Allemann, Design of photocontrolled RNA-binding peptidomimetics, *ChemBioChem* **2012**, 4, 515–519. DOI: 10.1002/cbic.201100800.
- [358] Alton Meister, Mary E. Anderson, Glutathione, *Annu. Rev. Biochem.* **1983**, 711–760. DOI: 10.1146/annurev.bi.52.070183.003431.
- [359] Cyril Boulègue, Markus Löweneck, Christian Renner, Luis Moroder, Redox potential of azobenzene as an amino acid residue in peptides, *ChemBioChem* **2007**, 6, 591–594. DOI: 10.1002/cbic.200600495.
- [360] Andrew A. Beharry, Loksum Wong, Vince Tropepe, G. A. Woolley, Fluorescence imaging of azobenzene photoswitching in vivo, *Angew. Chem. Int. Ed.* **2011**, 6, 1325–1327. DOI: 10.1002/anie.201006506.
- [361] David Bléger, Jutta Schwarz, Albert M. Brouwer, Stefan Hecht, *o*-Fluoroazobenzenes as readily synthesized photoswitches offering nearly quantitative two-way isomerization with visible light, *J. Am. Chem. Soc.* **2012**, 51, 20597–20600. DOI: 10.1021/ja310323y.
- [362] Lea Albert, Alberto Peñalver, Nemanja Djokovic, Laura Werel, Malte Hoffarth, Dusan Ruzic, Jing Xu, Lars-Oliver Essen, Katarina Nikolic, Yali Dou, Olalla Vázquez, Modulating Protein-Protein Interactions with Visible-Light-Responsive Peptide Backbone Photoswitches, *ChemBioChem* **2019**, 11, 1417–1429. DOI: 10.1002/cbic.201800737.
- [363] Ron Siewertsen, Hendrikje Neumann, Bengt Buchheim-Stehn, Rainer Herges, Christian Näther, Falk Renth, Friedrich Temps, Highly efficient reversible Z-E photoisomerization of a bridged azobenzene with visible light through resolved $S_1(n\pi^*)$ absorption bands, *J. Am. Chem. Soc.* **2009**, 43, 15594–15595. DOI: 10.1021/ja906547d.
- [364] Ron Siewertsen, Jan B. Schönborn, Bernd Hartke, Falk Renth, Friedrich Temps, Superior Z \rightarrow E and E \rightarrow Z photoswitching dynamics of dihydrodibenzodiazocine, a bridged azobenzene, by $S_1(n\pi^*)$ excitation at $\lambda = 387$ and 490 nm, *Phys. Chem. Chem. Phys.* **2011**, 3, 1054–1063. DOI: 10.1039/C0CP01148G.
- [365] Subhas Samanta, Chuanguang Qin, Alan J. Lough, G. A. Woolley, Bidirectional photocontrol of peptide conformation with a bridged azobenzene derivative, *Angew. Chem. Int. Ed.* **2012**, 26, 6452–6455. DOI: 10.1002/anie.201202383.
- [366] Gisela Cabré, Aida Garrido-Charles, Àngels González-Lafont, Widukind Moormann, Daniel Langbehn, David Egea, José M. Lluch, Rainer Herges, Ramon Alibés, Félix Busqué, Pau Gorostiza, Jordi Hernando, Synthetic Photoswitchable Neurotransmitters Based on Bridged Azobenzenes, *Org. Lett.* **2019**, 10, 3780–3784. DOI: 10.1021/acs.orglett.9b01222.
- [367] Ek R. Thapaliya, Jun Zhao, Graham C. R. Ellis-Davies, Locked-Azobenzene: Testing the Scope of a Unique Photoswitchable Scaffold for Cell Physiology, *ACS Chem. Neurosci.* **2019**, 5, 2481–2488. DOI: 10.1021/acschemneuro.8b00734.
- [368] Julie B. Trads, Katharina Hüll, Bryan S. Matsuura, Laura Laprell, Timm Fehrentz, Nicole Görltd, Krystian A. Kozek, C. D. Weaver, Nikolaj Klöcker, David M. Barber, Dirk Trauner, Sign Inversion in Photopharmacology: Incorporation of Cyclic Azobenzenes in Photoswitchable Potassium Channel Blockers and Openers, *Angew. Chem. Int. Ed.* **2019**, 43, 15421–15428. DOI: 10.1002/anie.201905790.
- [369] Charles R. Kissinger, Beishan Liu, Enrique Martin-Blanco, Thomas B. Kornberg, Carl O. Pabo, Crystal structure of an engrailed homeodomain-DNA complex at 2.8 Å resolution: A framework for understanding homeodomain-DNA interactions, *Cell* **1990**, 3, 579–590. DOI: 10.1016/0092-8674(90)90453-L.
- [370] Neil D. Clarke, Charles R. Kissinger, John Desjarlais, Gary L. Gilliland, Carl O. Pabo, Structural studies of the engrailed homeodomain, *Protein Sci.* **1994**, 10, 1779–1787. DOI: 10.1002/pro.5560031018.
- [371] Ishwar Radhakrishnan, Gabriela C. Pérez-Alvarado, David Parker, H. J. Dyson, Marc R. Montminy, Peter E. Wright, Solution structure of the KIX domain of CBP bound to the transactivation domain of CREB: A model for activator:coactivator interactions, *Cell* **1997**, 6, 741–752. DOI: 10.1016/S0092-8674(00)80463-8.
- [372] José Martinez-Oyanedel, Hui-Woog Choe, Udo Heinemann, Wolfram Saenger, Ribonuclease T₁ with free recognition and catalytic site: Crystal structure analysis at 1.5 Å resolution, *J. Mol. Biol.* **1991**, 2, 335–352. DOI: 10.1016/0022-2836(91)90215-R.
- [373] C. J. McKnight, Paul T. Matsudaira, Peter S. Kim, NMR structure of the 35-residue villin headpiece subdomain, *Nat. Struct. Biol.* **1997**, 3, 180–184. DOI: 10.1038/nsb0397-180.
- [374] Pascal Lentès, Philipp Frühwirth, Hilde Freißmuth, Widukind Moormann, Fabian Kruse, Georg Gescheidt, Rainer Herges, Photoswitching of diazocines in aqueous media, *J. Org. Chem.* **2021**, 5, 4355–4360. DOI: 10.1021/acs.joc.1c00065.
- [375] Nils Preußke, Widukind Moormann, Katrin Bamberg, Matthias Lipfert, Rainer Herges, Frank D. Sönnichsen, Visible-light-driven photocontrol of the Trp-cage protein fold by a diazocine cross-linker, *Org. Biomol. Chem.* **2020**, 14, 2650–2660. DOI: 10.1039/c9ob02442e.

8. Abbreviations

- [376] Pascal Lentès, Eduard Stadler, Fynn Röhrich, Arne Brahm, Jens Gröbner, Frank D. Sönnichsen, Georg Gescheidt, Rainer Herges, Nitrogen bridged diazocines: Photochromes switching within the near-infrared region with high quantum yields in organic solvents and in water, *J. Am. Chem. Soc.* **2019**, *34*, 13592–13600. DOI: 10.1021/jacs.9b06104.
- [377] Peter D. White, Weng C. Chan, Fmoc solid phase peptide synthesis: A practical approach, Oxford University Press, New York **2000**. ISBN: 978-0199637249.
- [378] A. J. Shaka, C. J. Lee, A. Pines, Iterative schemes for bilinear operators; application to spin decoupling, *J. Magn. Reson.* **1988**, *2*, 274–293. DOI: 10.1016/0022-2364(88)90178-3.

8. Abbreviations

A

AFP(s) - antifreeze protein(s)
AFP1-6 - isoform HPLC-6 of AFP type 1
AGC - automated gain control
AMP(s) - antimicrobial peptide(s)
AMSDb - antimicrobial sequences database
AMTC(s) - antimicrobial Trp-cage(s)
ANN(s) - artificial neural network(s)
AP-1 - activator protein 1
AP2 - adaptor protein 2
APD - antimicrobial peptides database
aPP - avian pancreatic polypeptide
aZIP - acidic region leucine zipper
A β - amyloid- β

B

B. megaterium - *Bacillus megaterium*
B. subtilis - *Bacillus subtilis*
BAK - Bcl-2 homologous antagonist/killer
BAP - β -arrestin-derived peptide
Bcl-2 - B-cell lymphoma 2
BH - Bcl-2 homology
bPP - bovine pancreatic polypeptide
BSA - bovine serum albumin
bZIP - basic region leucine zipper

C

CCP(s) - clathrin-coated pit(s)
CD - circular dichroism
cfu - colony forming units
CME - clathrin-mediated endocytosis
CPP(s) - cell-penetrating peptide(s)
CSD(s) - chemical shift deviation(s)

D

DCM - dichloromethane
dd-MS² - data-dependent tandem mass spectrometry

DIPEA - *N,N*-diisopropylethylamine
DIPS12 - decoupling in the presence of scalar interactions
DMF - *N,N*-dimethylformamide
DMSO - dimethyl sulfoxide
DNA - deoxyribonucleic acid
DPC - dodecylphosphocholine

E

E. coli - *Escherichia coli*
E6AP - E6-associated protein
EHEC - enterohemorrhagic *Escherichia coli*
EMA - European Medicines Agency
EPEC - enteropathogenic *Escherichia coli*
eq. - equivalent
EU - European Union

F

FC - fraction collection
FDA - U.S. Food and Drug Administration
FID - free induction decay
Fmoc - fluorenylmethoxycarbonyl
FWHM - full width at half maximum

G

GLP-1 - glucagon-like peptide 1
GSH - glutathione

H

HATU - hexafluorophosphate azabenzotriazole tetramethyl uronium
HDP(s) - host defense peptide(s)
HEK293T - human embryonic kidney 293T
HESI - heated electrospray ionization
HPV - human papillomavirus
hPYY - human polypeptide YY

I

IBP(s) - ice-binding protein(s)
IBTC(s) - ice-binding Trp-cage(s)
IC₅₀ - half maximal inhibitory concentration
IDR(s) - innate defense regulator(s)

K

KIH - knobs-into-holes

L

LB - lysogeny broth
LPS - lipopolysaccharide(s)

M

M. luteus - *Micrococcus luteus*
MBC - minimal bactericidal concentration
MD - molecular dynamics
MeCN - acetonitrile
MHC - minimal hemolytic concentration
MIC - minimal inhibitory concentration
MRSA - methicillin-resistant *Staphylococcus aureus*

N

NAC-diazocine acetylated N-diazocine
NAG - *N*-acetylglucosamine
NAM - *N*-acetylmuramic acid
NCE - normalized collision energy
NMR - nuclear magnetic resonance
NPY(s) - neuropeptide(s) Y

P

P. aeruginosa - *Pseudomonas aeruginosa*
PDB - Protein Data Bank
PP(s) - pancreatic polypeptide(s)
PPG(s) - photoremovable protecting group(s)
PPII - polyproline type II
pPYY - porcine polypeptide YY
PSS - photostationary state

PYY(s) - polypeptide(s) YY

Q

QSAR - quantitative structure-activity relationship

R

RBC(s) - red blood cell(s)
RCSB - Research Collaboratory for Structural
Bioinformatics
RNA - ribonucleic acid
RRE - Rev response element

S

S. aureus - *Staphylococcus aureus*
S. simulans - *Staphylococcus simulans*
SAR - structure-activity relationship
SCL(s) - synthetic combinatorial library(ies)
SDS - sodium dodecyl sulfate
S-layer - surface layer
SPPS - solid phase peptide synthesis
SUV(s) - small unilamellar vesicle(s)

T

TEM - transmission electron microscopy
Tf - transferrin
TFA - trifluoroacetic acid
TFE - 2,2,2-trifluoroethanol
TfR - transferrin receptor
TI - therapeutic index, $TI = MHC \cdot MIC^{-1}$
TIS - triisopropyl silane
TL - traffic light

U

UV - ultraviolet

α

αAMP(s) - α-helical antimicrobial peptide(s)